

28 June 2013 | \$10

Science

AAAS

EDITORIAL

- 1499 The Science of Sustainability
Christopher Dye and Marcia McNutt

NEWS OF THE WEEK

- 1506 A roundup of the week's top stories

NEWS & ANALYSIS

- 1508 Dueling Reviews for Controversial Flu Drug
1509 Chimeric Embryos May Soon Get Their Day in the Sun
1510 Minorities Run Up Significant Debt in Earning STEM Ph.D.s
1513 Light Beams With a Twist Could Give a Turbo Boost to Fiber-Optic Cables
>> Report p. 1545

NEWS FOCUS

- 1514 The Dizzying Journey to a New Cancer Arsenal
>> Science Podcast
1519 Scientists Bristle at Canadian Leader's Applied Research Push

LETTERS

- 1522 Coral Diseases Cause Reef Decline
C. S. Rogers and J. Miller
Reversing Excess Atmospheric CO₂
G. H. Rau and K. S. Lackner
Response
D. Matthews and S. Solomon
Good Grades for Dual Education
X. Chen and Q. Wang
1524 CORRECTIONS AND CLARIFICATIONS

BOOKS ET AL.

- 1525 Guano and the Opening of the Pacific World
G. T. Cushman,
reviewed by F. R. Davis
1526 Brainwashed
S. Satel and S. O. Lilienfeld,
reviewed by C. Gross

POLICY FORUM

- 1527 The Global Prevalence of Intimate Partner Violence Against Women
K. M. Devries et al.

PERSPECTIVES

- 1529 Garbage Truck of the Brain
M. Nedergaard
1530 More Can Be Better in N₂ Activation
M. D. Fryzuk
>> Report p. 1549
1531 Eliminating Malaria
D. A. Fidock
1533 Some Like It Hot, Some Not
J. Belnap
>> Report p. 1574; Video
1534 Translocation in Action
M. V. Rodnina
>> Research Articles
pp. 1542, 1543, and 1544
1535 Solving the Mascon Mystery
L. G. J. Montes
>> Report p. 1552

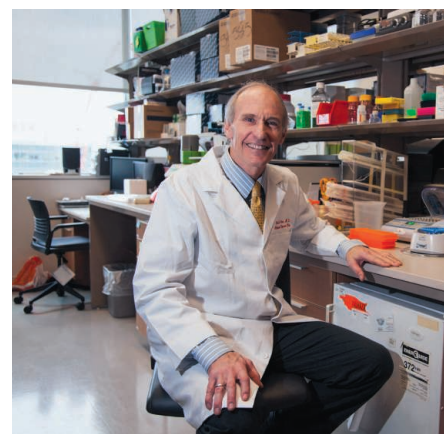
SCIENCE PRIZE ESSAY

- 1537 Investigating Ecosystems as a Blended Learning Experience
M. Pedaste et al.

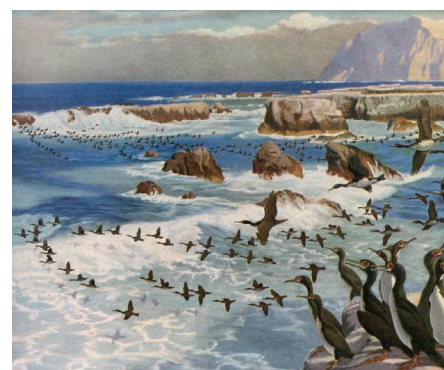
REVIEW

- 1541 From Gas to Stars Over Cosmic Time
M.-M. Mac Low
Review Summary; for full text:
<http://dx.doi.org/10.1126/science.1229229>
>> Video

CONTENTS continued >>



page 1514



page 1525

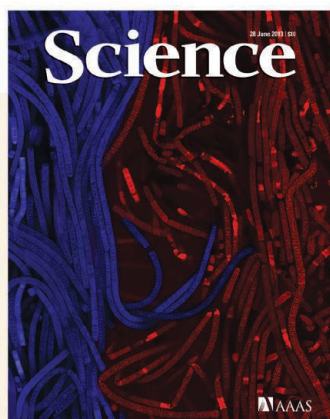
ON THE WEB THIS WEEK

>> Science Podcast

Listen to stories on the fate of topsoil microbes under climate change, observations from Voyager 1 at the fringes of the solar system, attacking cancer with T cells, and more.

>> Find More Online

Check out Science Express, our podcast, videos, daily news, our research journals, and Science Careers at www.sciencemag.org.



COVER

False-colored laser confocal fluorescence photomicrograph of *Microcoleus vaginatus* PCC9802 (blue) and *Microcoleus steenstrupii* SON82 (red) (image width: 0.3 millimeters). These two cyanobacterial strains are representative of the most abundant microbes in soil crusts of the arid lands in the western United States. *M. vaginatus* favors cooler climates, whereas *M. steenstrupii* prefers warmer areas. See pages 1533 and 1574.

Image: Estelle Couradeau and Ferran Garcia-Pichel/
W. M. Keck Bioimaging Laboratory, Arizona State University

DEPARTMENTS

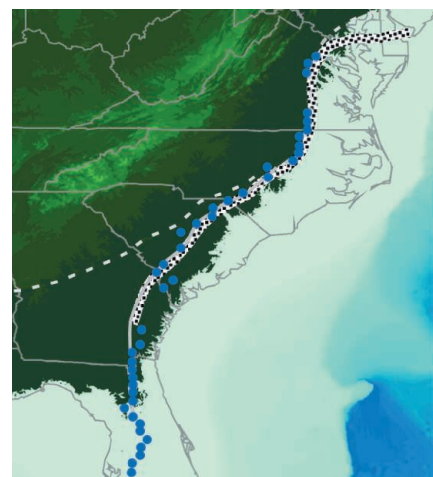
- 1497 This Week in Science
1500 Editors' Choice
1504 Science Staff
1539 AAAS News & Notes
1595 New Products
1596 Science Careers

RESEARCH ARTICLES

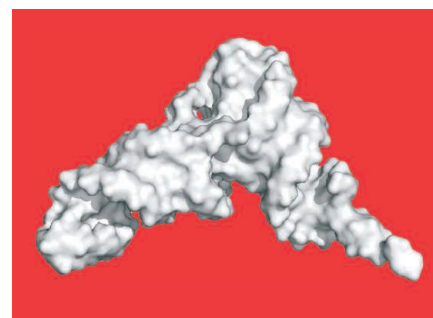
- 1542** Elongation Factor G Bound to the Ribosome in an Intermediate State of Translocation
D. S. Tourigny et al.
Research Article Summary; for full text:
<http://dx.doi.org/10.1126/science.1235490>
- 1543** Crystal Structures of EF-G-Ribosome Complexes Trapped in Intermediate States of Translocation
J. Zhou et al.
Research Article Summary; for full text:
<http://dx.doi.org/10.1126/science.1236086>
- 1544** Control of Ribosomal Subunit Rotation by Elongation Factor G
A. Pulk and J. H. D. Cate
Crystal structures reveal how messenger RNA and transfer RNAs transition through the prokaryotic ribosome during translation.
Research Article Summary; for full text:
<http://dx.doi.org/10.1126/science.1235970>
>> *Perspective p. 1534*

REPORTS

- 1545** Terabit-Scale Orbital Angular Momentum Mode Division Multiplexing in Fibers
N. Bozinovic et al.
Encoding data in the twist, or helicity, of photons provides a route to increase optical communication rates in fibers.
>> *News story p. 1513*
- 1549** Dinitrogen Cleavage and Hydrogenation by a Trinuclear Titanium Polyhydride Complex
T. Shima et al.
The collective reactivity of three hydride-bridged titanium centers cleaves dinitrogen under mild conditions.
>> *Perspective p. 1530*
- 1552** The Origin of Lunar Mascon Basins
H. J. Melosh et al.
A detailed model of impact basin formation explains the gravity signatures near two lunar craters.
>> *Perspective p. 1535*
- 1555** Continuous Permeability Measurements Record Healing Inside the Wenchuan Earthquake Fault Zone
L. Xue et al.
Measurements of permeability inside a fault zone after a major earthquake reveal rapid healing of fractures.
- 1560** Dynamic Topography Change of the Eastern United States Since 3 Million Years Ago
D. B. Rowley et al.
Mantle flow has deformed the presumed passive eastern margin of North America by up to 60 meters during the past 5 million years.
- 1564** Varied Response of Western Pacific Hydrology to Climate Forcings over the Last Glacial Period
S. A. Carolin et al.
Stalagmites from Borneo show how the climate of the western equatorial Pacific region changed over the past 100,000 years.
- 1567** Supercomplex Assembly Determines Electron Flux in the Mitochondrial Electron Transport Chain
E. Lapuente-Brun et al.
Ordered formation of supercomplexes of respiratory enzymes influences metabolic efficiency in response to food supply.
- 1570** Intrinsically Disordered Protein Threads Through the Bacterial Outer-Membrane Porin OmpF
N. G. Housden et al.
An antibacterial peptide can tunnel through cell-surface pores to deliver an epitope signal and initiate cell death.
- 1574** Temperature Drives the Continental-Scale Distribution of Key Microbes in Topsoil Communities
F. Garcia-Pichel et al.
Climate change is likely to shift the distribution of key cyanobacteria species in desert soils.
>> *Perspective p. 1533; Science Podcast*
- 1577** Mechanism of Eukaryotic RNA Polymerase III Transcription Termination
S. Nielsen et al.
Formation of the secondary structure of the transcribed RNA facilitates termination during transcription.
- 1580** Transcription Under Torsion
J. Ma et al.
RNA polymerase is a potent DNA-based torsional motor than can restart transcription after release of DNA supercoiling stress.
- 1583** Fe-S Cluster Biosynthesis Controls Uptake of Aminoglycosides in a ROS-Less Death Pathway
B. Ezraty et al.
The respiratory chain is required for antibiotic entry to the target cell rather than for its killing.



page 1560



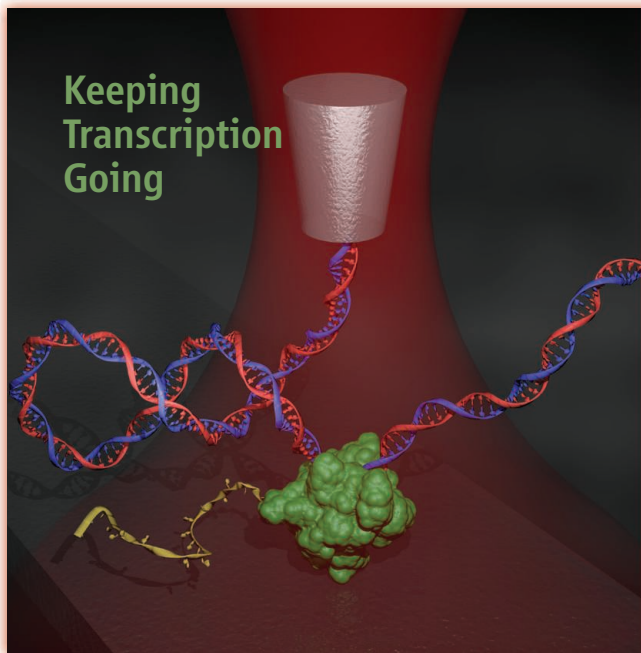
page 1577

- 1587** B Cells Use Mechanical Energy to Discriminate Antigen Affinities
E. Natkanski et al.
Mechanical forces allow immune B cells to extract high-affinity antigens from membrane surfaces.
- 1591** Deep Cortical Layers Are Activated Directly by Thalamus
C. M. Constantinople and R. M. Bruno
A direct pathway is used to evoke sensory responses in neurons in multiple layers of the rat barrel cortex.

SCIENCE (ISSN 0036-8075) is published weekly on Friday, except the last week in December, by the American Association for the Advancement of Science, 1200 New York Avenue, NW, Washington, DC 20005. Periodicals Mail postage (publication No. 484460) paid at Washington, DC, and additional mailing offices. Copyright © 2013 by the American Association for the Advancement of Science. The title SCIENCE is a registered trademark of the AAAS. Domestic individual membership and subscription (51 issues): \$149 (\$74 allocated to subscription). Domestic institutional subscription (51 issues): \$990; Foreign postage extra: Mexico, Caribbean (surface mail) \$55; other countries (air assist delivery) \$85. First class, airmail, student, and emeritus rates on request. Canadian rates with GST available upon request, GST #1254 88122. Publications Mail Agreement Number 1069624. Printed in the U.S.A.

Change of address: Allow 4 weeks, giving old and new addresses and 8-digit account number. Postmaster: Send change of address to AAAS, P.O. Box 96178, Washington, DC 20090-6178. Single-copy sales: \$10.00 current issue, \$15.00 back issue prepaid includes surface postage; bulk rates on request. Authorization to photocopy material for internal or personal use under circumstances not falling within the fair use provisions of the Copyright Act is granted by AAAS to libraries and other users registered with the Copyright Clearance Center (CCC) Transactional Reporting Service, provided that \$30.00 per article is paid directly to CCC, 222 Rosewood Drive, Danvers, MA 01923. The identification code for Science is 0036-8075. Science is indexed in the Reader's Guide to Periodical Literature and in several specialized indexes.

Keeping Transcription Going



In cells, the DNA double-stranded helix (dsDNA) is mostly supercoiled—either under- or overwound. RNA polymerase (RNAP) must transcribe through this supercoiled DNA. Furthermore, the act of transcription, which involves opening the double helix and threading the separated strands through the enzyme, generates supercoiling ahead and behind the polymerase. **Ma et al.** (p. 1580) used single-molecule methods to measure the upstream and downstream torque forces of *Escherichia coli* RNAP. The upstream torque was sufficient to disrupt dsDNA structure, and the stalled RNAP could also backtrack along the DNA. Release of the torsional stress allowed RNAP to resume transcription in vitro.

Revealed in Translation

The ribosome, with the help of transfer RNAs (tRNAs), converts the triple genetic code in messenger RNA (mRNA) into protein. Upon decoding of a codon, the mRNA and associated tRNAs must be moved through the ribosome, so that the next codon can be read, with a new charged tRNA taken in at the A (aminoacyl-tRNA) site, the newly extended peptidyl-tRNA moved into the P (peptidyl-tRNA) site, and the deacylated tRNA removed from the exit site in the ribosome (see the Perspective by **Rodnina**). Crystal structures from **Tourigny et al.** (p. 1542), **Pulk and Cate** (p. 1544), and **Zhou et al.** (p. 1543), variously capture the prokaryotic ribosome during this translocation phase, revealing the hybrid states of the tRNAs and the substantial motions of the 30S ribosomal subunit during the process, the role of elongation factor G, and suggest how the direction and reading frame of the mRNA is maintained.

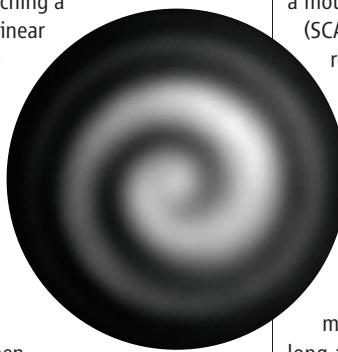
Titanium Cleaver

A century after its discovery, the Haber Bosch process is still used to produce ammonia from nitrogen for fertilizer. Nonetheless, the process requires high temperature and pressure, and chemists continue to look for synthetic analogs to microbial nitrogenase enzymes, which have managed to slice through the N_2 triple bond under ambient conditions for millennia. Most efforts in this vein have relied on a boost from the reducing power of alkali metals. **Shima et al.** (p. 1549; see the Perspective by **Fryzuk**) instead explored the reactivity of a titanium hydride

cluster, which cleanly slices through N_2 at room temperature and incorporates the separated N atoms into its framework. Though ammonia was not produced, the system offers hope in the search for mild nitrogen reduction catalysts.

A Twist on the Capacity Crunch

The rate at which data can be transmitted down optic fibers is approaching a limit because of nonlinear optical effects. Multiplexing allows data to be encoded in different modes of light such as polarization, wavelength, amplitude, and phase and to be sent down the fibers in parallel. Optical angular momentum (OAM) can provide another degree of freedom whereby the photons are given a well-defined twist or helicity. **Bozinovic et al.** (p. 1545) were able to transmit high-bandwidth data using OAM modes in long lengths of optical fibers, thus providing a possible route to get yet more capacity through optic fiber networks.



Lunar Mascons Explained

The origin of lunar mass concentrations (or mascons), which appear as prominent bull's-eye patterns on gravitational maps of both the near-

and far side of the Moon, has been a mystery since they were originally detected in 1968. Using state-of-the-art simulation codes, **Melosh et al.** (p. 1552, published online 30 May; see the Perspective by **Montesi**) developed a model to explain the formation of mascons, linking the processes of impact cratering, tectonic deformation, and volcanic extrusion.

By the Sea Side

The Atlantic coastal plain of North America has been thought of as a passive margin, responding mostly to the weight of deposited sediments. As a result, the fine-scale stratigraphy of the sediments has been used to infer changes in global sea level through the Cenozoic. However, recent work has shown that the coastal plain has deformed in response to flow in Earth's mantle. **Rowley et al.** (p. 1560, published online 16 May) used a model of flow in the mantle to show that the topography of the mid-Atlantic and Southern United States coast varied by 60 meters or more during the past 5 million years.

Respiration Refined

Cells derive energy from redox reactions mediated by mitochondrial enzymes that form the electron transport chain. The enzymes can form large complexes, known as supercomplexes, whose function has been controversial. **Lapiente-Brun et al.** (p. 1567) discovered that a mouse protein, supercomplex assembly factor I (SCAFI), specifically modulates assembly of respiratory complexes into supercomplexes. Formation of the supercomplexes appears to cause electrons to be processed differently, depending on the substrate from which they are derived.

B Cell Tug of War

High-affinity, protective antibodies made by B cells are critical for providing long-term protection against reinfection. In order to produce antibodies, B cells must first bind to and extract antigens from the surface of antigen-presenting cells. Using an in vitro system that allows B cells to bind to antigen-laden, flexible membranes, **Natkanski et al.** (p. 1587, published online 16 May) show that antigen extraction relies on myosin IIA-mediated contractile forces that pull upon the antigen-presenting membrane. These forces break the antigen-receptor bonds if affinity is low, thus ensuring that B cells only extract, internalize, and presumably respond to, high-affinity antigens.

Additional summaries

Water at the Bottom of a Well

Earthquakes generate numerous fractures as they propagate through an underground fault zone. These fractures strongly influence the way in which fluids flow in the subsurface, and the permeability of fault zones is often used as a proxy for the extent of fracturing. Following the 2008 M_w 7.9 Wenchuan earthquake in central China, several wells were drilled in and around the fault zone to understand the mechanics of the earthquake. Because the bottoms of these deep boreholes were open, the water levels in the wells were sensitive to tidal forces acting on the surrounding rock. Through continuous measurements of water levels over 1.5 years, **Xue et al.** (p. 1555) found that the rate at which water was pumped in and out of the borehole was proportional to the permeability of the fault zone, providing a direct way to measure the evolution of the hydrologic properties of a fault zone following a major earthquake. Permeability decreased ~25% during that time, suggesting that fractures generated in fault zones heal relatively rapidly.

Borneo Paleohydrology

Climate records of the last glacial cycle provide a good picture of how climate changed at high and middle latitudes, but fewer records of the tropics are available. **Carolin et al.** (p. 1564, published online 6 June) present data from a suite of precisely dated stalagmites from Borneo that reveal how the western tropical Pacific region behaved between 100,000 and 15,000 years ago, a period during which many abrupt climate changes occurred in other parts of the world. While the hydroclimate of Borneo changed in response to precessional forcing, it responded only weakly to the forces that produced glacial-interglacial changes in global climate.

Desert Soil Shuffle

Soil microorganisms make up a substantial fraction of global biomass, turning over carbon and other key nutrients on a massive scale. Although the soil protects them somewhat from daily temperature fluxes, the distribution of these communities will likely respond to gradual climate change. **Garcia-Pichel et al.** (p. 1574, see the cover; see the Perspective by **Belnap**) surveyed bacterial diversity across a range of North

American desert soils, or biocrusts—ecosystems in which photosynthetic bacteria determine soil fertility and control physical soil properties such as erodability and water retention. Most of the sites were dominated by one of two cyanobacte-

rial species, but their relative proportions were controlled largely by factors related to temperature. Laboratory enrichment cultures of the two species at different temperatures also showed temperature as a primary determining factor of bacterial diversity. It is unknown if temperature will affect the distribution of other soil microorganisms, but the marked shifts of these two keystone bacterial species suggest further change is in store for these delicate ecosystems.

Threading Through

Protein antibiotics (bacteriocins) are frequently deployed by Gram-negative bacteria to combat competitors, a trait common in pathogens such as *Escherichia coli*, *Yersinia pestis*, *Pseudomonas aeruginosa*, *Xanthomonas campestris*, and *Klebsiella pneumoniae*. As a result, bacteriocins are being developed as species-specific antibacterials. Bacteriocins must establish a translocon at the bacterial outer membrane in order to translocate into cells. Working in *E. coli*, **Housden et al.** (p. 1570) describe how the deoxyribonuclease, colicin E9, crosses the bacterial cell membrane by threading through a porin.

Stopping Transcription

It is as important to terminate any biological process as it is to start it. Transcription, copying information encoded in genes into RNA, requires accurate and timely termination. **Nielsen et al.** (p. 1577) present a mechanism for transcription termination by RNA polymerase III, the enzyme that synthesizes the majority of RNA molecules in eukaryotes. In this scenario, the folding of the RNA as it is transcribed by polymerase into a highly structured transcript causes termination at the end of its synthesis. This mechanism may serve as a control of proper folding of structural or catalytic RNAs synthesized by RNA polymerase III. Comparison with other organisms suggests that this mechanism emerged before divergence of bacteria and eukaryotes.

Unreactive Death

A controversial proposal that all bactericidal antibiotics kill by reactive oxygen species (ROS) and not by their primary cell target has recently attracted high-profile refutations. The ROS-death pathway implicated overstimulation of the electron transport in respiratory chains; a malfunction that leads to ROS releasing Fe from Fe-S clusters and causing cell death via Fenton chemistry.

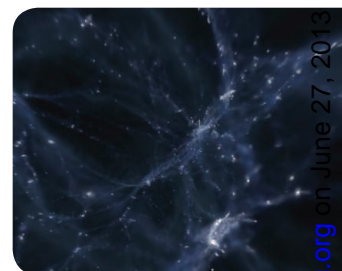
Ezraty et al. (p. 1583) show that electron transport chains and Fe-S clusters are key to killing by aminoglycoside antibiotics but not for the reasons envisioned in the ROS theory. Fe-S clusters are

essential for killing because they mature the respiratory chains that produce the necessary proton motive force for the energized uptake of aminoglycosides. Consequently, iron chelators protect against aminoglycosides, not because they scavenge the iron from Fenton chemistry, but because they block aminoglycoside uptake.

Understanding Star Formation

Understanding how galaxies and the chemical composition of the universe evolved through cosmic time relies on unraveling the history of star formation over the universe's almost

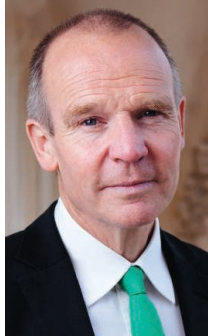
14-billion-year history. **Mac Low** (p. 1541) reviews the conditions of star formation in galaxies, focusing on the smaller-scale physics determining the conversion of gas into stars. Progress in understanding and modeling these processes and in observing galaxies at ever-earlier times are expected to lead to a convergence between model predictions and observations and to a full understanding of the cosmic history of star formation.



A Direct Line in the Brain

For decades, neuroscientists have assumed that there is a “canonical microcircuit” in the neocortex, in which information is transformed as excitation spreads serially along connections from thalamus, to cortical layer 4, then to layers 2/3, to layers 5/6, and finally to other brain regions. Each cortical layer is thought to transform sensory signals to extract behaviorally relevant information. Now, **Constantinople and Bruno** (p. 1591) challenge this dogma. In vivo whole-cell recordings revealed that sensory stimuli activate neurons in deep cortical layers simultaneously to those in layer 4 and that a large number of thalamic neurons converge onto deep pyramidal neurons, possibly allowing sensory information to completely bypass upper layers. Temporary blockade of layer 4 revealed that synaptic input to deep cortical layers derived entirely from the thalamus and not at all from upper cortical layers. This thalamically derived synaptic input reliably drove pyramidal neurons in layer 5 to discharge action potentials in the living animal. These deep layer neurons project to numerous higher-order brain regions and could directly mediate behavior.

CREDIT: MAC LOW



Christopher Dye is a director in the Office of Health Information in the Office of HIV/AIDS, Tuberculosis, Malaria and Neglected Tropical Diseases at the World Health Organization, Geneva, Switzerland. E-mail: dyec@who.int. The views expressed here do not necessarily represent the decisions, policy, or view of the World Health Organization.



Marcia McNutt is Editor-in-Chief of *Science*. E-mail: mmcnutt@aaas.org.

The Science of Sustainability

THE QUESTION OF WHAT CAN BE ACHIEVED IN 1000 DAYS HAS PREOCCUPIED KINGS, QUEENS, presidents, and, very recently, the Secretary-General of the United Nations (UN). Ban Ki-moon has not only appealed for a last big push to reach as many as possible of the UN's Millennium Development Goals (MDGs) by the deadline of 31 December 2015, he is advocating the establishment of objectives that should succeed the MDGs as well. Strong clues about the shape of the post-2015 agenda can be found in two recent reports, one published last month by a High-Level Panel* convened by Ban Ki-moon and chaired by the presidents of Indonesia and Liberia and the prime minister of the United Kingdom, and the other released this month by the Sustainable Development Solutions Network.† Both reports list the eradication of poverty as the number-one priority and set out complementary goals concerned with gender equality, education, health, food, water and sanitation, climate change, energy, employment, natural resources, governance, peace, and finance. These reports are unlikely to be the last contributions to the debate, but the proposed goals represent a call to action for the science community.

The plain truth is that it is not clear how these goals will be met, but it is evident that to fill the development gap, we must fill the knowledge gap from many different sources. More than ever, multidisciplinary research must be treated not as a formulaic insert on grant applications but as an immediate development necessity. Healthy lives do depend on food security. Poverty reduction does depend on jobs and equitable growth. Good governance is critical everywhere.

Two cross-disciplinary experiences amplify the point. Building resilience to natural hazards, such as hurricanes and earthquakes, and reducing deaths from them are subcomponents of eradicating poverty, because the poor suffer disproportionately from such events. Much progress has been made in building resiliency through collaborations between geoscientists, engineers, and architects; there are now early warning mechanisms, reinforced shelters, and improved modeling of complex events to target populations at risk. But the effectiveness of these remedies also depends on how vulnerable people weigh the risks to life and limb against the cost of abandoning property. So the best plans for risk mitigation should be informed by social sciences as well. Protecting people against risk is also central to achieving universal health coverage, a unifying goal in global health today. The twin questions of who is most at risk of impoverishment due to illness and what are the best ways to provide them with financial protection, call for a blend of epidemiology and welfare economics, set against the backdrop of societal preference. Universal health coverage requires services, not only for the treatment of illness but also for prevention, which may need a combination of educational, environmental, public health, and policy measures.

The two reports present a vast landscape of research possibilities. Research priorities must emerge from a global debate involving scientists, private investors, public funding agencies, and policy-makers, without forgetting the people who might benefit from the research. A guiding research agenda could stimulate fresh ideas and perhaps give renewed impetus to old ones. It would help strengthen research capacity around the world, fostering new institutions and networks, training high-caliber researchers, and generating data, ideally as an open and shared resource. It would also bring a responsibility, or at least an opportunity, to translate research results into action.

Although the post-2015 development agenda is still a draft, it is shaping up to be a huge and exciting challenge for science. For those ready to take it on, there is no need to wait until January 2016.

— Christopher Dye and Marcia McNutt

10.1126/science.1242219

*www.post2015hlp.org/wp-content/uploads/2013/05/UN-Report.pdf. †unsdsn.org/files/2013/06/130613-SDSN-An-Action-Agenda-for-Sustainable-Development-FINAL.pdf.



TOXICOLOGY

Teething Signs

Bisphenol A (BPA) is used in the production of polycarbonate plastics, which are widely used in the food packaging industry. Because of this, some developed-world populations have become extensively contaminated with BPA, which is a known endocrine-disrupting chemical. This class of chemicals has been linked to a set of adverse health effects, including infertility, obesity, and cancer. Jedeon *et al.* show that exposing rats to BPA in utero and during early life can affect the deposition of enamel on their teeth (amelogenesis), resulting in hypomineralization. This condition shares a number of features with the recently described human condition known as molar incisor hypomineralization, which manifests as patchy white opacities on the teeth of children at 6 to 8 years of age. Like molar incisor hypomineralization, the dental effect in rats is limited to a developmental window. BPA may act by interfering with the expression of an ameloblast protease that removes enamel-forming proteins from the enamel matrix; if these proteins were to persist, they would inhibit proper enamel deposition. If the defect in tooth development seen in rats is a good model for molar incisor hypomineralization, then this condition might provide a visible marker for infant exposure to BPA. — GR

Am. J. Pathol. **183**, 109 (2013).



GENETICS

Of Hinny's and Mules

Imprinting—the silencing of genes due to the methylation of specific DNA sequences coming from one parent—is known to play a crucial role in the development of the placenta in mammals. The offspring of matings between horses and donkeys are generally viable, but sterile. However, because of genetic differences between the species, estimated via RNA sequencing, Wang *et al.* were able to assess transcription differences and to identify equid-specific imprinted genes in the chorionic girdle that do not appear to be due to their

been observed for imprinted genes. Furthermore, imprinted genes appear to show specific differences between equids versus humans and mice, suggesting that equine hybrids may provide information on the evolutionary origins and maintenance of genomic imprinting. — LMZ

Proc. Natl. Acad. Sci. U.S.A. **110**, 10.1073/pnas.1308998110 (2013).

NEUROSCIENCE

A Less Selective Inhibitor

The most widely used antidepressant drugs are selective serotonin reuptake inhibitors. They block the high-affinity serotonin transporter and thereby prevent the retrieval of serotonin from the extracellular fluid into nerve terminals. Unfortunately, many individuals suffering from depression experience minimal or no improvement when taking these drugs; new medications would help patients who respond poorly to selective serotonin reuptake inhibitors. The organic cation transporters and the plasma membrane monoamine transporter have low affinity for serotonin but a high transport capacity. Decynium-22 is an inhibitor of this group of transporters and has been shown to block serotonin uptake

development of new antidepressant drugs. These drugs might act either in combination with existing antidepressants or perhaps all on their own by blocking one or more of the organic cation transporters or the plasma membrane monoamine transporter. — PRS

J. Neurosci. **33**, 10534 (2013).

CELL BIOLOGY

Centrosome Surfeit

Centrosome amplification is a hallmark of human tumors and is associated with aneuploidy and tumorigenesis. In fruit flies, even when extra centrosomes do not induce high levels of aneuploidy, spindle position defects cause an expansion of the neural stem cell (NSC) population and subsequent tumor formation. To investigate the consequences of centrosome amplification on mammalian NSCs during embryonic development, Marthiens *et al.* developed a mouse model in which centrosome numbers were increased in the developing central nervous system. Surprisingly, centrosome amplification caused microcephaly—a brain of reduced size but with otherwise normal architecture. This microcephaly resulted from defects in NSC division, which generated aneuploid cells that went on to die by apoptosis. These results may explain the etiology of certain types of microcephaly, which in humans have been associated with a number of centrosomal genes, and suggest that in the mammalian developing brain, centrosome amplification can cause depletion of the NSC pool. — SMH

Nat. Cell Biol. **15**, 10.1038/ncb2746 (2013).



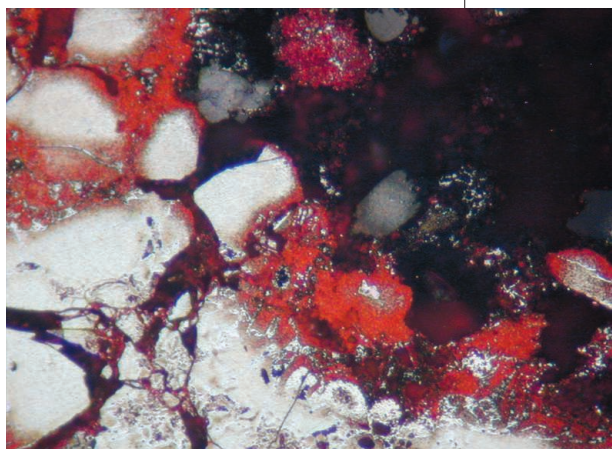
hybrid status. Of 40 known imprinted genes in humans and/or mice, only 15 were imprinted in the equine offspring. They also identified 93 imprinted genes, including 78 not previously described, that showed distribution across the genome and not in clusters, as had previously

into brain synaptosomes. Horton *et al.* report that the antidepressant-like effect of a selective serotonin reuptake inhibitor can be strengthened significantly by coadministration of decynium-22. This group of decynium-22-sensitive transporters may thus be a promising target for the

GEOCHEMISTRY

Siderite in Time

Banded iron formations are some of the oldest existing rocks that provide direct evidence of ancient sedimentary processes before Earth's atmosphere oxidized. The alternating layers of iron-rich minerals probably reflect changes in Precambrian seawater chemistry, but the numerous abiotic and potentially biotic reactions that resulted in their formation remain difficult to decipher. Based on high-pressure and high-temperature experiments, Köhler



et al. show that the iron-carbonate mineral siderite (FeCO_3) forms as a consequence of the concomitant burial of iron oxyhydroxide minerals and organic matter. Because the reactions depend on the amount of sedimentary organic matter, which was probably microbial in origin, these spheroidal siderite grains may serve as an indicator of ancient microbial metabolisms. In a series of related laboratory experiments, Kim *et al.* show that siderite in the Precambrian water column could photo-oxidize to form molecular hydrogen and iron oxide minerals that served as building blocks of banded iron formations. If global in scale, this abiotic process could have contributed to the early oxidation of Earth's atmosphere and provided an energy source for anaerobic microorganisms. — NW

Nat. Comm. **4**, 1741 (2013); *Proc. Natl. Acad. Sci. U.S.A.* **110**, 10.1073/pnas.1308958110 (2013).

ATMOSPHERIC SCIENCE

Green Gains

Satellite-based observations have shown that many regions of the terrestrial biosphere are getting greener; i.e., their above-ground vegetative mass is increasing. A number of factors, including changes in light, water, nutrients, and land use, could be causing that trend,

although the most obvious cause would seem to be the rising concentration of CO_2 in the atmosphere. Donohue *et al.* used gas exchange theory, which links vegetation mass to the concentration of atmospheric CO_2 through its effect on the water use efficiency of plants, to predict that the increase of atmospheric CO_2 between 1982 and 2010 should have produced an increase in the amount of green foliage between 5 and 10%. The authors then confirmed, based on satellite measurements, that the amount of vegetation increased by about 11% in warm, arid environments, where other factors affecting greenness should be unimportant. Although these findings cannot be used to explain changes in greenness in other regions, where different drivers may control vegetation, the principle still applies, and so the challenge is to develop a more general understanding of how increasing CO_2 is affecting vegetation in other environments, where the other forcing factors are more important. — HJS

Geophys. Res. Lett. **10.1002/grl.50563** (2013).

MATERIALS SCIENCE

Magnetic Titanium

The interface of SrTiO_3 and LaAlO_3 has puzzled physicists for some time now—it is not only highly conductive (and under certain circumstances even superconducting), it also exhibits magnetism even though neither of the two oxides is magnetic. Various explanations have been proposed for this unexpected magnetism, ranging from the presence of magnetic impurities or defects to an intrinsic property of the interface. Lee *et al.* used chemical-element-specific spectroscopic techniques to pinpoint the “host” of the magnetism. The analysis of the spectra indicated that the magnetic moments responsible for the magnetism were lying in the plane of the interface and were carried by Ti atoms, whereas comparison with calculations revealed similarities with spectra expected for the Ti^{3+} valence state of Ti. Furthermore, varying the thickness of the LaAlO_3 overlayer indicated that the Ti magnetic moments were located at the interface. Taken together, these results lend support to the intrinsic origin of the magnetism at the interface, although the role of, for example, oxygen defects cannot be entirely excluded. — JS

Nat. Mater. **10.1038/nmat3674** (2013).

**1200 New York Avenue, NW
Washington, DC 20005**
Editorial: 202-326-6550, FAX 202-289-7562
News: 202-326-6591, FAX 202-371-9227
**Bateman House, 82-88 Hills Road
Cambridge, UK CB2 1LQ**
+44 (0) 1223 326500, FAX +44 (0) 1223 326501

SUBSCRIPTION SERVICES For change of address, missing issues, new orders and renewals, and payment questions: 866-434-AAAS (2227) or 202-326-6417, FAX 202-842-1065. Mailing addresses: AAAS, P.O. Box 96178, Washington, DC 20090-6178 or AAAS Member Services, 1200 New York Avenue, NW, Washington, DC 20005

INSTITUTIONAL SITE LICENSES please call 202-326-6755 for any questions or information

REPRINTS: Author Inquiries 800-635-7181
Commercial Inquiries 803-359-4578

PERMISSIONS 202-326-6765, permissions@aaas.org

MEMBER BENEFITS AAAS Travels: Bethcart Expeditions 800-252-4910; Apple Store www.store.apple.com/us/go/epstore/aaas; NASA Federal: 1-888-NASA-FCU (1-888-627-2328) or www.nasafcu.com; Cold Spring Harbor Laboratory Press Publications www.cshlpress.com/affiliates/aaas.htm; GEICO Auto Insurance www.geico.com/landingpage/go51.htm?logo=17624; Hertz 800-654-2200 CDP#343457; Office Depot <https://bsd.officedepot.com/portalLogin.do>; Seabury & Smith Life Insurance 800-424-9883; Subaru VIP Program 202-326-6417; VIP Moving Services www.vipmymover.com/domestic/index.html; Other Benefits: AAAS Member Services 202-326-6417 or www.aaasmember.org.

science_editors@aaas.org (for general editorial queries)
science_letters@aaas.org (for queries about letters)
science_reviews@aaas.org (for returning manuscript reviews)
science_bookrevs@aaas.org (for book review queries)

Published by the American Association for the Advancement of Science (AAAS), *Science* serves its readers as a forum for the presentation and discussion of important issues related to the advancement of science, including the presentation of minority or conflicting points of view, rather than by publishing only material on which a consensus has been reached. Accordingly, all articles published in *Science*—including editorials, news and comment, and book reviews—are signed and reflect the individual views of the authors and not official points of view adopted by AAAS or the institutions with which the authors are affiliated.

AAAS was founded in 1848 and incorporated in 1874. Its mission is to advance science, engineering, and innovation throughout the world for the benefit of all people. The goals of the association are to: enhance communication among scientists, engineers, and the public; promote and defend the integrity of science and its use; strengthen support for the science and technology enterprise; provide a voice for science on societal issues; promote the responsible use of science in public policy; strengthen and diversify the science and technology workforce; foster education in science and technology for everyone; increase public engagement with science and technology; and advance international cooperation in science.

INFORMATION FOR AUTHORS

See pages 716 and 717 of the 8 February 2013 issue or access www.sciencemag.org/about/authors

SENIOR EDITORIAL BOARD

A. Paul Alivisatos, Lawrence Berkeley Nat'l. Laboratory
Ernst Fehr, Univ. of Zurich
Michael S. Turner, University of Chicago

BOARD OF REVIEWING EDITORS

Adriano Aguzzi, Univ. Hospital Zürich
Takuzo Aida, Univ. of Tokyo
Leslie Aiello, Wenner-Gren Foundation
Sonia Altizer, Univ. of Georgia
Virginia Armbrust, Univ. of Washington
Sebastian Amigorena, Institut Curie
Angelika Amon, MIT
Kathryn Anderson, Memorial Sloan-Kettering Cancer Center
Siv G. E. Andersson, Uppsala Univ.
Peter Andolfatto, Princeton Univ.
Meinrat O. Andreae, Max Planck Inst., Mainz
Paola Arlotta, Harvard Univ.
Johan Auwerx, EPFL
David Awschalom, Univ. of California Santa Barbara
Ben Barres, Stanford Medical School
Jordi Bascompte, Estación Biológica de Doñana, CSIC
Facundo Batista, London Research Inst.
Ray H. Baughman, Univ. of Texas, Dallas
David Baum, Univ. of Wisconsin
Mark Bear, Massachusetts Inst. of Technology
Yasmine Belkaid, NIAID, NIH
Philly Benfey, Duke Univ.
Stephen J. Benkovic, Penn State Univ.
Christophe Bernard, Aix-Marseille Univ.
Gregory C. Berzosa, Stanford Univ.
Gabriele Bergers, Univ. of California, San Francisco
Peer Bork, EMBL
Bernard Bourdon, Ecole Normale Supérieure de Lyon
Chris Bowler, Ecole Normale Supérieure
Ian Boyd, Univ. of St. Andrews
Christian Büchel, Universitätsklinikum Hamburg-Eppendorf
Joseph A. Burns, Cornell Univ.
William P. Butz, Population Reference Bureau
Giorgio Buzsáki, New York Univ., School of Medicine
Mats Carlsson, Univ. of Oslo
Miedred Cho, Stanford Univ.
David Clapham, Children's Hospital, Boston
David Clary, Univ. of Oxford
Jonathan D. Cohen, Princeton Univ.
Robert Cook-Deegan, Duke Univ.
James Collins, Boston Univ.
Alan Cowman, Walter & Eliza Hall Inst.
Robert H. Crabtree, Yale Univ.
Wolfgang Cramer, Mediterranean Inst. of Biodiversity and Ecology
Jeff L. Dangl, Univ. of North Carolina
Tom Daniel, Univ. of Washington
Frans de Waal, Emory Univ.
Stanislav Dehaene, Collège de France

Robert Desimone, MIT
Claude Desplan, New York Univ.
Ap Dijksterhuis, Radboud Univ. of Nijmegen
Dennis Discher, Univ. of Pennsylvania
Gerald W. Dorn II, Washington Univ. School of Medicine
Jennifer A. Doudna, Univ. of California, Berkeley
Julian Downard, Cancer Research UK
Bruce Dunn, Univ. of California, Los Angeles
Christopher Dye, WHO
Todd Ehlers, University of Tuebingen
David Eide, Carnegie Inst. of Washington
Tim Elston, Univ. of North Carolina at Chapel Hill
Gerhard Ertl, Fritz-Haber-Institut, Berlin
Barry Everitt, Univ. of Cambridge
Paul G. Falkowski, Rutgers Univ.
Ernst Fehr, Univ. of Zurich
Tom Fenchel, Univ. of Copenhagen
Michael Feuer, The George Washington Univ.
Alain Fischer, INSERM
Susan Fliske, Princeton Univ.
Anne C. Ferguson-Smith, Univ. of Cambridge
Peter Fratzl, Max Planck Inst.
Elaine Fuchs, Rockefeller Univ.
Wulfram Gerstner, EPFL Lausanne
Daniel Geschwind, UCLA
Andrew Gewirth, Univ. of Illinois
Karl-Heinz Glassmeier, TU Braunschweig
Elizabeth Grove, Univ. of Chicago
Kip Guy, St. Jude's Children's Research Hospital
Taejick Ha, Univ. of Illinois at Urbana-Champaign
Christian Haass, Ludwig Maximilians Univ.
Steven Hahn, Fred Hutchinson Cancer Research Center
Gregory J. Hannon, Cold Spring Harbor Lab.
Martin Heimann, Max Planck Inst., Jena
Vla Helariutta, Univ. of Finland
Isaac Held, NOAA
James A. Hendler, Rensselaer Polytechnic Inst.
Janet G. Hering, Swedish Fed. Inst. of Aquatic Science & Technology
Ray Hilborn, Univ. of Washington
Michael E. Himmel, National Renewable Energy Lab.
Kai-Uwe Hinrichs, Univ. of Bremen
Kei Hirose, Tokyo Inst. of Technology
David Hodell, Univ. of Cambridge
David Holden, Imperial College
Lora Hooper, UT Southwestern Medical Ctr at Dallas
Jeffrey A. Hubbell, EPFL Lausanne
Thomas Hudson, Ontario Inst. for Cancer Research
Raymond Huey, Univ. of Washington
Steven Jacobsen, Univ. of California, Los Angeles
Kai Johnsson, EPFL Lausanne
Peter Jonas, Inst. of Science & Technology (IST) Australia
Mark Kaerberlein, Univ. of Washington
William Kaelin Jr., Dana-Farber Cancer Inst.
Daniel Kahne, Harvard Univ.

Daniel Kammen, Univ. of California, Berkeley
Joel Kingsolver, Univ. of North Carolina at Chapel Hill
Robert Kingston, Harvard Medical School
Roberto Kolter, Harvard Medical School
Alberto R. Kornblith, Univ. of Buenos Aires
Leinid Kruglyak, Princeton Univ.
Thomas Langer, Univ. of Cologne
Mitchell A. Lazar, Univ. of Pennsylvania
David Lazer, Harvard Univ.
Virginia Lee, Univ. of Pennsylvania
Stanley Leibel, Univ. of North Carolina at Chapel Hill
Ottoline Leyser, Cambridge Univ.
Marcia C. Linn, Univ. of California, Berkeley
Jianguo Liu, Michigan State Univ.
Luis Liz-Marzan, CIC bioGUNE
Jonathan Losos, Harvard Univ.
Ke Lu, Chinese Acad. of Sciences
Christian Lüscher, Univ. of Geneva
Laura Machesky, CRUK Beatson Inst. for Cancer Research
Anne Magurran, Univ. of St. Andrews
Oscar Marin, CSIC & Univ. Miguel Hernández
Charles Marshall, Univ. of California, Berkeley
Chris Marshall, Inst. of Cancer Research
Martin M. Matzuk, Baylor College of Medicine
P. Robertson MacLean, Cincinnati College
Graham Medley, Univ. of Warwick
Yasushi Miyashita, Univ. of Tokyo
Richard Morris, Univ. of Edinburgh
Edward Morse, Norwegian Univ. of Science and Technology
Sean Munro, MRC Lab. of Molecular Biology
Thomas Murray, The Hastings Center
Naoto Nagaosa, Univ. of Tokyo
James Nelson, Stanford Univ. School of Med.
Daniel Neumark, Univ. of California, Berkeley
Stuart Newman, New York Medical College
Timothy W. Nilsen, Case Western Reserve Univ.
Pär Nordlund, Karolinska Inst.
Helga Nowotny, European Research Advisory Board
Luke O'Neill, Trinity College, Dublin
Stuart Newman, New York Medical College
N. Phuan Ong, Princeton Univ.
Joe Orenstein, Univ. of California, Berkeley & Lawrence Berkeley National Lab.
Harry Orr, Univ. of Minnesota
Andrew Oswald, Univ. of Warwick
Steve Palumbi, Stanford Univ.
Jane Parker, Max-Planck Inst. of Plant Breeding Research
Donald R. Paul, Univ. of Texas at Austin
P. David Pearson, Univ. of California, Berkeley
John H. J. Petrini, Memorial Sloan-Kettering Cancer Center
Simon Phillipot, Univ. of Florida
Joshua Plotkin, Univ. of Pennsylvania
Philippe Poulin, CNRS
Colin Renfrew, Univ. of Cambridge
Trevor Robbins, Univ. of Cambridge

EXECUTIVE PUBLISHER **Alan I. Leshner**
PUBLISHER **Beth Rosner**

FULFILLMENT SYSTEMS AND OPERATIONS (memberships@aaas.org); CUSTOMER SERVICE SUPERVISOR Pat Butler; SPECIALISTS LaToya Casteel, Michelle Oforidire, April Marshall; MANAGER, DATA ENTRY Mickie Napoleoni; DATA ENTRY SPECIALISTS JJ Regan, Jaimee Wise, Fiona Giblin

BUSINESS OPERATIONS AND ADMINISTRATION Director Deborah Rivera-Wienhold; BUSINESS SYSTEMS AND FINANCIAL ANALYSIS DIRECTOR Randy Yi; MANAGER OF FULFILLMENT SYSTEMS Neal Hawkins; SYSTEMS ANALYST Nicole Mehmedovich; MANAGER, BUSINESS ANALYSIS Eric Knott; MANAGER, BUSINESS OPERATIONS Jessica Tierney; BUSINESS ANALYSTS Cory Lipman, Cooper Tilton, Celeste Troxler; FINANCIAL ANALYST Jeremy Clay; RIGHTS AND PERMISSIONS: ASSISTANT DIRECTOR Emilie David; ASSOCIATE Elizabeth Sandler; MARKETING DIRECTOR Ian King; MARKETING MANAGER Alison Chandler, Julianne Wielga, Justin Sawyers; MARKETING ASSOCIATES Mary Ellen Crowley, Elizabeth Sattler, Rebecca Rifkin; SENIOR MARKETING EXECUTIVE Jennifer Reeves; DIRECTOR, SITE LICENSING Tom Ryan; DIRECTOR, CORPORATE RELATIONS Eileen Bernadette Moran; SENIOR PUBLISHER RELATIONS SPECIALIST Kiki Forsythe; PUBLISHER RELATIONS MANAGER Catherine Holland; PUBLISHER RELATIONS, EASTERN REGION Keith Layson; PUBLISHER RELATIONS, WESTERN REGION Ryan Rexroth; CUSTOMER RELATIONS MANAGER Iquo Edim; CUSTOMER RELATIONS ANALYSTS Simon Chong, Lana Guz; ASSOCIATE DIRECTOR, MARKETING Christina Schlecht; MARKETING ASSOCIATES Paulina Cotto, Mitchell Edmund; ELECTRONIC MEDIA DIRECTOR Elizabeth Harman; ASSISTANT MANAGER Lisa Stanford; PRODUCTION SPECIALISTS Antoinette Hodal, Nichele Johnston, Lori Murphy, Kimberly Oster; WEB AND NEW MEDIA: SENIOR PROJECT MANAGER Trista Smith, PROJECT LEADER Luke Johnson COMPUTER SPECIALISTS Walter Jones, Kai Zhang, Web Developer Chris Coleman; PROGRAM DIRECTOR, AAAS MEMBER CENTRAL Peggy Mihelich

DIRECTOR, GLOBAL COLLABORATION, CUSTOM PUBLICATIONS, ADVERTISING Bill Moran
EDITOR, CUSTOM PUBLISHING Sean Sanders: 202-326-6430

ASSISTANT EDITOR, CUSTOM PUBLISHING Tianna Hicklin 202-326-6463

SPONSORED CONTENT SPECIALIST Candice Nulsen 202-256-1528

ASSOCIATE DIRECTOR, COLLABORATION, CUSTOM PUBLICATIONS/CHINA/TAIWAN/KOREA/ SINGAPORE Ruolei Wu +86-1367-101-5294

PRODUCT (science_advertising@aaas.org); MIDWEST Rick Bongiovanni: 330-405-7080, FAX 330-405-7081; EAST COAST/E. CANADA Laurie Faraday: 508-747-9395, FAX 617-507-8189; WEST COAST/W. CANADA Lynne Stickrod: 415-931-9782, FAX 415-520-6940; UK EUROPE/ASIA Roger Gonçalves: TEL/ FAX +41 43 243 1358; JAPAN, Makiko Hara: +81 (0) 3 6802 4616, FAX +81 (0) 3 6802 4615; ads@sciencemag.jp; CHINA/TAIWAN Ruolei Wu: +86 1367 1015 294 ruw@aaas.org

WORLDWIDE ASSOCIATE DIRECTOR OF SCIENCE CAREERS Tracy Holmes +44 (0) 1223 326525, FAX +44 (0) 1223 326532

CLASSIFIED (advertise@sciencereaders.org); U.S./CANADA/SOUTH AMERICA Tina Burks: 202-326-6577; U.S. CORPORATE Candice Nulsen 202-256-1528; SALES ADMINISTRATOR Marci Gallun; EUROPE/ROW sales Axel Gesatzki; SALES ASSISTANT Kelly Grace; JAPAN Yuri Kobayashi +81 (0)90-9110-1719; careers@sciencemag.jp; CHINA/TAIWAN Ruolei Wu: +86 1367 1015 294 ruw@aaas.org; ADVERTISING SUPPORT MANAGER Karen Foote: 202-326-6740; ADVERTISING PRODUCTION OPERATIONS MANAGER Deborah Tompkins; SENIOR PRODUCTION SPECIALIST/GRAPHIC DESIGNER Amy Hardcastle; PRODUCTION SPECIALIST Yuse Lajimimuh; SENIOR TRAFFIC ASSOCIATE Christine Hall; SALES COORDINATOR Shirley Young; MARKETING MANAGER Allison Pritchard; MARKETING ASSOCIATE Aimee Aponte

AAAS BOARD OF DIRECTORS RETIRING PRESIDENT, CHAIR William H. Press; PRESIDENT Phillip A. Sharp; PRESIDENT-ELECT Gerald R. Fink; TREASURER David Evans Shaw; CHIEF EXECUTIVE OFFICER Alan I. Leshner; BOARD Bonnie L. Bassler, May R. Berenbaum, Claire M. Fraser, Elizabeth Loftus, Stephen L. Mayo, Raymond Orbach, Sue V. Rosser, Inder M. Verma



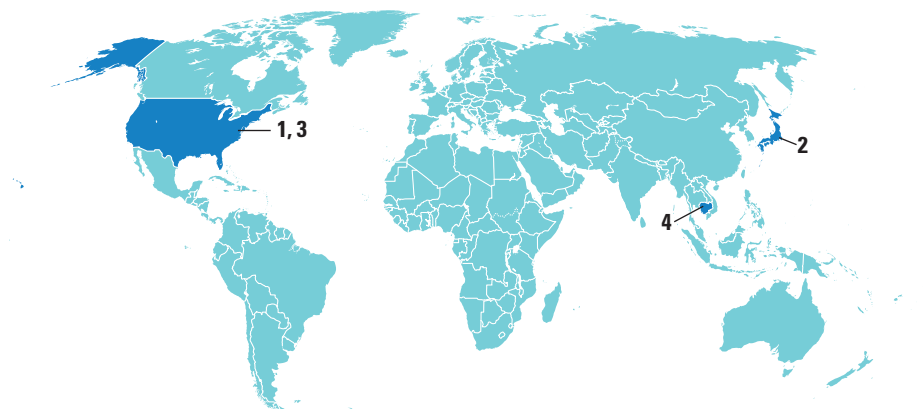
ADVANCING SCIENCE, SERVING SOCIETY

Jim Roberts, Fred Hutchinson Cancer Research Ctr.
Barbara A. Romanowicz, Univ. of California, Berkeley
Jens Rostrup-Nielsen, Haldor Topsøe
Mike Ryan, Univ. of Texas, Austin
Shimon Sakaguchi, Kyoto Univ.
Miquel Salmeron, Lawrence Berkeley National Lab
Jürgen Sandkühler, Max Planck Inst. of Vienna
Alexander Schier, Harvard Univ.
Randi Seeley, Univ. of Cincinnati
Vladimir Shalaev, Purdue Univ.
Joseph Silk, Institut d'Astrophysique de Paris
Denis Simon, Arizona State Univ.
Alison Smith, John Innes Centre
Davor Solter, Inst. of Medical Biology, Singapore
Peter Solter, Harvard Medical School
John Speakman, Univ. of Aberdeen
Allan C. Spradling, Carnegie Institution of Washington
Jonathan Sprent, Garvan Inst. of Medical Research
Eric Steig, Univ. of Washington
Paula Stephan, Georgia State Univ. and National Bureau of Economic Research
Elveth Stern, ETH Zürich
V. S. Subrahmanian, Univ. of Maryland
Ira Tabas, Columbia Univ.
Yoshiko Takahashi, Kyoto University
Sarah Teichmann, Cambridge Univ.
John Thomas, North Carolina State Univ.
Christopher Tyler-Smith, The Wellcome Trust Sanger Inst.
Herbert Virgin, Washington Univ.
Bert Vogelstein, Johns Hopkins Univ.
Cynthia Volkert, Univ. of Göttingen
Douglas D. Walker, Harvard Medical School
Bruce Wallace, Dalhousie Univ.
Ian Walmsley, Univ. of Oxford
David A. Wardle, Swedish Univ. of Agric Sciences
David Waxman, Fudan Univ.
Jonathan Weissman, Univ. of California, San Francisco
Keith Willis, Oxford Univ.
Ian A. Wilson, The Scripps Res. Inst.
Timothy D. Wilson, Univ. of Virginia
Rosemary Wyse, Johns Hopkins Univ.
Jan Zaenen, Leiden Univ.
Kenneth Zaret, Univ. of Penn. School of Medicine
Jonathan Zehr, Univ. of California, Santa Cruz
Maria Zuber, MIT

BOOK REVIEW BOARD

John Aldrich, Duke Univ.
David Bloom, Harvard Univ.
Angela Creager, Princeton Univ.
Richard Sweder, Univ. of Chicago
Ed Wasserman, DuPont
Lewis Wolpert, Univ. College London

AROUND THE WORLD



Washington, D.C. 1

DOE Labs Need Shakeup

A new report says that the U.S. Department of Energy needs to remove the red tape preventing its 17 national research laboratories from building stronger ties to industry. The report, from think tanks holding the left, right, and central ground politically, says that the labs are stuck in a Cold War-era



Energized. NREL is part of DOE network.

management structure that is particularly chafing in an era of tightening budgets. The report recommends a single bureaucratic overseer, greater flexibility for contractors, and market-based prices for industry to use the lab's extensive facilities. "The labs have been largely running on autopilot for

NOTED

>Speaking this week at Georgetown University about climate change, President Barack Obama reiterated how his administration plans to **limit carbon emissions from power plants and other sources**, improve the energy efficiency of appliances and buildings, create more green energy on federal lands, and promote mitigation and adaptation strategies without requiring action by Congress.

too long," the report's authors conclude. "A jolt to the system is needed now more than ever." <http://scim.ag/DOElabs>

Tokyo 2

Japanese Minister Defends Emphasis on Targeted Research

Japanese scientists want more details about a government proposal for a new funding entity to support applied biomedical research. The heads of 50 academic organizations want the government to maintain funding for investigator-initiated, innovative approaches as well as continuing its support for younger scientists.

"We have no intention to tie down the people who are involved in very fundamental research," says Akira Amari, minister for economic revitalization, about the government's plans for a Japanese version of the U.S. National Institutes of Health that would "strongly support the commercialization of innovative medical technologies." At the same time, Amari told scientists that "it is very important to have someone in [a research] group who can look at the industrialization or commercialization aspects and provide some direction to the research." <http://scim.ag/JapanResearch>

Washington, D.C. 3

House Panel Seeks Changes In NASA Programs

NASA would be forced to shelve an initiative to capture an asteroid and re-embark on a plan to establish a base on the moon under legislation authored by Republican lawmakers in the U.S. House of Representatives who have long butted heads with the Obama administration's vision for the space agency. The draft bill, vetted last week at a hearing



Moonstruck. Bill backs lunar base.

of the House science committee, would also downsize NASA's Earth Science portfolio—a program that the Obama administration would like to see grow—and redirect some of those funds to planetary science.

The bill's proponents are particularly opposed to NASA's proposal to capture an asteroid and drag it into a lunar orbit, calling it a "costly and complex distraction [that] lacks in details, a justification or support from NASA's advisory bodies." <http://scim.ag/NASACHanges>

Phnom Penh 4

New Treasures at Angkor Wat

Airborne laser imaging, or LiDAR, has revealed the imprint of a vast medieval cityscape surrounding Angkor Wat, Earth's largest religious monument. The findings were unveiled last week at a U.N. World Heritage meeting in Phnom Penh.

The Angkor kingdom was the heart of the Khmer Empire of the 9th to 15th centuries C.E., and Angkor was the most extensive city of its kind in the preindustrial world. The helicopter-borne survey, in April 2012, laid bare the imprints of a 9th century city, known from inscriptions as Mahendraparvata. The findings, in press at the *Proceedings of the National Academy of Sciences*, also lend weight to a hypothesis that the complexity of Angkor's vast waterworks was its ultimate undoing. <http://scim.ag/AngkorLiDAR>

THEY SAID IT

"The stem of the flower is STEM education, and the humanities are the blossom. Without the blossom, the STEM is completely useless."

—A new report from the American Academy of Arts and Sciences, *The Heart of the Matter*, makes the case for increased support for the humanities and social sciences.

CREDITS (TOP TO BOTTOM): NASA/RENDERING COURTESY OF BEHNAZ FARAH AND CONNOR WINGFIELD; DENNIS SCHROEDER/NREL

Downloaded from www.sciencemag.org on June 27, 2013

NEWSMAKERS

Into the Breach at Fermilab

The new director of the sole U.S. particle physics lab inherits an institution in transition. **Nigel Lockyer**, now director of the Canadian lab TRIUMF, takes the reins at the Fermi National Accelerator Laboratory (Fermilab) in Batavia, Illinois, on 3 September.



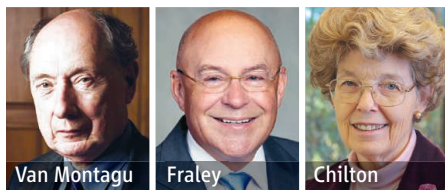
Lockyer, 60, a U.S. citizen who was raised in Canada, has long worked on experiments at Fermilab. Its Tevatron was shuttered in 2011, and the lab is struggling to launch its next mega-project, the Long-

Baseline Neutrino Experiment (LBNE), which has been chopped down from its original \$1.9 billion design. Since 2010, Fermilab's budget has fallen by 8% to \$366 million.

Particle physicist H. H. "Brig" Williams of the University of Pennsylvania thinks that Lockyer is up to the challenges. "He sleeps 4 or 5 hours and has tremendous energy," Williams says. "He can do things I wouldn't even try." In particular, Williams hopes that Lockyer will try to restore the original scope of LBNE. <http://scim.ag/NLockyer>

World Food Prize

Three scientists who made key contributions to the development of genetically modified crops will share this year's World Food Prize. Working at the Ghent University Medical School in Belgium, **Marc Van Montagu** and colleagues discovered in the



1970s that a ring of DNA, called a plasmid, in the microbe *Agrobacterium tumefaciens* caused a plant disease called crown gall. Then, in 1983, **Robert Fraley** of Monsanto and **Mary-Dell Chilton** at Washington University in St. Louis independently figured out how to use *Agrobacterium* to swap foreign genes into plants. The prize, founded by plant breeder Norman Borlaug in 1986 to recognize improvements to the amount and quality of food worldwide, is \$250,000. <http://scim.ag/FoodPrize>



Cracking Open Science

Championing the sharing of data can sometimes be a lonely pursuit, says art historian William Noel, one of 13 people honored by the White House last week for promoting so-called open science. "I feel like I've been handed the first telephone and have nobody to talk to," says Noel, who has helped digitize centuries-old scientific and medical tomes (digitalgalen.net).

The 20 June event, part of an Obama administration initiative called "Champions of Change," highlighted projects ranging from astrophysics to genomics. Some researchers have been slow to embrace the new technologies, says Noel, director of special collections at the University of Pennsylvania: "People have to relearn how to release their data." And pediatrician and bioinformaticist Atul Butte of Stanford University in California chided his fellow researchers for "having to come to the White House to talk about something we were taught to do in kindergarten." The 2-hour discussion is posted on the White House website, but the poster sessions and reception were by invitation only.

FINDINGS

Women Biologists Avoid Spotlight at Conferences

A new study finds that women are much less likely than men to accept invitations to speak at major biology conferences. A report in the *Journal of Evolutionary Biology* found that only 16% of invited speakers at the European Society for Evolutionary Biology Congress between 2001 and 2011 were women, half their presence in the overall pool of senior life scientists, and that they were twice as likely as their male counterparts to turn down an invitation to talk in slots reserved for presenting original and important work. At the same time, the number of female presenters of posters and uninvited talks was almost at parity with men.

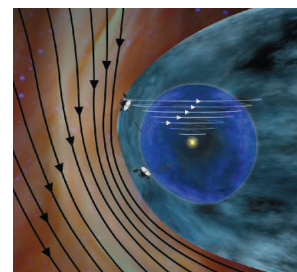
Possible reasons include the large number of such invitations, tight budgets, and anxiety about balancing the demands of family and work. The authors, Julia Schroeder of the Max Planck Institute for Ornithology in Germany and Hannah Dugdale of the University of Sheffield in the United Kingdom, say that the next step is to find out why so many women say no. "Then we [will] know what can be done to change their minds," Schroeder says. <http://scim.ag/BioWomen>

Voyager's Not Gone Yet

Last summer, it looked like the Voyager 1 spacecraft might have finally reached its ultimate destination. Thirty-five years out from Earth and three times farther from the sun than Pluto, the decrepit spacecraft reported a sharp drop in plasma blowing out from the sun and a sharp jump in cosmic rays streaming in from out in the galaxy.

But three papers published online this week in *Science* conclude that Voyager 1 has not left the heliosphere—the sun's magnetic bubble inflated by its blowing plasma—and entered interstellar space. That's because Voyager found no accompanying switch from the magnetic field spiraling out from the sun to the magnetic field of interstellar space.

Instead, Voyager has discovered a hybrid part of the heliosphere lying between the heliosphere proper and true interstellar space. And nobody knows how far that hybrid extends and when the spacecraft will actually make humankind's first contact with interstellar space.



INFLUENZA

Dueling Reviews for Controversial Flu Drug

BRUSSELS—Were the billions of dollars that governments spent on the antiviral drug Tamiflu to protect their populations from a flu pandemic a waste of money? For years now, an international group of researchers has said the answer may well be yes. Working under the umbrella of the Cochrane Collaboration, a global network of scientists reviewing medical evidence, the group says it's not clear that Tamiflu (also known as oseltamivir) can prevent complications from influenza or keep people out of the hospital. It has also waged a vigorous campaign calling on Roche, Tamiflu's manufacturer, to make public a series of unpublished trials on the drug.

But many influenza researchers believe that Tamiflu is beneficial—and now, they're planning an alternative review of the drug. At a meeting here on 18 June, several members of the new Multi-party Group for Advice on Science (MUGAS)—which also includes statisticians and epidemiologists—said that the Cochrane panel hasn't given Tamiflu a fair shake, and they questioned its expertise.

In turn, the Cochrane Acute Respiratory Infections Review Group—one of more than 50 Cochrane panels continuously sifting through medical evidence on therapies and devices—questions the new effort because it's sponsored by Roche, and three of the four people behind the initiative have ties to the company, including its chair, Albert Osterhaus of Erasmus MC in Rotterdam, the Netherlands. “This group is not independent,” says Tom Jefferson, an epidemiologist in Rome leading the Cochrane group. Jefferson and two other Cochrane invitees to the MUGAS meeting declined to attend.

The stakes are high, because the Cochrane analysis—and the fight over publication of the data—is eroding confidence in Tamiflu. At the recommendation of the World Health Organization and influenza scientists, many countries started building stockpiles of the drug after 2004, when fears of an H5N1 pandemic began running high. The Cochrane

analysis, published in 2009 and updated in 2012, has fed doubts about that decision. A parliamentary committee in the United Kingdom is now conducting an investigation into the decision to spend £500 million on Tamiflu; Peter Göttsche, director of the Nordic Cochrane Centre in Copenhagen, last year called on European governments to sue Roche to get their money back.



Worth the money? Many governments have stockpiled the influenza drug Tamiflu in case of a pandemic. But some scientists question how well it works.

The evidence for Tamiflu has never been all that impressive. Roche conducted 12 randomized controlled trials with Tamiflu in adults between 1997 and 2001, and it's beyond dispute that if given in the first 2 days after symptoms appear, the antiviral can shave about a day off the time that people feel sick—a modest gain, but enough to convince regulators to approve it for use in both seasonal and pandemic influenza.

The more important question, however, is whether Tamiflu can also prevent deaths from influenza, complications such as bacterial pneumonia or bronchitis, and hospitalizations, a major issue during pandemics because they can overburden the medical system. The trials weren't large enough to answer that question; very few flu patients die or have complications to begin with, and their numbers were too small to show a statistically significant benefit from Tamiflu.

However, by combining the studies in a so-called meta-analysis, a Roche-funded team led by Frederick Hayden and Laurent Kaiser of the University of Virginia found that Tamiflu reduced the risk of complications and hospitalizations. Their 2003 paper was widely cited in recommendations to stockpile the drug. The meta-analysis was repeated in 2011 by Miguel Hernán and Marc Lipsitch at Harvard University—this time without Roche funding and with a slightly different methodology—who also saw an effect on severe complications but did not draw conclusions on hospitalization.

Only two of the studies underlying these meta-analyses have been published, however; data from the rest were provided in confidence to the researchers by Roche. Having only the published studies to go on, the Cochrane researchers concluded in their 2009 report that there is no evidence to support the contention that Tamiflu prevents complications. They, with strong support from *BMJ*, have since lobbied Roche to release all the trial data. They scored a victory in March, when Roche issued a new data policy that gives scientists access to raw data on drug trials provided they have a solid analysis plan. (Privacy-sensitive or commercially important data will be redacted, however.) In early June, the company sent the Cochrane group a DVD with the first batch of Tamiflu data; “So far, [Roche] seems to do what they have promised,” Jefferson says. The Cochrane group plans to update its analysis.

Osterhaus agrees that it's time for another Tamiflu review, but he and others at the meeting were doubtful that the Cochrane group has the necessary expertise; for instance, there have been glaring errors in the group's statistical approach, says Stephen Senn, head of the Luxembourg government's Competence Center for Methodology and Statistics and a member of the MUGAS group.

In Brussels, the group decided that it will also take into consideration so-called observational studies, in which patients aren't randomized and blinded to their treatment. The Cochrane group considered only randomized controlled studies, the gold standard in medical evidence; observational studies carry a higher risk of bias but they shouldn't be simply disregarded, says Jonathan Nguyen-Van-Tam of the University of Nottingham in

the United Kingdom, a member of MUGAS. An as-yet unpublished analysis by Van-Tam's group of observational data from around the world has shown that Tamiflu prevented deaths during the 2009 H1N1 pandemic, a hectic period in which randomized studies would have been hard to organize or get ethical approval for.

Roche has promised MUGAS full access to all its Tamiflu data, but is also bankrolling the effort with an unrestricted grant. That, and some members' current or past

financial ties to the company, make the new review problematic, Jefferson says. Moreover, many of the members have been longtime advocates of Tamiflu, making it difficult for MUGAS to do an unbiased examination, says epidemiologist Peter Doshi of Johns Hopkins University in Baltimore, Maryland, another member of the Cochrane group. Given the billions spent, "there's a strong incentive to come to a conclusion that supports their earlier position," he says.

Osterhaus promises that the panel he chairs

will let the data speak and says MUGAS is transparent about its conflicts of interest; the review will be published regardless of the outcome. The group may tackle other issues as well, such as influenza vaccines—which the Cochrane group has also criticized as being far less effective than widely assumed. Can MUGAS settle such debates? "I'm not sure," says Hayden, who's also a member. "I'm afraid it will be our story and the Cochrane story—and the confusion will continue."

—MARTIN ENSERINK

STEM CELL RESEARCH

Chimeric Embryos May Soon Get Their Day in the Sun

TOKYO—Growing human body parts in pigs could alleviate a worldwide shortage of donated organs. But are such organ farms ethical?

Last week, a Japanese ethics panel decided that they are, recommending that the government lift a ban on certain experiments that mix human cells with those of other animals. But the scientist who is pioneering this research area and who pushed for an end to the ban, stem cell biologist Hiromitsu Nakauchi of the University of Tokyo, is planning to set up a lab in California, bringing the debate—and the possible benefits—to the United States.

Nakauchi has been pursuing the idea of implanting human pluripotent stem cells into pig embryos genetically engineered to be incapable of developing their own pancreases. These cells could be either embryonic stem cells or, preferably, induced pluripotent stem (iPS) cells. iPS cells derived from a patient's own skin or other tissue should avoid immune rejection, because the generated organ would genetically match the recipient. If all goes to plan, the stem cells would develop into human pancreases in the pig fetus. (Mouse experiments have shown that pluripotent cells can fill the developmental niche opened by the absence of an organ.) After the piglet's birth, the pancreas would be harvested and islet cells isolated for transplantation into human type 1 diabetes patients, whose islets either no longer produce insulin or produce too little of the sugar-regulating hormone.

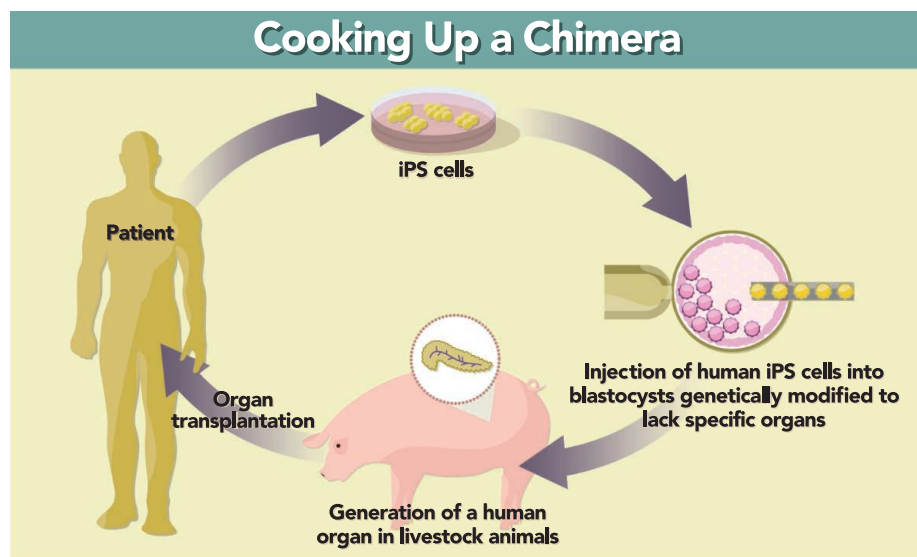
"The construction of tissues and organs in chimeric animals is a very promising approach," says Markus Grompe, a stem cell scientist at Oregon Health & Science University in Portland. "If successful, [Nakauchi's]

method would clearly be superior to in vitro differentiation." But the work is ethically fraught. "I suspect that a lot of scrutiny would be given to this research," says Nancy King, a bioethicist at Wake Forest University in Winston-Salem, North Carolina.

In a milestone on the road to a human-pig chimera, Nakauchi's team in a paper in *Cell*

Opinion in Genetics & Development.

Nakauchi's group has since gone further, generating pancreases for one pig species in apancreatic embryos of a different pig species, as they reported in the *Proceedings of the National Academy of Sciences* in February. Pig organs are similar in size to ours, so it should be possible to harvest a human organ



And a side of pancreas, please. To alleviate a shortage of donated organs, researchers aim to grow human organs in pigs. First up are pancreases. Human pluripotent stem cells would be implanted in pig embryos incapable of developing their own pancreases; the stem cells should develop into human pancreases in the pig fetus.

in 2010 described using rat stem cells to grow pancreases in apancreatic mouse embryos. "This work paves the way to the generation of human replacement organs within developing animals," wrote John Gurdon, a developmental biologist and Nobel laureate at the University of Cambridge in the United Kingdom, and colleagues last October in *Current*

grown for transplantation when it is the right size for an intended recipient. Getting the technique to work in pigs "is quite remarkable," says stem cell researcher Sean Wu of Stanford University in California, who feels that there is "a very reasonable chance" of generating human tissues from iPS cells. If the approach succeeds, Nakauchi and others

say, it might be applied to other organs, including kidneys and hearts.

Wu explains that there are difficulties getting stem cells to properly mature in vitro and challenges in generating them in the quantities needed for large organs. David Ayares, CEO of Revivacor, a regenerative medicine company in Blacksburg, Virginia, agrees that growing complex organs in vitro “requires more research.” Ayares says the challenges of growing tissues in vitro and the shortage of donated human organs has led several groups, including Revivacor, to study xenotransplantation: the transfer of living cells, tissues, or organs from one species, usually pigs, to humans. Nakauchi’s method is another alternative that could reach the clinic first. But working out the details of growing human organs in pigs, Wu warns, will be “extremely difficult.” There is a risk of inadvertently transplanting harmful pig pathogens into a human along with an organ. And the recipient’s immune system could reject a transplanted organ—even a genetic match—if it carries stray pig cells.

In Japan, current national guidelines governing stem cell research allow mixing human and animal material in vitro for 14 days but forbid in vivo experiments. “I have been asking the government to change the guidelines for 2-and-a-half years,” Nakauchi says. On 18 June, the Expert Panel on Bioethics of the Council for Science and Technology Policy, the nation’s highest science advisory body, took a step in that direction by recommending an overhaul.

Panel members acknowledge that a revision is long overdue. “The guidelines were written over 10 years ago, when there weren’t any examples of the kind of research Nakauchi wants to do,” says panelist Kaori



Chomping at the bit. After pushing the Japanese government to lift a ban on experiments essential to moving his research forward, Hiromitsu Nakauchi may continue his work at Stanford.

Muto, a research ethicist at the University of Tokyo. She says that the panel was responding not just to Nakauchi, but also to concerns that current restrictions are impeding several promising lines of stem cell research. The panel, which unanimously endorsed the decision, feels current rules are too restrictive and that ethical judgements should be based on “the specific research plan and the technology involved,” Muto says. The action now moves to an education ministry committee that will revise the guidelines—a process that Muto says could take a year or more.

Nakauchi is already anxious. His team’s papers offer a road map for exploiting the approach, and he knows of at least one group in China planning to follow up. To maintain momentum, Nakauchi is now negotiating to set up a lab at Stanford University, using a \$6.2 million, 6-year grant he has just won from the California Institute for Regenerative Medicine. (Such grants have to be used within California.)

U.S. approval for the controversial

research is not guaranteed. King notes that there are no relevant national laws, and the U.S. National Academies’ Guidelines for Human Embryonic Stem Cell Research do not prohibit creating human-animal chimeras. But they do flag for special attention any experiments that could introduce human cells into a chimera’s germ line—the genetic material passed on to offspring—or into the brain. According to the guidelines, the concern is that “human characteristics might be exhibited in the animal.” A worst-case scenario, Grompe says, is that “in theory we could end up with a human embryo gestating in a pig.”

The academies’ guidelines recommend that chimeras be prevented from breeding, to ensure human cells do not enter an animal’s germ line. Keeping human cells from migrating to the brain of a chimeric embryo might be more problematic. Nakauchi says that there are proven ways of doing this. One is attaching a “suicide gene” to the human stem cells that would destroy any differentiated cell that starts expressing neural proteins. Grompe says that an approach he is exploring—making chimeric embryos using differentiated cells—is less ethically contentious.

Nakauchi recognizes that he is stepping into controversial territory. “People think we’re making a human-pig monster,” he acknowledges, although he says most accept the idea once he explains what his team is trying to do. He is confident that he can make just as convincing a case to Stanford University’s review boards overseeing experiments involving human subjects, animals, and stem cells. “I haven’t submitted a research plan,” Nakauchi says, “but I’m sure they will allow it.”

—DENNIS NORMILE

U.S. GRADUATE EDUCATION

Minorities Run Up Significant Debt in Earning STEM Ph.D.s

Many African-Americans and Hispanics who pursue a career in science must wrestle with a dearth of role models, a lack of opportunity, and sometimes even outright discrimination. One factor not typically on that list of barriers to entry is the cost of a Ph.D. But a new study suggests that it should be, and that those groups, traditionally underrepresented in science, also owe much more than their white and Asian counterparts by the time they graduate.

Conventional wisdom holds that most

students can earn a doctoral degree in a science, technology, engineering, and mathematics (STEM) field without amassing large amounts of debt. This so-called free ride comes courtesy of a variety of mechanisms—notably student fellowships, institutional support, and research positions funded by grants to faculty members—designed to meet both the cost of tuition and living expenses. That financial freedom stands in sharp contrast to the widely publicized heavy debt often taken on by students obtaining advanced degrees in

the arts and humanities or those trained in the law, medicine, and other professions.

However, a new study of 19,000 newly minted Ph.D.s by a team at the American Institutes for Research (AIR) in Washington, D.C., suggests that the conventional wisdom is wrong and that minorities face a steeper climb onto the STEM career ladder. It finds that only 51% of African-Americans and 64% of Hispanics earning STEM Ph.D.s in 2010 graduated debt-free. In comparison, 73% of white and Asian STEM Ph.D.s avoided debt.

African-American women, who are part of two underrepresented minority groups in STEM fields, shoulder the heaviest burden, with 27% of them accumulating more than \$30,000 in debt. The comparable figure is 10% for white and Asian women.

The AIR researchers—Kristina Zeiser, Rita Kirshstein, and Courtney Tanenbaum—looked at self-reported data from students who earned their Ph.D.s in 2010 in either a STEM or SBE (social, behavioral, or economic) field. (Those in STEM fields account for 71% of the total.) The cohort is drawn from an annual survey conducted by the National Science Foundation (NSF) of all U.S. doctoral recipients that includes questions about their financial situation.

The AIR authors note that their findings suggest the cost of a degree needs to be a larger consideration in any initiative trying to attract more minorities and women into STEM careers. “If ... broadening participation ... is to remain a national priority, the policies and practices that aim to support students in financing their education need to be examined,” the AIR authors write in a May 2013 issue brief where their study results are offered (www.air.org/files/AIRPriceofPhDMay13.pdf). “Students’ concerns about debt accumulation during graduate school are not unfounded.”

So what explains the disparity in debt? Is there overt discrimination? Are underrepresented minorities more likely to borrow more money because they are poorer, or because they have additional financial responsibilities? Do they attend schools that provide less generous stipends, or where fewer faculty members have grants that can support them?

“We can’t explain these findings,” admits Tanenbaum, who expects to complete her doctoral degree in education next year at George Washington (GW) University in Washington, D.C. “This is just a first step in understanding what is going on.”

The few related studies addressing these issues have examined a different population and asked different questions. A pilot study released last month by the Council of Graduate Schools (CGS), for example, compared the completion and attrition rates of students seeking master’s degrees in STEM fields and business at five institutions. Although the CGS study was too small to include sub-

sets of underrepresented minorities in STEM fields, it did collect information on those who dropped out, a group that institutions rarely track. And what it found supports one potential explanation for the Ph.D. debt study.

For instance, while students who earned their STEM master’s ranked institutional support at the bottom of the list of factors affecting their ability to complete the program, a lack of funds is near the top of their list of reasons for leaving. “Wealth and access to capital is a huge factor” in enrollment decisions,

STEM Ph.D.s were more likely than whites and Asians to have taken on debt as undergraduates: 64% of the latter group compared with 51% of African-American and 57% of Hispanic Ph.D.s finished college without student debt. That fact alone shapes the graduate STEM pool, Malcom-Piqueux says. “Students with undergraduate debt are less likely to go to graduate school,” she notes. The AIR study reveals that, once enrolled, however, even debt-free minority students soon dig themselves a financial hole. One reason, Malcom-Piqueux says, is that “underrepresented minorities, on average, receive their Ph.D.s from less selective schools with fewer institutional resources.”

The type of support that graduate students receive can also make a big difference in how much debt they acquire. Research assistantships are generally more generous than teaching assistantships, for example, and extend through the summer. Research positions also help put students on the fast track academically, providing them with increased opportunities for publication, attendance at meetings, and networking with prominent figures in their field.

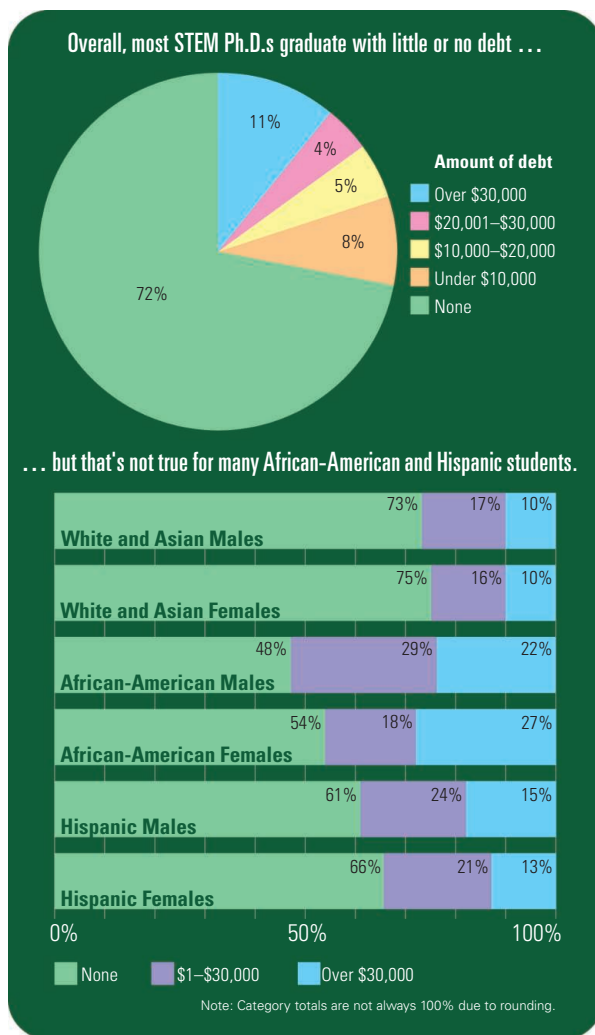
But much of what is known is based on anecdote rather than analysis. The NSF survey, for example, doesn’t even ask doctoral recipients for the amount of institutional support that they have received. “We haven’t figured out a good way to do it,” admits NSF’s Mark Fiegener.

For USC’s Dowd, race is the elephant in the room. “The [AIR] authors speculate on factors that may be causing the big differences in debt. But they omit labor market discrimination and favoritism,” she says. “If we white-wash out past and present discrimination when speculating on the results, we skew the nature of the debate.”

Some new data are expected soon. CGS hopes to have initial results later

this year on the financial situation of underrepresented minorities pursuing doctoral degrees in STEM fields at 21 institutions as part of a study on completion rates for those students. And this fall, CGS will launch a study sponsored by financial services giant TIAA-CREF that will measure the fiscal IQ of graduate students at 15 universities. “That has the potential to explore some of the questions raised by the AIR study,” says CGS’s Daniel Denecke. “Right now we just don’t know enough.”

—JEFFREY MERVIS



says Lindsey Malcom-Piqueux, an assistant professor of higher education administration at GW and Tanenbaum’s dissertation adviser. In 2012, she and Alicia Dowd of the University of Southern California (USC) in Los Angeles published a study on how undergraduate debt affects the pursuit of a graduate STEM degree. “White and Asian-Americans are more likely to borrow from their family because there are higher levels of wealth in those groups,” Malcom-Piqueux notes.

The AIR study found that minority

OPTICS

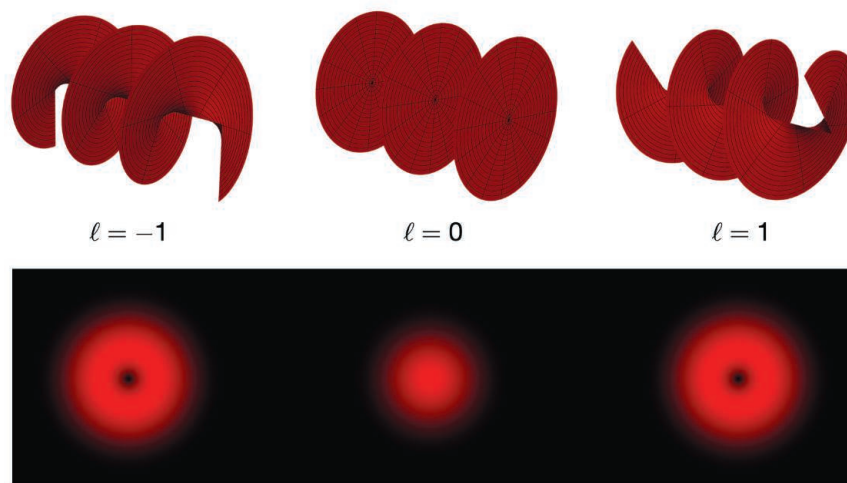
Light Beams With a Twist Could Give A Turbo Boost to Fiber-Optic Cables

The global flow of data traffic faces backups every bit as gnarly as an L.A. commute. Today, the worst traffic jams occur within data centers of companies such as Facebook, Amazon, and Google that must zip information back and forth between warehouses full of computer servers to sort out which data customers need most. This data travels through fiber optic cables at light speed. But with data center traffic rising exponentially, slowdowns are already being felt. Now, on page 1545, researchers describe a novel type of fiber optic line that allows them to encode data in a whole new way, using the way light waves corkscrew as they travel. Combined with more conventional ways of cramming extra data down fiber optics, the new approach could vastly increase data transmission rates.

"This is very impressive work," says Keren Bergman, an electrical engineer at Columbia University. "I'm really excited about it." Bergman notes that telecommunications companies made great strides in increasing data bandwidths after researchers showed in the 1990s that it was possible to send multiple data streams down the same fiber optic cable simply by encoding each data stream on a different color, or wavelength. Today, individual fibers use such wavelength division multiplexing to send hundreds of different data streams down a single fiber simultaneously. Telecom providers also encode information in light's polarization as well as in the height and width of light waves. Together, these encoding schemes allow today's fibers to carry 10,000 times as much information as they did 30 years ago. The new way of encoding data, which takes advantage of a property of light known as orbital angular momentum (OAM), "is a similar breakthrough," Bergman says. "It opens up another door to scaling."

OAM is harder to visualize than some of light's other properties. Slice through a traditional fiber optic and the beam looks

like one from a flashlight: most intense at the center and less concentrated at the edge. But by passing light through a hologram, researchers can force individual photons to corkscrew as they travel down the fiber. Different holograms control how many helices photons complete over a given distance. And light beams twisting at different rates create a unique pattern of light in any given slice, such as an intense spot in the center or a bull's-eye with a ring around



New twist. Passing light beams through holograms caused them to twist either clockwise (-1) or counterclockwise ($+1$) or to have no twist (0); each case produced a specific profile in an optical fiber.

it (see figure, above). OAM-encoded photons with different helices, or "modes," can carry a data stream without interfering with photons in other modes traversing the fiber simultaneously.

Optics researchers have encoded information in this manner for more than a decade. Last year, for example, a team led by Alan Willner, an electrical engineer at the University of Southern California in Los Angeles, reported in *Nature Photonics* that they had used OAM encoding to send more than 2.5 terabits of data (roughly five Blu-ray DVDs' worth) per second through open air. But when OAM has been tried in fibers, the backbone of modern communication transfer, the beams fell apart in less than a meter.

The problem is that in standard glass fibers, photons encoded with different OAM modes bleed into one another, corrupting the data. "So we asked, 'Can we make modes in a fiber that are distinct and make them behave like different colors?'" says Siddharth

Ramachandran, an electrical engineer at Boston University. In 2011, Ramachandran and a collaborator at OFS Fitel, a fiber production company in Brøndby, Denmark, did just that: They produced glass fibers with a unique combination of standard chemical additives arranged in several concentric rings. The additives change the speed at which light travels through the glass, creating separate pathways for different OAM modes to travel inside the fiber. That showed the fibers had potential.

For the current study, Ramachandran teamed up with Willner to show that the technique could enable high-speed data transfer. They sent 1.6 terabits of data per second in 10 different wavelengths and two

OAM modes down more than a kilometer of their specialized fibers. That's a tiny fraction of the distance needed for long-haul telecommunications lines. But it's more than enough for use within data centers and for other high-end users such as scientific institutions. "This is very impressive. I can imagine a huge commercial market," says Robert Boyd, a physicist at the University of Rochester in New York.

Ramachandran and Willner note that OAM isn't the only possible solution to alleviating data bottlenecks. In recent years, optics researchers have created optical fibers capable of supporting up to 12 modes. This approach, however, typically requires extensive computational power at the receiving end to unscramble the signals. Another approach has been to create "multicore" fibers with a series of "cores" that can each carry their own modes. Researchers in the United States used this approach last year to send more than 1 petabit of data per second (nearly 1000 times the current OAM demonstration). The approaches aren't mutually exclusive, says Willner, who envisions future fibers with multiple cores, each supporting several OAM modes in addition to allowing for all the more conventional data beams to flow through. If that becomes reality, it will make today's data rates seem as sluggish as a dial-up modem.

—ROBERT F. SERVICE



The Dizzying Journey To a New Cancer Arsenal

Carl June and others are on a quest to make T cell therapy a cancer treatment success. Getting there is filled with highs and lows and lots of uncertainty

ONE JANUARY AFTERNOON IN 2011, oncologists Carl June and David Porter settled themselves at a table at Gia Pronto, the coffee shop in the atrium of the Perelman Center for Advanced Medicine. The glass and steel building sits at the nerve center of the University of Pennsylvania's (Penn's) massive medical complex in West Philadelphia, a few blocks from the Schuylkill River that cuts the city in two. Outside, construction cranes rise up, a sign of Penn's ongoing expansion.

June and Porter had a problem. In an exhilarating 6 weeks in the summer of 2010, they had treated three men with leukemia who were out of options. In a cell therapy experiment, the patients' own T cells were genetically engineered in a lab to proliferate inside their bodies and seek and destroy cancer. The

strategy had worked beyond the doctors' wildest expectations, melting away pounds of tumor in each patient. In one case, the modified cells didn't grow well in the lab, and the patient, a 64-year-old scientist at a biotechnology company named Douglas Olson, received a mouse-sized dose. Now, he'd taken up running as a hobby and was teaching his grandchildren how to sail.

But generating the cells for all three patients had cost \$350,000. The scientists were out of money and out of "vector," the disabled HIV viruses that they were using to insert new genes into T cells. They had applied to the National Cancer Institute (NCI) and elsewhere for funding to continue their clinical trial, sharing unpublished data on patients 1, 2, and 3. Cancer had vanished

in Olson and one other patient. The third man responded partly but later died of his disease. Funders deemed the therapy too experimental and too impractical. Everywhere, Porter and June were turned down.

"It was one of these best of all times, worst of all times," says June, who had assembled his small team, including Porter, more than a decade ago. They weren't the first to test this radical new approach in people, but their results were the most striking. "We knew something worked," even if the remissions ended tomorrow, June says. "We knew it wasn't an accident."

Sipping coffee, Porter and June weighed their next step. They were itching to test the cell therapy in more people with leukemia, and to do that they needed money that they



Experimenting. A life of twists and turns has Carl June pressing forward with a radical cancer therapy.

Porter was en route to vacation in western Maryland with his family when the embargo lifted. His phone started ringing. “I was in the car for 8 hours that day,” he says. “I spent 8 hours straight on my phone, answering e-mail, answering phone calls. It was a story that took us all by surprise. It kind of went viral.” June fielded 5000 requests from patients and their families for the therapy. Eight hundred media outlets worldwide covered the story.

NCI reversed course and awarded June’s team nearly \$500,000 a year for 4 years, in part to create engineered T cells for patients. Pharmaceutical companies began courting June and his colleagues. Almost exactly a year after publication, Novartis signed a multimillion dollar agreement with Penn, licensing rights to the therapy with the goal of getting it approved by drug regulators. Three patients, two of them still in remission today, proved to be the tipping point that June had imagined.

Two years later, nearly all of the thousands of cancer patients desperate for engineered T cells are a long way from getting them. For one, the therapy can tackle only a subset of blood cancers, and it remains highly experimental. About three dozen people at Penn have received it, along with more than 50 elsewhere. Not everyone is helped, and many of those who are suffer serious side effects. In those whose disease has disappeared, no one knows yet how long the calm will last. “The medical literature is just littered with examples of drugs that look great on your first 10 patients, and they don’t pan out for one reason or another,” Porter says.

History may urge caution, but it’s hard not to be swept up in the moment. Despite the small numbers, many oncologists believe that what June’s team and others now replicating it have seen is unprecedented. No cell therapy has proliferated in the body, endured, and slain cancer quite like this one.

A looming question now is how to move engineered T cell therapy forward—how to test it in more patients, at more centers, in different forms of cancer. Drug companies “don’t care if it costs \$500 million to develop the first vial, as long as you can make the second vial for \$1,” says Steven Rosenberg, an NCI surgical oncologist in Bethesda, Maryland, who’s spent decades developing cell therapies. As Rosenberg knows well, that’s

not how T cell treatment works. Every batch is a distinctive drug, and right now, every step toward making it holds the chance of human error.

As academic cancer researchers and companies work to expand the therapy’s reach, June and his colleagues are in the public eye.

Online

sciencemag.org

Podcast interview with author Jennifer Couzin-Frankel (http://scim.ag/pod_6140).

Along with the accolades are critics charging that they’ve claimed more than their share of scientific credit and lawsuits alleging violations in agreements with collaborators. They are deeply driven to save lives; cancer looms large

in June’s own autobiography. But at stake, too, for the researchers and their institution, is money and scientific glory, and the chance to combat cancer with immunology on a grand scale.

T cells remodeled

The backbone of June’s work was forged in the mid-1980s by an Israeli immunologist. Zelig Eshhar was on sabbatical in Palo Alto, California, when he began toying with an unorthodox question: whether T cells, the sentries of the immune system, could be coaxed to destroy different targets. To accomplish this, Eshhar knew that he needed T cells to recognize and latch onto molecules that they normally ignore. And the only way to make that happen was by inserting foreign DNA into T cells, to alter the receptors they produced.

Eshhar returned home to the Weizmann Institute of Science in Rehovot, Israel, and got to work. Failure after failure followed. The technology to insert DNA was rudimentary. Then, in the late 1980s, Eshhar triumphed, adding a combination of gene sequences

“We knew something worked. . . . We knew it wasn’t an accident.”

—CARL JUNE,
ABRAMSON CANCER CENTER
UNIVERSITY OF PENNSYLVANIA

didn’t have. “We basically decided that we would just publish with three patients,” June says. Getting the word out, he hoped, could shift the dynamic in their favor. Porter was game to try, but skeptical that any reputable journal would accept a paper with an n of 3.

He turned out to be wrong. *The New England Journal of Medicine* welcomed a report about Olson and his mouse dose of T cells. *Science Translational Medicine*, *Science*’s sister journal, snapped up a manuscript detailing all three patients. The papers were published simultaneously on 10 August 2011. The university put out a news release that day. Its title: “Genetically Modified ‘Serial Killer’ T Cells Obliterate Tumors in Patients with Chronic Lymphocytic Leukemia, Penn Researchers Report.”

into a type of immortalized T cell that more readily accepts foreign DNA and endowing the cells with new targets they could kill. “The moment we realized it was working . . . we became, I don’t want to say obsessed, but really invested,” he recalls.

Eshhar’s feat was only the first step. To treat a disease like cancer, researchers needed to identify protein targets unique to certain tumor cells—otherwise, the modi-

fied T cells would destroy healthy tissue, too. They also had to ensure that the cells multiplied inside the body and persisted, wiping out every trace of cancer and preventing it from coming back.

Slowly, a handful of researchers picked up on Eshhar's accomplishment and carried it forward. At Memorial Sloan-Kettering Cancer Center in New York City, cell therapist and oncologist Michel Sadelain set to work introducing genes into human T cells. "It took me 3, 4 years to better transfer genes into more than 0.5% of the culture," Sadelain says. "Today, we can take a high school kid [and] in an afternoon, they know how to take T cells and blast genes in all of them." Sadelain pushed for a name, and "chimeric antigen receptor" cells, or simply CAR cells, stuck.

While Sadelain focused on cancer from the start, June got there circuitously. His career trajectory tracked Cold War history, and the reason for that was Vietnam. In 1971, when he was 18, a lottery gave June a near-certain chance of being drafted. He abandoned plans to enroll at Stanford University and applied to the U.S. Naval Academy in Annapolis, Maryland. The war ended 2 years later, but June remained with the military, which financed his medical education. With fears of nuclear attacks running high, he trained as an oncologist and a bone marrow transplant to treat those exposed to high doses of radiation. In 1989, the Berlin Wall collapsed. The Cold War ended soon after. The military "didn't care about bone marrow transplants after that," June says. He needed a new passion.

The Navy didn't fund cancer research, so June, then at the Naval Medical Research Institute in Bethesda, turned to HIV. The decision proved prescient, as he learned the ins and outs of T cells and the immune system, knowledge that would later serve him well. He spent a decade training T cells to flourish in HIV patients, whose own T cells are destroyed by the virus. An immunologist in the lab, Bruce Levine, explored how to grow T cells and what signals could best "activate" them,

turning them on outside the body to help them destroy their targets.

Then in 1995, June's personal and professional lives abruptly converged. His wife Cynthia was diagnosed with ovarian cancer. The couple had a 3-year-old daughter and two teenage sons. "I saw for the first time what it was like to be on the other side of the bed," he says. June was a believer in manipulating the immune system to treat cancer, but suitable immunotherapies weren't ripe at the time.

Cynthia June was 46 when she died in

Advances and acrimony

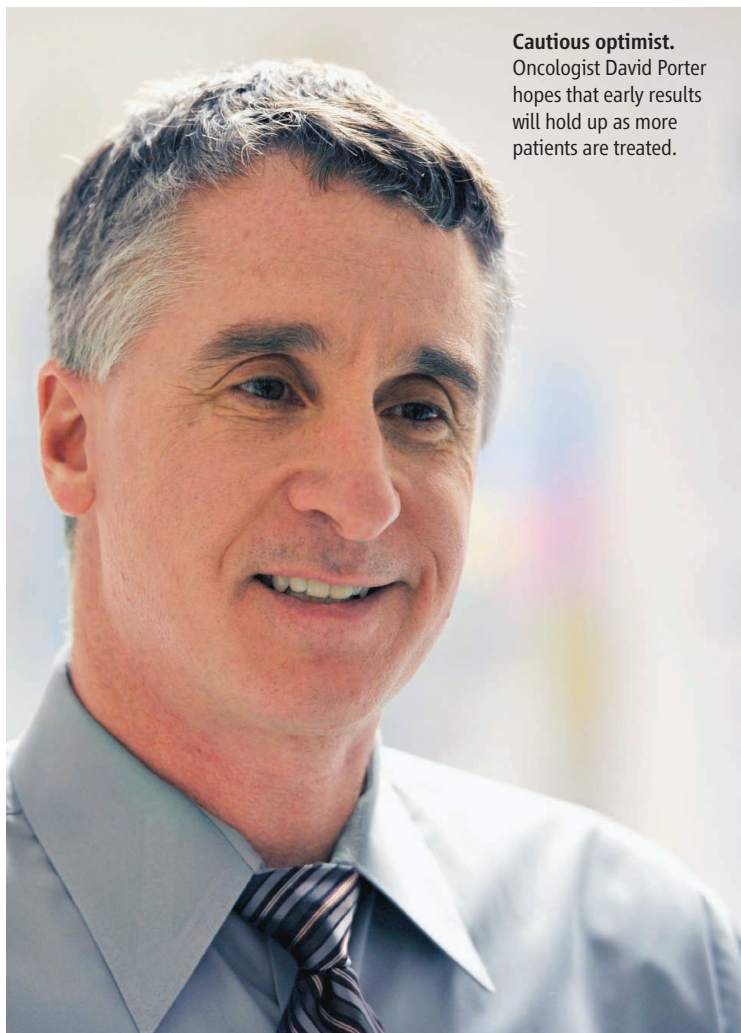
At Penn, June continued his HIV work but also threw himself into cancer, motivated by his wife's death and by a belief that the pieces were falling into place to successfully treat patients with CAR cells at last. He was enthusiastically welcomed by two oncologists: Porter, who cares for adults with blood cancer at Penn's Abramson Cancer Center, and Stephan Grupp with the Children's Hospital of Philadelphia (CHOP), who showed up at June's office door one day and asked to collaborate.

A handful of researchers elsewhere were also in the race to bring CAR therapy to people. In addition to June, they included Sadelain at Sloan-Kettering, Rosenberg at NCI, and Malcolm Brenner at Baylor College of Medicine in Houston, Texas. All were converging on the same cancer target, a marker called CD19. The only cells sporting CD19 are B cells, which proliferate dangerously in B cell leukemias. This was valuable for two reasons. The marker was a promising bull's-eye, because it was all but universal on these cancer cells. And although B cells are an important component of the immune system, they are not needed for survival—which was reassuring, because attacking CD19 would surely destroy healthy B cells, too.

How to design the very best CAR against CD19 was the big question. CARs "come in multiple flavors," Sadelain says. There are different ways to engineer a new receptor that will latch on to CD19. One important ingredient is the "co-stimulatory signal," which is embedded

in the CAR cells to activate them and keep them alive in a patient. Sadelain's group, like the others, studied a slew of possibilities in mice and settled on one, called CD28, which looked the most promising. Rosenberg and groups at two other centers picked CD28 as well. All four had clinical trials up and running when June's trial opened.

June chose a different co-stimulatory signal, called 4-1BB, in part to distinguish his efforts and also because lab studies suggested that it helped T cells proliferate. It



Cautious optimist.
Oncologist David Porter hopes that early results will hold up as more patients are treated.

2001, shortly after her husband left the Navy and the family relocated to Philadelphia. Their daughter was 9 years old. "It took a long time to recover," he says, speaking slowly as he thinks back on those years. "A lot of people helped me out."

The ripples hit those around June, too. "We knew Cindy, we had socialized with her," Levine says. "We saw what happened and what it did to Carl. Those are hugely significant events for people, and also for the program."

was a strong candidate in mice but not quite as impressive as CD28. A group at St. Jude Children's Research Hospital in Memphis, Tennessee, led by an oncologist named Dario Campana, had designed the first CAR construct with 4-1BB. Unlike the other groups, June's also used a disabled HIV virus to genetically engineer the T cells and a different recipe for growing them in the lab.

As it turned out, combatting cancer was in the details. The first to publish an anti-CD19 CAR therapy success was Rosenberg's team in 2010. They used the CD28 strategy, and one patient with a form of lymphoma achieved a long-lasting partial remission. But it was Penn's results in the three men with leukemia, with a 4-1BB CAR, that transfixed the cancer community and the wider world.

"It made a believer out of a lot of people who were pretty skeptical," says Ravi Bhatia, who treats blood cancers at City of Hope in Duarte, California, and counts himself among past doubters. His own hospital had been studying CAR cell therapy for several years, but there and elsewhere the transplanted T cells had quickly disappeared from the bloodstream. "That," Bhatia says, "was a big concern."

June, Porter, Levine, and Grupp—who was gearing up to treat the first children—sought to stay anchored amid the hype. "You try and keep your feet on the ground and say, 'We still have work to do,'" Levine says. The competition was fierce and not always friendly. In the pages of *The New England Journal of Medicine*, Rosenberg's group and June's sparred over whether Rosenberg's CAR therapy success, published 12 months before June's, was due to engineered T cells or attributable to chemotherapy that the patient received first, to make room for new cells. "There's acrimony out there," Sadelain says.

The most bitter came in July 2012. St. Jude sued the trustees of the University of Pennsylvania for breaching materials transfer agreements signed with St. Jude in 2003 and 2007, when Campana had shared his CAR materials with June.

Penn shot back with a lawsuit of its own, arguing that June's CAR cell construct was different than Campana's. Less than 3 weeks after that suit, in August 2012, Novartis and Penn unveiled an alliance to commercialize the T cell treatment. The company said that it would devote \$20 million to build a cell therapy research center at the university.

In the months that followed, the legal dueling continued. Then in March of this year came a turning point: St. Jude's application for a patent on Campana's T cell construct, with its 4-1BB signaling domain, was approved.

Three days later, Penn sued St. Jude again, claiming that the Campana patent was invalid. That lawsuit exposed an undercurrent of concern over who owned what. Penn's lawyers are seeking "a judicial determination" that they are not infringing on the St. Jude patent.

Neither June nor Campana, who is now at the National University of Singapore, would comment on the lawsuits. Novartis spokesman Scott Young wouldn't say much either—the company is not a party to any of the three suits—but he stressed in an e-mail message that "we have complete confidence in the viability of our collaboration with UPenn."

Jumping the hurdles

That collaboration is now moving swiftly ahead. At Novartis, dozens of people are strategizing over how to manufacture personalized T cells for patients. Novartis needs to determine how long the cells can hold up outside the body, because that determines how many

costly cell-processing facilities the company must open worldwide. It has to automate its method of growing and manipulating the cells as much as possible to reduce costs and the chance of human error. It has to consider whether the time from

"vein to vein," when the cells are removed until they're put back in, can be shortened. It now stands at about 3 weeks.

"All of this has to be thought through very carefully, not only for the U.S. but also on a global scale," says Manuel Litchman, who is overseeing the therapy's development program for Novartis Oncology. In the cramped lab at Penn, Levine is busy training Novartis employees. Company officials meet several times a week with June's team. In December, Novartis paid \$43 million for

an immunotherapy manufacturing facility in Morris Plains, New Jersey, which had been owned by a company, Dendreon, making a prostate cancer vaccine. "It's not going to look that different in Morris Plains than it looks in Bruce's lab," Litchman says. "It's just going to be replicated many, many times over, to fill up the suites there."

One top priority is consistency. Every batch of T cells will be different because each originates with a different patient. But other scientific and manufacturing variables—the vector that inserts the foreign DNA, techniques to grow the cells, how they're transported—can make the outcome unpredictable.

June's group learned this the hard way: After the fanfare around their

first three patients, they treated three more in January 2012 with a new vector lot. None responded. "I was just stumped out to the max," June says. He had no idea what had happened and still can't say whether something went awry with the vector material or whether the outcome was due to random fluctuations in the therapy's success. "All we knew was, it worked three times, and then it didn't work three times." All three of those patients later died of their disease.

Next in line was patient 7, who turned out to be another roller coaster. She was Emily Whitehead, a 6-year-old with end-stage leukemia whose parents turned to June's cell therapy as a last-ditch hope. The experimental treatment sent her body into a deadly immune overdrive. She spent 2 weeks on a ventilator in the CHOP intensive care unit while doctors tried everything they could think of to save her.

"We thought it was over," June says. He drafted an e-mail message to Penn's provost: "It is with regret that I inform you that our first pediatric patient on the CART19 trial will likely die," he wrote. "There is nothing to do at this point other than hope for a miracle." June pledged to "conduct a full investigation." It turned out that he didn't need to, and the e-mail was left unsent.

As doctors parsed Emily's lab results, they found that her revved up T cells were causing overproduction of a molecule called interleukin-6. She was saved, in a tale that became hospital lore, by an arthritis drug that disables it. June knew about the drug only

"The medical literature is just littered with examples of drugs that look great on your first 10 patients, and they don't pan out."

—DAVID PORTER,
ABRAMSON CANCER CENTER
UNIVERSITY OF PENNSYLVANIA

"You try and keep your feet on the ground and say, 'We still have work to do.'"

—BRUCE LEVINE,
UNIVERSITY OF PENNSYLVANIA

Survivor. Eight-year-old Emily Whitehead was the first child on the experimental Penn protocol, and she's now cancer-free 1 year later.



because his daughter Sarah had been diagnosed with rheumatoid arthritis shortly after her mother's death. Grupp happened upon it independently, when a colleague found it by Googling on his iPhone.

Emily remains in remission more than 1 year later, her hair long enough now for pigtails and her 8th birthday behind her. In her DNA, Grupp discovered a gene mutation that predisposes to a hyperactive immune response, which could help explain why the therapy sickened her as it did. Grupp has since switched to giving other children a tenth of the T cell dose that Emily received, although "in my heart of hearts I'm not sure the dose matters that much," because the cells multiply with abandon inside the body. All those on the Penn trial became deeply attached to Emily after her harrowing experience. Levine displays pictures of her in his office. June, who remarried and now has a 10-year-old daughter of his own, chokes up when he speaks of Emily and her family.

For the Penn team, Emily and the other patients are teaching laboratories, showing what the engineered T cells can do. "I've never been involved in anything like this in my life," Grupp says. In addition to the crush of media attention and hundreds of inquir-

ies from patients and families, Grupp was taken aback by parents reporting their child's progress on Facebook before he'd shared the news with the wider scientific world. "I am in a position of having my results publicly disclosed without having them subject to peer review," he says. "That's the aspect of

"When I'm doing informed consent with these families, the first thing I say is, 'Forget everything you've read about this.' Nothing could possibly be as promising as the various articles about this make it seem."

—STEPHAN GRUPP,
CHILDREN'S HOSPITAL OF PHILADELPHIA

this I was least prepared for," and it's one that makes him "extremely uncomfortable."

Grupp has treated 14 children with acute lymphoblastic leukemia so far. Of the five reported at scientific meetings or published, four went into remission but one of those later relapsed. Porter's most recent data on adults, presented at a meeting in May, includes 10 responders out of 17 treated, with five of those in complete remission for at least 3 months.

For every T cell infused, between 1000 and 93,000 leukemia cells die, showing just how dramatically the engineered T cells are multiplying inside the body. The group is still studying why their T cells proliferate like this, although they suspect that it's partly due to the 4-1BB construct that Campana pioneered. As expected, healthy B cells are destroyed, and the long-term effects of that remain uncertain. The expense of CAR treatment has plunged, but it still costs \$20,000 to \$40,000 to generate the cells. That doesn't include supportive care in the hospital after patients receive them.

In March, Sadelain reported on five patients with acute leukemia in *Science Translational Medicine*. That disease is more aggressive than chronic leukemia in adults, and oncologists were heartened by what they read: Four of the patients went into remission, a necessary precursor to getting a bone marrow transplant, which they then received. Three are still alive at least 5 months after treatment. "That it was verified at another center, at Memorial, was very important," says Bhatia at the City of Hope. It was "not just something strange that happened" in the people treated at Penn.

Still, physicians like Porter and Grupp are mindful that this isn't life-changing for everyone. "When I'm doing informed consent with these families, the first thing I say is, 'Forget everything you've read about this,'" Grupp says. "Nothing could possibly be as promising as the various articles about this make it seem." Only four people, including Emily, have been followed for more than a year. A looming question is whether CAR therapy can work in solid tumors, and June and others are opening clinical trials to try and find out.

Nearly 3 years after the summer that changed everything, the Penn group is still working flat out to keep up: enrolling as many patients on the trials as they can, working with drug regulators to discuss how best to study the cells with an eye toward approval, collaborating with Novartis to train their employees and streamline the cell-generating process. "I'm tired," says Porter, and he sounds it. June, a serious bike racer and runner, has scaled back his hobby, though he did manage to fit in a 34-mile ultramarathon last weekend. "I didn't used to work as many hours as I do" now, he says. "I mean, I used to work, but I'd take more time off." He's eagerly waiting for the hand-off, the day when Novartis starts processing T cells and making CARs. Neither June nor Novartis can say when that will be, but for June, it will mark a return to normalcy. "Until then," he says, "it's overdrive."

—JENNIFER COUZIN-FRANKEL

CANADA

Scientists Bristle at Canadian Leader's Applied Research Push

Prime Minister Stephen Harper has drawn criticism for an autocratic style and cuts to environmental research, but supporters applaud his focus on commercialization

OTTAWA—In the aftermath of the Boston Marathon bombings in April, newly minted Liberal Party leader Justin Trudeau proposed that Canada's researchers explore the root causes of terrorism. Prime Minister Stephen Harper mocked Trudeau's suggestion, declaring that "this is not a time to commit sociology."

That response was the latest—and quintessential—example of what Harper's critics have described variously as his "anti-intellectual," "antievience," or "antiscience" attitude. An economist turned politician, Harper became Canada's 22nd prime minister in February 2006. According to his opponents, Harper soon began waging a subtle "war on science" that has only intensified since his Conservative party captured a majority of Parliament in 2011.

That war has operated on many fronts, his detractors say. Stagnant budgets for the country's three granting councils have sent a message that academic research is not a priority for the Conservative government, they say. Climate and atmospheric research have been hit especially hard as part of what critics regard as an assault on environmental stewardship.

Many scientists believe that these and other policies threaten to marginalize the federal government's entire \$11-billion-a-year research portfolio. And last month, Harper's handpicked 18-member Science, Technology and Innovation Council (STIC) provided them with additional ammunition by reporting that Canada, since Harper's election, had fallen from 16th to 23rd among industrialized nations in overall research expenditures relative to gross domestic product.

But despite the widespread belief that Harper's government has been bad for science, the reality may be far more nuanced. Harper has generally maintained funding for the raft of multibillion dollar programs begun by the predecessor Liberal government.

They include efforts to rebuild the nation's scientific infrastructure (Canada Foundation for Innovation), reverse a perceived brain drain (Canada Research Chairs), and cover the indirect costs of research.

Harper's government has even built on the underlying premises of those original investments by giving \$10 million apiece over 7 years to 20 superstar researchers in four designated priority areas: the environment; natural resources and energy; health;



Arctic priority. Prime Minister Stephen Harper (center) in a tour last year of the High Arctic Research Station in Cambridge Bay, which boasts a fishing trawler refitted as a research vessel.

and information and communication technologies. And in 2011, the government announced its plans for a second competition to set up 10 more superstars.

The Harper government has also been eager to toss large pools of money at specific disciplines and groups, often without peer review. In 2007, Harper gave seven existing research institutes a total of \$105 million to establish Centres of Excellence for Commercialization and Research (CECRs) and then held a \$195 million competition that resulted in the creation of 14 more. In 2009, it launched a \$100 million brain research initiative led by a private foundation whose honorary chair was a former Conservative finance minister.

Taken together, these policies show that Harper is "a great supporter of science," says Gary Goodyear, Harper's minister of state for science and technology. A chiropractor who assumed his current post in 2008,

Goodyear says that his instructions were to ensure the health of the "entire ecosystem" of Canadian science, from fundamental to applied research. "And if you can create any jobs by Saturday, do it," he quips.

Scientific mercenaries?

For its part, the Harper government doesn't apologize for its focus on wealth creation. Study after study has shown that Canada's industrial sector is heavily based on natural resources and reluctant to invest in research. The only multinational juggernaut remaining in the country is besieged communications innovator BlackBerry (formerly Research In Motion).

Dealt a weak hand, the Harper government is simply trying to overcome chronic problems in Canada's innovation system, says Alan Bernstein, president of the Canadian Institute for Advanced Research in

Toronto. Those deeply rooted flaws, he says, include the fact that Canadians are "risk-averse" by nature, live in the shadow of a scientific superpower, and have a branch-plant economy with a weak venture capital community. Even the world's most generous R&D tax credits have done little to promote industrial research.

However, Harper's top-down initiatives and his demand that the academic community become more directly involved in the commercialization of research have infuriated scientists. Some argue that the government's propensity for large, elitist programs is an

assault on the fundamental tenets of investigator-initiated research that is eroding the health of the scientific base. Others are simply queasy about being nudged into becoming what some call "mercenaries for industry."

It's difficult to determine, however, if the changes pursued by Harper have affected the nature of research that Canadian scientists are conducting, says Timothy Caulfield, Canada Research Chair in Health Law and Policy at the University of Alberta. Some shifts may just be cosmetic, he says, involving minor modifications in the way that grants are written. "Researchers are nimble. They know how to get money."

Still, Caulfield is skeptical that the government will achieve the desired economic transformation. "Part of the package of justification is that it will lead to economic growth," he says. "But the evidence is thin that a commercialization directive from the government leads to economic growth."

Harper's Science Project



Playing favorites. Programs with the potential for economic payoff have received the most attention in the research garden of Canadian Prime Minister

Stephen Harper. At the same time, core research activities and many environmental initiatives have stagnated or withered away under his government.

Still, the Harper government has been nothing if not steadfast in using science as a tool to restructure the economy. It has heavily promoted academic collaborations with industry, including roughly \$255 million sunk into the 21 CECRs structured around subjects such as vaccine development, imaging technology, surgical innovation, and energy efficiency. The latest manifestation of that philosophy was last month's announcement that Canada's National Research Council (NRC), the government's primary in-house research arm, is being converted into a toolbox for industry.

Goodyear says that the government, having solidified support for fundamental research, is now turning its attention to the other end of the innovation chain. Transformation of NRC, efforts to spur industry-academic collaborations, and the creation of new pools of venture capital, like the \$400 million that the government set aside last year, are all designed to make industry more innovative and productive. More of the same will soon follow, Goodyear hints, possibly in the form of expanded procurement programs. "This isn't a picture or an x-ray," he says. "Our strategy is a video. You haven't seen the next chapter yet."

Scientists say that the book is quite clear when it comes to Harper's attitude toward environmental research and regulation. While Harper's supporters argue that the government's policies are simply a way to remove an impediment to economic development, most scientists regard them as an egregious example of a wrong-headed ideology and the prime minister's tight control over all government activities.

For example, when Harper announced in 2011 that Canada was bailing from the Kyoto Protocol, the global treaty to limit greenhouse gas emissions, (which Harper once called a "socialist conspiracy"), his rationale was that meeting the treaty's targets would cripple the country's economy. A similar rationale was offered in 2012, when government ministers gained the authority to override environmental assessments in approving industrial projects, and again this spring, when the government announced that it would withdraw from the U.N. Convention to Combat Desertification.

A slew of environmental programs have been axed since Harper earned a majority government, including the Canadian Foundation for Climate and Atmospheric Sciences (a nonprofit organization that dis-

tributed funds to research facilities such as the Polar Environment Atmospheric Research Laboratory), the National Round Table on the Environment and the Economy (which advocated the introduction of carbon taxes, which Harper finds anathema), the Ocean Contaminants and Marine Toxicology Program, the World Ozone and Ultraviolet Radiation Data Centre, and the Experimental Lakes Area program. Such moves are a far cry from Harper's decision in 2007, as head of a minority government, to spend \$2 billion on a pair of clean environmental technology programs that sought to develop "green energy generation and transmission infrastructure, carbon transmission and storage infrastructure."

Researchers say it's no coincidence that a policy requiring government scientists to obtain permission from Harper's office before speaking to the media seems so often to impinge on environmental researchers. Last year, 2000 researchers in lab coats descended on Parliament Hill for a mock funeral for the "death of evidence." The policy has spurred an ongoing investigation by the federal information commissioner into whether Harper has placed undue limits on the ability of federal scientists to disseminate findings.

CREDIT: G. GRULLON/SCIENCE

Goodyear dismisses the proposition that the government has trained its guns on the environmental sciences. “The perception is wrong,” he says, quickly pointing to the \$135 million that the Natural Sciences and Engineering Research Council of Canada (NSERC) set aside for climate change research.

One environmental area that has benefited from Harper’s policies is Arctic science. Harper’s support for consolidating Canadian control of its Arctic territory has long been tagged as his personal “legacy” project. That has translated into commitments such as building a Canadian High Arctic Research Station and launching three next-generation Constellation radar satellites, a project with an estimated price tag topping \$1 billion.

Those initiatives haven’t placated critics. Andrew Weaver, Canada Research Chair in Atmospheric Sciences at the University of Victoria and a member of the British Columbia legislature from the Green Party, accuses Harper of trying to “control the message” on climate and related issues by either ignoring or suppressing evidence that is antithetical to his objectives, such as developing Alberta’s oil sands.

To Scott Findlay, associate professor of biology at the University of Ottawa, Harper’s Arctic policy demonstrates his willingness to run roughshod over evidence if it challenges government priorities or orthodoxy. He and other scientists argue that the same ethic led to Harper’s decision in 2008 to eliminate the position of national science adviser, his scuttling of Statistics Canada’s mandatory long form census in 2010, and his axing this year of the Health Council of Canada.

Abolishing the national science adviser’s position was particularly egregious, says Kennedy Stewart, science critic for the opposition New Democratic Party. The result, he says, is that the Harper government is now crafting science policy “without getting advice from scientists.”

The shift to a voluntary census, meanwhile, prompted the resignation of then-Chief Statistician Munir Sheikh. It was ostensibly made because libertarian backbenchers within Harper’s caucus were fretting that a Canadian might be charged with failing to fill out a census form. And many fear that the elimination of the national health council, part of a broader policy to leave the provinces entirely in charge of health care, puts Canada on the fast track to becoming 14 splintered systems.

These and other policy moves have left many scientists feeling that they’re the victims of “bad science policy,” argues Cana-

dian Association of University Teachers Executive Director Jim Turk. Another poster child for those “bad” decisions, he and others say, is the loss of purchasing power by Canada’s granting councils, which fund academic science.

Years of flat budgets for NSERC, the Canadian Institutes of Health Research (CIHR) and the Social Sciences and Humanities Research Council (SSHRC), at about \$1 billion, \$1 billion, and \$700 million, respectively, mask an enormous transformation in their operations, Turk says. What modest increases they’ve received have often been tied to industrial programming or targeted at community colleges (which, prior to Harper, were precluded from tapping council budgets). In addition, as a general rule, the increases have merely offset the effects of multiyear cuts imposed during various deficit reduction exercises.

The councils have coped with no-growth budgets in different ways. CIHR, for example, has opted to help grantees keep up with rising costs by offering larger grants to fewer researchers, whereas NSERC has decided to increase the share of its budget going to promote industrial collaborations. Its so-called “fettered” research has grown in the past 5 years from \$208 million to \$360 million, while expenditures on basic research grants have dropped from \$389 million to \$322 million over the same period.

As a result, the core budgets of each council have plummeted since 2007: The drop is 6.4% for NSERC, 7.5% for CIHR, and 10.1% for SSHRC. Not surprisingly, the success rate for discovery grants has also sunk, from 21% to 9% at CIHR, from 73% to 62% at NSERC, and from 40% to 27% at SSHRC, Turk says.

Divided opinions

University of Toronto professor of mathematics James Colliander says that the largest impact of Harper’s policies on academic scientists has been a shift in the incentive system to reward those whose work has industrial application. “What the government is in some sense saying is: These eclectic people, with their ideas at the edge of knowledge of all human beings, are not important in Canada. Instead, we want those people in the academy that are closer to the business questions to be rewarded with funding. That’s the message that is illumi-

nating the exit signs for scientists and engineers to depart from Canada because their special skills aren’t valued.”

Gregory Marchildon, Canada Research Chair in Public Policy and Economic History at the University of Regina, says that the “federal government is dismantling key aspects of the scientific infrastructure” and that it will take “a generation or two to rebuild” the damage. The opposition’s Stewart says that the Harper government is coasting on investments past and that its strategy of “barking an order at someone” and telling them “to go from being a scientist to somebody who does industrial applications” is doomed to fail.

But Harper’s supporters say that the criticism of his policies is little more than overheated rhetoric from a disgruntled community that now finds itself forced to survive on

less-than-Cadillac budgets in an era of fiscal constraints. Canadian science is actually quite robust, argues Eliot Phillipson, Sir John and Lady Eaton Professor of Medicine Emeritus at the University of Toronto. Phillipson chaired a Council of Canadian Academies’ panel that

found only two fields—natural resources and environmental S&T—had lost ground between 2005 and 2010.

The expressions of anxiety are a function of a culture that is forever fretting about future funding, he adds. “It’s part of the scientific DNA.”

Harper’s critics see the 2015 election—and a new prime minister—as the only way to get the country’s scientific enterprise back on track. But Bernstein, who once led CIHR and the Global HIV Vaccine Enterprise, argues that the growing polarization and unease could be erased if Canada simply abandons its “out-of-date” debate over basic versus applied research and sets ambitious national science targets.

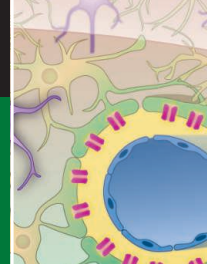
“I think we need to raise our sights,” he says. “I don’t think we should strive to be in the middle of the pack. It’s no different than the ‘Own the Podium’ approach that Canada used in the Olympics,” he explains, a strategy in which lavish funding for training produced an abundance of medal winners at the 2010 Vancouver Winter Games. “There’s no reason that Canada shouldn’t be at the very top, and we’re not.”

—WAYNE KONDRO

Wayne Kondro is a freelance writer in Ottawa.

“The evidence is thin that a commercialization directive from the government leads to economic growth.”

—Timothy Caulfield,
University of Alberta



LETTERS

edited by Jennifer Sills

Coral Diseases Cause Reef Decline

THERE HAS BEEN A GREAT DEAL OF DISCUSSION ABOUT THE ROLE OF BLEACHING IN CORAL REEF degradation worldwide (1–3), but little focus on the numerous other coral diseases that are also causing substantial declines.

In the late 1970s and 1980s, disease caused extensive mortality in elkhorn coral (*Acropora palmata*) and staghorn coral (*A. cervicornis*), radically changing the shallow Caribbean seascape (4). The damage was so severe that these species became the only corals listed as threatened under the U.S. Endangered Species Act (5). More recently, almost all stony coral (*Scleractinia*) species in the Caribbean have been affected by one or more diseases. White plague and Caribbean yellow band have been particularly devastating in the Caribbean, causing declines in living coral cover of more than 50 to 60% (6–8). Diseases are becoming more widespread on Pacific reefs as well (9).



Diseased reef-building coral in the Caribbean.

Bleaching occurs with the disintegration and expulsion of symbiotic microalgae from corals, usually in association with higher seawater temperatures. Bleached corals are still alive, and bleaching is reversible if temperatures cool quickly enough. Bleaching differs from diseases that are associated with initial tissue loss.

Disease outbreaks are not as predictable as bleaching episodes; sometimes extensive reef areas become diseased without any preceding bleaching event or several months after bleaching (8). Diseases can kill individual corals in the absence of any major outbreaks, causing inconspicuous but damaging incremental losses. Even low levels of disease can have serious consequences if they are chronic.

With climate change, seawater temperatures are predicted to increase and bleaching episodes are expected to become more frequent. However, the relationships among increasing seawater temperatures, bleaching, and disease have not been well-established (10).

To prevent and treat diseases as well as bleaching, we must conduct further research on the links between human actions and coral reef condition, as well as on the potential for reef resilience. Reducing stressors such as excess nutrients from sewage or high levels of sedimentation could make corals less likely to bleach or become diseased, and/or more likely to recover (11–14).

CAROLINE S. ROGERS^{1*} AND JEFF MILLER²

¹Southeast Ecological Science Center, U.S. Geological Survey, St. John, VI 00830, USA. ²SF/CN Inventory and Monitoring Network, National Park Service, St. John, VI 00830, USA.

*Corresponding author. E-mail: caroline_rogers@usgs.gov

References

1. C. Schmidt, *Science* **339**, 1517 (2013).
2. B. Polidoro, K. Carpenter, *Science* **340**, 34 (2013).
3. J. P. Gilmour *et al.*, *Science* **340**, 69 (2013).
4. R. B. Aronson, W. F. Precht, *Hydrobiologia* **460**, 25 (2001).
5. W. T. Hogarth, *Federal Register* **71**, 26852 (2006); www.nmfs.noaa.gov/pr/pdfs/fr/fr71-26852.pdf.
6. D. L. Ballantine *et al.*, *Coral Reefs of the USA*, B. Riegl, R. E. Dodge, Eds. (Springer, Dordrecht, 2008), chap. 9.
7. A. Cr  quer, E. Weil, *Dis. Aquat. Organisms* **83**, 209 (2009).
8. J. Miller *et al.*, *Coral Reefs* **28**, 925 (2009).
9. B. L. Willis *et al.*, in *Coral Health and Disease*, E. Rosenberg, L. Loya, Eds. (Springer, Berlin, 2004), chap. 3.
10. C. S. Rogers, *ISRN Oceanogr.* **2013** 10.5402/2013/739034 (2013).
11. J. F. Bruno *et al.*, *Ecol. Lett.* **6**, (2003).
12. J. E. Carilli *et al.*, *PLoS ONE* **4**, e6324 (2009).
13. S. A. Wooldridge, T. J. Done, *Ecol. Appl.* **19**, 1492 (2009).
14. J. Haapkyl   *et al.*, *PLoS One* **6**, e16893 (2011).

Reversing Excess Atmospheric CO₂

IN THEIR PERSPECTIVE “IRREVERSIBLE DOES not mean unavoidable” (26 April, p. 438, published online 28 March), H. D. Matthews and S. Solomon state that the effects of past anthropogenic CO₂ emissions are “irreversible on a time scale of at least 1000 years.” Recent research suggests that this may not be true. A variety of carbon cycle interventions have been proposed, which in theory could substantially add to the natural, slow removal of atmospheric CO₂ [e.g., (1–4)] and/or increase the retention of carbon on land or in the ocean [e.g., (5–8)].

The natural fluxes of CO₂ into and out of the atmosphere, each more than 700 Gt/year, are exquisitely balanced, and individually dwarf the annual CO₂ input from human activity (9). Creating a relatively small decrease in this ratio of input to output CO₂

by means of active management of natural fluxes [e.g., (2, 7, 8)], purely artificial strategies [e.g., (1, 3)], or hybrid approaches [e.g., (1, 5, 6)] could therefore hasten the removal of CO₂ from the atmosphere. Indeed, the sensitivity of atmospheric CO₂ concentration to natural variations in this ratio is clearly evident in this concentration's seasonal rise and fall (10).

The cost-effectiveness, safety, capacity, and environmental and societal desirability of proactively reducing atmospheric CO₂ input/output (in addition to reducing anthropogenic CO₂ emissions) have yet to be fully evaluated. Until these strategies are better understood, it is premature to conclude that removal of existing, excess atmospheric CO₂ cannot be accelerated. Such methods may indeed prove essential given our ongoing failure to reduce our CO₂ emissions and, hence, to stabilize if not lower historically unprecedented atmospheric CO₂ concentrations (10) and associated effects on climate and ocean chemistry.

GREG H. RAU¹* AND KLAUS S. LACKNER²

¹Institute of Marine Sciences, University of California, Santa Cruz, CA 95064, USA. ²Department of Earth and Environmental Engineering, Columbia University, New York, NY 10027, USA.

*Corresponding author. E-mail: ghrau@sbcbglobal.net

References

1. D. W. Keith, M. Ha-Duong, J. K. Stolaroff, *Clim. Change* **74**, 17 (2006).
2. T. M. Lenton, *Carbon Manage.* **1**, 145 (2010).
3. K. S. Lackner et al., *Proc. Natl. Acad. Sci. U.S.A.* **109**, 13156 (2012).
4. G. H. Rau, in *Handbook of Global Environmental Pollution, Vol. 1: Global Environmental Change*, B. Freeman, Ed. (Springer, New York, 2013); www.springerreference.com/docs/html/chapterdbid/303451.html.
5. S. E. Strand, G. Benford, *Environ. Sci. Technol.* **43**, 1000 (2009).
6. D. Woolf et al., *Nat. Commun.* **1**, 10.1038/ncomms1053 (2010).
7. J. M. Kimble, R. Lal, R. Birdsey, L. S. Heath, *The Potential of U.S. Forest Soils to Sequester Carbon and Mitigate the Greenhouse Effect* (CRC Press, Boca Raton, FL, 2010).
8. M. A. Liebig, A. J. Franzluebbers, R. Ronald, F. Follett, *Managing Agricultural Greenhouse Gases* (Academic Press, London, 2012).
9. I. C. Prentice et al., in *Climate Change 2001: The Scientific Basis: Contribution of Working Group I to the Third Assessment Report of the Intergovernmental Panel on Climate Change*, J. T. Houghton, Ed. (Cambridge Univ. Press, Cambridge, 2001), pp. 183–237.
10. Scripps Institution of Oceanography, Keeling Curve (<http://keelingcurve.ucsd.edu/>).

Response

RAU AND LACKNER SUGGEST THAT WE SHOULD qualify our statements about the irreversibility of anthropogenic climate change with a caveat acknowledging the possibility of future technological interventions that can either actively remove CO₂ from the atmosphere or artificially cool the planet by reflecting solar radiation. We agree that it is important to discuss and debate the potential utility and effectiveness of carbon dioxide removal technologies as a future strategy to decrease atmospheric CO₂ concentrations. However, we do not feel these technologies will be relevant for the time scales we discussed in our Perspective.

Geoengineering interventions involving solar reflection do not constitute true reversibility of climate change. This type of intervention would only temporarily decouple global temperatures from rising atmospheric CO₂ concentrations (1), would lead to continuing ocean acidification (2), and could increase the risk of damaging changes in rainfall patterns (3, 4).

Some carbon cycle geoengineering technologies may provide true reversibility by accelerating the removal of anthropogenic CO₂ from the atmosphere. If these technologies were combined with aggressive mitigation efforts, they could potentially meet long-term climate targets that would otherwise be inaccessible (5, 6). However, although such technologies may be effective in principle, and some have been subjected to limited tests, at present most remain far from development or implementation (7). In addition, many such technological interventions in the climate system also carry the potential for environmental damage that may far exceed the climate benefit of sequestered CO₂ (8).

Finally, technologies that hold the largest promise with the least potential for harmful side effects [notably those in the area of direct air CO₂ capture (9, 10)] are also thought to be very expensive and unlikely to be implemented on the time scale of the infrastructure commitments to carbon-intensive energy sources with which our article is concerned (5).

In a discussion of the potential for immediate or near-future action to slow the growth of atmospheric CO₂, we suggest that consideration of carbon dioxide removal (or other geoengineering) technologies would at best be not very relevant, and at worst could distract from the imperative of decreasing investment in energy technologies that lead to large CO₂ emissions.

DAMON MATTHEWS¹* AND SUSAN SOLOMON²

¹Department of Geography, Planning and Environment, Concordia University, Montreal, QC H3G 1M8, Canada.

²Department of Earth, Atmospheric and Planetary Sciences, Massachusetts Institute of Technology, Cambridge, MA 02139, USA.

*Corresponding author. E-mail: damon.matthews@concordia.ca

References

1. H. D. Matthews, K. Caldeira, *Proc. Natl. Acad. Sci. U.S.A.* **104**, 9949 (2007).
2. H. D. Matthews, L. Cao, K. Caldeira, *Geophys. Res. Lett.* **36**, L10706 (2009).
3. K. E. Trenberth, A. Dai, *Geophys. Res. Lett.* **34**, L15702 (2007).
4. A. Robock, L. Oman, G. L. Stenchikov, *J. Geophys. Res. Atmos.* **113**, D16101 (2008).
5. H. D. Matthews, *Carbon Manage.* **1**, 135 (2010).
6. T. M. Lenton, *Carbon* **1**, 145 (2010).
7. The Royal Society, "Geoengineering the climate: science, governance and uncertainty" (The Royal Society, London, 2009).
8. H. D. Matthews, S. E. Turner, *Environ. Res. Lett.* **4**, 045105 (2009).
9. D. Keith, M. Ha-Duong, J. Stolaroff, *Clim. Change* **74**, 17 (2006).
10. K. S. Lackner et al., *Proc. Natl. Acad. Sci. U.S.A.* **109**, 13156 (2012).

Good Grades for Dual Education

IN THE EUROPEAN UNION, 23.2% OF PEOPLE ages 15 to 24 (roughly 6 million people) are unemployed (1). Surprisingly, EU youth unemployment is higher in countries where more young people have university degrees. In France, Greece, and Spain, surveys show that 43, 42, and 39%, respectively, of people ages 25 to 35 have university degrees, compared with only 25% in Germany (2). However, the average youth unemployment has risen to 26.5% in France, 57.9% in Greece, and 55.9% in Spain, whereas in Germany it is only 7.6% (1).

One explanation for this discrepancy may be Germany's vocational education model. Referred to as dual education, this system combines classroom and business, theory and practice, and learning and working. It has been widely recognized as contributing to Germany's employment of young people (3, 4). More than 50% of German high school students enroll in the dual-education system instead of traditional higher education (5). In contrast, few high school graduates in

France choose vocational education (3, 6). Rather than improving youth skill through vocational education, the French government has relied on ambitious job creation plans for young people since the mid-1990s (4, 7). For example, the French government released a plan in 2009 to provide €1.3 billion (\$1.7 billion) in tax breaks and cash incentives for employers who hired young people. However, the track record of targeted programs is dismal, and youth unemployment in France has continued to rise (1).

Youth unemployment in the European Union reminds us that there is a deepening mismatch between what the labor mar-

ket needs and what the education system is producing. It is time to reform the current higher education system to prevent the most educated generation of young people from becoming a generation of the unemployed.

XI CHEN AND QIANG WANG*

Western Research Center for Energy and Eco-Environmental Policy, State Key Laboratory of Desert and Oasis Ecology, Xinjiang Institute of Ecology and Geography, Chinese Academy of Sciences, Urumqi 830011, China.

*Corresponding author. E-mail: qiangwang7@gmail.com

References

1. Eurostat, "Euro area unemployment rate at 12.2%" (2013); http://epp.eurostat.ec.europa.eu/cache/ITY_PUBLIC/3-31052013-BP/EN/3-31052013-BP-EN.PDF.

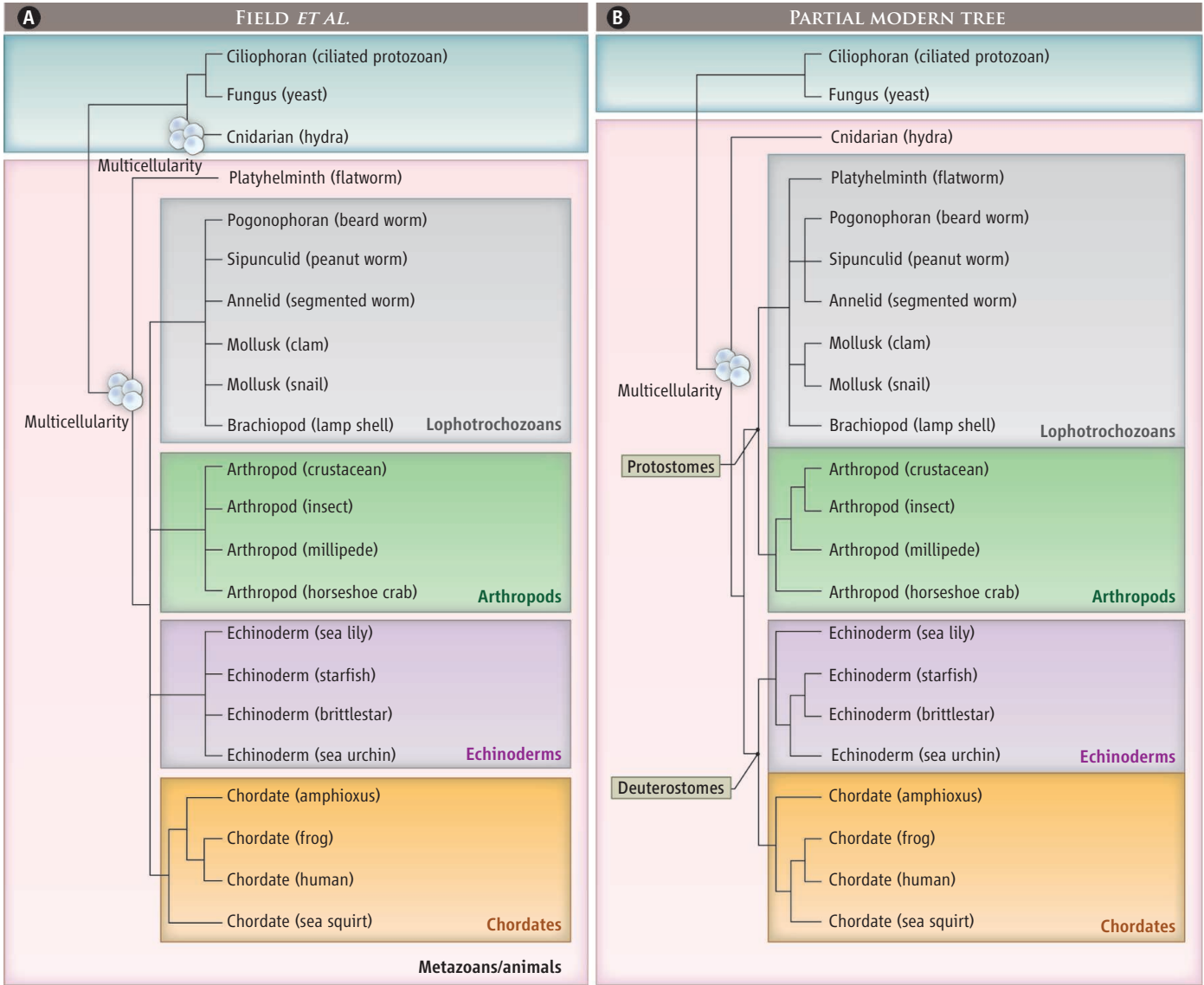
2. OECD, "Education at a Glance 2012 OECD indicators" (OECD Publishing, 2012); <http://dx.doi.org/10.1787/eag-2012-en>.
3. A. Wolf, "Review of vocational education: The Wolf report" (Department of Education, London, 2011).
4. Economist, "Youth unemployment: Generation jobless," *Economist* (27 April 2013).
5. M. Brockmann, L. Clarke, C. Winch, *Oxford Rev. Educ.* **34**, 547 (2008).
6. J. J. Powell, L. Graf, N. Bernhard, L. Coutrot, A. Kieffer, *Eur. J. Educ.* **47**, 405 (2012).
7. S. Bentolila, P. Cahuc, J. J. Dolado, T. Le Barbanchon, *Econ. J.* **122**, F155 (2012).

Letters to the Editor

Letters (~300 words) discuss material published in *Science* in the past 3 months or matters of general interest. Letters are not acknowledged upon receipt. Whether published in full or in part, Letters are subject to editing for clarity and space. Letters submitted, published, or posted elsewhere, in print or online, will be disqualified. To submit a Letter, go to www.submit2science.org.

CORRECTIONS AND CLARIFICATIONS

Perspectives: "The animal tree of life" by M. J. Telford (15 February, p. 764). In the original figure, the symbol indicating multicellularity in the main group of animals was misplaced in both panels. The symbols have now been placed in the correct position. The revised figure is shown here. The figure has been corrected in the HTML and PDF versions online.



ENVIRONMENTAL HISTORY

Worlds Built on Avian Excrement

Frederick R. Davis

Suppose you decided to write a global environmental history of the Pacific world. Suppose further that after you peeled away the layers of large-scale climate fluctuations, continent-island dynamics, and the displacement of indigenous cultures for imperial enterprise and colonization, you discovered the heart of the matter, in all its slimy, slippery, smelly glory: bird shit. For the faint of heart:

guano. In *Guano and the Opening of the Pacific World*, Gregory Cushman pursues this thought experiment with utterly magnificent results.

To be fair, Cushman (a historian at the University of Kansas) acknowledges from the outset that excrement, avian or not, hardly serves as a topic for polite conversation. Disclaimers out of the way, he plunges into his topic arguing for the fundamental role of nitrogenous waste in the development of agricultural systems. Appropriately, the originary story comes from indigenous sources in which a trickster escapes retribution with a disingenuous yet elemental excuse.

Guano covers grand expanses of time and space. The second chapter, for example, opens with Alexander von Humboldt's encounter with guano in Peru. Cushman then argues that after laboratories in Napoleonic Europe established Peruvian guano and nitrates as the two richest sources of nitrogen ever discovered, they fueled the Northern Hemisphere's ambitious demands for plantation crops, meat, sulfuric acid, high explosives, and imperial power. He concludes the chapter with the War of the Pacific (1879–1884), which was triggered by a devastating El Niño event and led to the withdrawal of Peru from the “guano age.” Notwithstanding his focus on major events and ideas, a charming element of family history surfaces here and elsewhere: Cushmans (some related, others not) dot the story like far-flung Pacific islands.

To explain how colonial regions in Australia, New Zealand, Chile, and the United

States consolidated and sustained their prosperity after exploiting the resources of initial colonization, Cushman offers “neo-ecological imperialism,” thereby refining a concept developed by Alfred Crosby (1). Indigenous peoples on Easter Island, Banaba, Niue, and other Pacific islands participated in the exploitative ecological regime for various reasons, thus securing survival despite suffering the onslaught

of microbes in the form of dysentery and other diseases as well as parasitic forms of colonial trade and government.

The 20th century ushered in the era of technocracy in the guano islands as Peru sought to capitalize on their benefits. Collaborating with agro-exporters and capitalists, foreign and local scientists and engineers helped buffer the islands from the exploitation of global capitalism and World War I. During the interwar period, a single company consolidated these efforts and laid the foundation for the scientific conservation of guano-producing birds. Although Peruvian technocrats continued to manage the “most valuable birds in the world,” populations remained vulnerable to the extreme regional climatic shifts in the region, which gave rise to boom and bust years (of birds and guano). For this and other reasons, Cushman argues, Peru could not hope to feed its burgeoning population, at least not solely on the basis of agricultural nutrients from guano.

The book reveals ornithologist William Vogt to be a strong candidate for the most underrated figure in the modern environmental movement. Vogt's Peruvian-funded research on the guano islands and subsequent conservation surveys in Latin America led him to present a Malthusian case in *The Road to Survival* (2), some 14 years before Rachel

Carson's renowned critique of pesticides. He follows the recommendations of Aldo Leopold (a longtime friend) with respect to species management. Moreover, Vogt believed that guano could help address the challenge of feeding a growing world population.

Insofar as ecology, in Cushman's view, has the power to shape culture, geopolitical events such as World War II transformed nature and culture in the Pacific world. During and after the war, Pacific islanders found themselves uprooted without respect to their livelihoods. On the roster of deracinated islanders, Cushman includes Yali, whose query regarding global inequalities motivated Jared Diamond (3). Cushman, contra Diamond, argues that given the opportunity Yali could have offered personal insights into the social inequities that prompted his question.

Guano played a substantial role in the Green Revolution in Mexico, which saw dramatically improved crop yields through the introduction of novel technologies in the form of new wheat cultivars, pesticides,



Most important source. Guanays (Peruvian cormorants), *Phalacrocorax bougainvillii*, make the largest contribution to Peru's guano. [Painting by Francis Lee Jacques from 1936 book by Robert Cushman Murphy (5).]

and, especially, fertilizers. Not surprisingly, Cushman suggests that Peru's Blue Revolution, the parallel expansion of marine resources through new inputs, also rested on a foundation of guano. Yet, technocrats made surprising choices in abandoning the guano birds to eliminate competition for Peru's chemical industry. Rather than revealing the need for intervention at the level of the state, as Garret Hardin argued in “The tragedy of the commons” (4), this displayed governmental technocratic overconfidence

Guano and the Opening of the Pacific World
A Global Ecological History

by Gregory T. Cushman
Cambridge University Press,
Cambridge, 2013. 414 pp.
\$99. ISBN 9781107004139.

in their ability to overcome dramatic swings in the ocean's productivity.

Given the book's remarkable breadth and depth, it is tragic that the exigencies of academic publishing have set the price beyond the reach of the casual reader. One can only hope that paperback and e-book editions are forthcoming. That said, *Guano and the Opening of the Pacific World* is a tour de force that deserves a wide audience. Cushman covers an expansive range of topics that flow from its humble source and offers persuasive arguments that challenge many aspects of received wisdom regarding natural versus cultural, indigenous versus colonial, island versus mainland, and local versus global.

References

1. A. W. Crosby, *Ecological Imperialism: The Biological Expansion of Europe, 900–1900* (Cambridge Univ. Press, Cambridge, ed. 2, 2004).
2. W. Vogt, *The Road to Survival* (W. Sloane, New York, 1948).
3. J. M. Diamond, *Guns, Germs, and Steel: The Fates of Human Societies* (Norton, New York, 1997).
4. G. Hardin, *Science* **162**, 1243 (1968).
5. R. C. Murphy, *Oceanic Birds of South America* (Macmillan and American Museum of Natural History, New York, 1936).

10.1126/science.1239339

NEUROSCIENCE

Between Brain and Imaging Hype

Charles Gross

Neurophilosophy, neuromarketing, neuroliterature, neurolaw, neurotheology, neuroaesthetics, neuroeconomics, neuromusicology, and neuropolitics are some of the applications of brain imaging now flooding academia and the popular press. A critical reaction against “neurohype,” “neuromania,” and “neurobollocks”—this imperialist attempt of “neuroscience” to swallow other disciplines—is also growing. *Brainwashed: The Seductive Appeal of Mindless Neuroscience* offers a set of cautionary essays on unproven or incorrect claims about the applications of neuroimaging, particularly functional magnetic resonance imaging (fMRI). Authors Sally Satel (a psychiatrist in Washington, D.C.) and Scott Lilienfeld (a clinical psychologist at Emory University) provide an elementary introduction to fMRI and discuss important problems and pitfalls

in the design and analysis of MRI studies. In general, they are hardly Luddites, being very sympathetic to the potential power of imaging to understand the brain.

Satel and Lilienfeld consider five areas of applications of neuroimaging, beginning with neuromarketing, the use of fMRI and electroencephalography (EEG) scans to assess customer preferences. The effectiveness of such growing techniques remains unclear, as most company data are kept secret. It is even uncertain whether they are more effective than focus groups. Although the authors' account is interesting, because the results of neuromarketing are unlikely to be more deceptive or misleading than other marketing techniques, there seems to be little to fuss over scientifically or ethically. At worst, the apparently high costs of neuromarketing research will be passed on to the consumer.

In their chapter on addiction, the authors very strongly oppose the view—advanced, for example, by the U.S. National Institute on Drug Abuse—that “addiction is a brain disease.” As they put it,

The neurocentric perspective encourages unwarranted optimism regarding pharmaceutical cures and oversells the need for professional help. It labels as “chronic” a condition that typically remits in early childhood. The brain-disease story gives short shrift to the reality that substances serve a purpose in addicts' lives and that neurobiological changes induced by alcohol and drugs can be overridden.

These claims seem doubtful. Most studies find a paucity of professional help for addicts, and some conventional diseases remit. The authors' belief that “the most effective interventions aim not at the brain but at the person” seems to contradict their admission that life experiences affect the brain. Do they really think that dealing with the personal and emotional needs of addicts is dealing with something other than a disturbed brain? Of course, talk therapy may be as effective for treating brain disturbances as pharmacology.

More valuable is the critique of the use of imaging for lie detection. In spite of the extraordinary claims of several lie-detecting firms, Satel and Lilienfeld cite overwhelming evidence that the use of imaging for reliable lie detection in the real world is inconceivable (at least for the foreseeable future).

In the chapter “My amygdala made me do it,” the authors discuss the increasing use of imaging in the courtroom. They note how, at least for mock juries in the laboratory, the presentation of imaging evidence can be very deceptive. They conclude that the potential for functional brain imaging to mislead currently exceeds its capacity to inform, although the ratio may eventually shift in favor of the value of scans for some purposes as technical advances emerge.

Because most biological scientists (including the authors) believe that behavior is a function of the brain whose properties are determined by genetics and experience, one wonders where that leaves moral responsibility and “free will.” In an unoriginal discussion, Satel and Lilienfeld favor “compatibilism”—as did Aristotle (384–322 BCE) and, more recently, Thomas Hobbes (1588–1679) and David Hume (1711–1776). In the authors' formulation,

Even if human beings lack ultimate freedom (that is, they lack the capacity to have done otherwise), we can consider mentally intact adults morally responsible because they have the abilities to engage in conscious deliberation, follow rules, and generally control themselves.

Perhaps most interesting is their attention, in their defense of retributive justice, to the emotional needs of crime victims.

The most valuable part of this timely series of essays is the extensive set of endnotes, which include important papers and books. However, many of the notes take a position different from or irrelevant to the text. Furthermore, given historical and other errors, it is not clear to what extent the authors are familiar with this material.

Unfortunately, *Brainwashed* includes little about major technical developments in the past decade, such as diffusion tensor analysis (a method of studying brain connections) or the analysis of the temporal relations among activity in different brain areas. And nowhere do the authors even mention the problems of relating fMRI activation to the underlying neuronal activity. Satel and Lilienfeld are correct that imaging claims garner many pop-science headlines. But in casting their critical net over “neuroscience,” they seem unaware that most contemporary neuroscientists are not (yet) brain imagers but molecular or systems neuroscientists.

10.1126/science.1240697

Brainwashed The Seductive Appeal of Mindless Neuroscience

by Sally Satel and
Scott O. Lilienfeld

Basic Books, New York,
2013. 250 pp. \$26.99, C\$30.
ISBN 9780465018772.

The reviewer is at the Department of Psychology and Princeton Neuroscience Institute, Princeton University, Princeton, NJ 08544, USA. E-mail: cggross@princeton.edu

GLOBAL HEALTH

The Global Prevalence of Intimate Partner Violence Against Women

K. M. Devries,^{1†} J. Y. T. Mak,¹ C. García-Moreno,^{2*} M. Petzold,³ J. C. Child,¹ G. Falder,¹ S. Lim,⁴ L. J. Bacchus,¹ R. E. Engell,⁴ L. Rosenfeld,⁴ C. Pallitto,^{2*} T. Vos,⁴ N. Abrahams,⁵ C. H. Watts¹

Violence against women is a phenomenon that persists in all countries (1). Since the 1993 World Conference on Human Rights and the Declaration on the Elimination of Violence against Women, the international community has acknowledged that violence against women is an important public health, social policy, and human rights concern. However, documenting the magnitude of violence against women and producing reliable comparative data to guide policy and monitor progress has been difficult.

The most common form of violence that women experience is from an intimate partner (IPV). This violence may be physical, sexual, or emotional. Most research to date has focused on assessing the prevalence and impacts of physical and/or sexual violence by partners. The short- and long-term health impacts of women's exposures to physical and/or sexual IPV are multiple (2). For example, it is a leading cause of homicide death in women globally (3) and is associated with increased levels of depression and suicidal behaviors (4). Prospective research from South Africa and Uganda shows that women exposed to physical and/or sexual IPV are more likely to acquire HIV infection (5, 6). The health and social impacts result in substantial economic costs, with one study estimating the cost of IPV at more than £15 billion in England and Wales in 2009 alone (7).

There are high-level global commitments to addressing violence against women and gender inequality, including IPV. The 2013 United Nations Commission on the Status of Women focused on prevention and elimination of all forms of violence against women

and girls; the UN Secretary General's UNiTE Campaign focuses on ending violence against women; and Millennium Development Goal 3 aims specifically "to promote gender equality and empower women." Similarly, many national governments have laws that explicitly criminalize intimate partner violence.

There is growing consensus in the research community on how to document the prevalence of women's exposures to physical and/or sexual partner violence in an ethically responsible way (8). "Gold standard" research methods include the conduct of one-on-one interviews in private, where women are asked direct, specific questions about their experience of a range of violent acts, including slaps, punches, kicks, the use of weapons, and forced or coerced sex (9).

As a result of this consensus and a greater global commitment to addressing violence against women, over the past decade, there has been a rapid expansion in the number of population studies examining IPV prevalence. However, existing surveys vary considerably in the specific measure of exposures to violence used, the populations sampled, and other characteristics. This has resulted in a large body of available prevalence data, but underlying challenges in interpretation, because of the lack of comparability across studies. We here present a synthesis of current evidence that provides new estimates of global and regional prevalence of IPV against women.

Synthesizing Evidence to Estimate Prevalence

Our research involved two main steps [all detailed in supplementary materials (SM)]. First, we did a systematic review of all available global prevalence data from studies representative at national or subnational levels. We searched 26 medical and social science databases, performed additional analysis of the WHO Multi-Country Study on Women's Health and Domestic Violence (10 countries), and requested additional analysis of the International Violence Against Women Surveys (8 countries); Gender, Culture and Alcohol: An International Study (16 countries); and the Demographic and Health Surveys to 2009 (20 countries) to obtain further prevalence estimates.

Data from 81 countries was used to estimate global prevalence of intimate partner violence against women.

Second, we used classical meta-regression methods to estimate women's lifetime prevalence of IPV (see SM). We modeled estimates for 21 global regions, adjusted for differences in study quality and characteristics, and provide age-standardized estimates, which reflect country age- and sex-specific population structures in 2010.

Data from 141 studies in 81 countries informed our estimates. Studies provided data on physical or sexual partner violence, or both, of different severity levels, occurring over different time periods and for age groups. The earliest study collected data in 1983; however, 96% of estimates that informed our model came from studies with data collected in 1999 or later. In all, 80% of estimates used a gold standard definition of IPV measurement (see SM).

The results show that globally, in 2010, 30.0% [95% confidence interval (CI) 27.8 to 32.2%] of women aged 15 and over have experienced, during their lifetime, physical and/or sexual intimate partner violence. There is considerable regional variation in the prevalence of physical and/or sexual partner violence (see the graph).

Implications for Policy

Given the high prevalence of IPV in all regions of the world, a greater focus on primary prevention is urgently needed alongside the provision of health, social, legal, and other support services (10). The prevention field is still in its nascence, but emerging evidence suggests several promising areas of intervention.

The strong association between exposure to violence in childhood and later experiences or perpetration of violence highlights the potential importance of interventions to prevent child maltreatment and witnessing of violence by their parents (10). For example, parenting interventions and social norm change to reduce the use of violence against children (10) and the provision of support to children living in violent families are possibilities.

Secondary education for women is consistently associated with lower levels of IPV, but women's employment has been shown to have the potential to either reduce or increase

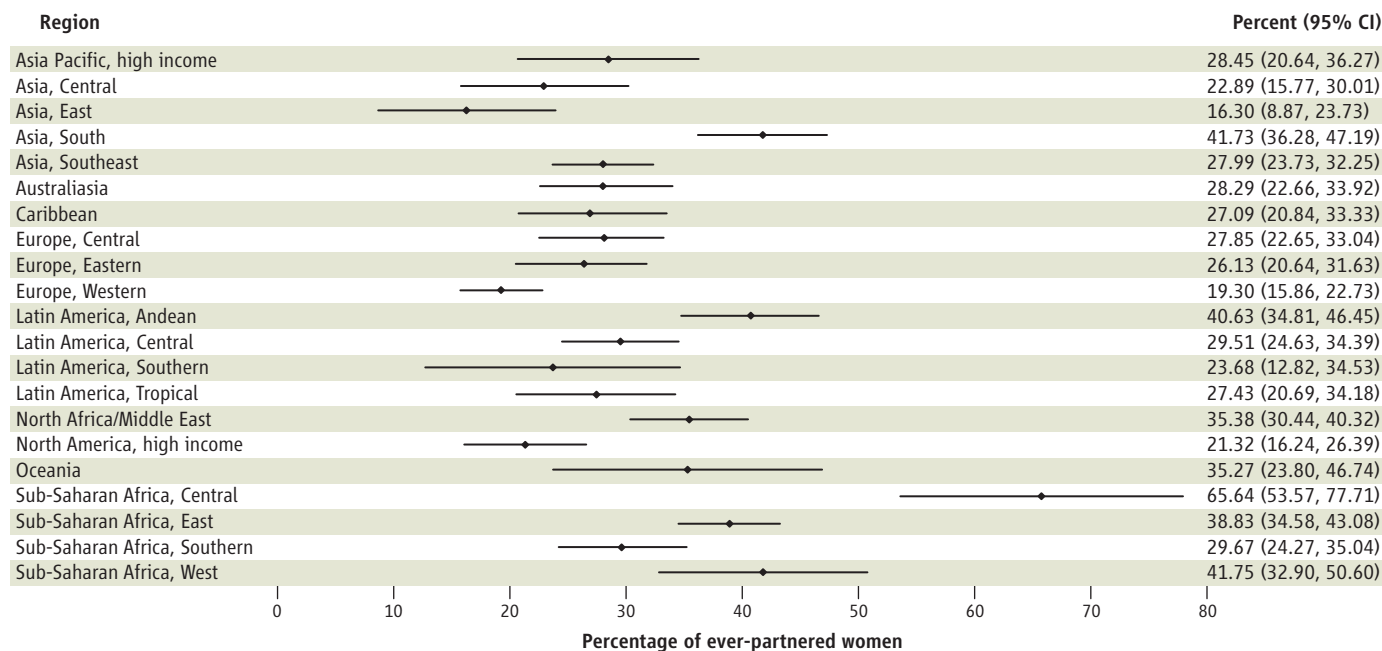
¹Gender Violence and Health Centre, London School of Hygiene and Tropical Medicine, London WC1E 7HT, UK.

²World Health Organization (WHO), 1211 Geneva, Switzerland.

³University of Gothenburg, 411 37 Gothenberg, Sweden.

⁴Institute for Health Metrics and Evaluation, University of Washington, Seattle, WA 98121, USA. ⁵Medical Research Council, Tygerberg 7505, South Africa.

*The author is a staff member of the World Health Organization. The author alone is responsible for the views expressed in this publication and they do not necessarily represent the views, decisions, or policies of the World Health Organization. †Author for correspondence: karen.devries@lshtm.ac.uk



Regional prevalence of IPV, percentage of ever-partnered women. See SM for details.

risk, depending upon geocultural context. In rural South Africa, an intervention that combined economic and social change program components showed a 55% reduction in past year levels of IPV over 2 years (11).

At the societal level, there is a need to challenge social norms that may condone some forms of IPV and male control over women, as well as norms that result in IPV being seen as a private issue, rather than a public concern. There are many promising social change interventions, including initiatives to support increased local activism against violence, to engage men and boys in violence prevention, and to use the media to promote nonviolent and gender equitable relationships and encourage neighbors to take action when violence occurs (10). Interventions to challenge social norms that promote problematic alcohol use among men, which is commonly associated with an increased severity and frequency of perpetration of IPV against female partners, are also needed (12).

The UN estimates that more than 600 million women live in countries where domestic violence is not considered a crime (13). Laws are important both to symbolize the unacceptability of IPV, as well as to provide a potential mechanism of legal recourse for women. At the national level, there is a need also to promote equal economic rights and entitlements for women—including equal access to formal wage employment, equal participation in schooling, and access to secondary education—and to address potentially discriminatory family law that may limit women's abil-

ity to divorce or maintain custody of their children (14).

Given the impacts and high prevalence of IPV it is likely that many women using health services are experiencing or have histories of abuse. The WHO, along with other professional health bodies, have produced guidance on how best to provide health care and support to women who have experienced violence (15). This work highlights the potential for health services to help identify, support, and refer women who are experiencing IPV and the need to support children growing up in households where there is IPV. It also identifies potential health sector entry points for an effective response.

IPV is a complex issue, and there are no quick-fix solutions. However, the global variation in the levels of violence highlight that IPV is not inevitable. There are multiple, important intervention entry points, and a concerted, multisectoral response is needed. Alongside the provision of services, an increased investment in violence prevention should form a central part of an expanded response. Research has a central role in this initiative, to support learning about the impact of different promising interventions being implemented globally, their costs, and how to take interventions to scale. Without such investments, the high levels of IPV documented here may continue unabated. The international community must honor commitments it has made over the past decade and devote resources to reducing violence against women, including IPV.

References and Notes

1. C. Watts, C. Zimmerman, *Lancet* **359**, 1232 (2002).
2. J. C. Campbell, *Lancet* **359**, 1331 (2002).
3. H. Stöckl et al., *Lancet* (2013). 10.1016/S0140-6736(13)61030-2
4. K. M. Devries et al., *PLoS Med.* **10**, e1001439 (2013).
5. R. K. Jewkes et al., *Lancet* **376**, 41 (2010).
6. F. G. Kouyoumdjian et al., *AIDS* **27**, 1331 (2013).
7. S. Walby, *The Cost of Domestic Violence: Up-date 2009* (Lancaster Univ., Lancaster, UK, 2010); www.lancs.ac.uk/fass/doc_library/sociology/Cost_of_domestic_violence_update.doc.
8. Department of Gender, Women, and Health, WHO, *Putting Women First: Ethical and Safety Recommendations for Research on Domestic Violence Against Women* (WHO, Geneva, 2001).
9. C. García-Moreno et al., *Science* **310**, 1282 (2005).
10. L. Heise, *What Works to Prevent Partner Violence? An Evidence Overview* (STRIVE, London School of Hygiene and Tropical Medicine, London, 2011).
11. J. C. Kim et al., *Am. J. Public Health* **97**, 1794 (2007).
12. K. Graham et al., *J. Interpers. Violence* **26**, 1503 (2011).
13. L. Turquet et al., *Progress of the World's Women 2011–2012: In Pursuit of Justice* (UN Women, New York, 2013).
14. L. Heise, *Determinants of Partner Violence in Low and Middle-Income Countries: Exploring Variation in Individual and Population Level Risk* (London School of Hygiene and Tropical Medicine, London, 2012).
15. WHO, "Responding to intimate partner and sexual violence against women: WHO clinical and policy guidelines" (WHO, Geneva, 2013).

Acknowledgments: We thank S. Kishor, K. Graham, H. Johnson, L. Heise, L. Petre, J. Astbury, J. Campbell, L. Davidson, M. Ellsberg, R. Jewkes, R. Naved, J. Mercy, H. Resnick, L. Sadowski, L. B. Schraiber, A. Taket, M. Yoshihama, the Economic and Social Research Council, Sigrid Rausing Trust, and the UN Development Programme, UN Population Fund, WHO, World Bank Special Programme of Research, Development, and Research Training in Human Reproduction.

Supplementary Materials

www.sciencemag.org/cgi/content/full/science.1240937/DC1

10.1126/science.1240937

NEUROSCIENCE

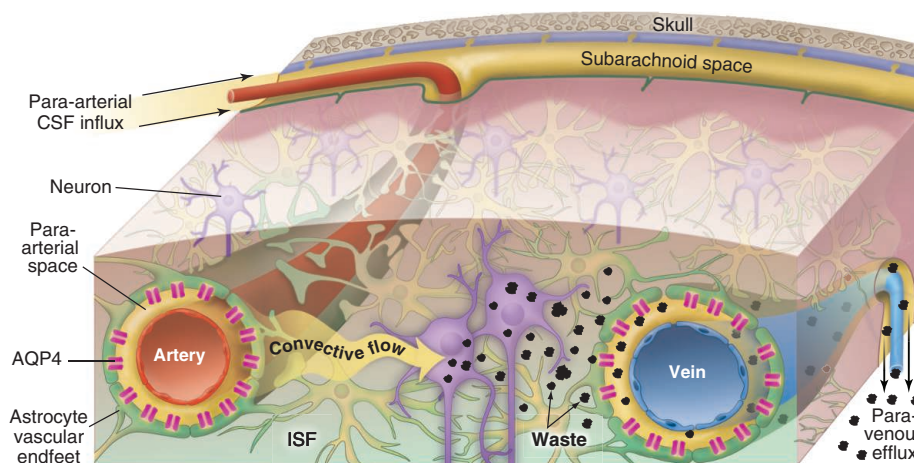
Garbage Truck of the Brain

Maiken Nedergaard

Essentially all neurodegenerative diseases are associated with misaccumulation of cellular waste products. Of these, misfolded or hyperphosphorylated proteins are among the most difficult for the brain to dispose. For example, tau and β -amyloid can accumulate as stable aggregates that are neurotoxic in conditions such as Alzheimer's disease (1). Intracellular proteasomal degradation and autophagy are considered the principal means for removing proteins in the central nervous system, and the dysfunction of each has been causally associated with neurodegeneration (2). Yet many cytosolic proteins are released into the interstitial space in the brain, suggesting that extracellular disposal routes may also eliminate waste (3).

Throughout the body's tissues, bulk flow of the fluid between cells, into the blood or lymph, plays an important role in the removal of potentially toxic metabolic by-products. Lymphatic vessels, which run in parallel with the blood vascular system, are the principal means by which tissues eliminate excess fluid and proteins. Although the density of lymph vessels generally correlates with tissue metabolic rate (4), the brain and spinal cord are curiously devoid of such a lymphatic tree. This is puzzling because the high metabolic activity of neurons predicts the need for rapid elimination of their metabolic by-products. It was long thought that movement of the cerebrospinal fluid (CSF), which is produced in the choroid plexus of the brain and flows through its ventricles and basal cisterns, constitutes a "sink" for waste products to diffuse from the brain, for eventual clearance to the general circulation. However, the large tissue distances in most of the brain prevent diffusion and bulk flow from making this process efficient. Albumin, for instance, would require more than 100 hours to diffuse through 1 cm of brain tissue (5).

Two-photon imaging of live mice through a closed cranial window has since permitted the direct observation of CSF movement through the intact brain. This technique revealed that CSF is exchanged rapidly with interstitial fluid (ISF) in the brain by a highly organized, brain-wide pathway



Go with the flow. Convective glymphatic fluxes of CSF and ISF propel the waste products of neuron metabolism into the paravenous space, from which they are directed into lymphatic vessels and ultimately return to the general circulation for clearance by the kidney and liver.

that consists of three serial elements: a para-arterial CSF influx route, a paravenous ISF clearance route, and an intracellular trans-astrocytic path that couples the two extracellular paravascular routes (6). Specifically, CSF passes through the para-arterial space that surrounds arteries; the space is bound by the abluminal surface of the blood vessel and the apical processes of astrocytes. Water channels called aquaporin 4 (AQP4) on the vascular endfeet of astrocytes (7) facilitate convective flow out of the para-arterial space and into the interstitial space (see the figure). As CSF exchanges with the ISF, vectorial convective fluxes drive waste products away from the arteries and toward the veins. ISF and its constituents then enter the paravenous space. As ISF exits the brain through the paravenous route, it reaches lymphatic vessels in the neck, and eventually returns its contents to the systemic circulation. Radio-label tracer studies indicate that 40 to 80% of large proteins and solutes are removed from the brain through this macroscopic clearance pathway (6). CSF can also exit through the arachnoid villi, which extend through the outer protective membrane layer of the brain and allow CSF to exit to the bloodstream, as well as at sites along the cavity and cranio-spinal nerve roots. Regardless of the route, its solutes and proteins ultimately reach the liver, where they are degraded. As such, the "glymphatic system"—so-named for its dependence on glial water channels and its

An intercellular "glymphatic" pathway clears cell waste from the brain and may reveal new targets for treating neurodegenerative diseases.

adoption of a clearance function similar to that of the peripheral lymphatic system—avoids the need for local protein processing and degradation. Instead, it facilitates transport to the same central excretion and recycling sites used by other tissues.

Studies of mice genetically engineered to lack AQP4 showed that fluid flux through the glymphatic pathway relies on specific expression of this water channel along the apical membrane of vascular endfeet of astrocytes (6). When AQP4 is mislocated to the cell body of astrocytes or to astrocytic processes that do not abut the vasculature, as observed in traumatic brain injury or stroke (8, 9), clearance of soluble proteins through the glymphatic system declines substantially.

An interesting question is whether the glymphatic system plays a role in spreading fibrillary tau aggregates through the interstitial space in neurodegenerative disease. The injection of brain extracts from mice containing an aggregation-prone form of human tau protein, into the brains of mice expressing wild-type human tau, induces self-assembly of the wild-type human tau into filaments. This results in the pathological spread of tau aggregates from the injection site to distant brain regions (2, 3, 10).

Perhaps the most persuasive example of CSF recycling as the cause of dispersing the initial seeds of tau tangles is after traumatic brain injury. As a result of axon damage, the tau concentration in CSF increases by as much

School of Medicine and Dentistry, University of Rochester Medical Center, Rochester, NY 14642, USA. E-mail: nedergaard@urmc.rochester.edu

as a factor of 40,000 (11). Consequently, as the heavily tau-laden CSF enters the brain tissue through the para-arterial space, it is taken up by cells closest to the paravascular boundary, thereby generating the typical paravascular predominance of tau-immunoreactive neurofibrillary tangles (12). Similarly, glymphatic CSF influx may also act as a constant source for delivering β -amyloid, which could contribute to the growth of para-arterial deposits in cerebral amyloid angiopathy. In turn, the same para-arterial space that normally functions as a low-resistance influx path for CSF will narrow as the amyloid plaques enlarge, slowing glymphatic clearance and thus accelerating amyloid deposition (13).

As such, studies of the multiple pathways involved in glymphatic clearance may identify new targets for treating neurodegenerative diseases. For example, mislocation of AQP4 water channels may contribute to neurodegenerative disease progression. Thus, potentiating the insertion and activity of AQP4 channels in astrocytic vascular endfeet might mitigate or even reverse the course of protein-associated neurodegenerative disorders.

Can the efficiency of glymphatic clearance be assessed? Preclinical analysis in rats shows that magnetic resonance imaging can provide a brain-wide map of both glymphatic influx and efflux, by which clearance kinetics can be derived and compared across subjects (14, 15). By extending this approach to humans, it may be possible to identify patients at risk for developing Alzheimer's disease who would benefit from therapeutic intervention before symptomatic neurodegeneration ensues. Similarly, this type of analysis might allow the monitoring of treatment responses, as well as the identification of genetic markers that predict enhanced susceptibility to glymphatic decline. Such an approach also may be suitable for victims of brain injury who develop chronic traumatic encephalopathy, which is characterized by paravascular tau tangles and premature neuronal degeneration (12). There are currently no definitive diagnostics that identify susceptible individuals, and thus no means by which to achieve early clinical intervention. Recognition that the brain, like all other organs, uses both local and organ-wide mechanisms for

clearing interstitial protein waste may offer new insights into the pathophysiology and prophylaxis of neurodegeneration, as well as injuries and proteinopathies of the human central nervous system.

References

1. L. Mucke, D. J. Selkoe, *Cold Spring Harb. Perspect. Med.* **2**, a006338 (2012).
2. B. Frost, M. I. Diamond, *Nat. Rev. Neurosci.* **11**, 155 (2010).
3. L. C. Walker, M. I. Diamond, K. E. Duff, B. T. Hyman, *J. Am. Med. Assoc. Neurol.* **70**, 304 (2013).
4. M. Loukas et al., *Clin. Anat.* **24**, 807 (2011).
5. H. F. Cserr, *Physiol. Rev.* **51**, 273 (1971).
6. J. J. Iliff et al., *Sci. Transl. Med.* **4**, 147ra111 (2012).
7. E. A. Nagelhus, T. M. Mathiesen, O. P. Ottersen, *Neuroscience* **129**, 905 (2004).
8. J. J. Iliff, M. Nedergaard, *Stroke* **44**, (Suppl 1), S93 (2013).
9. Z. Ren et al., *J. Cereb. Blood Flow Metab.* **33**, 834 (2013).
10. F. Clavaguera et al., *Nat. Cell Biol.* **11**, 909 (2009).
11. F. P. Zemlan et al., *Brain Res.* **947**, 131 (2002).
12. L. E. Goldstein et al., *Sci. Transl. Med.* **4**, 134ra60 (2012).
13. R. O. Weller, S. D. Preston, M. Subash, R. O. Carare, *Alzheimers Res. Ther.* **1**, 6 (2009).
14. J. J. Iliff et al., *J. Clin. Invest.* **123**, 1299 (2013).
15. L. Yang et al., *J. Transl. Med.* **11**, 107 (2013).

10.1126/science.1240514

CHEMISTRY

More Can Be Better in N₂ Activation

Michael D. Fryzuk

Nitrogen is essential for life, but only a few organisms can convert the abundant dinitrogen (N₂) molecules from the air into chemically usable forms of nitrogen. The Haber-Bosch process, developed over 100 years ago (1), combines N₂ and H₂ gases over activated iron surfaces to generate ammonia (NH₃) for use as fertilizer or to produce other chemicals, but this process is extremely energy intensive. Chemists have long searched for a low-energy process that converts N₂ to ammonia or higher-value nitrogen compounds such as N-heterocycles or amines. However, the intrinsic inertness of N₂ has made it challenging to discover metal complexes that can both bind and activate it. On page 1549, Shima et al. report a trititanium hydride cluster that cleaves N₂ and functionalizes it to form N-H bonds (2).

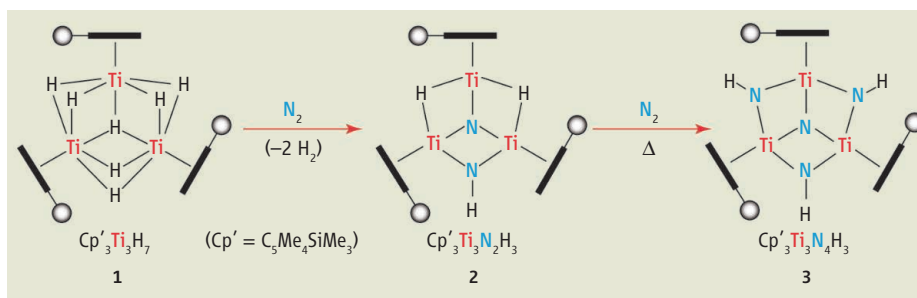
Since the discovery of the first dinitrogen complex [Ru(NH₃)₅N₂]²⁺ in 1965, many decades of research have been invested in

the search for soluble complexes that bind, activate, and functionalize N₂ (3). Generally, coordination of N₂ to a single metal center can result in mild activation, as determined by an increase in bond length or a decrease in stretching frequency from free N₂. Higher levels of activation have been found when N₂ binds to two or more metal centers.

The ability of hydride complexes to bind dinitrogen with loss of H₂ has been known since the late 1960s (4). In these early cases,

A soluble trititanium hydride cluster cleaves molecular nitrogen and forms N-H bonds.

the dinitrogen unit was only slightly activated upon coordination. A more recent study showed that ditantalum tetrahydride complex can activate N₂ but cannot cleave the very strong N-N triple bond (5). A dinibium tetrahydride complex has since been reported to cleave N₂ completely to generate a diniobium dinitride species, but without N-H bond formation (6). This work showed that N₂ could be activated by elimination of H₂, which is a source of two electrons for



How N₂ is caught and converted. Shima et al. show that trititanium heptahydride **1** can activate molecular nitrogen to generate trititanium imide-nitride **2**. The latter can further react with more N₂ to produce the trititanium triimide-nitride **3**. Both processes are unprecedented and will guide future studies in N₂ activation. Cp', tetramethyl(trimethylsilyl)cyclopentadienyl.

Department of Chemistry, The University of British Columbia, Vancouver, BC, Canada, V6T1Z1. E-mail: fryzuk@chem.ubc.ca

each H₂ unit lost; those electrons can be used to activate the N₂ unit.

Shima *et al.* show how the trimetallic heptahydride Cp'₃Ti₃H₇ (see the figure, 1) can activate and cleave one equivalent of N₂ under very mild conditions to form a complex with one nitride bound to the three titanium atoms at the center and one bridging imide (the Ti(NH)Ti unit, see the figure, 2), accompanied by the release of two equivalents of dihydrogen (H₂). Further reaction with N₂ under more forcing conditions (180°C, no solvent) results in a triimido-nitride species (see the figure, 3). The authors provide compelling experimental evidence on exactly how these reactions proceed and back up their experiments with computational results.

What is particularly appealing about this report is the data on proposed intermediates during the transformation that generates compound 2. Monitoring the reaction of ¹⁵N₂ with the heptahydride 1 at low temperatures shows evidence for the formation of two intermediates. The first intermediate is an end-on side-on bound N₂ complex formed through loss of

H₂. This is followed by scission of the N-N bond to generate a di-μ-nitride trihydride. The latter species slowly transforms to the imide-nitride 2 via a reductive elimination of one of the bridging hydrides to a nitride to generate a N-H bond. Both transformation processes are unprecedented in the dinitrogen activation literature. The N-H-forming process mimics one of the steps suggested on iron surfaces for the formation of ammonia in the Haber-Bosch process, albeit with different metals.

The biological process of nitrogen fixation involves the enzyme nitrogenase and a cofactor containing a multi-iron site that binds N₂ and converts it to ammonia. The detailed mechanism of ammonia formation from atmospheric N₂ by nitrogenase remains to be resolved, but it has recently been suggested (7) that the initial N₂ binding step involves H₂ elimination from the cofactor, perhaps from iron hydride moieties at the active site. The trititanium system reported by Shima *et al.* is by no means a model for nitrogenase, but both systems involve multimetallic sites,

which may be beneficial for N₂ reduction.

Clearly, having more than two metal centers and multiple hydrides present allows more N₂ to be activated, along with the formation of N-H bonds. But it is not as simple as more-is-better. Shima *et al.* report that tetrametallic hydride clusters of the formula Cp'₄M₄H₈, where M is Ti, Zr, and Hf, do not react with dinitrogen under any circumstances. Future studies should investigate how other multimetallic sites may be used to activate small molecules, especially nature's most inert diatomic molecule, N₂.

References

1. M. Peplow, *Chem. World*, 48 (May 2013).
2. T. Shima *et al.*, *Science* **340**, 1549 (2013).
3. M. D. Fryzuk, *Chem. Commun. (Camb.)* **49**, 4866 (2013).
4. J. Ballmann, R. F. Munhá, M. D. Fryzuk, *Chem. Commun. (Camb.)* **46**, 1013 (2010).
5. M. D. Fryzuk, *Acc. Chem. Res.* **42**, 127 (2009).
6. F. Akagi, T. Matsuo, H. Kawaguchi, *Angew. Chem. Int. Ed.* **46**, 8778 (2007).
7. B. M. Hoffman, D. Lukoyanov, D. R. Dean, L. C. Seefeldt, *Acc. Chem. Res.* **46**, 587 (2013).

10.1126/science.1240365

MICROBIOLOGY

Eliminating Malaria

David A. Fidock

Malaria kills more young children than any other infectious disease. The most pernicious causal agent, the protozoan parasite *Plasmodium falciparum*, is responsible for the death each year of more than half a million children, mostly in sub-Saharan Africa. Until recently, control efforts were thwarted by pyrimethamine- and chloroquine-resistant parasites, whose appearance in Africa was traced back to origins near the Thai-Cambodian border. Fortunately, the discovery of the potent antimalarial properties of artemisinin (1) has helped turn the tide against malaria. Artemisinin-based combination therapies (ACTs), which combine a potent but short-lived artemisinin derivative with a longer-lasting partner drug, have now been officially adopted across virtually the entire malaria-endemic world. Their deployment, along with efforts to distribute insecticide-treated bednets, is associated with recent substantial reductions in malaria burden. However, recent studies from

Cambodia and now Thailand show that once again resistance is looming as a major threat to global control efforts (see the figure) (2, 3).

Emerging resistance to artemisinins is defined as a reduced rate of parasite clearance after administration of an artemisinin derivative such as artesunate or an ACT. In western Cambodia, the epicenter of resistance, artesunate treatment yielded a mean clearance half-life of 5.9 hours in Pursat, as opposed to 2 hours for a comparator drug-sensitive cohort in Wang Pha, western Thailand (4). Delayed clearance translates into an increased proportion of individuals having microscopically detectable blood-stage infections by the third day of treatment and raises the risk of parasite recrudescence (i.e., disease reappearance). Major efforts are under way in this region to eliminate malaria while ACTs remain clinically effective, with the theory that nothing short of elimination will prevent its global dissemination.

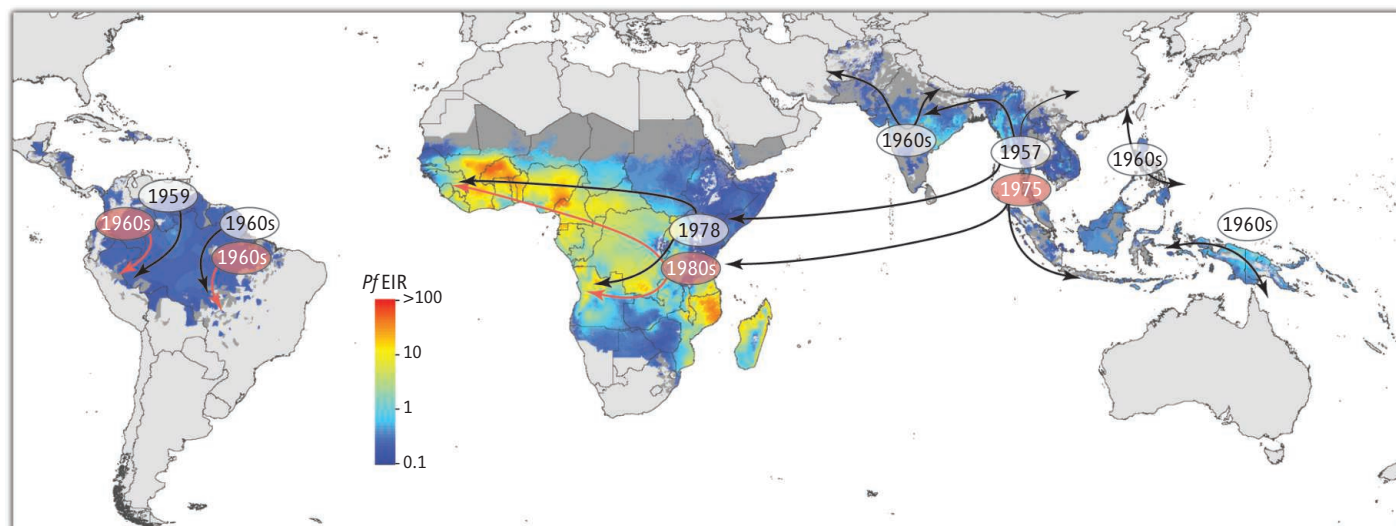
Mode-of-action studies, while controversial, mostly converge on the idea that artemisinins can be activated in the parasite via iron-mediated scission of the peroxide bridge following hemoglobin proteolysis

Global eradication requires concerted efforts to combat emerging resistance to the potent antimalarial artemisinin.

and release of ferric heme iron (5). This can lead to the formation of carbon-centered radicals that trigger cell death. This mechanism can account for drug action during most of the 48-hour intraerythrocytic developmental cycle, although how artemisinins act against the very early "ring" stages that form shortly after host cell invasion remains enigmatic.

In vitro studies on *P. falciparum* cultures exposed to high concentrations of artemisinin show that parasites can acquire an initial state of tolerance (6) whereby early ring-stage parasites adopt a drug-induced quiescent or dormant state and then resume normal growth upon drug removal (7). This trait is distinct from mechanisms of resistance to other antimalarials, which typically permit robust growth despite drug treatment and often involve genetic changes that alter drug targets or efflux systems (e.g., PfCRT or PfMDR1). Further research is needed to define the molecular basis of in vitro tolerance or resistance, understand its relation to delayed clearance rates, and model how resistance, parasite fitness, transmission intensity, and treatment coverage collectively influence the spread of resistance.

Department of Microbiology and Immunology and Division of Infectious Diseases, Department of Medicine, Columbia University Medical Center, New York, NY 10032, USA. E-mail: df2260@columbia.edu



Spread of *P. falciparum* resistance. Appearance and spread of resistance to former first-line antimalarials chloroquine and pyrimethamine (clear and orange ovals, respectively), showing migration from Southeast Asia to Africa. Emerging resistance to artemisinins is now documented in Southeast Asia, raising concerns about its future migration to Africa. Resistance patterns are overlaid onto a geostatistics map of *P. falciparum* entomological inoculation rates (EIR; numbers of infectious mosquito bites per individual per year) modeled for 2010 (16).

Recent high-density genotyping studies with clinically defined Southeast Asian patient isolates showed that parasite clearance rates have a predominantly heritable component, which was associated with a 35-kb region on chromosome 13 (8). A separate genome-wide association study also associated delayed clearance with single-nucleotide polymorphisms on chromosomes 13 and 10 (9). The chromosome 13 candidate markers identified in these two studies did not overlap, suggesting intrinsic difficulties in obtaining sufficiently high resolution to identify the causal gene and/or the presence of multiple genetic determinants on that chromosome.

Novel insights into the genetic basis of artemisinin resistance were recently provided by whole-genome sequencing of 825 parasite strains from Asia and Africa, which identified a highly unusual population structure in parasites from western Cambodia (10). This region harbors four genetically highly differentiated but nonetheless sympatric parasite subpopulations termed KH1 to KH4. Three (KH2, 3, and 4) showed a significant prolongation of parasite clearance half-life relative to the KH1 subpopulation that was commonly observed in largely artemisinin-sensitive neighboring regions. One explanation might be the presence of multiple genetic loci that collectively confer upon each subpopula-

tion the ability to survive artemisinin exposure; independent segregation of these genes during sexual recombination would thus be selected against during treatment. Alternatively, the lack of recombination may reflect relatively recent founder events that separately acquired a primary resistance determinant and that have not yet had time to recombine frequently and disrupt linkage disequilibrium. In KH2 parasites, chromosome 13 showed extensive linkage disequilibrium, with a single haplotype extending across half the 4-Mb chromosome; this makes the identification of specific changes associated with delayed clearance rates particularly challenging. Among the genome-wide candidates were several transporter genes that have highly differentiated sequences in the founder subpopulations, including the ABC transporters PfMDR1 and PF13_0271 that might restrict drug access to its site of action.

This study also identified substantial changes in the DNA mismatch repair pathway, including the repair heterodimer MutL α (consisting of PMS1 and MLH1) and its physical partner UvrD (10). Resistance-associated mutations in DNA repair pathways were separately observed for Rad5 (9), which is involved in the DNA damage tolerance pathway of postreplication repair (11). Mutations in this pathway have been implicated in cell cycle arrest in yeast and might play a similar role in *P. falciparum*. The presence of DNA repair variants in the KH1 subpopulation also suggests that some changes may predate artemisinin resistance—for example, by creating initial hypermutator strains that accelerate the frequency of resistance. This finding recalls the earlier report of an ARMD (accelerated resistance to multiple drugs) phenotype in some Southeast Asian parasites (12). Interestingly,

some MLH1 variants in yeast can suppress meiotic crossovers (11), raising the possibility that the changes in *P. falciparum* might be used to preserve linkage disequilibrium and polygenetic traits.

Molecular tools are urgently needed to monitor artemisinin resistance and to identify therapeutic approaches to contain it. Forward genetic methods, which entail crossing drug-resistant and drug-sensitive parasites and which previously localized the genetic determinants mediating resistance to chloroquine and pyrimethamine, would be useful if the trait followed a pattern of Mendelian inheritance. This trait could be quantified using an in vitro assay recently used to study parasite ring-stage susceptibility to artemisinins (7). Such crosses, which until now have required nonhuman primates, may be achievable using a new human hepatocyte- and erythrocyte-engrafted FRG NOD mouse model that permits mosquito-delivered *P. falciparum* parasites to progress through the liver and be recovered as blood-stage forms (13). Reverse genetic approaches, where candidate genes are modified via allelic exchange and phenotypic changes assessed, also benefit from the recent development of customized zinc finger nuclease-mediated gene editing in *P. falciparum* (14). This makes it feasible to assess a panel of candidates, with the goal of defining DNA sequence markers to inexpensively and rapidly screen for the spread of resistance, and begin to delineate its molecular basis. Finally, taking inspiration from approaches in *Mycobacterium tuberculosis* (15), new high-throughput screening approaches are required to identify antimalarial compounds that effectively eliminate artemisinin-tolerant quiescent parasites.

Emerging resistance to artemisinins has not yet compromised the outstanding

clinical efficacy of ACTs across most of the malaria-endemic regions of the world; even in western Cambodia most infections are reported to clear after ACT treatment. Malaria elimination remains an achievable goal, one that is critically dependent on an expanded and unified vision coordinated among funders, governments, health care providers, scientists, and the pharmaceutical industry. The issue of emerging artemisinin resistance highlights the necessity to intervene at all levels to prevent a looming disas-

ter, and an opportunity to bring about a truly global accomplishment that directly or indirectly benefits us all.

References

1. N. J. White, *Science* **320**, 330 (2008).
2. A. M. Dondorp *et al.*, *N. Engl. J. Med.* **365**, 1073 (2011).
3. A. P. Phyto *et al.*, *Lancet* **379**, 1960 (2012).
4. C. Amaratunga *et al.*, *Lancet Infect. Dis.* **12**, 851 (2012).
5. P. M. O'Neill, V. E. Barton, S. A. Ward, *Molecules* **15**, 1705 (2010).
6. Q. Cheng, D. E. Kyle, M. L. Gatton, *Int. J. Parasitol. Drugs Drug Resist.* **2**, 249 (2012).
7. B. Witkowski *et al.*, *Antimicrob. Agents Chemother.* **57**, 914 (2013).
8. I. H. Cheeseman *et al.*, *Science* **336**, 79 (2012).
9. S. Takala-Harrison *et al.*, *Proc. Natl. Acad. Sci. U.S.A.* **110**, 240 (2013).
10. O. Miotto *et al.*, *Nat. Genet.* **45**, 648 (2013).
11. S. Boiteux, S. Jinks-Robertson, *Genetics* **193**, 1025 (2013).
12. P. K. Rathod, T. McErlean, P. C. Lee, *Proc. Natl. Acad. Sci. U.S.A.* **94**, 9389 (1997).
13. A. M. Vaughan *et al.*, *J. Clin. Invest.* **122**, 3618 (2012).
14. J. Straimer *et al.*, *Nat. Methods* **9**, 993 (2012).
15. B. Gold *et al.*, *Proc. Natl. Acad. Sci. U.S.A.* **109**, 16004 (2012).
16. P. W. Gething *et al.*, *Malar. J.* **10**, 378 (2011).

10.1126/science.1240539

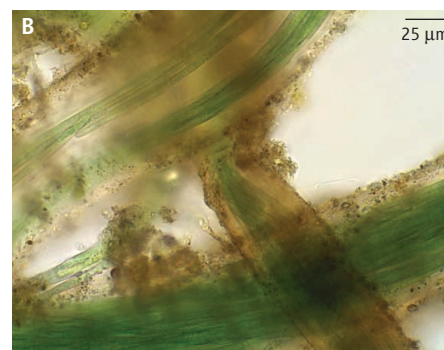
MICROBIOLOGY

Some Like It Hot, Some Not

Jayne Belnap

Dryland ecosystems cover over 40% of Earth's terrestrial landmass (1). Biocrusts—soil communities consisting of cyanobacteria, mosses, and lichens—can cover up to 70% of the ground in these ecosystems (see the figure, panel A) (2). The crucial role played by these and other very small organisms in nutrient, carbon, and water cycles has become increasingly clear in the past few decades (2, 3). Soil stability and the composition and performance of vascular plant communities also depend on biocrust health and activity. Yet, little is known about the identity, biology, ecophysiology, or distribution of the microbial components that dominate biocrusts (4, 5). Data are also needed to understand how they will respond to climate change. On page 1574 of this issue, Garcia-Pichel *et al.* (6) take a first step in filling this data gap.

Using samples from western U.S. desert sites across a range of climatic regimes, the authors compared DNA signatures of known cultivated cyanobacterial isolates to those in their field samples. They found a clear pattern of biogeographic segregation: At most sites, one of two cyanobacterial species dominated, with *Microcoleus vaginatus* (see the figure, panel B, and movie S1) prevalent at colder sites and *M. steenstrupii* at warmer



Hidden variation. (A) Soils covered by biological soil crusts near Moab, Utah. Because of low plant cover in drylands, biological soil crusts can comprise 70% or more of total cover and mediate most inputs and outputs from the soils. (B) *Microcoleus vaginatus*. Garcia-Pichel *et al.* show that biocrusts are dominated by *M. vaginatus* in colder deserts and *M. steenstrupii* in hotter deserts. As global temperatures increase, it is likely that *M. steenstrupii* will replace *M. vaginatus* in many deserts. Although the two species are morphologically similar, the ecological implication of this replacement is unknown. Movie S1 shows *M. vaginatus* filaments moving within a common polysaccharide sheath.

sites. The authors then conducted physiological studies to confirm that growth of *M. vaginatus* was, indeed, favored at lower temperatures and *M. steenstrupii* at higher temperatures. They predict that the latter will likely replace the former as temperatures increase in the future.

The study illustrates the need to know what microorganisms are present at a site and how they affect ecosystem function, rather than exclusively focusing on the more visible macroorganisms such as plants, animals, or even mosses and lichens (2, 4, 7). Modern genetic studies of microbes can quickly and cheaply produce overwhelming amounts of data, but adding the functional dimension to molecular diversity has been exceedingly difficult. There is an urgent need for usable, consistent, and agreed-upon taxonomic and functional categories for microbes.

As shown by Garcia-Pichel *et al.*, ecologically meaningful insights into microorganisms can be obtained by coupling new techniques (such as high-throughput molecular surveys of community DNA) with traditional techniques such as cultivation (7) and ecophysiological characterization of relevant isolates. (This approach, of course, is limited to organisms that can be cultured.) As it turns out, *M. steenstrupii* (and the nitrogen-fixing cyanobacterium *Scytonema*) appear to be far more important in hotter deserts than previously recognized.

Understanding the large difference in microbial composition in biocrusts from different regions will be crucial for managing these communities under future conditions. At colder sites, a shift from the dominant *M. vaginatus* to *M. steenstrupii* with warming could have a large effect on the ecosystem services provided by biocrusts. The extent of

U. S. Geological Survey, 2290 South Resource Boulevard, Moab, UT 84532, USA. E-mail: jayne_belnap@usgs.gov

this effect depends on how the two species differ in their ability to colonize bare soils, stabilize soils, and affect nutrient, water, and carbon cycles. In fact, given their genetic differences, the two species would be better placed in different families rather than in the same genus. However, the little research done has focused on *M. vaginatus*, with no work beyond description on *M. steenstrupii*, because its importance in biocrusts has not been recognized (8). *M. steenstrupii* constitutes a much more diverse phylogenetic clade than *M. vaginatus* (9), and it is likely to be much more genetically and functionally diverse. Renewed efforts should be made to characterize it in all its complexity.

There is also little information to date on the ecological consequences of changing the composition of the nitrogen-fixing cyanobacteria in biocrusts. Garcia-Pichel *et al.* did not directly address biogeographic patterns in these species, but their data show that *Scytonema* sp. appears favored at sites with higher temperatures and *Tolypothrix* sp. at sites with lower temperatures. Possible outcomes of replacing *Tolypothrix* sp. with *Scytonema* sp. include alteration of nitrogen, phospho-

rus, and carbon cycles. Again, most research has focused on one species, the ubiquitous *Nostoc*, with little information available for either *Scytonema* or *Tolypothrix*.

This lack of research also hampers efforts to actively restore disturbed biocrusts. Most attempts to cultivate and inoculate soils with cyanobacteria to “kickstart” soil stabilization and restoration in areas degraded by human impact use *M. vaginatus* and sometimes *Nostoc*. These efforts are surely at risk of failure if the site should be inoculated with *M. steenstrupii* and *Scytonema* (or possibly other species) instead, because cultivation, inoculation, and/or postinoculation techniques could differ substantially among various species. These situations thus call for a better understanding of which species are currently present at a site and their physiological tolerances.

Chemolithotrophic bacteria and Archaea involved in the nitrogen cycle (10) and biocrust fungi (11) are some other examples of potentially important groups that we know little about but that may also play pivotal roles in the structure and function of biocrusts and many other ecosystems. It is time

to tackle the difficult job of identifying the relevant microbes and their distributions and of establishing their functional roles to enable better management and restoration of dryland ecosystems.

References

1. S. B. Pointing, J. Belnap, *Nat. Rev. Microbiol.* **10**, 551 (2012).
2. J. Belnap, O. L. Lange, Eds., *Biological Soil Crusts: Structure, Function, and Management, Ecological Studies Series 150*, series edited by I. T. Baldwin *et al.* (Springer, Berlin, 2003).
3. W. Elbert *et al.*, *Nat. Geosci.* **5**, 459 (2012).
4. J. L. Green, B. J. Bohannan, R. J. Whitaker, *Science* **320**, 1039 (2008).
5. J. B. H. Martiny *et al.*, *Nat. Rev. Microbiol.* **4**, 102 (2006).
6. F. Garcia-Pichel *et al.*, *Science* **340**, 1574 (2013).
7. C. Parmesan, *Annu. Rev. Ecol. Evol. Syst.* **37**, 637 (2006).
8. J. Belnap, in *Biological Soil Crusts: Structure, Function, and Management*, J. Belnap, O. L. Lange, Eds. (Springer, Berlin, 2003), pp. 241–261.
9. F. Garcia-Pichel, M. F. Wojciechowski, *PLoS ONE* **4**, e7801 (2009).
10. Y. Marusenko *et al.*, *Ecol. Processes* **2**, 9 (2013).
11. S. L. Collins *et al.*, *J. Ecol.* **96**, 413 (2008).

Supplementary Materials

www.sciencemag.org/cgi/content/full/science.1240318/DC1
Movie S1

10.1126/science.1240318

BIOCHEMISTRY

Translocation in Action

Marina V. Rodnina

Ribosomes are macromolecular factories that translate the information encoded in messenger RNA (mRNA) into the amino acid sequence of proteins. Each time an amino acid has been transferred to the growing peptide chain, the mRNA and two transfer RNAs (tRNAs) move through the ribosome one codon at a time. This movement—called translocation—is promoted by elongation factor G (EF-G). Three papers in this issue, by Tourigny *et al.* on page 1542 (1), Pulk and Cate on page 1544 (2), and Zhou *et al.* on page 1543 (3), present high-resolution structures of translocation intermediates and provide insights into the underlying mechanism.

The translocation process occurs within milliseconds and entails a large number of structural rearrangements. During translocation, the small and large ribosomal subunits (SSU and LSU) rotate relative to each other (4). The SSU undergoes internal

motions (collectively called swiveling) of its head domain relative to the body (5). The tRNAs move from the A (aminoacyl) to the P (peptidyl), and from the P to E (exit) binding sites, and there are several intermediate positions that the tRNAs can adopt spontaneously (4, 6, 7) (see the figure). All these rearrangements are rapid and only loosely coupled, making it extremely challenging to obtain structural data on the trajectories of the movements.

To trap EF-G on the ribosome, all three groups (1–3) used nonhydrolyzable analogs of guanosine 5'-triphosphate (GTP) and placed a single tRNA on the mRNA codon in the P site of the ribosome. The structures show that the ribosome is trapped in a chimeric intermediate state (see the figure, panel B) that differs from the ground states before (panel A) and after (panel C) translocation. This means that the tRNAs move through a series of intermediates not only on the LSU (7) but on the SSU as well (8), providing new insight into the mechanics of tRNA translocation. One interesting possibility is that GTP

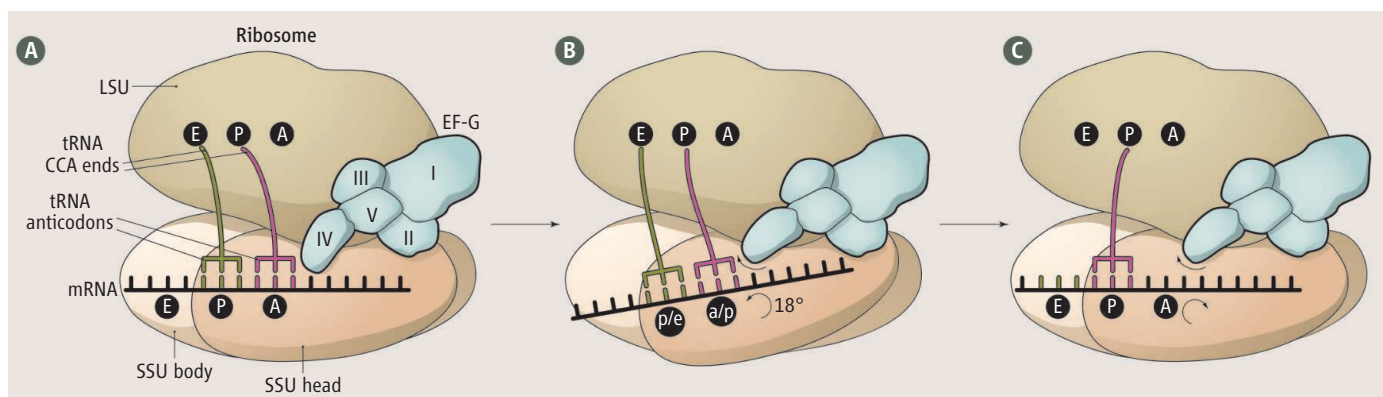
Structures of translocation intermediates reveal how tRNA molecules move through the ribosome during protein synthesis.

hydrolysis by EF-G is required to promote the backward rotation of the SSU head domain and the movement of the tRNA and mRNA into the posttranslocation state (see the figure, panel C). The results of experiments with a guanosine triphosphatase (GTPase)-deficient EF-G mutant appear to be consistent with this idea (9).

EF-G is a large, five-domain GTPase that changes its conformation in response to GTP hydrolysis (see the figure). Without GTP hydrolysis, translocation is slow and the release of EF-G from the ribosome is blocked (10). Like all GTPases, EF-G has the mobile switch 1 and 2 elements in its GTP-binding domain I. The switch regions are disordered in the unbound EF-G and become ordered in the complex with the ribosome. This transition causes reorientation of the EF-G domains, such that the tip of domain IV moves and the intermediate state of the ribosome is stabilized (see the figure, panel B).

The ribosome on its own allows the tRNAs to move in the forward or backward direction. EF-G provides the directionality

Max Planck Institute for Biophysical Chemistry, 37077 Goettingen, Germany. E-mail: rodnina@mpibpc.mpg.de



Translocation dynamics. (A) In the pretranslocation state of the ribosome, the tRNA anticodons are located in the A and P sites on the SSU, while the tRNA CCA ends oscillate between the A and P or P and E sites on the LSU. EF-G is in the GTP-bound conformation. (B) In the intermediate state of translocation, derived from the new crystal structures (1–3), the rotation of the SSU head domain brings the

tRNA anticodons and the mRNA codons into a state intermediate between A and P (called a/p) or between P and E (p/e) on the SSU. Domain IV of EF-G moves. (C) In the posttranslocation state (4, 14), only one tRNA is bound to the ribosome in the P site, the E-site tRNA is released, the SSU head domain is rotated backward, and EF-G has changed the conformation further before it dissociates from the ribosome (1–3).

of movement, and the new structures suggest how this is achieved. EF-G domain IV, which is essential for tRNA and mRNA translocation (10, 11), projects into the A site, thereby preventing the backward movement of the tRNA (1–3) (see the figure, panel C). In addition, elements of 16S ribosomal RNA in the SSU act as molecular pawls to fix the position of the mRNA, preventing backward movement of the mRNA (3).

The structures also show how GTP hydrolysis in EF-G may be activated by the ribosome. In the structures by Tourigny *et al.* (1) and Pulk and Cate (2), the conserved histidine residue from switch 2 is poised for hydrolysis. By contrast, in the structure by Zhou *et al.* (3), this histidine is too far from the γ -phosphate to act in catalysis, suggesting that a nonactivated intermediate was trapped. Mutations of the histidine residue in either EF-G or EF-Tu, another translational GTPase, abolish GTP hydrolysis and block the progression through the translation elongation cycle (9, 12), consistent with a catalytic role of the histidine. Key residues in EF-G and EF-Tu (13) form a nearly identical catalytic site, suggesting a common mechanism for the activation of translational GTPases by the ribosome.

The mechanism of translocation represents a case study of directed movement in large molecular machines. The new structures (1–3) suggest how GTP hydrolysis is coupled to translocation. The mechanism of coupling is reminiscent of motor proteins using ATP hydrolysis to drive directed movements (2). A remaining challenge is to determine the structure of a true pretranslocation complex (with tRNAs bound to both P and A sites and without EF-G occupying the A site of the SSU) and of intermediate states of

translocation. Another key question is how EF-G accelerates translocation. Answering this question will require comparison of intermediate states of EF-G-catalyzed and spontaneous translocation.

References

1. D. S. Tourigny, I. S. Fernández, A. C. Kelley, V. Ramakrishnan, *Science* **340**, 1542 (2013).
2. A. Pulk, J. H. D. Cate, *Science* **340**, 1544 (2013).
3. J. Zhou, L. Lancaster, J. P. Donohue, H. F. Noller, *Science* **340**, 1543 (2013).
4. J. Frank, R. K. Agrawal, *Nature* **406**, 318 (2000).
5. B. S. Schuwirth *et al.*, *Science* **310**, 827 (2005).
6. D. Moazed, H. F. Noller, *Nature* **342**, 142 (1989).
7. N. Fischer, A. L. Konevga, W. Wintermeyer, M. V. Rodnina, H. Stark, *Nature* **466**, 329 (2010).
8. A. H. Ratje *et al.*, *Nature* **468**, 713 (2010).
9. C. E. Cunha *et al.*, *Translation* **1**, e24315 (2013).
10. M. V. Rodnina, A. Savelsbergh, V. I. Katunin, W. Wintermeyer, *Nature* **385**, 37 (1997).
11. A. Savelsbergh, N. B. Matassova, M. V. Rodnina, W. Wintermeyer, *J. Mol. Biol.* **300**, 951 (2000).
12. T. Daviter, H. J. Wieden, M. V. Rodnina, *J. Mol. Biol.* **332**, 689 (2003).
13. R. M. Voorhees, T. M. Schmeing, A. C. Kelley, V. Ramakrishnan, *Science* **330**, 835 (2010).
14. Y. G. Gao *et al.*, *Science* **326**, 694 (2009).

10.1126/science.1240090

PLANETARY SCIENCE

Solving the Mascon Mystery

Laurent G. J. Montesi

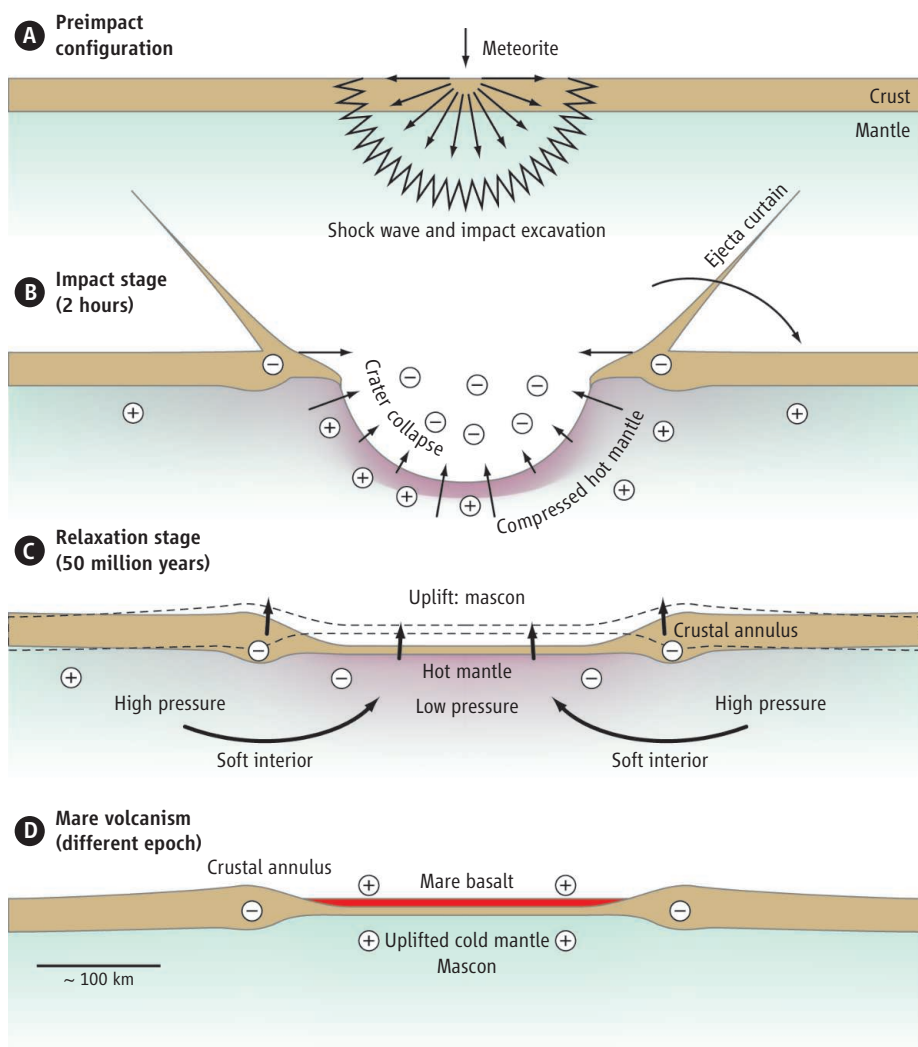
Modeling the formation of regions of mass concentration may lead to new estimates of early heat flux in the Moon.

When we look at the Moon, we can see images of a man, a rabbit, and countless other analogies. These images are the figments of our imagination, inspired by the distribution of thick lava sequences, the mare basalts, that fill ancient basins that formed by large meteorite impacts early in solar system history. Still, mysteries remain hidden beneath the lunar surface. The first spacecraft in orbit around the Moon felt a stronger pull of gravity when passing over these basins, implying that a mass concentration, or “mascon,” was present there (1).

Department of Geology, University of Maryland, College Park, MD 20742, USA. E-mail: montesi@geology.umd.edu

Subsequent studies added to the puzzle of mascons and provided partial explanations for their formation (2–4). On page 1552 of this issue, 45 years after the initial discovery, Melosh *et al.* (5) put all the pieces together and provide the first self-consistent model for the origin of mascons.

At first sight, the existence of mascons seems incompatible with the origin of the lunar basins in which they form. The impact process excavates a hole in the lunar crust and upper mantle, resulting in a mass deficit, not a mass concentration. The lunar mantle flows toward the basin interior and reduces the initial mass deficit. However, this flow process, which is similar to the rebound of



Mascon development. (A) A meteorite impact shocks the mantle and excavates a cavity that rapidly collapses while (B) depositing a curtain of crustal material that thickens the crust in an annulus at the edge of the basin. (C) Both the crust annulus and the shocked mantle drive mantle flow that uplifts the basin and forms a mascon. (D) Later mare basalts may add to the mass anomaly. The plus and minus symbols represent density anomalies over the initial configuration in (A).

Earth's mantle after the removal of ice caps at the end of the last glacial age, slows down as the mass anomaly decreases. How can a mass deficit in the basin turn into a mass excess?

As mare basalts are too thin to explain the mass excess, it was proposed that the mantle bounces above its isostatic level and is frozen in place (3, 6). Melosh *et al.* show that this dynamical process is not needed. Mascons can instead form as the result of slow mantle flow driven by two low-density regions generated by the impact process—an annulus of thick, low-density crust, and a low-density mantle under the basin (see the figure).

Both density anomalies drive uplift of the basin. However, the surface cools rapidly, essentially freezing in the contrast between the low-density crustal annulus and the high-

density basin interior. Deep-seated density differences continue to drive mantle flow, lifting the entire basin. The impact basin as a whole may end up being compensated (with deep density anomalies balancing out the surface mass deficit), but the frozen structure inside the basin produces a low-density ring surrounding the high-density interior, which forms a mascon.

Although none of the processes present in this model are fundamentally new, Melosh *et al.* put them all together in a start-to-finish model. The formation of a mascon hinges on the delicate balance between the strength and thermal structure of the lunar crust and upper mantle. The crust must be cold and strong enough to form and maintain a crustal annulus. The deeper mantle must be cold enough to relax over time scales much longer than

that of the initial cooling of the surface yet not so strong that it shears the crustal annulus away. The importance of the work by Melosh *et al.* is, therefore, not only that a mascon appears in this model but that it provides constraints on the conditions under which mascons can form.

The geological activity of planets and moons has changed dramatically during solar system history. Ancient volcanic activity shows that the interiors of the Moon, Mars, and Mercury were hotter 4 billion years ago than they are today. However, that heat is long gone. Ancient heat flux is usually estimated by matching the length scale of tectonic deformation (2, 7–9). Melosh *et al.* show that a mascon forms when the lunar heat flux is relatively high, with a surface geotherm of 30 K/km. It may now be possible to use mascons, which are detected on the Moon, Mars, and Mercury, as a new probe of the thermal history of these planets.

The model of Melosh *et al.* implies that as a planet cools, mascons may no longer form. When is it no longer possible to form a mascon? Is the mascon epoch different on Mars and Mercury? Mascons on Mars have a less well-developed low-density annulus than on the Moon (10). Is this an effect of the planet's size and surface modification processes on Mars? Melosh *et al.* lay the foundation for future work that will address these questions. As both the cratering and relaxation processes depend on the length scale of the mascon and on the acceleration of gravity, it may be possible to use the size of basins that produce mascons as a probe for strength stratification in the outer hundreds of kilometers of a planet in the distant past when these basins formed. It may also be possible to determine whether mascons could have formed in the larger and more active planets, such as Venus and Earth.

References

1. P. M. Muller, W. L. Sjogren, *Science* **161**, 680 (1968).
2. S. C. Solomon, J. W. Head, *Rev. Geophys.* **18**, 107 (1980).
3. G. A. Neumann, M. T. Zuber, D. E. Smith, F. G. Lemoine, *J. Geophys. Res.* **101**, 16841 (1996).
4. J. C. Andrews-Hanna, *Icarus* **222**, 159 (2013).
5. H. J. Melosh *et al.*, *Science* **340**, 1552 (2013); 10.1126/science.1235768.
6. M. A. Wieczorek, R. J. Phillips, *Icarus* **139**, 246 (1999).
7. L. G. J. Montesi, M. T. Zuber, *J. Geophys. Res.* **108**, 5048 (2003).
8. F. Nimmo, T. R. Watters, *Geophys. Res. Lett.* **31**, L02701 (2004).
9. S. C. Solomon *et al.*, *Science* **307**, 1214 (2005).
10. G. A. Neumann *et al.*, *J. Geophys. Res.* **109**, E08002 (2004).

Published online 30 May 2013

10.1126/science.1238099

IBI* SERIES WINNER

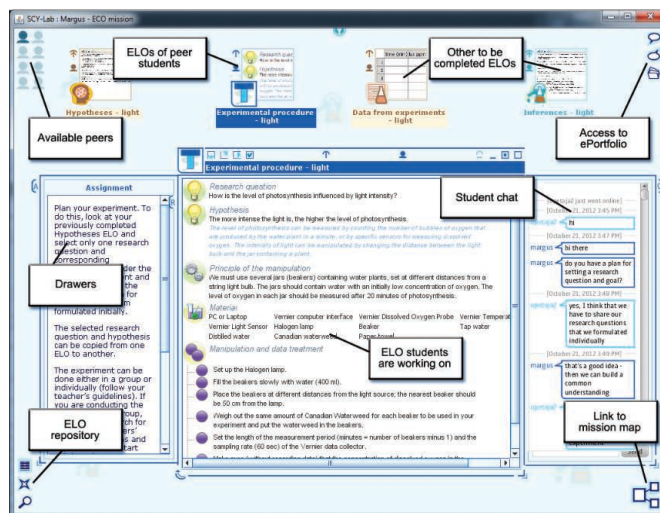
Investigating Ecosystems as a Blended Learning Experience

Margus Pedaste,^{1,†} Ton de Jong,² Tago Sarapuu,¹ Jaanika Piksööt,¹ Wouter R. van Joolingen,² Adam Giemza,³

Learning by inquiry, collaboration, and design are the central didactic principles of the software developed by the Science Created by You (SCY) project. In SCY technology-enhanced learning environments, or SCY missions, students learn by creating products that they can share and discuss with their peers. In order to do this, they make use of textual or multimedia learning materials and perform physical and virtual experiments.

Each SCY mission has a specific research or design goal, for example, to create a healthy pizza or a house where the CO₂ balance is close to zero. Along their way to this final product, students create many types of intermediate virtual products or Emerging Learning Objects (ELOs). ELOs can include concept maps, experimental procedures, models, and data sets from simulations or from real experiments. All activities in SCY missions, center around ELOs, which students can save, retrieve, and edit.

Four SCY missions have been developed around topics such as the greenhouse effect, food and nutritional values, and DNA [see (1) and www.scy-net.eu/]. Here, we focus on what we have called the ECO mission. This mission, for secondary school, ages 15 to 19, primarily addresses the area of ecology and includes chemistry and math subject matter. The ECO mission combines hands-on data collection with working in the SCY software environment. It starts by asking students to create a concept map of the different relations in a freshwater body that will present their initial knowledge about the domain. This can be done individually or collaboratively with student peers. Next, students follow four pre-defined different inquiry cycles on related



Example of a SCY mission interface (from the ECO mission). In the inquiry cycle on light, students collect data on light intensity, water temperature, and dissolved oxygen level. Canadian waterweed is placed in beakers of tap water. Light intensity is changed by moving the beakers different distances from a halogen lamp. Data are collected with mobile Vernier devices, and digital data can be imported into the SCY environment. Students can visualize the changing concentration of oxygen in the beakers and collect real data from which to infer the relation between light intensity and photosynthesis. These data also often prompt discussions on validity and limitations of scientific research.

topics: (i) the role of light in the level of photosynthesis, (ii) the concept of pH and pH changes in a water body, (iii) the influence of nutrient concentration on primary production, and (iv) relations between trophic levels in an ecosystem. These topics were selected on the basis of analysis of the curricula in Estonia, Cyprus, France, Norway, and the Netherlands and fine-tuned by means of expert interviews. After having gone through the four inquiry cycles, students return to their initial concept map to adapt it on the basis of the knowledge gathered in their inquiry.

In the interface that is shown in the screen shot above[ck], students design an experimental procedure during the inquiry cycle, for a hands-on experiment on the role of light in photosynthesis. The experimental procedure under development is open in the center of the screen. A guiding assignment and information sources for creating the ELO are located in “drawers,” or extendable windows attached to the ELO. Chat communication is available in a drawer, and peers are invited by dragging their avatar (top left corner) to the ELO. Navigation takes place through the mission map (bottom right corner), and the bottom left corner houses the ELO repository where students can save, search, and retrieve their own and their peers’ ELOs. More information on the SCY didactic principles and learning environment can be found in (1, 2).

In another physical experiment from the inquiry cycle on pH changes, students put sand, limestone fragments, and granite fragments in different beakers to discover the effect that the composition of a lake bottom could have on pH rise in the lake from acid precipitation. Distilled water is poured into the beakers, followed by different concentrations of sulfuric acid. The pH in all beakers is measured, and data analysis in the SCY environment enables students to understand why similar acid rain could have different effects on the life in various freshwater lakes.

In the inquiry cycle on nutrient concentration, students alter the concentration of nitrogen and phosphorus in water and observe the effect on algae biomass fluctuations. The simulation model takes into account the chemical affinity of nitrogen and phosphorus in forming compounds and the population growth and mortality characteristics. Here, students are provided with data that could otherwise only be collected in a lengthy real-life experiment.

In a simulation on trophic levels, values characterizing predator and prey in an ecosystem can be used as either input or output variables. Population gains and losses, ability to catch and feed on prey, natural growth and death factors, and the ability to convert prey biomass to predator biomass are specific elements in this simulation. Students can alter

¹University of Tartu, 50103 Tartu, Estonia. ²University of Twente, Post Office Box 217, 7500AE Enschede, Netherlands. ³University of Duisburg-Essen, 47048 Duisburg, Germany

*IBI, Science Prize for Inquiry-Based Instruction; www.sciencemag.org/site/feature/data/prizes/inquiry/.
†Corresponding author: margus.pedaste@ut.ee

the initial level of biomass of the components and then investigate changes for a specified time period.

The investigations done in each inquiry cycle (see the photos), together with scientific background information, are necessary for solving the problems introduced in each cycle's initial design or research goal. In addition, these outcomes should help students to redesign the concept map that they had created at the start. Students also develop a video report to illustrate their inquiry processes.

The ECO mission has been implemented in several schools in Estonia, the Netherlands, and Cyprus. Assessment in Estonia involved 64 students (ages 16 to 18) from secondary schools. In each trial site, students worked individually with the ECO mission for 4 hours. At the beginning of the session, an online pretest was completed. A posttest was completed online 2 weeks after the intervention.

Students' initial and final revised concept maps were analyzed in order to assess their conceptual knowledge. The results indicated a significant improvement in students' conceptual knowledge (Wilcoxon signed-rank test: $Z = -5.92$; $P < 0.001$). After working with the ECO mission, students were better able to organize and represent their knowledge about relations between biotic and abiotic factors in freshwater ecosystems.



Learning in a SCY mission. (A) A student planning an experiment. (B) Students measuring light intensity and dissolved oxygen level in water. (C) Waterweed in a beaker. (D) Vernier device for measuring dissolved oxygen level.

Pre- and posttests assessed changes in students' inquiry skills. In both tests, an everyday problem situation related to ecology was presented. Students were then asked to formulate research questions and hypotheses. Next, a graph with experimental data was presented, and students answered questions

about the graph in order to demonstrate their data analysis skills. The final task was to make inferences on the basis of the results of an experiment. Research questions were scored for three elements—the maximum score was given if a question related to the problem was formulated and if it included the correct dependent and independent factors. Hypotheses and inferences were scored on the basis of formulation (a sentence related to the research question), correct dependent and independent factors, and relation with background information. The comparison of pre- and posttests detected a statistically significant improvement in students' skills formulating research questions (Wilcoxon signed-rank test:

$Z = -3.67$; $P < 0.001$) and hypotheses ($Z = -2.78$; $P < 0.05$). As students' skills analyzing data and making inferences were already high before the intervention, significant improvement was not seen. The results indicated that after working on the ECO mission, students were better able to relate research questions and hypotheses and to correctly identify dependent and independent factors from background information. According to the teachers' feedback, the ECO mission enriches the school curriculum with innovative blended learning opportunities that combine learning in the classroom and the computer lab with authentic data collection.

Supplementary Materials

www.sciencemag.org/cgi/content/full/340/6140/1537/DC1

References and Notes

1. T. de Jong *et al.*, *Educ. Technol. Res. Dev.* **60**, 883 (2012).
2. T. de Jong *et al.*, *Br. J. Educ. Technol.* **41**, 909 (2010).

Acknowledgments: This study was conducted in the context of the SCY project, which was funded by the European Union (EU) under the Information and Communication Technologies theme of the 7th Framework Programme for R&D (grant agreement 212814). This document does not represent the opinion of the EU, and the EU is not responsible for any use that might be made of its content. We would like to acknowledge the SCY project members for their contributions, specifically, C. Geraedts, J. Heerink, T. Hovardas, R. Julien, P. Link, H.-A. Villako, A. Puusepp, M. Rinket, J. Sikken, M. Van der Zanden, M. Zinakov, and V. Vold made initial contributions to the ECO mission. L. Bollen and J. Sikken gave technical support in preparing this document. E. Fox corrected the English of this essay and the ECO mission statements. SCY has been developed in cooperation with a large set of schools around Europe but is a prototype system.

10.1126/science.1229908

About the authors



Margus Pedaste is professor of Technology Education at the University of Tartu, researching computer-supported inquiry learning. **Ton de Jong** is professor of Educational Psychology at the University of Twente, studying educational technology and science learning. **Tago Sarapuu** is an associate professor at the University of Tartu and lead research fellow at Tallinn University, focusing on design principles of virtual learning environments. **Jaanika Piksööt** is a Ph.D. student in science education at the University of Tartu concentrating on the analysis of visual

information in computer-based learning. **Wouter R. van Joolingen** is professor of Science Education at the University of Twente, researching modeling and computer-supported learning environments. **Adam Giemza** is a Ph.D. student at the University of Duisburg-Essen, studying heterogeneous architectures for collaborative and mobile learning.



MEDICAL RESEARCH

Research Offers Hope for More Effective Stroke Treatments

Many of the statistics about stroke are troubling. The disorder is the third leading cause of death in the world. And, because stroke risk rises sharply after age 60, countries with large “boomer” populations, such as the United States, are on course for a substantial increase in stroke prevalence in upcoming decades.

There are two bright spots on the horizon, however, which Walter Koroshetz, deputy director of the National Institute of Neurological Disorders and Stroke, explained at a 22 May Capitol Hill briefing hosted by AAAS in conjunction with Representative Chaka Fattah (D-PA) and with support from the Dana Foundation.

For one thing, up to 70% of strokes are preventable by fairly simple measures, such as blood pressure control, improved diet, and exercise.

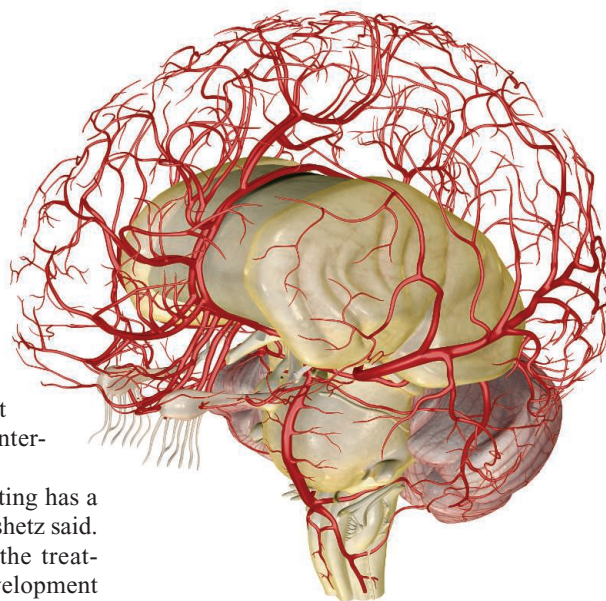
“The data for stroke show that if we really got our act together, we could make a huge difference because the science tells us that one’s annual stroke risk decreases dramatically as known risk factors are controlled,” Koroshetz said. “If we achieve optimal weight control, physical exercise, blood pressure, and diet earlier in life, then the health benefits to individuals, their families, and to the country as a whole would be enormous.”

A central understanding in this research field is that when one part of the brain dies in a stroke, another part of the brain can “learn” to take over its function. Much of what scientists are learning about this

dynamic rewiring of the brain comes from studying brain development in childhood, when connections between brain cells are being formed, strengthened, or pruned at an astounding rate as the child interacts with the environment.

“The stimulus the brain is getting has a lot to do with the rewiring,” Koroshetz said. That same principle applies in the treatment of stroke, where neural development patterns that have been suppressed since childhood can start working again and be enhanced and molded by intensive rehabilitation therapy. He noted an Emory University-led study with stroke patients who had a disabled arm. With their good arms immobilized, the patients gained dexterity in the affected arm, including some who started the treatment regime as long as 21 months after their strokes.

As scientists learn more about these intrinsic repair processes, they are finding more potential targets for drug therapies. But most relevant for patients right now, Koroshetz said, are the efforts to improve standard rehabilitation care. He noted a clinical trial of stroke patients from five hospitals in Florida and California, which showed that intensive rehabilitation, either with in-home exercises or on a treadmill, led to improved walking ability as compared to “standard of care” rehabilitation. Even 6 months after their strokes, patients who had received only the standard of care



could still make substantial improvements in walking by undergoing intensive treadmill training.

“This tells us that our standard of physical and rehabilitation therapy after a stroke is not optimal,” said Koroshetz. Patients often can benefit from more intensive therapy regimes, he said.

New technologies also offer promise. Koroshetz noted work with brain-machine interfaces using implanted electrodes that can record neuronal signals in the motor cortex of the brain. In a study reported last year, a woman paralyzed by a stroke learned to use her thoughts to generate neuronal signals to steer a robot arm to grab a bottle of coffee and lift it to her lips.

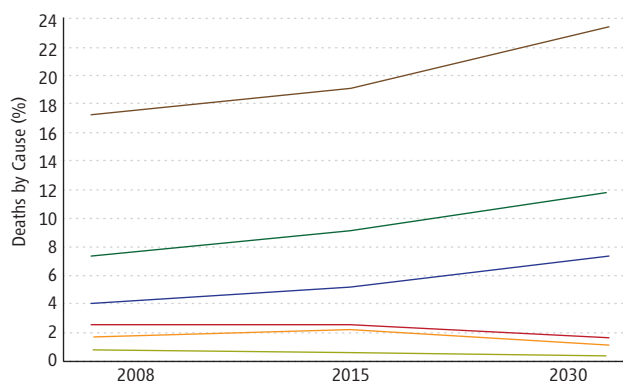
Other researchers have developed “therapeutic exoskeletons,” motor-powered mechanical braces that do much of the work of walking or lifting. The devices can help patients carry out the intensive activity they need to perhaps trigger some of the brain’s intrinsic repair mechanisms.

New recording technologies, such as optical probes that can detect tiny flashes of light by thousands of firing nerve cells, offer new possibilities for listening in on the electrochemical “language of the brain,” Koroshetz said. The BRAIN Initiative (Brain Research through Advancing Innovative Neurotechnologies), announced recently by President Barack Obama, should greatly expand the amount of information scientists can glean from these new technologies.

—Earl Lane and Kathy Wren

On the rise. The World Health Organization projects that deaths due to cardiovascular disease, including those caused by stroke, will continue to rise if appropriate measures are not taken.

— Cardiovascular diseases
— Cancer
— Chronic respiratory diseases
— Perinatal conditions
— HIV/AIDS
— Malaria



President of Poland Honors Long-Time AAAS Diplomat

In March 1967, Norman P. Neureiter arrived in Poland with his wife Georgine and their two young boys to serve as the first science attaché at the U.S. Embassy in Warsaw. During the next 2 years, Neureiter would develop many cooperative research projects bringing U.S. and Polish scientists together during some of the darkest days of the Cold War.

In recognition of this work and his subsequent support of Polish-American research, Neureiter, now a senior advisor to the AAAS Center for Science Diplomacy and director of the Center for Science, Technology and Security Policy, was on 6 June awarded the Officers Cross of the Order of Polonia Restituta (Polish Merit, one of the highest Polish State decorations) by the president of the Republic of Poland, Bronisław Komorowski.

By 1968, the student unrest in Western countries had spread in dramatic form to Poland and other parts of Eastern Europe. At the theater, Neureiter heard the audience cheer in response to anti-Russian sentiments in a play by beloved Polish poet Adam Mickiewicz. And, in Krakow, he watched as demonstrators were driven away by militias with red arm bands, leaving yellow flowers as a symbol of protest. In Czechoslovakia, where Neureiter was also assigned, he saw the start of the “Prague Spring” and its end with the Soviet invasion.

In the sciences, however, the prospects for progress were more auspicious. Neureiter broadened cooperation already beginning in agriculture, medicine, and health care and developed new areas, such as environmental protection and clean coal. After returning to the United States, he served as a U.S. Commissioner of the Maria Skłodowska-Curie Joint Fund II, which supported Polish-American research collaboration.

More recently, Neureiter helped to initiate a new awards program, announced last month, to be jointly administered by AAAS and the Foundation for Polish Science, recognizing scientists who have advanced science through U.S.-Polish cooperation.

Neureiter received the Officers Cross of the Order of Polish Merit during a ceremony at the historic Belvedere Presidential Palace in Warsaw. In his remarks, Neureiter



Committed to cooperation. Norman Neureiter (right) receives one of the highest Polish state decorations from the president of the Republic of Poland, Bronisław Komorowski.

stressed the value of science diplomacy in building and strengthening ties between nations, even in the face of severe strains in official relationships.

“I think your security people thought I was a spy determined to discover your scientific secrets,” he said. “But, in truth, my mission was just the opposite. It was to build friendly, cooperative relationships with the Polish science community and to foster cooperative projects wherever funding possibilities and joint scientific interests existed.”

“In those days, we did not have a special name for these activities; we just called them science cooperation. But, in fact, those projects were examples of what today we call science diplomacy: the use of science cooperation as a way of improving relations between countries.”

A research chemist in his early career, Neureiter entered the U.S. Foreign Service in the 1960s. Later, he served in President Richard Nixon’s Office of Science and Technology, where he helped to develop the scientific elements of historic agreements with the Soviet Union and China. He then spent more than 20 years with Texas Instruments, and in 2000, he was named science advisor to U.S. Secretary of State Madeleine Albright. He remained in that post under Albright’s successor, Colin Powell, and he joined AAAS in 2004.

Since that time, Neureiter has been a part of AAAS science-diplomacy delega-

tions to Iran, Cuba, Syria, Myanmar, North Korea, and other countries. In 2008, Neureiter received the National Academy of Sciences Public Welfare Medal in recognition of his efforts as a science advisor and champion for international research cooperation. He also received Japan’s Order of the Rising Sun, Gold and Silver Star decoration in 2010, for his efforts to advance U.S.–Japan relations and joint scientific efforts. Last year, Neureiter was awarded the Austrian Cross of Honour for Science and Art 1st Class for his efforts to support the International Institute for Applied Systems Analysis, a Vienna-based organization that addresses global challenges.

—Kathy Wren

BUDGET POLICY

AAAS Op-Ed: Don’t Devalue Basic Research

Hefty federal deficits in Canada and the United States pose a significant threat to fundamental, basic research as some policy-makers seem to value near-term, industry-focused science more highly. That’s shortsighted and will likely have damaging consequences for both countries, AAAS CEO Alan I. Leshner wrote in a 19 May op-ed published by Canada’s largest daily newspaper, the *Toronto Star*.

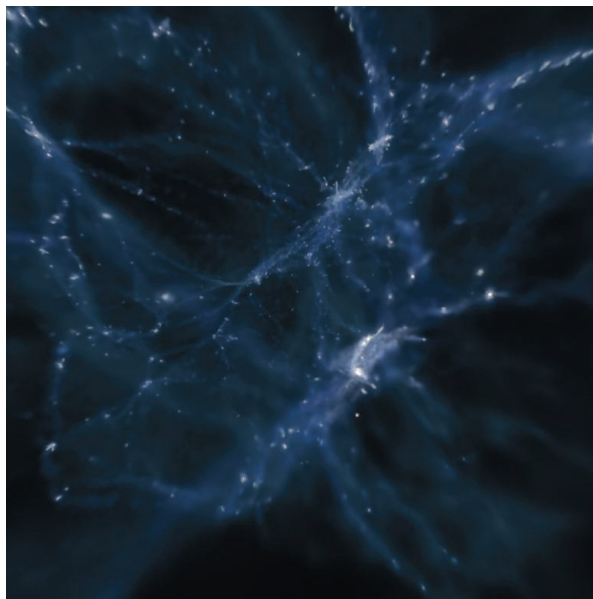
From Gas to Stars Over Cosmic Time

Mordecai-Mark Mac Low

Background: Immediately after the Big Bang, the universe was uniform, homogeneous, and completely free of stars. The gravitational collapse of dark matter gathered gas with it that cooled, collapsed further, and formed stars. Observations over the past 20 years have revealed the dynamic star-formation history of the universe. The star-formation rate peaked 10 billion years ago, when stars formed an order of magnitude faster than in the modern universe. Deep observations have begun to reveal the early history of star formation, but how quickly star formation started remains controversial, with results from observations of early galaxies suggesting a slower start than distributions of distant gamma-ray bursts that trace young stars. However, simulations using standard prescriptions for energetic feedback from star formation (from stellar explosions and ionizing radiation) have tended to predict a substantially earlier peak than either of these methods shows.

Advances: Energetic feedback drives turbulence in diffuse gas that both promotes and inhibits star formation, with inhibition dominating over promotion, so that star formation does not efficiently trigger further star formation. Insufficient numerical resolution in simulations causes unphysical radiative cooling to occur in multiple ways, reducing the effectiveness of feedback in driving turbulence. Other mechanisms—such as magnetorotational instability, radiative heating, or accretion from the intergalactic medium—must also contribute to the observed gas velocity dispersions. Radiation pressure appears likely to be only modestly effective because of Rayleigh-Taylor instability in gas accelerated by it. Observed correlations between gas surface density and star-formation rate surface density can be reproduced by models including gravitational instability. Molecule formation may occur as a result of gravitational collapse rather than initiating it. Thus, gravitational instability seems to determine star formation, with the level of turbulence setting the critical density for instability.

Outlook: Determining the early history of star formation will require the efforts of the largest ground- and space-based telescopes under construction, such as the James Webb Space Telescope, the European Extremely Large Telescope, and the Large Synoptic Survey Telescope. Progress in models requires both better algorithms and larger computers. Adaptive meshes, both structured and unstructured, will play a critical role, as will hybrid algorithms that can take full advantage of the shared memory nodes of massively parallel computer clusters. A clear picture of star formation will underpin our understanding of the evolution of galaxies, including our own Milky Way, and of the history of the production and distribution of the elements heavier than helium, including those necessary for planet formation and for life.



The peak of star formation. Some 10 billion years ago, stars formed in the universe at a rate more than 20 times higher than the modern era. Star-forming galaxies light up the sky, whereas fainter filaments trace the distribution of dark matter that draws the gas together gravitationally in this numerical model. Understanding the history of star formation over cosmic time remains a major theoretical and observational challenge. [Credit: American Museum of Natural History/National Astronomical Observatory of Japan]



READ THE FULL ARTICLE ONLINE
<http://dx.doi.org/10.1126/science.1229229>

Cite this article as M.-M. Mac Low, *Science* **340**, 1229229 (2013). DOI: 10.1126/science.1229229

ARTICLE OUTLINE

Star-Formation History of the Universe

Numerical Simulations

How Does Stellar Feedback Inhibit Star Formation?

What Are the Sources of the Interstellar Turbulence?

Star-Formation Laws

Gravitational Instability

Outlook

ADDITIONAL RESOURCES

Special issue on Galaxy Evolution, *Science* **333**, 169–185 (8 July 2011); particularly J. S. Dunlop's Review, "The cosmic history of star formation" (pp. 178–181).

The Hayden Planetarium show "Journey to the Stars" covers the formation of the first stars and the star-formation history of the universe along with other aspects of stellar and solar astrophysics. It is available to educators on DVD or by streaming at www.journeytothestars.org.

From Gas to Stars Over Cosmic Time

Mordecai-Mark Mac Low^{1,2}

From the time the first stars formed over 13 billion years ago to the present, star formation has had an unexpectedly dynamic history. At first, the star-formation rate density increased dramatically, reaching a peak 10 billion years ago of more than 10 times the present-day value. Observations of the initial rise in star formation remain difficult, poorly constraining it. Theoretical modeling has trouble predicting this history because of the difficulty in following the feedback of energy from stellar radiation and supernova explosions into the gas from which further stars form. Observations from the ground and space with the next generation of instruments should reveal the full history of star formation in the universe, and simulations appear poised to accurately predict the observed history.

Once, there were no stars. This simple, yet profound, statement is an inevitable consequence of Big Bang cosmology. Observations of the cosmic microwave background reveal that, at the time of its emission some 300,000 years after the Big Bang, the universe was filled with hydrogen and helium having a density uniform to a few parts in 10^5 (1, 2). Understanding how that gas evolved into the universe filled with stars that we observe today, 13.798 \pm 0.037 billion years later (3, 4), remains one of the most important goals of modern astrophysics.

The ordinary matter from which stars form makes up only 4.63 \pm 0.0024% of the total mass energy of the universe and 17% of the matter (5), with the rest being made up of not-yet-identified cold dark matter and dark energy. Star formation (Box 1) traces the gravitational collapse of the dark matter into the cosmic web in a universe whose expansion is currently dominated by dark energy.

The collapse of dark matter from small perturbations into the gravitationally bound structures first identified as halos around galaxies can be followed by the Press-Schechter (6, 7) analytic excursion-set formalism. However, the properties of the stellar populations that form within those halos, in visible galaxies, depend critically on nonlinear physics, including magnetized gas dynamics, radiative transfer, and nuclear fusion. We are ultimately forced to rely on numerical simulations of galaxy formation incorporating approximate treatments of these processes in order to predict the observable outcomes of cosmological theory.

The approximations used in these models rely on a detailed understanding of the smaller-scale physics determining star formation. Feedback of energy into the interstellar and intergalactic gas from ionizing ultraviolet (UV) radiation and supernova explosions from stars, and from high-

velocity outflows and radiation from supermassive black holes, has been extremely difficult to model well enough to predict the star-formation history of galaxies. Models that neglect feedback or understate its importance predict far too much star formation at early times (8, 9). Because of its central importance to modern models of star formation, I explore this topic in some detail in this review.

Star-Formation History of the Universe

Star formation in the universe can be described by using the star-formation rate (SFR) density at any time, often expressed in units of solar masses per cubic megaparsec per year. After a slow start, the SFR density in the observed universe peaked some 10 billion years ago, when stars formed an order of magnitude faster than they do in the present epoch (10–12). Light emitted then has been redshifted by the expansion of the universe to longer wavelengths by a factor of $(1+z)=3$, so we refer to that era (13) as being at redshift $z=2$. The time dependence of the SFR at higher redshifts (greater lookback times) remains uncertain, leaving the time of formation of the first stars poorly constrained (12, 14, 15). Two major lines of evidence, from imaging galaxies and gamma-ray bursts, give apparently conflicting results (15–17) that in turn must agree with two constraints: the range of time over which the intergalactic medium was reionized by UV ra-

diation from stars and the well-observed density of stars at $z=4$.

The first line of evidence relies on the detection of high redshift galaxies by photometry in multiple colors. Even broadband photometry can detect the sharp cutoff in galactic emission in the far UV beyond the 91.2-nm Lyman limit, the wavelength of light that can ionize hydrogen, the most abundant element, and thus will be absorbed by it. Galaxies at high redshifts have this Lyman break redshifted into visible or even infrared light, where it can be observed from large, ground-based telescopes. A galaxy that is bright in colors with wavelengths longer than the redshifted break, but that disappears below it, can be identified as being at a specific redshift (18). Lyman break galaxies observed out to $z>8$ (6×10^8 years after the Big Bang) can be used to determine the SFR density as a function of redshift [e.g., (19)]. However, the faintest galaxies at each redshift cannot be detected, so their contribution must be extrapolated from the distribution of the brighter observed galaxies. Only taking into account the directly observed galaxies leads to the conclusion that the SFR drops off rather quickly at high redshift (15, 16, 20) as shown by the blue points in Fig. 1. However, this is in tension with the first constraint, because it would imply a reionization redshift somewhat later than the current concordance value $z=10.1 \pm 1.0$ (5).

Gamma-ray bursts provide the second line of evidence. These intense flashes of tightly beamed, gamma-ray light produced in occasional supernova explosions (21) are bright enough to be observed back to $z>8$. Derivation of the SFR associated with the host galaxies of such high-redshift gamma-ray bursts depends on calibrations at lower redshifts, though, so extension of these calibrations to high redshift requires determination of how the incidence of gamma-ray bursts as a function of the SFR evolves with redshift (15–17). One hypothesis is that gamma-ray bursts occur primarily in galaxies with low abundances of heavy elements, which form a greater fraction of the population at high redshift. However, the SFR derived from that hypothesis (the red points in Fig. 1) violates the second constraint, predicting too high

Box 1. Star formation.

Stars form when gravity causes interstellar gas and dust—the interstellar medium—to collapse toward regions of higher density, while radiative cooling prevents the temperature from increasing as densities get higher, so that pressure cannot prevent collapse. Collapse ultimately continues until central temperatures and pressures rise high enough for nuclear fusion to begin, heating the gas sufficiently to counterbalance the force of gravity and maintain hydrostatic equilibrium. This process occurs over a time of order the free-fall time of the gas $t_{\text{ff}} \sim (G\rho)^{-1/2}$, depending only on ρ , the mass density of the gas, where G is the gravitational constant. The mass of a region capable of gravitational collapse is given by the Jeans (122) mass

$$M_J = (\pi/6) G^{-3/2} \rho^{-1/2} c_s^3$$

where c_s is the sound speed of the gas, which depends on the temperature as $T^{1/2}$.

¹Department of Astrophysics, American Museum of Natural History, 79th Street at Central Park West, New York, NY 10024, USA. ²Zentrum der Astrophysik der Universität Heidelberg, Institut für Theoretische Astrophysik, Albert-Ueberle-Str. 2, 69121 Heidelberg, Germany.

E-mail: mordecai@amnh.org

a stellar density by $z = 4$ (17). Similarly, the model shown by the green line in Fig. 1, which includes this hypothesis as well as a physically motivated minimum mass of dark matter halo in which stars can form, still predicts slightly less star formation than suggested by the red points. This suggests that some other effect must also be acting (15, 17). The strength of this effect can be empirically derived by measuring the fraction of gamma-ray burst host galaxies detectable at redshifts $z = 5$ and $z = 6$ (15).

Numerical Simulations

Numerical simulations a decade ago [e.g., (9)] predicted that the peak in star formation should occur at $z \sim 6$. The contradiction to the observations of the well-observed peak at $z \sim 2$ occurs in large part because neglecting feedback, or including it by standard recipes (22), leads to overproduction of stars at early times. The alternative to date has been reliance on ad hoc models of strong feedback, both from stars and supermassive black holes, to suppress that early star formation in order to agree with the observations.

This is because simulations capturing cosmological scales have been unable to model the interstellar medium within galaxies with sufficient resolution to follow the energetics of stellar feedback successfully. This leads to the classical overcooling problem. Without local feedback that transfers realistic amounts of energy to the interstellar medium, the SFR can be an order of magnitude higher than observed, even in models of modern galaxies (9, 23–29).

Another reason for requiring ad hoc models of energetic feedback, which I will not focus on here, is that accretion into clusters of galaxies produces huge reservoirs of hot gas. The accretion of this low-density hot gas onto massive elliptical galaxies must be throttled. It is much easier to prevent accretion onto galaxies of low-density gas that cannot radiatively cool easily than it is to reheat and expel already cooled and accreted gas. The required heating likely comes from the jets driven by supermassive black holes in active galactic nuclei rather than stars.

Feedback models typically fail because of unphysical cooling in poorly resolved regions of hot gas. Interstellar and intergalactic gas cools radiatively (30, 37): Inelastic collisions excite electrons into higher energy levels while slowing down the colliding particles (effectively reducing the temperature of the gas). The excited electrons then drop back to the ground state, releasing photons. So long as the densities are low enough for collisions not to deexcite the electrons before radiation and the opacity of

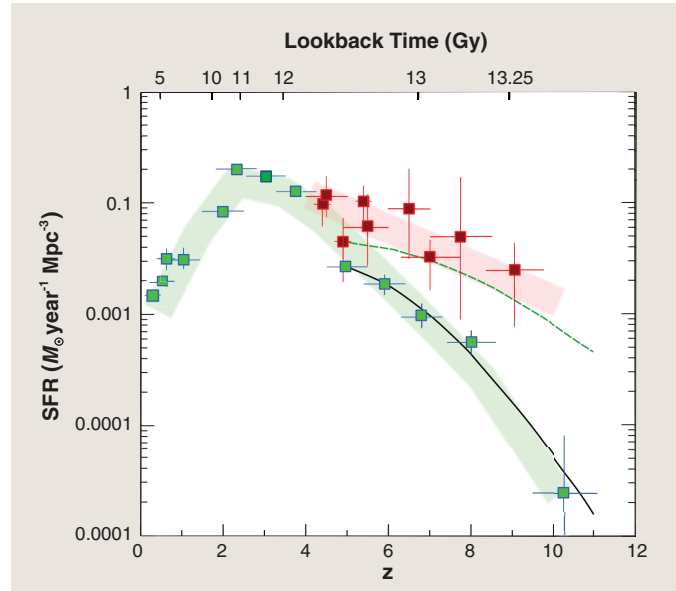


Fig. 1. Cosmic history of star formation. The cosmic history of star formation in the universe versus redshift z or lookback time (15). Star formation peaked some 10 billion years ago at a rate 10 times as high as the modern era. At high redshift, the lower estimates outlined in green rely on observations of high-redshift Lyman break galaxies, neglecting those below the detection limit (19), whereas the upper estimates outlined in red depend on the star-formation intensity per gamma-ray burst (16). The lines show model predictions (17, 129) integrated over either the range of galaxies included in the Lyman break galaxy survey (black solid) or down to the expected lower limit for the mass of star-forming galaxies (green dashed). M_\odot indicates solar mass.

the gas and dust is low enough to allow escape of the photons from the system, these inelastic collisions lead to energy loss and thus cooling. Interstellar and intergalactic gas away from the very densest cores of star-forming regions typically satisfies both of these conditions.

Because radiative cooling relies on collisions, its strength, $\dot{E} = -n^2 \Lambda(T)$, depends on the square of the number density n , as well as having a strong temperature dependence, $\Lambda(T)$, from the distribution of available energy levels for electron excitation. Crucially, the value of $\Lambda(T)$ for $T = 10^5$ K gas in ionization equilibrium exceeds by more than an order of magnitude that for hot 10^6 K or cool 10^4 K gas (Fig. 2A) (31). The elevated cooling around 10^5 K occurs because of the ability of collisions in that temperature range to excite the strong resonance lines of lithium-like ions of carbon, oxygen, and nitrogen, the most common elements heavier than helium.

The temperature and density dependence of the cooling function leads to two serious problems for numerical simulations. First, supernova explosions drive blast waves that shock gas to temperatures above 10^6 K, so that it only cools with difficulty. However, if stellar feedback energy is fed into the grid of a numerical simulation too slowly or over too large a volume, it will only raise the temperature into the 10^5 K range or lower, so that the energy will promptly radiate without exerting dynamical effects. Sec-

ond, simulations of gas flow usually require several zones to resolve interfaces between gas with different properties, such as hot and rarefied or cold and dense. Within such an interface, the resolution of the numerical grid rather than the physics of the interface determines the amount of intermediate temperature gas (Fig. 2B). In poorly resolved models, such interfaces capture large volumes of gas that cools unphysically. Over 25 years ago, Tomisaka (32) already demonstrated that the evolution of superbubbles formed by multiple supernova explosions from an association of OB stars could not be adequately simulated with 5-pc (16-light-year) resolution because of such strong numerical overcooling (33). For models of the diffuse interstellar medium of the Milky Way Galaxy ($0.01 < n < 100 \text{ cm}^{-3}$), it has been demonstrated that 2-pc (6.5-light-year) grid cells resolve interfaces well enough to avoid dynamically important loss of energy from hot gas (34–36). Such a model, from (36), is shown in Movie 1.

How Does Stellar Feedback Inhibit Star Formation?

Energetic feedback from stars heats the interstellar gas through radiative ionization and drives strong shock waves through it from supernova explosions, leaving it in a characteristic state of supersonic, highly compressible turbulence. This differs in its properties from the almost-incompressible turbulence familiar from the terrestrial atmosphere and ocean because of the strong density fluctuations produced by the shock waves and the strong vorticity sheets produced at shock intersections.

Such highly compressible turbulence both promotes and prevents gravitational collapse. We can heuristically estimate which effect wins by examining the dependence of the Jeans critical mass for gravitational collapse (Eq. 1), $M_J \propto \rho^{-1/2} c_s^3$, on the root-mean-square turbulent velocity, v_{rms} (37). In the classical picture, turbulence is treated as an additional pressure (38, 39) so that we can define an effective sound speed, $c_{s,\text{eff}}^2 = c_s^2 + v_{\text{rms}}^2/3$. This additional effective pressure increases the Jeans mass by $M_J \propto v_{\text{rms}}^3$, inhibiting collapse. On the other hand, shock waves with Mach number $\mathcal{M} = v_s/c_s$ in an isothermal medium cause density enhancements with density ratio $\rho_s/\rho_0 = \mathcal{M}^2$. These turbulent compressions decrease the Jeans mass by $M_J \propto \rho_s^{-1/2}$, assuming that the shocks typically have shock velocity $v_s \cong v_{\text{rms}}$.

When we combine the effects of increased pressure and increased density, we find that

$$M_J \propto \left(\frac{c_s}{v_{\text{rms}}} \right) \left(c_s^2 + \frac{v_{\text{rms}}^2}{3} \right)^{3/2} \propto v_{\text{rms}}^2 \quad (1)$$

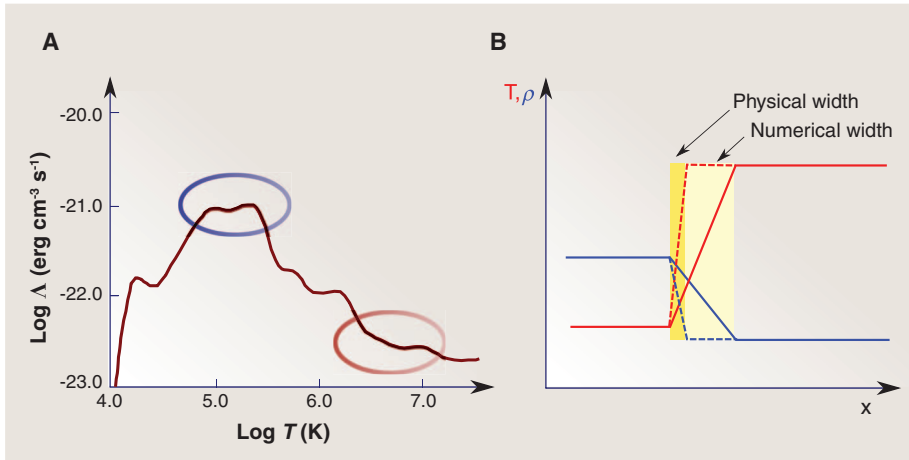


Fig. 2. Cooling of interstellar gas. (A) The temperature dependence of the cooling function $\Lambda(T)$ from (31), showing the order-of-magnitude higher cooling rate at around 10^5 K (red circle) compared with 10^6 to 10^7 K (blue circle). (B) Sketch of how unphysical cooling can occur at poorly resolved numerical interfaces when too much intermediate temperature gas is present.

Movie 1. Visualization of supernova driving of turbulence in a magnetized, stratified atmosphere representative of a cross-section through a galactic disk. Temperature is shown along a vertical cut through the region nearest the disk midplane of a three-dimensional simulation performed using the adaptive mesh refinement code FLASH, with the region within 0.05 kpc of the plane resolved at 1.95-pc resolution. This is model bx50 in (37).

for $v_{\text{rms}} \gg c_s$. Thus, highly supersonic turbulence strongly inhibits collapse. Because turbulence acts intermittently, it still promotes collapse locally, in shock-compressed regions, even though its net effect is to inhibit collapse globally. Therefore, a region with mass lower than the Jeans mass globally because of turbulence can still have isolated regions of local collapse, as shown in isothermal simulations (40). The role of compression was isolated in simulations described in (41), in which the average density was increased with the dependence on the Mach number required to balance the turbulent support term. Even higher-resolution simulations using adaptive mesh refinement (42) show that the star-formation efficiency can be expressed in terms of the ratio of the crossing time, $t_x = L = 2v_{\text{rms}}$, for a region of size L to the free-fall time t_{ff} .

The net suppression of star formation by turbulence has consequences in the diffuse, stratified interstellar medium of galaxies. This was demonstrated (35) with a well-resolved model of supernova driving of turbulence, including a treatment of radiative heating and cooling but not self-gravity of the gas, run with the adaptive mesh refinement gas dynamics simulation code FLASH (43). The turbulent flow indeed compressed gas into Jeans-unstable regions of cold, dense gas with sizes comparable to observed star-forming clouds. However, if the SFR expected for those regions is computed, it is an order of magnitude less than the rate required to produce the assumed number of supernovas driving the turbulence. This is consistent with the results of uniformly driven,

self-gravitating turbulence described in the preceding paragraph. Turbulence triggers star formation inefficiently; it does not lead to stochastic propagating waves of star formation as once proposed (44).

At the scale of single star-forming clouds, the question of triggering has also been studied (45). In such clouds, the most important effect is heating of the gas from under 100 to around 10^4 K when UV radiation from newly formed massive stars ionizes it (46). The resulting huge increase in pressure drives a blast wave outward. This strongly disturbs the morphology of the gas cloud. However, the actual difference in the SFR is small, accelerating the formation of stars by only 20% of the free-fall time of the cloud.

Quantitative observational studies support the conclusion that triggering does not represent a major mode of star formation. Although triggered star formation clearly occurs around regions of massive star formation, it is a relatively small effect that does not explain most star formation, consistent with the 10% effectiveness previously found (35). For example, even under favorable circumstances, compression of gas by nearby massive stars triggers less than a quarter of star formation in the Elephant Trunk Nebula (47). At the galactic scale, multiple supernova explosions sweep up supershells in the Large Magellanic Cloud. Only 12 to 25% of the star-forming gas traced by the emission of the molecule carbon monoxide in the supershells formed as a direct result of supershell formation, corresponding to no more than 11% of the total star-forming gas in this galaxy (48).

What Are the Sources of the Interstellar Turbulence?

If turbulence limits star formation, then understanding sources of turbulence, both in the diffuse gas and in dense clouds of star-forming, molecular gas, will help us to understand star formation.

Supernova explosions effectively drive turbulence in the diffuse gas (37). A study (49) of the velocity dispersion resulting from supernova rates ranging from the Milky Way value to 512 times higher, as would be seen in extreme starburst galaxies having SFRs hundreds of times that of the Milky Way, showed that, regardless of the supernova rate, supernova driving resulted in a rather uniform velocity dispersion: $v_{\text{rms}} = 5$ to 10 km s^{-1} . This work varied the surface density of the gas disks following the Kennicutt-Schmidt law (50) relating the surface density to the SFR and thus the supernova rate. To simulate observations in the 21-cm line of atomic hydrogen, they fit single Gaussian components to the velocity of gas in the atomic temperature range (roughly 10^2 to 10^4 K). The resulting simulated observations showed spectral line widths equivalent to 10 to 20 km s^{-1} , agreeing with most observations (51, 52), aside from extreme starbursts where elevated 21-cm line widths are observed (53).

The driving of interstellar turbulence in nearby galaxies was more generally studied by (52) in a sample of galaxies observed with the Spitzer Infrared Nearby Galaxies Survey (54) and The H I Nearby Galaxies Survey (55). The energy input from supernovas can explain the observed density of kinetic energy of the interstellar gas within the star-forming inner regions of the observed disk galaxies. However, in the primarily gaseous outer disks—where star formation drops off strongly, so there are few supernova explosions—some other mechanism has to be stirring the gas to maintain the observed density of kinetic energy.

Two possibilities have been proposed for this alternative mechanism. One possibility is magnetorotational instability (56), which transfers energy from differential rotation into turbulence whenever the angular velocity decreases outward in rotating, magnetized gas. Galactic disks have flat rotation curves, with constant orbital velocity, because they lie within massive haloes of dark matter. Therefore, their angular velocity decreases outward, so magnetorotational instability can drive substantial turbulence (57).

However, the strength of this turbulence depends on the thermal properties of the gas. The temperature dependence of the cooling curve for interstellar gas at $T < 10^4$ K leads to the possibility of a two-phase medium in which the gas has two stable equilibria with the radiative heating (58), one cold ($T \sim 10^2$ K) and dense ($n \sim 100 \text{ cm}^{-3}$) phase and one warm ($T \sim 10^4$) and lower density ($n \sim 1 \text{ cm}^{-3}$) phase. Simulations have shown that velocity dispersions of the magnitudes observed in 21-cm emission can be reached if such a two-phase medium forms (59).

The energy input from the magnetorotational instability appears sufficient to explain the kinetic energy seen in the outer disks of galaxies beyond the star-forming region where supernovas are expected (52).

Another possibility is that radiative heating from external sources of UV radiation such as quasars or starburst galaxies can by itself maintain the observed velocity dispersion as thermal motion (60, 61). Under this hypothesis, gas in the outer disk must lie predominantly in the warm phase, and the transition to a two-phase medium as density increases marks the radius at which star formation begins. This model can be distinguished observationally from magnetorotational instability by its prediction of an absence of gas in the cold, dense phase in outer disks. However, the discovery of finite rates of star formation in outer disks by the GALEX satellite UV observatory (62) suggests the presence of the cold, dense phase, supporting magnetorotational instability as the second driving mechanism.

Recently, radiation pressure from the light emitted by the most massive star clusters reflecting off of dust grains in the interstellar gas has been argued to play a major, or even dominant, role in limiting star formation in galaxies (53). However, this conclusion depends on how well radiation can couple to the dust and thence with the gas by collisions of moving dust grains with the surrounding gas particles. If each photon from the massive stars only scatters once off of a dust grain before escaping the system, then the radiation pressure from a star cluster with luminosity L is proportional to L/c , where $c = 3 \times 10^5 \text{ km s}^{-1}$ is the speed of light. This is sometimes called the momentum-driven limit, because this conserves the momentum of the radiation, but much of its energy escapes. If, on the other hand, the dust is extremely optically thick so that the photons continue scattering off of the dust until they lose almost all their energy, then the radiation pressure is far higher, proportional to L/v_{rms} , which is called the energy-driven limit. Because the turbulent motions in interstellar gas have $v_{\text{rms}} \sim 10 \text{ km s}^{-1}$, this represents a huge difference.

Although it is unlikely that the energy-driven limit is ever reached in real star-forming galaxies, the argument for the importance of radiation pressure relies on the expectation that the number of times the photons scatter is comparable to the infrared optical depth, τ_{IR} , of the most massive star-forming regions in the galaxies, which can be over 100. This assumption suggests a radiation pressure proportional to $\tau_{\text{IR}}L/c$. However, several groups (63, 64) argued for the momentum-driven limit actually being the appropriate one, suggesting that radiation pressure is far less important in galactic evolution.

Recent multidimensional simulations of radiation pressure acting on a layer of gas with $\tau_{\text{IR}} \gg 1$ (65) showed that the radiation acts as a rarefied fluid accelerating a dense fluid, which causes Rayleigh-Taylor instability. The instability

overturns and fragments the dense gas, stirring it but allowing the radiation to escape far more quickly than would be expected from its initial optical depth. As a result of this overturn, although radiation pressure is more effective than the momentum-driven limit, it is typically at least an order of magnitude less efficient than suggested by the assumption of proportionality to $\tau_{\text{IR}}L/c$. This calls into serious question results based on that assumption.

The gravitational interaction of the gas with itself can temporarily drive turbulence even in the absence of outside energy inputs. Such gravitationally driven turbulence occurs in disks that are dense and cool enough to be subject to gravitational instability (26). The resulting turbulence produces a distribution of surface-density fluctuations consistent with observations of atomic gas in the Magellanic Clouds. However, turbulence decays in roughly a gravitational free-fall time (66), so turbulence driven by internal gravitational motions cannot effectively delay gravitational collapse and subsequent star formation on its own.

On the other hand, accretion of gas from the intergalactic medium onto galaxies, a process that appears to continue to the present day, carries substantial kinetic energy with it, so it could feed gravitationally driven turbulence. Even if that energy only couples to the interstellar gas with 10% efficiency, the velocity dispersion observed in the gas of galaxies comparable in mass to the Milky Way could be maintained if they accrete gas at the same rate as they form stars (67). Lower-mass dwarf galaxies have lower accretion velocities, though, and so gain less energy. Nevertheless, they have the same observed velocity dispersion, which cannot be explained by this mechanism. Such dwarf galaxies represent the dominant location for star formation over cosmic time (68), so mechanisms other than accretion, such as supernova driving, must play an important role in its regulation.

However, accretion may dominate the dynamics of individual star-forming clouds. They appear to continually accrete gas from the surrounding interstellar medium at a rate sufficient to drive the turbulent motions of 1 to 5 km s^{-1} observed within them (67, 69, 70). This results in longer lifetimes than would be expected for isolated clouds of the same mass, because the driven turbulence inhibits collapse and star formation. Still, other forms of feedback such as ionization heating appear necessary to explain how star formation within these clouds comes to an end and the dense gas disperses.

Models of galactic evolution do lead to one firm conclusion: Driving of turbulence by internal gravity or accretion onto galaxies must be supplemented by other energy sources, as has been argued must be true at least for dwarf galaxies (67). Otherwise, standard simulations performed without stellar feedback or other energy sources beyond gravity would be sufficient to reproduce observed galaxies, which is not the

case, as summarized in (29) and simulated at high resolution in small, isolated dwarfs in (71). Insufficient numerical resolution leading to excessive dissipation of turbulent energy may play a role in massive galaxies but not in the well-resolved dwarf simulations. Ultimately, gravity must compete with stellar feedback and other energy sources to determine the progression of collapse and star formation.

Star-Formation Laws

Star formation correlates well with gas surface density in galaxies. The most well-known version of this correlation, the Kennicutt-Schmidt law (50), relates the SFR surface density, Σ_{SFR} , to the total (both atomic and molecular) gas surface density Σ_{gas} averaged over either the entire disks of normal or starburst galaxies or entire galactic centers (Box 2) to derive the empirical law

$$\Sigma_{\text{SFR}} \propto \Sigma_{\text{gas}}^{1.4} \quad (2)$$

Although variations around this law have been repeatedly found, for example, in (72), it nevertheless appears to broadly hold (73). As observations reached higher resolution and were able to resolve regions a few thousand light-years on a side in nearby galaxies, a similar correlation was found for them (74). However, in this case (Fig. 3A), regions with the lowest gas surface densities have lower SFR densities than would be expected from the power-law correlation, whereas the highest gas surface densities have higher than expected rates. Comparison to nearby star-forming regions in the Milky Way shows that individual molecular clouds dozens of light-years in size form stars far more efficiently than the larger regions observable in external galaxies (75). The rates observed in local clouds have been successfully simulated by using high-resolution simulations of super-Alfvénic, isothermal turbulence (76). Star formation deviates from the power-law correlations with total gas in extreme cases, but it correlates linearly with H_2 surface density over the entire range of observed values (74, 77–80), although with more than an order of magnitude scatter among individual regions. This has been interpreted to mean that H_2 formation causes or controls star formation (63, 81–83). However, one must ask whether correlation actually implies causation.

Other measurements of high-density gas ($n > 10^4 \text{ cm}^{-3}$) also show linear correlations of the column density of the gas with star formation. These include a linear correlation between HCN emission, which only occurs above a critical density $n_c \sim 10^5 \text{ cm}^{-3}$, and Σ_{SFR} (84) and a direct correlation between the number of young stellar objects in a region and the mass of material along lines of sight with sufficient dust to obscure background stars by greater than 0.8 magnitude in near-infrared light measured in the 2- μm K-band (85).

Examination of the physics of star formation reveals that molecule formation is not vital to

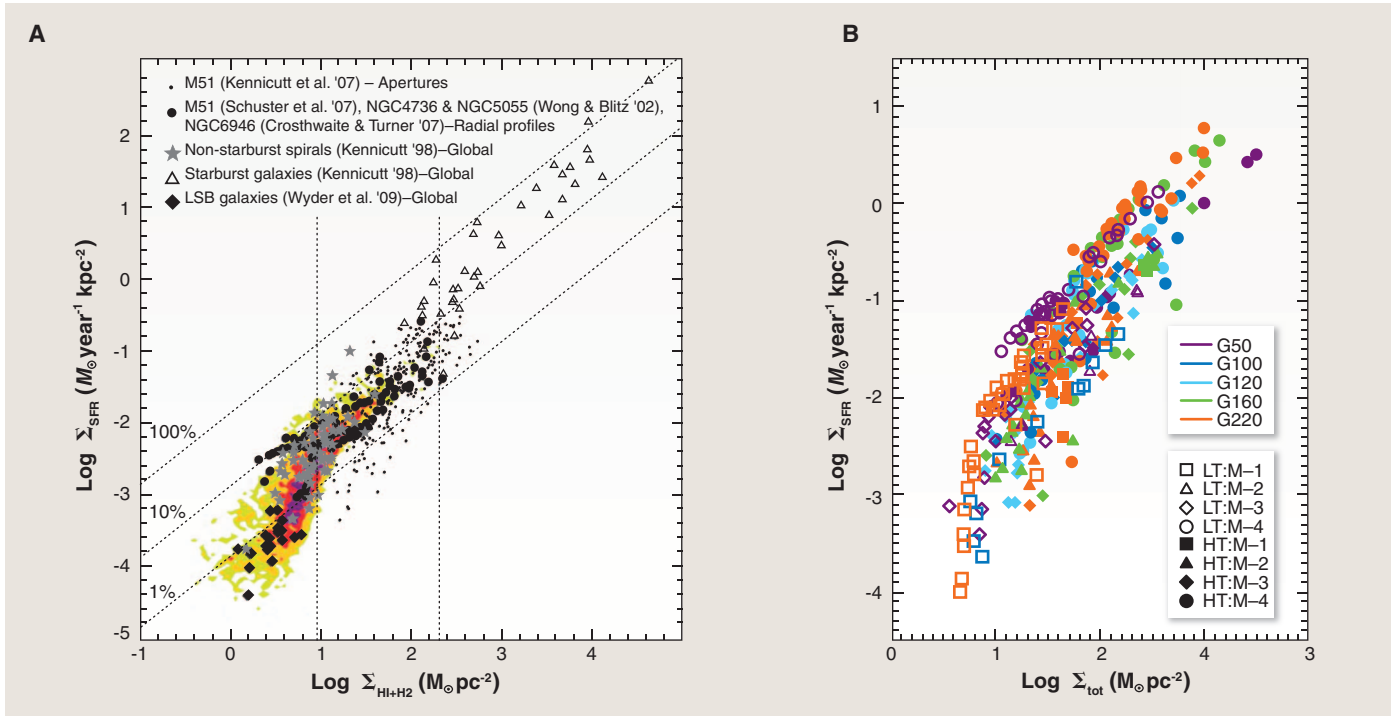


Fig. 3. Star-formation correlations. (A) A comparison of SFR surface density, Σ_{SFR} , to total gas surface density, Σ_{gas} , from observations presented in (74), showing the combined data from that paper in colored contours along with points from the observations described in the legend (50, 78, 130–133).

The dashed lines show what percentage of the gas would be consumed at that SFR over a period of 10^8 years. (B) Radial profiles across model disks simulated with isothermal gas, live stellar disks, and dark matter halos (134), showing the same drop in star-formation efficiency at low gas-surface density.

the process of gravitational collapse so long as heavy elements such as carbon and oxygen are present even in trace quantities $>10^{-5}$ the solar abundance. It had been argued that low-energy molecular lines were required to allow radiative cooling of star-forming gas to only a few tens of degrees above absolute zero. Molecular gas does in fact dominate the cooling of such high-density gas, but this is coincidental: Pure atomic gas at the same densities cools almost as effectively by radiation from fine structure lines of heavy elements. Instead, the key factor for star formation seems to be shielding of the cold gas by dust from heating by background UV light (86, 87). Removing molecular cooling from models changes the minimum temperature from 5 to 7 K, whereas removing the shielding increases the minimum temperature by more than an order of magnitude (87). Indeed, well-resolved galaxy formation simulations reached virtually the same result whether star formation was limited to occur only in molecular gas or allowed to occur in all dense gas (88).

The correlation observed between H_2 and SFR surface densities appears not to be causal but rather to occur because both have a common cause. Formation of H_2 occurs over a time scale (89) of $t_f = (1 \text{ Gy})/(n/1 \text{ cm}^{-3})$. When stars form through gravitational collapse, high densities are inevitably reached, and H_2 then forms quickly (90). This happens almost independent of the dust-to-gas ratio (91), which is largely controlled by the abundance of heavy elements,

Box 2. Star-formation law observations.

Observers derive SFRs from different observational indicators that trace either directly or indirectly the ionizing UV radiation from massive stars. Such stars have short lifetimes of only a few million years, so their presence traces recent star formation. The dense gas and dust immediately around newly forming stars absorbs UV light efficiently, ionizing and heating up in the process and reemitting the energy in the far infrared. Eventually, the expanding bubble of ionized gas escapes the cloud. That gas can be observed in the $\text{H}\alpha$ line (the 2-1 transition of recombining atomic hydrogen), which lies in the red portion of the visible spectrum. After the young stars have entirely escaped their natal gas, they can be directly observed in the UV.

Determination of the total gas surface density depends on observation of not just the atomic hydrogen that dominates the diffuse interstellar gas but also the H_2 that forms in the dense, star-forming clouds. However, the lowest rotational lines from the low-mass H_2 molecule lie at such high energies that they are not excited at the low temperatures typical of molecular gas [e.g., (73)]. Instead, emission from the next most common molecule, carbon monoxide, is used as a tracer of the molecular gas. This requires the use of a conversion factor, X_{CO} , that has been found to be roughly constant in the Milky Way. However, it has recently been demonstrated (123–126) that the conversion factor rises sharply in regions with low absorption because of either low column density of gas and dust or low heavy-element abundance leading to low dust fractions in the gas. Conversely, it seems to drop in high column density regions dominated by molecular gas (127), such as in starburst galaxies (128).

even though H_2 formation depends on dust surfaces. The dust grains provide the necessary catalyst for formation of a homonuclear molecule at densities low enough that three-body collisions hardly ever occur. (An exception to the need for dust surfaces occurs in the almost radiation-free environment of the early universe, where electrons and protons can act as catalysts in gas-phase reactions involving the fragile H^- and H_3^+ ions.)

Collapse occurs within a free-fall time (92). However, at solar elemental abundances, cooling occurs far more quickly, with the cooling time $t_{\text{cool}} < t_{\text{ff}}$ for abundances as low as 10^{-4} of the solar abundance, characteristic of the early universe or the very lowest abundance dwarf galaxies in the local neighborhood. In such low-abundance gas, molecule formation is delayed severely compared with the near solar abundance gas characteristic of the Milky Way. Then H_2 only forms in

the very densest cores of the collapsing region, leading to low integrated molecular fractions, despite ongoing star formation.

Gravitational Instability

The gravitational instability of the gas and stars in galaxies does appear to control star formation directly. We can heuristically derive (37, 61) the criterion for stability of a differentially rotating galactic disk (93, 94) by comparing the free-fall time required for collapse of a region to the time required for it to shear apart or for a pressure wave to cross it. We consider a thin galactic disk with uniform c_s and surface density Σ . The Jeans criterion for gravitational instability requires that the time scale for collapse of a density perturbation of size λ

$$t_{\text{ff}} = (\lambda/G\Sigma)^{1/2} \quad (3)$$

not exceed the time required for the gas to respond to the collapse by changing its pressure, the sound crossing time,

$$t_s = \lambda/c_s \quad (4)$$

This implies that regions can collapse if they have size

$$\lambda > c_s^2/G\Sigma \quad (5)$$

In a rotating disk, collapsing perturbations effectively rotate around themselves because of Coriolis forces (93, 95), causing centrifugal motions that can also support against gravitational collapse if t_{ff} exceeds the rotational period $t_{\text{rot}} = 2\pi/\kappa$, where the epicyclic frequency κ is of order the rotational frequency of the disk Ω . Thus, for collapse to proceed,

$$\lambda < 4\pi^2 G\Sigma/\kappa^2 \quad (6)$$

Gravitational instability occurs if there are regions with sizes that satisfy both of these criteria simultaneously, having

$$\frac{c_s^2}{G\Sigma} < \lambda < \frac{4\pi^2 G\Sigma}{\kappa^2} \quad (7)$$

This occurs if the Toomre parameter (93)

$$Q \equiv c_s \kappa / (2\pi G\Sigma) < 1 \quad (8)$$

The full criterion for instability derived from linear analysis of the equations of motion of gas in shearing disks gives a factor of π rather than 2π in the denominator (94, 96), whereas the use of kinetic theory for collisionless stellar disks gives a factor of 3.36 (93).

When collisionless stars and collisional gas both contribute to gravitational instability, as in most galactic disks, a rather more complicated formalism is required to accurately capture their combined action (97, 98). This has been successfully approximated with simple algebraic combinations of the stellar and gas Toomre parameters (99, 100). Gas supported by turbulent flows rather than pure thermal pressure has no formal minimum wavelength for gravitational collapse in

the presence of turbulent dissipation (95), although finite disk thickness does act to stabilize the smallest wavelengths against collapse.

Numerical simulations display the relationship between global gravitational instability and star formation. An example is given in (101), which describes simulations of the behavior of exponential gas disks embedded in live stellar disks with the turbulent velocity in the disk modeled by using an isothermal equation of state having a 6 to 12 km s⁻¹ sound speed. The strength of the gravitational instability was varied, and the amount of gas that collapsed gravitationally was measured in models that resolved the Jeans length to densities of $n \sim 10^7$ cm⁻³. Not only did all the models fall cleanly on the global Kennicutt-Schmidt correlation between total gas and SFR surface density but also (Fig. 3B) analysis of azimuthal rings in the models predicts the falloff in star formation at low gas densities observed at kiloparsec scales (74).

Another example of the strength of the hypothesis that gravitational instability controls star formation lies in the unusual morphologies of many high-redshift galaxies. Clumpy, irregular galaxies occur far more frequently at $z \sim 2$ than in modern times (102). Galaxies then tended to be far more gas-rich than now because gas accreted far more quickly in the denser high-redshift universe. As a result, high-redshift galaxies are more likely to be strongly gravitationally unstable. Well-resolved adaptive-mesh computations show that such conditions naturally lead to the formation of giant, gravitationally bound clumps (103) consistent with the observed morphologies.

An extended version of the gravitational instability hypothesis (104–107) proposes that star formation is controlled by the combination of gravitational instability and thermal equilibrium in a two-phase medium. This occurs because stellar feedback increases as star formation increases, which in turn is driven by gravitational instability. However, as the feedback increases, it heats and stirs the gas. This reduces its gravitational instability as its effective pressure increases and ultimately prevents gravitational instability entirely if the pressure increases beyond the range available to a two-phase medium. Thus, in this model, the SFR adjusts until a steady-state rate of star formation is reached.

Outlook

Understanding the cosmic history of star formation requires a statistical description of the luminosity function of galaxies, particularly of faint galaxies at early times. These faint galaxies dominate cosmic reionization (108) and can explain most of the apparent difference between star formation histories derived from gamma-ray burst statistics and Lyman break galaxies (15). Heroic efforts with the final instrument set on the Hubble Space Telescope are yielding our first glimpses into this territory (108, 109), but real progress will occur with the next generation of ground and space-based telescopes, such as the

James Webb Space Telescope (110), the European Extremely Large Telescope (111) and other 30-m telescopes, and the Large Synoptic Survey Telescope (112).

Resolving feedback in simulations reaching cosmological scales remains tremendously difficult, but computers are slowly becoming sufficiently powerful and algorithms well developed enough for this to fall within the realm of the possible. Simulations of star formation over cosmic time that result in realistic star formation histories for single galaxies (88, 113) and even clusters of galaxies (114) have started appearing. Expanding these to statistically representative samples of the universe containing both clusters and voids remains a huge challenge that is just starting to be met (115). Use of adaptive spatial resolution on either structured (116, 117) or unstructured (115, 118) meshes (119) will clearly play a central role in making progress. Also required will be use of hybrid algorithms to take full advantage of massively parallel computer clusters made up of nodes with multiple processors sharing memory or even graphics coprocessors.

As our understanding of star formation comes into focus, we will be able to apply the knowledge gained to a series of outstanding questions. One is the evolution of heavy-element abundances in galaxies, ultimately leading to planet formation around stars with sufficient rock-forming elements (120). Another is understanding the structure and origins of our own Milky Way Galaxy, and a third is understanding how gas between galaxies both in clusters and in the field gets polluted with heavy elements and heated up to observed abundances and temperatures. Last, the very structure of the cores of dark-matter halos appears intertwined with star formation and feedback. Thus, improving our understanding of star formation will provide the key to unlocking the story of our own origins and those of the universe around us.

References and Notes

1. G. F. Smoot *et al.*, Structure in the COBE differential microwave radiometer first-year maps. *Astrophys. J.* **396**, L1 (1992). doi: [10.1086/186504](https://doi.org/10.1086/186504)
2. D. N. Spergel *et al.*, Three-Year Wilkinson Microwave Anisotropy Probe (WMAP) observations: Implications for cosmology. *Astrophys. J. Suppl.* **170**, 377 (2007). doi: [10.1086/513700](https://doi.org/10.1086/513700)
3. N. Jarosik *et al.*, Seven-Year Wilkinson Microwave Anisotropy Probe (WMAP) observations: Sky maps, systematic errors, and basic results. *Astrophys. J. Suppl.* **192**, 14 (2011). doi: [10.1088/0067-0049/192/2/14](https://doi.org/10.1088/0067-0049/192/2/14)
4. Planck Collaboration (2013), <http://arxiv.org/abs/1303.5062>.
5. C. L. Bennett *et al.* (2012), <http://arxiv.org/abs/1212.5225>.
6. W. H. Press, P. Schechter, Formation of galaxies and clusters of galaxies by self-similar gravitational condensation. *Astrophys. J.* **187**, 425 (1974). doi: [10.1086/152650](https://doi.org/10.1086/152650)
7. J. R. Bond, S. Cole, G. Efstathiou, N. Kaiser, Excursion set mass functions for hierarchical Gaussian fluctuations. *Astrophys. J.* **379**, 440 (1991). doi: [10.1086/170520](https://doi.org/10.1086/170520)
8. S. D. M. White, C. S. Frenk, Galaxy formation through hierarchical clustering. *Astrophys. J.* **379**, 52 (1991). doi: [10.1086/170483](https://doi.org/10.1086/170483)
9. V. Springel, L. Hernquist, The history of star formation in a cold dark matter universe. *Mon. Not. R. Astron. Soc.* **339**, 312 (2003). doi: [10.1046/j.1365-8711.2003.06207.x](https://doi.org/10.1046/j.1365-8711.2003.06207.x)

10. P. Madau *et al.*, High-redshift galaxies in the *Hubble Deep Field*: Colour selection and star formation history to $z \sim 4$. *Mon. Not. R. Astron. Soc.* **283**, 1388 (1996). doi: [10.1093/mnras/283.4.1388](#)
11. S. J. Lilly, O. Le Fevre, F. Hammer, D. Crampton, The Canada-France Redshift Survey: The luminosity density and star formation history of the Universe to $z \sim 1$. *Astrophys. J.* **460**, L1 (1996). doi: [10.1086/309975](#)
12. A. M. Hopkins, J. F. Beacom, On the normalization of the cosmic star formation history. *Astrophys. J.* **651**, 142 (2006). doi: [10.1086/506610](#)
13. The exact relationship between redshift and lookback time is nonlinear and depends on the actual expansion law of the universe.
14. V. Bromm, M. Yoshida, The first galaxies. *Annu. Rev. Astron. Astrophys.* **49**, 373 (2011). doi: [10.1146/annurev-astro-081710-102608](#)
15. M. Trenti, R. Perna, E. M. Levesque, J. M. Shull, J. T. Stocke, Gamma-ray burst host galaxy surveys at redshift $z \geq 4$: Probes of star formation rate and cosmic reionization. *Astrophys. J.* **749**, L38 (2012). doi: [10.1088/2041-8205/749/L38](#)
16. M. D. Kistler, H. Yüksel, J. F. Beacom, A. M. Hopkins, J. S. B. Wyithe, The star formation rate in the reionization era as indicated by gamma-ray bursts. *Astrophys. J.* **705**, L104 (2009). doi: [10.1088/0004-637X/705/2/L104](#)
17. B. E. Robertson, R. S. Ellis, Connecting the gamma ray burst rate and the cosmic star formation history: Implications for reionization and galaxy evolution. *Astrophys. J.* **744**, 95 (2012). doi: [10.1088/0004-637X/744/2/95](#)
18. C. C. Steidel, M. Giavalisco, M. Pettini, M. Dickinson, K. L. Adelberger, Spectroscopic confirmation of a population of normal star-forming galaxies at redshifts $z > 3$. *Astrophys. J.* **462**, L17 (1996). doi: [10.1088/1538-4357/462/1/L17](#)
19. R. J. Bouwens *et al.*, Ultraviolet luminosity functions from $132 < z < 7$ and $z \sim 8$ Lyman-break galaxies in the ultra-deep HUDF09 and Wide-Area Early Release Science WFC3/IR observations. *Astrophys. J.* **737**, 90 (2011). doi: [10.1088/0004-637X/737/2/90](#)
20. B. P. Moster, T. Naab, S. D. M. White, Galactic star formation and accretion histories from matching galaxies to dark matter haloes. *Mon. Not. R. Astron. Soc.* **428**, 3121 (2012).
21. E. Costa *et al.*, Discovery of an X-ray afterglow associated with the γ -ray burst of 28 February 1997. *Nature* **387**, 783 (1997). doi: [10.1038/42885](#)
22. R. Cen, J. P. Ostriker, Cold dark matter cosmology with hydrodynamics and galaxy formation: The evolution of the intergalactic medium and background radiation fields. *Astrophys. J.* **417**, 404 (1993). doi: [10.1086/173321](#)
23. N. Katz, D. H. Weinberg, L. Hernquist, Cosmological simulations with TreeSPH. *Astrophys. J.* **105** (suppl.), 19 (1996). doi: [10.1086/192305](#)
24. R. S. Somerville, J. R. Primack, Semi-analytic modelling of galaxy formation: the local Universe. *Mon. Not. R. Astron. Soc.* **310**, 1087 (1999). doi: [10.1046/j.1365-8711.1999.03032.x](#)
25. D. Kereš, N. Katz, R. Davé, M. Fardal, D. H. Weinberg, Galaxies in a simulated Λ CDM universe - II. Observable properties and constraints on feedback. *Mon. Not. R. Astron. Soc.* **396**, 2332 (2009). doi: [10.1111/j.1365-2966.2009.14924.x](#)
26. F. Bournaud, B. G. Elmegreen, R. Teyssier, D. L. Block, I. Puerari, ISM properties in hydrodynamic galaxy simulations: turbulence cascades, cloud formation, role of gravity and feedback. *Mon. Not. R. Astron. Soc.* **409**, 1088 (2010). doi: [10.1111/j.1365-2966.2010.17370.x](#)
27. C. L. Dobbs, A. Burkert, J. E. Pringle, The properties of the interstellar medium in disc galaxies with stellar feedback. *Mon. Not. R. Astron. Soc.* **417**, 1318 (2011). doi: [10.1111/j.1365-2966.2011.19346.x](#)
28. E. J. Tasker, Star formation in disk galaxies. II. The effect of star formation and photoelectric heating on the formation and evolution of giant molecular clouds. *Astrophys. J.* **730**, 11 (2011). doi: [10.1088/0004-637X/730/1/11](#)
29. C. B. Hummels, G. L. Bryan, Adaptive mesh refinement simulations of galaxy formation: Exploring numerical and physical parameters. *Astrophys. J.* **749**, 140 (2012). doi: [10.1088/0004-637X/749/2/140](#)
30. A. Dalgarno, R. A. McCray, Heating and ionization of H I regions. *Annu. Rev. Astron. Astrophys.* **10**, 375 (1972). doi: [10.1146/annurev-aa.10.090172.002111](#)
31. R. S. Sutherland, M. A. Dopita, Cooling functions for low-density astrophysical plasmas. *Astrophys. J. Suppl.* **88**, 253 (1993). doi: [10.1086/191823](#)
32. K. Tomisaka, S. Ikeuchi, Evolution of superbubble driven by sequential supernova explosions in a plane-stratified gas distribution. *Publ. Astron. Soc. Jpn.* **38**, 697 (1986).
33. M.-M. Mac Low, R. McCray, M. L. Norman, Superbubble blowout dynamics. *Astrophys. J.* **337**, 141 (1989). doi: [10.1086/167094](#)
34. M. A. de Avillez, Disc-halo interaction - I. Three-dimensional evolution of the Galactic disc. *Mon. Not. R. Astron. Soc.* **315**, 479 (2000). doi: [10.1046/j.1365-8711.2000.03464.x](#)
35. M. K. R. Joing, M.-M. Mac Low, Turbulent structure of a stratified supernova-driven interstellar medium. *Astrophys. J.* **653**, 1266 (2006). doi: [10.1086/508795](#)
36. A. S. Hill *et al.*, Vertical structure of a supernova-driven turbulent, magnetized interstellar medium. *Astrophys. J.* **750**, 104 (2012). doi: [10.1088/0004-637X/750/2/104](#)
37. M.-M. Mac Low, R. S. Klessen, Control of star formation by supersonic turbulence. *Rev. Mod. Phys.* **76**, 125 (2004). doi: [10.1103/RevModPhys.76.125](#)
38. S. Chandrasekhar, The gravitational instability of an infinite homogeneous turbulent medium. *Proc. R. Soc. London Ser. A* **210**, 26 (1951). doi: [10.1098/rspa.1951.0228](#)
39. C. F. von Weizsäcker, The evolution of galaxies and stars. *Astrophys. J.* **114**, 165 (1951). doi: [10.1086/145462](#)
40. R. S. Klessen, F. Heitsch, M.-M. Mac Low, Gravitational collapse in turbulent molecular clouds. I. Gasdynamical turbulence. *Astrophys. J.* **535**, 887 (2000). doi: [10.1086/308891](#)
41. C. Federrath, R. S. Klessen, On the star formation efficiency of turbulent magnetized clouds. *Astrophys. J.* **763**, 51 (2013). doi: [10.1088/0004-637X/763/1/51](#)
42. P. Padoan, T. Haugbelle, Å. Nordlund, A simple law of star formation. *Astrophys. J.* **759**, L27 (2012). doi: [10.1088/2041-8205/759/L27](#)
43. B. Fryxell *et al.*, FLASH: An adaptive mesh hydrodynamics code for modeling astrophysical thermonuclear flashes. *Astrophys. J.* **131** (suppl.), 273 (2000). doi: [10.1086/317361](#)
44. H. Gerola, P. E. Seiden, Stochastic star formation and spiral structure of galaxies. *Astrophys. J.* **223**, 129 (1978). doi: [10.1086/156243](#)
45. J. E. Dale, P. C. Clark, I. A. Bonnell, Ionization-induced star formation - II. External irradiation of a turbulent molecular cloud. *Mon. Not. R. Astron. Soc.* **377**, 535 (2007). doi: [10.1111/j.1365-2966.2007.11515.x](#)
46. B. G. Elmegreen, C. J. Lada, Sequential formation of subgroups in OB associations. *Astrophys. J.* **214**, 725 (1977). doi: [10.1086/155302](#)
47. K. V. Getman *et al.*, The Elephant Trunk nebula and the Trumpler 37 cluster: Contribution of triggered star formation to the total population of an H II region. *Mon. Not. R. Astron. Soc.* **426**, 2917 (2012). doi: [10.1111/j.1365-2966.2012.21879.x](#)
48. J. R. Dawson *et al.*, Supergiant shells and molecular cloud formation in the large Magellanic Cloud. *Astrophys. J.* **763**, 56 (2013). doi: [10.1088/0004-637X/763/1/56](#)
49. M. R. Joing, M.-M. Mac Low, G. L. Bryan, Dependence of interstellar turbulent pressure on supernova rate. *Astrophys. J.* **704**, 137 (2009). doi: [10.1088/0004-637X/704/1/137](#)
50. R. C. Kennicutt Jr., The global Schmidt law in star-forming galaxies. *Astrophys. J.* **498**, 541 (1998). doi: [10.1086/305588](#)
51. A. O. Petric, M. P. Rupen, H I velocity dispersion in NGC 1058. *Astron. J.* **134**, 1952 (2007). doi: [10.1086/518558](#)
52. D. Tamburro *et al.*, What is driving the H I velocity dispersion? *Astron. J.* **137**, 4424 (2009). doi: [10.1088/0004-6256/137/5/4424](#)
53. N. Murray, E. Quataert, T. A. Thompson, The disruption of giant molecular clouds by radiation pressure & the efficiency of star formation in galaxies. *Astrophys. J.* **709**, 191 (2010). doi: [10.1088/0004-637X/709/1/191](#)
54. R. C. Kennicutt Jr. *et al.*, SINGS: The SIRTIF Nearby Galaxies Survey. *Publ. Astron. Soc. Pac.* **115**, 928 (2003). doi: [10.1086/376941](#)
55. F. Walter *et al.*, THINGS: The H I Nearby Galaxy Survey. *Astron. J.* **136**, 2563 (2008). doi: [10.1088/0004-6256/136/6/2563](#)
56. S. A. Balbus, J. F. Hawley, Instability, turbulence, and enhanced transport in accretion disks. *Rev. Mod. Phys.* **70**, 1 (1998). doi: [10.1103/RevModPhys.70.1](#)
57. J. A. Sellwood, S. A. Balbus, Differential rotation and turbulence in extended H I disks. *Astrophys. J.* **511**, 660 (1999). doi: [10.1086/306728](#)
58. G. B. Field, Thermal instability. *Astrophys. J.* **142**, 531 (1965). doi: [10.1086/148317](#)
59. R.-A. Piontek, E. C. Ostriker, Models of vertically stratified two-phase ISM disks with MRI-driven turbulence. *Astrophys. J.* **663**, 183 (2007). doi: [10.1086/518103](#)
60. B. G. Elmegreen, A. Parravano, When star formation stops: Galaxy edges and low surface brightness disks. *Astrophys. J.* **435**, L121 (1994). doi: [10.1086/187609](#)
61. J. Schaye, Star formation thresholds and galaxy edges: Why and where. *Astrophys. J.* **609**, 667 (2004). doi: [10.1086/421232](#)
62. S. Boissier *et al.*, Radial variation of attenuation and star formation in the largest late-type disks observed with GALEX. *Astrophys. J. Suppl.* **173**, 524 (2007). doi: [10.1086/516642](#)
63. M. R. Krumholz, C. F. McKee, J. Tumlinson, The star formation law in atomic and molecular gas. *Astrophys. J.* **699**, 850 (2009). doi: [10.1088/0004-637X/699/1/850](#)
64. S. M. Fall, M. R. Krumholz, C. D. Matzner, Stellar feedback in molecular clouds and its influence on the mass function of young star clusters. *Astrophys. J.* **710**, L142 (2010). doi: [10.1088/2041-8205/710/L142](#)
65. M. R. Krumholz, T. A. Thompson, Direct numerical simulation of radiation pressure-driven turbulence and winds in star clusters and galactic disks. *Astrophys. J.* **760**, 155 (2012). doi: [10.1088/0004-637X/760/2/155](#)
66. M.-M. Mac Low, The energy dissipation rate of supersonic, magnetohydrodynamic turbulence in molecular clouds. *Astrophys. J.* **524**, 169 (1999). doi: [10.1086/307784](#)
67. R. S. Klessen, P. Hennebelle, Accretion-driven turbulence as universal process: galaxies, molecular clouds, and protostellar disks. *Astron. Astrophys.* **520**, A17 (2010). doi: [10.1051/0004-6361/200913780](#)
68. A. Karim *et al.*, The star formation history of mass-selected galaxies in the COSMOS field. *Astrophys. J.* **730**, 61 (2011). doi: [10.1088/0004-637X/730/2/61](#)
69. E. Vázquez-Semadeni, P. Colín, G. C. Gómez, J. Ballesteros-Paredes, A. W. Watson, Molecular cloud evolution. III. Accretion versus stellar feedback. *Astrophys. J.* **715**, 1302 (2010). doi: [10.1088/0004-637X/715/2/1302](#)
70. N. J. Goldbaum, M. R. Krumholz, C. D. Matzner, C. F. McKee, The global evolution of giant molecular clouds. II. The role of accretion. *Astrophys. J.* **738**, 101 (2011). doi: [10.1088/0004-637X/738/1/101](#)
71. C. M. Simpson *et al.* (2013), <http://arxiv.org/abs/1211.1071>.
72. R. Shetty, B. C. Kelly, F. Bigiel, Evidence for a non-universal Kennicutt-Schmidt relationship using hierarchical Bayesian linear regression. *Mon. Not. R. Astron. Soc.* **430**, 288 (2013). doi: [10.1093/mnras/sts617](#)
73. R. C. Kennicutt Jr., N. J. Evans II, Star formation in the Milky Way and nearby galaxies. *Annu. Rev. Astron. Astrophys.* **50**, 531 (2012). doi: [10.1146/annurev-astro-081811-125610](#)
74. F. Bigiel *et al.*, The star formation law in nearby galaxies on sub-kpc scales. *Astron. J.* **136**, 2846 (2008). doi: [10.1088/0004-6256/136/6/2846](#)
75. A. Heiderman, N. J. Evans II, L. E. Allen, T. Huard, M. Heyer, The star formation rate and gas surface density relation in the Milky Way: Implications for extragalactic studies. *Astrophys. J.* **723**, 1019 (2010). doi: [10.1088/0004-637X/723/2/1019](#)
76. C. Federrath, R. S. Klessen, The star formation rate of turbulent magnetized clouds: Comparing theory, simulations, and observations. *Astrophys. J.* **761**, 156 (2012). doi: [10.1088/0004-637X/761/2/156](#)

77. B. K. Rownd, J. S. Young, The star formation efficiency within galaxies. *Astron. J.* **118**, 670 (1999). doi: [10.1086/300957](https://doi.org/10.1086/300957)
78. T. Wong, L. Blitz, The relationship between gas content and star formation in molecule-rich spiral galaxies. *Astrophys. J.* **569**, 157 (2002). doi: [10.1086/339287](https://doi.org/10.1086/339287)
79. A. K. Leroy *et al.*, The star formation efficiency in nearby galaxies: Measuring where gas forms stars effectively. *Astron. J.* **136**, 2782 (2008). doi: [10.1088/0004-6256/136/6/2782](https://doi.org/10.1088/0004-6256/136/6/2782)
80. F. Bigiel *et al.*, A constant molecular gas depletion time in nearby disk galaxies. *Astrophys. J.* **730**, L13 (2011). doi: [10.1088/2041-8205/730/2/L13](https://doi.org/10.1088/2041-8205/730/2/L13)
81. B. E. Robertson, A. V. Kravtsov, Molecular hydrogen and global star formation relations in galaxies. *Astrophys. J.* **680**, 1083 (2008). doi: [10.1086/587796](https://doi.org/10.1086/587796)
82. N. Y. Gnedin, A. V. Kravtsov, On the Kennicutt-Schmidt relation of low-metallicity high-redshift galaxies. *Astrophys. J.* **714**, 287 (2010). doi: [10.1088/0004-637X/714/1/287](https://doi.org/10.1088/0004-637X/714/1/287)
83. C. Christensen *et al.*, Implementing molecular hydrogen in hydrodynamic simulations of galaxy formation. *Mon. Not. R. Astron. Soc.* **425**, 3058 (2012). doi: [10.1111/j.1365-2966.2012.21628.x](https://doi.org/10.1111/j.1365-2966.2012.21628.x)
84. Y. Gao, P. M. Solomon, The star formation rate and dense molecular gas in galaxies. *Astrophys. J.* **606**, 271 (2004). doi: [10.1086/382999](https://doi.org/10.1086/382999)
85. C. J. Lada, M. Lombardi, J. F. Alves, On the star formation rates in molecular clouds. *Astrophys. J.* **724**, 687 (2010). doi: [10.1088/0004-637X/724/1/687](https://doi.org/10.1088/0004-637X/724/1/687)
86. M. R. Krumholz, A. K. Leroy, C. F. McKee, Which phase of the interstellar medium correlates with the star formation rate? *Astrophys. J.* **731**, 25 (2011). doi: [10.1088/0004-637X/731/1/25](https://doi.org/10.1088/0004-637X/731/1/25)
87. S. C. O. Glover, P. C. Clark, Is molecular gas necessary for star formation? *Mon. Not. R. Astron. Soc.* **421**, 9 (2012).
88. P. F. Hopkins, E. Quataert, N. Murray, Self-regulated star formation in galaxies via momentum input from massive stars. *Mon. Not. R. Astron. Soc.* **417**, 950 (2011). doi: [10.1111/j.1365-2966.2011.19306.x](https://doi.org/10.1111/j.1365-2966.2011.19306.x)
89. D. Hollenbach, E. E. Salpeter, Surface recombination of hydrogen molecules. *Astrophys. J.* **163**, 155 (1971). doi: [10.1086/150754](https://doi.org/10.1086/150754)
90. S. C. O. Glover, M.-M. Mac Low, Simulating the formation of molecular clouds. II. Rapid formation from turbulent initial conditions. *Astrophys. J.* **659**, 1317 (2007). doi: [10.1086/512227](https://doi.org/10.1086/512227)
91. S. C. O. Glover, P. C. Clark, Star formation in metal-poor gas clouds. *Mon. Not. R. Astron. Soc.* **426**, 377 (2012). doi: [10.1111/j.1365-2966.2012.21737.x](https://doi.org/10.1111/j.1365-2966.2012.21737.x)
92. M. R. Krumholz, Star formation in atomic gas. *Astrophys. J.* **759**, 9 (2012). doi: [10.1088/0004-637X/759/1/9](https://doi.org/10.1088/0004-637X/759/1/9)
93. A. Toomre, On the gravitational stability of a disk of stars. *Astrophys. J.* **139**, 1217 (1964). doi: [10.1086/147861](https://doi.org/10.1086/147861)
94. P. Goldreich, D. Lynden-Bell, I. Gravitational stability of uniformly rotating disks. *Mon. Not. R. Astron. Soc.* **130**, 97 (1965).
95. B. G. Elmegreen, Gravitational instabilities in two-component galaxy disks with gas dissipation. *Astrophys. J.* **737**, 10 (2011). doi: [10.1088/0004-637X/737/1/10](https://doi.org/10.1088/0004-637X/737/1/10)
96. V. S. Safronov, On the gravitational instability in flattened systems with axial symmetry and non-uniform rotation. *Ann. Astrophys.* **23**, 979 (1960).
97. C. F. Gammie, The formation of giant molecular clouds, thesis, Princeton University, Princeton, NJ (1992).
98. R. R. Rafikov, The local axisymmetric instability criterion in a thin, rotating, multicomponent disc. *Mon. Not. R. Astron. Soc.* **323**, 445 (2001). doi: [10.1046/j.1365-8711.2001.04201.x](https://doi.org/10.1046/j.1365-8711.2001.04201.x)
99. B. Wang, J. Silk, Gravitational instability and disk star formation. *Astrophys. J.* **427**, 759 (1994). doi: [10.1086/174182](https://doi.org/10.1086/174182)
100. A. B. Romeo, J. Wiegert, The effective stability parameter for two-component galactic discs: is $Q^{-1} \sim Q_{\text{stars}}^{-1} + Q_{\text{gas}}^{-1}$? *Mon. Not. R. Astron. Soc.* **416**, 1191 (2011). doi: [10.1111/j.1365-2966.2011.19120.x](https://doi.org/10.1111/j.1365-2966.2011.19120.x)
101. Y. Li, M.-M. Mac Low, R. S. Klessen, Star formation in isolated disk galaxies. II. Schmidt laws and efficiency of gravitational collapse. *Astrophys. J.* **639**, 879 (2006). doi: [10.1086/499350](https://doi.org/10.1086/499350)
102. D. M. Elmegreen *et al.*, Clumpy galaxies in GOODS and GEMS: Massive analogs of local dwarf irregulars. *Astrophys. J.* **701**, 306 (2009). doi: [10.1088/0004-637X/701/1/306](https://doi.org/10.1088/0004-637X/701/1/306)
103. O. Agertz, R. Teyssier, B. Moore, Disc formation and the origin of clumpy galaxies at high redshift. *Mon. Not. R. Astron. Soc.* **397**, L64 (2009). doi: [10.1111/j.1745-3933.2009.00685.x](https://doi.org/10.1111/j.1745-3933.2009.00685.x)
104. E. C. Ostriker, C. F. McKee, A. K. Leroy, Regulation of star formation rates in multiphase galactic disks: A thermal/dynamical equilibrium model. *Astrophys. J.* **721**, 975 (2010). doi: [10.1088/0004-637X/721/2/975](https://doi.org/10.1088/0004-637X/721/2/975)
105. E. C. Ostriker, R. Shetty, Maximally star-forming galactic disks. I. Starburst regulation via feedback-driven turbulence. *Astrophys. J.* **731**, 41 (2011). doi: [10.1088/0004-637X/731/1/41](https://doi.org/10.1088/0004-637X/731/1/41)
106. C.-G. Kim, W.-T. Kim, E. C. Ostriker, Regulation of star formation rates in multiphase galactic disks: Numerical tests of the thermal/dynamical equilibrium model. *Astrophys. J.* **743**, 25 (2011). doi: [10.1088/0004-637X/743/1/25](https://doi.org/10.1088/0004-637X/743/1/25)
107. R. Shetty, E. C. Ostriker, Maximally star-forming galactic disks. II. Vertically resolved hydrodynamic simulations of starburst regulation. *Astrophys. J.* **754**, 2 (2012). doi: [10.1088/0004-637X/754/1/2](https://doi.org/10.1088/0004-637X/754/1/2)
108. R. J. Bouwens *et al.*, Lower-luminosity galaxies could reionize the universe: Very steep faint-end slopes to the UV luminosity functions at $z \geq 5-8$ from the HUDF09 WFC3/IR observations. *Astrophys. J.* **752**, L5 (2012). doi: [10.1088/2041-8205/752/1/L5](https://doi.org/10.1088/2041-8205/752/1/L5)
109. M. Trenti *et al.*, The brightest of reionizing galaxies survey: Design and preliminary results. *Astrophys. J.* **727**, L39 (2011). doi: [10.1088/2041-8205/727/2/L39](https://doi.org/10.1088/2041-8205/727/2/L39)
110. J. P. Gardner *et al.*, The James Webb Space Telescope. *Space Sci. Rev.* **123**, 485 (2006). doi: [10.1007/s11214-006-8315-7](https://doi.org/10.1007/s11214-006-8315-7)
111. M. Lyubenova, M. Kissler-Patig, Eds., *An Expanded View of the Universe: Science with the European Extremely Large Telescope* (European Southern Observatory, Garching bei München, Germany, 2009).
112. J. Tyson, Large Synoptic Survey Telescope: Overview. *Proc. SPIE* **4836**, 10 (2002). doi: [10.1117/12.456772](https://doi.org/10.1117/12.456772)
113. F. Governato *et al.*, Cuspy no more: How outflows affect the central dark matter and baryon distribution in A cold dark matter galaxies. *Mon. Not. R. Astron. Soc.* **422**, 1231 (2012). doi: [10.1111/j.1365-2966.2012.20696.x](https://doi.org/10.1111/j.1365-2966.2012.20696.x)
114. R. Cen, Environmentally driven global evolution of galaxies. *Astrophys. J.* **741**, 99 (2011). doi: [10.1088/0004-637X/741/2/99](https://doi.org/10.1088/0004-637X/741/2/99)
115. M. Vogelsberger, D. Sijacki, D. Keres, V. Springel, L. Hernquist, Moving mesh cosmology: Numerical techniques and global statistics. *Mon. Not. R. Astron. Soc.* **425**, 3024 (2012). doi: [10.1111/j.1365-2966.2012.21590.x](https://doi.org/10.1111/j.1365-2966.2012.21590.x)
116. A. V. Kravtsov, A. A. Klypin, A. M. Khokhlov, Adaptive refinement tree: A new high-resolution N -body code for cosmological simulations. *Astrophys. J. Suppl.* **111**, 73 (1997). doi: [10.1086/313015](https://doi.org/10.1086/313015)
117. B. W. O'Shea *et al.*, in *Adaptive Mesh Refinement: Theory and Applications*, T. Plewa, T. Linde, V. G. Weirs, Eds. (Lecture Notes in Computational Science and Engineering, Springer, Heidelberg, Germany, 2004), pp. 341–350.
118. V. Springel, *E pur si muove*: Galilean-invariant cosmological hydrodynamical simulations on a moving mesh. *Mon. Not. R. Astron. Soc.* **401**, 791 (2010). doi: [10.1111/j.1365-2966.2009.15715.x](https://doi.org/10.1111/j.1365-2966.2009.15715.x)
119. See www.cfa.harvard.edu/ttc/research/movingmeshcosmology/ for visualizations of galaxies from unstructured mesh simulations.
120. L. A. Buchhave *et al.*, An abundance of small exoplanets around stars with a wide range of metallicities. *Nature* **486**, 375 (2012). PMID: [22722196](https://pubmed.ncbi.nlm.nih.gov/22722196/)
121. M.-M. Mac Low, in *Molecular Gas, Dust, and Star Formation in Galaxies*, J. Ott, T. Wong, Eds. (Proceedings of the International Astronomical Union, Cambridge Univ. Press, Cambridge, 2013), pp. 3–15.
122. J. H. Jeans, The stability of a spherical nebula. *Philos. Trans. R. Soc. London Ser. A* **199**, 1 (1902). doi: [10.1098/rsta.1902.0012](https://doi.org/10.1098/rsta.1902.0012)
123. S. C. O. Glover, M.-M. Mac Low, On the relationship between molecular hydrogen and carbon monoxide abundances in molecular clouds. *Mon. Not. R. Astron. Soc.* **412**, 337 (2011). doi: [10.1111/j.1365-2966.2010.17907.x](https://doi.org/10.1111/j.1365-2966.2010.17907.x)
124. D. Narayanan, M. Krumholz, E. C. Ostriker, L. Hernquist, The CO-H₂ conversion factor in disc galaxies and mergers. *Mon. Not. R. Astron. Soc.* **418**, 664 (2011). doi: [10.1111/j.1365-2966.2011.19516.x](https://doi.org/10.1111/j.1365-2966.2011.19516.x)
125. A. Schruha *et al.*, A molecular star formation law in the atomic gas dominated regime in nearby galaxies. *Astron. J.* **142**, 37 (2011). doi: [10.1088/0004-6256/142/2/37](https://doi.org/10.1088/0004-6256/142/2/37)
126. R. Shetty, S. C. Glover, C. P. Dullemond, R. S. Klessen, Modelling CO emission - I. CO as a column density tracer and the X factor in molecular clouds. *Mon. Not. R. Astron. Soc.* **412**, 1686 (2011). doi: [10.1111/j.1365-2966.2010.18005.x](https://doi.org/10.1111/j.1365-2966.2010.18005.x)
127. D. Narayanan, M. R. Krumholz, E. C. Ostriker, L. Hernquist, A general model for the CO-H₂ conversion factor in galaxies with applications to the star formation law. *Mon. Not. R. Astron. Soc.* **421**, 3127 (2012). doi: [10.1111/j.1365-2966.2012.20536.x](https://doi.org/10.1111/j.1365-2966.2012.20536.x)
128. D. Downes, P. M. Solomon, Rotating nuclear rings and extreme starbursts in ultraluminous galaxies. *Astrophys. J.* **507**, 615 (1998). doi: [10.1086/306339](https://doi.org/10.1086/306339)
129. M. Trenti *et al.*, The galaxy luminosity function during the reionization epoch. *Astrophys. J.* **714**, L202 (2010). doi: [10.1088/2041-8205/714/2/L202](https://doi.org/10.1088/2041-8205/714/2/L202)
130. R. C. Kennicutt Jr. *et al.*, Star formation in NGC 5194 (M51a). II. The spatially resolved star formation law. *Astrophys. J.* **671**, 333 (2007). doi: [10.1086/522300](https://doi.org/10.1086/522300)
131. K. F. Schuster, C. Kramer, M. Hitschfeld, S. Garcia-Burillo, B. Mookerjee, A complete ¹²CO 2-1 map of M 51 with HERA. *Astron. Astrophys.* **461**, 143 (2007). doi: [10.1051/0004-6361/20065579](https://doi.org/10.1051/0004-6361/20065579)
132. L. P. Crosthwaite, J. L. Turner, CO(1-0), CO(2-1), and neutral gas in NGC 6946: Molecular gas in a late-type, gas-rich, spiral galaxy. *Astron. J.* **134**, 1827 (2007). doi: [10.1086/521645](https://doi.org/10.1086/521645)
133. T. K. Wyder *et al.*, The star formation law at low surface density. *Astrophys. J.* **696**, 1834 (2009). doi: [10.1088/0004-637X/696/2/1834](https://doi.org/10.1088/0004-637X/696/2/1834)
134. Y. Li, M.-M. Mac Low, R. S. Klessen, Star formation in isolated disk galaxies. I. Models and characteristics of nonlinear gravitational collapse. *Astrophys. J.* **626**, 823 (2005). doi: [10.1086/430205](https://doi.org/10.1086/430205)

Acknowledgments: An early version of this review was presented at International Astronomical Union Symposium 292 (121). I have benefited over the past 15 years from discussions and collaborations on these topics with M. A. Avillez, B. G. Elmegreen, C. Federrath, S. C. O. Glover, F. Heitsch, A. S. Hill, M. R. Joung, R. S. Klessen, M. R. Krumholz, Yueying Li, T. Peters, and E. Vázquez-Semadeni. I thank J. Beacom, C. Federrath, S. C. O. Glover, and J. C. Ibañez Mejía for useful comments on the manuscript and the anonymous referees for detailed and constructive reviews that improved this work. I was partially supported by NSF grant AST11-09395, NASA Chandra Theory grant TMO-11008X, and Deutsche Forschungsgemeinschaft (DFG) Sonderforschungsbereich 881—The Milky Way System.

Supplementary Materials
www.sciencemag.org/content/340/6140/1229229/suppl/DC1
 Movie 1

10.1126/science.1229229

Elongation Factor G Bound to the Ribosome in an Intermediate State of Translocation

David S. Tourigny, Israel S. Fernández, Ann C. Kelley, V. Ramakrishnan*

Introduction: After peptidyl transfer, the movement of messenger RNA (mRNA) and transfer RNAs (tRNAs) with respect to the ribosome places the next mRNA codon in the A site. This process of translocation proceeds via an intermediate state in which the acceptor ends of the tRNAs have moved with respect to the 50S subunit but not the 30S subunit, to result in A/P and P/E tRNA hybrid states. The guanosine triphosphatase elongation factor G (EF-G) catalyzes the subsequent movement of mRNA and tRNA with respect to the 30S subunit. How EF-G binds to the intermediate state of the ribosome and how this results in guanosine 5'-triphosphate (GTP) hydrolysis and translocation are questions that will be greatly facilitated by a high-resolution structure of the complex.

Methods: *Thermus thermophilus* ribosomes lacking protein L9 were crystallized in an intermediate state with mRNA, a hybrid P/E tRNA, and EF-G with the nonhydrolyzable GTP analog GDPCP. The structure was solved by molecular replacement and refined to 2.9 Å resolution.

Results: The 50S and 30S ribosomal subunits are rotated relative to each other, as was expected from previous cryo-electron microscopy studies. The L1 stalk on the 50S subunit moves inward to stabilize the P/E hybrid-state tRNA, and atomic details of this interaction can now be seen. Domain IV of EF-G takes up an orientation intermediate between that of the isolated form of EF-G and that of EF-G bound to the ribosome in the fully translocated state. The catalytic center of EF-G shows that key switch regions surrounding the γ -phosphate of GDPCP are clearly visible and therefore ordered. Moreover, key conserved residues in EF-G, including a histidine and an aspartate, change conformation relative to both the isolated and fully translocated structure. These activated conformations appear to be stabilized by the highly conserved sarcin-ricin RNA loop (SRL) of the 50S subunit.

Discussion: Comparison with the posttranslocational state suggests that interactions between the tRNA and L1 stalk are preserved throughout translocation and that these are probably an essential feature of translocation required for stabilization of the hybrid P/E state.

In the isolated structure of EF-G, domain IV, because of its orientation, would largely avoid a clash with A-site tRNA, as would be required for formation of a transient initial complex. In our structure, domain IV partly extends into the A site, which is consistent with the observation that EF-G facilitates translocation at a slow rate even without GTP hydrolysis.

The catalytic center of EF-G has essentially the same structure as that previously observed for elongation factor Tu (EF-Tu), with the highly conserved histidine stabilized by the SRL in an orientation that coordinates a water molecule in position for hydrolysis of GTP. This shows that although EF-Tu and EF-G bind to very different states of the ribosome, the mechanism of activation of GTP hydrolysis is probably the same for these two factors, and possibly for other translational GTPases.

READ THE FULL ARTICLE ONLINE
<http://dx.doi.org/10.1126/science.1235490>

Cite this article as D. S. Tourigny *et al.*, *Science* **340**, 1235490 (2013). DOI: 10.1126/science.1235490

FIGURES AND TABLE IN THE FULL ARTICLE

Fig. 1. Unbiased difference Fourier maps.

Fig. 2. EF-G bound to the rotated state of the ribosome.

Fig. 3. Dynamics of the L1 stalk during tRNA translocation.

Fig. 4. Interactions of EF-G with L6, L11, and L12.

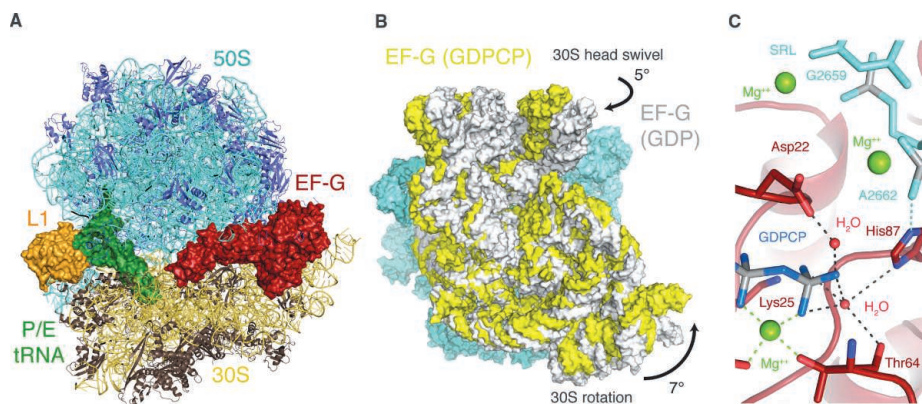
Fig. 5. Conformational changes in EF-G during translocation.

Fig. 6. The active site of EF-G.

Table 1. Summary of crystallographic data and refinement.

SUPPLEMENTARY MATERIALS

Movies S1 to S3



Structure of EF-G with GDPCP bound to the ribosome in an intermediate state of translocation. (A) Overview of the structure with a hybrid P/E tRNA. (B) Rotation of the body and swiveling of the head of the 30S subunit (yellow), compared to the canonical state (gray). (C) Catalytic site showing conserved residues around the GDPCP molecule stabilized in an activated conformation.

MRC Laboratory of Molecular Biology, Cambridge CB2 0QH, UK.

*Corresponding author. E-mail: ramak@mrc-lmb.cam.ac.uk

Elongation Factor G Bound to the Ribosome in an Intermediate State of Translocation

David S. Tourigny, Israel S. Fernández, Ann C. Kelley, V. Ramakrishnan*

A key step of translation by the ribosome is translocation, which involves the movement of messenger RNA (mRNA) and transfer RNA (tRNA) with respect to the ribosome. This allows a new round of protein chain elongation by placing the next mRNA codon in the A site of the 30S subunit. Translocation proceeds through an intermediate state in which the acceptor ends of the tRNAs have moved with respect to the 50S subunit but not the 30S subunit, to form hybrid states. The guanosine triphosphatase (GTPase) elongation factor G (EF-G) catalyzes the subsequent movement of mRNA and tRNA with respect to the 30S subunit. Here, we present a crystal structure at 3 angstrom resolution of the *Thermus thermophilus* ribosome with a tRNA in the hybrid P/E state bound to EF-G with a GTP analog. The structure provides insights into structural changes that facilitate translocation and suggests a common GTPase mechanism for EF-G and elongation factor Tu.

Following peptidyl transfer, translocation of tRNAs on the ribosome was shown to occur spontaneously with respect to the 50S subunit, while the anticodon ends and mRNA remain anchored in their original sites in the 30S subunit, resulting in the formation of A/P and P/E tRNA hybrid states (1). The hybrid tRNA states are accompanied by a rotation of the ribosomal subunits relative to one another, together with a series of conformational changes in the L1 stalk and main body of the ribosome (2, 3).

In the second step of translocation, the guanosine triphosphatase (GTPase) elongation factor G (EF-G) catalyzes the movement of mRNA and tRNAs with respect to the 30S subunit, thereby placing the next codon of mRNA in the A site and restoring the ribosome to the canonical, unrotated state. Various experiments suggest that EF-G with GTP stabilizes the rotated state of the ribosome (4) with hybrid tRNAs (5–7). EF-G is structurally similar to the ternary complex of elongation factor Tu (EF-Tu), tRNA, and GTP, with its domain IV mimicking the anticodon stem-loop of tRNA (8–10). The structures of EF-G bound to the ribosome in both the canonical and rotated states have been observed by cryo-electron microscopy (cryo-EM) (11–13). Whereas these studies have greatly advanced our understanding of the changes in the ribosome induced by EF-G binding, a high-resolution structure can provide greater details of the interactions of EF-G with the rotated state of the ribosome and insights into the molecular mechanisms that lead to translocation.

It was originally assumed that EF-G simply lowers the free-energy barrier of the spontaneous reaction and that GTP hydrolysis is required to release EF-G from the posttranslocated ribosome (14, 15). The currently prevailing view, based on kinetic experiments suggesting that GTP hydrolysis precedes and accelerates translocation (16–18), is that the rotated-state ribosome plays the role of a GTPase activator for EF-G. Rapid GTP hydrolysis upon ribosome binding is thought to accelerate rate-limiting conformational changes that result in an unlocking of the ribosome leading to translocation (17).

How GTP hydrolysis is activated by the ribosome remains somewhat controversial. Mutation of the highly conserved His⁸⁴ of EF-Tu to alanine resulted in a 10⁶-fold reduction in catalytic activity (19). The structure of the ternary complex bound to the ribosome showed that His⁸⁴ in the switch II region was involved in hydrogen-bonding interactions both with A2662 of the sarcin-ricin loop (SRL) of 23S ribosomal RNA (rRNA) and a water molecule positioned for hydrolysis of the γ -phosphate of the GTP analog β - γ -methyleneguanosine 5'-triphosphate (GDP-CP) (20). Suggestions that the histidine might play a role as a catalytic base were later questioned (21–23). Subsequently, a structure of release factor 3 (RF3) bound to a rotated-state ribosome (24) placed the histidine in a very different position, suggesting that it was unlikely to play a direct role in catalysis and that any mechanism of GTP hydrolysis is not general, as was first proposed (20).

A breakthrough in determining high-resolution structures of the ribosome bound to EF-G in various states was made when the crystal structure of guanosine diphosphate (GDP)-bound EF-G stalled on a posttranslocated ribosome was solved

(25). Here, we report a crystal structure refined using data to 2.9 Å, of the ribosome bound to EF-G with GDP-CP. In addition, the structure consists of an mRNA with a phenylalanine codon in the P site and a tRNA^{Phe} in the P/E hybrid state. As was done in previous cryo-EM structures (11, 12), the A-site tRNA was left out in order to obtain the intermediate rotated state of the ribosome, because in its presence with wild-type EF-G, the ribosome proceeds within seconds to the posttranslocational canonical state even without GTP hydrolysis (16, 26). This structure with EF-G bound to the rotated state of the ribosome before GTP hydrolysis lacks an A-site tRNA, but otherwise represents a key hitherto missing high-resolution structure in the elongation cycle.

Results

Overall Structure

Crystallographic data are shown in Table 1. After molecular replacement using the 50S and 30S subunits as search models, the P/E tRNA, mRNA, EF-G, and GDP-CP were clearly visible in difference Fourier maps (Fig. 1; mRNA not shown), and the entire structure was built and refined (Fig. 2A). The main body of the 30S subunit is rotated $\sim 7^\circ$ counterclockwise with respect to the 50S (as viewed from the solvent side) (Fig. 2B and movie S1). Although the precise rotation angles differ, the intersubunit interactions and central bridges are similar to those previously seen in the rotated state with ribosome recycling factor (RRF) (27) or RF3 (24, 28), suggesting a ratcheting motion that is conserved across the translational pathway. The head of the 30S is swiveled by $\sim 5^\circ$ as compared to the canonical state (Fig. 2C and movie S2). Two separate ratcheted states that differ in the degree of head swiveling have been identified by cryo-EM of an EF-G-ribosome complex (13). As displayed in Fig. 2C, the 30S head of this structure has a conformation similar to that of the TI^{PRE} state in that cryo-EM study [root mean square deviation (RMSD) of 1.7 Å as opposed to 11.1 Å when compared to TI^{POST} state]. Recently, it was shown that the TI^{PRE} state also closely resembles cryo-EM reconstructions of ribosomes containing both P/E and A/P hybrid tRNAs after peptidyl transfer (29), which is further evidence that our structure represents a valid model for the main intermediate state of translocation. The head swivel is thought to widen a constriction in the 30S to allow translocation of the P-site tRNA to the E site (13, 30, 31). In the rotated state seen here, this constriction is widened by ~ 2.7 Å compared to the canonical state, suggesting that further widening must occur at some point to allow translocation of the anticodon stem-loop of tRNA from the P to the E site. It has been proposed that intersubunit ratcheting and 30S head swiveling are sequential events that provide directionality to mRNA and tRNA translocation (32).

MRC Laboratory of Molecular Biology, Cambridge CB2 0QH, UK.

*Corresponding author. E-mail: ramak@mrc-lmb.cam.ac.uk

Table 1. Summary of crystallographic data and refinement.

	Data set 1	Data set 2	70S-tRNA-EF-G-GDPCP (merged)
Data collection			
Beamline	ID14-4 (ESRF)	IO4 (DLS)	
Space group	$P2_1$	$P2_1$	$P2_1$
<i>Cell dimensions</i>			
<i>a</i> , <i>b</i> , <i>c</i> (Å)	203.42, 243.05, 309.97	201.58, 241.65, 305.80	201.58, 241.65, 305.80
α , β , γ (°)	90.00, 99.53, 90.00	90.00, 99.48, 90.00	90.00, 99.48, 90.00
Resolution (Å)	39.6–3.1 (3.2–3.1)	39.6–2.9 (3.0–2.9)*	39.6–2.9 (3.0–2.9)†
<i>R</i> _{sym} (%)	17.8 (58.7)	24.1 (138.4)	22.4 (137.8)
<i>I</i> / σ (<i>I</i>)	8.15 (2.42)	4.93 (1.08)	7.56 (1.02)
Completeness (%)	99.6 (97.1)	97.8 (98.9)	99.8 (98.9)
Refinement			
Resolution (Å)			39.6–2.9
No. unique reflections			635,092
<i>R</i> _{work} / <i>R</i> _{free}			19.6/24.5
No. atoms			150,122
<i>B</i> values			
RNA			37.8
Protein			51.4
Bond length RMSD (Å)			0.004
Bond angles RMSD (°)			1.488

**I*/ σ (*I*) = 2.15 at 3.1 Å (using a bin from 3.2 to 3.1 Å resolution). †*I*/ σ (*I*) = 3.31 at 3.1 Å (using a bin from 3.2 to 3.1 Å resolution).

Interaction of the L1 Stalk with the P/E Hybrid tRNA

The tRNA^{Phe} in the P/E conformation is distorted, with a twist in the D-stem of the main body enabling the acceptor arm to swing ~35° toward the E site of the 50S subunit, similar to that seen in the hybrid states with RRF (27) or RF3 (28) (RMSD of 0.81 and 1.55 Å, respectively). The elbow of the P/E tRNA is cradled by the L1 stalk of the 50S ribosomal subunit, which has pivoted about the base of helix H76 (Fig. 3A) and swung into the fully closed conformation seen in lower-resolution studies (11, 12). In structures with a canonical E-site tRNA in the posttranslocational state, the L1 stalk is in a “half-closed” conformation (25). Relative to that conformation, the distal part of the L1 stalk has moved inward by ~25 Å to interact with the P/E tRNA (Fig. 3B), resulting in an angle of ~17.4° between these two positions. Moreover, there is a distance of ~37 Å between the closed conformation seen here and the fully open conformation observed in structures of the ribosome with a vacant E site (30). This dynamical nature of the L1 stalk has been studied in two kinds of single-molecule fluorescence resonance energy transfer experiments and demonstrated to have a mechanistic role during translocation (33, 34). In the absence of any factor, the L1 stalk fluctuates between half-closed and closed conformations corresponding to non-ratcheted and ratcheted states of the ribosome; binding of EF-G shifts this equilibrium toward the closed conformation of the ratcheted state. Our structure supports the notion that the L1 stalk-tRNA interaction persists throughout translocation (33). However, a separate study suggests that hybrid state formation and L1 stalk closure are not tightly coupled (35).

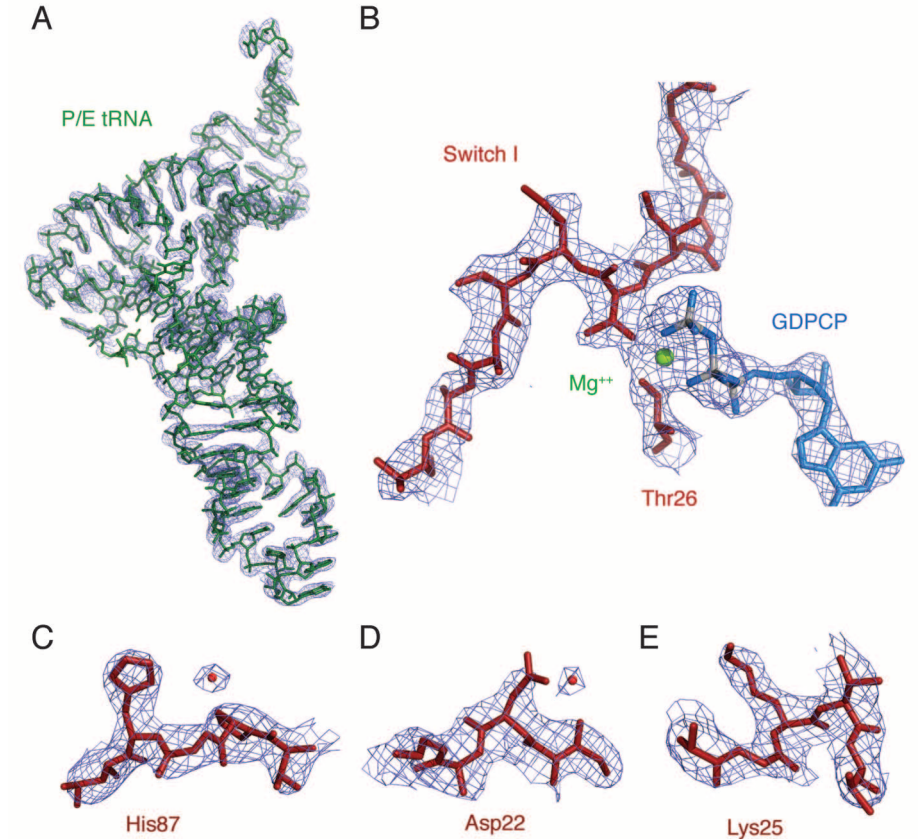


Fig. 1. Unbiased difference Fourier maps. Unbiased difference Fourier maps obtained after initial refinement with an empty ribosome as a starting model, showing (A) P/E tRNA, (B) switch I and GDP in the active site, and (C to E) key conserved residues in the active site with water molecules.

A detailed description of the interactions between the L1 protein and tRNA is made possible by the stabilization of the stalk in the closed conformation, resulting in excellent maps that show side-chain conformations (Fig. 3C). Most of these interactions are electrostatic, such as

Fig. 2. EF-G bound to the rotated state of the ribosome.

(A) Overall view of EF-G and the ribosome. Shown are EF-G (red), the 50S subunit (cyan), 30S subunit (yellow), P/E-site tRNA (green), and ribosomal protein L1 (orange). (B) Global conformational changes in the 70S ribosome upon GTP hydrolysis as viewed from the perspective of the 23S RNA (cyan). (C) Change in the swivel angle of the head of the 30S in various states of the ribosome, showing the rotated state with EF-G in this study

(yellow), the posttranslocated state with EF-G and GDP [light gray; Protein Data Bank (PDB) code 2WRI] (25), the “Tl^{Pre}” state of a cryo-EM structure of EF-G with GPDNP bound to a rotated state (green) (13), and the “Tl^{Post}” state of the same study (red). For clarity, only the rRNA is shown in (B) and (C).

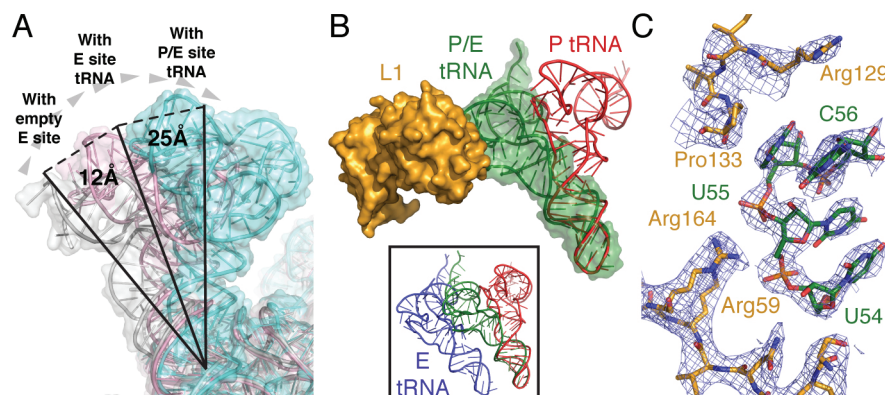
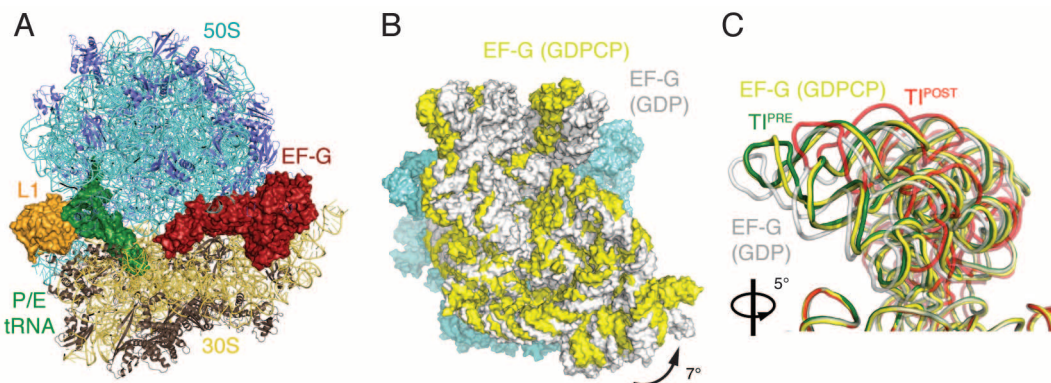


Fig. 3. Dynamics of the L1 stalk during tRNA translocation. (A) Three distinct conformations of the L1 stalk, showing the open (gray; PDB code 2WA4) (30), the half-closed (pink; PDB code 2WRI) (25), and fully closed conformations (cyan; this study). (B) The ribosomal protein L1 (orange) stabilizes the distorted P/E tRNA (green) halfway between the canonical P-site (red) and E-site (blue, see inset) conformations. (C) Details of interactions between the L1 protein (orange) and elbow of the P/E tRNA (green). The unbiased $F_o - F_c$ difference Fourier map is contoured at 2.5σ .

Arg⁵⁹, Arg¹²⁹, and Arg¹⁶⁴ forming salt bridges with the negatively charged phosphate backbone of the tRNA, but there is also a stacking interaction between base C56 and the imino ring of Pro¹³³. Such contacts are probably maintained as the L1 stalk chaperones the P/E tRNA to the E/E conformation during translocation (33), because superposing the current structure with that docked into the posttranslocated ribosome structure reveals that the backbone of the L1 protein does not change upon the transition.

Interactions of EF-G with L11, L12, and L6

On the other side of the 50S subunit from the L1 stalk, the interaction of EF-G with L6, L11, and the L12 stalk are indistinguishable from those previously described for the posttranslocational state (25) (Fig. 4). In particular, the C-terminal domain of one of the L12 molecules is seen interacting with EF-G and the N-terminal domain of L11, and on the opposite side, L6, at the base of the L12 stalk, also interacts with EF-G through a flexible C-terminal domain extension.

Changes in the Conformation of Domain IV of EF-G

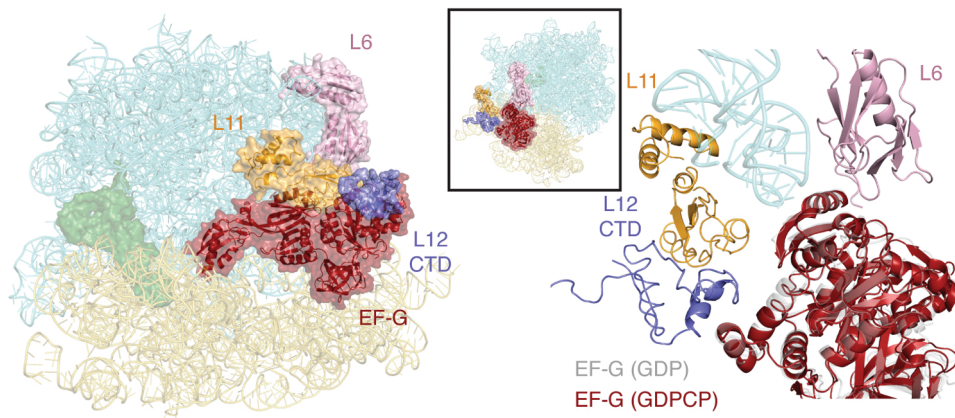
Details of the structural changes in EF-G during translocation can be discerned by superposing domains I and II of EF-G in this structure with those of the isolated factor (36) or in the posttranslocational state (25). In this superposition, the isolated structure of EF-G would have a conformation of domain IV that would largely avoid a steric clash with A-site tRNA (Fig. 5A). Presumably this orientation of domain IV resembles the transient state immediately after EF-G binds to the rotated state and just before translocation occurs in the 30S. In the structure described here, domain IV has moved partly into the A site and would clash with A-site tRNA (Fig. 5A and movie S1), which explains why slow translocation can occur even without GTP hydrolysis. Thus, ribosome binding alone must promote a conformation of EF-G that partially facilitates translocation. However, the fragmented density and high B factors for domain IV suggest that it has a dynamical nature, consistent with its requirement for being able to coexist transiently with A-site tRNA.

A comparison with EF-G in the posttranslocational state (25) shows that the tip of domain IV has moved by another ~ 6.6 Å and more fully occupies the A site (Fig. 5B and movie S1). This further movement is a result of the rotation of the superdomain I-II relative to domains III-V that presumably occurs after GTP hydrolysis.

Changes in the Catalytic Site

The catalytic site of EF-G shows distinct differences from the posttranslocated GDP form (25) or the isolated EF-G with GPDNP (36) that yield insights into activation of GTP hydrolysis. The switch I region was unresolvable in previous crystal structures of both posttranslocated and isolated EF-G, but is ordered in this structure from Met⁵⁵ onward. The switch I region adopts a single turn of a 3_{10} helix that contacts helix B₃ of domain III, as in the isolated structure of the EF-G homolog EF-G-2 in the GTP form and as also seen at lower resolution by cryo-EM studies of a ribosomal complex similar to the structure described here (12). The γ -phosphate of GDDCP is surrounded by several highly conserved residues, notably His⁸⁷ of switch II and Asp²² and Lys²⁵ in the P loop (Fig. 6, A and B). His⁸⁷ and Asp²² point away from bound nucleotide in the isolated and posttranslocated states of EF-G, but have moved by ~ 6.4 and ~ 3.3 Å, respectively, toward the γ -phosphate of GDDCP upon ribosome binding (Fig. 6C and movie S3) to assume a conformation very similar to that seen before in EF-Tu (Fig. 6D) (20). As with EF-Tu, the conformation of the activated His⁸⁷ is stabilized by hydrogen bonding interactions with both A2662 of the SRL and the catalytic water molecule poised for hydrolysis of the phosphate ester (Fig. 6B). Two Mg²⁺ ions uniquely positioned by the GAGA tetrad of the SRL stabilize the inward conformation of Asp²² where it coordinates a second water molecule above the γ -phosphate of GDDCP (Fig. 6B). This second water could play a further role in catalysis by donating a hydrogen bond to the γ -phosphate O2. The structure strongly suggests that the change in orientation of Asp²² and His⁸⁷ upon EF-G binding is part of GTPase activation by the ribosome

Fig. 4. Interactions of EF-G with L6, L11, and L12. Interactions of EF-G with ribosomal proteins L11, L6, and the L12 C-terminal domain (CTD) near the base of the L7/L12 stalk. A single CTD of L12 is seen to interact with both EF-G and the N-terminal domain of L11 (far right).



and that the mechanism of GTP hydrolysis is essentially the same for both EF-Tu and EF-G.

Although the final activated state of EF-Tu and that of EF-G GTP are highly similar, in EF-Tu the equivalent Asp²¹ has its activated conformation even in the isolated ternary complex. Thus, different steps may be required to reach the same activated state. Interestingly, the toxin ricin depurinates A2660 of the GAGA tetrad. It is likely that depurination of A2660 prevents the surrounding region from adopting the conformation required to bind the metal ions necessary to stabilize Asp²² and neighboring regions of EF-G in the activated form. EF-Tu does not make these interactions, explaining why ricin only affects EF-G function (37).

Although a proposal was made that His⁸⁷ might be acting as a general base in EF-Tu (20), the structure is consistent with an alternate mechanism that was proposed subsequently (21). In this mechanism, the environment of the SRL may result in an increase in the acid dissociation constant (pK_a) of His⁸⁷ and stabilize the protonated state of its N_δ, thus enabling His⁸⁷ to donate a hydrogen bond to the hydrolytic water. The water can in turn donate a hydrogen bond to the carbonyl oxygen of Thr⁶⁴ and to one of the three oxygen atoms on the γ -phosphate. Under these circumstances, the occurrence of a substrate-promoted catalytic mechanism, whereby the γ -phosphate abstracts a proton from the water molecule to generate a hydroxide ion that in turn cleaves the phosphate ester, appears feasible. It has also been suggested that the role of the histidine is not to behave as a donor or acceptor of protons at all, but to contribute to an allosteric effect that results in stabilization of the transition state by the general electrostatic effect of the P loop (23). This scenario is compatible with the observation that in EF-G-2, a ribosome-activated GTPase that can substitute for EF-G in polyU-directed protein synthesis in vitro (12), the histidine and aspartate have been replaced by tyrosine and glycine, respectively (Fig. 6A).

Discussion

The structure sheds light on the GTPase mechanism of EF-G and on its role in translocation.

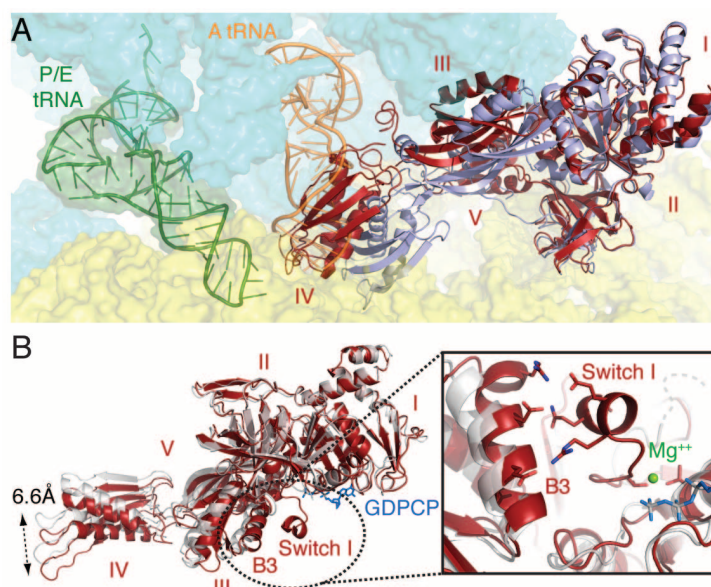


Fig. 5. Conformational changes in EF-G during translocation. (A) Comparison of isolated EF-G structure (light blue; PDB code 2BV3) (36) with EF-G in this study (red). (B) Comparison of EF-G in this study (red) with that in the posttranslocated state (gray; PDB code 2WRI) (25) reveals an interdomain rotation about domain III leading to changes in the orientation of domain IV. Inset (right) shows that in the GDP-CP-bound EF-G (this study), switch I forms a 3_{10} helix that stabilizes helix B3 in an altered conformation.

Globally, a distinctive feature is that the interactions of the L1 stalk with the P/E tRNA appear to be the same as those with the posttranslocational E-site tRNA (25), implying that the interactions are preserved throughout translocation, as previously suggested (33). This also suggests that the stabilization of the closed conformation of the L1 stalk through its interaction with the P/E tRNA is an essential feature of translocation through the stabilization of hybrid states.

Another large-scale movement is the swiveling of the head, which is required to open a constriction that allows passage of the P-site tRNA to the E site in the 30S subunit (13, 38). It has previously been suggested that spectinomycin, an antibiotic that inhibits translocation, may act by inhibiting the movement of the head by binding to a crucial hinge point (39, 40). Our structure shows that in the rotated state, the swivel

angle of the head would cause a steric clash with spectinomycin, thus supporting this idea.

Notably, key residues in EF-Tu and EF-G change conformation in different ways upon binding to very different states of the ribosome to form a nearly identical catalytic site (Fig. 6D), suggesting a common mechanism for activation of translational GTPases by the ribosome. This mechanism also implies that the SRL plays a crucial role in stabilizing key residues of the catalytic site in their activated conformations, which would be in keeping with their very high degree of conservation.

Recently, lethal mutations in the SRL were found not to affect GTP hydrolysis (41), suggesting that the SRL does not play a direct role in stabilizing the transition state for GTP hydrolysis. However, the interactions with the SRL occur via phosphate backbone interactions

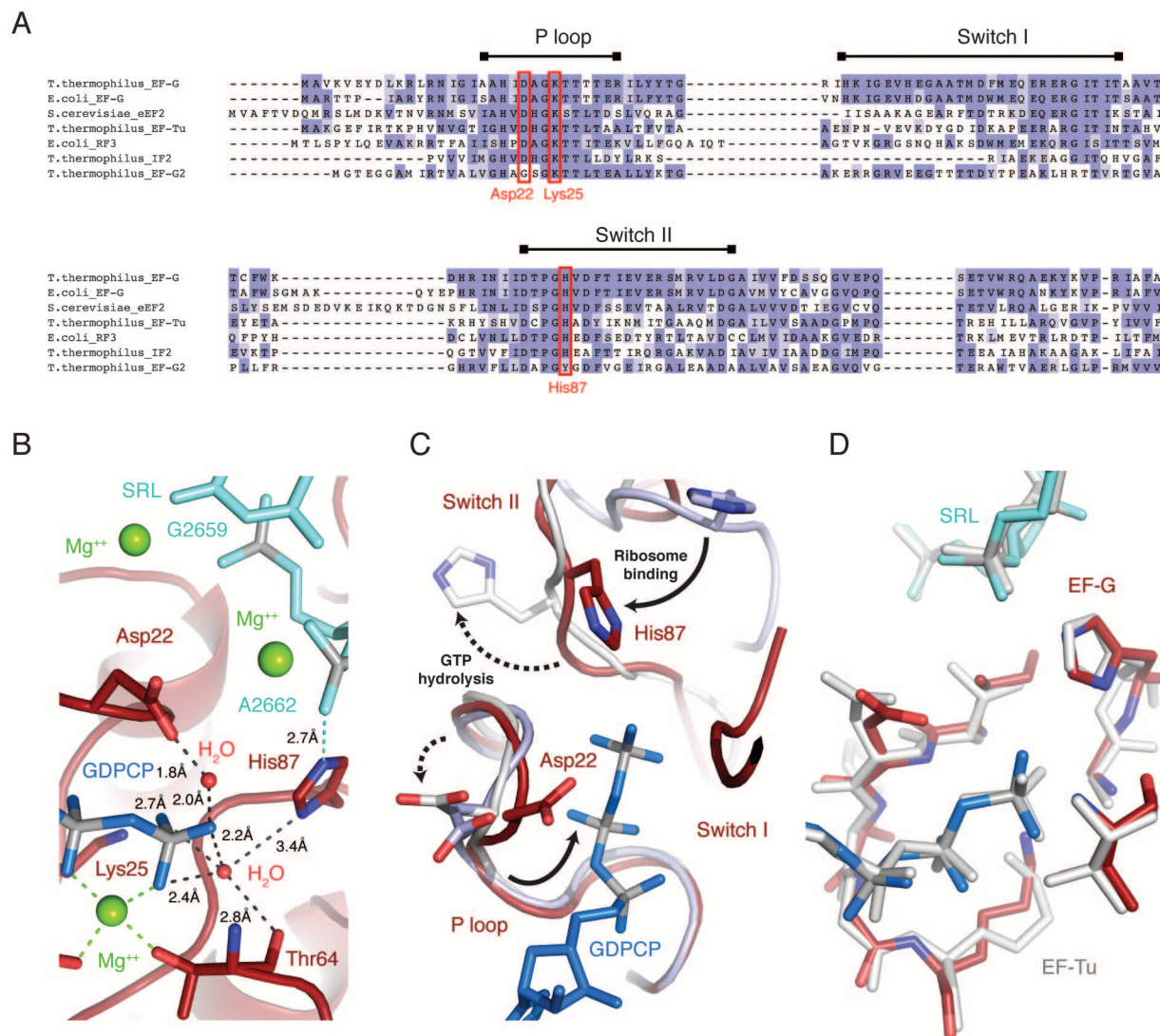


Fig. 6. The active site of EF-G. (A) Sequence alignment of G domains from several translational GTPases shows conservation of residues Asp²², Lys²⁵, and His⁸⁷, except in EF-G-2. *T. thermophilus*, *Thermus thermophilus*; *E. coli*, *Escherichia coli*; and *S. cerevisiae*, *Saccharomyces cerevisiae*. (B) Details of the catalytic site around the γ -phosphate of GTP (blue) with relevant distances displayed as dashes. EF-G residues and waters are in red, Mg²⁺ ions are in green, and residues of the SRL are in cyan. (C) Comparison of the active site of isolated EF-G with GDPNP (light blue; PDB code 2BV3) (36), EF-G with GTP

in this structure (red), and EF-G in the GDP posttranslocated state (gray; PDB code 2WRI) (25) shows that His⁸⁷ and Asp²² move toward the γ -phosphate of GTP (blue) on ribosome binding and away from it upon GTP hydrolysis. (D) Similarity of the activated catalytic sites of EF-G (red; this structure) and EF-Tu (gray; PDB code 2XQD) (20), suggesting a common mechanism of GTPase activation for the two factors. Abbreviations for the amino acid residues are as follows: A, Ala; C, Cys; D, Asp; E, Glu; F, Phe; G, Gly; H, His; I, Ile; K, Lys; L, Leu; M, Met; N, Asn; P, Pro; Q, Gln; R, Arg; S, Ser; T, Thr; V, Val; W, Trp; and Y, Tyr.

rather than specific bases, so it is possible that in these mutant ribosomes, other nucleotides of the mutated SRL play the role of key residues in the wild-type ribosome.

In contrast to EF-Tu and EF-G, the catalytic site of RF3 on the ribosome appears different; the histidine is far from the γ -phosphate of GTP and makes different interactions with the SRL (24). It is therefore possible that the GTPase mechanism for RF3 is different or that the structure, which lacks the expected P/E tRNA, does not represent the GTPase-activated state of RF3.

The structure reported here offers some clues into how conformational changes associated with GTP hydrolysis could facilitate translocation.

GTP hydrolysis results in changes in switch I, switch II, and P-loop regions that form an interface between the ribosome, domain III, and GTP. These changes in switch I and II may be communicated to domain III and cause the large movements of the helices that serve to bridge the I-II and III-V superdomains (Fig. 5). This would account for the relative change in the orientation of these superdomains upon GTP hydrolysis (Fig. 5). Deletion of domain III decreases EF-G activity 10³-fold on the ribosome (42), supporting the notion that this region may couple GTP hydrolysis to the interdomain movements that allow domain IV to adopt the favored conformation of the posttranslocational state. Such a conformation may be adopted after tRNA

translocation has occurred transiently, allowing domain IV to enter the A site and prevent a reversal of translocation. Details of the mechanism of action of EF-G will require concerted studies by many complementary techniques.

In conclusion, this work provides an atomic model of EF-G bound to the ribosome in a rotated state before GTP hydrolysis. It has enabled a complete description of the inward movement of the L1 stalk, stabilization of the P/E tRNA, and conformational changes in EF-G that are the key steps in facilitating translocation. GTP hydrolysis leads to a series of changes in the switch I, switch II, and P-loop regions of EF-G, which result in an interdomain reorientation about domain III that is expected to promote translocation

of any tRNA bound at the ribosomal A site. Local conformational changes at the GTP-binding site of EF-G have implicated key residues Asp²², Lys²⁵, and His⁸⁷ in GTPase activation, whose precise roles can be tested by biochemical and mutagenesis experiments. Finally, despite their action on conformationally very different states of the elongating ribosome, the structure supports a common mechanism of GTP hydrolysis by both EF-G and EF-Tu.

Materials and Methods

Full-length EF-G, tRNA^{Phe}, and ribosomes from *Thermus thermophilus* harboring a C-terminal truncation of protein L9 were prepared as previously described (25, 31). mRNA with the sequence 5'-GGCAAGGAGGUAAAAUGUUCAAAA-3' was purchased from Dharmcon (Thermo Scientific), where the phenylalanine codon in the P site is underlined.

Ribosomes (4.0 μM) and mRNA (8.0 μM) were incubated at 55°C for 6 min before addition of tRNA^{Phe} (16.0 μM) and a further incubation at 55°C for 20 min. Separately, EF-G (20.0 μM) was incubated with GTPCP (6.0 mM) for 20 min at 37°C and mixed with the ribosome complex for a final incubation at 37°C for 20 min in buffer G [50 mM KCl, 10 mM NH₄Cl, 10 mM Mg-acetate, 5 mM HEPES (pH 7.5)]. Immediately before crystallization, the detergent HEGA-9 was added (46 mM). All concentrations refer to the final values in the sample. Typical total sample volumes used for crystallization experiments did not exceed 500 μl.

Crystals were grown by streak seeding and vapor diffusion in sitting-drop trays by mixing 3 μl of sample with 3 μl of reservoir solution [100 mM MES (pH 6.3), 75 mM KCl, 6.0 to 6.5% (w/v) polyethylene glycol (PEG) molecular weight 20,000 (20K)]. Crystals of plate morphology grew to full size (~200 μm by 100 μm by 50 μm) over a period of 3 weeks and were cryoprotected in a stepwise fashion by sequentially increasing the concentrations of PEG 20K and PEG 400 in the crystallization buffer to 6.8 and 30%, respectively, while maintaining the concentration of other components. Crystals were plunged into liquid nitrogen and stored until data collection.

Two independently complete sets of data were collected from single crystals on beam line ID 14-4 at the European Synchrotron Radiation Facility (43) and on beam line IO4 at the Diamond Light Source, Harwell, United Kingdom, respectively. Data were integrated, merged, and scaled using XDS (44) and found to be consistent with space group *P*2₁ and unit cell dimensions *a* = 201.58 Å, *b* = 241.65 Å, *c* = 305.80 Å and β = 99.48°.

Molecular replacement was performed with MOLREP (45) in two stages, first with the 50S subunit of the 70S *T. thermophilus* structure (31) as a search model, followed by inclusion of the 30S. The solution showed a single ribosome in the asymmetric unit in the fully rotated conformation. Refinement was carried out in alternat-

ing cycles of automated refinements with either PHENIX (46) or REFMAC5 (47), with manual refinement and model building in COOT (48). A summary of refinement and data collection statistics is displayed in Table 1. All figures were generated with PyMOL (49) or Jalview for sequence alignments (50).

References and Notes

1. D. Moazed, H. F. Noller, Intermediate states in the movement of transfer RNA in the ribosome. *Nature* **342**, 142 (1989). doi: [10.1038/342142a0](#); pmid: [2682263](#)
2. P. Julián *et al.*, Structure of ratcheted ribosomes with tRNAs in hybrid states. *Proc. Natl. Acad. Sci. U.S.A.* **105**, 16924 (2008). doi: [10.1073/pnas.0809587105](#); pmid: [18971332](#)
3. X. Agirrezabala *et al.*, Visualization of the hybrid state of tRNA binding promoted by spontaneous ratcheting of the ribosome. *Mol. Cell* **32**, 190 (2008). doi: [10.1016/j.molcel.2008.10.001](#); pmid: [18951087](#)
4. J. Frank, R. K. Agrawal, A ratchet-like inter-subunit reorganization of the ribosome during translocation. *Nature* **406**, 318 (2000). doi: [10.1038/35018597](#); pmid: [10917535](#)
5. S. Dorner, J. L. Brunelle, D. Sharma, R. Green, The hybrid state of tRNA binding is an authentic translation elongation intermediate. *Nat. Struct. Mol. Biol.* **13**, 234 (2006). doi: [10.1038/nsmb1060](#); pmid: [16501572](#)
6. P. C. Spiegel, D. N. Ermolenko, H. F. Noller, Elongation factor G stabilizes the hybrid-state conformation of the 70S ribosome. *RNA* **13**, 1473 (2007). doi: [10.1261/rna.601507](#); pmid: [17630323](#)
7. D. N. Ermolenko *et al.*, Observation of intersubunit movement of the ribosome in solution using FRET. *J. Mol. Biol.* **370**, 530 (2007). doi: [10.1016/j.jmb.2007.04.042](#); pmid: [17512008](#)
8. M. Lindahl *et al.*, Crystal structure of the ribosomal protein S6 from *Thermus thermophilus*. *EMBO J.* **13**, 1249 (1994). pmid: [8137808](#)
9. J. Czworkowski, J. Wang, T. A. Steitz, P. B. Moore, The crystal structure of elongation factor G complexed with GDP, at 2.7 Å resolution. *EMBO J.* **13**, 3661 (1994). pmid: [8070396](#)
10. P. Nissen *et al.*, Crystal structure of the ternary complex of Phe-tRNA^{Phe}, EF-Tu, and a GTP analog. *Science* **270**, 1464 (1995). doi: [10.1126/science.270.5241.1464](#); pmid: [7491491](#)
11. M. Valle *et al.*, Locking and unlocking of ribosomal motions. *Cell* **114**, 123 (2003). doi: [10.1016/S0092-8674\(03\)00476-8](#); pmid: [12859903](#)
12. S. R. Connell *et al.*, Structural basis for interaction of the ribosome with the switch regions of GTP-bound elongation factors. *Mol. Cell* **25**, 751 (2007). doi: [10.1016/j.molcel.2007.01.027](#); pmid: [17349960](#)
13. A. H. Ratje *et al.*, Head swivel on the ribosome facilitates translocation by means of intra-subunit tRNA hybrid sites. *Nature* **468**, 713 (2010). doi: [10.1038/nature09547](#); pmid: [21124459](#)
14. N. Inoue-Yokosawa, C. Ishikawa, Y. Kaziro, The role of guanosine triphosphate in translocation reaction catalyzed by elongation factor G. *J. Biol. Chem.* **249**, 4321 (1974). pmid: [4605331](#)
15. J. Czworkowski, P. B. Moore, The conformational properties of elongation factor G and the mechanism of translocation. *Biochemistry* **36**, 10327 (1997). doi: [10.1021/bi970610k](#); pmid: [9254632](#)
16. M. V. Rodnina, A. Savelsbergh, V. I. Katunin, W. Wintermeyer, Hydrolysis of GTP by elongation factor G drives tRNA movement on the ribosome. *Nature* **385**, 37 (1997). doi: [10.1038/385037a0](#); pmid: [8985244](#)
17. A. Savelsbergh *et al.*, An elongation factor G-induced ribosome rearrangement precedes tRNA-mRNA translocation. *Mol. Cell* **11**, 1517 (2003). doi: [10.1016/S1097-2765\(03\)00230-2](#); pmid: [12820965](#)
18. C. Chen *et al.*, Single-molecule fluorescence measurements of ribosomal translocation dynamics. *Mol. Cell* **42**, 367 (2011). doi: [10.1016/j.molcel.2011.03.024](#); pmid: [21549313](#)
19. T. Daviter, H. J. Wieden, M. V. Rodnina, Essential role of histidine 84 in elongation factor Tu for the chemical step of GTP hydrolysis on the ribosome. *J. Mol. Biol.* **332**, 689 (2003). doi: [10.1016/S0022-2836\(03\)00947-1](#); pmid: [12963376](#)
20. R. M. Voorhees, T. M. Schmeing, A. C. Kelley, V. Ramakrishnan, The mechanism for activation of GTP hydrolysis on the ribosome. *Science* **330**, 835 (2010). doi: [10.1126/science.1194460](#); pmid: [21051640](#)
21. A. Liljas, M. Ehrenberg, J. Åqvist, Comment on "The mechanism for activation of GTP hydrolysis on the ribosome". *Science* **333**, 37 (2011). doi: [10.1126/science.1202472](#); pmid: [21719661](#)
22. R. M. Voorhees, T. M. Schmeing, A. C. Kelley, V. Ramakrishnan, Response to Comment on "The mechanism for activation of GTP hydrolysis on the ribosome". *Science* **333**, 37 (2011). doi: [10.1126/science.1202472](#); pmid: [21719661](#)
23. A. J. Adamczyk, A. Warshel, Converting structural information into an allosteric-energy-based picture for elongation factor Tu activation by the ribosome. *Proc. Natl. Acad. Sci. U.S.A.* **108**, 9827 (2011). doi: [10.1073/pnas.1105714108](#); pmid: [21617092](#)
24. J. Zhou, L. Lancaster, S. Trakhanov, H. F. Noller, Crystal structure of release factor RF3 trapped in the GTP state on a rotated conformation of the ribosome. *RNA* **18**, 230 (2012). doi: [10.1261/rna.031187.111](#); pmid: [22187675](#)
25. Y. G. Gao *et al.*, The structure of the ribosome with elongation factor G trapped in the posttranslocational state. *Science* **326**, 694 (2009). doi: [10.1126/science.1179709](#); pmid: [19833919](#)
26. D. N. Ermolenko, H. F. Noller, mRNA translocation occurs during the second step of ribosomal intersubunit rotation. *Nat. Struct. Mol. Biol.* **18**, 457 (2011). doi: [10.1038/nsmb.2011](#); pmid: [21399643](#)
27. J. A. Dunkle *et al.*, Structures of the bacterial ribosome in classical and hybrid states of tRNA binding. *Science* **332**, 981 (2011). doi: [10.1126/science.1202692](#); pmid: [21596992](#)
28. H. Jin, A. C. Kelley, V. Ramakrishnan, Crystal structure of the hybrid state of ribosome in complex with the guanosine triphosphatase release factor 3. *Proc. Natl. Acad. Sci. U.S.A.* **108**, 15798 (2011). doi: [10.1073/pnas.1112185108](#); pmid: [21903932](#)
29. X. Agirrezabala *et al.*, Structural characterization of mRNA-tRNA translocation intermediates. *Proc. Natl. Acad. Sci. U.S.A.* **109**, 6094 (2012). doi: [10.1073/pnas.1201288109](#); pmid: [22467828](#)
30. B. S. Schuwirth *et al.*, Structures of the bacterial ribosome at 3.5 Å resolution. *Science* **310**, 827 (2005). doi: [10.1126/science.1117230](#); pmid: [16272117](#)
31. M. Selmer *et al.*, Structure of the 70S ribosome complexed with mRNA and tRNA. *Science* **313**, 1935 (2006). doi: [10.1126/science.1131127](#); pmid: [16959973](#)
32. Z. Guo, H. F. Noller, Rotation of the head of the 30S ribosomal subunit during mRNA translocation. *Proc. Natl. Acad. Sci. U.S.A.* **109**, 20391 (2012). doi: [10.1073/pnas.1218999109](#); pmid: [23188795](#)
33. J. Fei, P. Kosuri, D. D. MacDougall, R. L. Gonzalez Jr., Coupling of ribosomal L1 stalk and tRNA dynamics during translation elongation. *Mol. Cell* **30**, 348 (2008). doi: [10.1016/j.molcel.2008.03.012](#); pmid: [18471980](#)
34. P. V. Cornish *et al.*, Following movement of the L1 stalk between three functional states in single ribosomes. *Proc. Natl. Acad. Sci. U.S.A.* **106**, 2571 (2009). doi: [10.1073/pnas.0813180106](#); pmid: [19190181](#)
35. J. B. Munro *et al.*, Spontaneous formation of the unlocked state of the ribosome is a multistep process. *Proc. Natl. Acad. Sci. U.S.A.* **107**, 709 (2010). doi: [10.1073/pnas.0908597107](#); pmid: [20018653](#)
36. S. Hansson, R. Singh, A. T. Gudkov, A. Liljas, D. T. Logan, Crystal structure of a mutant elongation factor G trapped with a GTP analogue. *FEBS Lett.* **579**, 4492 (2005). doi: [10.1016/j.febslet.2005.07.016](#); pmid: [16083884](#)
37. D. Moazed, J. M. Robertson, H. F. Noller, Interaction of elongation factors EF-G and EF-Tu with a conserved loop in 23S RNA. *Nature* **334**, 362 (1988). doi: [10.1038/334362a0](#); pmid: [2455872](#)
38. W. Zhang, J. A. Dunkle, J. H. Cate, Structures of the ribosome in intermediate states of ratcheting. *Science* **325**, 1014 (2009). doi: [10.1126/science.1175275](#); pmid: [19696352](#)

39. A. P. Carter *et al.*, Functional insights from the structure of the 30S ribosomal subunit and its interactions with antibiotics. *Nature* **407**, 340 (2000). doi: [10.1038/35030019](https://doi.org/10.1038/35030019); pmid: [11014183](https://pubmed.ncbi.nlm.nih.gov/11014183/)
40. M. A. Borovinskaya, S. Shoji, J. M. Holton, K. Fredrick, J. H. Cate, A steric block in translation caused by the antibiotic spectinomycin. *ACS Chem. Biol.* **2**, 545 (2007). doi: [10.1021/cb700100n](https://doi.org/10.1021/cb700100n); pmid: [17696316](https://pubmed.ncbi.nlm.nih.gov/17696316/)
41. X. Shi, P. K. Khade, K. Y. Sanbonmatsu, S. Joseph, Functional role of the sarcin-ricin loop of the 23S rRNA in the elongation cycle of protein synthesis. *J. Mol. Biol.* **419**, 125 (2012). doi: [10.1016/j.jmb.2012.03.016](https://doi.org/10.1016/j.jmb.2012.03.016); pmid: [22459262](https://pubmed.ncbi.nlm.nih.gov/22459262/)
42. K. A. Martemyanov, A. T. Gudkov, Domain III of elongation factor G from *Thermus thermophilus* is essential for induction of GTP hydrolysis on the ribosome. *J. Biol. Chem.* **275**, 35820 (2000). doi: [10.1074/jbc.M002656200](https://doi.org/10.1074/jbc.M002656200); pmid: [10940297](https://pubmed.ncbi.nlm.nih.gov/10940297/)
43. A. A. McCarthy *et al.*, A decade of user operation on the macromolecular crystallography MAD beamline ID14-4 at the ESRF. *J. Synchrotron Radiat.* **16**, 803 (2009). doi: [10.1107/S0909049509035377](https://doi.org/10.1107/S0909049509035377); pmid: [19844017](https://pubmed.ncbi.nlm.nih.gov/19844017/)
44. W. Kabsch, XDS. *Acta Crystallogr. D Biol. Crystallogr.* **66**, 125 (2010). doi: [10.1107/S0907444909047337](https://doi.org/10.1107/S0907444909047337); pmid: [20124692](https://pubmed.ncbi.nlm.nih.gov/20124692/)
45. A. Vagin, A. Teplyakov, Molecular replacement with MOLREP. *Acta Crystallogr. D Biol. Crystallogr.* **66**, 22 (2010). doi: [10.1107/S0907444909042589](https://doi.org/10.1107/S0907444909042589); pmid: [20057045](https://pubmed.ncbi.nlm.nih.gov/20057045/)
46. P. D. Adams *et al.*, PHENIX: A comprehensive Python-based system for macromolecular structure solution. *Acta Crystallogr. D Biol. Crystallogr.* **66**, 213 (2010). doi: [10.1107/S0907444909052925](https://doi.org/10.1107/S0907444909052925); pmid: [20124702](https://pubmed.ncbi.nlm.nih.gov/20124702/)
47. G. N. Murshudov *et al.*, REFMAC5 for the refinement of macromolecular crystal structures. *Acta Crystallogr. D Biol. Crystallogr.* **67**, 355 (2011). doi: [10.1107/S0907444911001314](https://doi.org/10.1107/S0907444911001314); pmid: [21460454](https://pubmed.ncbi.nlm.nih.gov/21460454/)
48. P. Emsley, B. Lohkamp, W. G. Scott, K. Cowtan, Features and development of Coot. *Acta Crystallogr. D Biol. Crystallogr.* **66**, 486 (2010). doi: [10.1107/S0907444910007493](https://doi.org/10.1107/S0907444910007493); pmid: [20383002](https://pubmed.ncbi.nlm.nih.gov/20383002/)
49. W. L. DeLano, The PyMOL Molecular Graphics System; www.pymol.org (2006).
50. A. M. Waterhouse, J. B. Procter, D. M. Martin, M. Clamp, G. J. Barton, Jalview Version 2—a multiple sequence alignment editor and analysis workbench. *Bioinformatics* **25**, 1189 (2009). doi: [10.1093/bioinformatics/btp033](https://doi.org/10.1093/bioinformatics/btp033); pmid: [19151095](https://pubmed.ncbi.nlm.nih.gov/19151095/)

Acknowledgments: We are indebted to P. R. Elliott and the beamline staff on IO4 at Diamond Light Source and ID14-4 at the European Synchrotron Radiation Facility for help and advice with data collection, and to R. M. Voorhees and C. Spahn for critical comments. This work was supported by grants to V.R. from the UK Medical Research Council (U105184332), a program grant and Senior Investigator Award from the Wellcome Trust, the Agouron Institute, and the Louis-Jeantet Foundation. Coordinates and structure factors have been deposited in the PDB with codes 4JUW and 4JUX.

Supplementary Materials

www.sciencemag.org/content/340/6140/1235490/suppl/DC1
Movies S1 to S3

22 January 2013; accepted 3 May 2013
[10.1126/science.1235490](https://doi.org/10.1126/science.1235490)

Crystal Structures of EF-G–Ribosome Complexes Trapped in Intermediate States of Translocation

Jie Zhou, Laura Lancaster, John Paul Donohue, Harry F. Noller*

READ THE FULL ARTICLE ONLINE
<http://dx.doi.org/10.1126/science.1236086>

Cite this article as J. Zhou *et al.*, *Science* **340**, 1236086 (2013). DOI: 10.1126/science.1236086

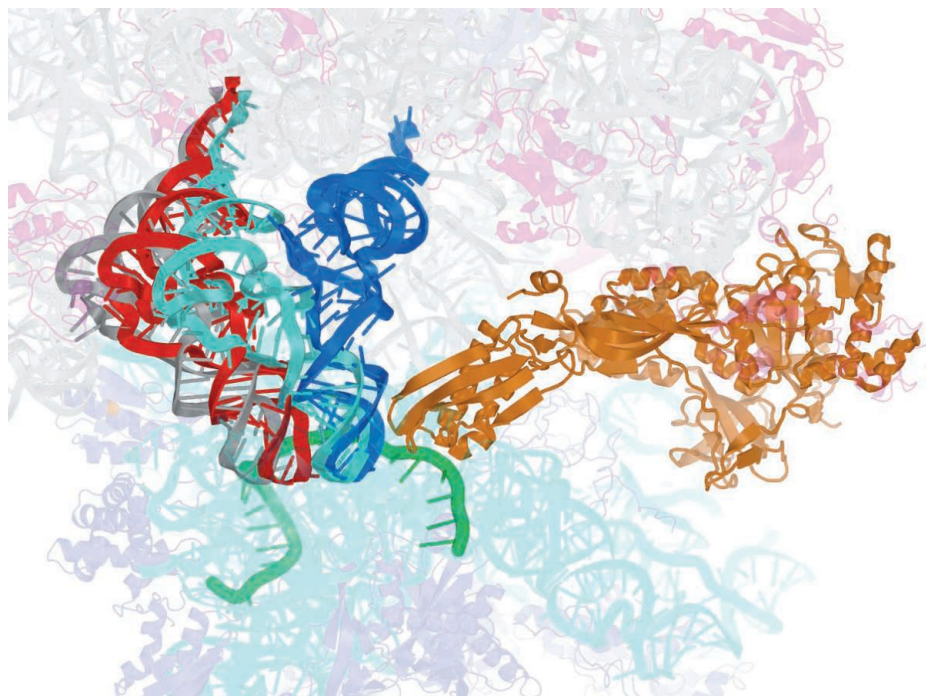
Introduction: One of the most critical and complex steps of protein synthesis is the coupled translocation of messenger RNA and transfer RNAs (mRNA and tRNAs) through the ribosome, catalyzed by the guanosine triphosphatase (GTPase) elongation factor EF-G. Although several of the main steps have been identified, the underlying molecular mechanisms of translocation are poorly understood. A central question is how structural rearrangements in the ribosome are coupled to movement of mRNA and tRNA.

Methods: We trapped and crystallized complexes of *Thermus thermophilus* ribosomes bound with EF-G, mRNA, and tRNA, using the antibiotic fusidic acid (which prevents release of EF-G after GTP hydrolysis) or the nonhydrolyzable GTP analog GDPNP, in intermediate states of translocation. Their crystal structures were determined to resolutions from 3.5 to 4.1 Å.

Results: The structures of the fusidic acid complex (Fus) and two GDPNP complexes (GDPNP-I and GDPNP-II) reveal conformational changes occurring during intermediate states of translocation, including large-scale (15° to 18°) rotation of the 30S subunit head and 3° to 5° rotation of the 30S body. In all complexes, the tRNA acceptor end has moved from the 50S subunit P site to the 50S E site, while the anticodon stem loop (ASL) and mRNA move with the head of the 30S subunit to positions between the P and E sites, forming chimeric pe*/E intermediate states. The elongated, mobile domain IV of EF-G moves to contact the head of the 30S subunit and the backbone of the mRNA. Two universally conserved bases of 16S rRNA that intercalate between bases of the mRNA may act as “pawls” of a translocational ratchet. In the GDPNP complexes, structuring of the conserved switch loop I segment, which was disordered in previous structures, completes the cage that encloses GDPNP and fixes the relative geometry of EF-G domains I, III, and V. In the Fus complex, the position of fusidic acid overlaps that of switch loop I, stabilizing contacts between domains I and III that are normally made by the structured switch loop.

Discussion: Our structures capture intermediate states of the rate-limiting step of translocation, in which movement of the tRNA ASL and mRNA is coupled to rotational movement of the 30S subunit head. Slippage of the translational reading frame during reverse rotation of the head during translocation may be prevented by intercalation of bases C1397 and A1503 of 16S rRNA, which project from the body of the 30S subunit, between mRNA bases. The antibiotic fusidic acid appears to stabilize binding of EF-G to the ribosome in the GDP state by mimicking the structure of the conserved core of switch loop I of EF-G in the GTP state.

EF-G-catalyzed translocation. Overall view of the positions of mRNA (green) and tRNA bound in the classical P/P (blue), hybrid P/E (cyan), chimeric pe*/E (red), and classical E/E (gray) states in the ribosome (transparently rendered). The position of elongation factor EF-G (orange) bound to the ribosome in an intermediate state of translocation trapped with the nonhydrolyzable GTP analog GDPNP is shown.



FIGURES IN THE FULL ARTICLE

- Fig. 1. Structures of trapped 70S ribosome–EF-G complexes.
- Fig. 2. Movement of tRNA from the P/P to the pe*/E state.
- Fig. 3. Flexing of tRNA during translocation.
- Fig. 4. Interactions of mRNA with the 30S subunit.
- Fig. 5. EF-G interactions and dynamics.
- Fig. 6. Structuring of switch loop I.

SUPPLEMENTARY MATERIALS

Figs. S1 to S11
 Table S1

The list of author affiliations is available in the full article online.

*Corresponding author. E-mail: harry@nuvolari.ucsc.edu

Crystal Structures of EF-G–Ribosome Complexes Trapped in Intermediate States of Translocation

Jie Zhou, Laura Lancaster, John Paul Donohue, Harry F. Noller*

Translocation of messenger and transfer RNA (mRNA and tRNA) through the ribosome is a crucial step in protein synthesis, whose mechanism is not yet understood. The crystal structures of three *Thermus* ribosome–tRNA–mRNA–EF-G complexes trapped with β,γ -imidoguanosine 5'-triphosphate (GDPNP) or fusidic acid reveal conformational changes occurring during intermediate states of translocation, including large-scale rotation of the 30S subunit head and body. In all complexes, the tRNA acceptor ends occupy the 50S subunit E site, while their anticodon stem loops move with the head of the 30S subunit to positions between the P and E sites, forming chimeric intermediate states. Two universally conserved bases of 16S ribosomal RNA that intercalate between bases of the mRNA may act as "pawls" of a translocational ratchet. These findings provide new insights into the molecular mechanism of ribosomal translocation.

One of the most critical and complex steps of protein synthesis is the coupled translocation of mRNA and tRNAs through the ribosome, catalyzed by the guanosine triphosphatase (GTPase) elongation factor EF-G. Although several of the main steps have been identified, the underlying molecular mechanisms of translocation are poorly understood. Immediately after peptide bond formation, the A (aminoacyl-tRNA) site is occupied by the newly extended peptidyl-tRNA and the P (peptidyl-tRNA) site by a deacylated tRNA. In the first step of translocation, the acceptor end of the deacylated tRNA moves into the 50S subunit E (exit) site, forming the P/E hybrid state, and the acceptor end of the peptidyl-tRNA moves into the 50S P site, forming the A/P hybrid state (1, 2). The formation of hybrid states can occur spontaneously and reversibly in vitro (1, 3, 4) and is correlated with intersubunit rotational movement (4–6). Although this step can proceed in the absence of EF-G or guanosine triphosphate (GTP), the observation that EF-G favors the formation of hybrid states (5) suggests that it is catalyzed by EF-G in vivo. Translocation is completed when the anticodon stem loops (ASLs) of the tRNAs move from the 30S A and P sites to the P and E sites, respectively, coupled to movement of their associated mRNA codons. The latter step is rate-limiting (7) and is strongly dependent on EF-G. There is increasing evidence that it is coupled to a rotational movement of the head of the small subunit (8–11).

Although several cryoelectron microscopy (cryo-EM) reconstructions of EF-G–ribosome complexes have been determined (8, 12–14), until now only a single crystal structure has been

reported, for a posttranslocation complex in which EF-G was trapped on the ribosome with fusidic acid in the nonrotated state (15). Here, we describe crystal structures for three ribosome complexes containing EF-G, mRNA, and tRNA trapped in intermediate states in which the 30S subunit head undergoes large-scale (15° to 18°) intrasubunit rotations and the 30S body undergoes smaller (3° to 5°) intersubunit rotations. Our findings provide insights into the molecular mechanisms of EF-G–catalyzed translocation.

Results

EF-G–Dependent Structural Changes in the Ribosome

Ribosomes from *Thermus thermophilus* were co-crystallized with the 27-nucleotide mv27 mRNA, elongator tRNA^{Met}, and EF-G in the presence of GTP and the antibiotic fusidic acid, which allows GTP hydrolysis but prevents release of EF-G (16), or with EF-G and β,γ -imidoguanosine 5'-triphosphate (GDPNP), a nonhydrolyzable analog of GTP. Crystals of the fusidic acid complex (Fus) diffracted to 3.6 Å; those of the two other complexes, GDPNP-I and GDPNP-II, which crystallized under slightly different conditions, diffracted to 3.5 Å and 4.1 Å, respectively (table S1). The most notable structural change is a large-scale counterclockwise rotation of the 30S head domain by 15° (Fus and GDPNP-I) or 18° (GDPNP-II) relative to the classical-state ribosome (17), around an axis roughly parallel to the long axis of the subunit (Fig. 1, C to E). This is accompanied by smaller 3° (Fus and GDPNP-I) or 5° (GDPNP-II) counterclockwise rotations of the 30S body relative to the 50S subunit. These rotational movements resemble those observed for an EF-G–ribosome cryo-EM reconstruction (8) and for an RF3-ribosome crystal structure (18). Additional large-scale changes include a 14 Å inward movement

of the 50S subunit L1 stalk to contact the elbow of the tRNA (fig. S1) and a 12 Å inward movement of the L11 stalk to avoid clash with its contact site on domain V of EF-G. Rotation of the 30S head results in 25 to 30 Å displacements of the contacts forming intersubunit bridge B1a between 30S protein S13 and the A-site finger (helix H38 of 23S rRNA), resulting in the formation of a new bridge with protein S19 and an 11 Å upward movement of H38 in the Fus and GDPNP-I complexes; in the GDPNP-II complex, this increases to 14 Å because of greater rotation of the 30S head.

Trapping of tRNA in the Chimeric pe*/E Intermediate State of Translocation

Binding of EF-G to the ribosome with either GTP and fusidic acid or as a GDPNP complex, under the conditions of complex formation and crystallization, results in movement of the tRNA from its initial binding state in the classical P site (P/P state) into new binding states. During rotation of the head of the 30S subunit, the P-site contacts between the ASL and the head (19, 20) are maintained, while those between the ASL and the 30S body and platform are disrupted. In the classical-state ribosome, a 14 Å constriction between nucleotides 790 in the platform and 1340 in the head blocks movement of the ASL between the 30S P and E sites (21). Rotation of the 30S head widens this gap to 22 Å in the Fus and GDPNP-I complexes and to 24 Å in GDPNP-II, allowing sufficient room for the ASL to move between the P and E sites (Fig. 2). The ASL precisely follows the rotational movement of the 30S subunit head, placing it midway between the positions of the classical P and E sites (Fig. 2). The positions of the ASLs in the Fus and GDPNP-I complexes superimpose closely, whereas the ASL in GDPNP-II is displaced further toward the E site. Interactions between tRNA and the 50S subunit are similar to the E-site interactions observed for tRNA bound in the classical E/E and hybrid P/E states (fig. S1) (19, 20). Because the ASL is simultaneously bound to P-site elements of the 30S head and to features that lie between the P and E sites of the 30S body and platform, we refer to this new state as a chimeric pe*/E hybrid state. Repositioning of the tRNA is promoted not only by structural changes in the ribosome but also by conformational changes in the tRNA itself. We imagine that the pe*/E state represents an intermediate between the P/E and E/E states.

Aligning the structures of tRNAs bound in these three states on their ASLs (Fig. 3) shows that the body of the E/E tRNA bends downward and sideways toward the P site, relative to the P/E tRNA (Fig. 3, A and D). The pe*/E tRNA closely matches the downward bend of the E/E tRNA (Fig. 3, C and F), but with a sideways bend half the magnitude of that of the E/E tRNA, consistent with its intermediate state of translocation. The main position of flexing of the tRNAs is localized to the junction between their D and anticodon stems at the noncanonical 26-44 base pair, as has

Center for Molecular Biology of RNA and Department of Molecular, Cell and Developmental Biology, University of California, Santa Cruz, CA 95064, USA.

*Corresponding author. E-mail: harry@nuvolari.ucsc.edu

been seen for kinking of the A/T-state tRNA in the EF-Tu ternary complex during tRNA selection (22, 23). These findings provide further evidence that tRNA does not transit the ribosome as a rigid body during protein synthesis, but rather exhibits considerable flexibility.

mRNA Interactions

Well-resolved electron density allowed fitting of 23 of the 27 nucleotides of the mv27 mRNA in

the GDPNP-I and Fus complexes (Fig. 4 and figs. S2 and S3). The path of the mRNA and its contacts with the 30S body and platform (which serve as static reference points for mRNA movement) in the Fus complex (fig. S11) can be compared with those of a mRNA from a previously determined structure of a complex containing tRNAs bound in classical states (Fig. 4) (17). In the classical-state complex, protein S11 contacts the mRNA upstream from the E site at positions –6 and –7

(where position +1 is defined as the 5' nucleotide of the P-site codon in the initially formed complex); in the EF-G–Fus complex, the corresponding contacts are made with positions –3 and –4, respectively, indicating a displacement of the mRNA by three nucleotides, or one codon. Using another landmark, 16S nucleotide U1498 packs against riboses +1 and +2 of the mRNA in the classical complex; in the Fus and GDPNP-I complexes, U1498 packs against ribose +4 and

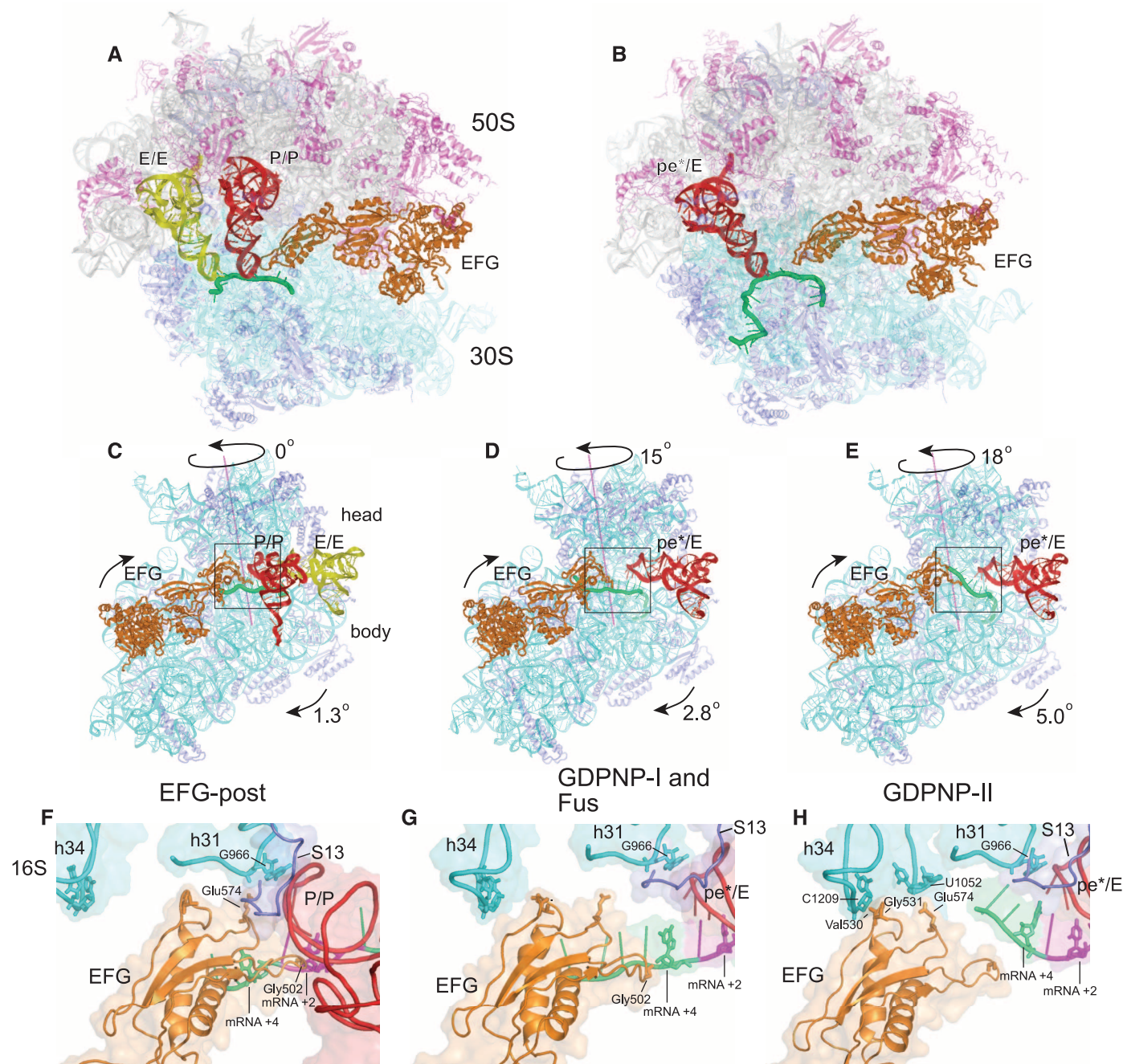


Fig. 1. Structures of trapped 70S ribosome-EF-G complexes. (A and B) Overall views of (A) the nonrotated 70S-EF-G-post complex (15) and (B) the Fus 70S-EF-G complex with tRNA bound in the pe*/E state. (C to E) Interface views showing 30S subunit body and head rotation in (C) the EF-G-post state (15), (D) the GDPNP-I and Fus complex, and (E) the GDPNP-II complex. (F to H) Close-up views of EF-G domain IV interactions with the 30S subunit head in (F) the EF-G-post complex (15), (G) the GDPNP-I and Fus complex, and (H) the GDPNP-II complex. Cyan, 16S rRNA; blue, 30S proteins; gray, 23S rRNA; magenta, 50S proteins; green, mRNA; red, P/P or pe*/E tRNA; yellow, E/E tRNA; orange, EF-G.

phosphate +5, corresponding again to translocation of nearly three nucleotides, or one codon. However, calibration against G926 gives a smaller displacement; in the classical complex, G926 forms hydrogen bonds with phosphate +1, whereas in the EF-G-Fus complex, it interacts with phosphate +3. This net displacement of the mRNA by about two nucleotides in the EF-G-Fus complex extends through the downstream region to position +11, while upstream of the P site, the mRNA translocates by about three nucleotides, or one full codon. This difference may be due to flexibility in the downstream part of the mRNA chain caused by the sparse downstream contacts resulting from

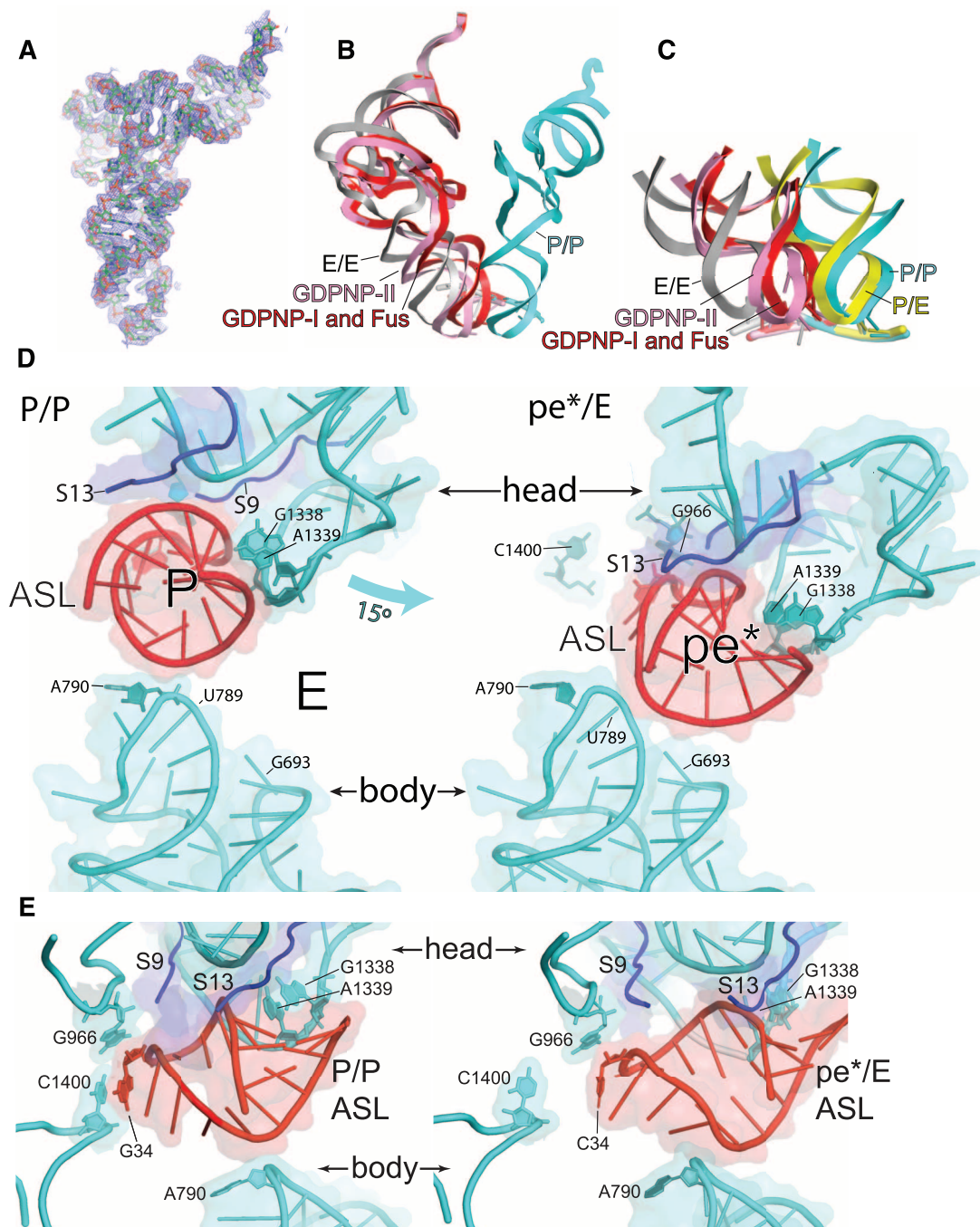
a vacant A site. Codon-anticodon base pairing is disrupted in the Fus and GDPNP-I complexes; however, pairing with the first two codon bases is retained in the GDPNP-II complex (fig. S4).

An important question concerning the mechanics of translocation is how the translational reading frame is maintained. Slippage of the reading frame will occur if the movements of mRNA and tRNAs are not precisely synchronized, resulting in translation of a stream of incorrect codons and, most likely, an out-of-frame termination codon that risks creating a dominant, toxic product. Of potential relevance to this question is the intercalation of two bases from 16S rRNA be-

tween bases at two positions of the mRNA (Fig. 4 and fig. S5). In the Fus and GDPNP-I complexes, C1397 stacks on A+10 (Fig. 4), partially intercalating between bases +9 and +10; it is not clear whether this interaction occurs in the GDPNP-II complex because of disorder in this region of its mRNA. Intercalation of C1397 was also observed in a termination complex formed with release factor RF2 (24). Previously unreported is the intercalation of A1503 between positions -1 and -2 (Fig. 4), which is observed in all three complexes. These interactions would block mRNA movement in either the forward or reverse direction. We propose that they act as "pawls" of a translocational

Fig. 2. Movement of tRNA from the P/P to the pe*/E state.

(A) Electron density map ($2F_{\text{obs}} - F_{\text{calc}}$) contoured at 1.5σ for pe*/E tRNA from the Fus complex. (B) Superimposition of tRNA positions for the P/P (blue), E/E (gray), and pe*/E states from the Fus (red) and GDPNP-II (pink) complexes, aligned on the 23S rRNAs from each complex. The pe*/E tRNAs move from the P site to positions midway between the P and E sites. (C) Positions of the ASLs of tRNA in the Fus (red) and GDPNP-II (pink) pe*/E states compared with those of the classical P/P (blue) and E/E (gray) (17) and hybrid-state P/E (yellow) (6) tRNAs, aligned on the 30S subunit body. (D) Interactions of (left) a P/P classical-state ASL (17) and (right) the pe*/E ASL from the 70S-EF-G Fus complex with the 30S subunit. The 15° rotation of the 30S subunit head in the EF-G opens the constriction blocking passage of the tRNA from the P site to the E site from 14 Å to 22 Å, allowing translocation. (E) Side views of the complexes shown in (D). Rotation of the head moves the tRNA ASL away from its contacts with C1400 and A790 in the body and platform as it translocates into the pe*/E state.



ratchet to prevent reversal of the movement of the mRNA chain during translocation. In the classical-state complex (17), where both the extended structure of the mRNA and bases 1397 and 1503 are well resolved, both bases are retracted from their intercalated conformations, a state that would permit mRNA movement; in the state observed for our EF-G-containing complexes, their intercalation would lock the register of the mRNA, preventing slippage of the translational reading frame. At some point prior to the next round of translocation, the bases would need to retract from their intercalated state to allow mRNA movement. The universal conservation of bases 1397 and 1503, from bacteria to archaea to eukarya, is consistent with such a critical role. Both bases project from the tips of conserved, compact, tertiary hairpin-like structures that seem optimized to facilitate intercalation (Fig. 4, C and D). Moreover, the two hairpins are connected by a conserved, tertiary Watson-Crick base pair between C1399 and G1504, which suggests that their movements could be coordinated during translocation.

Structuring of Switch Loop I of EF-G

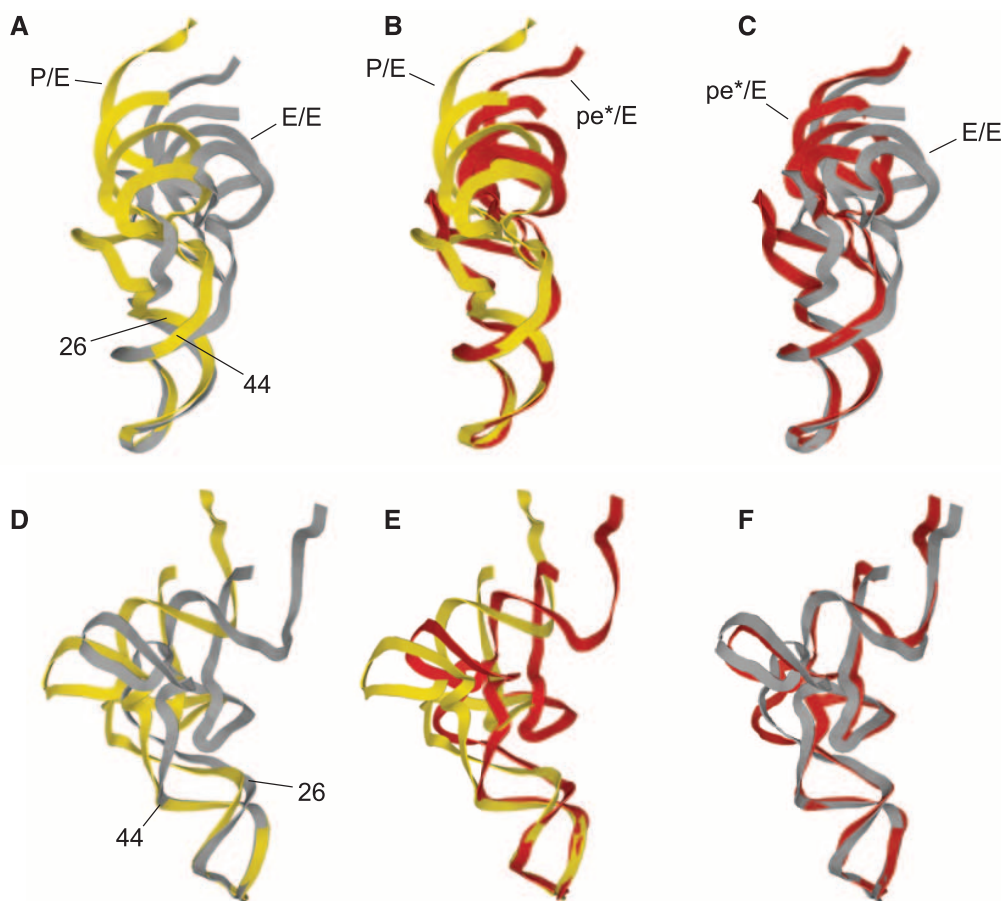
EF-G is bound in the subunit interface of the ribosome, where its domain I binds to the sarcin-ricin loop (SRL) (fig. S8) and protein L6 of the 50S subunit, domains II and III bind to 16S rRNA helices h5 and h15 and protein S12 in the 30S

subunit, domain IV binds to the mRNA and helix h34 in the 30S subunit, and domain V binds to the L11 stalk of the 50S subunit (Fig. 5, A and B). In all previous structures of EF-G, the switch loop I region (25) was disordered. This functionally important feature of EF-G (residues 40 to 67 in *T. thermophilus* EF-G) is now well resolved in the GDPNP-I complex, revealing its contacts with other regions of EF-G, with the ribosome, and with GDPNP (Fig. 6). Structuring of the conserved core of switch loop I (positions 59 to 67 in *T. thermophilus* EF-G) completes the cage that encloses GDPNP and fixes its position with a network of hydrogen-bonded and van der Waals interactions (Fig. 6B). Arg⁶¹ in switch loop I interacts with the phosphate of G2663 in the SRL, while Thr⁶⁴ contacts the β - and γ -phosphates of GDPNP via a coordinated magnesium ion. The NKXD motif (residues 137 to 140) interacts with the guanosine end, and the phosphate-binding loop (residues 20 to 27) wraps around the triphosphate end of the nucleotide cofactor (Fig. 6B). The position of the conserved His⁸⁷ in switch loop II does not allow it to act as a general base, as in a previously proposed universal mechanism for the GTPase reaction (26) (fig. S9). Structuring of switch loop I appears to fix the relative geometry of domains I, III, and V through contacts with domain III. Comparison with the crystal structure of EF-G-GDP in its free form (27), whose

switch loop I is unstructured, shows rearrangement of domains III and V relative to domain I (Fig. 6, E and F). In the GDP form, contacts between domain III and the 30S subunit, and between domain V and the L11 stalk, are disrupted, likely causing release of EF-G from the ribosome. The position of fusidic acid in the Fus complex overlaps that of residues 63 to 66 in the conserved core of switch loop I, mimicking the stabilizing contacts between domains I and III made by the structured switch loop (Fig. 6, C and D). This finding explains how fusidic acid stabilizes a conformation virtually identical to that of the GDPNP-I complex, allowing EF-G to bind stably to the ribosome in the presence of GDP.

Comparison of the folds of the crystal structures of the four different translational G proteins in which switch loop I is ordered shows that although the conserved core of switch loop I (residues 59 to 67) is positioned similarly in all four cases, the N-terminal folds of the switch loop (residues 40 to 58) diverge into two classes (fig. S10). In one class, which includes EF-G and EF-Tu (26), the N-terminal region of the loop continues in the direction of the $\alpha 1$ helix, then loops back toward the β -phosphate of GDPNP, where it joins the conserved core. The other class comprises EF-G-2 (28) and RF3 (18), in which the loop runs parallel to the $\alpha 1$ helix and then forms a complex fold that packs against GDPNP

Fig. 3. Flexing of tRNA during translocation. (A and D) Comparison of the conformations of tRNA in the hybrid P/E and classical E/E states, aligned on their respective ASLs. (B and E) Comparison of the conformations of tRNA in the chimeric pe*/E and P/E states, aligned on their respective ASLs. (C and F) Comparison of the conformations of tRNA in the pe*/E and E/E states, aligned on their respective ASLs. The main site of flexing is localized to the noncanonical base pair at positions 26 to 42, between the D and anticodon stems. The P/E and E/E structures are from (6, 15).



before joining the conserved core. The crystal structure of free EF-G-2-GTP was fitted to the electron density for EF-G from a cryo-EM reconstruction of an EF-G-ribosome complex (28). However, the resulting interdomain geometry for EF-G-2 differs from that of the EF-G structures, particularly for domain III, which is shifted by as much as 9 Å relative to that seen in GDPNP-I. Details of the interactions between the C-terminal domain (CTD) of protein L12 and the G' domain of EF-G, which are believed to be important for recruiting EF-G to the ribosome and for stimulating GTP hydrolysis (29, 30), can be visualized in both the Fus and GDPNP-I complexes (Fig. 5, A and B, and fig. S6). These involve residues Ala⁶⁷, Lys⁷¹, Thr⁸², Lys⁸⁷, and Lys⁹⁰ of the CTD with Lys²¹⁵, Glu²¹⁸, Asp²²², Tyr²³¹, and Val²³² of the G' domain, the majority of which are universally conserved.

Interdomain Movement in EF-G

Comparison of the different structures of EF-G in its ribosome-bound state shows that the largest conformational changes occur in domains III and IV, between the EF-G-post complex (15) and the Fus and GDPNP-I complexes. Domain IV moves

upward toward the head of the 30S subunit by ~6 Å and domain III by ~3 Å (Fig. 1G, Fig. 5C, and fig. S7). At the tip of domain IV, the loop containing the conserved Gly⁵⁰² moves by ~5 Å between the post and GDPNP-I and Fus structures, as its contact with the mRNA backbone switches from position +2 to +4 (Fig. 1, F and G). Although the largest displacement of domain IV in the ribosome is seen in the GDPNP-II complex, this is mainly a result of the overall rotational movement of EF-G relative to the ribosome, rather than internal movement of the EF-G molecule. In the GDPNP-II complex, 23S rRNA features that contact EF-G (including the SRL, the L11 stalk, and H89) move by 2 to 4 Å in concert with movement of EF-G, which follows the increased intersubunit rotation of the 30S subunit; on the 30S side, this results in shifting of contacts between domain III of EF-G and protein S12. Rotation of the 30S subunit head and body in the GDPNP-II complex brings the tip of domain IV into contact with helix 34 of 16S rRNA in the GDPNP-II complex, as observed previously by cryo-EM (8), where the backbone oxygens of Val⁵³⁰ and the universally conserved Gly⁵³¹ form hydrogen bonds with ribose 1209 of 16S rRNA,

and the side chain of Glu⁵⁷⁴ forms hydrogen bonds with ribose 1052 (Fig. 1H). This interaction appears to participate in fixing the position of the head of the 30S subunit in the rotational state observed for the GDPNP-II complex. Finally, the side chains of Glu⁵⁷⁹, Ser⁵⁷⁸, and Arg⁵⁰⁴ form hydrogen bonds with nucleotides 1492, 1493, and 1494, respectively.

Discussion

In the absence of continuous rotary motion (31) (which is unlikely for an asymmetric structure such as the ribosome), translocation of mRNA and tRNA through the ribosome must be based on some kind of ratchet mechanism, as was realized many decades ago (32). Intersubunit rotational movement, which is coupled to the formation of hybrid states, has been termed “ratcheting” (4, 6, 12, 33–35); however, ribosomes containing bound tRNAs have been observed to undergo spontaneous, reversible, back-and-forth intersubunit rotation in the absence of EF-G or GTP (3), unlike the behavior of a true ratchet. Moreover, the step of translocation that is critically dependent on catalysis by EF-G is the movement of mRNA, coupled to that of the tRNA ASLs, on

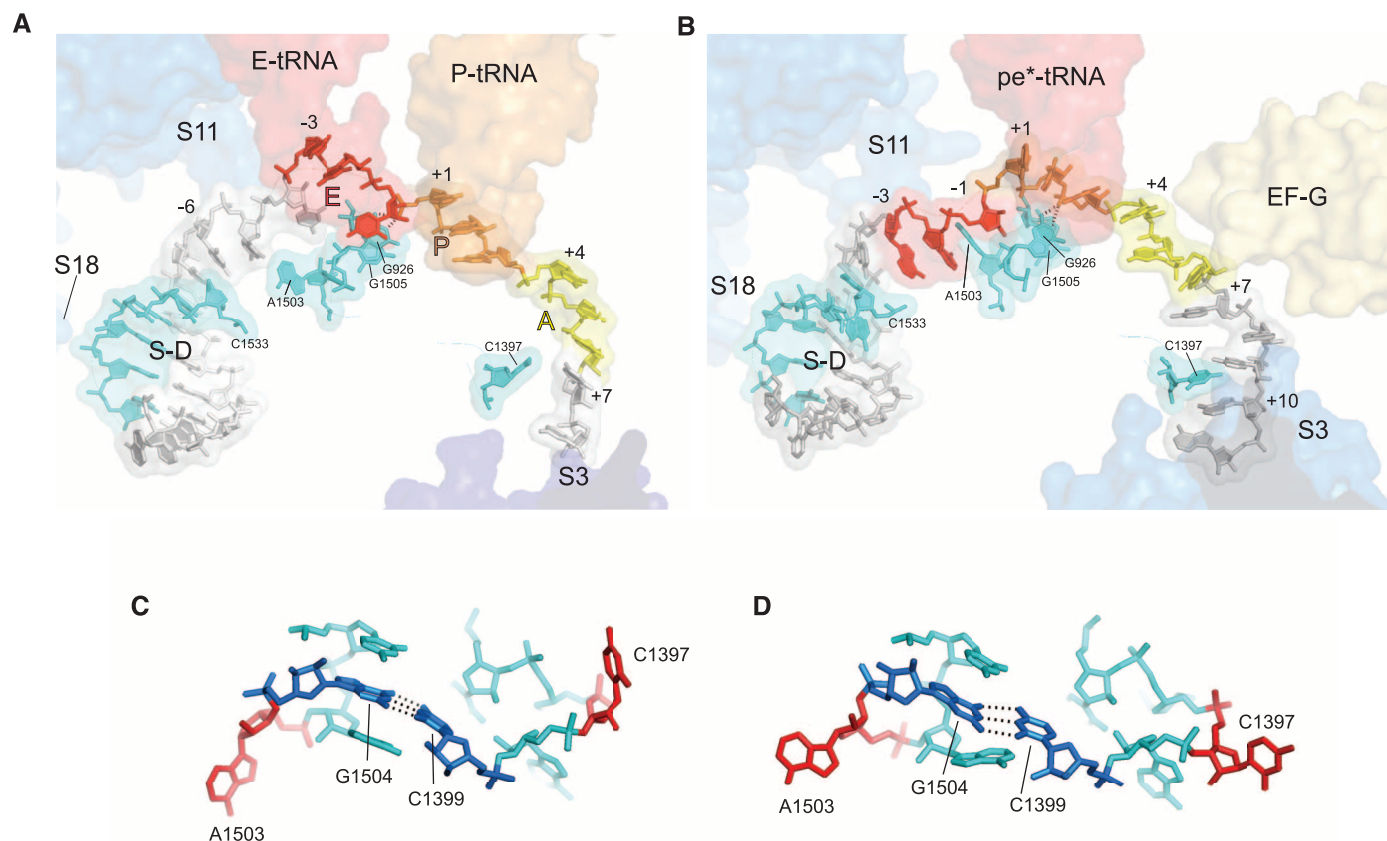


Fig. 4. Interactions of mRNA with the 30S subunit. (A) mRNA bound to a classical-state 70S ribosome (17). (B) mRNA bound to the Fus complex with EF-G and pe*/E tRNA. The positions of proteins S3, S11, and S18 are shown as blue transparent molecular surfaces. Also shown are the positions of EF-G; the anticodon stem loops of EF-G, P-tRNA, E-tRNA, and pe*/E tRNA; and the Shine-Dalgarno helix (S/D). Elements of 16S rRNA are shown in cyan. The A-, P-, and E-site codons for the mRNAs during complex formation are shown in yellow,

orange, and red, respectively. The mRNAs are numbered with +1 corresponding to the 5' nucleotide of the P-site codon. (C and D) The conformations of the tertiary hairpin-like structures containing the intercalating bases C1397 and A1503 (shown in red) in (C) the classical-state ribosome and (D) the 70S-EF-G Fus complex. The structures of these features in the GDPNP-I and GDPNP-II complexes are similar to those of the Fus complex. The universally conserved C1399-G1504 base pair is shown in dark blue.

the 30S subunit (1, 7). In a cryo-EM reconstruction of fusidic acid-trapped EF-G complexes, Spahn and co-workers resolved a previously unobserved subpopulation of particles in which rotation of the 30S subunit head was accompanied by movement of the ASL of a P-site tRNA into a novel intermediate state (8). Because the tRNA maintained contact with the P site on the 30S head and simultaneously established interaction with the E site on the 30S platform, they termed this the “pe/E” hybrid state. In our crystal structures, head rotation in the three different trapped EF-G complexes results in movement of the ASLs to positions midway between the 30S P and E sites (Fig. 2); accordingly, we term these states chimeric pe*/E hybrid states. Close comparison with the cryo-EM structure (8) shows that the ASL in their pe/E state is positioned 5 Å farther toward the E site from the pe*/E ASL in the GDPNP-I and Fus structures, and 2.7 Å farther in the GDPNP-II structure. The pe/E and pe*/E states appear to represent intermediate states between the hybrid P/E and classical E/E states, near the completion of the EF-G-catalyzed translocation of a P-site tRNA. The larger body rotations observed for some ribosome complexes (6, 18, 36), together with the large head rotation observed in the GDPNP-II complex, may be sufficient to complete the movement of tRNA fully into the eventual E/E state, as predicted from the rotational values observed for a ribosome-RF3 complex (18). Finally, our structures suggest that C1397 and A1503 act as molecular pawls to fix the po-

sition of the mRNA ratchet; we do not know whether there are separate pawls to prevent backslippage of tRNA during reverse rotation of the 30S head, or indeed, whether the movements of mRNA and tRNA are coupled simply through their codon-anticodon interactions, or instead are translocated by separate structural features of the translation apparatus, albeit in a coordinated fashion.

Methods

Construction of *Thermus thermophilus* Strain HB27_L9d

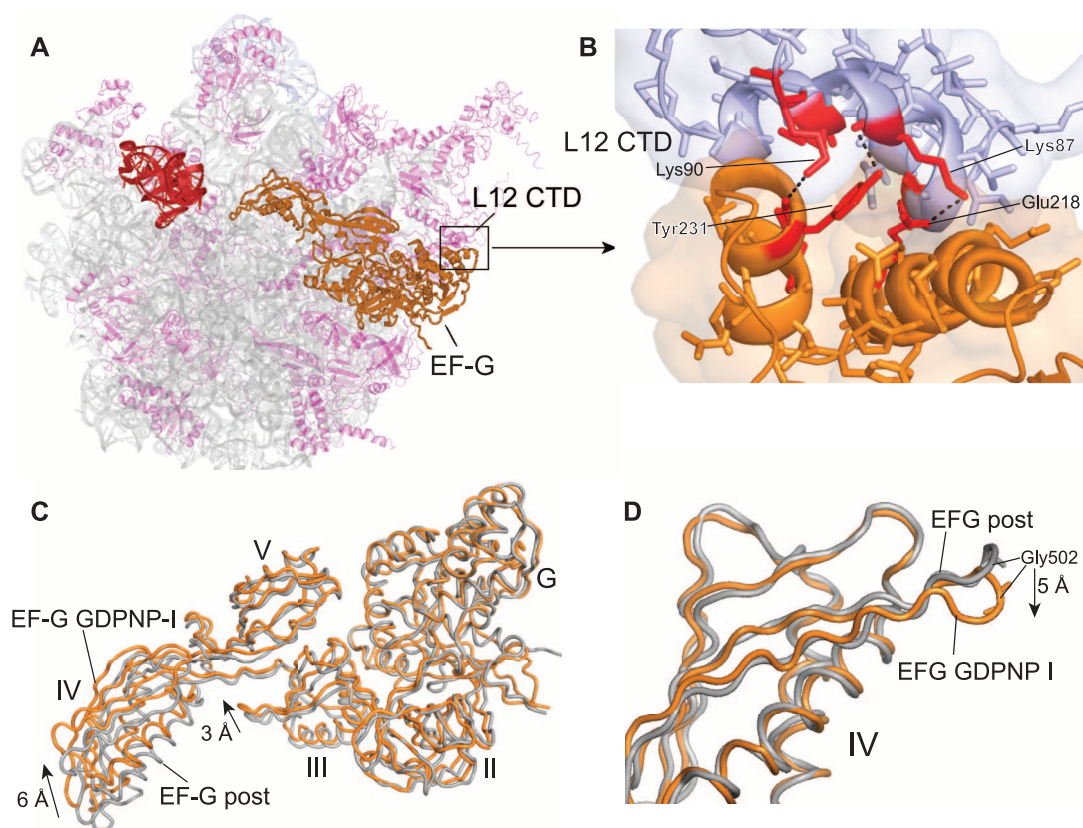
The L9 protein-coding region plus an additional 1000 nucleotides upstream and 2200 nucleotides downstream was amplified by polymerase chain reaction (PCR) from *Thermus thermophilus* HB27 genomic DNA with primers 5'TTGAATTCTAGACGCCATT-TGGACCTGACCCTCGCCGGTCAGG and 5'TTTCCATTTAAGCTTGGCTTCGCAACATGGGAGACCCTGGCTAGCCC, which add Xba I and Hind III sites to facilitate cloning. Site-directed mutagenesis (37) with oligo 5'GGAGGGGCGCTAAGGGGTTTGCCCTGCAGCGTTCACCCCTACTTCCGCACC was used to delete the entire L9 protein-coding region and replace it with a Pst I restriction site, generating plasmid pL9d. The KAT cassette (coding for thermostable kanamycin adenyl transferase downstream of a *T. thermophilus* promoter) was cut from plasmid pKT1 (38) and ligated into the Pst I site of pL9d to generate plasmid

pL9d_KAT. For unknown reasons, pL9d_KAT made *E. coli* (DH5alpha) cells very sick, and plasmid prepped from the transformed *E. coli* strain contained a mixture of pL9d and pL9d_KAT. HB27 cells were transformed with pL9d/pL9d_KAT as described (38), plated on ATCC 697 medium plus kanamycin (20 µg/ml), and grown at 70°C for 24 hours. Kanamycin-resistant colonies were screened for deletion of L9 by PCR, using primers that flank the L9-coding region. Surprisingly, we did not detect colonies that contain the KAT protein-coding sequence inserted into the genome at the L9 position, but instead obtained “clean deletions” of L9 in which the genomic copy of L9 was replaced with a Pst I restriction site. The resulting HB27 L9 deletion strain was only transiently kanamycin-resistant, and we suspect it arose from double transformation with pL9d and pL9d_KAT.

Purification of *Thermus thermophilus* EF-G

Thermus thermophilus EF-G, cloned into pET24b (Novagen), was expressed in *E. coli* strain BLR (DE3) by induction with IPTG (1 mM final concentration). Cells were lysed in 25 mM Tris-Cl (pH 7.5), 60 mM NH₄Cl, 10 mM MgCl₂, and 5 mM βME, and ribosomes were removed (pelleted) by centrifugation in a Ti70 (Beckman) rotor at 55,000 rpm for 2 hours at 4°C. The supernatant was heated at 65°C for 20 min to denature *E. coli* proteins, which were removed (pelleted) by centrifugation in a JA20 rotor at 30,000g for 20 min at 4°C. EF-G was purified by FPLC chromatography using a 6-ml Resource-Q

Fig. 5. EF-G interactions and dynamics. (A) Overall view of the position of EF-G on the 50S subunit. (B) Detailed view of the contact surface between the G' domain of EF-G and the C-terminal domain (CTD) of one of the four copies of protein L12. The L12 CTD is shown in magenta in (A) and blue in (B). Gray, 23S rRNA; magenta, 50S proteins; orange, EF-G. (C) Superimposition of EF-G from the fusidic acid post complex (gray) (15) with EF-G from the GDPNP-I complex (orange) by alignment on their domains I shows rearrangements in the orientation of domains III and IV. (D) Alignment of the same two EF-G structures in (C) on their respective domains IV shows local rearrangement of the loop containing the conserved Gly⁵⁰² and Gly⁵⁰³ residues (see Fig. 1, F to H).



anion exchange column (Pharmacia) and eluted with a 200-ml salt gradient from 60 to 300 mM KCl in buffer A [25 mM Tris-Cl (pH 7.5), 60 mM NH₄Cl, and 5 mM β ME]. EF-G-containing fractions were concentrated to less than 0.4 ml with an Amicon Ultra 15 concentrator (Millipore; 10,000 molecular weight cutoff), before additional purification on a 24-ml Superdex 75 gel filtration column (Pharmacia) preequilibrated in buffer A. Aliquots were flash-frozen in liquid nitrogen and stored at -80°C .

Ribosome Preparation

Ribosomes were prepared from *T. thermophilus* strain HB27_L9d. Cells were resuspended in buf-

fer B [25 mM Tris-Cl (pH 7.5), 100 mM NH₄Cl, 52.5 mM MgCl₂, 2.5 mM EDTA, and 5 mM β ME], lysed, and pelleted through cushions containing 1.1 M sucrose and buffer B supplemented with NH₄Cl to 1 M. Ribosomes were purified over a Toyopearl Butyl-650S column and eluted with a gradient of 0.7 M to 0.2 M ammonium sulfate. To remove endogenous tRNA, ribosomes were dissociated into subunits by dialysis against buffer C [55 mM Tris-Cl (pH 7.5), 100 mM NH₄Cl, 1 mM MgCl₂, and 5 mM β ME], then pelleted through cushions containing 25% sucrose in buffer C. The pellets were resuspended in buffer D [20 mM KHepes (pH 7.5), 100 mM NH₄Cl, 10 mM MgCl₂, 1 mM spermine, and 5

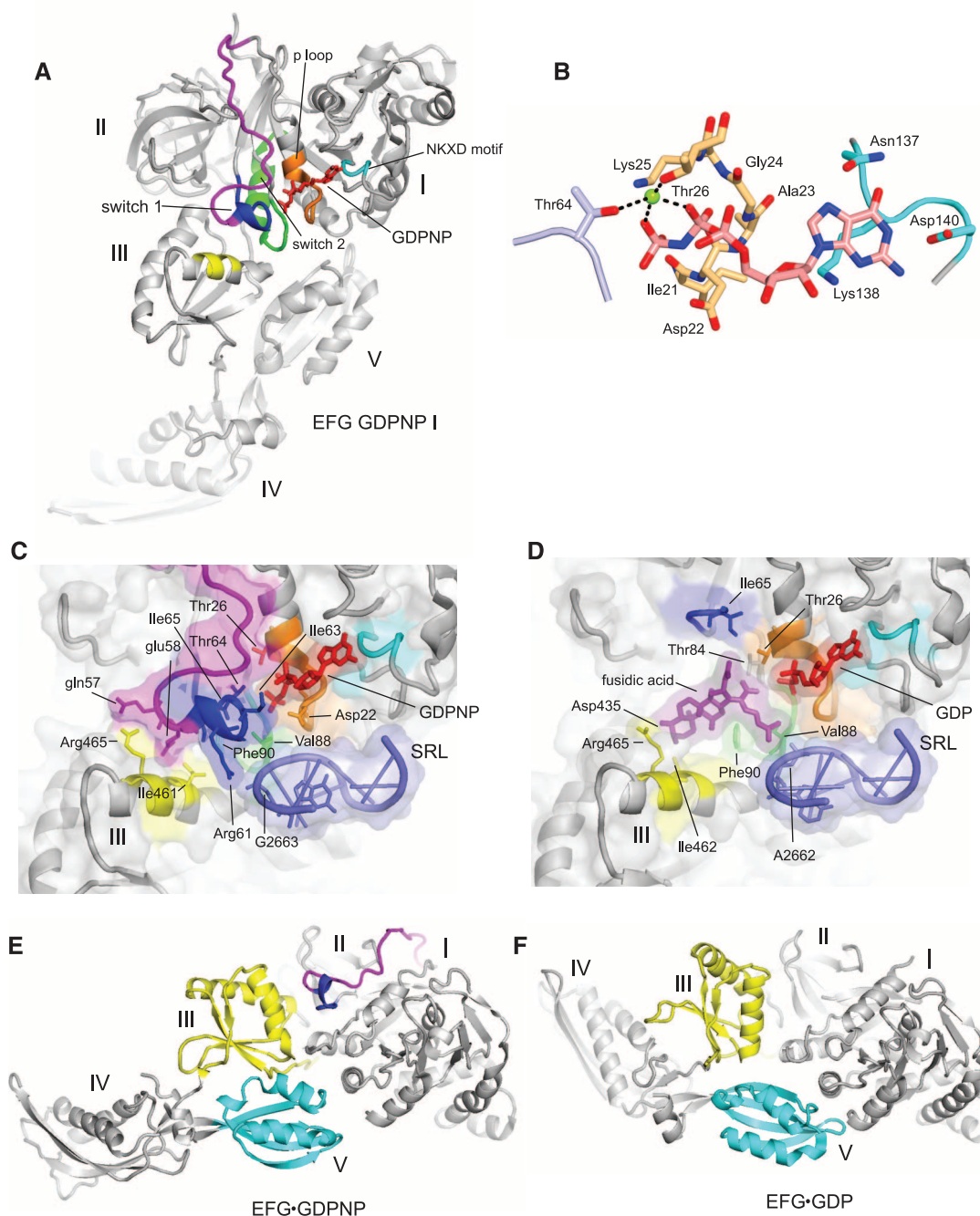
mM β ME] and ribosomes were reassociated by heating at 65°C for 5 min before loading onto gradients containing 10 to 35% sucrose in buffer D. The 70S ribosome peak was collected and the ribosomes were pelleted, resuspended in buffer D, flash-frozen in liquid nitrogen, and stored at -80°C .

Complex Formation

Ribosomes (400 pmol), tRNA-Met (MP Biomedicals; 800 pmol), and mRNA mv27 (GGCAAG-GAGGUAAAAAUGGUAAAAA; IDT) (1000 pmol) were incubated at 37°C for 30 min in 10 mM KHepes (pH 7.5), 100 mM NH₄Cl, 5 mM MgCl₂, and 1 mM spermine. EF-G (3000 pmol) preincubated for 30 min at 37°C with either GTP

Fig. 6. Structuring of switch loop I.

(A) EF-G GDPNP-I showing the path of switch loop I (residues 40 to 67), which was disordered in all previous EF-G structures. The conserved core (residues 59 to 67) is shown in blue and the rest of switch loop I (residues 40 to 58) in magenta. (B) Structure of the GDPNP binding pocket, showing interactions with switch loop I (light blue), the guanine recognition motif (cyan), and P loop (orange). A magnesium ion coordinating the β and γ phosphates of GDPNP is shown as a green sphere. (C) The switch I region in the GDPNP-I complex. (D) The fusidic acid binding site in the Fus complex, in the same view as for (C). These views show the conserved core of switch loop I (blue) and the rest of switch loop I (magenta), guanine recognition motif (cyan), phosphate binding loop (orange), and switch loop 2 (green) and domain III contacts (yellow); the components are shown with transparent molecular surface representations. (E) EF-G from the GDPNP-I structure containing a structured switch loop I (blue, magenta). (F) The structure of free EF-G-GDP containing a disordered switch loop I (27) showing movement of domains III (yellow), IV, and V (cyan).



plus fusidic acid, or GDPNP, in 10 mM KHepes (pH 7.5) and 100 mM NH_4Cl was added to the ribosome-tRNA complex and incubated at 37°C for 15 min. The final conditions were 10 mM KHepes (pH 7.5), 100 mM NH_4Cl , 1 to 1.5 mM MgCl_2 (GDPNP-I and Fus complexes) or 0.5 mM MgCl_2 (GDPNP-II complex), 0.5 to 0.8 mM spermine, 2 mM dithiothreitol, 0.25 mM fusidic acid, and 0.5 mM GTP, or 1 mM GDPNP in a total volume of 100 μl . In complexes containing viomycin, it was added to a final concentration of 0.5 to 1 mM. Deoxy Big Chap (Hampton) was added to 0.5 mM just before crystallization.

Crystallization

Both the EF-G-GDPNP-ribosome-mRNA-tRNA and EF-G-GDP-fusidic acid-ribosome-mRNA-tRNA complexes were grown via vapor diffusion in 96-well plates by adding 1 to 2 μl of reservoir solution [100 mM Tris (pH 7.0), 200 mM KSCN, 2.9% PEG20K, 2.8% PPG P400, 5.1% PEG550MME) to 1 to 2 μl of sample. Viomycin-containing complexes were crystallized under the same conditions. After 10 days at 22°C, crystals grew to dimensions of up to 1000 $\mu\text{m} \times 600 \mu\text{m} \times 60 \mu\text{m}$. After slowly adding PEG 400 to a final concentration of 25% (v/v) for the GDPNP-I and Fus complexes or 20% for the GDPNP-II complex, the crystals were harvested and flash-frozen in liquid nitrogen.

Crystal Screening and Data Collection

Crystals were screened at beamline 12-2 at the Stanford Synchrotron Radiation Laboratory (SSRL) and at beamline 12-3-1 at the Advanced Light Source (ALS), Lawrence Berkeley National Laboratory. Data were collected at beamline 12-3-1 at the ALS and at beamline 23ID-D at the Advanced Photon Source at Argonne National Laboratory using 0.3° oscillations. Diffraction data were indexed and integrated in XDS (39) and scaled in SCALA (40).

Molecular Replacement, Model Building, and Structure Refinement

The 50S and 30S models from previously published structures (24) were used as initial search models for molecular replacement using the program Phaser (41). Two 70S ribosomes were found per asymmetric unit in space group C_2 . Clear density was visible in unbiased $F_{\text{obs}} - F_{\text{calc}}$ difference electron density maps for EF-G, mRNA, and tRNA in all of the above complexes. Four-rigid-body refinements were performed initially in Phenix (42), and the refined models were subjected to 600-rigid-body refinement and TLS group, B group, and B individual minimization refinements in Phenix and in CNS (43).

Models for tRNA, mRNA, EF-G (domain IV and switch loop), GDPNP, GDP, and fusidic acid were initially built manually in O (44) or Coot (45) against simulated-annealing $F_{\text{obs}} - F_{\text{calc}}$ omit maps calculated in Phenix. The C-terminal domain of L12 was built manually on the basis of a previous poly(Ala) model (15).

Inclusion of viomycin improved the resolution of EF-G complex crystals, as found previously for crystals of RF3-ribosome complexes (18). The sole structural differences detected between viomycin-containing or viomycin-free structures are that 16S rRNA bases A1492 and A1493 and 23S rRNA base A1913 are flipped out in the viomycin complexes while retaining their original positions in the viomycin-free complexes. Statistics for the fusidic acid complex crystallized in the absence of viomycin are shown in table S1 for comparison.

References and Notes

1. D. Moazed, H. F. Noller, Intermediate states in the movement of transfer RNA in the ribosome. *Nature* **342**, 142 (1989). doi: [10.1038/342142a0](#); pmid: [2682263](#)
2. S. Dorner, J. L. Brunelle, D. Sharma, R. Green, The hybrid state of tRNA binding is an authentic translation elongation intermediate. *Nat. Struct. Mol. Biol.* **13**, 234 (2006). doi: [10.1038/nsmb1060](#); pmid: [16501572](#)
3. P. V. Cornish, D. N. Ermolenko, H. F. Noller, T. Ha, Spontaneous intersubunit rotation in single ribosomes. *Mol. Cell* **30**, 578 (2008). doi: [10.1016/j.molcel.2008.05.004](#); pmid: [18538656](#)
4. X. Agirrezabala *et al.*, Visualization of the hybrid state of tRNA binding promoted by spontaneous ratcheting of the ribosome. *Mol. Cell* **32**, 190 (2008). doi: [10.1016/j.molcel.2008.10.001](#); pmid: [18951087](#)
5. P. C. Spiegel, D. N. Ermolenko, H. F. Noller, Elongation factor G stabilizes the hybrid-state conformation of the 70S ribosome. *RNA* **13**, 1473 (2007). doi: [10.1261/rna.601507](#); pmid: [17630323](#)
6. J. A. Dunkle *et al.*, Structures of the bacterial ribosome in classical and hybrid states of tRNA binding. *Science* **332**, 981 (2011). doi: [10.1126/science.1202692](#); pmid: [21596992](#)
7. M. V. Rodnina, W. Wintermeyer, The ribosome as a molecular machine: The mechanism of tRNA-mRNA movement in translocation. *Biochem. Soc. Trans.* **39**, 658 (2011). doi: [10.1042/BST0390658](#); pmid: [21428957](#)
8. A. H. Ratje *et al.*, Head swivel on the ribosome facilitates translocation by means of intra-subunit tRNA hybrid sites. *Nature* **468**, 713 (2010). doi: [10.1038/nature09547](#); pmid: [21124459](#)
9. Z. Guo, H. F. Noller, Rotation of the head of the 30S ribosomal subunit during mRNA translocation. *Proc. Natl. Acad. Sci. U.S.A.* **109**, 20391 (2012). doi: [10.1073/pnas.1218999109](#); pmid: [23188795](#)
10. M. A. Borovinskaya, S. Shoji, J. M. Holton, K. Fredrick, J. H. Cate, A steric block in translation caused by the antibiotic spectinomycin. *ACS Chem. Biol.* **2**, 545 (2007). doi: [10.1021/cb700100n](#); pmid: [17696316](#)
11. D. J. Taylor *et al.*, Structures of modified EF2 80S ribosome complexes reveal the role of GTP hydrolysis in translocation. *EMBO J.* **26**, 2421 (2007). doi: [10.1038/sj.emboj.7601677](#); pmid: [17446867](#)
12. J. Frank, R. K. Agrawal, A ratchet-like inter-subunit reorganization of the ribosome during translocation. *Nature* **406**, 318 (2000). doi: [10.1038/35018597](#); pmid: [10917535](#)
13. H. Gao, M. Valle, M. Ehrenberg, J. Frank, Dynamics of EF-G interaction with the ribosome explored by classification of a heterogeneous cryo-EM dataset. *J. Struct. Biol.* **147**, 283 (2004). doi: [10.1016/j.jsb.2004.02.008](#); pmid: [15450297](#)
14. H. Stark, M. V. Rodnina, H. J. Wieden, M. van Heel, W. Wintermeyer, Large-scale movement of elongation factor G and extensive conformational change of the ribosome during translocation. *Cell* **100**, 301 (2000). doi: [10.1016/S0092-8674\(00\)80666-2](#); pmid: [10676812](#)
15. Y. G. Gao *et al.*, The structure of the ribosome with elongation factor G trapped in the posttranslocational state. *Science* **326**, 694 (2009). doi: [10.1126/science.1179709](#); pmid: [19833919](#)
16. J. W. Bodley, F. J. Zieve, L. Lin, S. T. Zieve, Formation of the ribosome-G factor-GDP complex in the presence of fusidic acid. *Biochem. Biophys. Res. Commun.* **37**, 437 (1969). doi: [10.1016/0006-291X\(69\)90934-6](#); pmid: [4900137](#)
17. L. B. Jenner, N. Demeshkina, G. Yusupova, M. Yusupov, Structural aspects of messenger RNA reading frame maintenance by the ribosome. *Nat. Struct. Mol. Biol.* **17**, 555 (2010). doi: [10.1038/nsmb.1790](#); pmid: [20400952](#)
18. J. Zhou, L. Lancaster, S. Trakhanov, H. F. Noller, Crystal structure of release factor RF3 trapped in the GTP state on a rotated conformation of the ribosome. *RNA* **18**, 230 (2012). doi: [10.1261/ma.031187.111](#); pmid: [22187675](#)
19. A. Korostelev, S. Trakhanov, M. Laurberg, H. F. Noller, Crystal structure of a 70S ribosome-tRNA complex reveals functional interactions and rearrangements. *Cell* **126**, 1065 (2006). doi: [10.1016/j.cell.2006.08.032](#); pmid: [16962654](#)
20. M. Selmer *et al.*, Structure of the 70S ribosome complexed with mRNA and tRNA. *Science* **313**, 1935 (2006). http://www.ncbi.nlm.nih.gov/entrez/query.fcgi?cmd=Retrieve&db=PubMed&list_uids=16959973&dopt=Abstract; doi: [10.1126/science.1131127](#); pmid: [16959973](#)
21. B. S. Schuwirth *et al.*, Structures of the bacterial ribosome at 3.5 Å resolution. *Science* **310**, 827 (2005). doi: [10.1126/science.1117230](#); pmid: [16272117](#)
22. T. M. Schmeing *et al.*, The crystal structure of the ribosome bound to EF-Tu and aminoacyl-tRNA. *Science* **326**, 688 (2009). http://www.ncbi.nlm.nih.gov/entrez/query.fcgi?cmd=Retrieve&db=PubMed&list_uids=19833920&dopt=Abstract; doi: [10.1126/science.1179700](#); pmid: [19833920](#)
23. J. C. Schuette *et al.*, GTPase activation of elongation factor EF-Tu by the ribosome during decoding. *EMBO J.* **28**, 755 (2009). doi: [10.1038/emboj.2009.26](#); pmid: [19229291](#)
24. A. Korostelev *et al.*, Crystal structure of a translation termination complex formed with release factor RF2. *Proc. Natl. Acad. Sci. U.S.A.* **105**, 19684 (2008). doi: [10.1073/pnas.0810953105](#); pmid: [19064930](#)
25. H. R. Bourne, D. A. Sanders, F. McCormick, The GTPase superfamily: Conserved structure and molecular mechanism. *Nature* **349**, 117 (1991). doi: [10.1038/349117a0](#); pmid: [1898771](#)
26. R. M. Voorhees, T. M. Schmeing, A. C. Kelley, V. Ramakrishnan, The mechanism for activation of GTP hydrolysis on the ribosome. *Science* **330**, 835 (2010). doi: [10.1126/science.1194460](#); pmid: [21051640](#)
27. M. Laurberg *et al.*, Structure of a mutant EF-G reveals domain III and possibly the fusidic acid binding site. *J. Mol. Biol.* **303**, 593 (2000). doi: [10.1006/jmbi.2000.4168](#); pmid: [11054294](#)
28. S. R. Connell *et al.*, Structural basis for interaction of the ribosome with the switch regions of GTP-bound elongation factors. *Mol. Cell* **25**, 751 (2007). doi: [10.1016/j.molcel.2007.01.027](#); pmid: [17349960](#)
29. D. Mohr, W. Wintermeyer, M. V. Rodnina, GTPase activation of elongation factors Tu and G on the ribosome. *Biochemistry* **41**, 12520 (2002). doi: [10.1021/bi026301y](#); pmid: [12369843](#)
30. M. Helgstrand *et al.*, The ribosomal stalk binds to translation factors IF2, EF-Tu, EF-G and RF3 via a conserved region of the L12 C-terminal domain. *J. Mol. Biol.* **365**, 468 (2007). doi: [10.1016/j.jmb.2006.10.025](#); pmid: [17070545](#)
31. H. Noji, R. Yasuda, M. Yoshida, K. Kinoshita Jr., Direct observation of the rotation of F1-ATPase. *Nature* **386**, 299 (1997). doi: [10.1038/386299a0](#); pmid: [9069291](#)
32. C. Woese, Molecular mechanics of translation: A reciprocating ratchet mechanism. *Nature* **226**, 817 (1970). doi: [10.1038/226817a0](#); pmid: [5444622](#)
33. J. Frank, Intermediate states during mRNA-tRNA translocation. *Curr. Opin. Struct. Biol.* **22**, 778 (2012). doi: [10.1016/j.sbi.2012.08.001](#); pmid: [22906732](#)
34. P. Julián *et al.*, Structure of ratcheted ribosomes with tRNAs in hybrid states. *Proc. Natl. Acad. Sci. U.S.A.* **105**, 16924 (2008). doi: [10.1073/pnas.0809587105](#); pmid: [18971332](#)

35. A. Korostelev, H. F. Noller, Analysis of structural dynamics in the ribosome by TLS crystallographic refinement. *J. Mol. Biol.* **373**, 1058 (2007). doi: [10.1016/j.jmb.2007.08.054](https://doi.org/10.1016/j.jmb.2007.08.054); pmid: [17897673](https://pubmed.ncbi.nlm.nih.gov/17897673/)
36. H. Jin, A. C. Kelley, V. Ramakrishnan, Crystal structure of the hybrid state of ribosome in complex with the guanosine triphosphatase release factor 3. *Proc. Natl. Acad. Sci. U.S.A.* **108**, 15798 (2011). doi: [10.1073/pnas.1112185108](https://doi.org/10.1073/pnas.1112185108); pmid: [21903932](https://pubmed.ncbi.nlm.nih.gov/21903932/)
37. T. A. Kunkel, K. Bebenek, J. McClary, Efficient site-directed mutagenesis using uracil-containing DNA. *Methods Enzymol.* **204**, 125 (1991). doi: [10.1016/0076-6879\(91\)04008-C](https://doi.org/10.1016/0076-6879(91)04008-C); pmid: [1943776](https://pubmed.ncbi.nlm.nih.gov/1943776/)
38. I. Lasa, J. R. Castón, L. A. Fernández-Herrero, M. A. de Pedro, J. Berenguer, Insertional mutagenesis in the extreme thermophilic eubacteria *Thermus thermophilus* HB8. *Mol. Microbiol.* **6**, 1555 (1992). doi: [10.1111/j.1365-2958.1992.tb00877.x](https://doi.org/10.1111/j.1365-2958.1992.tb00877.x); pmid: [1625584](https://pubmed.ncbi.nlm.nih.gov/1625584/)
39. W. Kabsch, Automatic processing of rotation diffraction data from crystals of initially unknown symmetry and cell constants. *J. Appl. Crystallogr.* **26**, 795 (1993). doi: [10.1107/S0021889893005588](https://doi.org/10.1107/S0021889893005588)
40. P. Evans, Scaling and assessment of data quality. *Acta Crystallogr. D* **62**, 72 (2006). doi: [10.1107/S0907444905036693](https://doi.org/10.1107/S0907444905036693); pmid: [16369096](https://pubmed.ncbi.nlm.nih.gov/16369096/)
41. A. J. McCoy *et al.*, Phaser crystallographic software. *J. Appl. Cryst.* **40**, 658 (2007). doi: [10.1107/S0021889807021206](https://doi.org/10.1107/S0021889807021206)
42. P. D. Adams *et al.*, PHENIX: A comprehensive Python-based system for macromolecular structure solution. *Acta Crystallogr. D* **66**, 213 (2010). doi: [10.1107/S0907444909052925](https://doi.org/10.1107/S0907444909052925); pmid: [20124702](https://pubmed.ncbi.nlm.nih.gov/20124702/)
43. A. T. Brünger *et al.*, Crystallography & NMR system: A new software suite for macromolecular structure determination. *Acta Crystallogr. D* **54**, 905 (1998). doi: [10.1107/S0907444998003254](https://doi.org/10.1107/S0907444998003254); pmid: [9757107](https://pubmed.ncbi.nlm.nih.gov/9757107/)
44. T. A. Jones, J. Y. Zou, S. W. Cowan, M. Kjeldgaard, Improved methods for building protein models in electron density maps and the location of errors in these models. *Acta Crystallogr. A* **47**, 110 (1991). doi: [10.1107/S0108767390010224](https://doi.org/10.1107/S0108767390010224); pmid: [2025413](https://pubmed.ncbi.nlm.nih.gov/2025413/)
45. P. Emsley, K. Cowtan, Coot: Model-building tools for molecular graphics. *Acta Crystallogr. D* **60**, 2126 (2004). doi: [10.1107/S0907444904019158](https://doi.org/10.1107/S0907444904019158); pmid: [15572765](https://pubmed.ncbi.nlm.nih.gov/15572765/)

Acknowledgments: We thank H. Amiri for critical reading of the manuscript, S. Mohan for helpful discussions, and the synchrotron beamline staffs at the ALS, APS, and SSRL for expert help with data collection. Supported by NIH grants GM-17129 and GM-59140. Synchrotron facilities were supported by the U.S. Department of Energy and by NIH grants Y1-CO-1020 and Y1-GM-1104 (to the APS), and GM-105404 (to the ALS), and P41-GM-103393 (to the SSRL). Coordinates and structure factors have been deposited with the following PDB accession codes: (GDPNP-I) 4KCY, 4KCZ, 4KDO, 4KD2; (GDPNP-2) 4KBT, 4KBU, 4KBV, 4KBW; (Fus-3.6) 4KD8, 4KD9, 4KDA, 4KDB; (Fus-4.2) 4KDG, 4KDH, 4KDJ, 4KDK.

Supplementary Materials

www.sciencemag.org/content/340/6140/1236086/suppl/DC1
Figs. S1 to S11
Table S1

4 February 2013; accepted 3 May 2013
10.1126/science.1236086

Control of Ribosomal Subunit Rotation by Elongation Factor G

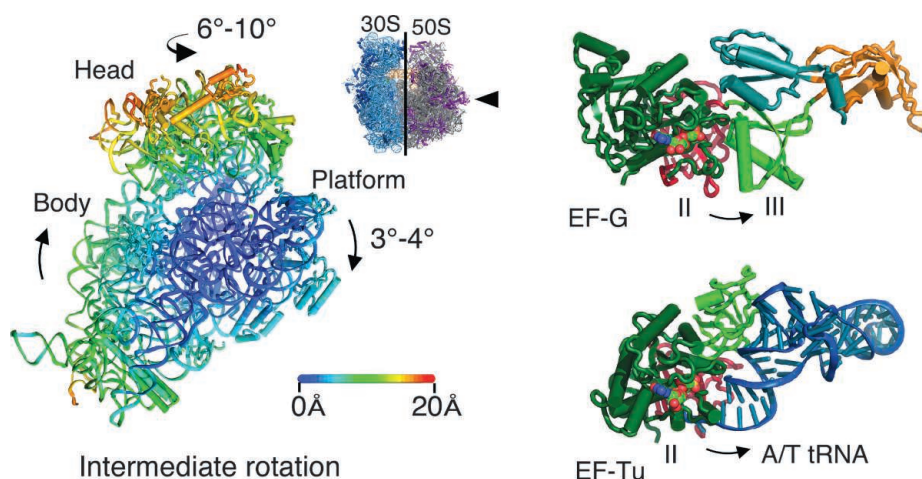
Arto Pulk and Jamie H. D. Cate*

Introduction: During protein synthesis, the guanosine triphosphatase (GTPase) elongation factor G (EF-G) promotes translocation of messenger RNA (mRNA) and transfer RNA (tRNA) on the ribosome. Translocation requires multiple steps that involve large-scale rearrangements of the ribosome that are directed by EF-G. The structural basis for how the GTPase active site in EF-G, composed of mobile “switch” elements that coordinate the guanosine 5′-triphosphate (GTP) and positioned by the large (50S) ribosomal subunit, connects to events on the small (30S) subunit remain unclear at a molecular level.

Methods: Ribosomes from *Escherichia coli* lacking the C-terminal region of protein L9 were complexed with EF-G, the nonhydrolyzable GTP analog β , γ -methyleneguanosine 5′-triphosphate (GMPPCP), and the antibiotic and translation inhibitor viomycin. Two crystal forms, each containing four unique copies of the ribosome/EF-G/GMPPCP complex, along with different stoichiometries of bound viomycin, were used to solve eight ribosome structures by molecular replacement using diffraction data to 3 Å resolution.

Results: Binding of EF-G in the GMPPCP state to the ribosome orders switch elements in the GTPase active site that are unfolded in the GDP-bound state. The GTPase switch elements contact the 50S subunit in an activated conformation, as seen in ribosome structures with elongation factor Tu (EF-Tu) and aminoacyl-tRNA during mRNA codon decoding. Folding of the switch regions also causes EF-G to adopt a rigid conformation with many new contacts between domains in the protein that form a new hydrophobic core. In the structures, EF-G/GMPPCP binds the ribosome in three different states of ribosomal subunit rotation but is more ordered in the intermediate and fully rotated states than in the unrotated state. Domain IV of EF-G is positioned in the aminoacyl-tRNA binding site (A site) on the small ribosomal subunit, where mRNA decoding occurs, but does not contact the head domain of the 30S subunit.

Discussion: The rigid conformation of EF-G/GMPPCP positions EF-G domain IV in the 30S subunit A site, a conformation incompatible with early steps of translocation. This rigid conformation may represent the activated GDP•P_i form, with EF-G domain IV decoupling tRNA movement from the 30S subunit platform and allowing the intrinsic dynamics of the 30S subunit head domain to translocate tRNAs into the peptidyl and exit sites. After GTP hydrolysis and inorganic phosphate (P_i) dissociation, unfolding of the GTPase center in EF-G would release EF-G interdomain contacts in a trajectory that matches that of aminoacyl-tRNA release from EF-Tu during mRNA decoding. The relaxed state of EF-G/GDP would then allow the 30S subunit to revert to the unrotated conformation and EF-G/GDP to dissociate from the ribosome.



READ THE FULL ARTICLE ONLINE
<http://dx.doi.org/10.1126/science.1235970>

Cite this article as A. Pulk and J. H. D. Cate, *Science* 340, 1235970 (2013). DOI: 10.1126/science.1235970

FIGURES AND TABLE IN THE FULL ARTICLE

Fig. 1. Global structural rearrangements in the ribosome in EF-G/GMPPCP complexes.

Fig. 2. Compact arrangement of EF-G domains I and III in the GTP state.

Fig. 3. A network of contacts between EF-G domains extends from the GTPase center toward the small ribosomal subunit.

Fig. 4. Contacts between EF-G and the 30S subunit are maintained during ribosomal subunit rotation.

Fig. 5. Conformational rigidity of EF-G/GMPPCP in the intermediate rotational state.

Fig. 6. Model of EF-G-controlled translocation of mRNA and tRNA.

Table 1. X-ray diffraction data and refinement statistics.

SUPPLEMENTARY MATERIALS

Materials and Methods

Figs. S1 to S4

Table S1

References

Intermediate states of translation. (Left) Ribosome in an intermediate state of 30S subunit rotation stabilized by EF-G bound to GMPPCP, viewed from the 50S subunit. Color coding is by the distance between corresponding atoms in the unrotated state of the ribosome. **(Right)** Opening of domains II and III in EF-G after GTP hydrolysis follows the same trajectory of tRNA release from EF-Tu during mRNA decoding.

The list of author affiliations is available in the full article online.

*Corresponding author. E-mail: jcate@lbl.gov

Control of Ribosomal Subunit Rotation by Elongation Factor G

Arto Pulk¹ and Jamie H. D. Cate^{1,2,3*}

Protein synthesis by the ribosome requires the translocation of transfer RNAs and messenger RNA by one codon after each peptide bond is formed, a reaction that requires ribosomal subunit rotation and is catalyzed by the guanosine triphosphatase (GTPase) elongation factor G (EF-G). We determined 3 angstrom resolution x-ray crystal structures of EF-G complexed with a nonhydrolyzable guanosine 5'-triphosphate (GTP) analog and bound to the *Escherichia coli* ribosome in different states of ribosomal subunit rotation. The structures reveal that EF-G binding to the ribosome stabilizes switch regions in the GTPase active site, resulting in a compact EF-G conformation that favors an intermediate state of ribosomal subunit rotation. These structures suggest that EF-G controls the translocation reaction by cycles of conformational rigidity and relaxation before and after GTP hydrolysis.

Guanosine triphosphatases (GTPases)—enzymes that catalyze the hydrolysis of guanosine 5'-triphosphate (GTP)—are widespread in biology and use GTP hydrolysis as a “switch” between functional states driven by protein conformational changes (1). Protein biosynthesis by the ribosome is controlled by GTPase translation factors in all stages of translation (2). Although the GTPase catalytic core is highly conserved, translation factors have evolved unique domain architectures for separate and nonoverlapping functions in translation initiation, elongation, termination, and ribosome recycling. The distinctions between translation factors, both within the translation process and between different domains of life, are targets for numerous families of antimicrobial compounds (3, 4). However, the structural basis for how GTPase translation factors use a highly conserved GTP hydrolysis mechanism to control distinct steps of translation remains unclear.

During polypeptide elongation, bacterial elongation factors EF-Tu and EF-G alternate in catalyzing accurate messenger RNA (mRNA) decoding and mRNA and transfer RNA (tRNA) translocation, respectively. The GTPase center of EF-Tu is coupled to distortions in aminoacyl-tRNA that contribute to the accuracy of mRNA decoding (5, 6). By contrast, EF-G promotes movement of mRNA and tRNA on the ribosome in steps that involve large-scale rearrangements of the ribosome (7–11). Biochemical and genetic experiments have shown that the GTPase centers of EF-Tu and EF-G, although highly conserved, are not interchangeable (12), whereas key amino acids in the GTPase active site of the eukaryotic

translocase eEF2 can be mutated to those of EF-G and retain function (13). Furthermore, whereas EF-Tu hydrolyzes GTP rapidly only during accurate mRNA decoding, the GTPase activity of EF-G is greatly accelerated even by vacant ribosomes (14, 15). Together with the divergent architectures of EF-Tu and EF-G outside of the GTPase active site (16), these results indicate that EF-G has evolved considerably different means for linking GTP hydrolysis to ribosome dynamics.

mRNA and tRNA translocation occurs in multiple steps (17). First, the 3' acceptor ends of the tRNAs move with respect to the large ribosomal (50S) subunit, so that the peptidyl-site (P-site) and aminoacyl-site (A-site) tRNA termini move to the exit (E) and P sites, respectively, creating a hybrid P/E and A/P tRNA binding state (18). This hybrid state requires a rotation of the small ribosomal (30S) subunit relative to the 50S subunit (7) and an orthogonal rotation of the 30S

subunit head domain (9, 19, 20) (Fig. 1A), conformational changes that are conserved in the eukaryotic ribosome (21). When complexed with GTP, EF-G binds the ribosome and favors ribosomal subunit rotation, a state associated with tRNA binding in the hybrid A/P and P/E sites (22–25). GTP hydrolysis by EF-G, subsequent ribosome dynamics (10), and phosphate release are then required to translocate mRNA and the tRNA anticodons on the small ribosomal subunit to complete the translocation reaction and to release EF-G/guanosine diphosphate (GDP) from the ribosome, respectively (26, 27).

The structural basis for EF-G/GTP stabilization of rotated states of the ribosome is known only at low resolution (9, 10, 28). Cryogenic electron microscopy (cryo-EM) reconstructions revealed EF-G domain positions in late stages of tRNA translocation but do not provide a molecular understanding of how the GTPase active site in EF-G, positioned by the 50S ribosomal subunit, is connected to events on the 30S subunit required for mRNA and tRNA translocation. Here, we determined structures of the ribosome in multiple states of subunit rotation, in complexes with EF-G bound to the nonhydrolyzable GTP analog β,γ -methylene guanosine 5'-triphosphate (GMPPCP). These structures reveal that GTP binding rearranges switch regions in EF-G to promote EF-G interdomain packing and ribosomal subunit rotation, an allosteric mechanism reminiscent of motor proteins that use adenosine 5'-triphosphate hydrolysis to drive mechanical events common in biology.

Results and Discussion

Global Conformations of the Ribosome Complexes

We determined two crystal structures of the *Escherichia coli* 70S ribosome in complexes with EF-G, the nonhydrolyzable GTP analog GMPPCP,

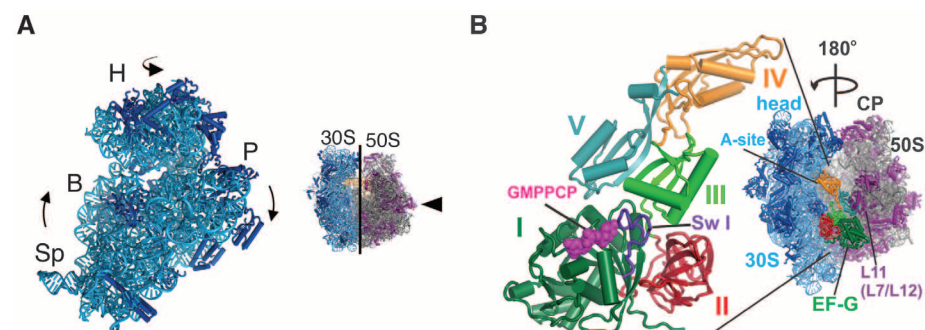


Fig. 1. Global structural rearrangements in the ribosome in EF-G/GMPPCP complexes. (A) Schematic illustrating two degrees of freedom in the 30S subunit within the 70S ribosome. 30S subunit rotation encompasses the body (B) and platform (P) domains, whereas the 30S subunit head domain (H) swivels around a nearly orthogonal rotational axis. (B) EF-G is shown bound to the 70S ribosome oriented 180° from the view shown to the left. Domains in EF-G are numbered: domain I (dark green), domain II (red), domain III (light green), domain IV (orange), and domain V (light blue). Switch I (sw I) (amino acids 38 to 64) in domain I is highlighted in purple, with GMPPCP as magenta spheres. The 30S subunit is in blue, and the 50S subunit is in gray and magenta. Single-letter abbreviations for the amino acid residues are as follows: A, Ala; C, Cys; D, Asp; E, Glu; F, Phe; G, Gly; H, His; I, Ile; K, Lys; L, Leu; M, Met; N, Asn; P, Pro; Q, Gln; R, Arg; S, Ser; T, Thr; V, Val; W, Trp; and Y, Tyr.

¹Department of Molecular and Cell Biology, California Institute for Quantitative Biosciences, University of California, Berkeley, CA 94720, USA. ²Physical Biosciences Division, Lawrence Berkeley National Laboratory, Berkeley, CA 94720, USA. ³Department of Chemistry, University of California, Berkeley, CA 94720, USA.

*Corresponding author. E-mail: jcate@lbl.gov

and the antibiotic viomycin to a resolution of 3 Å (Table 1) (29). Each crystal form contains four unique copies of the ribosome in the crystallographic asymmetric unit that adopt different conformations with respect to 30S subunit rotation and swiveling of the 30S subunit head domain (fig. S1). Rotation of the 30S subunit body and platform domains ranges from ~0° to ~8°, whereas the head domain of the 30S subunit is swiveled by ~6° to ~11° (table S1). EF-G, a five-domain protein, is bound to all eight copies of the ribosome, with the GTPase domain (domain I or G domain) and domains II, III, and V positioned adjacent to the 50S subunit L11 arm, while domain IV projects into the 30S subunit mRNA decoding site (A site) (Fig. 1B). All of the copies of EF-G contain clear electron density for GMPPCP visible in the GTPase active site.

Ordering of the GTPase Switch Regions and EF-G Domain Packing

The GTPase active site in EF-G contains mobile “switch” elements termed switch I (amino acids 38 to 64) and switch II (amino acids 84 to 107) and a P loop that coordinates the triphosphate (amino acids 12 to 27) (30). In EF-G, the switch elements are thought to convert the free energy of GTP hydrolysis in the G domain into the unidirectional translocation of the ribosome along an mRNA and the rapid cycling of EF-G during protein synthesis (9, 15, 27, 31). In the present structures, the G domain of EF-G contacts the sarcin-ricin loop (SRL) in 23S ribosomal RNA (rRNA) of the large ribosomal subunit. Nucleotide A2662 in the SRL coordinates a catalytic histidine in switch II (His92) in EF-G and positions its imidazole ring in the correct location to activate a nucleophilic water molecule putatively required for GTP hydrolysis, similar to the structure of the GTPase EF-Tu bound to the ribosome in the GTP state (6) (Fig. 2A). By contrast, this catalytic histidine is oriented away from the active site in a structure of the *Thermus thermophilus* 70S ribosome trapped with EF-G in a GDP state by the antibiotic fusidic acid (32). Binding of the GTP analog also orders much of switch I in EF-G (amino acids 49 to 64), closing the GTP binding pocket (Fig. 2, B and C), as previously observed at low resolution by cryo-EM with a paralog of EF-G (9). During translocation, GTP hydrolysis by EF-G is rapid and is followed by a rate-limiting conformational rearrangement of the translocation complex that is coupled to EF-G in an activated GDP•P_i (inorganic phosphate) state (27, 33). After GTP hydrolysis and translocation, switch I becomes disordered (31), which greatly accelerates release of EF-G/GDP from the post-translocational ribosome (27, 31). In the structure of EF-G trapped on the ribosome with GDP by fusidic acid, switch I is entirely disordered (32). Thus, the current complexes likely represent either the pre-GTP hydrolysis configuration of EF-G on the ribosome, or the GDP•P_i state.

The folding of EF-G switch I results in multiple new interdomain contacts throughout EF-G. Arginine 59 (R59) from switch I, universally

conserved in canonical translation GTPases (34), interacts with the backbone of SRL nucleotide A2663 on one side, as seen with EF-Tu (6), and forms a salt bridge with aspartate 467 (D467) in EF-G domain III (Fig. 2D), which occupies the space where the 3'-acceptor end of tRNA binds EF-Tu (6) (Fig. 2E). Although mutations of R59 in EF-Tu and EF-G do not affect GTP hydrolysis (35), mutations of R59 in EF-G decrease translocation by a factor of up to 50 (35), similar to the rate that occurs in the absence of GTP or with a non-hydrolyzable GTP analog (35). The rate of translocation is decreased by a factor of only 5 when R59 is replaced with lysine, showing that the salt bridge with D467 in domain III is important for EF-G function. A second salt bridge forms between glutamate 58 and arginine 475 (Fig. 2D), an interaction absent in EF-Tu (6). Further differences between the geometry of switch I in EF-G and EF-Tu occur in amino acids adjacent to the α-phosphate of GMPPCP and the P loop (fig. S2), which may explain the observation that replacement of EF-G switch I amino acids 44 to 55 with those from EF-Tu renders EF-G functionally inactive (12).

The folding of EF-G switch I further induces close hydrophobic packing between domains I, II, and III, capped by the side chain of R59 and centered on switch II residue phenylalanine 95 (F95) which is thought to contribute to GTPase

activation (36) (Fig. 3A). In the ribosome complex of EF-G with GDP and fusidic acid, this interface is broken and occupied by the antibiotic, which packs against F95 (32). Notably, mutations in this interface, including F95, confer fusidic acid resistance to cells (36). In some cases, these mutations make EF-G an intrinsically active GTPase (36) while at the same time drastically reducing EF-G's ability to accelerate translocation, indicating that GTP hydrolysis must be linked with ribosomal conformational changes for effective translocation (36). An additional network of polar and hydrophobic interactions surrounds salt bridges between switch II residues arginine 101 (R101), glutamate 98 (E98), and domain II residue lysine 323 (K323), which are held in place by residues from switches I and II (threonine 64 and serine 65, and isoleucine 97) and domains II and III (threonine 393 and the backbone of glutamate 441) (Fig. 3B). The contacts between these conserved residues in EF-G are lost upon GTP hydrolysis and P_i release, when switch I becomes disordered and domains II and III move apart (32).

EF-G Coupling to the Conformation of the 70S Ribosome

Formation of these extensive interfaces between domains I to III in EF-G in the GMPPCP complexes results in large-scale movement of domains II and III that couple to rotation of the body of

Table 1. X-ray diffraction data and refinement statistics. a.s.u., crystallographic asymmetric unit; CC(1/2), correlation coefficient; I/σ, mean signal-to-noise value of measured intensities; R, refinement R factor; R_{free} refinement free R factor; R_{merge}, measurement R factor; RMS, root mean square.

	Crystal I	Crystal II
Space group	P 2 ₁	P 2 ₁
Unit cell (a, b, c in Å) (α, β, γ in degrees)	90.0, 103.566, 90.0 361.60, 361.77, 433.20	90.0, 103.217, 90.0 361.14, 360.51, 429.73
Resolution (Å) (high-resolution shell)*	70 – 3.0 (3.1 – 3.0)	70 – 3.0 (3.1 – 3.0)
R _{merge} [†]	15.2 (100.9)	17.3 (132)
I/σ (I)	6.49 (0.84)	5.84 (0.58)
CC(1/2) (%)	99.4 (42.7)	99.3 (30.4)
Completeness (%)	83.7 (60.7)	89.6 (71.5)
Measurement redundancy	3.1 (1.5)	3.9 (2.3)
Unique reflections	1,799,385 (122,106)	1,904,514 (142,145)
No. crystals used	20	24
Refinement		
Resolution (Å) [†]	70 – 2.9	70 – 2.9
No. reflections	1,874,109	1,984,535
Molecules per a.s.u	4	4
R _{free} set	8,386	8,583
R/R _{free} (%)	0.230/0.278	0.221/0.270
Average B factor		
RNA	27.4	31.8
Protein	30.3	38.5
Other	12.6	15.1
RMS deviations		
Bond lengths (Å)	0.008	0.009
Bond angles (°)	1.304	1.376

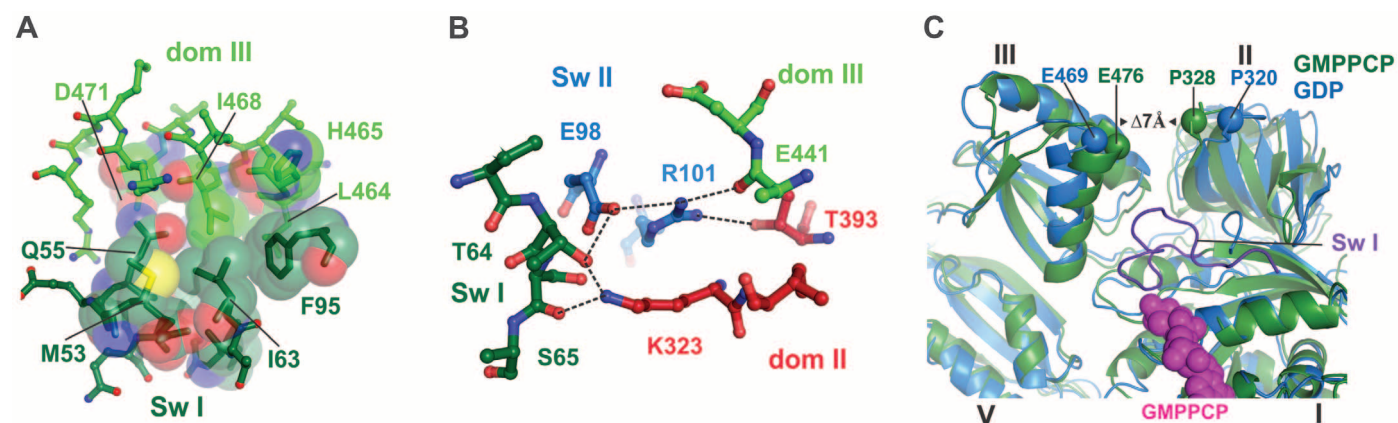
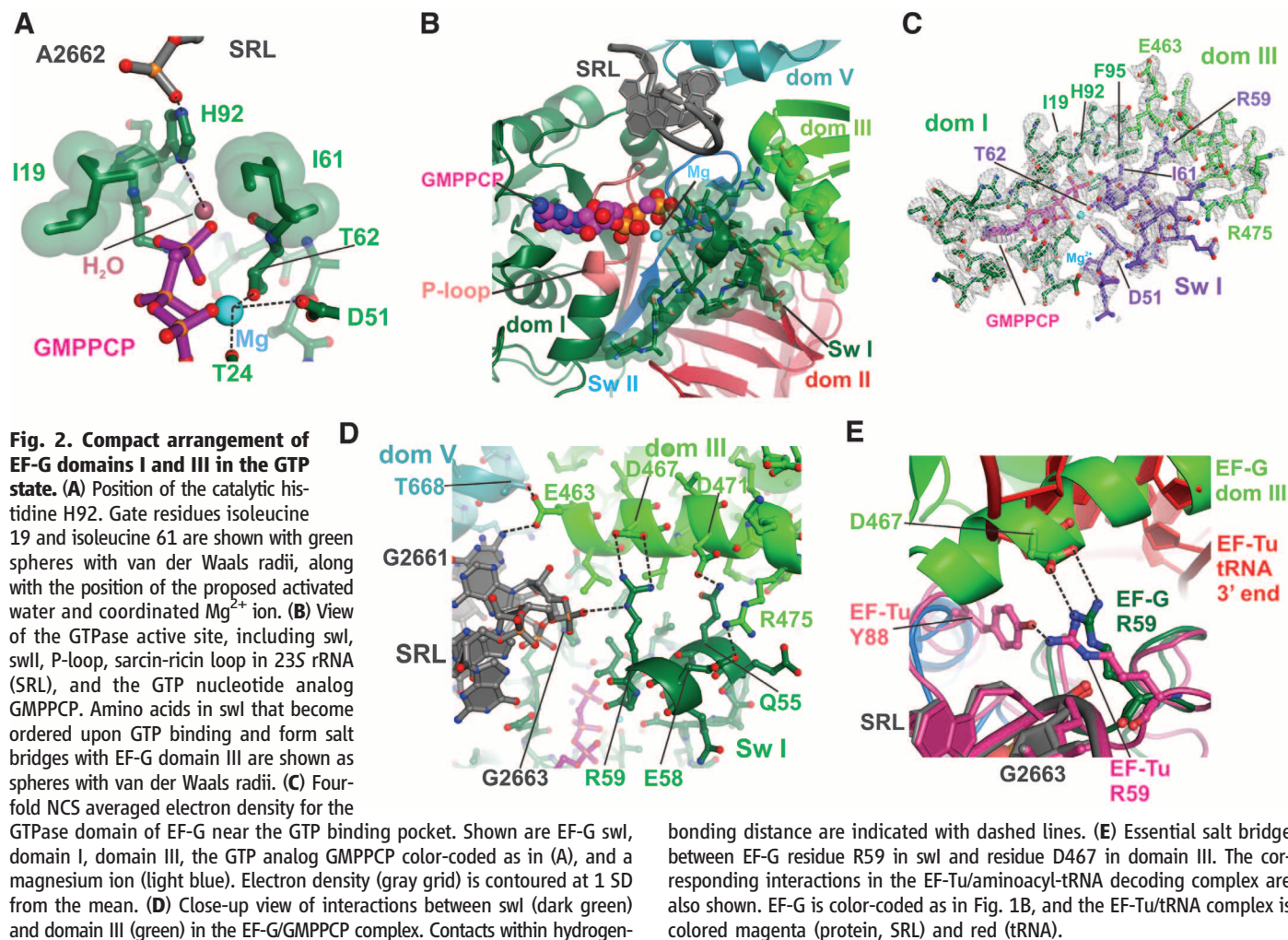
*Data beyond the high-resolution shell in parentheses were used for refinement and map calculation and extend to a CC(1/2) value of about 24.5% (54).
[†]All statistics not in parentheses include data over the whole reported resolution range. Crystal form I contains higher occupancy for viomycin and II lower occupancy for viomycin.

the 30S ribosomal subunit. Domain II of EF-G complexed with GMPPCP moves ~ 7 Å closer to domain III at its extremity, when compared to the ribosome complex with EF-G, GDP, and fusidic acid, which corresponds to a post-translocation

state with P- and E-site tRNAs and the ribosome in an unrotated conformation (32) (Fig. 3C). EF-G domains II and III move together with the body of the 30S subunit, which is rotated by 3° to 8° , and maintain contacts with 16S rRNA

helices 4, 5, and 15 and ribosomal protein S12 (Fig. 4, A and B) (9, 10, 32).

In the structure of the unrotated 70S ribosome in the present crystals, EF-G domain II is largely disordered, and the G domain is partially disordered



domains II and III in the GTP state, color-coded as in Fig. 1B. Dashes indicate atoms within hydrogen-bonding distance. (C) Closure of domains II and III due to binding of the GMPPCP form of EF-G to the ribosome (7 Å) is indicated. The structure of the ribosome with EF-G/GDP/fusidic acid is shown in blue (32). The ribosome in an intermediate rotation state with EF-G/GMPPCP is in green.

domains II and III in the GTP state, color-coded as in Fig. 1B. Dashes indicate atoms within hydrogen-bonding distance. (C) Closure of domains II and III due to binding of the GMPPCP form of EF-G to the ribosome (7 Å) is indicated. The structure of the ribosome with EF-G/GDP/fusidic acid is shown in blue (32). The ribosome in an intermediate rotation state with EF-G/GMPPCP is in green.

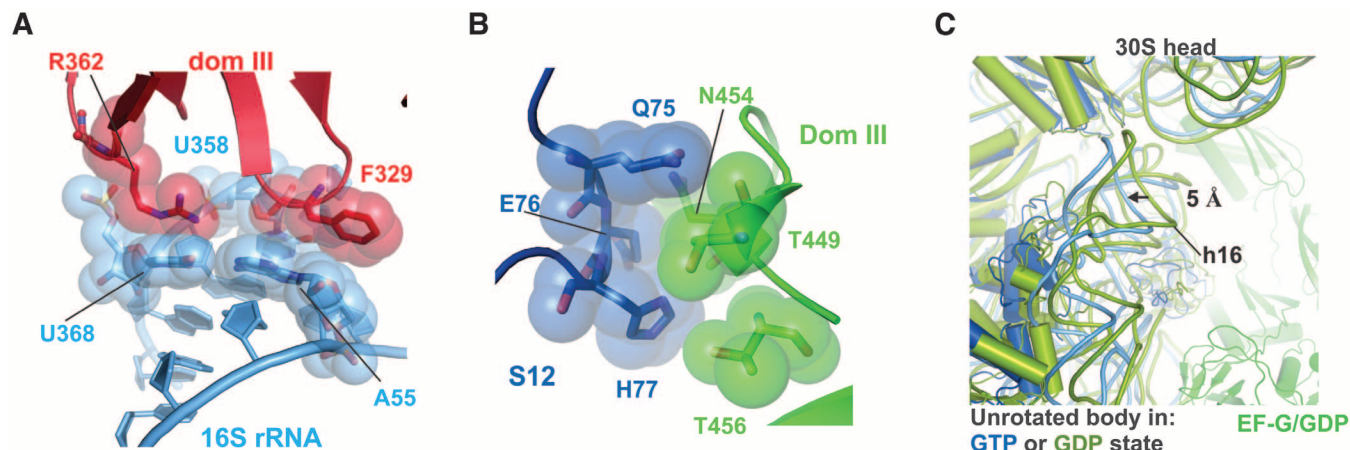


Fig. 4. Contacts between EF-G and the 30S subunit are maintained during ribosomal subunit rotation. (A) Contacts between EF-G domain II (red) and 16S rRNA (light blue) near helices h5 (A55 or U358) and h15 (U368). (B) Contacts between EF-G domain III (green) and ribosomal protein S12 (blue) for the ribo-

some in an intermediate state of rotation. (C) Movement of the 30S subunit body domain away from the subunit interface in the unrotated state induced by EF-G binding in the GTP state (blue). For comparison, the structure of the ribosome with EF-G/GDP/fusidic acid in the unrotated state is shown in green and olive (32).

(fig. S3A), as is domain IV. Furthermore, the 30S subunit body domain is forced away from the 50S subunit interface by 5 Å when compared to EF-G bound with GDP/fusidic acid to the unrotated post-translocation state (Fig. 4C), consistent with evidence that EF-G/GTP binding favors rotated states of the ribosome (22–25). In the two structures of the ribosome in a fully rotated state determined here, domains II and IV of EF-G are more ordered when compared to the unrotated state (fig. S3B). EF-G/GMPPCP also adopts a well-defined conformation when bound to intermediate rotated states (Fig. 5A). Thus, the interactions between EF-G and the 30S ribosomal subunit couple the nucleotide status of the GTPase center (GDP versus GTP or GDP•P_i) to inter-domain stabilization of EF-G and the rotational state of the ribosome.

Position of EF-G Domain IV in the Ribosomal A Site

In the present structures, domain IV in EF-G, which is essential for tRNA and mRNA translocation (37), projects toward the 30S subunit and occupies the position of A-site tRNA (8–10, 32) (Fig. 5B). The orientation of domain IV is stabilized primarily by salt bridges with domain III and domain V (Fig. 5C), with only a few interactions occurring to the tip of h44 in 16S rRNA in the 30S subunit A site. Binding of the antibiotic viomycin in the vicinity of these weak interactions with 16S rRNA helix h44 (fig. S4) does not seem to stabilize them, since the interactions remain weak whether viomycin is bound to h44 or not (fig. S4) (29). Although the head domain of the 30S subunit adopts large swiveling angles in these structures (fig. S1 and table S1), there are no clear contacts between EF-G domain IV and the head domain in seven of the eight ribosomes observed here (Fig. 5D). Instead, the position of domain IV seems to function almost exclusively to preclude tRNA occupancy in the ribosomal A site (8–10, 32). In the various struc-

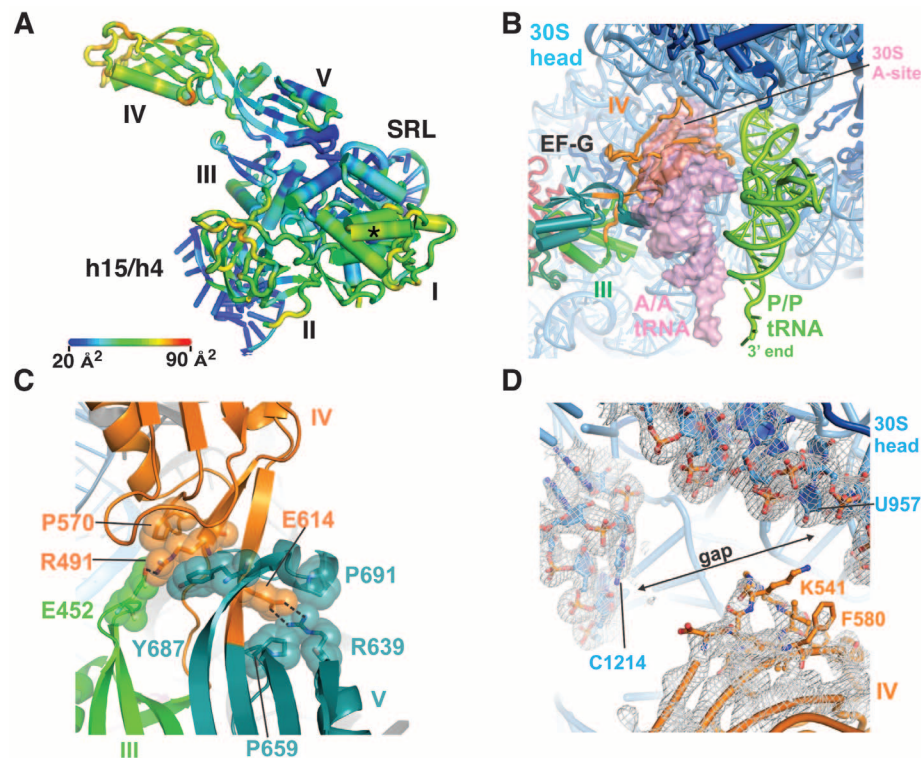


Fig. 5. Conformational rigidity of EF-G/GMPPCP in the intermediate rotational state. (A) Atomic displacement parameters (B factors) of EF-G/GMPPCP bound to the ribosome in an intermediate state of subunit rotation. Scale bar indicates the range of color-coded B factors. Domains in EF-G and helices in 16S and 23S rRNA are indicated. The asterisk indicates the site of interaction seen between EF-G and ribosomal proteins L7/L12 in (32). (B) Position of EF-G domain IV (orange) in the ribosomal A site. The position of tRNAs in the A site (A/A tRNA, transparent pink surface) and P site (P/P tRNA, green) are derived from the superposition of the ribosome structure in (55) with the ribosome in an intermediate state of subunit rotation, using the 30S subunit platform as a frame of reference. (C) Salt bridges between EF-G domain III (green) residue E452, domain IV (orange) residues R491 or E614, and domain V (aqua) residue R639, buttressed by hydrophobic packing. (D) Lack of contacts between EF-G domain IV and the head domain of the 30S subunit of a representative ribosome in an intermediate state of rotation. Difference electron density ($2F_{\text{obs}} - 2F_{\text{calc}}$) is shown at a contour of 1 SD from the mean.

tures of EF-G with GMPPCP and GDP/fusidic acid, the specific interactions between EF-G and platform elements of the 30S subunit A site near

helix h44 also vary in detail and are poorly ordered in nearly all of the present structures, again suggesting that EF-G domain IV serves as a

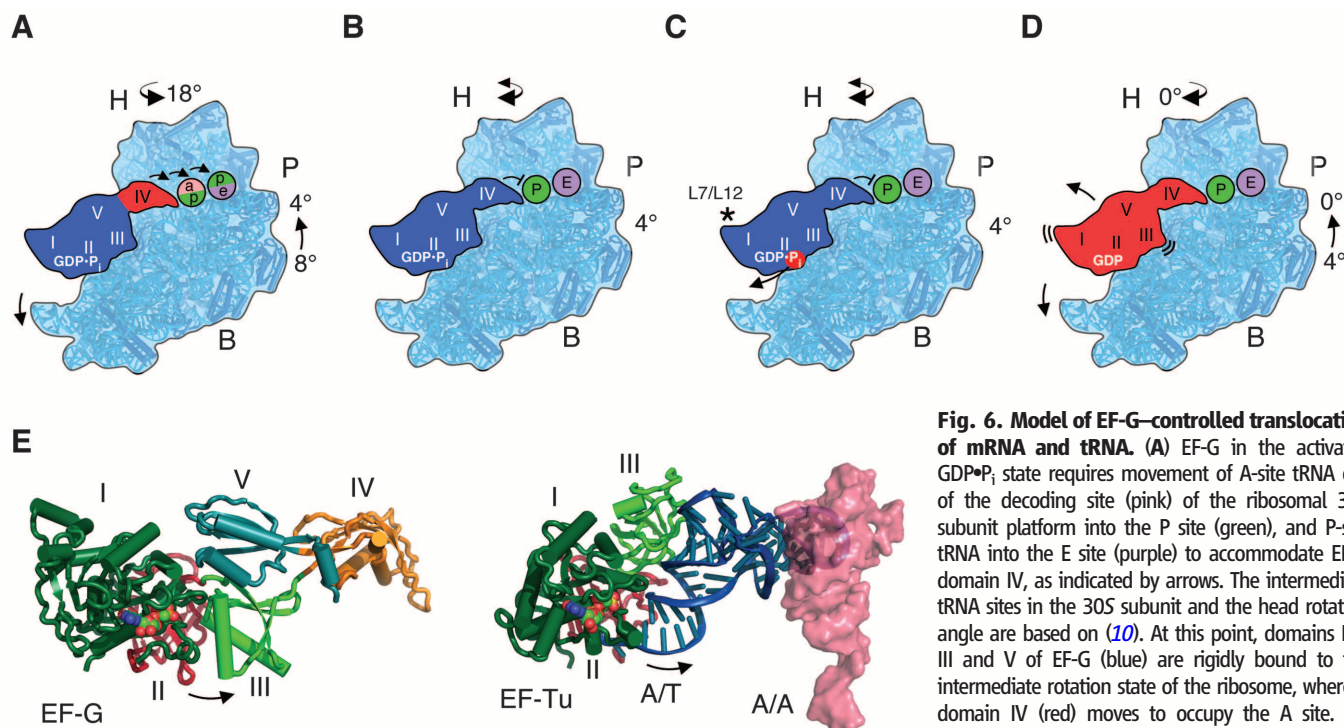


Fig. 6. Model of EF-G-controlled translocation of mRNA and tRNA.

(A) EF-G in the activated GDP•P_i state requires movement of A-site tRNA out of the decoding site (pink) of the ribosomal 30S subunit platform into the P site (green), and P-site tRNA into the E site (purple) to accommodate EF-G domain IV, as indicated by arrows. The intermediate tRNA sites in the 30S subunit and the head rotation angle are based on (10). At this point, domains I to III and V of EF-G (blue) are rigidly bound to the intermediate rotation state of the ribosome, whereas domain IV (red) moves to occupy the A site. (B) Stable interactions between EF-G domain IV and

the remainder of EF-G position domain IV to prevent back-translocation of P-site tRNA. The 30S subunit head domain may remain dynamic in this post-translocation state (46, 51, 56). (C) Phosphate release from the GTPase domain of EF-G, stimulated by proteins L7/L12 (asterisk), disrupts interdomain contacts in EF-G, allowing the ribosome to revert to the unrotated state, (D), from which EF-G/GDP dissociates from the ribosome. In panels (A) to (D), the lowercase letters indicate tRNA contacts to the 30S head and body domains, in that order. Uppercase letters indicate tRNA contacts to the P or E sites in both the 30S head and 30S body domains. (E) Opening of domains II and III in EF-G after GTP hydrolysis follows the same trajectory as tRNA release from EF-Tu during mRNA decoding. The position of A-site tRNA (pink, PDB entry 318G) (57) was compared to that for EF-Tu in an mRNA decoding complex with the GTP analog GMPPCP (6).

steric block to control movements of the ribosome and tRNA substrates in later steps of translocation (32, 37).

Model of mRNA and tRNA Translocation

Translocation of mRNA and tRNA on the ribosome can occur in the absence of EF-G, but the rate of EF-G-independent translocation is too slow to support cell growth (38, 39) and is highly reversible (40, 41). Thus, although the process of translocation is intrinsic to the ribosome, EF-G increases translocation efficiency and biases it in the forward direction. Kinetic experiments revealed that EF-G-catalyzed translocation involves multiple steps, with GTP hydrolysis occurring rapidly, followed by a rate-limiting conformational change in the ribosome that precedes mRNA and tRNA translocation (27, 33, 42). However, the relationships between these kinetically defined events and structural changes in ribosome translocation complexes remain to be determined (43–46). Several lines of evidence indicate that, although EF-G/GTP may bind the ribosome in the unrotated state (47), EF-G/GTP binds more favorably to the ribosome in an intermediate step of the translocation reaction, after tRNAs occupy hybrid A/P and P/E sites and the ribosomal subunits are in a rotated state (10, 11, 46, 48). The present structures reveal that EF-G/GMPPCP can bind to vacant ribosomes in multiple states of

subunit rotation, including the unrotated state. However, the rigid arrangement of EF-G observed here is incompatible with pretranslocation complexes in which tRNA occupies the A site in the 30S subunit (49) (Fig. 5B).

The present structural data suggest that the intermediate state of rotation may be preferred before GTP hydrolysis by EF-G. However, in kinetic experiments GTP hydrolysis is rapid and precedes the rate-limiting conformational change in translocation (27, 33, 42). It is possible that the GTP and GDP•P_i states of EF-G may be in equilibrium (47), analogous to the situation with eukaryotic initiation factor eIF2 (50). Thus, the present structures of the partially and fully rotated states may represent EF-G/GDP•P_i bound to the ribosome as tRNAs move into the ap/P and pe/E sites in the 30S/50S subunits as defined in (10), when the 30S head domain adopts extremely rotated positions (10, 28) (Fig. 6A). Consistent with the intermediate state of rotation observed previously by cryo-EM (10), it is likely that the activated (GDP•P_i) form of EF-G stabilizes the intermediate state of rotation (Fig. 6A) (27). However, the present structures reveal that EF-G binding to partially rotated ribosomes is independent of the position of the 30S head domain. Because EF-G domain IV only makes substantial contact to the 30S subunit head domain in the post-translocation state (30), and not when the

head is swiveled (8–10, 28) (Fig. 5D), domain IV of the EF-G/GDP•P_i complex may simply act to decouple tRNA movement from the 30S subunit platform and allow the intrinsic dynamics of the 30S subunit head domain (51, 52) to translocate tRNAs into the P and E sites (10, 28). EF-G domain IV would then prevent translocated P-site tRNA from reverting its position to the A site, as suggested by previous structures (8–10, 32, 37) (Fig. 6B). P_i release, accelerated by switch I unfolding (Fig. 6C), and accompanied by switch I unfolding (Fig. 6C), would then cause EF-G to relax due to loss of interdomain contacts and allow the 30S subunit to reverse its rotation to 0°. The relaxed state of EF-G/GDP would then dissociate from the ribosome as domain III and V contacts with the ribosome are destabilized (Fig. 6D).

Conclusion

The model of EF-G cycling between rigid and relaxed conformations is comparable to the changes in tRNA conformation that occur during mRNA decoding by EF-Tu. During mRNA decoding, GTP hydrolysis by EF-Tu releases tRNA from a bent conformation that relaxes as the tRNA is accommodated into the ribosomal A site (5, 6). The trajectory of tRNA motion after release from EF-Tu corresponds to the direction of domains II and III opening in EF-G (Fig. 6E). It will be important to determine whether similar cycles

may occur with other translation GTPases. In the case of EF-G, future structural and biophysical insights will also be needed to elucidate the contribution of tRNAs to translocation and to understand the role of EF-G in its distinct functional role in ribosome recycling (53).

Materials and Methods

Escherichia coli ribosomes lacking the C terminus of ribosomal protein L9 (amino acids 56 to the C terminus) were purified and used for complex formation with *E. coli* EF-G, the nonhydrolyzable GTP analog GMPPCP, and viomycin. Purification and crystallization of the complexes are described in the supplementary materials. Two ribosome crystal forms, each containing four unique copies of the ribosome, were used for x-ray diffraction measurements and structure determination by molecular replacement. Details of the data measurement, structure determination, refinement, and ribosome superpositions are given in the supplementary materials.

References and Notes

- H. R. Bourne, D. A. Sanders, F. McCormick, The GTPase superfamily: Conserved structure and molecular mechanism. *Nature* **349**, 117 (1991). doi: [10.1038/349117a0](#); pmid: [1898771](#)
- N. Clementi, N. Polacek, Ribosome-associated GTPases: The role of RNA for GTPase activation. *RNA Biol.* **7**, 521 (2010). doi: [10.4161/rna.7.5.12467](#); pmid: [20657179](#)
- H. Liang, Sordarin, an antifungal agent with a unique mode of action. *Beilstein J. Org. Chem.* **4**, 31 (2008). doi: [10.3762/bjoc.4.31](#); pmid: [18941619](#)
- D. Sohmen, J. M. Harms, F. Schlünzen, D. N. Wilson, Enhanced SnapShot: Antibiotic inhibition of protein synthesis II. *Cell* **139**, 212, e1 (2009). doi: [10.1016/j.cell.2009.08.009](#); pmid: [19804764](#)
- T. M. Schmeing *et al.*, The crystal structure of the ribosome bound to EF-Tu and aminoacyl-tRNA. *Science* **326**, 688 (2009). doi: [10.1126/science.1179700](#); pmid: [19833920](#)
- R. M. Voorhees, T. M. Schmeing, A. C. Kelley, V. Ramakrishnan, The mechanism for activation of GTP hydrolysis on the ribosome. *Science* **330**, 835 (2010). doi: [10.1126/science.1194460](#); pmid: [21051640](#)
- J. Frank, R. K. Agrawal, A ratchet-like inter-subunit reorganization of the ribosome during translocation. *Nature* **406**, 318 (2000). doi: [10.1038/35018597](#); pmid: [10917535](#)
- M. Valle *et al.*, Locking and unlocking of ribosomal motions. *Cell* **114**, 123 (2003). doi: [10.1016/S0092-8674\(03\)00476-8](#); pmid: [12859903](#)
- S. R. Connell *et al.*, Structural basis for interaction of the ribosome with the switch regions of GTP-bound elongation factors. *Mol. Cell* **25**, 751 (2007). doi: [10.1016/j.molcel.2007.01.027](#); pmid: [17349960](#)
- A. H. Ratje *et al.*, Head swivel on the ribosome facilitates translocation by means of intra-subunit tRNA hybrid sites. *Nature* **468**, 713 (2010). doi: [10.1038/nature09547](#); pmid: [21124459](#)
- J. B. Munro, M. R. Wasserman, R. B. Altman, L. Wang, S. C. Blanchard, Correlated conformational events in EF-G and the ribosome regulate translocation. *Nat. Struct. Mol. Biol.* **17**, 1470 (2010). doi: [10.1038/nsmb.1925](#); pmid: [21057527](#)
- A. Kolesnikov, A. Gudkov, Elongation factor G with effector loop from elongation factor Tu is inactive in translocation. *FEBS Lett.* **514**, 67 (2002). doi: [10.1016/S0014-5793\(02\)02300-1](#); pmid: [11904183](#)
- G. Bartish, O. Nygård, Importance of individual amino acids in the Switch I region in eEF2 studied by functional complementation in *S. cerevisiae*. *Biochimie* **90**, 736 (2008). doi: [10.1016/j.biochi.2008.01.006](#); pmid: [18267126](#)
- M. S. Rohrbach, J. W. Bodley, Steady state kinetic analysis of the mechanism of guanosine triphosphate hydrolysis catalyzed by *Escherichia coli* elongation factor G and the ribosome. *Biochemistry* **15**, 4565 (1976). doi: [10.1021/bi00666a003](#); pmid: [9976](#)
- M. V. Rodnina, A. Savelsbergh, V. I. Katunin, W. Wintermeyer, Hydrolysis of GTP by elongation factor G drives tRNA movement on the ribosome. *Nature* **385**, 37 (1997). doi: [10.1038/385037a0](#); pmid: [8985244](#)
- M. Kjeldgaard, J. Nyborg, B. F. Clark, The GTP binding motif: Variations on a theme. *FASEB J.* **10**, 1347 (1996). pmid: [8903506](#)
- A. Petrov *et al.*, Dynamics of the translational machinery. *Curr. Opin. Struct. Biol.* **21**, 137 (2011). doi: [10.1016/j.sbi.2010.11.007](#); pmid: [21256733](#)
- D. Moazed, H. F. Noller, Intermediate states in the movement of transfer RNA in the ribosome. *Nature* **342**, 142 (1989). doi: [10.1038/342142a0](#); pmid: [2682263](#)
- J. A. Dunkle *et al.*, Structures of the bacterial ribosome in classical and hybrid states of tRNA binding. *Science* **332**, 981 (2011). doi: [10.1126/science.1202692](#); pmid: [21596992](#)
- X. Agirrezabala *et al.*, Structural characterization of mRNA-tRNA translocation intermediates. *Proc. Natl. Acad. Sci. U.S.A.* **109**, 6094 (2012). doi: [10.1073/pnas.1201288109](#); pmid: [22467828](#)
- T. Budkevich *et al.*, Structure and dynamics of the mammalian ribosomal pretranslocation complex. *Mol. Cell* **44**, 214 (2011). doi: [10.1016/j.molcel.2011.07.040](#); pmid: [22017870](#)
- D. N. Ermolenko *et al.*, Observation of intersubunit movement of the ribosome in solution using FRET. *J. Mol. Biol.* **370**, 530 (2007). doi: [10.1016/j.jmb.2007.04.042](#); pmid: [17512008](#)
- P. V. Cornish, D. N. Ermolenko, H. F. Noller, T. Ha, Spontaneous intersubunit rotation in single ribosomes. *Mol. Cell* **30**, 578 (2008). doi: [10.1016/j.molcel.2008.05.004](#); pmid: [18538656](#)
- J. Fei, P. Kosuri, D. D. MacDougall, R. L. Gonzalez Jr., Coupling of ribosomal L1 stalk and tRNA dynamics during translation elongation. *Mol. Cell* **30**, 348 (2008). doi: [10.1016/j.molcel.2008.03.012](#); pmid: [18471980](#)
- J. B. Munro, R. B. Altman, C. S. Tung, K. Y. Sanbonmatsu, S. C. Blanchard, A fast dynamic mode of the EF-G-bound ribosome. *EMBO J.* **29**, 770 (2010). doi: [10.1038/emboj.2009.384](#); pmid: [20033061](#)
- F. Peske, A. Savelsbergh, V. I. Katunin, M. V. Rodnina, W. Wintermeyer, Conformational changes of the small ribosomal subunit during elongation factor G-dependent tRNA-mRNA translocation. *J. Mol. Biol.* **343**, 1183 (2004). doi: [10.1016/j.jmb.2004.08.097](#); pmid: [15491605](#)
- B. Wilden, A. Savelsbergh, M. V. Rodnina, W. Wintermeyer, Role and timing of GTP binding and hydrolysis during EF-G-dependent tRNA translocation on the ribosome. *Proc. Natl. Acad. Sci. U.S.A.* **103**, 13670 (2006). doi: [10.1073/pnas.0606099103](#); pmid: [16940356](#)
- D. J. Ramrath *et al.*, The complex of tmRNA-SmpB and EF-G on translocating ribosomes. *Nature* **485**, 526 (2012). pmid: [22622583](#)
- Materials and methods are available as supplementary materials on Science Online.
- I. R. Vetter, A. Wittinghofer, The guanine nucleotide-binding switch in three dimensions. *Science* **294**, 1299 (2001). doi: [10.1126/science.1062023](#); pmid: [11701921](#)
- C. Ticu, R. Nechifor, B. Nguyen, M. Desrosiers, K. S. Wilson, Conformational changes in switch I of EF-G drive its directional cycling on and off the ribosome. *EMBO J.* **28**, 2053 (2009). doi: [10.1038/emboj.2009.169](#); pmid: [19536129](#)
- Y. G. Gao *et al.*, The structure of the ribosome with elongation factor G trapped in the posttranslocational state. *Science* **326**, 694 (2009). doi: [10.1126/science.1179709](#); pmid: [19833919](#)
- A. Savelsbergh *et al.*, An elongation factor G-induced ribosome rearrangement precedes tRNA-mRNA translocation. *Mol. Cell* **11**, 1517 (2003). doi: [10.1016/S1097-2765\(03\)00230-2](#); pmid: [12820965](#)
- T. Margus, M. Remm, T. Tenson, A computational study of elongation factor G (EF-G) duplicated genes: Diverged nature underlying the innovation on the same structural template. *PLoS ONE* **6**, e22789 (2011). doi: [10.1371/journal.pone.0022789](#); pmid: [21829651](#)
- D. Mohr, W. Wintermeyer, M. V. Rodnina, Arginines 29 and 59 of elongation factor G are important for GTP hydrolysis or translocation on the ribosome. *EMBO J.* **19**, 3458 (2000). doi: [10.1093/emboj/19.13.3458](#); pmid: [10880458](#)
- C. Ticu, M. Murataliev, R. Nechifor, K. S. Wilson, A central interdomain protein joint in elongation factor G regulates antibiotic sensitivity, GTP hydrolysis, and ribosome translocation. *J. Biol. Chem.* **286**, 21697 (2011). doi: [10.1074/jbc.M110.214056](#); pmid: [21531717](#)
- A. Savelsbergh, N. B. Matassova, M. V. Rodnina, W. Wintermeyer, Role of domains 4 and 5 in elongation factor G functions on the ribosome. *J. Mol. Biol.* **300**, 951 (2000). doi: [10.1006/jmbi.2000.3886](#); pmid: [10891280](#)
- S. Pestka, Studies on the formation of transfer ribonucleic acid-ribosome complexes. VI. Oligopeptide synthesis and translocation on ribosomes in the presence and absence of soluble transfer factors. *J. Biol. Chem.* **244**, 1533 (1969). pmid: [4886309](#)
- L. P. Gavrilova, A. S. Spirin, Stimulation of "non-enzymic" translocation in ribosomes by p-chloromercuribenzoate. *FEBS Lett.* **17**, 324 (1971). doi: [10.1016/0014-5793\(71\)80177-1](#); pmid: [11946059](#)
- S. Shoji, S. E. Walker, K. Fredrick, Reverse translocation of tRNA in the ribosome. *Mol. Cell* **24**, 931 (2006). doi: [10.1016/j.molcel.2006.11.025](#); pmid: [17189194](#)
- A. L. Konevega *et al.*, Spontaneous reverse movement of mRNA-bound tRNA through the ribosome. *Nat. Struct. Mol. Biol.* **14**, 318 (2007). doi: [10.1038/nsmb.1221](#); pmid: [17369838](#)
- A. Savelsbergh, D. Mohr, U. Kothe, W. Wintermeyer, M. V. Rodnina, Control of phosphate release from elongation factor G by ribosomal protein L7/12. *EMBO J.* **24**, 4316 (2005). doi: [10.1038/sj.emboj.7600884](#); pmid: [16292341](#)
- C. Chen *et al.*, Single-molecule fluorescence measurements of ribosomal translocation dynamics. *Mol. Cell* **42**, 367 (2011). doi: [10.1016/j.molcel.2011.03.024](#); pmid: [21549313](#)
- J. Fei, A. C. Richard, J. E. Bronson, R. L. Gonzalez Jr., Transfer RNA-mediated regulation of ribosome dynamics during protein synthesis. *Nat. Struct. Mol. Biol.* **18**, 1043 (2011). doi: [10.1038/nsmb.2098](#); pmid: [21857664](#)
- D. N. Ermolenko, H. F. Noller, mRNA translocation occurs during the second step of ribosomal intersubunit rotation. *Nat. Struct. Mol. Biol.* **18**, 457 (2011). doi: [10.1038/nsmb.2011](#); pmid: [21399643](#)
- L. Wang, R. B. Altman, S. C. Blanchard, Insights into the molecular determinants of EF-G catalyzed translocation. *RNA* **17**, 2189 (2011). doi: [10.1261/rna.029033.111](#); pmid: [22033333](#)
- S. E. Walker, S. Shoji, D. Pan, B. S. Cooperman, K. Fredrick, Role of hybrid tRNA-binding states in ribosomal translocation. *Proc. Natl. Acad. Sci. U.S.A.* **105**, 9192 (2008). doi: [10.1073/pnas.0710146105](#); pmid: [18591673](#)
- X. Agirrezabala, J. Frank, Elongation in translation as a dynamic interaction among the ribosome, tRNA, and elongation factors EF-G and EF-Tu. *Q. Rev. Biophys.* **42**, 159 (2009). doi: [10.1017/S0033583509990060](#); pmid: [20025795](#)
- H. Stark, M. V. Rodnina, H. J. Wieden, M. van Heel, W. Wintermeyer, Large-scale movement of elongation factor G and extensive conformational change of the ribosome during translocation. *Cell* **100**, 301 (2000). doi: [10.1016/S0092-8674\(00\)80666-2](#); pmid: [10676812](#)
- M. A. Algire, D. Maag, J. R. Lorsch, Pi release from eIF2, not GTP hydrolysis, is the step controlled by start-site selection during eukaryotic translation initiation. *Mol. Cell* **20**, 251 (2005). doi: [10.1016/j.molcel.2005.09.008](#); pmid: [16246727](#)
- I. S. Gabashvili, R. K. Agrawal, R. Grassucci, J. Frank, Structure and structural variations of the *Escherichia coli*

- 30 S ribosomal subunit as revealed by three-dimensional cryo-electron microscopy. *J. Mol. Biol.* **286**, 1285 (1999). doi: [10.1006/jmbi.1999.2538](https://doi.org/10.1006/jmbi.1999.2538); pmid: [10064696](https://pubmed.ncbi.nlm.nih.gov/10064696/)
52. N. Fischer, A. L. Konevega, W. Wintermeyer, M. V. Rodnina, H. Stark, Ribosome dynamics and tRNA movement by time-resolved electron cryomicroscopy. *Nature* **466**, 329 (2010). doi: [10.1038/nature09206](https://doi.org/10.1038/nature09206); pmid: [20631791](https://pubmed.ncbi.nlm.nih.gov/20631791/)
53. F. Peske, M. V. Rodnina, W. Wintermeyer, Sequence of steps in ribosome recycling as defined by kinetic analysis. *Mol. Cell* **18**, 403 (2005). doi: [10.1016/j.molcel.2005.04.009](https://doi.org/10.1016/j.molcel.2005.04.009); pmid: [15893724](https://pubmed.ncbi.nlm.nih.gov/15893724/)
54. P. A. Karplus, K. Diederichs, Linking crystallographic model and data quality. *Science* **336**, 1030 (2012). doi: [10.1126/science.1218231](https://doi.org/10.1126/science.1218231); pmid: [22628654](https://pubmed.ncbi.nlm.nih.gov/22628654/)
55. R. M. Voorhees, A. Weixlbaumer, D. Loakes, A. C. Kelley, V. Ramakrishnan, Insights into substrate stabilization from snapshots of the peptidyl transferase center of the intact 70S ribosome. *Nat. Struct. Mol. Biol.* **16**, 528 (2009). doi: [10.1038/nsmb.1577](https://doi.org/10.1038/nsmb.1577); pmid: [19363482](https://pubmed.ncbi.nlm.nih.gov/19363482/)
56. W. Zhang, J. A. Dunkle, J. H. Cate, Structures of the ribosome in intermediate states of ratcheting. *Science* **325**, 1014 (2009). doi: [10.1126/science.1175275](https://doi.org/10.1126/science.1175275); pmid: [19696352](https://pubmed.ncbi.nlm.nih.gov/19696352/)
57. L. B. Jenner, N. Demeshkina, G. Yusupova, M. Yusupov, Structural aspects of messenger RNA reading frame maintenance by the ribosome. *Nat. Struct. Mol. Biol.* **17**, 555 (2010). doi: [10.1038/nsmb.1790](https://doi.org/10.1038/nsmb.1790); pmid: [20400952](https://pubmed.ncbi.nlm.nih.gov/20400952/)

Acknowledgments: We thank J. Doudna for helpful discussions and comments, J. Holton and G. Meigs for help with x-ray data collection, and P. Afonine and J. Headd for advice on crystallographic refinement. This work was supported by NIH grant R01-GM65050 to J.H.D.C., by the NIH project MINOS grant R01GM105404 for the Structural Integrated

Biology for Life Sciences (SIBYLS) and 8.3.1 beam lines at the Advanced Light Source (ALS), and by the U.S. Department of Energy (DEAC02-05CH11231 for the SIBYLS and 8.3.1 beam-lines at the ALS). Coordinates for the ribosomes have been deposited in the Protein Data Bank (PDB): 4KIX, 4KIY, 4KIZ, 4KJ0, 4KJ1, 4KJ2, 4KJ3, 4KJ4, 4KJ5, 4KJ6, 4KJ7, 4KJ8, 4KJ9, 4KJA, 4KJB, and 4KJC.

Supplementary Materials

www.sciencemag.org/content/340/6140/1235970/suppl/DC1

Materials and Methods

Figs. S1 to S4

Table S1

References (58–71)

1 February 2013; accepted 3 May 2013
10.1126/science.1235970

Terabit-Scale Orbital Angular Momentum Mode Division Multiplexing in Fibers

Nenad Bozinovic,^{1*} Yang Yue,^{2*} Yongxiong Ren,² Moshe Tur,³ Poul Kristensen,⁴ Hao Huang,² Alan E. Willner,^{2†} Siddharth Ramachandran^{1†}

Internet data traffic capacity is rapidly reaching limits imposed by optical fiber nonlinear effects. Having almost exhausted available degrees of freedom to orthogonally multiplex data, the possibility is now being explored of using spatial modes of fibers to enhance data capacity. We demonstrate the viability of using the orbital angular momentum (OAM) of light to create orthogonal, spatially distinct streams of data-transmitting channels that are multiplexed in a single fiber. Over 1.1 kilometers of a specially designed optical fiber that minimizes mode coupling, we achieved 400-gigabits-per-second data transmission using four angular momentum modes at a single wavelength, and 1.6 terabits per second using two OAM modes over 10 wavelengths. These demonstrations suggest that OAM could provide an additional degree of freedom for data multiplexing in future fiber networks.

The data-carrying capacity of single-mode optical fibers has increased by four orders of magnitude in the past three decades (1), primarily because of multiplexing techniques that use wavelength, amplitude, phase, and polarization of light to encode information (Fig. 1A). As

the capacity of the current optical fiber systems reaches limits imposed by nonlinear effects (2), the possibility of spatial-division-multiplexing methods by use of multicore (3) and multimode (4) fibers has emerged to address the forthcoming capacity crunch. Although multicore fibers potentially require more complex manufacturing than do circularly symmetric multimode fibers, conventional multimode fibers suffer from mode coupling caused by random perturbations in fibers or incomplete mode-conversion (5). Methods that have been developed to address the problem of mode coupling so far have been dependent on computationally intensive digital signal processing (DSP) algorithms, and have been based either on

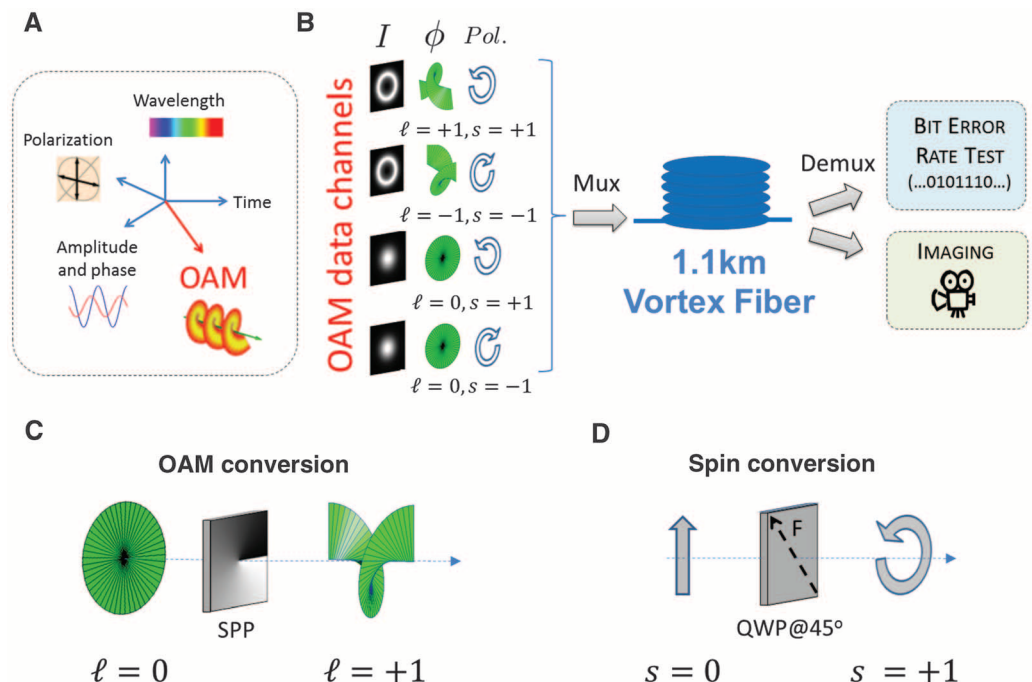
adaptive optics feedback (6) or complex multiple-input multiple-output (MIMO) methodologies (4).

We show a method that offers a means of increasing network throughput without using complex DSP algorithms, but instead by using fiber modes that carry orbital angular momentum (OAM). As one of the most fundamental physical quantities in classical and quantum electrodynamics, OAM of light has initiated widespread interest in many areas, including optical tweezers, atom manipulation, and optical communications (7). Photons that carry OAM have a helical phase of electric field proportional to $\exp(i\ell\phi)$, where ℓ is topological charge, and ϕ is the azimuthal angle (7). Several classical (8) and quantum (9) communications experiments have exploited the inherent orthogonality of OAM modes in free space by multiplexing information in this additional degree of freedom, increasing the capacity of free-space communications links. In fibers, however, OAM beams were considered to be completely unstable owing to mode coupling, and only short-length fiber propagation, without data transmission, has been demonstrated (10–14).

The OAM mode-division multiplexing (OAM-MDM) concept used here is illustrated in Fig. 1B and is based on multiplexing two fundamental fiber modes of opposite spins (circular polarizations), with the two OAM fiber modes of opposite topological charges $\ell = \pm 1$. The three key enablers for our demonstration are (i) a multiplexing setup, comprising spatial light modulators (SLMs) and conventional free-space optics (conceptually illustrated in Fig. 1, C and D), that enabled <21 dB of multiplexing crosstalk; (ii) a circularly symmetric specialty fiber fabricated on a commercial manufacturing setup that minimized mode coupling, leading to <10 dB of crosstalk

Fig. 1. The OAM-MDM principle.

(A) OAM may be considered as an orthogonal degree of freedom for data multiplexing. (B) Simplified OAM-MDM setup: four modes with distinct values of OAM (ℓ) and spin (or circular polarization, s) are multiplexed into a specialty fiber, transmitted for 1.1 km, demultiplexed, and analyzed at the output by using BER testers and cameras. (C) OAM conversion of $\ell = 0 \rightarrow 1$ is achieved by using spiral phase patterns (SPPs) (the spiral pattern has opposite helicity for the $\ell = 0 \rightarrow 1$ case). (D) Spin conversion to $s = \pm 1$ is implemented with a quarter wave plate (QWP) whose fast axis is oriented $\pm 45^\circ$ with respect to the input (linear) polarization.



among modes after 1.1 km of propagation; and (iii) a demultiplexing setup that enabled sorting of the modes with high purity at the output by using free-space polarization and OAM sorters. The detailed experimental setup is available in fig. S1 (15). Conventional single-mode fibers (SMFs) support propagation of two distinct, degenerate polarization states of the fundamental mode (LP_{01}^{\pm}), designated by their spin $s = \pm 1$. The few-mode fiber that we use (“vortex fiber”) additionally supports the first-order antisymmetric modes: one transverse magnetic mode (TM_{01}), two OAM^{\pm} modes (denoted by their $\ell = \pm 1$ topological charge), and one transverse electric (TE_{01}) mode (“0” and “1” in the subscript “01” refer to azimuthal and radial indices, respectively, denoting the number of nulls in the electric field in the two orthogonal directions). However, unlike traditional few-mode fibers, the vortex fiber was designed to lift the near-degeneracy between the desired OAM^{\pm} and parasitic TM_{01} and TE_{01} , hence minimizing modal crosstalk between them (16). Thus, this fiber yields two new degenerate states (OAM^{\pm}) in addition to the conventional degenerate LP_{01}^{\pm} modes.

The index profile of our vortex fiber (Fig. 2, A and B) has a characteristic high-index ring that serves to lift the debilitating near-degeneracy between the desired OAM^{\pm} and parasitic TM_{01} and TE_{01} responsible for mode coupling in conventional fibers (5). Effective index differences (Δn_{eff}) of the first-order modes with respect to the LP_{01}^{\pm} modes were numerically calculated and compared with the experimentally measured values (Fig. 2C). In the vortex fiber, the OAM^{\pm} states are separated from the LP_{01}^{\pm} states by $\Delta n_{eff} \approx 3 \times 10^{-3}$ (at 1550 nm) and from the parasitic TE_{01} and TM_{01} states by $\Delta n_{eff} \approx 1.6 \times 10^{-3}$. These values of Δn_{eff} are larger than those in polarization-maintaining fibers that preserve distinct polarization modes and, by analogy, indicate that all distinct modes in the vortex fiber should be resistant to distributed mode coupling (16). This is in contrast to conventional fibers and hence indicative of the fact that OAM modes would be preserved in these vortex fibers. The degenerate pair of OAM^{\pm} states inevitably mix into each other because of fiber birefringence (13). However, this coupling can be compensated for by

using a fiber polarization controller (we achieve ~ 20 dB of crosstalk between the two OAM^{\pm} states at the output of the 1.1-km bare-fiber spool). Polarization controller feedback-based correction techniques are commonly used in conventional polarization-division multiplexed systems (17). We used a previously developed mode-purity characterization technique that analyzes spatial intensity variations at the fiber output arising from intermodal interference in order to study the effects of distributed mode coupling (13). Relative mode powers as a function of a fiber length (iteratively measured via cutback) is shown in Fig. 2D for the case of high-purity (>21 dB) OAM^{\pm} mode excitation at 1550 nm. After 1.1 km of propagation of the desired OAM modes, less than ~ 10 dB of the input power leaked into the LP_{01}^{\pm} and the parasitic TM_{01} and TE_{01} modes. The relative mode powers are also measured in time (Fig. 2E), indicating temporal stability on the order of hours, although polarization controller adjustments were necessary for longer periods of time. Having confirmed the capability of the fiber to carry individual OAM states over long distances

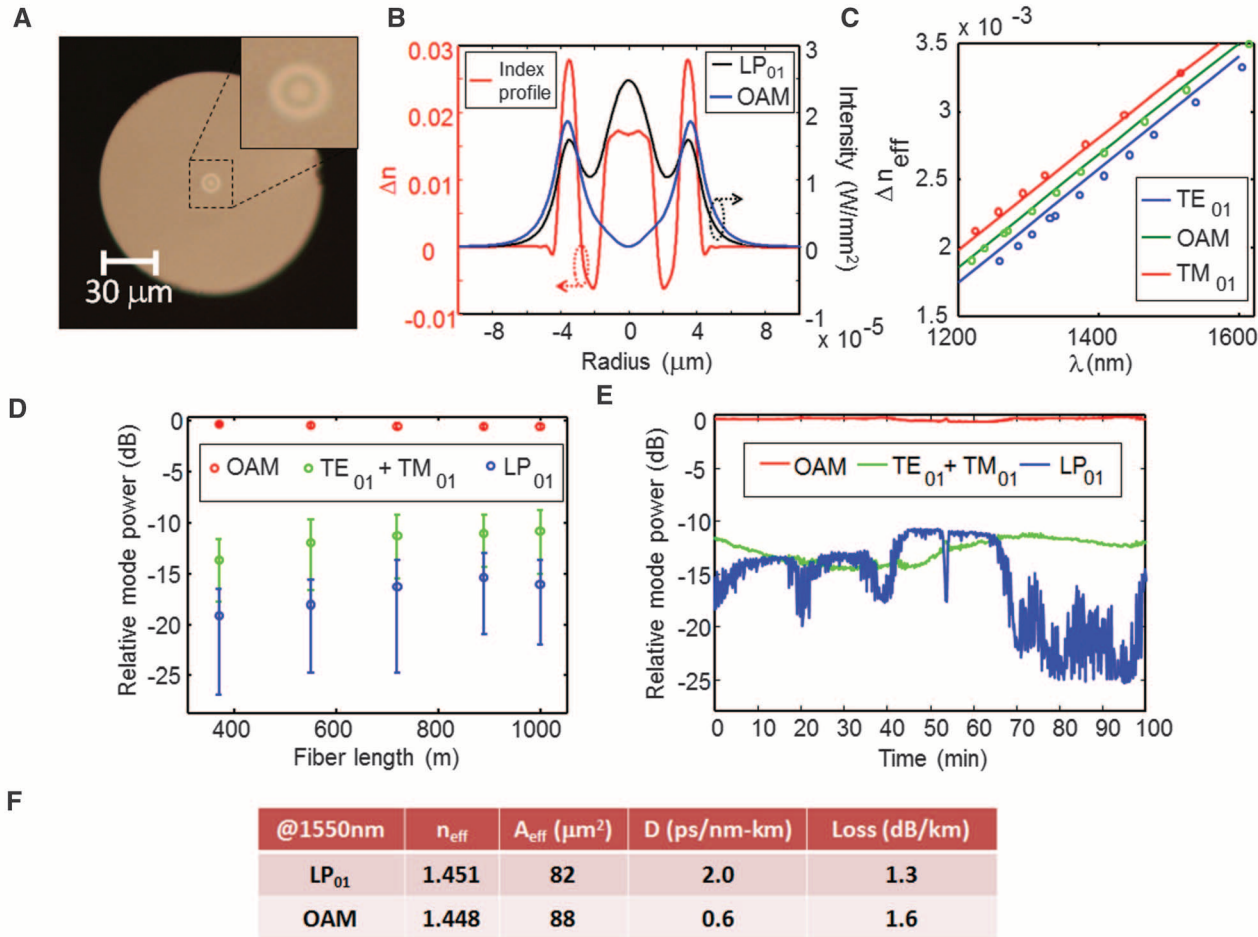


Fig. 2. Vortex fiber characteristics. (A) Microscope image of the vortex fiber facet. (B) Measured fiber refractive index and numerically calculated mode profiles. (C) Measured (open circles) and numerically calculated (solid lines) effective index differences (Δn_{eff}) of the first-order modes— TE_{01} , OAM, and TM_{01} —with respect to the fundamental mode (LP_{01}); large Δn_{eff} between modes lowers mode-coupling distortions. (D) Measured modal power ratios as

a function of fiber length for the case of OAM^+ mode excitation at 1550 nm (OAM power refers to combined OAM^+ and OAM^- mode powers, and LP_{01} refers to combined powers of the two LP_{01}^{\pm} states). (E) Relative mode powers with respect to time, showing the temporal stability of the OAM modes. (F) Table of vortex fiber properties at 1550 nm, including numerically calculated effective area and dispersion and experimentally measured loss.

with low mode-coupling, we investigate the prospects of multiplexing four guided modes—namely, the two LP_{01}^{\pm} and the two OAM^{\pm} modes—and using them as four distinct channels for OAM-MDM data transmission. We used a commercial SLM and free-space optics for OAM mode generation and multiplexing (Fig. 1, B and C, and fig. S1). The detailed alignment procedure is available in (15).

After 1.1 km of propagation, the vortex fiber output is imaged onto a camera when only one channel is enabled at a time. Examples of images from the LP_{01}^{\pm} and OAM^+ channels are shown in Fig. 3, A and B (images from all four channels are available in fig. S2). To reveal the transverse phase of the OAM^+ channel outputs, interference with an expanded Gaussian beam reference was recorded (Fig. 3, C and D), with the vortex fiber polarization controller adjusted to yield ~ -20 dB OAM^{\pm} crosstalk. The spiral interference patterns clearly indicate that the OAM^+ (OAM^-) state was obtained at the output in the case when the individual OAM^+ (OAM^-) mode was sent at the channel input.

With all four channels enabled simultaneously, the demuxing system sorts the modes according to their OAM (l) and spin (s) values, using another SLM and a combination of a quarter-wave plate and a polarizer, respectively (15). In the example of the OAM^+ channel, the resulting output maps back into a conventional Gaussian-shaped beam with a planar phase (Fig. 3, E and F), which we can now route to a coherent receiver by

coupling into an SMF. This enables a quantitative measure of mode purity by observing channel output power versus time (Fig. 3G), which reveals how much power leaked into other channels (crosstalk), as well as how much power leaked out-and-back, during fiber propagation, into an individual channel [multi-path interference (MPI)] (18, 19). MPI is a fundamental property arising from fiber design, whereas crosstalk depends on both the fiber and the multiplexing (or demultiplexing) setup design. Both crosstalk and MPI increase bit error rate (BER) in the absence of MIMO corrective algorithms (measured values for all the modes are given in Fig. 3E).

We have demonstrated OAM-MDM data transmission feasibility of the system described above by sending 50-GBaud, quadrature-phase-shift-keyed (QPSK) data at a single wavelength and over four mode channels (Fig. 4A) (15, 20). BERs were measured for two cases: when only one channel was used for data transmission (single-channel case) and when all four channels were simultaneously populated with distinct (decorrelated) data streams (all-channels case). In the single-channel case, the largest received power penalty for achieving a BER of 3.8×10^{-3} [the threshold BER level at which forward-error-correction (FEC) algorithms ensure error-free data transmission] is 2.5 dB, mainly due to MPI. In the all-channel case, this largest power penalty increased to 4.1 dB, mainly due to crosstalk. In the latter case, a total transmission capacity at 400 Gbit/s below the FEC limit is achieved.

In addition to the single-wavelength demonstration, we used wavelength-division multiplexing (WDM) to further extend the capacity of our system (Fig. 4C) (20). Recall that we used a conventional polarization controller to achieve ~ -20 dB crosstalk between the OAM^{\pm} modes. However, optimizing our system to yield two orthogonal, pure OAM^{\pm} states at one wavelength implies that at other wavelengths, the OAM^{\pm} states will, to a certain extent, couple with each other. A more advanced transmitter with individual wavelength channel polarization control could, in principle, be used to mitigate this effect. In addition, extraneous contributory factors such as the wavelength dependence of the SLM and other free-space optical components can also affect the crosstalk. For these reasons, only two OAM modes and 10 WDM channels (from 1546.64 to 1553.88 nm) were chosen for our WDM experiment (Fig. 4D, boxed region, which illustrates wavelengths at which crosstalk was low) (15). Reduction to two modes allowed us to choose a more complex modulation format (16-quadrature amplitude modulation) for data transmission, yielding higher spectral efficiency, albeit at a lower baud rate of 20 GBaud. Although the BER of the two modes varied somewhat because of crosstalk (Fig. 4E), transmission of 20 channels (OAM-MDM and WDM) resulted in a total transmission capacity of 1.6 Tb/s under the FEC limit.

Our results indicate that simple, low-complexity DSP coherent detection methods can be used to achieve OAM-MDM in fibers. Our demonstration

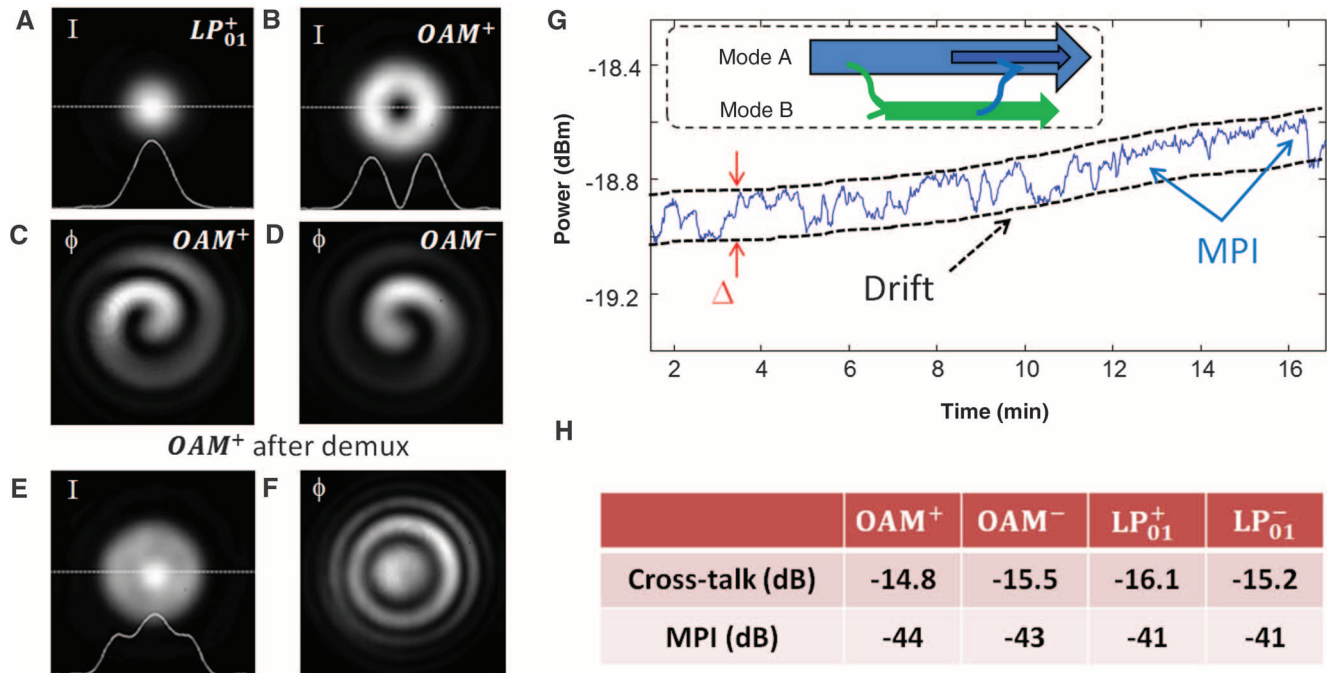


Fig. 3. Transmission channel characterization. (A and B) Intensity of LP_{01}^{\pm} and OAM^+ channel outputs (collimated). (C and D) Interference patterns between an expanded Gaussian beam reference and the OAM^+ and OAM^- channel outputs, respectively. The handedness of the spiral is indicative of the OAM value ($l = +1$ or -1) carried by each beam. Clear spiral images are also indicative of high mode purity. (E and F) Intensity and phase of the OAM^+ channel output after demulti-

plexing. All images taken when only one channel is enabled at a time. (G) Example of the LP_{01}^+ channel power drift (attributed to crosstalk and free-space optics) and power fluctuations (due to MPI). (Inset) Illustration of crosstalk and MPI mechanisms; mode A can couple into mode B, producing crosstalk, but a certain amount of the power can couple back into mode A, interfering with the original signal and producing MPI. (H) Table of measured values for crosstalk and MPI for all four modes.

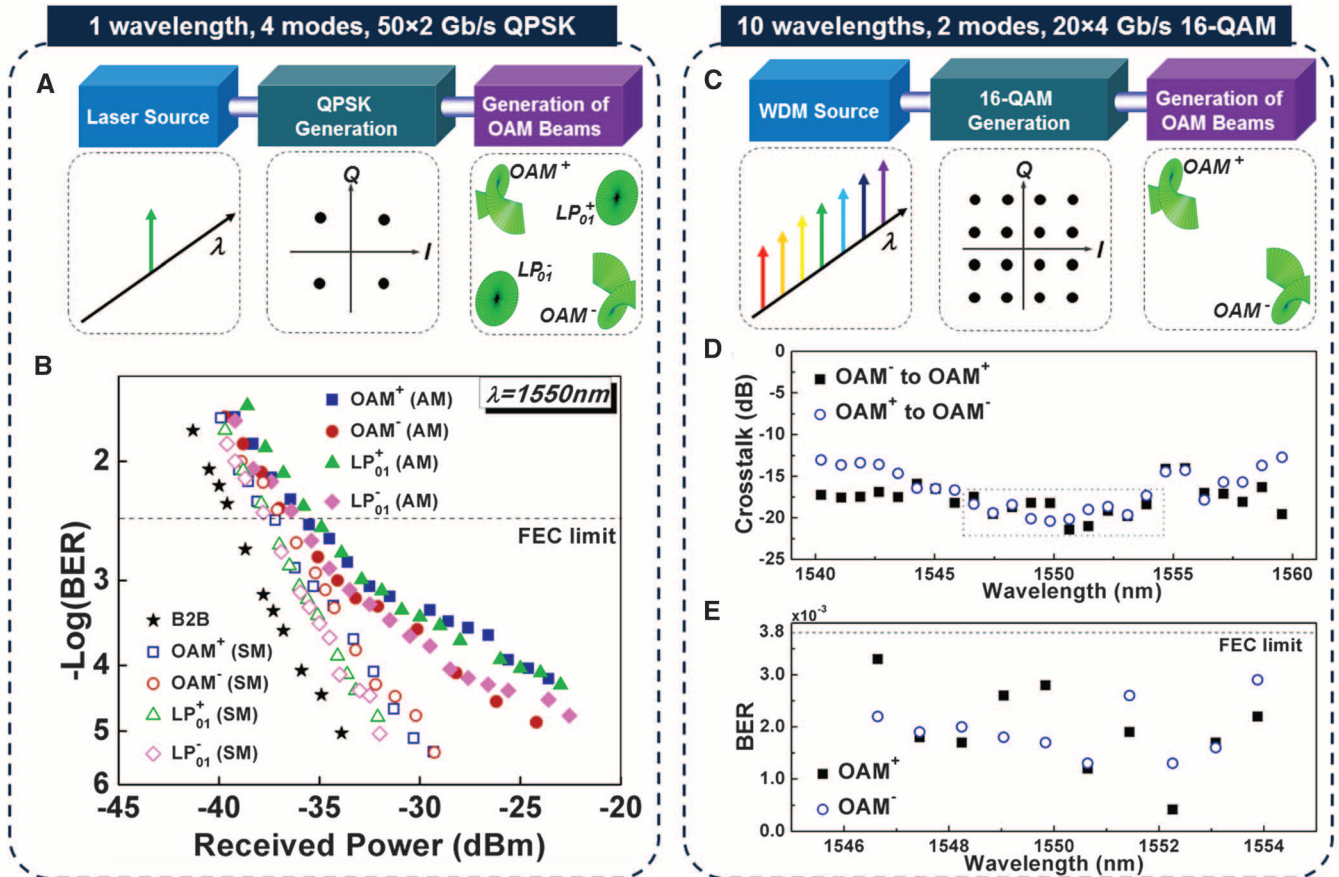


Fig. 4. Data-transmission experiments. (A) Block diagram of 50×2 Gbaud QPSK signal transmission over a single wavelength carrying four modes in the vortex fiber. (B) Measured BER as a function of received power for the single-channel (SC) and all-channels (AC) transmission case. (C) Block diagram

of 20×4 Gbaud 16-QAM signal transmission over 10 wavelengths carrying two modes in the vortex fiber. (D) Measured crosstalk between OAM^\pm modes as a function of wavelength. (E) BER as a function of wavelength for OAM^\pm modes in the WDM system.

used no computationally intensive DSP corrective algorithms, such as MIMO. Furthermore, because our OAM-MDM scheme primarily required that the vortex fiber we used enabled mode-coupling-free propagation of OAM modes, we expect this scheme to be scalable in number of modes, and thus data capacity, given recent developments on fiber designs that may be able to support propagation of multiple OAM modes with $\ell \gg 1$ (22). Because our primary goal is that of demonstrating the viability of fiber-based data transmission of independent OAM modes, we used conventional, commercial components (SLMs and wave retarders) for muxing and demuxing, which are inherently lossy as the number of OAM modes is scaled. Recent demonstrations of theoretically lossless OAM muxing devices, based on waveguides (23) or free-space optics (24), indicate that the required component technology is concurrently developing to enable realistic deployments of scalable networks based on OAM-MDM.

References and Notes

- R. Essiambre, R. Tkach, *Proc. IEEE* **100**, 1035 (2012).
- D. J. Richardson, *Science* **330**, 327 (2010).
- J. Sakaguchi *et al.*, *J. Lightwave Technol.* **30**, 658 (2012).
- R. Ryf *et al.*, *J. Lightwave Technol.* **30**, 521 (2012).
- D. Marcuse, *Appl. Opt.* **23**, 1082 (1984).
- J. Carpenter, B. C. Thomsen, T. D. Wilkinson, Degenerate mode-group division multiplexing, *J. Lightwave Technol.* **30**, 3946 (2012).
- D. Andrews, *Structured Light and Its Applications* (Academic Press, New York, 2008).
- J. Wang *et al.*, *Nat. Photonics* **6**, 488 (2012).
- S. Gröblacher, T. Jennewein, A. Vaziri, G. Weihs, A. Zeilinger, *New J. Phys.* **8**, 75 (2006).
- D. McGloin, N. B. Simpson, M. J. Padgett, *Appl. Opt.* **37**, 469 (1998).
- P. Z. Dashti, F. Alhassen, H. P. Lee, *Phys. Rev. Lett.* **96**, 043604 (2006).
- N. Bozinovic, P. Kristensen, S. Ramachandran, in *Frontiers in Optics 2011/Laser Science XXVII*, OSA Technical Digest (online) (Optical Society of America, 2011), paper LWL3; available at <http://dx.doi.org/10.1364/LS.2011.LWL3>.
- N. Bozinovic, S. Golowich, P. Kristensen, S. Ramachandran, *Opt. Lett.* **37**, 2451 (2012).
- G. K. L. Wong *et al.*, *Science* **337**, 446 (2012).
- Materials and methods are available as supplementary materials on Science Online.
- S. Ramachandran, P. Kristensen, M. F. Yan, *Opt. Lett.* **34**, 2525 (2009).
- H. Sunnerud, C. Xie, M. Karlsson, R. Samuelsson, P. A. Andrekson, *J. Lightwave Technol.* **20**, 368 (2002).
- S. Ramachandran, J. W. Nicholson, S. Ghalimi, M. F. Yan, *IEEE Photon. Technol. Lett.* **15**, 1171 (2003).
- S. Ramachandran, S. Ghalimi, J. Bromage, S. Chandrasekhar, L. L. Buhl, *IEEE Photon. Technol. Lett.* **17**, 238 (2005).
- N. Bozinovic *et al.*, in *European Conference and Exhibition on Optical Communication*, OSA Technical Digest (online), (Optical Society of America, 2013), paper Th.3.C.6; available at <http://dx.doi.org/10.1364/ECEOC.2012.Th.3.C.6>.
- Y. Yue *et al.*, in *Conference on Optical Fiber Communications*, OSA Technical Digest, paper OTh4G.2 (Optical Society of America, Washington, DC, 2013).
- P. Gregg *et al.*, in *Conference on Lasers and Electro-Optics 2013*, OSA Technical Digest (online) (Optical Society of America, 2013), paper CTu2K.2.
- T. Su *et al.*, *Opt. Express* **20**, 9396 (2012).
- G. C. Berkhout, M. P. Lavery, J. Courtial, M. W. Beijersbergen, M. J. Padgett, *Phys. Rev. Lett.* **105**, 153601 (2010).

Acknowledgments: We thank S. Golowich, P. Gregg, and P. Steinvurzel for insightful discussions and M. V. Pedersen for the numerical waveguide simulation tool. This work was funded by the Defense Advanced Research Projects Agency-InPho program. M.T. acknowledges support from the Chief Scientist Office of the Israeli Ministry of Industry, Trade and Labor within the "Tera Santa" consortium. All data related to the experiments described in this manuscript are recorded in laboratory notebooks of members in S.R.'s group, and all associated digital data are stored on networked computers at Boston University, whose contents are archived daily.

Supplementary Materials

www.sciencemag.org/cgi/content/full/340/6140/1545/DC1
Materials and Methods
Figs. S1 to S6

15 March 2013; accepted 29 May 2013
10.1126/science.1237861

Dinitrogen Cleavage and Hydrogenation by a Trinuclear Titanium Polyhydride Complex

Takanori Shima,^{1,2*} Shaowei Hu,^{1,2*} Gen Luo,³ Xiaohui Kang,^{2,3} Yi Luo,³ Zhaomin Hou^{1,2,3†}

Both the Haber-Bosch and biological ammonia syntheses are thought to rely on the cooperation of multiple metals in breaking the strong N≡N triple bond and forming an N–H bond. This has spurred investigations of the reactivity of molecular multimetallic hydrides with dinitrogen. We report here the reaction of a trinuclear titanium polyhydride complex with dinitrogen, which induces dinitrogen cleavage and partial hydrogenation at ambient temperature and pressure. By ¹H and ¹⁵N nuclear magnetic resonance, x-ray crystallographic, and computational studies of some key reaction steps and products, we have determined that the dinitrogen (N₂) reduction proceeds sequentially through scission of a N₂ molecule bonded to three Ti atoms in a μ-η¹:η²:η²-end-on-side-on fashion to give a μ₂-N/μ₃-N dinitrido species, followed by intramolecular hydrogen migration from Ti to the μ₂-N nitrido unit.

Dinitrogen (N₂) is the most abundant component (78%) of Earth's atmosphere and is largely chemically inert under ordinary conditions. Certain microbial organisms can reduce N₂ to ammonia (NH₃) by using nitrogenase enzymes at ambient temperature and pressure (1–7). In this transformation, six electrons and six protons are required to produce two equivalents of NH₃ per N₂. Industrially, NH₃ is produced in ~10⁸ tons/year quantities from N₂ and H₂ by the Haber-Bosch process, in which H₂ serves as the source of both electron and proton (8–10). This process requires relatively harsh conditions (350° to 550°C and 150 to 350 atm) to activate N₂ on the solid catalyst surface, making it energy intensive. Indeed, the Haber-Bosch ammonia synthesis consumes more than 1% of the world's annual energy supply. Both the biological and Haber-Bosch processes are thought to take place through the cooperation of multiple metal sites.

To further explore the mechanism of N₂ reduction at the molecular level and thereby develop milder chemical processes for ammonia synthesis, extensive studies on the activation of N₂ with organometallic complexes have been carried out over the past decades. By use of low-valent transition metal species or a combination of transition metal complexes with strong reducing reagents, such as KC₈, Na/Hg, or Mg, the activation of N₂ has been achieved under mild conditions (11–22). The catalytic transformation of N₂ to NH₃ has also been accomplished by using a Mo–N₂ complex (23, 24). However, these reaction systems generally require a stoichiometric excess of strong reducing agents and extra proton sources to afford NH₃. An alternative approach is the di-

rect reduction of N₂ by transition metal hydrides, which avoids the use of extra reducing agents and proton sources and may provide an entry to homogeneous catalyst systems for the synthesis of NH₃ from a mixture of N₂ and H₂. Previously, various metal hydride complexes have been reported for the activation of N₂ (25). However, most of these N₂-activating hydrides were mononuclear transition metal complexes and did not lead to N–N bond cleavage. A binuclear niobium tetrahydride complex has been reported to enable N–N bond cleavage with loss of two H₂ molecules, but the hydrogenation of the resulting nitrido species did not take place (26). A metal hydride complex that can induce both N≡N bond cleavage and N–H bond formation remains unknown, and the use of a polynuclear rather than binuclear metal hydride complex for the activation of N₂ has not been reported to date. In view of the fact that both Haber-Bosch and biological ammonia syntheses likely rely on the cooperation of multiple metal sites in the activation and hydrogenation of N₂, the investigation of the reactivity of multimetallic hydride complexes with N₂ is of great interest and importance. We report here a trinuclear titanium polyhydride complex that reacts with N₂ through N≡N bond cleavage and N–H bond formation under mild conditions without additional reducing agents or proton sources. The Ti-bound N₂ activation products and some key reaction steps have been elucidated by ¹H and ¹⁵N nuclear magnetic resonance (NMR), x-ray crystallographic, and computational studies.

We have previously reported that the hydrogenolysis of the C₅Me₄SiMe₃-ligated half-sandwich rare-earth dialkyl complexes such as [(C₅Me₄SiMe₃)Ln(CH₂SiMe₃)₂(THF)] (Ln indicates Sc, Y, Gd, Tb, Dy, Ho, Er, Tm, Yb, or Lu; Me, methyl group; and THF, tetrahydrofuran) with H₂ could easily afford the corresponding tetranuclear rare-earth octahydride complexes of a general formula {[C₅Me₄SiMe₃)Ln]₄(μ-H)₈} (27–29). The analogous tetranuclear zirconium and hafnium octahydride complexes {[C₅Me₄SiMe₃)M]₄(μ-H)₈}

(M = Zr, Hf) could also be obtained similarly by the hydrogenolysis of the alkyl precursors [(C₅Me₄SiMe₃)M(CH₂SiMe₃)₃] (30). In an attempt to synthesize a titanium analog, we carried out the hydrogenolysis of the titanium alkyl complex [(C₅Me₄SiMe₃)Ti(CH₂SiMe₃)₃] (**1**) under similar conditions (4:1 H₂:N₂ mixture at 5 atm) in an autoclave. A mixed di-imido/tetrahydrido tetranuclear titanium complex {[C₅Me₄SiMe₃)Ti]₄(μ₃-NH)₂(μ₂-H)₄} (**2**) was obtained in 90% yield as dark purple crystals (Fig. 1A), whereas the expected octahydride complex {[C₅Me₄SiMe₃)Ti]₄(μ-H)₈} was not observed. In this reaction, one N₂ molecule was formally reduced to two [NH]^{2–} imido units by H₂. The hydrogenolysis of **1** in the presence of ¹⁵N₂ afforded the isotopically enriched ¹⁵N-imido complex {[C₅Me₄SiMe₃)Ti]₄(μ₃-¹⁵NH)₂(μ₂-H)₄} (**2**-¹⁵N) [¹⁵N NMR, with a chemical shift in parts per million (δ) of 52.7 (using MeNO₂ as a standard reference) and a coupling constant of NH (*J*_{NH}) = 66.5 Hz]. Similarly, the reaction of **1** with D₂ and N₂ gave the corresponding deuterated analog {[C₅Me₄SiMe₃)Ti]₄(μ₃-ND)₂(μ₂-D)₄} (**2**-d₆). These results suggest that the NH imido units in **2** are formed by the hydrogenation of molecular nitrogen with H₂. Protonolysis of **2** and **2**-¹⁵N with anhydrous hydrochloric acid almost quantitatively afforded almost NH₄Cl and ¹⁵NH₄Cl, respectively, together with the formation of [(C₅Me₄SiMe₃)TiCl₃].

To further clarify the mechanism for the formation of **2**, we then carried out the hydrogenolysis of **1** with H₂ (4 atm) under N₂-free conditions, which afforded a nitrogen-free trinuclear titanium heptahydride complex {[C₅Me₄SiMe₃)Ti]₃(μ₃-H)(μ₂-H)₆} (**3**) in 69% yield as dark brown crystals (Fig. 1A) together with a small amount of the tetranuclear titanium octahydride complex {[C₅Me₄SiMe₃)Ti]₄(μ-H)₈} (**4**) (10%, dark purple crystals) (31). An x-ray diffraction study revealed one μ₃-H and six μ₂-H ligands in **3**, with each Ti atom also coordinated by a C₅Me₄SiMe₃ ligand (Fig. 1B). Formally, one of the three Ti atoms in **3** should be in the 4+ oxidation state, and two Ti atoms should be in the 3+ oxidation state in view of the total negative charge (10[–]) of all the ligands. However, there is no significant difference in the three Ti–Ti separation distances, which exhibit an average value (2.6479 Å) comparable with those found in the Ti(III) hydride complexes reported to have metal–metal bonding interactions (32). A density functional theory (DFT) study on a model compound {[C₅H₄SiH₃)Ti]₃(μ₃-H)(μ₂-H)₆} (**3m**) implied that the electron cloud of the highest occupied molecular orbital (HOMO) is delocalized among the three Ti metals, with Wiberg bond indexes (WBI) for the Ti–Ti bonds of 1.1058 (Ti1–Ti2), 1.1213 (Ti1–Ti3), and 1.1233 (Ti2–Ti3), respectively, consistent with Ti–Ti bonding interactions in **3**.

In agreement with the presence of Ti(III)–Ti(III) bonding interactions observed by the x-ray and DFT analyses, **3** exhibited diamagnetic behavior and showed well-resolved signals in the ¹H NMR spectrum in toluene-*d*₈. The seven hydrides appeared equivalently as a singlet at δ_H

¹Advanced Catalysis Research Group, RIKEN Center for Sustainable Resource Science, 2-1 Hirosawa, Wako, Saitama 351-0198, Japan.

²Organometallic Chemistry Laboratory, RIKEN, 2-1 Hirosawa, Wako, Saitama 351-0198, Japan. ³State Key Laboratory of Fine Chemicals and School of Pharmaceutical Science and Technology, Dalian University of Technology, Dalian 116024, China.

*These authors contributed equally to this work.

†Corresponding author. E-mail: houz@riken.jp

2.66 over a temperature range from 22° to –80°C, suggesting rapid μ_2 -H/ μ_3 -H site exchange.

The tetranuclear Ti(III) octahydride complex **4** is an analog of the zirconium and hafnium complexes $\{[(C_5Me_4SiMe_3)M]_4(\mu-H)_8\}$ reported previously (30), neither of which showed activity toward N_2 at room or even high temperatures (~120°C). In contrast, the trinuclear mixed valence Ti(III)/Ti(IV) heptahydride complex **3** showed high reactivity with N_2 , affording the imido/nitrido complex $\{[(C_5Me_4SiMe_3)Ti]_3(\mu_2-NH)(\mu_3-N)(\mu_2-H)_2\}$ (**5**) in 91% yield as dark blue crystals, upon exposure to a N_2 atmosphere (1 atm) at room temperature for 12 hours (Fig. 1B). Single crystals of **5** suitable for x-ray diffraction study were obtained by recrystallization in THF. In the solid-state structure, the nitrido atom (N1) is bonded to three Ti atoms, with one N–Ti bond [N1–Ti1: 2.071(5) Å] significantly longer than the other two almost equivalent N–Ti bonds [N1–Ti2: 1.883(5), N1–Ti3: 1.883(5) Å] (Fig. 1B). The NH imido ligand (N2) bridges one of the three Ti–Ti sides of the Ti_3 triangle [Ti2–N2: 1.937(6), Ti3–N2: 1.926(6) Å], and the other two Ti–Ti sides are each bridged by a

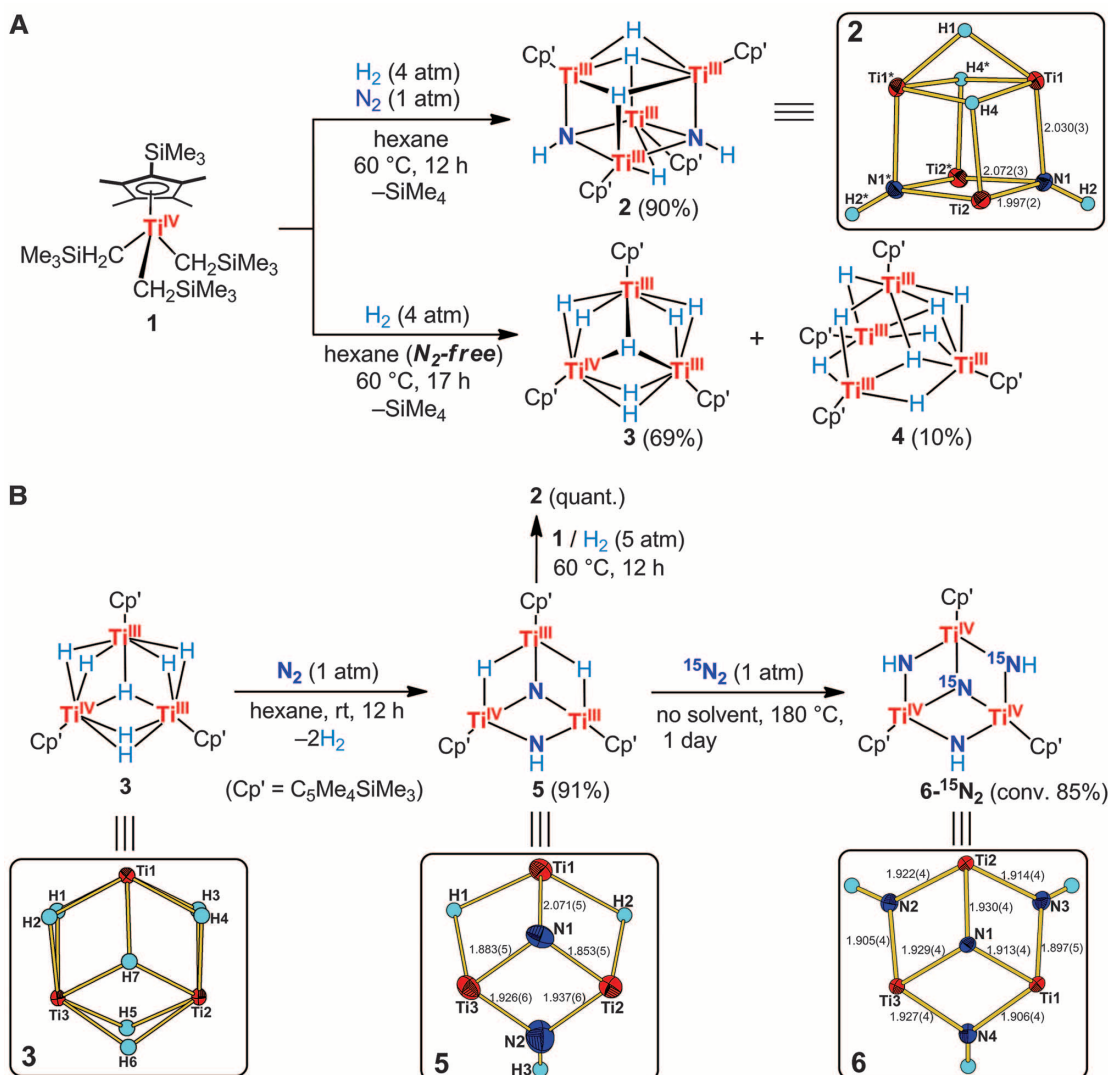
μ_2 -H ligand [Ti1–H1: 1.91(4), Ti3–H1: 1.90(4) Å; Ti1–H2: 1.92(4), Ti2–H2: 1.91(4) Å].

The reaction of **3** with $^{15}N_2$ under the similar conditions afforded the corresponding ^{15}N -enriched complex $\{[(C_5Me_4SiMe_3)Ti]_3(\mu_2-^{15}NH)(\mu_3-^{15}N)(\mu_2-H)_2\}$ (**5**- ^{15}N), confirming that the imido and nitrido units in **5** are formed by the reduction of N_2 . The ^{15}N NMR spectrum of **5**- ^{15}N in THF- d_8 at –50°C showed two broad signals at δ 402.9 and δ 46.9, which are assignable to the nitrido (μ_3 -N) and imido (μ_2 -NH) units, respectively (33). The 1H NMR spectrum of **5**- ^{15}N at –50°C showed a doublet at δ 17.62 with J_{NH} = 63.6 Hz for the imido group.

To gain more information on the formation of **5**, we monitored the reaction of **3** with $^{15}N_2$ by 1H and ^{15}N NMR spectroscopy in THF- d_8 at low temperatures (Fig. 2). The reaction of **3** with $^{15}N_2$ took place even at –30°C, leading to formation of a dinitrogen complex $\{[(C_5Me_4SiMe_3)Ti]_3-(\mu-\eta^1:\eta^2-^{15}N_2)(\mu-H)_3\}$ (**7**- ^{15}N) with release of two equivalents of H_2 (observed at δ_H 4.5) [the x-ray structure of a trimetallic Ti N_2 complex was reported recently; see (34)]. In this process,

$N\equiv N$ was formally reduced to $[N^{2-}-N^{2-}]$ by four electrons generated by reductive elimination of two molecules of H_2 from **3**. The ^{15}N NMR spectrum of **7**- ^{15}N at –30°C showed two doublets at δ_N 73.1 and 262.9 with J_{NN} = 21.5 Hz. This J_{NN} value and the large difference in chemical shift between the two ^{15}N NMR signals of **7**- ^{15}N are comparable to those observed in the binuclear tantalum end-on-side-on dinitrogen complex $\{[NPN]TaH_2\}_2N_2$ {where $[NPN]$ = $PhP(CH_2SiMe_2NPh)_2$, δ_N –20.4 and 163.6, and J_{NN} = 21.5 Hz} (35). The three hydride ligands in **7**- ^{15}N gave two singlets with a 1:2 integration ratio at δ_H 9.73 (1 H) and –13.80 (2 H) in the 1H NMR spectrum at –30°C. When the temperature was raised from –30° to –10°C, nitrogen–nitrogen bond cleavage took place to give the dinitrido (N^{3-}) complex $\{[(C_5Me_4SiMe_3)Ti]_3(\mu_3-N)(\mu_2-N)(\mu_2-H)_3\}$ (**8**- ^{15}N) almost quantitatively in 2 hours with disappearance of **7**- ^{15}N . This transformation was accompanied by the oxidation of the two Ti(III) sites to two Ti(IV) units. The ^{15}N NMR spectrum of **8**- ^{15}N at –50°C showed two singlet peaks at δ_N 593.4 and 444.8, which could be assigned to the two bridging nitrido

Fig. 1. N_2 activation by Ti complexes **1 and **3**.** (A) Hydrogenolysis of **1** in the presence of N_2 affords an imido complex **2** ($Cp' = C_5Me_4SiMe_3$), the x-ray core structure of which is shown in the square frame (Cp' ligands omitted for clarity; the N1–Ti bond lengths, with standard deviations in the parentheses, are given in angstroms). Hydrogenolysis under an N_2 -free atmosphere gives mainly a trinuclear heptahydride complex **3** together with a tetranuclear octahydride **4**.



ligands. No cross-peak with any protons was observed by ^1H - ^{15}N two-dimensional NMR spectroscopy. The three hydride units in $8\text{-}^{15}\text{N}$ showed one triplet and one doublet at δ_{H} 4.65 (1 H) and 2.67 (2 H) with $J_{\text{HH}} = 28.0$ Hz, respectively, in the ^1H NMR spectrum at -70°C . When the temperature was raised to 20°C , one of the two nitrido units in

$8\text{-}^{15}\text{N}$ was hydrogenated (or protonated) by an H ligand, yielding the mixed imido/nitrido/dihydrido complex $5\text{-}^{15}\text{N}$. In this reaction, a hydride (H^-) is oxidized to a proton (H^+), whereas the two Ti(IV) ions bridged by the hydride are formally reduced to Ti(III) (Fig. 2A), demonstrating that a hydride ligand can serve as a formal proton source

through metal reduction. The related N-H bond formation in the reactions of zirconium- N_2 and hafnium silylimido species with H_2 has been reported previously (15, 17, 36).

To have a better understanding of the mechanistic details, we performed DFT computations on a model compound of **3**, namely $[(\text{C}_5\text{H}_4\text{SiH}_3)_3\text{Ti}_3\text{H}_7]$ (**3m**). The Kohn-Sham orbital analysis revealed that the lowest unoccupied molecular orbital (LUMO) of **3m** concentrates on the Ti3 atom, facilitating access of N_2 in an end-on manner (Fig. 3A) (37). After the coordination of N_2 to Ti3, the rearrangement of some hydride ligands takes place, leading to release of one molecule of H_2 and formation of the pentahydride/dinitrogen complex $[(\text{C}_5\text{H}_4\text{SiH}_3)_3\text{Ti}_3\text{H}_5(\mu\text{-}\eta^1\text{-}\eta^2\text{-N}_2)]$ (**3m'-N**), in which the dinitrogen is bonded to two Ti atoms (Ti2 and Ti3) in a side-on-end-on fashion (Fig. 3B). The whole process is exergonic by 3.89 kcal/mol. Subsequently, release of another molecule of H_2 from **3m'-N** takes place to give the trihydride/dinitrogen complex $[(\text{C}_5\text{H}_4\text{SiH}_3)_3\text{Ti}_3\text{H}_3(\mu\text{-}\eta^1\text{-}\eta^2\text{-N}_2)]$ (**7m**), which is equivalent to the dinitrido complex $[(\text{C}_5\text{H}_4\text{SiH}_3)_3\text{Ti}_3\text{H}_3(\mu_3\text{-N})(\mu_2\text{-N})]$ (**8m**). This process is accompanied by migration of a Ti-H bond from Ti3 to Ti1. The subsequent migration of a $\mu_2\text{-H}$ ligand, which bridges Ti1 and Ti2, to the $\mu_2\text{-N}$ nitrido atom in **8m** affords the imido/nitrido product $[(\text{C}_5\text{H}_4\text{SiH}_3)_3\text{Ti}_3\text{H}_2(\mu_3\text{-N})(\mu_2\text{-NH})]$ (**5m**). To see whether N-H bond formation could precede N-N bond cleavage, we also computed the energetics of migration of an H atom to an N atom in **7m** (dashed line, Fig. 3B). However, this reaction path requires overcoming an energy barrier as high as 47.55 kcal/mol and is therefore kinetically less favorable. These computational results are in good agreement with the experimental observation of the dinitrido/trihydrido intermediate species $8\text{-}^{15}\text{N}$ as described above (Fig. 2).

The sequential N-N bond cleavage and N-H bond formation observed in the present reaction of the titanium hydride cluster **3** with N_2 stands in contrast with the reaction mechanisms previously observed in other homogeneous or surface-supported organometallic N_2 -activating systems or the FeMo nitrogenase enzymes, in which N-H bond formation generally took place before N-N bond cleavage (5, 38). In the heterogeneous Haber-Bosch process, N_2 reduction is also thought to take place on the catalyst surface first through $\text{N}\equiv\text{N}$ bond cleavage then followed by hydrogenation of the resulting nitrido species (8, 38), although details are not clear because of the difficulty in identifying the true active sites and reaction intermediates.

The dihydrido/imido/nitrido complex **5** is stable at room temperature. However, when it was heated at 180°C under N_2 (1 atm) overnight, further incorporation and reduction of N_2 took place to give the tri-imido/nitrido complex $\{[(\text{C}_5\text{Me}_4\text{SiMe}_3)\text{Ti}]_3(\mu_3\text{-N})(\mu_2\text{-NH})_3\}$ (**6**) in 85% yield. When **5** was heated with $^{15}\text{N}_2$ under the

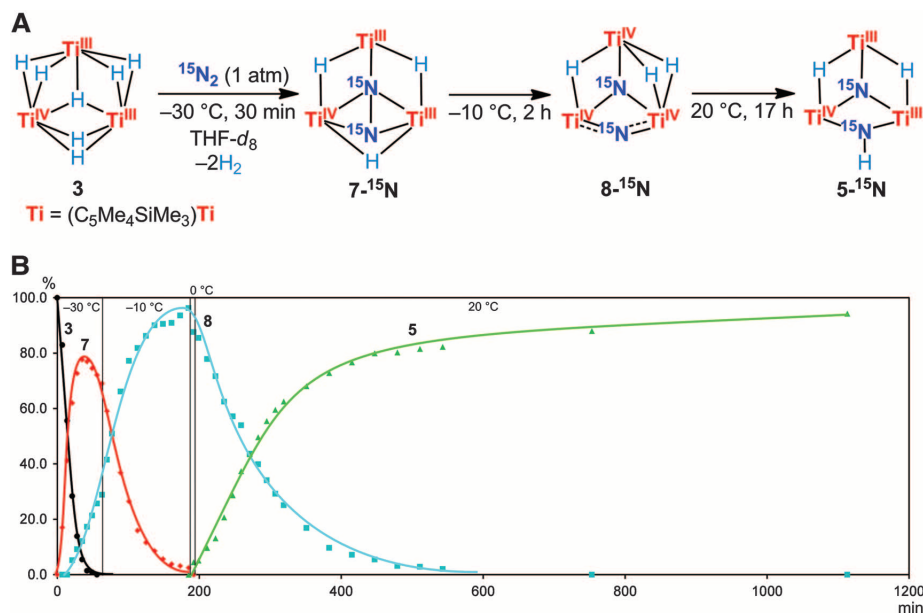


Fig. 2. NMR monitoring of reaction kinetics of **3 with N_2 .** (A) Observed intermediates in the reaction with $^{15}\text{N}_2$; oxidation states of the Ti metals are assigned formally. (B) Conversion versus time curves at the indicated temperatures. The solid lines are interpolations of the experimental data.

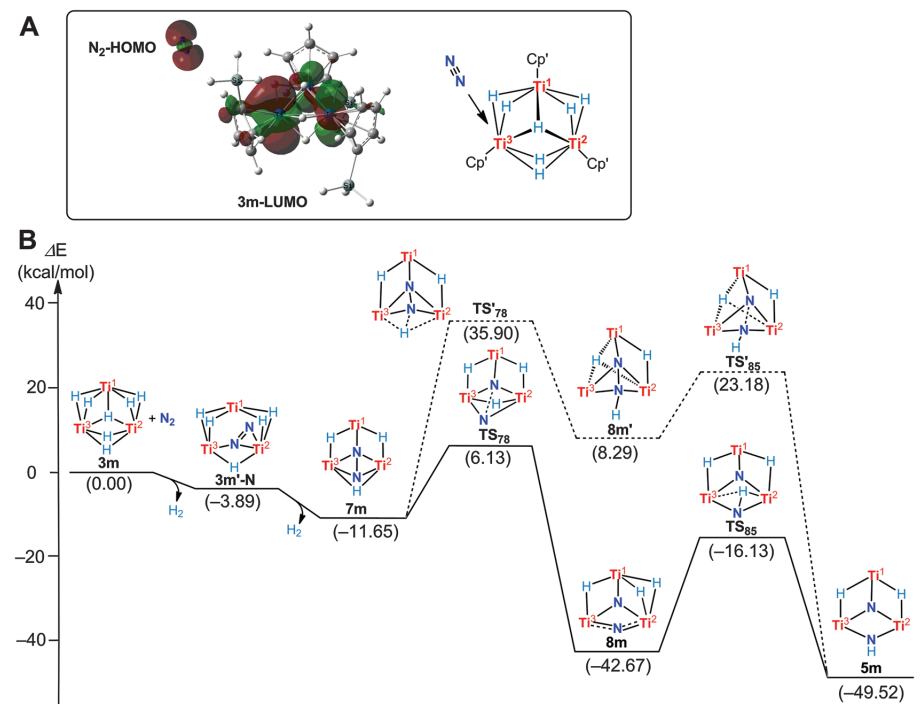


Fig. 3. Computational analysis of the reaction of **3 with N_2 .** (A) Coordination of N_2 could occur at the Ti3 atom through interaction of the LUMO of **3m** and the HOMO of N_2 . (B) DFT calculated energy profile for the reaction of **3m** with N_2 . The $\text{C}_5\text{H}_4\text{SiH}_3$ ligands have been omitted for clarity.

same conditions, the ^{15}N -enriched analog $\{[(\text{C}_5\text{Me}_4\text{SiMe}_3)\text{Ti}]_3(\mu_3\text{-}^{15}\text{N})(\mu_2\text{-}^{15}\text{NH})(\mu_2\text{-NH})_2\}(\text{6-}^{15}\text{N}_2)$ was obtained (Fig. 1B). The ^{15}N NMR spectrum of $\text{6-}^{15}\text{N}_2$ showed a singlet at δ_{N} 424.6 and a doublet at δ_{N} 101.3 with $J_{\text{NH}} = 64.0$ Hz, which could be assigned to a $\mu_3\text{-N}$ nitrido and a $\mu_2\text{-NH}$ imido unit, respectively. These results suggest that the newly incorporated N_2 molecule is split into a $\mu_3\text{-N}$ nitrido unit and a $\mu_2\text{-NH}$ imido unit, whereas the nitrido unit originally existing in **5** is hydrogenated to a $\mu_2\text{-NH}$ imido group. No apparent reaction between **5** or **6** and H_2 (up to 8 atm) was observed at room or higher temperatures (up to 150°C). However, when the hydrogenolysis of the trialkyl complex **1** with H_2 was carried out in the presence of 1 equiv of **5**, the tetranuclear di-imido complex **2** was formed quantitatively (Fig. 1B), possibly through hydrogenation of the nitrido group of **5** with a mononuclear Ti hydride species such as $(\text{C}_5\text{Me}_4\text{SiMe}_3)_3\text{TiH}_3$ formed in situ by hydrogenolysis of **1** (39). These results could account for the formation of **2** in the hydrogenolysis of **1** with H_2 in the presence of N_2 (Fig. 1A), in view of the facile formation of **3** in the hydrogenolysis of **1** in the absence of N_2 and the high reactivity of **3** with N_2 to give **5**. Although the origin of the unusually high reactivity of the trinuclear mixed valence Ti(IV)/Ti(III) heptahydride complex **3** is subject to further studies, our findings demonstrate that hydride ligands in a metal hydride cluster can serve as the source of both electron and proton and that multimetallic transition metal hydride complexes can serve as a platform for nitrogen fixation.

References and Notes

- B. K. Burgess, D. J. Lowe, *Chem. Rev.* **96**, 2983 (1996).
- R. R. Eady, *Chem. Rev.* **96**, 3013 (1996).
- J. B. Howard, D. C. Rees, *Chem. Rev.* **96**, 2965 (1996).
- J. B. Howard, D. C. Rees, *Proc. Natl. Acad. Sci. U.S.A.* **103**, 17088 (2006).
- R. R. Schrock, *Angew. Chem. Int. Ed.* **47**, 5512 (2008).
- K. M. Lancaster *et al.*, *Science* **334**, 974 (2011).
- T. Spatzal *et al.*, *Science* **334**, 940 (2011).
- G. Ertl, *Angew. Chem. Int. Ed.* **47**, 3524 (2008).
- K. Honkala *et al.*, *Science* **307**, 555 (2005).
- R. Schlögl, *Angew. Chem. Int. Ed.* **42**, 2004 (2003).
- J. Chatt, J. R. Dilworth, R. L. Richards, *Chem. Rev.* **78**, 589 (1978).
- M. Hidai, Y. Mizobe, *Chem. Rev.* **95**, 1115 (1995).
- T. A. Bazhenova, A. E. Shilov, *Coord. Chem. Rev.* **144**, 69 (1995).
- B. A. MacKay, M. D. Fryzuk, *Chem. Rev.* **104**, 385 (2004).
- M. D. Fryzuk, J. B. Love, S. J. Rettig, V. G. Young, *Science* **275**, 1445 (1997).
- A. Caselli *et al.*, *J. Am. Chem. Soc.* **122**, 3652 (2000).
- J. A. Pool, E. Lobkovsky, P. J. Chirik, *Nature* **427**, 527 (2004).
- M. Mori, *J. Organomet. Chem.* **689**, 4210 (2004).
- W. J. Evans *et al.*, *J. Am. Chem. Soc.* **126**, 14574 (2004).
- G. B. Nikiforov, I. Vidyaratne, S. Gambarotta, I. Korobkov, *Angew. Chem. Int. Ed.* **48**, 7415 (2009).
- M. M. Rodriguez, E. Bill, W. W. Brennessel, P. L. Holland, *Science* **334**, 780 (2011).
- C. E. Laplaza, C. C. Cummins, *Science* **268**, 861 (1995).
- D. V. Yandulov, R. R. Schrock, *Science* **301**, 76 (2003).
- K. Arashiba, Y. Miyake, Y. Nishibayashi, *Nat. Chem.* **3**, 120 (2011).
- J. Ballmann, R. F. Munhá, M. D. Fryzuk, *Chem. Commun.* **46**, 1013 (2010).
- F. Akagi, T. Matsuo, H. Kawaguchi, *Angew. Chem. Int. Ed.* **46**, 8778 (2007).
- M. Nishiura, Z. Hou, *Nat. Chem.* **2**, 257 (2010).
- Z. Hou, M. Nishiura, T. Shima, *Eur. J. Inorg. Chem.* **2007**, 2535 (2007).
- M. Nishiura, J. Baldamus, T. Shima, K. Mori, Z. Hou, *Chem. Eur. J.* **17**, 5033 (2011).
- S. Hu, T. Shima, Y. Luo, Z. Hou, *Organometallics* **32**, 2145 (2013).
- The hydrogenolysis of **1** under a higher H_2 pressure (80 atm) at 60°C led to formation of a larger amount of the octahydride **4** (~20%) and a smaller amount of the heptahydride **3** (~50%).
- T. Matsuo, H. Kawaguchi, *Organometallics* **22**, 5379 (2003).
- H. W. Roesky, Y. Bai, M. Noltemeyer, *Angew. Chem. Int. Ed. Engl.* **28**, 754 (1989).
- S. P. Semproni, C. Milsman, P. J. Chirik, *Organometallics* **31**, 3672 (2012).
- M. D. Fryzuk, S. A. Johnson, S. J. Rettig, *J. Am. Chem. Soc.* **120**, 11024 (1998).
- S. P. Semproni, E. Lobkovsky, P. J. Chirik, *J. Am. Chem. Soc.* **133**, 10406 (2011).
- A similar DFT study showed that the reaction of the tetranuclear Ti octahydride complex **4** with N_2 is less favored, because its LUMO is distributed on the four Ti atoms with competitive orbital contribution and is unsuitable in orbital shape for an overlap with the HOMO of N_2 (see fig. S26 and table S3 in the supplementary materials).
- P. Avenier *et al.*, *Science* **317**, 1056 (2007).
- The hydrogenation of the nitrido group of **5** with a mixed alkyl/hydride species formed in situ by partial hydrogenolysis of **1** followed by further hydrogenolysis of the alkyl species could not be ruled out in this case.

Acknowledgments: This work was supported by a Grant-in-Aid for Young Scientists (B) (no. 21750068) and a Grant-in-Aid for Scientific Research (S) (no. 21225004) from the Japan Society for the Promotion of Science, an Incentive Research Grant from RIKEN, and grants from the National Natural Science Foundation of China (nos. 21028001 and 21174023). We gratefully appreciate access to the RIKEN Integrated Cluster of Clusters and the Network and Information Center of Dalian University of Technology for computational resources. Metrical parameters for the structures of compounds **2** to **6** are available free of charge from the Cambridge Crystallographic Data Centre under reference nos. CCDC-937384 to 937388. Correspondence on DFT calculations should be sent to Y.L. (luoyi@dlut.edu.cn). Z.H., T.S., and S.H. conceived and designed the experiments. S.H. carried out most of the experiments. T.S. carried out the x-ray analyses and part of the experiments. G.L., X.K., and Y.L. performed the DFT calculations. Z.H., T.S., and S.H. analyzed the data and co-wrote the manuscript. Z.H. directed the project.

Supplementary Materials

www.sciencemag.org/cgi/content/full/340/6140/1549/DC1
Materials and Methods
Figs. S1 to S26
Tables S1 to S3
Scheme S1
References (40–50)

3 April 2013; accepted 13 May 2013
10.1126/science.1238663

The Origin of Lunar Mascon Basins

H. J. Melosh,^{1,2*} Andrew M. Freed,¹ Brandon C. Johnson,² David M. Blair,¹ Jeffrey C. Andrews-Hanna,³ Gregory A. Neumann,⁴ Roger J. Phillips,⁵ David E. Smith,⁶ Sean C. Solomon,^{7,8} Mark A. Wieczorek,⁹ Maria T. Zuber⁶

High-resolution gravity data from the Gravity Recovery and Interior Laboratory spacecraft have clarified the origin of lunar mass concentrations (mascons). Free-air gravity anomalies over lunar impact basins display bull's-eye patterns consisting of a central positive (mascon) anomaly, a surrounding negative collar, and a positive outer annulus. We show that this pattern results from impact basin excavation and collapse followed by isostatic adjustment and cooling and contraction of a voluminous melt pool. We used a hydrocode to simulate the impact and a self-consistent finite-element model to simulate the subsequent viscoelastic relaxation and cooling. The primary parameters controlling the modeled gravity signatures of mascon basins are the impactor energy, the lunar thermal gradient at the time of impact, the crustal thickness, and the extent of volcanic fill.

High-resolution gravity data obtained from NASA's dual Gravity Recovery and Interior Laboratory (GRAIL) spacecraft now provide unprecedented measurements of the gravity anomalies associated with lunar

impact basins (*1*). These gravity anomalies are the most striking and consistent features of the Moon's large-scale gravity field. Positive gravity anomalies in basins partially filled with mare basalt, such as Humorum (Fig. 1), have been

known since 1968, when lunar mass concentrations, or "mascons," were discovered (*2*). Mascons have subsequently been identified in association with impact basins on Mars (*3*) and Mercury (*4*). Previous analysis of lunar gravity and topography data indicated that at least nine such mare basins possess central positive anomalies, exceeding that attributable to lava emplacement

¹Department of Earth, Atmospheric, and Planetary Sciences, Purdue University, 550 Stadium Mall Drive, West Lafayette, IN 47907, USA. ²Department of Physics, Purdue University, 525 Northwestern Avenue, West Lafayette, IN 47907, USA. ³Department of Geophysics, Colorado School of Mines, 1500 Illinois Street, Golden, CO 80401-1887, USA. ⁴Solar System Exploration Division, NASA Goddard Space Flight Center, Greenbelt, MD 20771, USA. ⁵Planetary Science Directorate, Southwest Research Institute, Boulder, CO 80302, USA. ⁶Department of Earth, Atmospheric and Planetary Sciences, Massachusetts Institute of Technology, Cambridge, MA 02139-4307, USA. ⁷Department of Terrestrial Magnetism, Carnegie Institution of Washington, Washington, DC 20015, USA. ⁸Lamont-Doherty Earth Observatory, Columbia University, Palisades, NY 10964, USA. ⁹Institut de Physique du Globe de Paris, Sorbonne Paris Cité, Université Paris Diderot, 75205 Paris Cedex 13, France.

*Corresponding author. E-mail: jmelosh@purdue.edu

alone (5). This result is confirmed with GRAIL observations over basins that lack basaltic infilling, such as Freundlich-Sharonov (Fig. 1), which are also characterized by a central positive free-air gravity anomaly surrounded by a concentric gravity low. These positive anomalies indicate an excess of subsurface mass beyond that required for isostatic (mass) balance—a “superisostatic” state. Mascon formation seems ubiquitous in lunar basins, whether mare-filled or not, despite their formation by impacts (a process of mass removal that leaves a topographic low, which normally implies a negative gravity anomaly), making mascons one of the oldest puzzles of lunar geophysics. Their elucidation is one of the goals of the GRAIL mission.

The gravity anomaly structure of lunar mascon basins was previously attributed to mantle rebound during collapse of the transient crater cavity (5, 6). This process requires a lithosphere beneath the basin capable of supporting a superisostatic load immediately after impact, a proposal that conflicts with the expectation that post-impact temperatures were sufficiently high to melt both crustal and mantle rocks (7). Alternatively, it was proposed (8) that mascons are created by flexural uplift of a thickened annulus of subisostatic (a deficiency of the subsurface mass required for isostasy) crust surrounding the basin, concomitantly lifting the basin interior as it cooled and the underlying lithosphere became stronger. This alternative model emphasizes the annulus of

anomalously low gravitational acceleration surrounding all mascons (Fig. 1) (1, 9, 10), a feature previously attributed to thickened crust (5, 6) or perhaps brecciation of the crust during impact. Many mascons also exhibit an annulus of positive gravitational acceleration surrounding the annulus of negative gravity anomaly, so the gravity structure of most lunar basins resembles a bullseye target (Fig. 1).

The role of uplift in the formation of mascon basins has been difficult to test because little is known about the mechanical state of basins immediately after cavity collapse. Here, we couple GRAIL gravity and lunar topography data from the Lunar Orbiter Laser Altimeter (LOLA) (11) with numerical modeling to show that the gravity anomaly pattern of a mascon is the natural consequence of impact crater excavation in the warm Moon, followed by post-impact isostatic adjustment (12) during cooling and contraction (13) of a voluminous melt pool. In mare-filled basins, this stage in basin evolution was followed by emplacement of mare-basalt lavas and associated subsidence and lithospheric flexure.

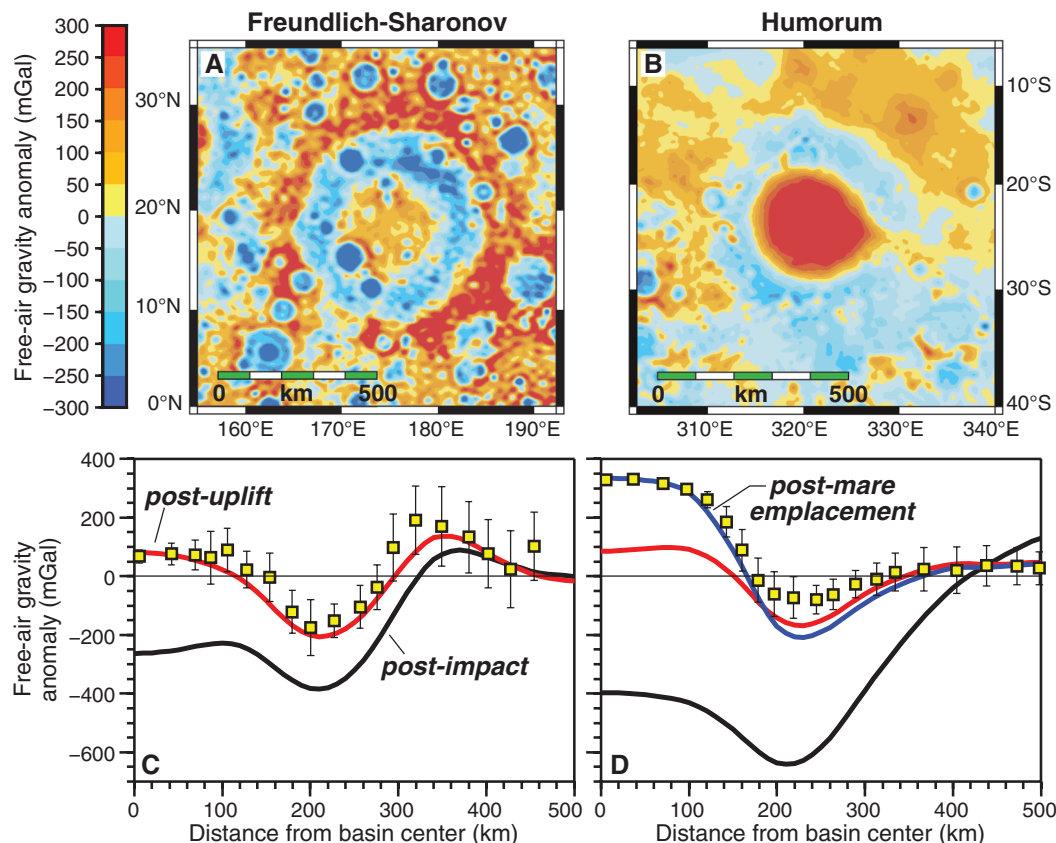
We used the axisymmetric iSALE hydrocode (14–16) to simulate the process of crater excavation and collapse. Our models used a typical lunar impact velocity of 15 km/s (17) and a two-layer target simulating a fractured gabbroic lunar crust (density = 2550 kg/m³) (18) and a dunite mantle (3200 kg/m³). Our objective was to simulate the cratering process that led to the

Freundlich-Sharonov and Humorum basins, which are located in areas where the crustal thickness is 40 and 25 km, respectively, as inferred from GRAIL and LOLA observations (18). We sought a combination of impactor diameter and lunar thermal gradient that yielded an annulus of thickened crust at a radius of ~200 km, a result which is consistent with the annulus of negative free-air gravity anomaly around those basins.

The dependence of material strength on temperature and pressure has the most marked effect on the formation of large impact basins (19). With little certainty regarding the temperature–depth profile of the early Moon or the diameter of the impactor, we considered impactor diameters ranging from 30 to 80 km and three possible shallow thermal gradients (20)—10, 20, and 30 K/km—from a 300 K surface. To avoid melted material in the mantle, the thermal profile was assumed to follow that for a subsolidus convective regime (0.05 K/km adiabat) at temperatures above 1300 K. We found that impact at vertical incidence of a 50-km-diameter impactor in conjunction with a 30 K/km initial thermal gradient best matched the extent of the annular gravity low and led to an increase in crustal thickness of 10 to 15 km at a radial distance of 200 to 260 km from both basin centers (Fig. 2), despite the differences in initial crustal thickness (21).

A crucial aspect of the model is the formation of the subisostatic collar of thickened crust surrounding the deep central pool of melted mantle

Fig. 1. Free-air gravity anomalies over (A) the mare-free Freundlich-Sharonov basin (radius to the center of the free-air gravity low is 210 km) and (B) the mare-filled Humorum basin (radius to the center of the annular free-air gravity low is 230 km) from GRAIL observations (2). (C and D) Comparison of observed and calculated free-air gravity anomalies for the Freundlich-Sharonov and Humorum basins, respectively. The observed anomalies and associated 1-SD ranges were derived from averages of the data within concentric rings at different radial distances. The black lines represent the predicted gravity anomaly just after impact and transient cavity collapse, from the hydrocode calculation. The red lines represent the predicted anomaly after isostatic response and cooling, a state which is appropriate for comparison with the Freundlich-Sharonov data. The blue line in (D) represents the predicted gravity anomaly after mare emplacement in the Humorum basin and is appropriate for comparison with data from that basin.



rock. The crust is thickened as the impact ejects crustal material onto the cool, strong, preexisting crust. The ejected material forms a wedge ~15 km thick at its inner edge that thins with increasing distance from the center. The preexisting crust is drawn downward and into the transient crater cavity because of a combination of loading by ejecta and inward flow of the underlying mantle, deforming it into a subsisostatic configuration. This arrangement is maintained by the frictional strength of the cool (but thoroughly shattered) crust, as well as by the viscoelastic mantle that requires time to relax. It is the subsequent relaxation of the mantle that leads to a later isostatic adjustment. The result is a thick, low-density crustal collar around the central hot melt pool that is initially prevented from mechanically rebounding from its disequilibrium state. The higher thermal gradient of 30 K/km, somewhat counterintuitively, yields a thicker subsisostatic crustal collar than the thermal gradients of 10 and 20 K/km. This difference occurs because the weaker mantle associated with a higher thermal gradient flows more readily during the collapse of the transient crater, exerting less inward drag on the crustal collar, which consequently experiences less stretching and thinning.

Calculations suggest that the impact into relatively thin crust at Humorum basin fully exposed mantle material in the central region of the basin (Fig. 2B), whereas a ~15-km-thick cap of crustal material flowed over the central region of the Freundlich-Sharonov basin (Fig. 2A). This crustal cap was warm, weak, lower crustal material that migrated to the basin center during crater collapse (fig. S1). At the end of the crater collapse process, the basins (defined by their negative topography) were 6 to 7 km deep out to 150 km from the basin center, with shallow negative topography continuing to a radial distance of 350 to 400 km, approximately twice the excavation radius. A substantial melt pool, defined as mantle at temperatures above 1500 K, developed in both basins. This melt pool extended out to ~150 km from the basin center and to more than 100 km depth (Fig. 2).

To model the subsequent evolution of the basins, we used the finite element code Abaqus (22, 23). We developed axisymmetric models of the Humorum and Freundlich-Sharonov basins from the hydrocode output, adjusting the thermal structure of the melt to account for rapid post-impact convection and thermal homogenization of the melt pool. The density of solid and liquid silicate material was calculated from the bulk composition of the silicate Moon (21, 24).

Our models (Fig. 1, C and D) show that the depressed basin topography, the thickened crustal collar, and the lower density of heated material combine to create a substantial negative free-air gravity anomaly at the basin centers (21). The post-impact free-air anomaly is slightly positive outside of the basin owing to ejecta supported by the cool, strong crust and mantle. The overall shape of the modeled post-impact free-air gravity

anomaly is similar to that observed but is much more negative, suggesting that the general pattern of the observed gravity anomaly is the result of the impact, but that subsequent evolution of the basin drove the central anomalies positive.

As the impact-heated mantle beneath the basin cooled, the pressure gradient from its exterior to its interior drove viscoelastic flow toward the basin center, uplifting the basin floor. The inner basin (where the central mascon develops) cannot rise above isostatic equilibrium solely because of forces from its own subsisostatic state. However, mechanical coupling between the inner and outer basin—where the collar of thickened crust was also rising isostatically—provided additional lift to the inner basin floor, enabling it to achieve a supersisostatic state. This mechanical coupling is

achieved if the lithosphere above the melt pool thickened sufficiently as it cooled. In the case of the Freundlich-Sharonov basin, the 15-km-thick layer of cool crust provided an initial (if thin) lithosphere from the beginning, which thickened as the underlying mantle cooled. For Humorum basin, the melt pool reached the surface and thus there was initially no lithosphere, although one developed during cooling. Our calculations show that if the viscosity of the mantle outside the melt pool is consistent with dry dunite, its viscoelastic strength would delay isostatic uplift of the basin floor so that lithospheres sufficient for development of a mascon develop over the melt pools in both basins. In addition to these isostatic forces, cooling increases the density of the melt through contraction; given a strong lithosphere that hin-

Fig. 2. Vertical cross section of crust and mantle geometry and thermal structure after crater collapse (2 hours after impact) for the (A) Freundlich-Sharonov basin (40-km-thick original crust) and (B) Humorum basin (25-km-thick original crust), according to the hydrocode calculation.

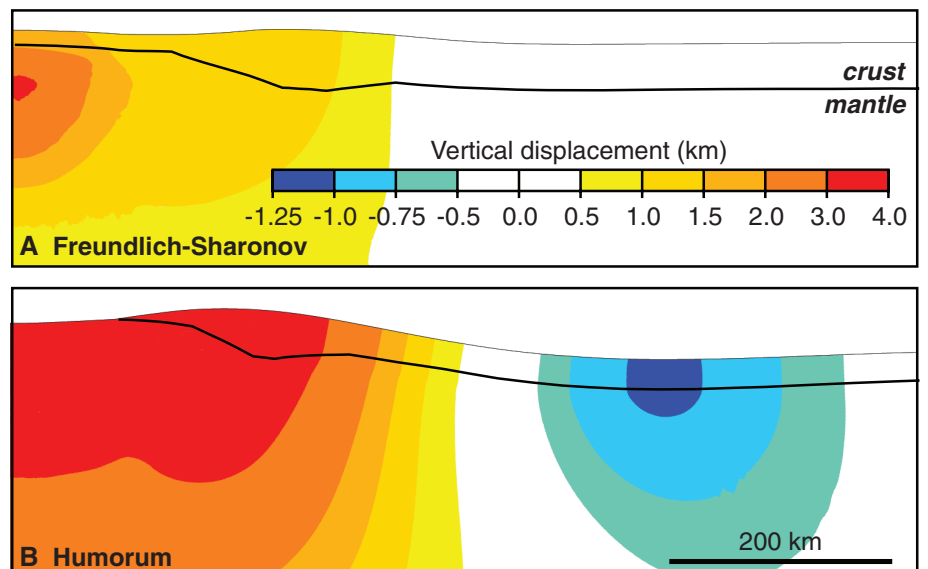
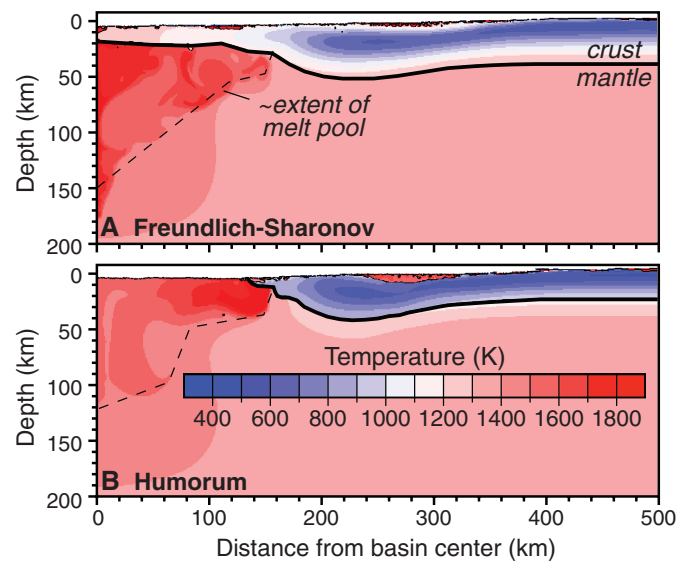


Fig. 3. Vertical displacement calculated by the finite element model relative to the initial post-crater-collapse configuration predicted by the hydrocode for the unfilled (A) Freundlich-Sharonov basin and (B) Humorum basin. The deformation is exaggerated by a factor of 10.

ders the sinking of this higher-density material, this process further increases the gravity anomaly at the basin center. The net effect is that isostatic uplift of the surrounding depressed surface topography and crustal collar, combined with cooling and contraction of the melt pool, create the central positive free-air anomaly. The flexural strength that enables the inner basin to rise into a superisostatic state prevents the outer basin from fully rising to isostatic equilibrium, leaving the observed ring of negative free-air anomaly that surrounds the inner basin.

Isostatic uplift raised the surface topography of the Freundlich-Sharonov basin by ~2 km at the center of the basin (Fig. 3A). These effects place the final basin depth at just over 4 km, a value which is consistent with LOLA elevation measurements (11, 21). For the Humorum basin, the inner basin was calculated to rise ~3 km (Fig. 3B). This uplift distribution would have left the Humorum basin ~4 km deep before mare fill. Infilling of a 3-km-thick mare unit and associated subsidence brings the floor depth of the Humorum basin to just over 1.5 km deep, modestly deeper than the 1 km depth measured by LOLA (21).

The free-air gravity anomalies of both basins increased markedly after crater collapse as a result of cooling and isostatic uplift. The free-air anomaly of the Freundlich-Sharonov basin is predicted to have risen to a positive 80 mGal in the inner basin and ~200 mGal in the outer basin above the thickened crust, which are figures in excellent agreement with GRAIL observations (Fig. 1C, red line) (1). Furthermore, the model predicts an outer annulus of positive anomalies, which is also in agreement with observations. A similar post-impact increase in the free-air anomaly is observed in our model of Humorum basin (Fig. 1D, red line), although this gravity anomaly cannot be verified because the Humorum basin was subsequently partially filled with mare basalt. Our results support the inference that lunar basins possess a positive gravity anomaly in excess of the mare load (5). As a final step in our analysis, we emplaced a mare unit 3 km thick and 150 km in radius (tapered to zero thickness over the outermost 50 km in radial distance) within the Humorum basin. The addition of the mare increases the mascon at the center of the Humorum basin to 320 mGal (Fig. 1D, blue line), matching GRAIL measurements (1).

This basin evolution scenario depends primarily on the energy of the impactor, the thermal gradient of the Moon at the time of the impact, and the thickness of the crust. A high thermal gradient enables weaker mantle to flow more readily during the collapse of the transient crater, resulting in less inward motion and thinning of the crust. In contrast to hydrocode parameters that control crater excavation and collapse, such as the energy of the impactor and the initial thermal gradient, the close match of our predicted free-air gravity anomalies to those observed by GRAIL is not a product of finding a special combination of finite-element model parameters as-

sociated with isostatic uplift and cooling. These processes are controlled by the evolution of the density and viscosity structure in the model, which follow from the mineralogy of the lunar crust and mantle and the evolution of temperature as the region conductively cools.

References and Notes

1. M. T. Zuber *et al.*, *Science* **339**, 668 (2013).
2. P. M. Muller, W. L. Sjogren, *Science* **161**, 680 (1968).
3. D. E. Smith *et al.*, *J. Geophys. Res.* **98**, 20,871 (1993).
4. D. E. Smith *et al.*, *Science* **336**, 214 (2012).
5. G. A. Neumann, M. T. Zuber, D. E. Smith, F. G. Lemoine, *J. Geophys. Res.* **101**, 16,841 (1996).
6. M. A. Wieczorek, R. J. Phillips, *Icarus* **139**, 246 (1999).
7. E. Pierazzo, H. J. Melosh, *Icarus* **145**, 252 (2000).
8. J. C. Andrews-Hanna, *Lunar Planet. Sci.* **43**, 2804 (2012).
9. W. L. Sjogren, R. N. Wimbey, W. R. Wollenhaupt, *Moon* **9**, 115 (1974).
10. M. T. Zuber, D. E. Smith, F. G. Lemoine, G. A. Neumann, *Science* **266**, 1839 (1994).
11. D. E. Smith *et al.*, *Geophys. Res. Lett.* **37**, L18204 (2010).
12. "Isostatic adjustment" as used here is the process by which the stresses imparted in a non-isostatic crust-mantle volume are relieved as they drive density boundaries toward mass balance (isostasy). The level of isostasy achieved depends on viscosity-controlled flow and also on the finite strength of the system as characterized by lithospheric flexure. This "isostatic adjustment" includes the uplift of the basin center to a superisostatic position as a result of its flexural coupling to the subisostatic annulus.
13. H. J. Melosh, D. M. Blair, A. M. Freed, *Lunar Planet. Sci.* **43**, 2596 (2012).
14. A. A. Amsden, H. M. Ruppel, C. W. Hirt, *LANL Rep. LA-8095*, 101 pp., Los Alamos Natl. Lab., Los Alamos, N. M. (1980).
15. G. S. Collins, H. J. Melosh, B. A. Ivanov, *Meteorit. Planet. Sci.* **39**, 217 (2004).
16. K. Wünnemann, G. S. Collins, H. J. Melosh, *Icarus* **180**, 514 (2006).
17. The precise value of the impact velocity is not critical for this computation because a lower impact velocity can be compensated by a larger impactor, and vice versa. The impact velocity distribution on the Moon is strongly skewed toward high velocities, with a mode at 10 km/s and a median of ~15 km/s (25).
18. M. A. Wieczorek *et al.*, *Science* **339**, 671 (2013).
19. B. A. Ivanov, H. J. Melosh, E. Pierazzo, in *Large Meteorite Impacts and Planetary Evolution IV*, W. U. Reimold, R. L. Gibson, Eds. (Special Paper 465, Geological Society of America, Boulder, Colo., 2010), pp. 29–49.
20. G. Schubert, D. L. Turcotte, P. Olson, *Mantle Convection in the Earth and Planets* (Cambridge Univ. Press, Cambridge, 2001).
21. More detailed descriptions of these models and methods are available as supplementary materials on Science Online.
22. A. M. Freed, S. C. Solomon, T. R. Watters, R. J. Phillips, M. T. Zuber, *Earth Planet. Sci. Lett.* **285**, 320 (2009).
23. A. M. Freed *et al.*, *J. Geophys. Res.* **117**, E00L06 (2012).
24. S. R. Taylor, *Planetary Science: A Lunar Perspective* (Lunar and Planetary Institute, Houston, TX, 1982).
25. M. Le Feuvre, M. A. Wieczorek, *Icarus* **214**, 1 (2011).

Acknowledgments: The GRAIL mission is supported by NASA's Discovery Program and is performed under contract to the Massachusetts Institute of Technology and the Jet Propulsion Laboratory. The Lunar Reconnaissance Orbiter LOLA investigation is supported by the NASA Science Mission Directorate under contract to the NASA Goddard Space Flight Center and Massachusetts Institute of Technology. Data from the GRAIL and LOLA missions have been deposited in the Geosciences Node of NASA's Planetary Data System.

Supplementary Materials

www.sciencemag.org/cgi/content/full/science.1235768/DC1
Supplementary Text
Figs. S1 to S6
Tables S1 to S4
References (26–43)

28 January 2013; accepted 16 May 2013
Published online 30 May 2013;
10.1126/science.1235768

Continuous Permeability Measurements Record Healing Inside the Wenchuan Earthquake Fault Zone

Lian Xue,^{1,2*} Hai-Bing Li,² Emily E. Brodsky,¹ Zhi-Qing Xu,² Yasuyuki Kano,³ Huan Wang,² James J. Mori,³ Jia-Liang Si,² Jun-Ling Pei,⁴ Wei Zhang,^{2,5} Guang Yang,^{2,6} Zhi-Ming Sun,⁴ Yao Huang⁷

Permeability controls fluid flow in fault zones and is a proxy for rock damage after an earthquake. We used the tidal response of water level in a deep borehole to track permeability for 18 months in the damage zone of the causative fault of the 2008 moment magnitude 7.9 Wenchuan earthquake. The unusually high measured hydraulic diffusivity of 2.4×10^{-2} square meters per second implies a major role for water circulation in the fault zone. For most of the observation period, the permeability decreased rapidly as the fault healed. The trend was interrupted by abrupt permeability increases attributable to shaking from remote earthquakes. These direct measurements of the fault zone reveal a process of punctuated recovery as healing and damage interact in the aftermath of a major earthquake.

The initiation and propagation of earthquakes depend critically on the hydrogeologic properties of the fault zone, including the fracture-dominated damage zone (1–6). Fault zone permeability serves as a proxy for fracturing and healing, as the fault regains strength

during one of the most unconstrained phases of the earthquake cycle (7). In addition, permeability and storage help to govern the pore pressure and effective stress on a fault. Because earthquakes generate fractures in a damage zone around a fault, it is reasonable to expect that after a large

earthquake, the fault zone permeability transiently increases. Over time, the permeability may decrease as a result of a combination of chemical and mechanical processes (7). However, measuring in situ fault zone hydrogeologic properties requires post-earthquake rapid-response drilling, and appropriate data have not previously been recorded continuously immediately after a large earthquake.

¹Department of Earth and Planetary Sciences, University of California, Santa Cruz, CA 95064, USA. ²State Key Laboratory of Continental Tectonic and Dynamics, Institute of Geology, Chinese Academy of Geological Sciences, Beijing 100037, China. ³Disaster Prevention Research Institute, Kyoto University, Gokasho, Uji, Kyoto 6110011, Japan. ⁴Institute of Geomechanics, Chinese Academy of Geological Sciences, Beijing 100081, China. ⁵Shandong Provincial Lunan Geo-engineering Exploration Institute, Yanzhou, Shandong 272100, China. ⁶Guangdong Zhuhai Engineering Investigation Institute, Zhuhai 519000, China. ⁷No. 6 Brigade of Jiangsu Geology and Mineral Resources Bureau, Lianyungang, Jiangsu 222023, China.

*Corresponding author. E-mail: lxue3@ucsc.edu

Fig. 1. Location and sketch of the WFSD-1 site.

Red lines in the inset indicate the main rupture zone; the red star is the epicenter of the Wenchuan earthquake. In the sketch, the black line is the fault core, which is surrounded by the damage zone. The borehole is 1201 m deep, and 800 to 1201 m is the open interval where water can flow into the hole from the formation (white arrows). The fault that was most likely active during the Wenchuan earthquake is the major lithological boundary between the pre-Cambrian Pengguan complex and the Triassic sediments at 590 m.

The devastating moment magnitude 7.9 Wenchuan earthquake occurred on 12 May 2008 and was the largest seismic event in China in the past 50 years. Shortly afterward, the Wenchuan earthquake Fault Scientific Drilling Project (WFSD) constructed a series of boreholes penetrating the main rupture zone. The first borehole (WFSD-1; 31.1°N, 103.7°E) is 1201 m deep and nearly vertical, in a locale with 6 m of vertical displacement at the surface (8). The borehole is open to fluid flow in the formation below 800 m (Fig. 1) and provides a unique opportunity to directly measure fault zone permeability over time. The borehole intersects the likely principal slip zone at a depth of 590 m, which is a major lithological boundary between the upthrust Pre-Cambrian Pengguan granitic and volcanic complex and the underlying Triassic sediments (8, 9). The fault breccia extends to 760 m, and the fracture density remains high to the bottom of the borehole (8). Mature faults have damage zones extending at least ~100 m from the

edge of the fault core (10). Therefore, the damage zone of this site is expected to extend into the open interval beginning at 800 m.

We measured the water level response to tidal forcing in WFSD-1 to constrain the average hydrogeologic properties of the damage zone between 800 and 1200 m below the ground surface [~200 to 600 m below the principal slip zone (8, 9)]. We used these measurements to infer the hydraulic diffusivity and permeability variations inside the Wenchuan earthquake fault zone from 1 January 2010 to 6 August 2011. The WFSD-1 pressure transducer recorded data with a sample rate of 2 min and at a resolution of 6 mm (Fig. 2). Data gaps occurred every month or two, when the instruments were removed from the well to retrieve the data and measure temperature profiles. The raw records show clear tidal oscillations superimposed on the long-term recharge trend (Fig. 2).

The tidal oscillations serve as probes of the fault's hydrogeologic properties. The tidal forcing

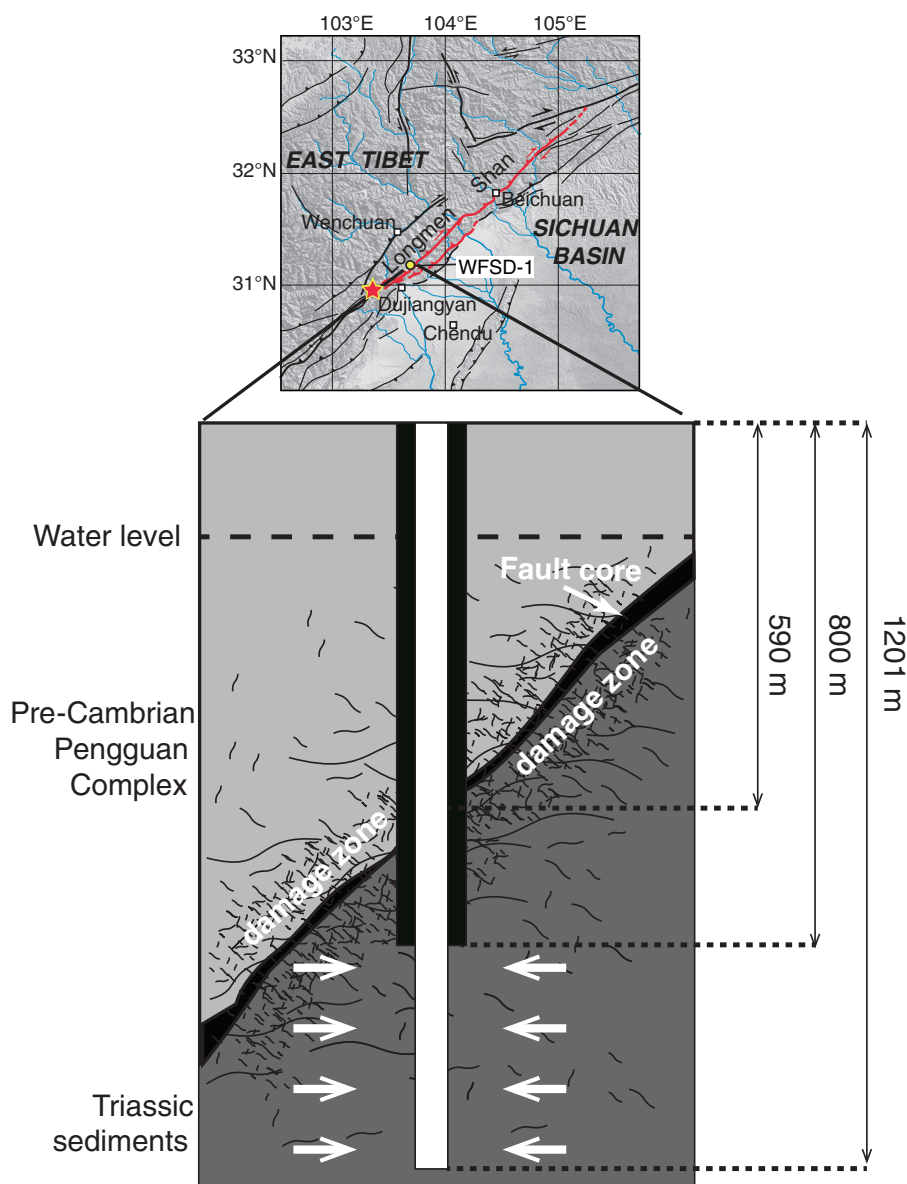


Fig. 2. Water levels from WFSD-1 recorded from 1 January 2010 to 6 August 2011. The oscillations in the inset are generated by Earth tides. The precision of the water level measurement is 6 mm. Water level is assumed to be continuous across the data gaps. The measured water level is the height of water above the pressure transducer.

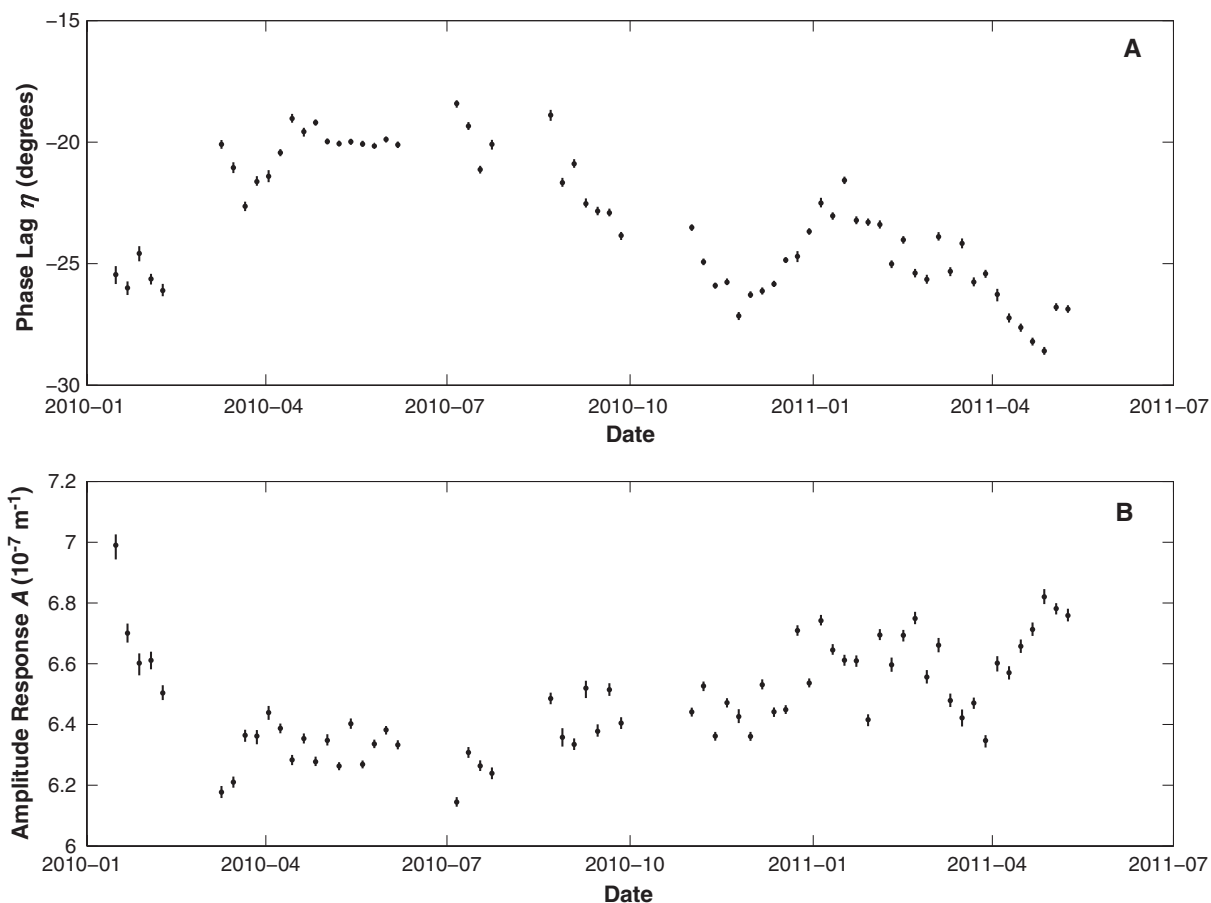
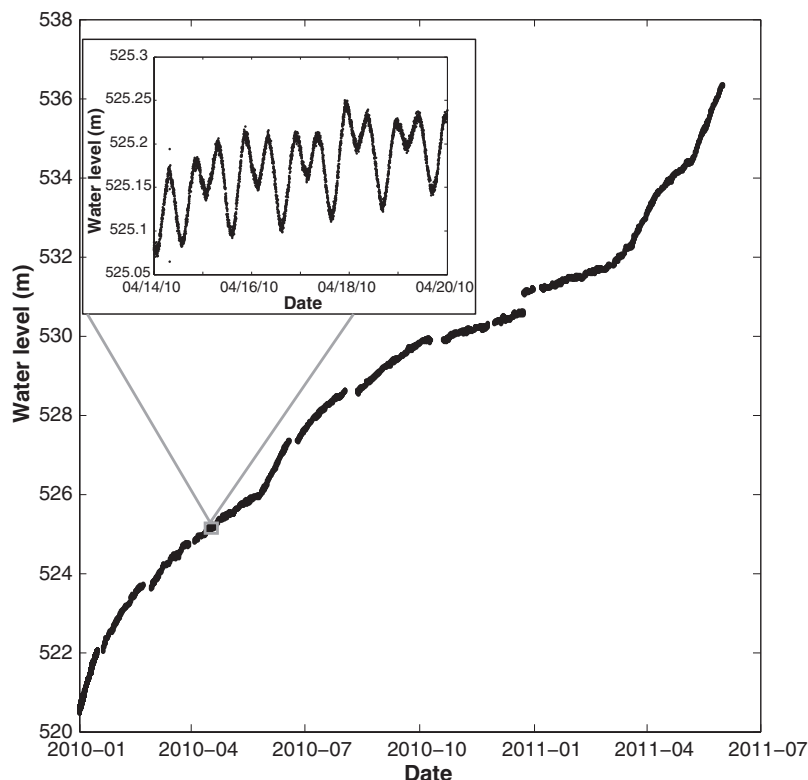


Fig. 3. Water level response relative to semidiurnal tidal dilatation strain. (A) Phase lag; (B) amplitude response. Values were calculated using a Bayesian Monte Carlo Markov chain inversion method in the time

domain (13). The inversion was applied by 29.6-day segments overlapping by 80%, respectively. The error bars represent the 95% confidence interval.

imposes a dilatational strain on the surrounding rock formation that pumps water cyclically in and out of the well through the rock around the uncased portion of the borehole below 800 m depth. The clear oscillations indicate that the aquifer is well-confined. The transmissivity and storage coefficient determine the phase and amplitude response of the water level to the tidal loading (11). To first order, phase lag is inversely related to transmissivity, and amplitude response is proportional to storage coefficient. Using tidal response to measure hydrogeologic properties has two distinct advantages: (i) Tidal response is passive and records the in situ properties undisturbed by repeated pump tests or water injections, and (ii) tidal response provides a continuous record of temporal changes of hydrogeologic properties in the rocks below the main rupture zone.

We translated the phase and amplitude responses into transmissivity and storage coefficient values on the basis of the analytical solution for a two-dimensional isotropic, homogeneous, and

laterally extensive aquifer (12, 13). The observed phase lag ranged from -20° to -30° , where negative values indicate that the water level oscillations lag behind the imposed dilatational strain; the amplitude response ranged from 5.5×10^{-7} to $6.3 \times 10^{-7} \text{ m}^{-1}$ (Fig. 3). The corresponding transmissivity T varied systematically over a range of 3.6×10^{-6} to $6.8 \times 10^{-6} \text{ m}^2 \text{ s}^{-1}$, with an average value of $5.1 \times 10^{-6} \text{ m}^2 \text{ s}^{-1}$ (Fig. 4). In contrast, the storage coefficient S did not evolve systematically, having an average value of 2.2×10^{-4} with small fluctuations about this mean (standard deviation = 5.7×10^{-6}). The different behavior for storage and transmissivity is the result of the weak sensitivity of the solution to variations in storage coefficient (12) and little real variation of the storage coefficient. Accordingly, we fixed S to the average value to more robustly solve for T and found that the resulting values of transmissivity were unchanged from the original inversion (Fig. 4). Because of the geometrical idealizations of the model, the absolute values are lower bounds

(13), although relative variations over time are more robust.

For the average values of T and S over the observation period, the average hydraulic diffusivity, $D = T/S$, is $2.4 \times 10^{-2} \text{ m}^2 \text{ s}^{-1}$. On the basis of this observed hydraulic diffusivity, the tidal observations sense a zone extending $\sim 40 \text{ m}$ from the well and thus are sensitive to mesoscale fractures (13). The most transmissive units in the damage zone control the tidally driven flow. The estimate of D is two orders of magnitude larger than that of the most directly comparable post-earthquake fault zone study [$7 \times 10^{-5} \text{ m}^2 \text{ s}^{-1}$ on the Chelungpu fault slip zone after the 1999 Chi-Chi earthquake from a cross-hole experiment (14)]. Our diffusivity value implies that as soon as the currently observed level of damage developed during the earthquake, coseismic drainage was important. However, the diffusivity may be small enough that advective flow through the fault zone does not have a major impact on the postseismic temperature measurements that

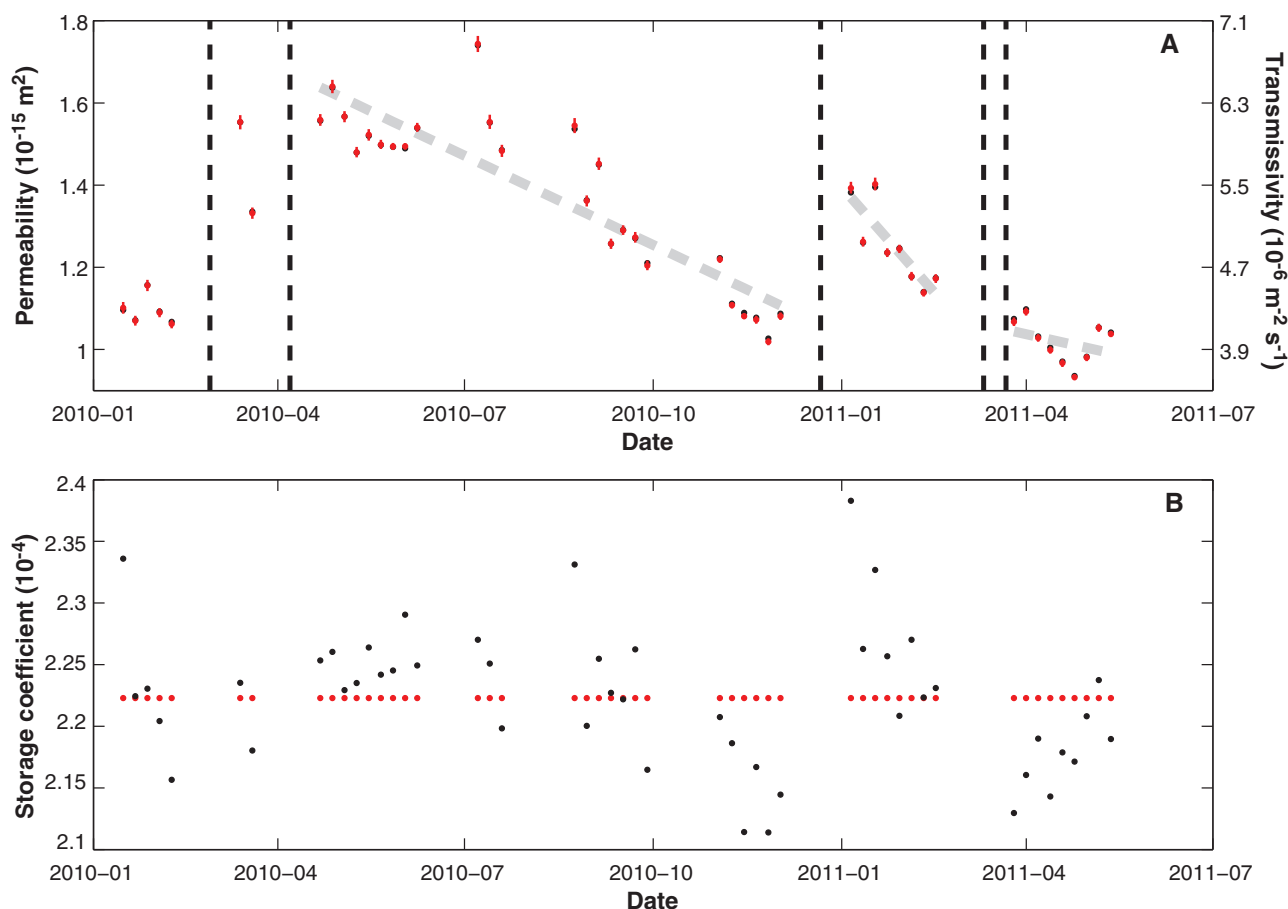


Fig. 4. Hydrogeologic properties of the well-aquifer system over time. (A) Permeability and transmissivity; (B) storage coefficient. Values were inverted from the phase and amplitude of each 29.6-day segment based on the analytical model (9). Segments that overlap the remote earthquakes (vertical dashed lines) were not inverted [see (13) for inversion results including these times]. The black dots denote an unconstrained inversion; the red dots are the results of inversion with the storage coefficient fixed to

a single value. Because the two separate inversions have identical results for transmissivity, the red dots cover the black dots in (A). The vertical dashed lines show the time of the selected teleseismic events, which correspond to sudden increases in permeability. The best-fit linear trends between each set of permeability increases are shown as light gray dashed lines. Permeability errors are estimated by propagating the range of phase errors.

are another objective of post-earthquake studies (15). Previous modeling work has shown that hydraulic diffusivities comparable to the observed effective D could suppress the temperature anomaly by at most a factor of 2 relative to a conductively cooled model (13, 16), and therefore thermal anomalies in the fault zone could be observable if the fault friction is comparable to laboratory values.

The effective permeability k is related to transmissivity T by

$$k = \frac{\mu}{\rho g d} T \quad (1)$$

where μ is the fluid dynamic viscosity, d is the thickness of the open interval of the well, and ρ is the density of fluid. Using $\mu = 10^{-3}$ Pa·s at 20°C, $\rho = 10^3$ kg m⁻³, $g = 9.8$ m s⁻², and $d = 400$ m, the average value of the effective permeability is 1.4×10^{-15} m² (Fig. 4). Permeability errors are estimated by propagating the range of phase errors. This approach is appropriate for measuring the precision of the inversion, and these errors are useful for assessing time variability. The absolute value of the permeability is more strongly affected by the limitations of the flow model (13). The observation constrains the effective permeability averaged over the entire open interval and is therefore a lower bound for the effective permeability of the highly fractured regions.

Our observed fault zone permeability is much larger than core-scale laboratory measurements of permeability from active-fault core samples (17), which range from 10^{-19} to 10^{-18} m²; it is also larger than the previously measured average permeability of 1.9×10^{-16} m² for the intact upper Triassic rock near the Wenchuan drilling site (18). The difference is likely due to mesoscale fractures and highlights the importance of damage in determining the field-scale behavior (6).

There are also substantial temporal changes in transmissivity, which we interpret as permeability changes because the formation thickness and fluid properties are unlikely to vary during the observation period. During most of the study period, the permeability trends downward and is most easily interpreted as a reduction in fracture aperture and connectivity during the continuous evolution since the original earthquake. Seismic studies in Wenchuan suggest that damage healed over a protracted time after the earthquake (19), and permeability does not generally evolve in time in the absence of a disturbance (20). The only candidate perturbation besides the earthquake is the drilling itself, which could potentially produce transient damage. However, drilling-induced fractures are expected to extend at most a few borehole radii away from the hole (21) (i.e., <0.3 m) and cannot account for the phase change of the long-period tidal response that senses average properties up to ~40 m from the borehole.

This decreasing permeability may reflect the healing process of the fault zone after the Wenchuan earthquake due to a combination of fracture closure, sealing, precipitation, biogenic

growth, and pressure solution (7). The healing rates range from 4.1×10^{-16} m² year⁻¹ to 2.1×10^{-17} m² year⁻¹, using linear fits to each interval between perturbation events (Fig. 4) (13). Previous work (22, 23) modeled fault zone healing as an exponential recovery process with decay times on the order of decades or longer. However, our data are best fit with much shorter exponential decay times of 0.6 to 2.5 years, indicating a much more rapid process than anticipated (table S2). The short exponential decay times might indicate a fast healing process, such as removal of props trapped in fractures, or crack sealing with a strongly disequibrated fluid to allow mass transfer with the observed characteristic times.

Fault zone healing has been documented in seismic velocity changes (24, 25) and has been suspected on the basis of discrete repeated active formation tests (26). After the 1995 Kobe (Hyogoken-Nambu) earthquake, water injection experiments in 1997 and 2000 tracked fluid flow in the hanging wall 50 m from the Nojima fault core and found that the permeability in 2000 had decreased to 50% of the value in 1997 (26). Seismic studies document seismic velocity decreases around the fault after an earthquake continuing for years, which can also be interpreted as a consequence of fracture closure (19, 24, 25). In Wenchuan, the repeated seismic velocity measurements made in the first year are consistent with such healing (19).

The sudden increases in permeability result in an overall rate of decrease that is more gradual than the short-term trends by a factor of 1.5 to 7.5. Previous work suggests that permeability might be enhanced by remote or regional earthquakes (20, 27). Plausible mechanisms include fracture unclogging due to the rapid, oscillatory flow driven by the seismic waves as they pass through the fault zone (27, 28). The times of the four permeability increases in Fig. 4 are correlated with the four teleseismic earthquakes that produced the largest integrated seismic shaking at the drilling site during the observation period (table S2). However, like many hydrogeologic observations, the magnitudes of the perturbations are not simply proportional to that of the peak amplitude of the seismic wave (27). Most important, our observations imply that any physical modeling of precipitation, fracture closure, or any other healing process of a fault zone needs to match the much more rapid healing rate that is only visible in the continuously recorded data.

An interplay between permeability evolution and fault strength has previously been suggested on geological and theoretical grounds (29). The Wenchuan earthquake Fault Scientific Drilling Project captured the permeability evolution in the critical post-earthquake period, when damage heals and the stage is set for the next earthquake. The unexpectedly high average hydraulic diffusivity (2.4×10^{-2} m² s⁻¹) measured here also implies substantial fluid circulation in the evolving fault zone. If this value represents the hydrogeologic

properties during the earthquake, fluid flow should take place during the earthquake rupture.

References and Notes

1. M. K. Hubbert, W. W. Rubey, *Geol. Soc. Am. Bull.* **70**, 115 (1959).
2. D. Andrews, *J. Geophys. Res.* **107**, 2363 (2002).
3. J. R. Rice, *J. Geophys. Res.* **111**, B05311 (2006).
4. A. W. Rempel, J. R. Rice, *J. Geophys. Res.* **111**, B09314 (2006).
5. C. Marone, D. M. Saffer, in *The Seismogenic Zone of Subduction Thrust Faults*, T. H. Dixon, J. C. Moore, Eds. (Columbia Univ. Press, New York, 2007), pp. 346–369.
6. J. S. Caine, J. P. Evans, C. B. Forster, *Geology* **24**, 1025 (1996).
7. J. P. Gratier, *Oil Gas Sci. Technol. Rev. IFP Energies Nouvelles* **66**, 491 (2011).
8. H. Li et al., *Tectonophysics* **584**, 23 (2013).
9. Z. Xu et al., *Episodes* **31**, 291 (2008).
10. H. M. Savage, E. E. Brodsky, *J. Geophys. Res.* **116**, B03405 (2011).
11. Transmissivity is a measure of the rate of volumetric flow through a unit width of aquifer under a unit hydraulic gradient and is directly proportional to permeability. Storage coefficient is the volume of water released from storage per unit surface area of aquifer per unit imposed head (30).
12. P. A. Hsieh, J. D. Bredehoeft, J. M. Farr, *Water Resour. Res.* **23**, 1824 (1987).
13. See supplementary materials on Science Online.
14. M. Doan, E. Brodsky, Y. Kano, K. Ma, *Geophys. Res. Lett.* **33**, L16317 (2006).
15. E. E. Brodsky, J. Mori, P. M. Fulton, *Eos* **91**, 237 (2010).
16. P. M. Fulton, R. N. Harris, D. M. Saffer, E. E. Brodsky, *J. Geophys. Res.* **115**, B09402 (2010).
17. D. Lockner, H. Naka, H. Tanaka, H. Ito, R. Ikeda, in *Proceedings of the International Workshop on the Nojima Fault Core and Borehole Data Analysis Tsukuba, Japan*, H. Ito, K. Fujimoto, H. Tanaka, D. A. Lockner, Eds. (U.S. Geol. Surv. Open File Rep., 1999), pp. 22–23.
18. Z. Rukai et al., *Petrol. Explor. Dev.* **36**, 46 (2009).
19. Y. Li, *Imaging, Modeling and Assimilation in Seismology* (China High Education Press, Beijing, 2012), vol. 1, pp. 151–198.
20. J. E. Elkhoury, E. E. Brodsky, D. C. Agnew, *Nature* **441**, 1135 (2006).
21. M. Brudy, M. Zoback, *Int. J. Rock Mech. Min. Sci.* **36**, 191 (1999).
22. F. Renard, J. P. Gratier, B. Jamveit, *J. Struct. Geol.* **22**, 1395 (2000).
23. J. P. Gratier, P. Favreau, F. Renard, *J. Geophys. Res.* **108**, 2104 (2003).
24. F. Brenguier et al., *Science* **321**, 1478 (2008).
25. Y. G. Li, J. E. Vidale, K. Aki, F. Xu, T. Burdette, *Science* **279**, 217 (1998).
26. Y. Kitagawa, K. Fujimori, N. Koizumi, *Geophys. Res. Lett.* **29**, 1483 (2002).
27. M. Manga et al., *Rev. Geophys.* **50**, RG2004 (2012).
28. J. E. Elkhoury, A. Niemeijer, E. E. Brodsky, C. Marone, *J. Geophys. Res.* **116**, B02311 (2011).
29. R. Sibson, *Tectonophysics* **211**, 283 (1992).
30. R. A. Freeze, J. A. Cherry, *Groundwater* (Prentice-Hall, Upper Saddle River, NJ, 1977).

Acknowledgments: Supported by the National Science and Technology Planning Project in China (H.-B.L.) and NSF grant EAR1220642 (E.E.B.). Seismic data from the Chinese national network are archived and distributed by Incorporated Research Institutions for Seismology (IRIS) Data Management System.

Supplementary Materials

www.sciencemag.org/cgi/content/full/340/6140/1555/DC1
Materials and Methods
Supplementary Text
Figs. S1 and S2
Tables S1 and S2
References (31–34)

1 March 2013; accepted 17 May 2013
10.1126/science.1237237

Dynamic Topography Change of the Eastern United States Since 3 Million Years Ago

David B. Rowley,^{1*} Alessandro M. Forte,² Robert Moucha,³ Jerry X. Mitrovica,⁴ Nathan A. Simmons,⁵ Stephen P. Grand⁶

Sedimentary rocks from Virginia through Florida record marine flooding during the mid-Pliocene. Several wave-cut scarps that at the time of deposition would have been horizontal are now draped over a warped surface with a maximum variation of 60 meters. We modeled dynamic topography by using mantle convection simulations that predict the amplitude and broad spatial distribution of this distortion. The results imply that dynamic topography and, to a lesser extent, glacial isostatic adjustment account for the current architecture of the coastal plain and proximal shelf. This confounds attempts to use regional stratigraphic relations as references for longer-term sea-level determinations. Inferences of Pliocene global sea-level heights or stability of Antarctic ice sheets therefore cannot be deciphered in the absence of an appropriate mantle dynamic reference frame.

The continental margin of the East Coast of the United States is the archetypal Atlantic-type or passive-type continental margin (1). Such margins have been thought to overlay a mantle that is entirely passive (2). As a consequence, passive-type margins are generally inter-

preted as having simple stratigraphic histories controlled by the interplay between thermally driven subsidence, sediment loading, compaction, and sea-level variations (3, 4). Flexural responses of the lithosphere resulting from off-shore sediment loading (5, 6) and, less frequently, onshore ero-

sional unloading (7) are also recognized as potentially important (4–6). These assumptions underpin the rationale for the use of the U.S. East Coast margin in determining global long-term [≥ 0.1 million years (My)] sea-level variations (4–6, 8, 9).

The mantle is not a passive player. Mantle flow influences surface topography, through perturbations of the dynamic topography, in a manner that varies both spatially and temporally. As a result, it is difficult to invert for the global long-term sea-level signal and, in turn, the size of the Antarctic Ice Sheet by using East Coast shoreline data (10). Factors that need to be considered include flow associated with the negative buoyancy of the subducted Farallon slab (10–14) and the coupled shallower westward flow of hotter man-

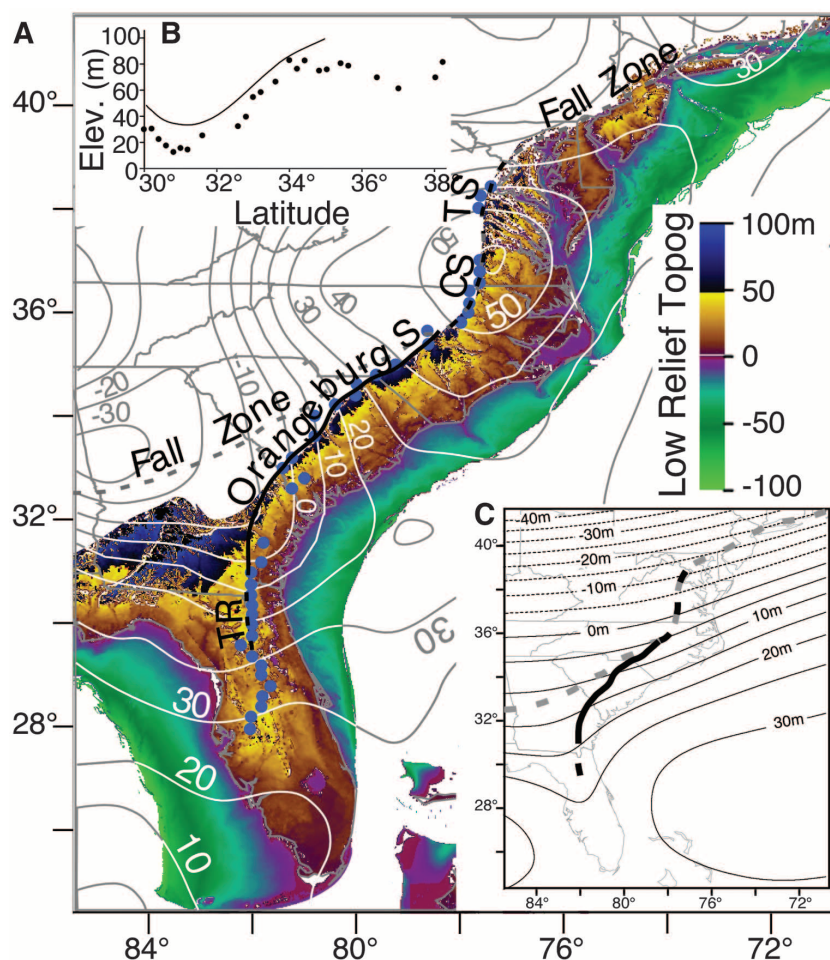
¹Department of the Geophysical Sciences, 5734 South Ellis Avenue, The University of Chicago, Chicago, IL 60637, USA.

²GÉOTOP—Université du Québec à Montréal CP 8888, succursale Centre-Ville Montréal, Québec H3C 3P8, Canada.

³Department of Earth Sciences, 204 Heroy Geology Laboratory, Syracuse University, Syracuse, NY 13244, USA. ⁴Department of Earth and Planetary Sciences, Harvard University, 20 Oxford Street, Cambridge, MA 02138, USA. ⁵Atmospheric, Earth, and Energy Division, Lawrence Livermore National Laboratory, Livermore, CA 94551, USA. ⁶Jackson School of Geological Sciences, University of Texas at Austin, Austin, TX 78712, USA.

*Corresponding author. E-mail: drowley@uchicago.edu

Fig. 1. Post-mid-Pliocene warping and incision of the Coastal Plain. (A) Present topography based on ETOPO1 emphasizing the incised, low-relief, mid-Pliocene flooding surface of the East Coast Coastal Plain, highlighting (black solid and dashed line) the locations of the Orangeburg, Chippenham (CS), Thornburg (TS) wave-cut scarps and Trail Ridge (TR) and (blue dots) sites with preserved mid-Pliocene (Yorktown, Duplin, Chortlon, and Cypresshead Formations) strata. Superimposed are contours showing an estimate of the amplitude of the post-3-Ma change in the dynamic topography based on TX2007 V2 model. The dynamic topography change is shown by the contours with a 10-m contour interval, white where they are superimposed on the topography. (B) Inset graph of the height of the Orangeburg Scarp as a function of latitude (solid line) based on (26) and the highest preserved mid-Pliocene marine sedimentary rocks as a function of latitude (dots). (C) Contours of GIA-induced relative sea level change based on the V2 viscosity profile (supplementary text) with a 5-m contour interval. The Orangeburg, Chippenham, and Thornburg Scarps are indicated by the thick black line; the Fall Zone is the thick dashed gray line.



tle (10, 12, 15). The latter produces, at least locally, changes in buoyancy and associated shorter wavelength changes in dynamic topography. Both factors confound local estimates of long-term sea-level variations (15).

The Coastal Plain is characterized by a sequence of marine and nonmarine sedimentary units that range from at least Early Cretaceous to present in age. These units generally thicken eastward to more than 12 km (16–19). This package unconformably overlies pre-Mesozoic crystalline rocks, as well as Triassic/Jurassic rift-basin strata, and pinches out to the west along the Fall Zone (Fig. 1A). Models of the depositional architecture of this margin have been developed on the basis of combinations of seismic stratigraphy and drilling (9, 18, 19) in order to better understand its evolution (4–6, 20). These models have also been used to infer global sea-level history by solving for the contributions of thermal subsidence, sediment loading and compaction, flexural loading, and sediment delivery while assuming that the only remaining unknown is the contribution from changes in sea level. Most attempts have fo-

cused on the New Jersey segment of this margin (4–6, 9, 21). A local and temporally limited sea-level estimate has been made by using the mid-Pliocene Orangeburg Scarp as a marker (8). In this particular example, after correction for $\sim 50 \pm 18$ m of post-mid-Pliocene uplift derived from a local estimate of stream incision rate (22), the Orangeburg Scarp has been inferred to have had an elevation of 35 ± 18 m, which has been taken to indicate the height of the mid-Pliocene sea level (8). This height would imply collapse of the Greenland and West Antarctic Ice Sheets and potentially considerable melting of the East Antarctic Ice Sheet during the mid-Pliocene climate optimum (23–25). However, the Pliocene strandline and immediately adjacent shallow marine sediments are not preserved at constant elevation along the Coastal Plain (Fig. 1B) (26). Thus, the Orangeburg Scarp is not a good reference for sea-level determinations for the Pliocene. Instead, we used the scarp as a marker for characterizing the processes that have warped the continental margin subsequent to 4 to 3 million years ago (27).

To assess the processes responsible for the post-mid-Pliocene warping of this margin, we developed a model of the Coastal Plain that accounts for mantle dynamics (10) and glacial isostatic adjustment (GIA) (28). Formation of karsts can also induce uplift (29). However, because carbonates are scarce north of Florida, we ignored this effect. Potential contributions from flexural warping because of offshore sediment loading and erosional unloading (7, 30) were assessed (supplementary text) but were deemed too uncertain to yield reliable estimates for the current analysis. In addition, it is shown below that the majority of the warping can be accounted for by dynamic topography and GIA alone.

Our analysis focused on the variably incised, mid-Pliocene, low-relief flooding surface that characterizes the geomorphology of the eastern seaboard coastward of the Orangeburg and equivalent wave-cut scarps that define the landward edge of this surface (Fig. 1A). The Orangeburg and correlative scarps would have been horizontal at the time of formation; the adjacent mid-Pliocene shallow marine rocks and associated flooding surface would have been largely undissected and would have sloped gently eastward in a manner comparable to the modern shallow shelf. Therefore, the warping (Fig. 1B) and incision of this low-relief flooding surface primarily reflects post-mid-Pliocene relative uplift together with erosional down-cutting by rivers and streams that traverse the eastern Coastal Plain. A reasonable test of our modeling will be the retrodiction of this flooding surface to a configuration comparable to the modern shelf.

We calculated global mantle convective flow by following the approach of (10, 15, 31, 32) with the tomography models TX2007 (33) and TX2008 (34), in which global seismic data together with a range of convection-related observables (present-day surface topography, free air gravity, plate velocities, and core-mantle boundary excess ellipticity) were jointly inverted to yield the three-dimensional (3D) distribution of density in the mantle (34) that is consistent with seismic, geodynamic, and mineral physics data. The underlying physical basis of this model is described in detail by Forte (35). We considered two different models of the radial distribution of viscosity, V1 and V2 (10, 31, 32), and these, together with the two different inversions (TX2007 and TX2008) for mantle density, provide four alternative models for predictions of time varying dynamic topography (see supplementary materials).

The 3D distribution of mantle buoyancy, when integrated with estimates of the radial distribution of viscosity, allows the computation of the instantaneous global flow field (31). With this in hand, we iteratively computed a global backward advection solution brought forward in time with a full convection calculation to estimate the vertical stresses acting on the base of the crust arising from flow in the mantle (10, 32). These time-dependent vertical stresses generate a globally distributed dynamic topography that warps Earth's

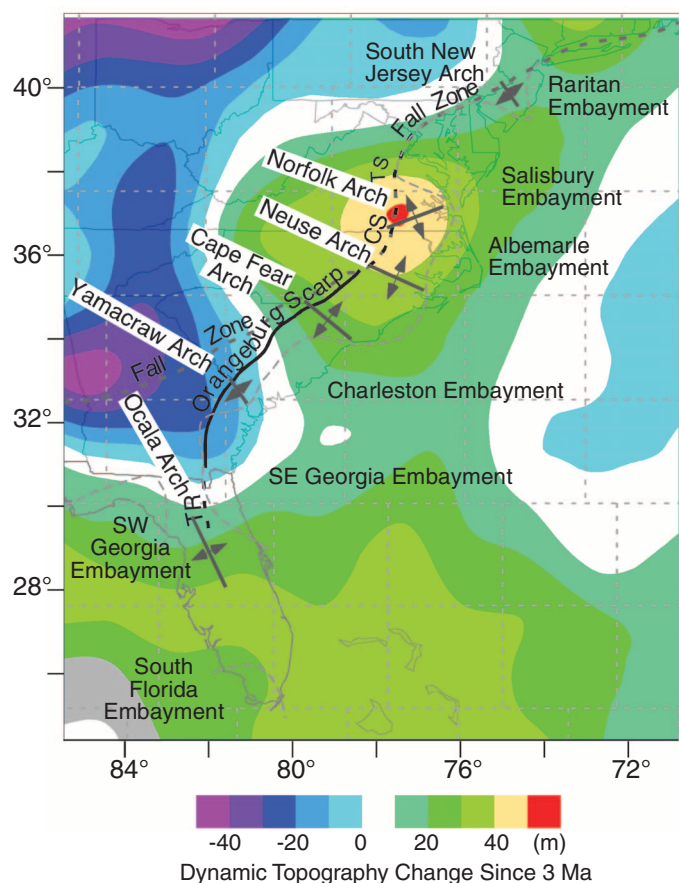


Fig. 2. Calculated dynamic topography change since 3 Ma. Locations of features associated with East Coast Coastal Plain geology after (36). The Fall Zone marks the approximate landward erosional edge of the Early Cretaceous to Cenozoic Coastal Plain strata. Color image is the distribution of retrodicted dynamic topography change based on TX 2007 V2 results. Dashed gray rectangular boxes outline the underlying resolution of the Simmons *et al.* (33, 34) joint seismic-geodynamic tomography inversion. The Orangeburg and correlative scarps pass over the center of the maximum of retrodicted dynamic topography change since 3 Ma.

surface. The difference between the present-day dynamic topography and estimates of past dynamic topography yields the change in dynamic topography as a function of time (Figs. 1 and 2 and fig. S1). The variations in height of the Orangeburg Scarp and related sediments (Fig. 1B) is well correlated, in latitude, with our estimates of the dynamic topography change since 3 million years ago (Ma). Both are high in Florida, decrease toward the north in the Southeast Georgia Embayment (~31°N), and then rise again farther north in the vicinity of the Cape Fear, Neuse, and Norfolk arches (Fig. 2).

The height of the Orangeburg Scarp rises more quickly starting north of 32°N than the estimates of dynamic topography change since 3 Ma (fig. S1). We attribute this misfit primarily to differences in the spatial scales of these data sets and to uncertainties in the tomography-based flow calculation. The joint seismic-geodynamic constrained tomography model has a minimum horizontal spatial resolution of 270 km by 270 km (34) (Fig. 2). It thus resolves mantle heterogeneity on a length scale substantially greater than the geological data being considered, whose variations are known to less than a kilometer resolution. In this regard, it is important to emphasize that our estimates of dynamic topography change are derived from full global mantle convection solutions and have not been adjusted or in any way tuned to yield better fits to the observed warping of the Orangeburg and correlative scarps.

Despite the longer-wavelength character of the seismic tomography constrained mantle flow calculations, there is a good spatial correlation between the maxima of the estimated changes in dynamic topography since 3 Ma and relative incision of the mid-Pliocene flooding surface (Fig. 1). Regions in Georgia with limited retrodicted changes in dynamic topography are characterized by limited fluvial incision into this surface. In contrast, farther north, where the retrodicted amplitude of dynamic topography change increases, the intensity of dissection increases concomitantly, and both reach a maximum in the vicinity of Chesapeake Bay (Figs. 1 and 2). The amount of incision of the low-relief flooding surface is about 50 ± 10 m in this region, in accord with the retrodicted amplitude of dynamic topography change since 3 Ma. This implies that a large fraction of the Coastal Plain geomorphology, at least shoreward of the Orangeburg Scarp, is a result of the interaction between flooding-related planation and subsequent dynamic topography induced uplift and fluvial incision within the last 3 My.

The principal outstanding feature of the dynamic topography retrodictions is the pattern of variable uplift along the East Coast of the United States (fig. S1). The origin of this uplift can be directly traced to the existence of hot, buoyant material in the shallow (<250 km) mantle under this region, with additional contributions resulting from the “far-field” advection of hot mantle rising from beneath Bermuda (figs. S2 and S3).

The impact of this active, buoyant material on the upper-mantle convective flow field is shown in fig. S2, where one may note that the centers of upwelling mantle under the eastern margin of the United States are directly correlated with (and contributing to) the pattern of recent, post-Pliocene uplift of the coastal plain (fig. S3). We conclude that this aspect of the mantle flow field has played a large role in the topographic evolution of the eastern seaboard.

GIA refers to the deformational, gravitational, and rotational adjustment of Earth in consequence of the Late Pleistocene glacial cycles. The U.S. East Coast is mostly located on the peripheral bulge of the Laurentide ice complex, and it has been continuously subsiding since the end of the last glacial maximum at 21 thousand years ago (28). A numerical simulation of the GIA process (see supplementary text) based on the V2 model predicts a variation of ~15 m of the current topography along the Orangeburg Scarp, *sensu stricto*, and an additional ~20 m along the Chippenham and Thornburg Scarps farther north (Fig. 1C). The total along-strike variation is ~35 m. However, uncertainty in the

Laurentide ice history and, in particular, the radial profile of mantle viscosity can lead to changes (~10 to 25 m) in the predicted amplitude of the GIA signal (27) (fig. S6).

We retrodicted the paleogeography of the East Coast of the United States at maximum flooding by subtracting contributions from GIA and dynamic topography change since 3 Ma from the present topography (Fig. 3). On a regional scale, there is good correspondence between geological data that constrain the known distribution of marine mid-Pliocene sediments, inferred shoreline positions based on the geology (27, 36), and the position of the retrodicted shoreline relative to present sea level. This correspondence suggests that dynamic topography and GIA can account for the vast majority of the warping of the Orangeburg and correlative scarps and the low-relief flooding surface.

Models that retrodict only dynamic subsidence of the U.S. East Coast (11, 13, 14) over this time interval are not compatible with the observed geology. Furthermore, these models (13, 14) track mantle flow over long time scales (>50 My) starting from the present, and thus any misfit with more

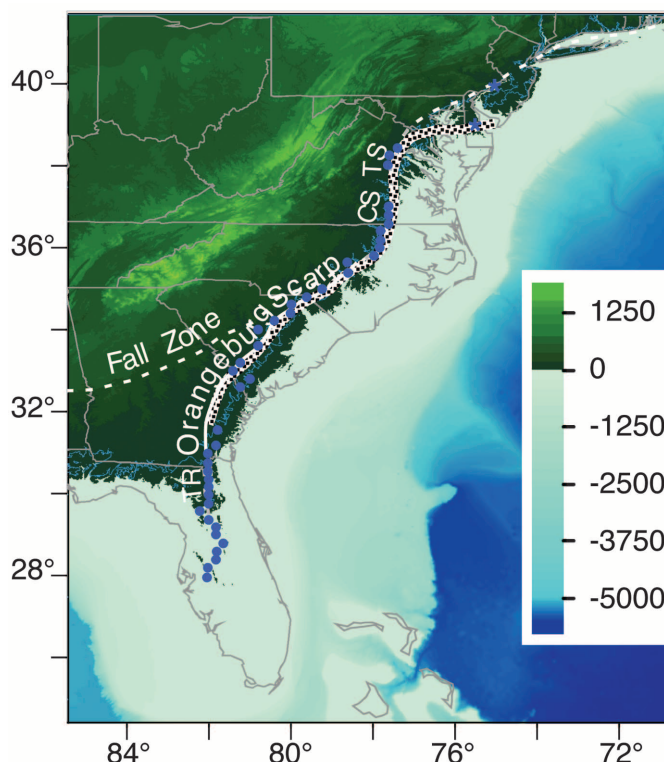


Fig. 3. Retrodicted paleogeography of the Coastal Plain at 3 Ma. Paleogeographic reconstruction of the eastern United States at 3 Ma. Retrodicted topography from which differential dynamic topography based on TX 2007 V2 results and a GIA signal have been subtracted. Scale bar is in meters. No attempt has been made to remove effects of subsequent river and stream incision. Thick dotted line is the shoreline inferred geologically (23, 29) that essentially follows the Orangeburg and correlative scarps. The thin blue line is the +25 m contour on the retrodicted topography. Blue dots are locations for which there are independent outcrop or borehole constraints on the presence of Pliocene marine sediments. Blue stars in southern Delaware and New Jersey are locations of Pliocene estuarine sediments (38, 42).

recent times (<5 My) implies that these models are unlikely to accurately retrodict dynamic topography at any older time. Our analyses do not support large amplitudes of dynamic topographic subsidence along the Atlantic shelf margin of North America, either on time scales considered here or on longer time scales (30 My) (10).

Our simulations have implications for inferences of long-term sea-level change. As can be seen from the retrodicted paleogeography, the Orangeburg and correlative scarps and marine mid-Pliocene localities lie close to the +25 m (Fig. 3 and fig. S4). It would be premature to conclude that this supports an estimate of +25 m for mid-Pliocene sea level because of inherent uncertainties in the various modeling parameters, particularly the mantle viscosity adopted in the dynamic topography and GIA retrodictions, and because we have not included a topographic correction for sediment loading and erosional unloading (supplementary text). Given these uncertainties, our view is that we cannot, as yet, place robust limits on the maximum height of mid-Pliocene sea level.

In the area of the Norfolk Arch, where the largest amplitude of retrodicted dynamic topography change is centered (Fig. 2), the predicted rate of uplift is ~60 m/My (supplementary text). This value is about three times the inferred maximum rate of change of long-term global sea level since the base of the Jurassic (37). Moreover, it is greater than ~85% of the rate of change of the short-term global sea-level height when this is averaged over 0.1-My intervals (37). Thus, the regression from the Albemarle and southern Salisbury Embayments since mid-Pliocene, which from the local sequence stratigraphic perspective would be directly linked to a significant global sea-level fall, is instead dominated by dynamic topographic uplift and GIA (Fig. 3).

The mid-Pliocene stratigraphy of New Jersey is dominated by regressive sequences, marked by denudation and incision of earlier Miocene flooding surfaces and by deposition of the Pensauken fluvial clastics (38). Accepting that New Jersey was rising out of the water (Fig. 3), while Virginia and points south were transgressed, then some other processes, including, but perhaps not limited to, dynamic topography were controlling the sequence stratigraphy of this margin. Because the average slope of the shelf surface is about $0.05^\circ \pm 0.025^\circ$, even relatively small changes (~20 to 40 m) in dynamic topography beneath the shelf would move the shoreline laterally by tens of km. The regression of the Pliocene and younger sequences from the Albemarle Embayment appears to specifically reflect such an effect, thereby calling into question inferences of sea-level change based on sequence stratigraphic approaches.

Coastal scarps, similar to the Orangeburg scarp but at lower elevations, have often been interpreted as reflecting progressive drops in sea level (39, 40). Alternatively, they may reflect the gradual emergence of the coast under relatively constant sea level at interglacial highstands (41).

Likely both processes were operating, but it is difficult to disentangle the effects of each over time without also quantifying the mantle dynamic contributions.

Our retrodicted paleogeography at 3 Ma (Fig. 3) closely matches the well-known distribution of mid-Pliocene marine strata in the Albemarle and southern Salisbury Embayments. We suggest that assessments of the height of mid-Pliocene global sea level, and thus the size and stability of the East Antarctic Ice Sheet during this period of relative warmth, must be based on global analyses that account for globally consistent, mantle convection-driven topography, rather than on local investigations.

Note added in proof: Figures 1 and 3 were revised so that the figures in the main text are based on the same dynamic topography and glacial isostatic adjustment calculations.

References and Notes

1. C. L. Drake, M. Ewing, G. H. Sutton, in *Physics and Chemistry of the Earth* (Pergamon, Elmsford, NY, 1959), vol. 3, pp. 110–198.
2. D. McKenzie, *Earth Planet. Sci. Lett.* **40**, 25 (1978).
3. J. V. Browning *et al.*, *Basin Res.* **20**, 227 (2008).
4. M. A. Kominz *et al.*, *Basin Res.* **20**, 211 (2008).
5. A. B. Watts, M. S. Steckler, in *Deep Drilling Results in the Atlantic Ocean; Continental Margins and Paleoenvironment*, M. Talwani, W. Hay, W. B. F. Ryan, Eds. (American Geophysical Union, Washington, DC, 1979), vol. 3, pp. 218–234.
6. A. B. Watts, J. Thorne, *Mar. Pet. Geol.* **1**, 319 (1984).
7. F. Pazzaglia, T. Gardner, *J. Geophys. Res.* **99**, 12143 (1994).
8. H. J. Dowsett, T. Cronin, *Geology* **18**, 435 (1990).
9. K. G. Miller *et al.*, *Science* **310**, 1293 (2005).
10. R. Moucha *et al.*, *Earth Planet. Sci. Lett.* **271**, 101 (2008).
11. C. P. Conrad, C. Lithgow-Bertelloni, K. E. Loudon, *Geology* **32**, 177 (2004).
12. R. Moucha, A. M. Forte, S. Quéré, J. X. Mitrovica, D. B. Rowley, *EOS Trans. Am. Geophys. Union* **87**, T53D (2006).
13. R. D. Müller, M. Sdrolias, C. Gaina, B. Steinberger, C. Heine, *Science* **319**, 1357 (2008).
14. S. Spasojević, L. Liu, M. Gurnis, R. D. Müller, *Geophys. Res. Lett.* **35**, 6 (2008).
15. A. M. Forte, J. X. Mitrovica, R. Moucha, N. A. Simmons, S. P. Grand, *Geophys. Res. Lett.* **34**, 5 (2007).
16. W. Dillon, P. Popenoe, "The Blake Plateau Basin and Carolina Trough," in *The Atlantic Continental Margin; U.S., R. Sheridan, J. Grow, Eds., of The Geology of North America* (Geological Society of America, Boulder, CO, 1988), vols. I–2, pp. 291–328.
17. K. O. Emery, E. Uchupi, *The Geology of the Atlantic Ocean* (Springer-Verlag, New York, 1984).
18. C. Poag, W. Sevon, *Geomorphology* **2**, 119 (1989).
19. L. J. Poppe, P. Popenoe, C. W. Poag, B. A. Swift, *Mar. Pet. Geol.* **12**, 677 (1995).
20. N. H. Sleep, *Geophys. J. Int.* **24**, 325 (1971).
21. K. G. Miller, "Sea level change, last 250 million years," in *Encyclopedia of Paleoclimatology and Ancient Environments*, V. Gornitz, Ed. (Springer, Berlin, 2008), pp. 879–893.
22. D. A. Soller, *Geologic and Tectonic History of the Lower Cape Fear Valley, Southeastern North Carolina* (U.S. Geological Survey Professional Paper 1466-A, Government Printing Office, Washington, DC, 1988).
23. H. Dowsett *et al.*, *Stratigraphy* **7**, 123 (2010).
24. D. Fox, *Science* **328**, 1630 (2010).
25. D. J. Hill, A. M. Haywood, R. C. A. Hindmarsh, P. J. Valdes, "Characterizing ice sheets during the Pliocene: Evidence from data and models," in *Deep-Time Perspectives on Climate Change: Marrying the Signal from Computer Models and Biological Proxies*,

- M. Williams, A. M. Haywood, F. J. Gregory, D. N. Schmidt, Eds. (Geological Society Publishing House, Bath, UK, 2007), pp. 517–538.
26. C. Winker, J. Howard, *Geology* **5**, 123 (1977).
27. D. Krantz, *Quat. Sci. Rev.* **10**, 163 (1991).
28. M. E. Raymo, J. X. Mitrovica, M. J. O'Leary, R. M. Deconto, P. J. Hearty, *Nat. Geosci.* **4**, 328 (2011).
29. P. Adams, N. Opdyke, J. Jaeger, *Geology* **38**, 531 (2010).
30. F. J. Pazzaglia, T. W. Gardner, in *Geomorphology and Global Tectonics*, M. A. Summerfield, Ed. (Wiley Interscience, Chichester, UK, 2000), pp. 284–302.
31. A. M. Forte *et al.*, *Earth Planet. Sci. Lett.* **295**, 329 (2010).
32. R. Moucha *et al.*, *Geophys. Res. Lett.* **36**, L19310 (2009).
33. N. A. Simmons, A. M. Forte, S. P. Grand, *Geophys. Res. Lett.* **34**, 5 (2007).
34. N. A. Simmons, A. M. Forte, S. P. Grand, *Geophys. J. Int.* **177**, 1284 (2009).
35. A. M. Forte, in *Treatise on Geophysics*, G. Schubert, Ed. (Elsevier, Amsterdam, 2007), pp. 805–858.
36. L. W. Ward, R. H. Bailey, J. G. Carter, in *The Geology of the Carolinas: Carolina Geological Society 50th Anniversary Volume*, J. W. Horton Jr., V. A. Zullo, Eds. (Univ. of Tennessee Press, Knoxville, TN, 1991), pp. 274–289.
37. B. Haq, A. Al-Qahtani, *Georabia* **10**, 127 (2005).
38. S. D. Stanford, G. M. Ashley, G. J. Brenner, *J. Geol.* **109**, 265 (2001).
39. R. Oaks, N. Coch, J. Sanders, R. Flint, in *Post-Miocene Stratigraphy, Central and Southern Atlantic Coastal Plain*, R. Q. Oaks Jr., J. R. DuBar, Eds. (Utah State Univ. Press, Logan, Utah, 1974), pp. 53–87.
40. R. Oaks, J. DuBar, *Post-Miocene Stratigraphy, Central and Southern Atlantic Coastal Plain* (Utah State Univ. Press, Logan, Utah, 1974), pp. 232–245.
41. M. E. Raymo, L. E. Lisiecki, K. H. Nisancioglu, *Science* **313**, 492 (2006); 10.1126/science.1123296.
42. J. J. Groot, R. R. Jordan, *The Pliocene and Quaternary Deposits of Delaware: Palynology, Ages, and Paleoenvironments*, D. G. Survey, Ed. (Delaware Geological Survey Report of Investigations, Newark, DE, 1999), vol. 58.

Acknowledgments: D.B.R., A.M.F., and J.X.M. thank the Canadian Institute for Advanced Research (CIFAR) for research support and a postdoctoral fellowship to R.M. and members of the Earth Systems Evolution Program of CIFAR for discussions and encouragement. We also acknowledge funding from Natural Sciences and Engineering Research Council of Canada and the Canada Research Chair Program (A.M.F.), the U.S. Department of Energy under contract DE-AC52-07NA27344 (N.A.S.), NSF grants EAR0309189 (S.P.G.) and OCE-1202632 (J.X.M.), and Harvard University (J.X.M.). Work by N.A.S. is performed under the auspices of the U.S. Department of Energy by Lawrence Livermore National Laboratory under contract DE-AC52-07NA27344. Data are available online in the supplementary materials. D.B.R. was responsible for the geology and data integration and thanks T. Komacek for help compiling Pliocene marine localities along the Coastal Plain; A.M.F. and R.M. were responsible for the dynamic topography calculations; J.X.M. for glacial isostatic adjustment calculations; and N.A.S. and S.P.G., for the global seismic tomography, which, working together with A.M.F., yielded the buoyancy field that underlies the dynamic topography calculations.

Supplementary Materials

www.sciencemag.org/cgi/content/full/science.1229180/DC1
Materials and Methods
Supplementary Text
Figs. S1 to S6
Table S1
References (43–49)

22 August 2012; accepted 30 April 2013
Published online 16 May 2013;
10.1126/science.1229180

Varied Response of Western Pacific Hydrology to Climate Forcings over the Last Glacial Period

Stacy A. Carolin,^{1*} Kim M. Cobb,¹ Jess F. Adkins,² Brian Clark,³ Jessica L. Conroy,¹ Syria Lejau,³ Jenny Malang,³ Andrew A. Tuen⁴

Atmospheric deep convection in the west Pacific plays a key role in the global heat and moisture budgets, yet its response to orbital and abrupt climate change events is poorly resolved. Here, we present four absolutely dated, overlapping stalagmite oxygen isotopic records from northern Borneo that span most of the last glacial cycle. The records suggest that northern Borneo's hydroclimate shifted in phase with precessional forcing but was only weakly affected by glacial-interglacial changes in global climate boundary conditions. Regional convection likely decreased during Heinrich events, but other Northern Hemisphere abrupt climate change events are notably absent. The new records suggest that the deep tropical Pacific hydroclimate variability may have played an important role in shaping the global response to the largest abrupt climate change events.

The response of the tropical Pacific to changes in Earth's climate system remains highly uncertain. The most recent glacial-interglacial cycle encompasses several precessional cycles; changes in ice volume, sea level, global temperature, and atmospheric partial pressure of CO₂; and millennial-scale climate events, thus providing insights into the tropical Pacific response to a variety of climate forcings. Chinese stalagmites show that East Asian monsoon strength closely tracks precessional insolation forcing over several glacial-interglacial cycles and exhibits prominent millennial-scale variability (1, 2). The timing and structure of these abrupt climate changes are nearly identical to millennial-scale events recorded in the Greenland ice cores [Dansgaard-Oeschger (D/O) events] (3) and in sediment records that document ice-rafted debris across the North Atlantic (Heinrich events) (4, 5). A Borneo stalagmite record spanning the past 27,000 years provides a markedly different view of hydrology in the western tropical Pacific, with the Heinrich 1 excursion and spring-fall precessional insolation forcing explaining much of the variability (6). At its most basic, this finding illustrates the complexity of regional responses to various climate forcings, especially at sites located far from the North Atlantic, and demands a more exhaustive tropical Pacific hydrologic record encompassing a full glacial-interglacial cycle.

Here, we present four overlapping stalagmite oxygen isotopic ($\delta^{18}\text{O}$) records from Gunung Buda and Gunung Mulu national parks, located in northern Borneo (4°N, 115°E) (fig. S1), that together span most of the last glacial cycle. The research site is located near the center of the west Pacific warm pool (WPWP), where changes in sea surface temperatures and sea-level pressure have consid-

erable impacts on large-scale atmospheric circulation and global hydrology (7). Using multiple stalagmites from different caves, we distinguish shared climate-related features from cave-specific signals in the overlapping $\delta^{18}\text{O}$ records.

The four stalagmite records span portions of the last glacial cycle with many intervals of overlap, based on U-series dates (Fig. 1). Stalagmites were recovered from Secret Cave at Gunung Mulu [SC02, 37 to 94 thousand years before the present (ky B.P.), and SC03, 32 to 100 ky B.P.] and from Bukit Assam (BA02, 15 to 46 ky B.P.) and Snail Shell Cave (SCH02, 31 to 73 ky B.P.) at Gunung Buda, 25 km from Gunung Mulu (fig. S2). The deglacial and Holocene $\delta^{18}\text{O}$ records from stalagmite SCH02 were presented in (6). Eighty-six new U/Th dates measured across the four stalagmites fall in stratigraphic order within 2 σ errors (8). Large uncertainties in the $^{230}\text{Th}/^{232}\text{Th}$ ratio of the contaminant phases translate into large uncertainties associated with the correction for detrital thorium contamination. Fourteen isochrons measured across stalagmites from three separate caves give initial $^{230}\text{Th}/^{232}\text{Th}$ atomic ratios of 56 ± 11 (2 σ) for Bukit Assam Cave, 59 ± 13 (2 σ) for Snail Shell Cave, and 111 ± 41 (2 σ) $\times 10^{-6}$ for Secret Cave (8), which fall within the range of previously published values from our site (6). Absolute age errors for each U/Th date were calculated with a Monte Carlo approach that combined multiple sources of error. The resulting dating errors average ± 200 , ± 250 , ± 400 , and ± 500 years (2 σ) for BA02, SCH02, SC02, and SC03, respectively. Age models were initially constructed by linearly interpolating between each date and were refined by aligning five major millennial-scale $\delta^{18}\text{O}$ excursions visible across all four records within age error (8). The fact that both chronologies fall nearly completely within the StalAge (9) algorithm's 95% confidence interval (figs. S3 to S6) adds credibility to our assigned chronologies and associated error estimates. With our 1-mm sampling interval, the temporal resolution of the associated $\delta^{18}\text{O}$ records averages 60 years per sample for the faster-growing

stalagmites BA02 and SCH02 and 200 years per sample for the slower-growing stalagmites SC02 and SC03. During the 50- to 38-ky B.P. interval, SC02 and SC03 were sampled at 0.5-mm to achieve a resolution of ~ 100 years per sample. Ultraslow growth intervals ($< 10 \mu\text{m}/\text{year}$ for the faster-growing stalagmites and $< 3 \mu\text{m}/\text{year}$ for the slower growing stalagmites) may represent unresolved hiatuses and, as such, were excluded from the resulting paleoclimate reconstructions (8), following (6).

The stalagmite $\delta^{18}\text{O}$ records provide reconstructions of rainfall $\delta^{18}\text{O}$ variability at the research site, which, in turn, tracks the strength of regional convective activity (10). Consistent with the tropical amount effect (11, 12), rainfall $\delta^{18}\text{O}$ variations measured at the site from 2006 to 2011 are significantly anticorrelated with regional precipitation amount and closely track the El Niño–Southern Oscillation on monthly time scales (10). A weak semi-annual seasonal cycle in rainfall $\delta^{18}\text{O}$ is characterized by relative minima in June to July and November to January and relative maxima in February to April and August to October. Such a pattern suggests that the twice-yearly passage of the Intertropical Convergence Zone (ITCZ) over the site is associated with shifts in the moisture sources and/or trajectories that drive the observed seasonal fractionations (10). Dripwater $\delta^{18}\text{O}$ values match rainfall $\delta^{18}\text{O}$ values averaged over the preceding 2 to 6 months (13), suggesting a short residence time of dripwater $\delta^{18}\text{O}$ relative to our centennial-scale sampling of stalagmite $\delta^{18}\text{O}$. Time series of Buda and Mulu stalagmite $\delta^{18}\text{O}$ are highly reproducible (6, 14), strongly supporting their interpretation as rainfall $\delta^{18}\text{O}$ reconstructions and, by extension, as records of past regional convective activity.

The overlapping Borneo stalagmite $\delta^{18}\text{O}$ records show orbital-scale variability related to precessional insolation forcing and glacial-interglacial (G-I) changes (Fig. 2). The similarity of our stalagmite $\delta^{18}\text{O}$ time series to indices of G-I variability greatly diminishes after removing the mean $\delta^{18}\text{O}$ of seawater due to changes in ice volume (8, 15) from the Borneo $\delta^{18}\text{O}$ records (Fig. 2 and fig. S7). After this correction, Last Glacial Maximum (LGM) $\delta^{18}\text{O}$ values are nearly identical to $\delta^{18}\text{O}$ values at ~ 85 ky B.P., despite the presence of substantially larger ice sheets, cooler regional temperatures (16, 17), and a completely exposed Sunda Shelf during the LGM. In particular, Sunda Shelf emergence has been implicated in shaping glacial western tropical Pacific hydroclimate in previous studies (6, 18, 19). However, we find little correspondence between Borneo stalagmite $\delta^{18}\text{O}$ and an index of Sunda Shelf areal extent over the entire glacial cycle (fig. S7). For example, Borneo stalagmite $\delta^{18}\text{O}$ variations in the 70- to 90-ky B.P. interval bear little resemblance to reconstructed sea-level changes, especially from ~ 71 to 76 ky B.P. (20), when a large drop in sea level almost doubled the size of the exposed shelf (fig. S7). As such, the new Borneo $\delta^{18}\text{O}$ records suggest that the cumulative influence of G-I

¹School of Earth and Atmospheric Sciences, Georgia Institute of Technology, Atlanta, GA 30332, USA. ²Division of Geological and Planetary Sciences, California Institute of Technology, Pasadena, CA 91125, USA. ³Gunung Mulu National Park, Sarawak, Malaysia. ⁴Institute of Biodiversity and Environmental Conservation, Universiti Malaysia Sarawak, Sarawak, Malaysia.

*Corresponding author. E-mail: stacy.carolin@gatech.edu

boundary conditions, including changes in global temperature and CO_2 , did not drive considerable changes in rainfall $\delta^{18}\text{O}$ at our site. However, given the complexities of influences on rainfall $\delta^{18}\text{O}$ (10), LGM climate may have been characterized by two or more competing influences on regional rainfall $\delta^{18}\text{O}$. For example, regional drying during the LGM inferred from WPWP sediment cores (21) and modeling studies (19) may have increased rainfall $\delta^{18}\text{O}$, whereas longer moisture trajectories associated with the emergence of the Sunda Shelf may have decreased rainfall $\delta^{18}\text{O}$.

The Borneo stalagmite $\delta^{18}\text{O}$ records vary in phase with insolation at the equator during boreal fall in stage 5 and the Holocene, when precessional forcing is relatively strong (Fig. 2C). The impact of precessional forcing on Borneo stalagmite $\delta^{18}\text{O}$ is weak during stage 3, in part owing to reduced precessional amplitude during this time. Precessional forcing is also apparent in older glacial-interglacial stalagmite $\delta^{18}\text{O}$ reconstructions from Borneo (14). Taken together, the Borneo

records suggest that precession may be the dominant source of orbital-scale hydroclimate variability in the WPWP. The implied sensitivity of northern Borneo hydrology to boreal fall insolation is consistent with results from a previous modeling study (22). Moreover, results from a long-term rainfall $\delta^{18}\text{O}$ monitoring program at Mulu demonstrate that mean annual rainfall $\delta^{18}\text{O}$ values depend, in part, on the magnitude of rainfall $\delta^{18}\text{O}$ enrichments during the boreal spring-fall seasons (10). In this sense, the observed sensitivity to boreal fall insolation may represent a direct response of mean annual rainfall $\delta^{18}\text{O}$ to local changes in seasonal moisture sources and trajectories. However, El Niño–Southern Oscillation and the Madden-Julian Oscillations (23) have large impacts on modern Mulu rainfall $\delta^{18}\text{O}$ variability (10), such that Borneo stalagmite $\delta^{18}\text{O}$ signals may represent a combination of one or more climatic influences.

The Borneo stalagmite $\delta^{18}\text{O}$ records are dominated by six millennial-scale increases in $\delta^{18}\text{O}$ that coincide with Heinrich events, inferring a

decrease in regional convection during these abrupt climate changes (Fig. 2). A nearby Sulu Sea sediment core (Fig. 2E) also documents increased planktonic foraminiferal $\delta^{18}\text{O}$ values during Heinrich events (24), consistent with a reduction in regional convective activity. The dominant paradigm to explain millennial-scale tropical hydroclimate anomalies is that they are driven from the North Atlantic region, either from weakening of the Atlantic thermohaline circulation or from a dramatic albedo change due to sea-ice cover, both of which drive a southward migration of the ITCZ that dries most of the northern tropics (25, 26). A similar chain of events is used to describe D/O abrupt climate changes that are well documented outside of the tropical Pacific, most notably in Chinese and Peruvian stalagmite $\delta^{18}\text{O}$ records (1, 2, 27) and in a high-resolution ice core $\delta^{18}\text{O}$ record from the south Atlantic sector of Antarctica (28). However, the Borneo stalagmite $\delta^{18}\text{O}$ records lack any coherent signature of D/O events (Fig. 2 and fig. S8). The Borneo stalagmite $\delta^{18}\text{O}$ records show no consistent response to D/O events 8 and 12, the prominent D/O events that occur on the heels of Heinrich events 4 and 5 (fig. S8). Of particular note, the records show little millennial-scale variability from ~30 to 40 ky B.P. across D/O events 5 to 8 (fig. S8). The records do bear a strong resemblance to the Chinese $\delta^{18}\text{O}$ records during the 50- to 60-ky B.P. interval, as both records contain a distinct $\delta^{18}\text{O}$ increase at ~55 ky B.P. This shared $\delta^{18}\text{O}$ enrichment may reflect the influence of an additional Heinrich event, referred to as “Heinrich 5a” in one study (29), or may indicate a regional hydrological sensitivity to the relatively prolonged D/O events that occurred during this time interval. Contrary to inferences drawn from a deglacial Borneo stalagmite $\delta^{18}\text{O}$ record (6), there is no evidence for a Southern Hemisphere influence on millennial-scale variability in Borneo hydroclimate over the last glacial cycle (fig. S8).

The unambiguous signature of Heinrich events in the Borneo stalagmite $\delta^{18}\text{O}$ records stands in stark contrast to the lack of consistent D/O-related signals in the records, implying a selective response of WPWP hydrology to high-latitude abrupt climate change forcing. Specifically, the absence of any readily identifiable D/O signals in the Borneo $\delta^{18}\text{O}$ record represents a clear challenge to our understanding of abrupt climate change mechanisms. The new Borneo records suggest that one of two possibilities must be true: (i) If D/O events reflect a similar mechanism to Heinrich events, then they must not be strong enough to affect northern Borneo hydrology appreciably, or (ii) D/O events and Heinrich events are characterized by fundamentally different climate mechanisms and feedbacks.

The largest millennial-scale anomaly in the Borneo records is not a Heinrich event, but rather an abrupt increase in $\delta^{18}\text{O}$ that occurs at 73.42 ± 0.30 (2 σ) ky B.P., coincident with a similarly large and abrupt increase in Chinese stalagmite $\delta^{18}\text{O}$ (Fig. 2). Whether this event is associated with the

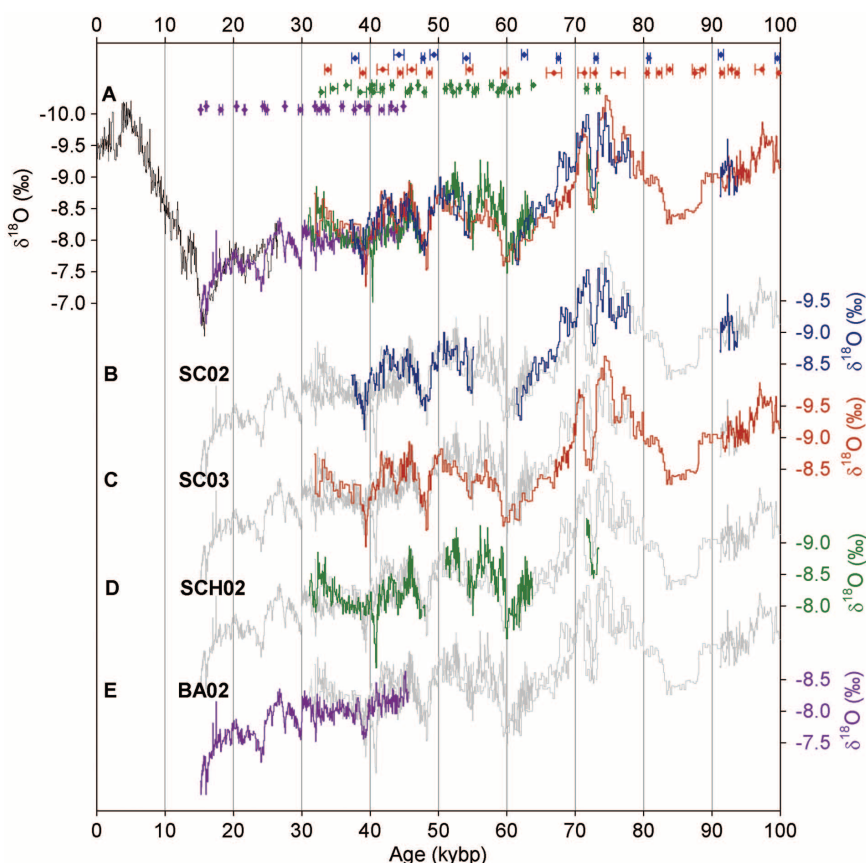


Fig. 1. Comparison of four overlapping stalagmite $\delta^{18}\text{O}$ records from northern Borneo. (A) $\delta^{18}\text{O}$ records from SC02 (blue), SCH02 (green), and BA02 (purple) are overlain after aligning five major millennial-scale $\delta^{18}\text{O}$ excursions shared across all four stalagmites to within 2 σ dating errors (8), plotted with previously published stalagmite $\delta^{18}\text{O}$ data from our site (black) (6). SC03 and SC02 mean $\delta^{18}\text{O}$ have been offset +0.2 per mil (‰), and BA02 mean $\delta^{18}\text{O}$ has been offset –0.45‰ to match the absolute value of SCH02, consistent with the prior use of SCH02 as a benchmark for the deglacial–Holocene Borneo records (6). (B) The $\delta^{18}\text{O}$ record for SC02, plotted using its raw age model (blue), shown with the three other overlapping Borneo stalagmite $\delta^{18}\text{O}$ records using their raw age models (gray). (C) Same as (B), but for SC03 (red). (D) Same as (B), but for SCH02 (green). (E) Same as (B), but for BA02 (purple). The U–Th–based age model was used to construct the composite $\delta^{18}\text{O}$ record plotted in corresponding colors at the top, shown with 2 σ uncertainty limits (8). The x axis indicates age in thousand years before the present (kybp).

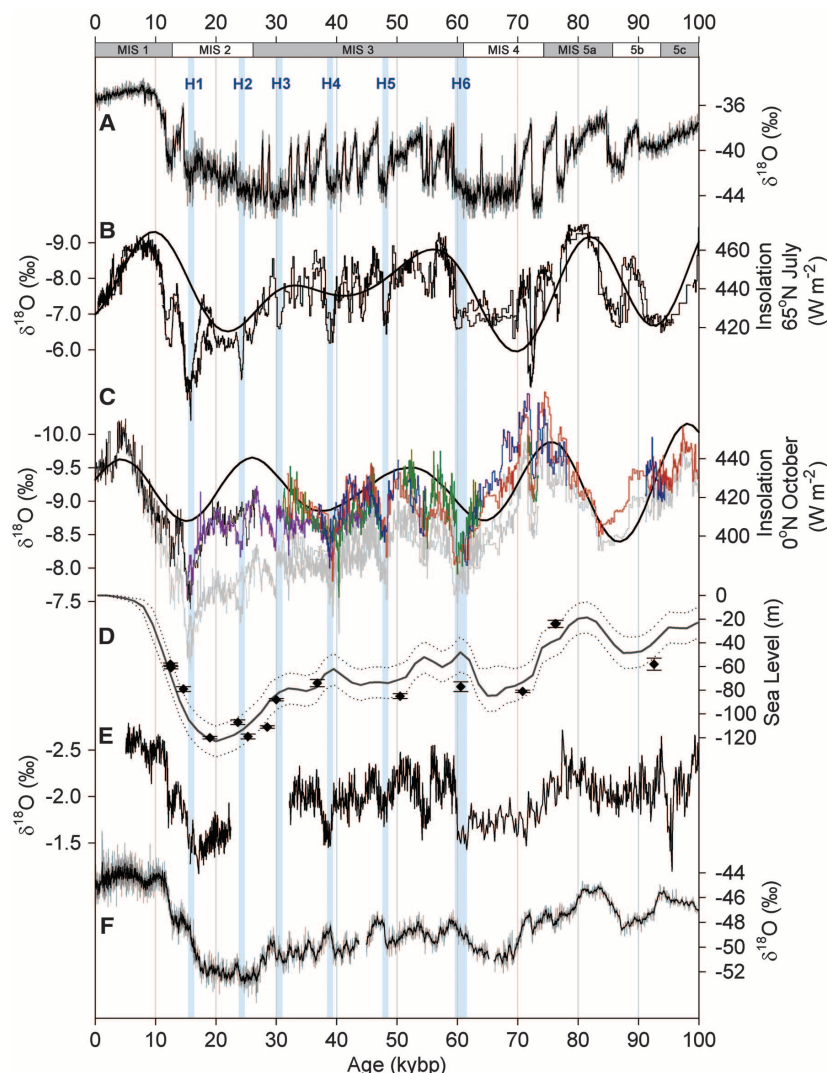


Fig. 2. Comparison of Borneo stalagmite $\delta^{18}\text{O}$ records to climate forcings and records of paleoclimate from key regions. (A) Greenland NGRIP (North Greenland Ice Core Project) ice core $\delta^{18}\text{O}$ (gray) (31) with 100-year averages (black), plotted using the GICC05modelext age model (32). (B) Hulu–Sanbao cave stalagmite $\delta^{18}\text{O}$ records from China (1, 2) (Sanbao has been offset by +1.6‰ to match Hulu), plotted with July insolation at 65°N (33). (C) Borneo stalagmite $\delta^{18}\text{O}$ records, plotted with age models aligned and adjusted to account for ice-volume-related changes in global seawater $\delta^{18}\text{O}$ (8). Also plotted are October insolation at 0°N (black) (33) and Borneo stalagmite $\delta^{18}\text{O}$ records (gray) that have not been corrected for ice volume. (D) Coral-based estimates of paleo-sea-level record (20, 34, 35) (black symbols) and global mean sea-level record (15) (solid line, average; dotted lines, minimum and maximum). (E) Sulu Sea planktonic foraminifera $\delta^{18}\text{O}$ (24), plotted with a revised age model using updated IntCal09 calibration curve 41–ky B.P. modern and aligning 60–ky B.P. $\delta^{18}\text{O}$ excursion to the Hulu–Sanbao stalagmite $\delta^{18}\text{O}$ records. (F) EPICA (European Project for Ice Coring in Antarctica) Dronning Maud Land (EDML) ice core $\delta^{18}\text{O}$ (gray) (28) with 7-year averages (black). Vertical blue bars indicate the timing of Heinrich events H1 to H6 (5), as recorded by the Hulu–Sanbao stalagmite $\delta^{18}\text{O}$ records (1, 2).

Toba supereruption, dated at 73.88 ± 0.64 (2 σ) ky B.P. (30), and/or a prominent early abrupt climate change event visible in Greenland ice core $\delta^{18}\text{O}$ (Fig. 2A) merits investigation in additional high-resolution paleoclimate records from the Indo-Pacific.

The Borneo composite records demonstrate the sensitivity of western equatorial Pacific hydrology to both high-latitude and low-latitude forcings. However, the response of northern Borneo hydroclimate to these forcings is not uniform: Glacial conditions and D/O events apparently

had much smaller impacts on regional hydrology than either insolation or Heinrich-related forcing. Our results imply that once the hydrological response threshold is reached, then climate feedbacks internal to the tropics may serve to amplify and prolong a given climate change event, whether the trigger originates from internal dynamics or external radiative forcing.

References and Notes

1. Y. J. Wang *et al.*, *Science* **294**, 2345 (2001).
2. Y. J. Wang *et al.*, *Nature* **451**, 1090 (2008).

3. W. Dansgaard *et al.*, *Nature* **364**, 218 (1993).
4. H. Heinrich, *Quat. Res.* **29**, 142 (1988).
5. S. R. Hemming, *Rev. Geophys.* **42**, RG1005 (2004).
6. J. W. Partin, K. M. Cobb, J. F. Adkins, B. Clark, D. P. Fernandez, *Nature* **449**, 452 (2007).
7. M. Cane, A. C. Clement, *Geophys. Monogr. Ser.* **112**, 373 (1999).
8. Materials and methods are available as supplementary materials on Science Online.
9. D. Scholz, D. L. Hoffmann, *Quat. Geochronol.* **6**, 369 (2011).
10. J. W. Moerman *et al.*, *Earth Planet. Sci. Lett.* **369–370**, 108 (2013).
11. W. Dansgaard, *Tellus* **16**, 436 (1964).
12. K. Rozanski, L. Araguás-Araguás, R. Gonfiantini, *Science* **258**, 981 (1992).
13. K. M. Cobb, J. F. Adkins, J. W. Partin, B. Clark, *Earth Planet. Sci. Lett.* **263**, 207 (2007).
14. A. N. Meckler, M. O. Clarkson, K. M. Cobb, H. Sodemann, J. F. Adkins, *Science* **336**, 1301 (2012).
15. C. Waelbroeck *et al.*, *Quat. Sci. Rev.* **21**, 295 (2002).
16. M. Zhao, C.-Y. Huang, C.-C. Wang, G. Wei, *Palaeogeogr. Palaeoclimatol. Palaeoecol.* **236**, 39 (2006).
17. D. W. Oppo, Y. B. Sun, *Geology* **33**, 785 (2005).
18. A. B. G. Bush, R. G. Fairbanks, *J. Geophys. Res. D Atmos.* **108**, 4446 (2003).
19. P. N. DiNezio *et al.*, *Paleoceanography* **26**, PA3217 (2011).
20. K. B. Cutler *et al.*, *Earth Planet. Sci. Lett.* **206**, 253 (2003).
21. P. De Deckker, N. J. Tapper, S. Van der Kaars, *Global Planet. Change* **35**, 25 (2003).
22. J. E. Tierney *et al.*, *J. Geophys. Res. D Atmos.* **117**, D19108 (2012).
23. R. A. Madden, P. R. Julian, *J. Atmos. Sci.* **29**, 1109 (1972).
24. S. Dannenmann, B. K. Linsley, D. W. Oppo, Y. Rosenthal, L. Beaufort, *Geochim. Geophys. Geosyst.* **4**, 1 (2003).
25. R. Zhang, T. L. Delworth, *J. Clim.* **18**, 1853 (2005).
26. J. C. H. Chiang, C. M. Bitz, *Clim. Dyn.* **25**, 477 (2005).
27. L. C. Kanner, S. J. Burns, H. Cheng, R. L. Edwards, *Science* **335**, 570 (2012).
28. C. Barbante *et al.*; EPICA Community Members, *Nature* **444**, 195 (2006).
29. H. Rashid, R. Hesse, D. J. W. Piper, *Paleoceanography* **18**, 1077 (2003).
30. M. Storey, R. G. Roberts, M. Saidin, *Proc. Natl. Acad. Sci. U.S.A.* **109**, 18684 (2012).
31. K. K. Andersen *et al.*; North Greenland Ice Core Project members, *Nature* **431**, 147 (2004).
32. E. W. Wolff, J. Chappellaz, T. Blunier, S. O. Rasmussen, A. Svensson, *Quat. Sci. Rev.* **29**, 2828 (2010).
33. A. Berger, M. F. Loutre, *Quat. Sci. Rev.* **10**, 297 (1991).
34. E. Bard, B. Hamelin, R. G. Fairbanks, A. Zindler, *Nature* **345**, 405 (1990).
35. E. Bard, B. Hamelin, R. G. Fairbanks, *Nature* **346**, 456 (1990).

Acknowledgments: We thank N. Meckler, J. Partin, and S. Clark (Gunung Mulu National Park) for field assistance; J. Partin for assistance in sample analysis; G. Paris, M. Raven, S. Hines, and A. Subhas for assistance in U-Th dating; and J. Lynch-Stieglitz for providing comments on early versions of the manuscript. S.A.C., K.M.C., and J.F.A. were involved in the writing and design of this study; A.A.T. and B.C. facilitated the fieldwork for this study; S.A.C., K.M.C., S.L., and J.M. collected samples; and S.A.C. analyzed the samples. The research was funded by NSF PECASE Award no. 0645291 to K.M.C., NSF AGS award no. 0903099 to J.F.A., and a NSF Graduate Research Fellowship to S.A.C. Permits for this work were granted by the Malaysian Economic Planning Unit, the Sarawak State Planning Unit, and the Sarawak Forestry Department. All data reported in this paper are archived at the National Climatic Data Center (<http://ftp.ncdc.noaa.gov/pub/data/paleo/speleothem/pacific/borneo2013.txt>).

Supplementary Materials

www.sciencemag.org/cgi/content/full/science.1233797/DC1
Materials and Methods
Figs. S1 to S12
Tables S1 to S4
References (36–38)

7 December 2012; accepted 21 May 2013
Published online 6 June 2013;
10.1126/science.1233797

Supercomplex Assembly Determines Electron Flux in the Mitochondrial Electron Transport Chain

Esther Lapuente-Brun,^{1,2*} Raquel Moreno-Loshuertos,^{2*} Rebeca Acín-Pérez,¹ Ana Latorre-Pellicer,¹ Carmen Colás,¹ Eduardo Balsa,^{1,3} Ester Perales-Clemente,¹ Pedro M. Quirós,⁵ Enrique Calvo,¹ M. A. Rodríguez-Hernández,⁴ Plácido Navas,⁴ Raquel Cruz,⁶ Ángel Carracedo,⁶ Carlos López-Otín,⁵ Acisclo Pérez-Martos,² Patricio Fernández-Silva,² Erika Fernández-Vizarra,⁷ José Antonio Enriquez^{1,2†}

The textbook description of mitochondrial respiratory complexes (RCs) views them as free-moving entities linked by the mobile carriers coenzyme Q (CoQ) and cytochrome c (cyt c). This model (known as the fluid model) is challenged by the proposal that all RCs except complex II can associate in supercomplexes (SCs). The proposed SCs are the respirasome (complexes I, III, and IV), complexes I and III, and complexes III and IV. The role of SCs is unclear, and their existence is debated. By genetic modulation of interactions between complexes I and III and III and IV, we show that these associations define dedicated CoQ and cyt c pools and that SC assembly is dynamic and organizes electron flux to optimize the use of available substrates.

Electron transport in the mitochondria cannot be fully explained by the classical fluid model (1) or the solid model, which proposes that the respirasome is the only functional mitochondrial electron transport chain (mETC) (2, 3). However, both models can be regarded as extremes of a more dynamic situation in which the respirasome [containing complexes I, III, and IV (CI, CIII, and CIV)], the other supercomplexes (SCs) (CI and CIII or CIII and CIV), and free respiratory complex (RC) populations coexist (4). Although CI is unstable in the absence of CIII or CIV (5–7), definitive evidence for physical association between RCs in vivo has been lacking, and their putative functions remain unclear (2, 4, 8–12).

To investigate interaction between CI and CIII, we used mitochondria from mouse fibroblasts with constitutively abnormal low expression of CIII (S cells) (supplementary materials and fig. S1). Blue-native gel electrophoresis (BNGE) detected fewer CI-containing SCs in S cells than

in control cells; moreover, no free CIII was detected (Fig. 1A), suggesting that CI sequesters the limited amount of CIII. Oxygen consumption was measured in permeabilized S cells incubated with either the mETC substrates glutamate and malate, which generate intramitochondrial NADH (reduced form of nicotinamide adenine dinucleotide) to feed electrons to CI, thus promoting respiration through CI, CIII, and CIV, or succinate, which feeds electrons to CII, via flavin adenine dinucleotide (FAD), promoting respiration through CII, CIII, and CIV (fig. S1D). Combined with the use of specific inhibitors, this allowed us to measure respiration through alternate routes to CIV and also to spectrophotometrically determine electron flux through mETC components, both individually (CI, CII, CIII, or CIV) and in combination (CI with CIII or CII with CIII) (fig. S1F). The low content of CIII in S cells disrupted respiration from succinate and the activity of CII combined with CIII, indicating that the limited CIII is unavailable to electrons from CII (or other sources that deliver electrons to FAD, such as glycerol-3-phosphate dehydrogenase) (Fig. 1B). We ruled out that changes in coenzyme Q (CoQ) levels would explain this behavior (fig. S1G).

If physical association of CI with CIII creates separate populations of CIII molecules (the bound population dedicated to CI, the unbound to other enzymes), depletion of CII would not increase CIII-bound CI nor the flux between CI and CIII, but depletion of CI would release CIII and increase electron transport through CII and CIII. Small interfering RNA (siRNA)-mediated depletion of CII in control fibroblasts reduced activity of CII and CII with CIII without affecting CI or CI with CIII (fig. S1, H and I). In contrast, in a cell line in which CI was stably depleted by 60% (I3), CIII activity was normal and CII activity slightly increased, although combined activity of CI and CIII was normal and the linked

activity of CII with CIII was increased (Fig. 1B). These results support the idea that electron flux from CI to CIII takes place within SCs, whereas electrons flow from CII to CIII not associated with CI. If this is so, depletion of CI in S cells would release CIII to reactivate electron transfer from CII. To test this, we used siRNA to deplete the CI subunit *NDUFS3* from S cells. BNGEs revealed that depletion of CI released CIII from CI-SC (Fig. 1, C and D). This was accompanied by decreased electron flux through CI and CIII and increased flux through CII and CIII (Fig. 1E). CIII thus associates preferentially with CI in CoQ-containing supercomplexes (those containing CI and III or those with CI, III, and IV), establishing preferential electron flux from CI to CIII. To confirm this, we depleted CIII from control cells with siRNA (fig. S2A). Low CIII induced specific loss of supercomplex III+IV (fig. S2B) and a greater decrease in the combined activity of CII with CIII than that of CI with CIII (fig. S2C). Supercomplexes therefore define two functional CoQ populations: CoQ dedicated to transferring electrons originating from NADH (CoQ_{NADH}), which is trapped in SCs containing CI, and free CoQ in the inner mitochondrial membrane for use by CII and other enzymes that use FAD (CoQ_{FAD}) (Fig. 1F).

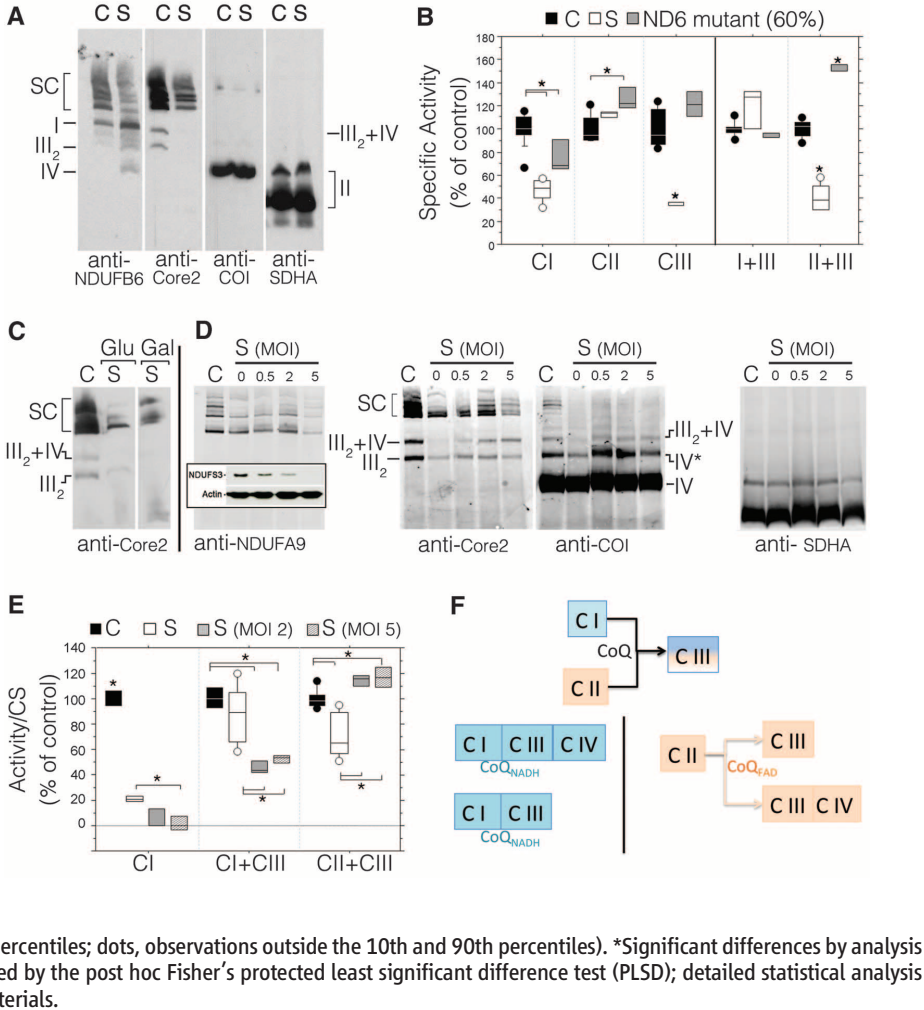
To investigate interaction between CIII and CIV, we screened for proteins present in SCs but not in free complexes (fig. S3, A and B). Mitochondrial samples prepared in the presence of digitonin, which preserves the integrity of RC and SC associations, were fractionated by BNGE, and individual bands were analyzed by proteomic methods. The screen identified cytochrome c oxidase subunit VIIa polypeptide 2-like (Cox7a2l) in the respirasome and in SC CIII+CIV, but not in free complexes III or IV (fig. S3). In parallel, we fortuitously discovered a Cox7a2l mutation in a screen of immortalized mouse fibroblasts derived from six littermates with mixed genetic background (C57BL/6 and 129Sv strains) (fig. S4A). Three cell lines had the reported pattern of SC interactions on immunoblots after one-dimensional BNGE (SC⁺ cells). However, the other three lines (SC⁻ cells) showed no association between CIII and CIV (fig. S4, A and B). A search for single-nucleotide polymorphisms (SNPs) differentiating SC⁺ and SC⁻ cells identified most in chromosome 17, which contains the *Cox7a2l* gene (fig. S4C). The SC⁻ lines were homozygous for a *Cox7a2l* version 6 base pairs shorter than that found in heterozygosis in SC⁺ cell lines (fig. S5A); these proteins encode proteins of 111 and 113 amino acids, respectively. Our proteomic analysis detected only the long isoform (fig. S3D). Immunoblotting detected Cox7a2l protein only in SC⁺ cell lines, indicating that the short isoform may be unstable (fig. S5B). Purebred C57BL/6 mice contained the short allele and 129Sv mice the long one, both in homozygosis, and accordingly these mice exclusively showed the SC⁻ or SC⁺ phenotype, respectively (Fig. 2, A and B). Based on these findings, we propose that

¹Centro Nacional de Investigaciones Cardiovasculares Carlos III, Madrid, Spain. ²Departamento de Bioquímica y Biología Molecular y Celular, Facultad de Ciencias, Universidad de Zaragoza, Zaragoza 50009, Spain. ³Servicio de Inmunología, Hospital Universitario de La Princesa, Universidad Autónoma de Madrid, Instituto de Investigación Sanitaria Princesa (IIS-IP), Madrid 28006, Spain. ⁴Centro Andaluz de Biología del Desarrollo, Universidad Pablo de Olavide-CSIC and Centro de Investigación Biomédica en Red de Enfermedades Raras, ISCIII, Sevilla 41013 Spain. ⁵Departamento de Bioquímica y Biología Molecular, Instituto Universitario de Oncología (IUOPA), Universidad de Oviedo, 33006-Oviedo, Spain. ⁶Grupo de Medicina Xenómica, Facultad de Medicina, Centro de Investigación Biomédica en Red de Enfermedades Raras, Universidad de Santiago de Compostela 15782 Santiago de Compostela, A Coruña, Spain. ⁷IIS Aragón, Unidad de Investigación Traslacional Instituto Aragonés de Ciencias de la Salud, Hospital Universitario Miguel Servet, Zaragoza 50009, Spain.

*These authors contributed equally to this work.

†Corresponding author. E-mail: jaenriquez@cnic.es

Fig. 1. Separate CoQ pools supply electrons from CI and CII to CIII. (A) Immunoblot of assembled supercomplexes in digitonin-permeabilized mitochondria separated by BNGE and probed with monoclonal antibodies for CI (anti-NDUFB6), CIII (anti-Core2), CIV (anti-COI), and CII [anti-SDHA (130)]. (B) Box plot representation of mitochondrial complex activities, either alone or in combination with CIII, in C, S, and heteroplasmic ND6 mutant cells (lacking the CI subunit *ND6-M*, and thus partially depleted for CI) (19–21). Activities were measured spectrophotometrically in the presence of specific electron donors and complex inhibitors (see supplementary materials). When cells were grown in medium containing glucose instead of galactose—to allow them to survive through glycolysis—free CIII was detectable in S cells. SC, supercomplexes containing CI; III₂+IV, supercomplex III+IV; III₂, dimeric CIII. (C) BNGE immunoblot of CIII-containing supercomplexes in S cells grown with glucose or galactose. (D) BNGE immunoblots showing distribution of CI, CIII, CIV, and CII in control cells (C) and S cells shRNA-depleted for the CI subunit NDUF53 (S) at the indicated multiplicity of infection (MOI). IV and IV*, nonsuperassembled complex IV. (Inset) SDS–polyacrylamide gel electrophoresis (SDS–PAGE) immunoblot of NDUF53 (actin was the loading control). (E) Activities of isolated CI, CI+CIII, and CII+CIII in control cells and NDUF53-interfered S cells (CI-K_d). Respiration capacity of S cells was lower than in (B) because they were in glucose medium. (F) Ubiquinone exists in independent pools, one for NADH (blue) and other for FAD-containing enzymes (brown). Data in (B) and (E) are presented as box plots (horizontal bar, median; box limits, 25th and 75th percentiles; whiskers, 10th and 90th percentiles; dots, observations outside the 10th and 90th percentiles). *Significant differences by analysis of variance (ANOVA). Paired differences were assessed by the post hoc Fisher’s protected least significant difference test (PLSD); detailed statistical analysis for all figures is described in the supplementary materials.



Cox7A21 be renamed supercomplex assembly factor I (SCAFI). The yeast proteins *rcf1* and *rcf2*, previously proposed to be supercomplex III:IV assembly factors, also affect individual CIV assembly (14–16).

Mice derived from 129sv:C57BL/6 intercrosses showed normal supercomplex formation or no association of CIII with CIV (Fig. 2B), demonstrating tight correlation between absence of 113 amino acid SCAFI and failed CIII-CIV interaction. The long form of SCAFI and the SC⁺ phenotype were present in CBA, 129, NZB, and CD1 mice, whereas C57BL/6J and Balb/cJ mice were homozygous for the short form and had the SC[−] phenotype (Fig. 3, A and B). SC[−] cells were unaffected by overexpression of the short form, whereas overexpression of the long form restored the assembly of SCs containing CIV (Fig. 2, C and D).

Respiration rates were higher in liver mitochondria lacking SCAFI, both when incubated with pyruvate and malate (pyr+mal) (for which electrons are carried by NADH) or succinate (for which electrons are carried by FAD) (Fig. 3C). Respiration was higher in C57BL/6J fibroblasts transfected with short-SCAFI than in those transfected with long-SCAFI (fig. S6, A and B).

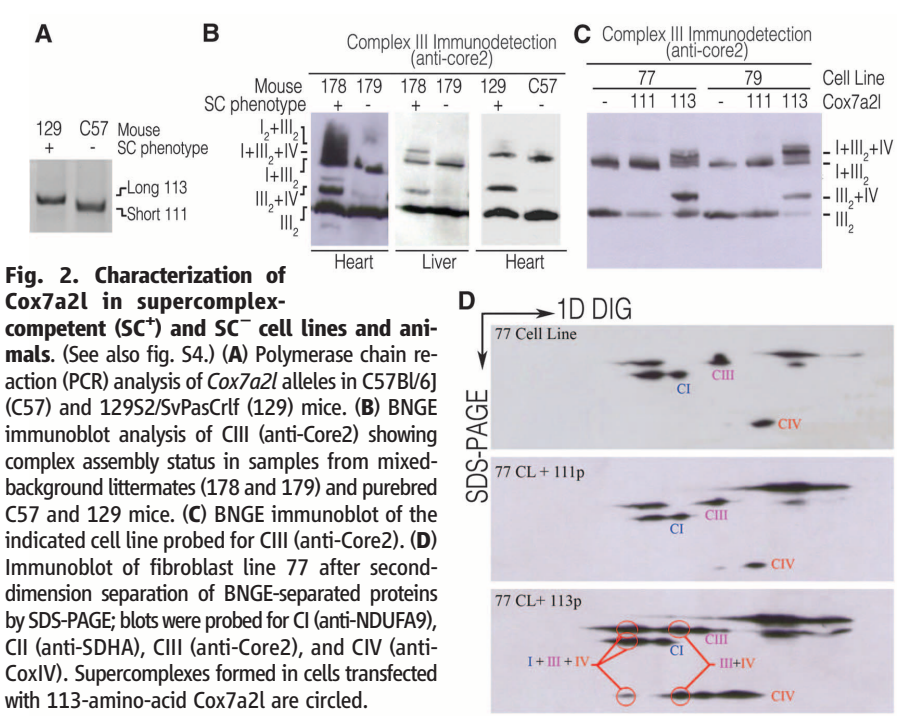


Fig. 2. Characterization of Cox7a21 in supercomplex-competent (SC⁺) and SC[−] cell lines and animals. (See also fig. S4.) (A) Polymerase chain reaction (PCR) analysis of *Cox7a21* alleles in C57BL/6J (C57) and 129Sv/CvPasCrlf (129) mice. (B) BNGE immunoblot analysis of CIII (anti-Core2) showing complex assembly status in samples from mixed-background littermates (178 and 179) and purebred C57 and 129 mice. (C) BNGE immunoblot of the indicated cell line probed for CIII (anti-Core2). (D) Immunoblot of fibroblast line 77 after second-dimension separation of BNGE-separated proteins by SDS-PAGE; blots were probed for CI (anti-NDUFA9), CII (anti-SDHA), CIII (anti-Core2), and CIV (anti-CoxIV). Supercomplexes formed in cells transfected with 113-amino-acid Cox7a21 are circled.

In contrast, CIV respiration driven by the specific electron donor tetramethylphenylenediamine (TMPD) was similar regardless of SCAFI expression. Thus, cells expressing functional SCAFI do not use the full potential of CIV when fed with glucose (fig. S6B). In permeabilized C57BL/6J-derived fibroblasts expressing short-SCAFI, adenosine triphosphate (ATP) production was near maximal with pyr+mal or succinate as substrates, whereas maximal respiration and ATP production in cells expressing long-SCAFI required substrates for both the NADH and the FAD routes (fig. S6C).

In the absence of SCAFI, no CIV will assemble in SCs, and electrons from NADH or FAD will pass through a single pool of cyt c to a single pool of CIV (Fig. 3D). In contrast, in the presence of SCAFI, a fraction of CIV interacts with CIII and two SCs would form: I+III+IV (the respirasome) and III+IV (Fig. 3D). Because CIV-

containing SCs also contain cyt c (4, 17), this will define three CIV populations: one receiving electrons exclusively from NADH (CIV_{NADH}), another from FAD-dependent enzymes (CIV_{FAD}), and a third from NADH and FAD (Fig. 3D). Confirming this, simultaneous exposure of SCAFI⁺ mitochondria to succinate and pyr+mal had an additive effect on respiration and ATP synthesis, an effect not seen in the absence of CIII+CIV superassembly (Fig. 3C).

The ability of SCAFI to segment the mETC into three CIV populations may prevent saturation by one substrate, thereby promoting simultaneous oxidation of multiple substrates at optimum rates. To test this, we evaluated fumarate synthesis in SCAFI⁺ and SCAFI⁻ liver mitochondria supplied with succinate alone or with pyr+mal. With succinate alone, SCAFI⁻ mitochondria generated fumarate at higher rates than SCAFI⁺ mitochondria (Fig. 3E). Simultaneous addition

of succinate and pyr+mal did not alter fumarate synthesis in SCAFI⁺ mitochondria but significantly reduced it in SCAFI⁻ mitochondria (Fig. 3E), demonstrating that SCAFI-mediated assembly of CIV into SCs minimizes competitive inhibition of respiration between pyruvate and succinate.

The ratio of NADH:FAD electrons feeding the mETC is higher when glucose is the respiratory substrate and lower for fatty-acid (FA) oxidation. Adjustment of mETC superassembly would provide a mechanism to ensure efficient oxidation of available substrates. To test this, we analyzed respiration capacity through the FAD and NADH routes in liver mitochondria from CD1 and C57BL/6J mice fed ad libitum or fasted for 18 hours to activate FA degradation. In mitochondria from fed animals of both strains, the respiration rate was higher with succinate than with pyr+mal (Fig. 4, A and B). Simultaneous use of both substrates produced an additive effect on maximum respiration in CD1 (Fig. 4A) but not C57BL/6J mitochondria (Fig. 4B). In mitochondria from fasted animals, respiration driven by pyr+mal was significantly lower in both strains, whereas succinate respiration was enhanced by fasting in CD1 but not C57BL/6J mitochondria (Fig. 4, A and B). These results support the existence of separate electron routes and are consistent with the predicted shift to the FAD route upon switching to FA degradation.

In CD1 mitochondria, fasting reduced maximal CI and CI+CIII activities without influencing CII or CII+CIII (Fig. 4A), but this effect was not seen in C57BL/6J mitochondria (Fig. 4B). Accordingly, fasting reduced the proportion of CIII assembled with CI (NADH route) only in CD1 mitochondria (Fig. 4, A and B). Pyruvate dehydrogenase (PDH) activity is down-regulated by phosphorylation by PDH kinase during starvation (Fig. 4C) (18). This may explain the lower respiration rate with pyr+mal in both C57BL/6J and CD1 mitochondria, despite the fact that CI activity is down-regulated only in CD1 mice (Fig. 4, A and C). An alternative way to generate intramitochondrial NADH+H⁺ is to feed mitochondria with glutamate, which is converted to α -ketoglutarate by glutamate dehydrogenase, an enzyme not regulated by starvation (Fig. 4C). Because starvation reduced CI activity only in CD1 mice, glutamate-dependent respiration should be affected only in this strain. This was confirmed in liver mitochondria from starved CD1 animals, in which pyruvate- and glutamate-driven synthesis of ATP was decreased, whereas only pyruvate-dependent ATP synthesis was decreased in C57BL/6J-derived organelles (Fig. 4D).

Our results provide genetic evidence for the existence of mitochondrial respiratory superassemblies, supporting the plasticity model of mETC organization and identifying dynamic supercomplex assembly as a mechanism through which cells might adapt to varying carbon sources and tailor the mETC to specific cell-type requirements. The lack of this mechanism in commonly used mouse strains

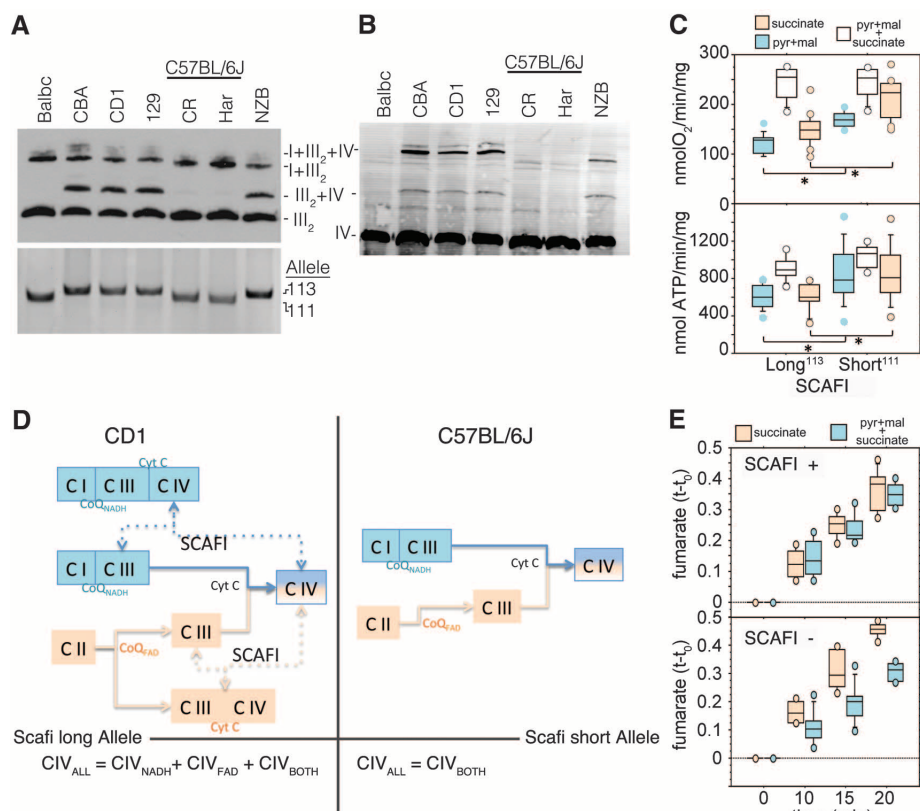


Fig. 3. Cox7a2/SCAFI depletion alters mitochondrial respiratory function. (A) (Top) BNGE immunoblot of CIII (anti-Core2) in different mouse strains, showing complex assembly in liver mitochondria. (Bottom) Genotyping (PCR) of the Cox7a2l allele. **(B)** BNGE immunoblot of CIV (anti-NDUFA4), showing complex assembly in liver mitochondria. **(C)** Substrate-driven rates of oxygen consumption and ATP synthesis in liver mitochondria from Cox7a2/SCAFI-deficient (Short) and Cox7a2/SCAFI-expressing (Long) mice. **(D)** Plasticity model of mETC organization, showing CI associations with a dedicated CoQ pool [blue, the respirasome (CI+III+IV) and CI+III] coexisting with CIII+CIV associations and free CII, CIII, and CIV. (Left) Normal situation (CD1 mice), in which Cox7a2/SCAFI modulates CIV-containing supercomplexes, thereby regulating the proportions of free CIII and CIV and generating three states for CIV. (Right) Extreme situation of C57BL/6J mice, where SCAFI is absent and no CIV-containing supercomplexes form, making all CIV available to any substrate. **(E)** Time profile ($t-t_0$) of fumarate production by isolated liver mitochondria from SCAFI-proficient and SCAFI-deficient mice in the presence of succinate or succinate and pyr+mal. Data in (C) and (E) are presented as box plots; marks and symbols same as for Fig. 1. *Significant differences by ANOVA. Paired differences were assessed by PLSD.

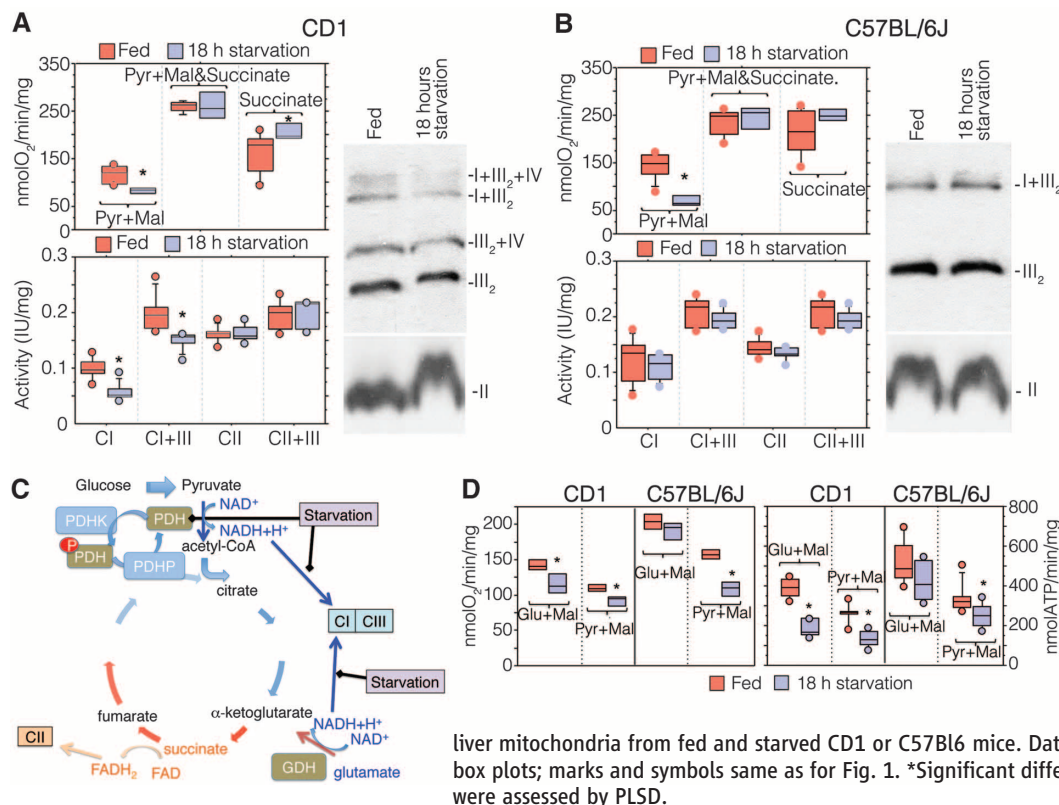


Fig. 4. mETC activity and super-complex distribution in response to fasting. (A and B) (Top left) Oxygen-dependent (coupled) respiration in isolated liver mitochondria from fed and starved CD1 (A) or C57BL/6J mice (B) driven by pyr+mal, succinate, or both. (Bottom left) Activities of mitochondrial complexes (CI and CII), individually and in combination with CIII (CI+III and CII+III), expressed as international units (IU) per milligram mitochondrial protein. (Right) BNGE immunoblots showing CIII associations (anti-Core2). CII (anti-SDHA) is shown on the same blot as a loading control. (C) Sites for mitochondrial generation of $\text{NADH}+\text{H}^+$ or FADH_2 from different substrates and processes potentially targeted by starvation. PDHK/D, PDH kinase/dehydrogenase; GDH, glutamate dehydrogenase. (D) Oxygen-dependent (coupled) respiration (left) and ATP production rate (right) driven by pyr+mal or glutamate in isolated

liver mitochondria from fed and starved CD1 or C57BL/6J mice. Data in (A), (B) and (D) are presented as box plots; marks and symbols same as for Fig. 1. *Significant differences by ANOVA. Paired differences were assessed by PLSD.

has potential implications for studies of metabolic processes and is of interest for research into human diseases affecting mitochondrial function.

References

1. C. R. Hackenbrock, B. Chazotte, S. S. Gupte, *J. Bioenerg. Biomembr.* **18**, 331 (1986).
2. H. Schagger, K. Pfeiffer, *EMBO J.* **19**, 1777 (2000).
3. G. Lenaz, M. L. Genova, *Am. J. Physiol. Cell Physiol.* **292**, C1221 (2007).
4. R. Acín-Pérez, P. Fernández-Silva, M. L. Peleato, A. Pérez-artos, J. A. Enriquez, *Mol. Cell* **32**, 529 (2008).
5. R. Acín-Pérez et al., *Mol. Cell* **13**, 805 (2004).
6. F. Díaz, H. Fukui, S. Garcia, C. T. Moraes, *Mol. Cell. Biol.* **26**, 4872 (2006).
7. U. D. Vempati, X. Han, C. T. Moraes, *J. Biol. Chem.* **284**, 4383 (2009).
8. H. Eubel, J. Heinemeyer, H. P. Braun, *Plant Physiol.* **134**, 1450 (2004).
9. N. V. Dudkina, H. Eubel, W. Keegstra, E. J. Boekema, H. P. Braun, *Proc. Natl. Acad. Sci. U.S.A.* **102**, 3225 (2005).
10. E. Schäfer et al., *J. Biol. Chem.* **281**, 15370 (2006).
11. E. Schäfer, N. A. Dencher, J. Vonck, D. N. Parcej, *Biochemistry* **46**, 12579 (2007).
12. N. V. Dudkina, M. Kudryashev, H. Stahlberg, E. J. Boekema, *Proc. Natl. Acad. Sci. U.S.A.* **108**, 15196 (2011).
13. R. Acín-Pérez et al., *Hum. Mol. Genet.* **12**, 329 (2003).
14. Y.-C. Chen et al., *Cell Metab.* **15**, 348 (2012).
15. V. Strogolova, A. Furness, M. Robb-McGrath, J. Garlich, R. A. Stuart, *Mol. Cell. Biol.* **32**, 1363 (2012).
16. M. Vukotic et al., *Cell Metab.* **15**, 336 (2012).
17. T. Althoff, D. J. Mills, J.-L. Popot, W. Kühlbrandt, *EMBO J.* **30**, 4652 (2011).
18. M. S. Patel, L. G. Korotchkina, *Biochem. Soc. Trans.* **34**, 217 (2006).
19. M. E. Gallardo et al., *Hum. Mutat.* **27**, 575 (2006).
20. M. P. Bayona-Bafaluy et al., *Nucleic Acids Res.* **31**, 5349 (2003).
21. R. Staden, K. F. Beal, J. K. Bonfield, *Methods Mol. Biol.* **132**, 115 (2000).

Supplementary Materials

www.sciencemag.org/cgi/content/full/340/6140/1567/DC1
Materials and Methods
Supplementary Text
Figs. S1 to S6

Table S1

References (22–27)

18 September 2012; accepted 25 April 2013
10.1126/science.1230381

Intrinsically Disordered Protein Threads Through the Bacterial Outer-Membrane Porin OmpF

Nicholas G. Housden,¹ Jonathan T. S. Hopper,² Natalya Lukyanova,³ David Rodriguez-Larrea,² Justyna A. Wojdyla,¹ Alexander Klein,¹ Renata Kaminska,¹ Hagan Bayley,² Helen R. Saibil,³ Carol V. Robinson,² Colin Kleanthous^{1*}

Porins are β -barrel outer-membrane proteins through which small solutes and metabolites diffuse that are also exploited during cell death. We have studied how the bacteriocin colicin E9 (ColE9) assembles a cytotoxic translocon at the surface of *Escherichia coli* that incorporates the trimeric porin OmpF. Formation of the translocon involved ColE9's unstructured N-terminal domain threading in opposite directions through two OmpF subunits, capturing its target TolB on the other side of the membrane in a fixed orientation that triggers colicin import. Thus, an intrinsically disordered protein can tunnel through the narrow pores of an oligomeric porin to deliver an epitope signal to the cell to initiate cell death.

Porins mediate the diffusion of nutrients and ions into cells and organelles and the expulsion of xenobiotics through a central pore (1, 2). We studied the mechanism by which the endonuclease [deoxyribonuclease (DNase)] bacteriocin ColE9 exploits the porin OmpF in the outer membrane (OM) of *Escherichia coli*.

OmpF is one of the most abundant proteins in the *E. coli* OM (>100,000 copies per cell), with related porins widespread in bacteria (3, 4). Composed of three identical 16-stranded β -barrels, each with a narrow pore that traverses the OM, OmpF subunits restrict the passive diffusion of molecules to those <600 daltons. Nevertheless,

some colicins use OmpF, or its homolog OmpC, to enter the periplasm after their initial binding to the vitamin B₁₂ receptor BtuB (Fig. 1A) (5, 6). Colicins are potent cytotoxins that are expressed and released by *E. coli* in response to environmental stress that target closely related organisms during interbacterial competition (7–10). ColE9 (60 kDa) is released bound to the immunity protein Im9, a high-affinity inhibitor [dissociation constant (K_d) $\sim 10^{-14}$ M] that neutralizes the DNase domain in the colicin-producing host (11). ColE9 recruits OmpF through an intrinsically unstructured translocation domain (IUTD) in order to contact TolB in the periplasm (Fig. 1A), thereby forming a translocon complex that initiates cell entry (12–15). Colicin translocons are transient, unstable species involving protein-protein interactions on either side of the OM (fig. S1). We thus devised a strategy to stabilize the translocon for ColE9, enabling its purification and subsequent biophysical and structural analysis (Fig. 1A).

We designed a disulfide bond trap that would form between the periplasmically located TolB-binding epitope (TBE) of ColE9 and TolB after

recruitment of OmpF in the OM. The covalent bond did not induce any structural changes relative to the wild-type complex (fig. S2 and table S1) (13). The ColE9 cysteine mutant was allowed to form its translocon at the OM of *E. coli* cells, was trapped by disulfide bond formation with the corresponding TolB cysteine mutant, and the entire complex was extracted from the membrane and purified, exploiting a histidine tag on the C terminus of TolB (fig. S1B). The ColE9 translocon was deemed homogeneous by blue native polyacrylamide gel electrophoresis (BN-PAGE) (Fig. 1B). The individual components of the translocon were identified by matrix-assisted laser desorption/ionization mass spectrometry of protein bands excised from SDS-PAGE gels; the latter also confirmed the presence of the trapping disulfide bond (Fig. 1C). The isolated translocon was a heptameric assembly composed of single copies of the ColE9-Im9 complex, BtuB, OmpF trimer, and TolB as determined by size-exclusion chromatography–multiangle light scattering (SEC-MALS) (fig. S3A) and native-state electrospray ionization mass spectrometry (ESI-MS) (16, 17) (Fig. 1D). The mass of the translocon obtained by ESI-MS ($296,983 \pm 80$ daltons) agreed closely with that calculated for the complex but included additional mass of ~ 3.5 kDa, which is likely to be a single molecule of lipopolysaccharide bound noncovalently to the BtuB receptor (fig. S4).

Limited proteolysis was used to probe the organization of the ColE9 translocon. Trypsin

digestion yielded a stable subcomplex when analyzed by BN-PAGE (Fig. 2A), which corresponded to intact TolB and OmpF and a ~ 11 -kDa fragment of ColE9 (fig. S5, A, C, and E). The ColE9 IUTD is known to house two OmpF-binding sites (OBS1, residues 2 to 18, and OBS2, residues 54 to 63) that flank the TolB-binding epitope (TBE; residues 32 to 47) (12) (fig. S6). The ~ 11 -kDa fragment of the digested translocon encompassed residues 2 to 122 from the ColE9 T domain (ColE9 T₂₋₁₂₂), which includes all the identified binding epitopes as well as additional sequences corresponding to extracellular regions of the colicin. ESI-MS and SEC-MALS confirmed the native mass of the digested translocon (Fig. 2B, fig. S3B, and table S2). It has previously been proposed that the colicin's IUTD passes through OmpF (Fig. 1D and fig. S6, A to C) (6, 12). SDS-PAGE of the digested translocon, in combination with heat treatment and a reducing agent, confirmed that the colicin had indeed passed through its bound porin; TolB and OmpF only comigrated when the disulfide between TolB and the ColE9 T₂₋₁₂₂ fragment was intact and OmpF was a folded trimer (Fig. 2C).

Two trypsin sites, one in each OBS, remained undigested when the translocon was treated with trypsin, whereas the same sites were readily proteolyzed in a disulfide-bonded complex containing just ColE9 and TolB (fig. S5, B, D, and F). These differential protease accessibility results are incompatible with a simple sequential translocation

Fig. 1. Isolation and characterization of the ColE9 translocon from the OM of *E. coli*. (A) Strategy for the capture and isolation of the ColE9 translocon. Nuclease colicins such as ColE9 (brown) contain a hairpin receptor-binding (R-) domain; an N-terminal translocation (T-) domain that includes the IUTD, shown as a dotted line; and a C-terminal cytotoxic DNase domain to which is bound the immunity protein Im9 (yellow). The engineered cysteines for disulfide bond formation between the TolB-binding epitope of ColE9 and histidine-tagged TolB (purple) are shown as red circles. (B) BN-PAGE of the isolated translocon showing that the complex contains the ColE9-Im9 complex, BtuB, OmpF, and TolB. (C) 12% SDS-PAGE of the translocon \pm β -mercaptoethanol (β -Me), confirming the presence of the disulfide between ColE9 and TolB. (D) Native-state ESI-MS spectrum of the ColE9 translocon. Colored inserts give assignments for species observed in the spectrum, all devoid of detergent: orange hexagon, the intact complex that includes a single molecule of lipopolysaccharide; red circle, translocon from which BtuB and lipopolysaccharide have dissociated in the gas phase; blue square, dissociated BtuB. See table S2 for masses.

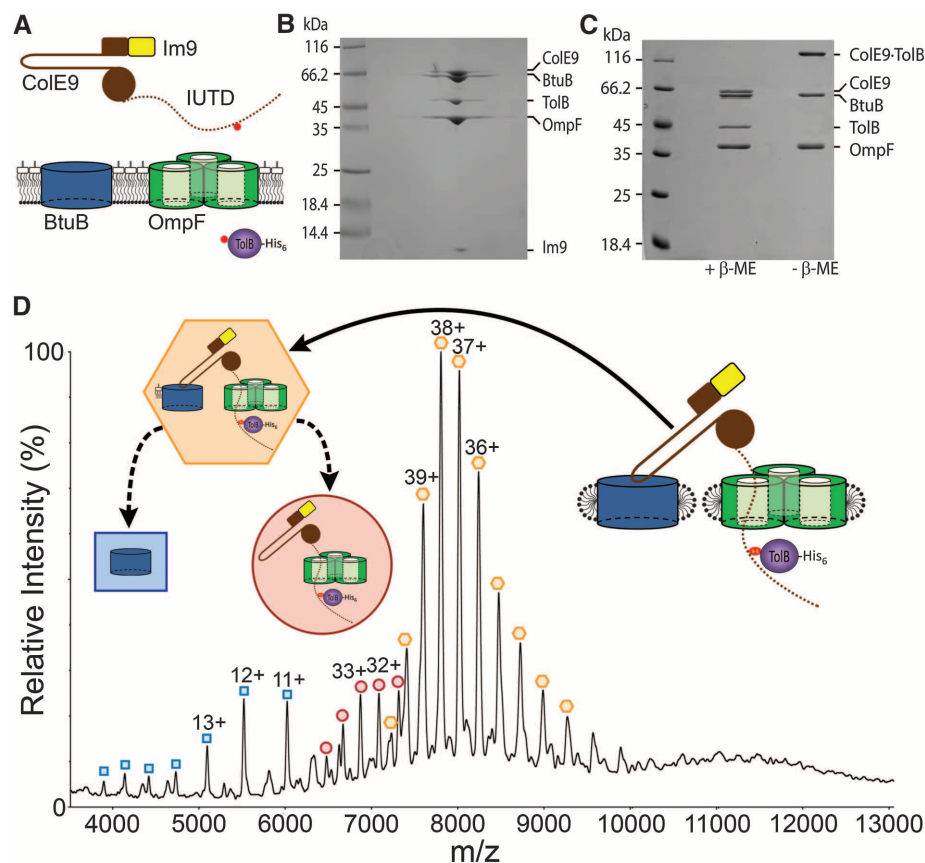


Fig. 2. Formation of the ColE9 translocon involves passage of the colicin through OmpF. (A) BN-PAGE showing the time course for limited proteolysis of the translocon by trypsin (100:1) at 30°C. (B) Native-state ESI-MS data for the trypsin-digested translocon (containing TolB, OmpF, and ColE9 T₂₋₁₂₂) along with a graphical representation of the complex. The observed and expected masses for the complex were 166,528 ± 81 daltons and 166,572 daltons, respectively. (C) 12% SDS-PAGE of the digested translocon and its comparison to control TolB and OmpF proteins ± reducing agent (β-Me) and/or heat denaturation. In the absence of boiling, OmpF migrates as a trimer. TolB and the OmpF trimer only migrate together within the proteolysed translocon when connected by ColE9 T₂₋₁₂₂ that has passed through the trimer and formed a trapping disulfide with TolB (last lane). Reduced ColE9 T₂₋₁₂₂ migrates off the end of this gel and so is not resolved.

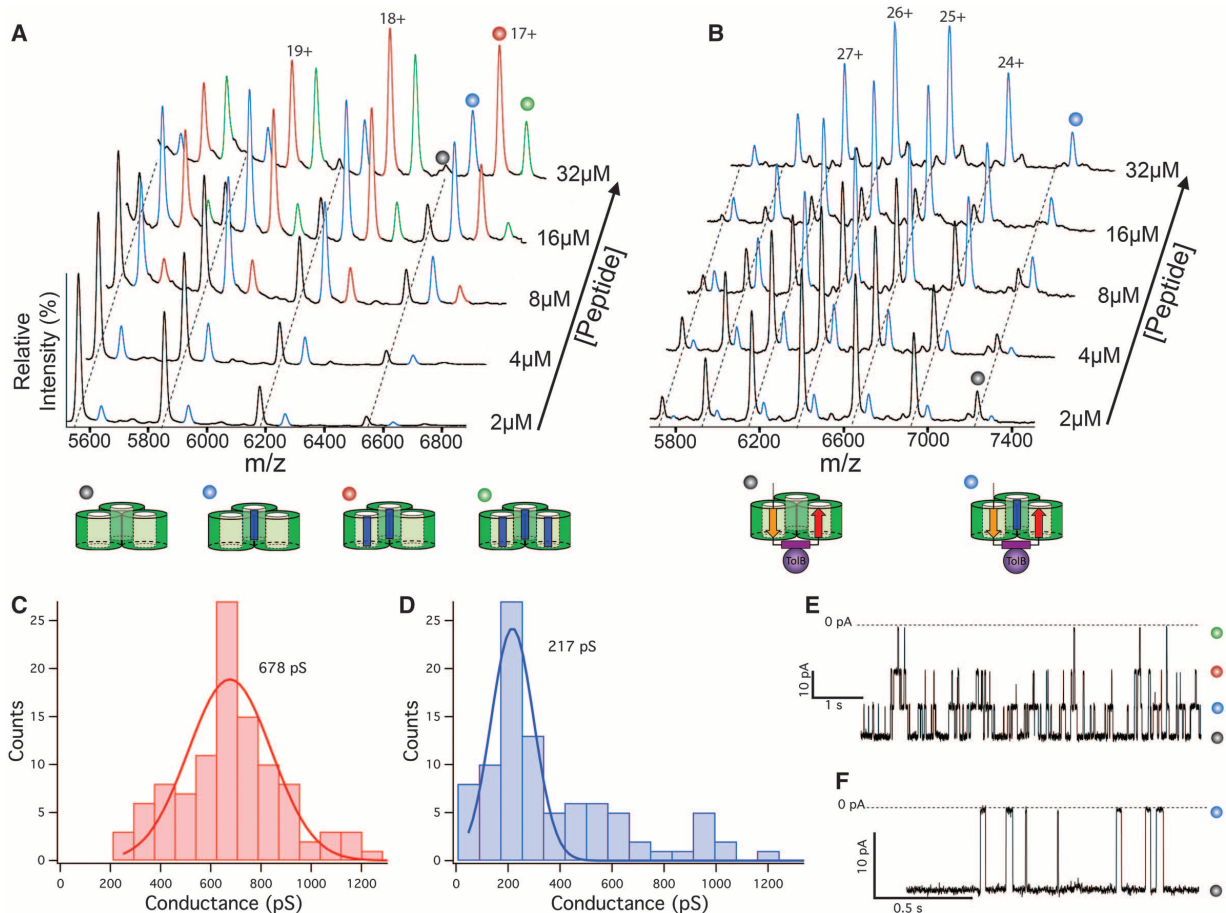
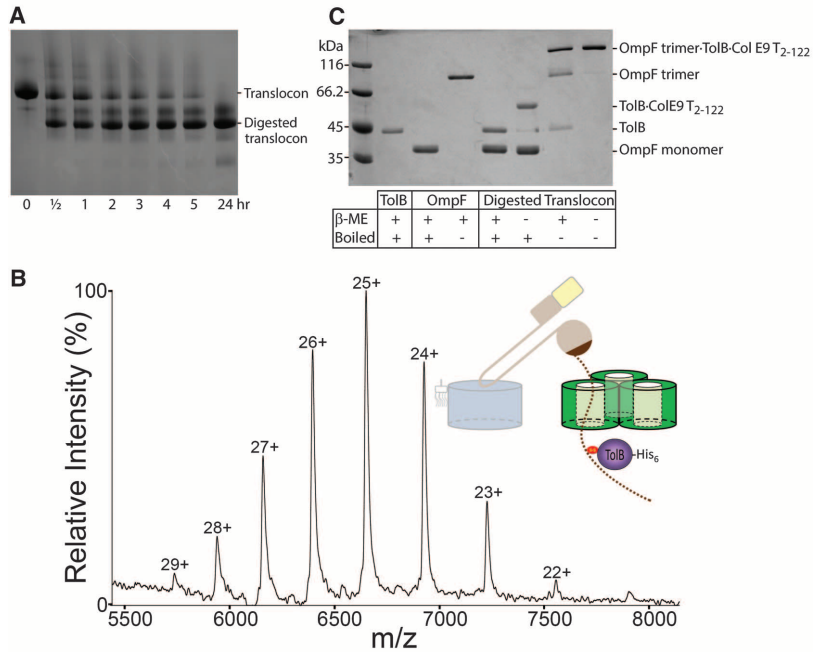


Fig. 3. ColE9 occupies two subunits of an OmpF trimer. (A) ESI-MS titration showing binding of up to three OBS1 peptides to OmpF in the gas phase (see table S2 for masses). Peak assignments are shown below the data (OBS1 is represented as a blue rectangle). (B) ESI-MS titration showing the binding of one OBS1 peptide to the proteolysed translocon. Peak assignments are shown below the data (see fig. S6 for color coding of the ColE9 IUTD-binding epitopes). (C) Histogram showing a Gaussian distribution of unitary conductance (in pS) mea-

surements for OmpF trimers in planar lipid bilayers. (D) Histogram showing the Gaussian distribution of unitary conductance (in pS) measurements for the digested ColE9 translocon, where the mean value is one-third the OmpF conductance observed in (C). (E) Electrical recording (–50 mV) for a single OmpF trimer showing the blockade of its three channels by the OBS1 peptide, states assigned as in (A). (F) Electrical recording (–50 mV) for the tryptic-digested translocon showing the blockade of its single OmpF channel by the OBS1 peptide, states assigned as in (B).

model in which OBS2 is anchored in the porin and OBS1 merely passes unhindered to the periplasm (fig. S6, A to C). Instead, a single OmpF trimer may bind to both OBS sequences simultaneously (fig. S6, A, B, D, and E). To test this hypothesis, we used ESI-MS and electrical recordings in planar lipid bilayers to compare how many pores were available in OmpF and the proteolysed translocon to bind a 17-residue ColE9 OBS1 peptide. ESI-MS data of OmpF yielded well-resolved spectra and a mass very close to that predicted for the trimer (Fig. 3A and table S2). When the OBS1 peptide was titrated into OmpF, additional mass/charge ratio (m/z) states appeared, corresponding to noncovalent binding of OBS1 in all three of its pores. In contrast, when the OBS1 peptide was added to the trypsin digested translocon, a single peptide was bound, indicating that only one of the OmpF pores remained accessible (Fig. 3B). Furthermore, we were able to determine a K_d for the digested translocon complex with the OBS1 peptide by ESI-MS, which matched that for the OmpF-OBS1 complex obtained by ITC under the same buffer conditions ($K_d \sim 1 \mu\text{M}$) (fig. S7). Thus, the interactions of the OBS1 sequence within the porin remain fundamentally the same in the two complexes.

In a parallel approach, the electrical activity of OmpF and the proteolysed ColE9 translocon were compared. OmpF produces voltage-gated ion channels when incorporated into planar lipid bilayers that can be blocked by a variety of molecules, including colicin IUTD sequences (18). Purified OmpF had a mean conductance of $\sim 678 \pm 13$ pS, representing the ion conductivity of all three pores within the trimer (Fig. 3C). In contrast, the mean unitary conductance for the trypsin-digested translocon was one-third this value (217 ± 7 pS), consistent with the translocon having only one of its three OmpF subunits able to conduct ions (Fig. 3D). When the OBS1 peptide was added to OmpF, we saw sequential blockades and reopenings of each of its three conducting subunits (Fig. 3E and fig. S8). The proteolysed translocon channel was also blocked by OBS1, but its blockade was manifested as a simple two-state current trace consistent with the peptide occluding one OmpF pore (Fig. 3F). Thus, the ColE9 translocon involves its porin-binding sequences occupying two of the three subunits of OmpF (fig. S6E). As a consequence, the colicin's IUTD must traverse the hydrophobic bilayer of the OM twice, its many charged and polar residues, typical of intrinsically disordered

protein sequences (19), sequestered within the solvated pores of the oligomeric porin. This threading mechanism also implies that OBS1 has the ability to insert into an OmpF subunit in either orientation; N-to-C when the colicin first docks (fig. S6A), as observed in the crystal structure of the OmpF-OBS1 complex (12), and then C-to-N when it passes into a neighboring subunit from the periplasmic side of the porin (fig. S6E).

Negative stain electron microscopy (EM) structural analysis of the proteolysed translocon highlighted several important features of the assembly (Fig. 4A). First, TolB was well resolved, held ~ 20 Å from OmpF by ColE9, for which connecting density was also observed. Second, TolB was positioned asymmetrically relative to OmpF, tilted $\sim 45^\circ$ with respect to the membrane. TolB is part of the Tol-Pal system that includes the inner membrane TolQ-TolR-TolA complex and the lipoprotein Pal, which together help stabilize the OM (7). The ColE9 TBE is an allosteric activator of TolB, inducing its association with TolA (20), thereby connecting the colicin to the proton motive force across the inner membrane (Fig. 4B) (21). Formation of this network initiates colicin entry by triggering release of the tightly bound Im9 in a step that probably involves remodeling of the nuclease (22, 23). Tethering TolB to OmpF via the colicin's two porin-binding sites ensures that TolB does not rotate but rather is presented to TolA in a fixed orientation. Although neither OBS sequence is essential for ColE9 activity (at least one must be present), cell killing is significantly enhanced by having both present (12), suggesting that restricting TolB rotation increases the efficiency of translocation. Third, the intrinsically disordered ColE9 TBE has a kinetic advantage in binding TolB relative to Pal, the endogenous binding partner of TolB with which it competes (24, 25). Constraining the ColE9 TBE through two OmpF attachment points might further enhance such competition by lowering the entropic penalties associated with binding TolB.

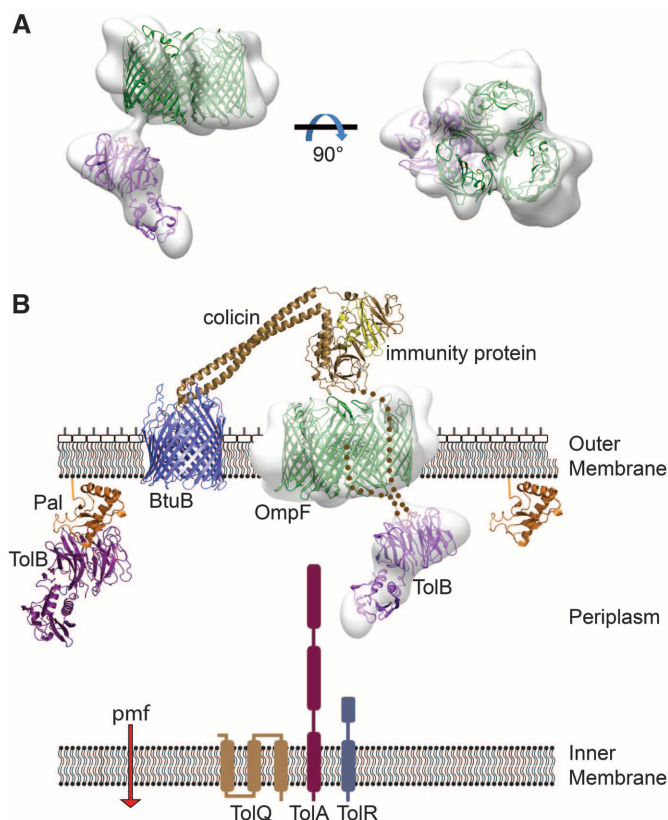


Fig. 4. ColE9 uses OmpF to capture TolB on the other side of the membrane in a defined orientation. (A) Negative-stain EM structure at ~ 20 Å resolution of the trypsin-digested ColE9 translocon composed of the OmpF trimer and TolB connected by ColE9 T₂₋₁₂₂, seen in side (left) and face (right) views of the membrane plane. OmpF and TolB crystal structures have been manually docked into the density as rigid bodies. (B) Structural representation of the ColE9 translocon [the structure for the related ColE3-Im3 bound to BtuB is shown (PDB accession code 1UJW)] and its protein-protein interaction network across the Gram-negative cell envelope (see text for details) (14, 21).

References and Notes

- G. E. Schulz, *Curr. Opin. Cell Biol.* **5**, 701 (1993).
- K. Zeth, M. Thein, *Biochem. J.* **431**, 13 (2010).
- H. Nikaïdo, *Microbiol. Mol. Biol. Rev.* **67**, 593 (2003).
- F. A. Schabert, C. Henn, A. Engel, *Science* **268**, 92 (1995).
- N. G. Housden, S. R. Loftus, G. R. Moore, R. James, C. Kleanthous, *Proc. Natl. Acad. Sci. U.S.A.* **102**, 13849 (2005).
- G. Kurisu *et al.*, *Nat. Struct. Biol.* **10**, 948 (2003).
- E. Cascales *et al.*, *Microbiol. Mol. Biol. Rev.* **71**, 158 (2007).
- B. C. Kirkup, M. A. Riley, *Nature* **428**, 412 (2004).
- B. Stecher *et al.*, *Proc. Natl. Acad. Sci. U.S.A.* **109**, 1269 (2012).
- D. M. Cornforth, K. R. Foster, *Nat. Rev. Microbiol.* **11**, 285 (2013).
- C. Kleanthous *et al.*, *Nat. Struct. Biol.* **6**, 243 (1999).
- N. G. Housden *et al.*, *Proc. Natl. Acad. Sci. U.S.A.* **107**, 21412 (2010).
- S. R. Loftus *et al.*, *Proc. Natl. Acad. Sci. U.S.A.* **103**, 12353 (2006).
- C. Kleanthous, *Nat. Rev. Microbiol.* **8**, 843 (2010).
- E. Yamashita, M. V. Zhaltina, S. D. Zakharov, O. Sharma, W. A. Cramer, *EMBO J.* **27**, 2171 (2008).

16. N. P. Barrera, N. Di Bartolo, P. J. Booth, C. V. Robinson, *Science* **321**, 243 (2008).
17. A. Laganowsky, E. Reading, J. T. S. Hopper, C. V. Robinson, *Nat. Protoc.* **8**, 639 (2013).
18. S. D. Zakharov *et al.*, *Biophys. J.* **87**, 3901 (2004).
19. H. J. Dyson, P. E. Wright, *Nat. Rev. Mol. Cell Biol.* **6**, 197 (2005).
20. D. A. Bonsor *et al.*, *EMBO J.* **28**, 2846 (2009).
21. K. S. Jakes, W. A. Cramer, *Annu. Rev. Genet.* **46**, 209 (2012).
22. M. Vankemmelbeke *et al.*, *J. Biol. Chem.* **284**, 18932 (2009).
23. O. E. Farrance *et al.*, *PLoS Biol.* **11**, e1001489 (2013).
24. G. Papadakos, N. G. Housden, K. J. Lilly, R. Kaminska, C. Kleanthous, *J. Mol. Biol.* **418**, 269 (2012).
25. D. A. Bonsor, I. Grishkovskaya, E. J. Dodson, C. Kleanthous, *J. Am. Chem. Soc.* **129**, 4800 (2007).

Acknowledgments: We thank S. Johnson (Department of Pathology, University of Oxford) for help with SEC-MALS experiments and D. Ashford (Department of Biology, York University) for LC-MS data. N.G.H. acknowledges the Department of Biochemistry (University of Oxford) for financial support. D.R.-L. was supported by the National Institutes of Health (grant R01 HG003709). C.V.R. acknowledges the Medical Research Council, European Research Council (ERC) Impress, and the Royal Society for financial support. H.R.S. acknowledges support from the Biotechnology and Biological Sciences Research Council (BBSRC) (BB/D00873/1), ERC (294408), and The Wellcome Trust (079605/2/06/2). This

work was supported by grants to C.K. from The Wellcome Trust (WT082045) and the BBSRC (BB/G020671/1). Atomic coordinates and structural amplitudes have been deposited in the Protein Data Bank (PDB) under accession number 4JML. The EM map has been deposited in the EM databank under accession number EMD-2372.

Supplementary Materials

www.sciencemag.org/cgi/content/full/340/6140/1570/DC1

Materials and Methods

Figs. S1 to S10

Tables S1 and S2

References (26–51)

15 March 2013; accepted 7 May 2013

10.1126/science.1237864

Temperature Drives the Continental-Scale Distribution of Key Microbes in Topsoil Communities

Ferran Garcia-Pichel,^{1*} Virginia Loza,^{1,2} Yevgeniy Marusenko,¹ Pilar Mateo,^{1,2} Ruth M. Potrafka¹

Global warming will likely force terrestrial plant and animal species to migrate toward cooler areas or sustain range losses; whether this is also true for microorganisms remains unknown. Through continental-scale compositional surveys of soil crust microbial communities across arid North America, we observed a latitudinal replacement in dominance between two key topsoil cyanobacteria that was driven largely by temperature. The responses to temperature of enrichment cultures and cultivated strains support this contention, with one cyanobacterium (*Microcoleus vaginatus*) being more psychrotolerant and less thermotolerant than the other (*M. steenstrupii*). In view of our data and regional climate predictions, the latter cyanobacterium may replace the former in much of the studied area within the next few decades, with unknown ecological consequences for soil fertility and erodibility.

Plant interspaces in arid lands can be colonized by cryptic photosynthetic assemblages known as biological soil crusts (biocrusts) (1, 2). These largely microbial communities help stabilize the soil against erosion (3), are net exporters of biologically fixed carbon and nitrogen (4, 5), and modify the hydrological properties of soil (6), all of which are crucial roles for the fertility and sustainability of desert ecosystems. Because of the extent of arid lands, the biogeochemical contributions of soil biocrusts are important globally and not only locally (7). Some of the macroscopic biotic components typical of old-growth biocrusts, such as lichens or mosses, are known to display geographic patterns of distribution (8), which likely drive the patterns in biocrust fungi recently detected by using molecular surveys (9). As with most free-living microorganisms (10, 11), the geographic distributions of biocrust microbes remain largely undefined, even for the pioneer primary producer microbes that start biocrust formation.

We undertook a continental-scale survey of biocrust bacterial diversity based on 16S rRNA gene diversity in community DNA (Fig. 1) and

characterized each site by a range of parameters related to soil type, geochemistry, and texture, as well as geography and climate (table S1). An initial analysis of bacterial community composition resolved at the phylum level yielded neither statistically discernible geographic patterns nor any strong taxon-parameter associations (table S2). This was perhaps not surprising given the large functional diversity contained in many bacterial phyla (12). For the Bacteria in general it was not possible to achieve deeper taxonomic resolution.

Because much prior descriptive work was available for Cyanobacteria (13–17), which made up the biocrust's dominant phylum, we could develop ad hoc bioinformatic algorithms that allowed robust assignment of the large majority of sequences to well-defined generic or subgeneric entities (Fig. 1). The phototroph community was dominated by two oscillarian (filamentous, non-heterocystous) cyanobacteria: *Microcoleus vaginatus* and *M. steenstrupii*. The former is considered to be the most common and widespread cyanobacterium in biocrusts (13) (18), but the second is known to dominate at least some locations of the Lower Sonoran region (14). In spite of sharing a generic name, these two cyanobacteria are not closely related phylogenetically and in fact likely belong in different families. But both species are rope-

formers, a convergent trait that helps them to stabilize the soil on contact (17) and to become biocrust pioneers. They are in this sense keystone species. Other phototrophs detected include several heterocystous (N₂-fixing) cyanobacteria and also eukaryotic algae (as plastid rRNA sequences), most of which were closely allied to *Klebsormidium* spp. (*Streptophyta*), a known inhabitant of some biocrusts (19). In fact, the algal contribution overwhelmingly came from just two sites (9 and 12), where streptophytes were dominant. Similarity ordination of the phototroph community structure revealed three groups of self-similar sites (Fig. 1, bottom). One was defined by the dominance of streptophytes (sites 9 and 12). Most of the other sites could be cleanly split into those dominated by *M. steenstrupii* (12 sites, mostly southern latitudes), and those dominated by *M. vaginatus* (8 sites, mostly northern). This is consistent with prior molecular surveys carried out in a site of the Sonoran (14) versus one in the Colorado Plateau (15). Similarity in community composition between sites did not correlate well with geographic distance between them ($R^2 = 0.2$).

A canonical correspondence analysis (CCA) ordinated most sites along a line on a plane, the axes of which explained 82 (60 and 22) % of the variability in site community composition (Fig. 2). Algae-dominated sites mapped away from this line. *M. steenstrupii* was among the community members characterizing one end of the main distribution, whereas *M. vaginatus* mapped at the opposite end. CCA also identified several climatic parameters related to temperature as important community composition drivers; precipitation and geochemical factors were much less influential (Fig. 2). Simple correlation and multiple regression analyses applied to the distribution of individual taxa (table S3) also showed the relevance of temperature. This influence was most conspicuous for the pioneer, crust-forming oscillarian cyanobacteria: Among all parameters, *M. steenstrupii* (Pearson coefficient = 0.81) and *M. vaginatus* (−0.56) abundances correlated best with mean annual temperature (MAT) (Fig. 2). In fact, there was a replacement in relative representation between these two cyanobacteria along the MAT range, with a tipping range around 13° to 15°C. This dominance shift was not absolute: Both cyanobacteria were detected in all samples, precluding a lack of dispersal as an explanation

¹School of Life Sciences, Arizona State University, Tempe, AZ 85287, USA. ²Departamento de Biología, Facultad de Ciencias, Universidad Autónoma de Madrid, Madrid, Spain.

*Corresponding author. E-mail: ferran@asu.edu

for the replacement. Rather, environmental selection likely lead to niche separation.

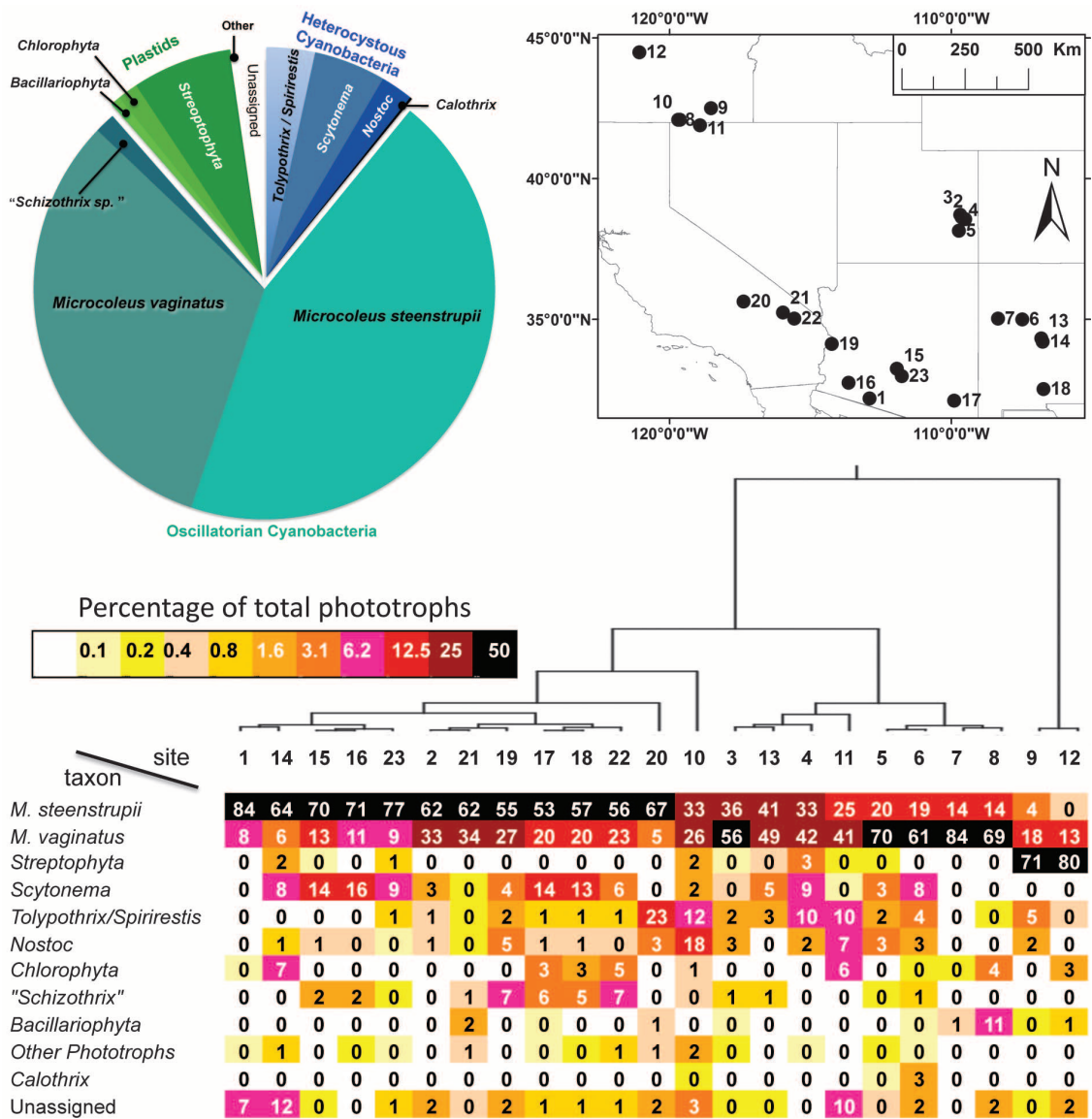
One of the comparative advantages of studying climate and geography patterns in microbes is that ecophysiological hypotheses can be tested directly by using cultures, adding a capacity for causal attribution to the correlative patterns detected statistically (20). To test the temperature segregation hypothesis, we used two cultivation avenues: the outcome of enrichment cultures as a function of incubation temperature and the determination of thermophysiological traits of newly isolated, pedigreed strains. We hypothesized, on the basis of results in Fig. 2, that incubation of field samples in standard minimal media maintained below the apparent inflexion range of 13° to 15°C should result in a preferential enrichment of *M. vaginatus* over *M. steenstrupii* regardless of the geographic origin of inoculum and that the opposite outcome would result from incubations at higher temperature. Results of such enrichments (Table 1) confirmed this pre-

diction. A collection of 22 oscillatorian, rope-forming isolates (fig. S1) were pedigreed and determined to fall into three of the phylotypes recognized in the field communities: *M. vaginatus* (5 strains), *M. steenstrupii* (12 strains), and a minor group that could be assigned to the morphogenus “*Schizothrix*” (5 strains). These strains were subjected to a battery of tests designed to highlight any significant differences in their thermal physiology. All strains survived freezing, so this was not quantified further. By contrast, we found a differential response to high temperature. No *M. vaginatus* survived incubation for 12 days at 40°C, bleaching completely and losing viability, whereas all other strains remained viable (Fig. 3). Because of their clumpy, adherent, and slow mode of growth, standard microbiological growth curves based on subsampling were not possible; instead we carried out sacrificial, end-point-yield determinations. Although there was some level of interstrain variability, trends did appear. At low temperature (10°C, Fig. 3),

M. vaginatus strains grew more than most strains of *M. steenstrupii*, the latter scoring poorly. In the psychrophilic range (5° to 15°C), average yields of all *M. vaginatus* were significantly higher ($P < 0.05$; t test) than those of *M. steenstrupii*. The situation reversed at high temperature, where four of the five best-performing strains at 35°C belonged to *M. steenstrupii* and *M. vaginatus* performed poorly or failed to grow. Between 30° and 35°C, *M. steenstrupii* strains grew significantly ($P < 0.05$; t test) more than those of *M. vaginatus*. Strains belonging to the *Schizothrix* clade, by contrast, performed uniformly well, indicating that this organism was not as influenced by temperature. The overall inference from our culture studies is that, as predicted by their geographic distribution, *M. vaginatus* represents an inherently more psychrotolerant taxon than *M. steenstrupii*, whose members are more thermotolerant.

The distributional and ecophysiological evidence gathered here allows us to logically predict that a few degrees of temperature increase

Fig. 1. Community composition of microbial phototrophs in arid soil biocrusts of the U.S. southwestern region. Site locations depicted as points in map (top right) encompassed several biogeographic regions (the Sonoran, Mojave, and Chihuahuan deserts, as well as the Great Basin and the Colorado Plateau). The pie chart (top left) shows an average distribution of phylotypes for all sites, each given equal weight. The explicit community composition for each site is in the heat map table (bottom), with sites arranged horizontally according to a similarity analysis (the similarity tree crowns the table heading).



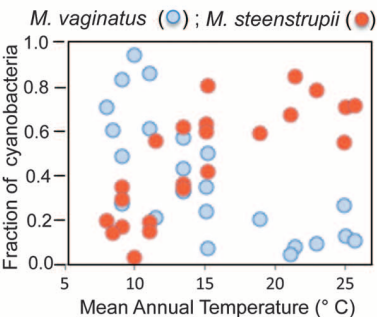
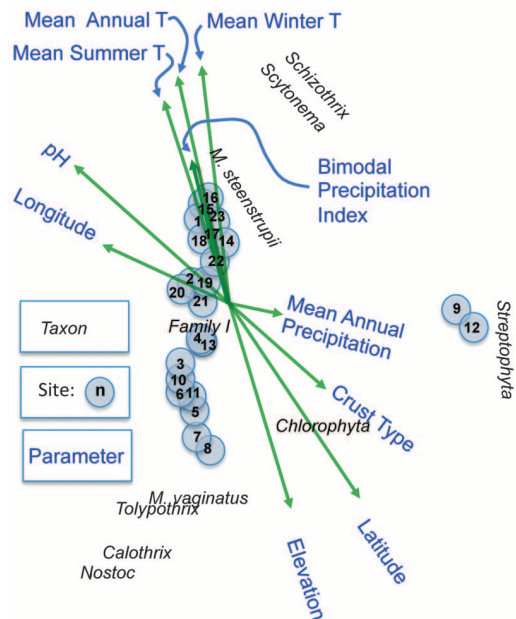


Fig. 2. Environmental factors driving community structure. CCA of the compositional and environmental data set for the survey of sites (**left**) yields a significant model (trace $P = 0.008$), where (with the exception of communities dominated by algae, sites 9 and 12) most communities ordinate along a continuum driven most strongly by vectors related to temperature and typified by the presence of one of the two major oscillarian phylotypes at opposite ends in the distribution. CCA used data from all 23 sites and from 10 environmental variables preselected among those that showed some level of correlation with community composition in preliminary tests. An explicit depiction at the abundance of these two phylotypes as a function of site mean annual temperature (**right**) reveals a pattern of mutual exclusion or niche separation, with a tipping range around 13° to 15°C.

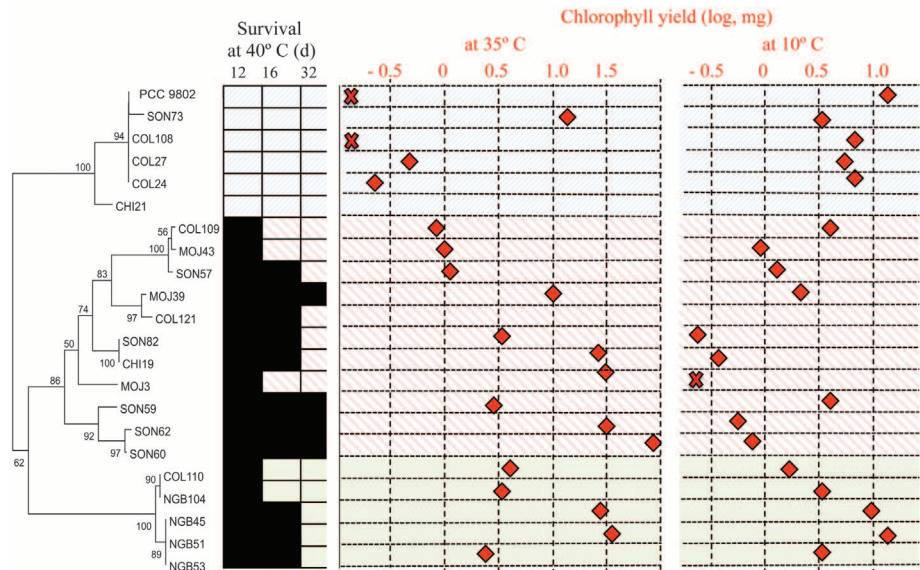


Fig. 3. Temperature physiology of biocrust-relevant strains. Strains tested are arranged vertically according to phylogenetic placement (a simplified tree is shown at left, with bootstrap support at the nodes, a full tree is in fig. S1): strains of *M. vaginatus* are at the top (data in blue background), those of *M. steenstrupii* in the middle (pink background), with “*Schizothrix*” strains below (green background). Charts show strain sensitivity to extreme heat (Survival at 40°C, positive for survival is darkened) and their ability to grow at low (yield at 10°C) and high (yield at 35°C) temperatures. Crosses indicate a value lower than the detection limit.

Table 1. Ratio of *M. vaginatus* over *M. steenstrupii* attained in enrichment cultures after 1 to 2 months of incubation as a function of temperature and inoculum source. Original ratios have their basis in data for the sites (shown in Fig. 1).

Inoculum source	Original	Ratio		
		After enrichment		
		at 4°C	at 15°C	at 30°C
Site 7 (Colorado Plateau)	6.00	27	11	0.20
Site 3 (Colorado Plateau)	1.55	48	35	0.16
Site 15 (Sonoran Desert)	0.19	9	2	0.03
Site 20 (Mojave Desert)	0.07	*	20	0.17

*Insufficient biomass development for counts

can result in a replacement in the dominance of *M. vaginatus* by *M. steenstrupii* on the cooler side of the current boundary (Fig. 2). In fact, warming in the southwestern United States is among the most marked on record (21), and a variety of climate models predict further increases in aridity and a warming in the order of about a degree per decade (22, 23). This rate should translate in a complete replacement of *M. vaginatus* dominance from the area studied here in some 50 years. In this sense, terrestrial cyanobacteria respond differently than macroscopic vegetation in the area, whose biogeography is most heavily influenced by rainfall patterns, as is the sensitivity to global change of biocrust mosses (24). Given that both cyanobacterial species are found through the study range, populational shifts should proceed unimpeded by dispersal. Although some of the physiological and genetic properties of *M. vaginatus*, long recognized as important, have been determined (25–28), practically nothing is known about *M. steenstrupii*. Therefore, the consequences of replacement in such keystone species cannot be predicted at this time. In the short term, *M. steenstrupii* should also be considered as inoculum by land managers, in addition to *M. vaginatus*, for soil management and restoration efforts in arid lands.

References and Notes

1. J. Belnap, O. L. Lange, Eds., *Biological Soil Crusts: Structure, Function, and Management* (Springer-Verlag, Berlin, 2001), vol. 150.
2. F. Garcia-Pichel, in *Encyclopedia of Environmental Microbiology*, G. Bitton, Ed. (Wiley, New York, 2002), pp. 1019–1023.
3. J. Belnap, D. A. Gillette, *J. Arid Environ.* **39**, 133 (1998).
4. S. Strauss, T. Day, F. Garcia-Pichel, *Biogeochemistry* **108**, 171 (2012).
5. S. L. Johnson, S. Neuer, F. Garcia-Pichel, *Environ. Microbiol.* **9**, 680 (2007).
6. J. Belnap, *Hydrol. Processes* **20**, 3159 (2006).

7. W. Elbert *et al.*, *Nat. Geosci.* **5**, 459 (2012).
8. B. Büdel, in *Biological Soil Crusts: Structure, Function, and Management*, J. Belnap, O. L. Lange, Eds. (Springer-Verlag, Berlin, 2001), pp. 141–152.
9. S. T. Bates, T. H. Nash 3rd, F. Garcia-Pichel, *Mycologia* **104**, 353 (2012).
10. J. B. H. Martiny *et al.*, *Nat. Rev. Microbiol.* **4**, 102 (2006).
11. J. L. Green, B. J. M. Bohannan, R. J. Whitaker, *Science* **320**, 1039 (2008).
12. L. Philippot *et al.*, *Nat. Rev. Microbiol.* **8**, 523 (2010).
13. F. Garcia-Pichel, A. López-Cortés, U. Nübel, *Appl. Environ. Microbiol.* **67**, 1902 (2001).
14. M. L. Nagy, A. Pérez, F. Garcia-Pichel, *FEMS Microbiol. Ecol.* **54**, 233 (2005).
15. S. R. Gundlapally, F. Garcia-Pichel, *Microb. Ecol.* **52**, 345 (2006).
16. C. M. Yeager *et al.*, *FEMS Microbiol. Ecol.* **60**, 85 (2007).
17. F. Garcia-Pichel, M. F. Wojciechowski, *PLoS ONE* **4**, e7801 (2009).
18. J. Belnap, J. S. Gardner, *Great Basin Nat.* **53**, 40 (1993).
19. S. M. Smith, R. M. M. Abed, F. Garcia-Pichel, *Microb. Ecol.* **48**, 200 (2004).
20. C. Parmesan, *Annu. Rev. Ecol. Evol. Syst.* **37**, 637 (2006).
21. J. Overpeck, B. Udall, *Science* **328**, 1642 (2010).
22. A. W. Ellis, T. W. Hawkins, R. C. Balling Jr., P. Gober, *Clim. Res.* **35**, 227 (2008).
23. R. Seager, G. A. Vecchi, *Proc. Natl. Acad. Sci. U.S.A.* **107**, 21277 (2010).
24. S. C. Reed *et al.*, *Nature Clim. Change* **2**, 752 (2012).
25. T. D. Brock, *J. Phycol.* **11**, 316 (1975).
26. F. Garcia-Pichel, O. Pringault, *Nature* **413**, 380 (2001).
27. L. Chen, D. Li, Y. Liu, *J. Arid Environ.* **55**, 645 (2003).
28. S. R. Starkenburg *et al.*, *J. Bacteriol.* **193**, 4569 (2011).

Acknowledgments: This work was supported by a grant (NSF-Biodiversity Surveys and Inventories) to F.G.-P. P.M. acknowledges the support of Universidad Autónoma de Madrid for a sabbatical leave at Arizona State University. Data are available in the supplementary materials and at the Desert Soil Microbe Web page and database (<http://garcia-pichel.lab.asu.edu/databases.html>).

Supplementary Materials

www.sciencemag.org/cgi/content/full/340/6140/1574/DC1

Materials and Methods

Fig. S1

Tables S1 to S3

References (29–42)

11 February 2013; accepted 8 May 2013

10.1126/science.1236404

Mechanism of Eukaryotic RNA Polymerase III Transcription Termination

Soren Nielsen, Yulia Yuzenkova, Nikolay Zenkin*

Gene expression in organisms involves many factors and is tightly controlled. Although much is known about the initial phase of transcription by RNA polymerase III (Pol III), the enzyme that synthesizes the majority of RNA molecules in eukaryotic cells, termination is poorly understood. Here, we show that the extensive structure of Pol III–synthesized transcripts dictates the release of elongation complexes at the end of genes. The poly-T termination signal, which does not cause termination in itself, causes catalytic inactivation and backtracking of Pol III, thus committing the enzyme to termination and transporting it to the nearest RNA secondary structure, which facilitates Pol III release. Similarity between termination mechanisms of Pol III and bacterial RNA polymerase suggests that hairpin-dependent termination may date back to the common ancestor of multisubunit RNA polymerases.

Termination of transcription is an obligatory step after synthesis of the transcript, which leads to dissociation of RNA polymerase (RNAP) and the transcript from the template DNA. However, evolutionarily conserved multisubunit RNAPs from bacteria and Archaea and three eukaryotic RNAPs use different mechanisms to terminate transcription

(1–3). Eukaryotic polymerase III (Pol III) terminates after synthesis of a poly-U stretch (4, 5), and most studies have focused on the efficiency of recognition of the poly-T (on the nontemplate strand) termination signal (6, 7). However, the events leading to termination on the poly-T signal; that is, dissociation of Pol III from the template, are not known.

We used in vitro–assembled elongation complexes, which have been successfully used to investigate various RNAPs (8–11), to examine this problem. These complexes—assembled with purified RNAP, synthetic complementary template and nontemplate DNA strands, and RNA—allow us to skip the initiation step, therefore excluding any accessory factors from the reaction. We immobilized complexes on streptavidin beads through biotin on the 5′ end of the nontemplate strand, and we labeled RNA by incorporation of radioactive nucleoside monophosphates (scheme in Fig. 1A) (12). We analyzed transcription through poly-T signals of various lengths by purified *Saccharomyces cerevisiae* Pol III. As seen in Fig. 1, A and B, transcripts finishing after T₆ to T₁₀ were transcribed (compare to fig. S1).

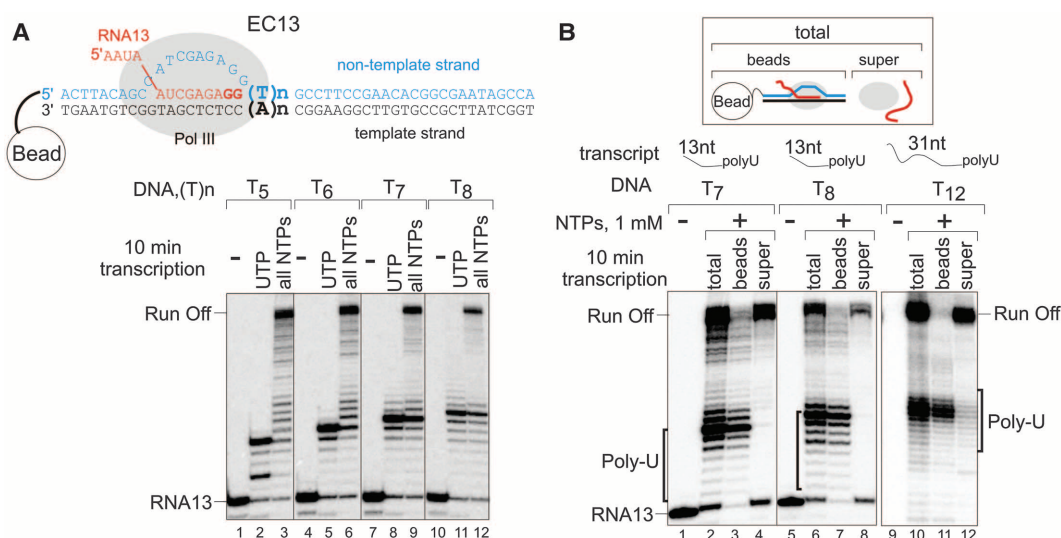
To test if transcripts ending with a poly-U stretch were released from the template as a result of termination, we analyzed RNA in the

Centre for Bacterial Cell Biology, Institute for Cell and Molecular Biosciences, Newcastle University, Baddiley-Clark Building, Richardson Road, Newcastle upon Tyne, NE2 4AX, UK.

*Corresponding author. E-mail: n.zenkin@ncl.ac.uk

Fig. 1. Pol III pauses on the poly-T signal but does not terminate.

(A) Scheme of assembled elongation complexes (EC13) containing 13-nt-long RNA (RNA13) is shown at the top. RNA was radiolabeled at the 3′ end of guanosine monophosphates (bold) (12). Complexes were immobilized on beads through biotin on the 5′ end of the nontemplate strand. Transcription occurred for 10 min on templates with poly-T signals of different lengths in the presence of 1 mM of either uridine triphosphate (UTP) or all nucleoside triphosphates (NTPs). Hereafter, black vertical lines separate parts of a single gel that were brought together. (B) After 10 min of transcription on the templates depicted above the gels (12), released transcripts (supernatant, “super”) were separated from transcripts that remained in the immobilized complexes (“beads”) (scheme in the frame above the gels). The length of RNA preceding the poly-U tract is depicted above the gels.



supernatant and immobilized fractions of the reaction (scheme of Fig. 1B). As seen in Fig. 1B, although RNAs resulting from transcription to the end of template (run-off products) were released in the supernatant, transcripts ending at the poly-T signal remained part of the elongation complex (even after prolonged incubation), independently of the length of the transcript or sequences surrounding the poly-T signal (12). The inability of Pol III and RNA to leave DNA was not due to the deficiency in the upstream DNA duplex restoration or to formation of an extended RNA-DNA hybrid (13) (fig. S2, A and B). These results indicate that Pol III pauses rather than terminates at the poly-T signal.

We analyzed transcription of the full-length 5S and tRNA^{Tyr} (*SUP4*) genes. Given the length of each gene, as a template we used streptavidin-bead-immobilized, double-stranded polymerase chain reaction product with a single-stranded extrusion at the 3' end of the template strand and an RNA primer complementary to this extrusion (12, 14) (scheme in Fig. 2A). Transcription ended in the poly-T signal; however, the full-length 5S and tRNA^{Tyr} RNAs were readily released from the template (Fig. 2A, lanes 1 to 3 and 7 to 9, respectively). The abolished release of the run-

off products is explained by immobilization of complexes via the 5' end of the template strand.

Transcript release during bacterial transcription termination is facilitated by an RNA hairpin that forms behind the poly-U tract (15). All transcripts synthesized by Pol III, as per their functions (structural or tRNAs), have extensive secondary structures, so that the poly-U tract is preceded by RNA hairpins and/or stems (fig. S3 and table S1). We therefore hypothesized that, as in the case of bacterial termination, termination by Pol III may also be facilitated by an RNA hairpin and/or stem, in this case, provided by the structure of RNA itself. To test this hypothesis, we changed the sequence of the 5S and tRNA^{Tyr} genes to eliminate formation of RNA secondary structures close to poly-U stretch of the transcript (5S-HP and tRNA^{Tyr}-HP templates; -HP, no hairpin). The release of the transcripts ending in the poly-U signals of the mutant genes was indeed abolished (Fig. 2A, lanes 4 to 6 and 10 to 12).

To test the requirement for the RNA secondary structure during Pol III termination in the presence of transcription factors, we analyzed transcription in more native conditions by using *S. cerevisiae* nuclear lysates and promoter-containing DNA templates (scheme in Fig. 2B). Given that any

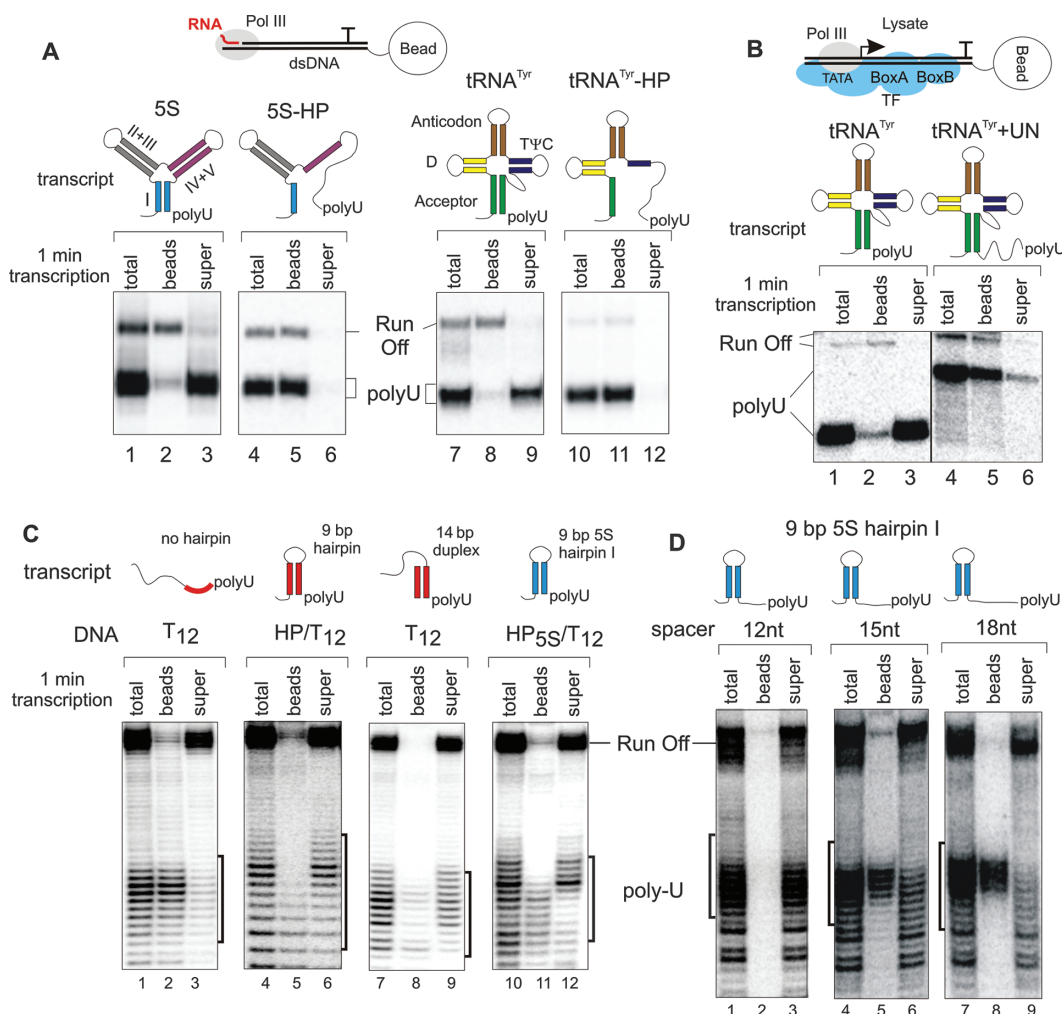
alterations to the secondary structure of tRNA^{Tyr} destroy the internal promoter of Pol III, an unstructured spacer was introduced between the body of tRNA^{Tyr} and the poly-U stretch. In full agreement with the results obtained with purified Pol III, the secondary structure preceding the poly-U tract was essential for termination (Fig. 2B).

To directly test the role of an RNA hairpin in termination by Pol III, we changed the sequence of template T₁₂, which did not allow for release (Fig. 2C, lanes 1 to 3), so that the synthesized transcript formed a 9-base pair-long hairpin before the poly-U stretch. This led to the release of the transcript ending in the poly-T signal; that is, to termination (HP/T₁₂ template; Fig. 2C, lanes 4 to 6). Addition of a short RNA complementary to the hairpin-less transcripts upstream of (but not far away from; see fig. S4) the poly-U stretch, which mimics a termination hairpin (16), also resulted in efficient termination (Fig. 2C, lanes 7 to 9). The 5S helix I, formed by the most proximal 5' and 3' parts of 5S RNA (scheme in Fig. 2A), placed upstream of the poly-T signal also caused efficient termination (Fig. 2C, lanes 10 to 12).

For efficient termination by bacterial RNAP, an RNA hairpin has to be immediately upstream of

Fig. 2. Termination by Pol III is facilitated by the secondary structure of the transcript. (A and B)

Termination by Pol III on full-length genes and their mutant variants lacking secondary structure before poly-U of the transcripts [lacking hairpin (-HP) 5S-HP and tRNA^{Tyr}-HP or having unstructured spacer (+UN) tRNA^{Tyr}+UN] (12). Here and below, release was analyzed after 1 min. (A) Transcription was initiated by purified Pol III on the construct with the single-stranded overhang (scheme above the gels). dsDNA, double-stranded DNA. (B) Transcription was performed in yeast nuclear lysate on templates carrying the promoter (scheme shown above the gels; TATA, Box A, and Box B are Pol III promoter elements bound by transcription factors, TF). (C) Absence of release of transcript without a hairpin (lanes 1 to 3) and release of transcripts containing an arbitrary hairpin (lanes 4 to 6), an RNA duplex formed by an externally added oligonucleotide (lanes 7 to 9), or helix I of 5S RNA [lanes 10 to 12; see also the scheme in (A)] before the poly-U tract (12). bp, base pair. (D) Termination of transcripts bearing spacers of different lengths between the poly-U tract and the termination hairpin (5S helix I) (12). See also fig. S4.



the poly-U stretch (1, 17). Consistently, a hairpin immediately upstream in the poly-U tract also causes termination by Pol III (Fig. 2C). To test the requirements for the distance between a hairpin and the poly-U tract, we introduced unstructured spacers of different lengths (Fig. 2D). We found that a distance as large as ~12 base pairs between the poly-U stretch and the hairpin allows for efficient termination (Fig. 2D, lanes 1 to 3). Longer spacers result in diminished termination (Fig. 2D, lanes 4 to 9; see also fig. S4). These results suggest that an RNA hairpin formed within ~12 nucleotides (nt) upstream of the poly-U stretch is sufficient for termination of the poly-T-paused complex, which is consistent with lengths of spacers between the poly-U tract and the nearest secondary structure found in transcripts synthesized by Pol III (table S1).

The ability of the termination hairpin to act on the paused complex at a distance of ~20 nt from the 3' end of the transcript suggests that the paused complex should slide backward to approach the hairpin. We analyzed the geometry of the paused elongation complexes carrying 8U (EC^{8U}) and 10U (EC^{10U}) tracts on the 3' ends of their hairpin-less transcripts. To map the position of the Pol III active center, we used the ability of the RNAP active center to immobilize Fe^{2+} ion (instead of the native Mg^{2+}), which, by generating hydroxyl radicals, induces cleavage of the transcript in the vicinity of the active center (18). As seen in Fig. 3A, transcripts in EC^{8U} and EC^{10U} were cleaved in the 5' proximal part of the poly-U tract (lanes 4 and 9), indicating that the active center of Pol III has backtracked from the 3' end of RNA. Protection from ribonuclease

A (RNase A), which cleaves single-stranded RNA after pyrimidines, was also consistent with the backtracked conformation, as bodies and poly-U tracts of the transcripts of EC^{8U} and EC^{10U} were mostly protected from RNase A (Fig. 3A, lanes 2 and 7, and fig. S5). In agreement with the length of the secondary channel (19), the 3' end proximal Us in EC^{10U} , but not in EC^{8U} , were exposed to RNase A (Fig. 3A, lanes 2 and 7, and fig. S5). Backtracking of the termination complex thus explains a loose (anywhere within ~12 nt) requirement for the positioning of the termination hairpin and/or stem upstream of the poly-T signal.

Note that the backtracking of EC^{polyU} is unusual because the highly efficient hydrolytic activity of the Pol III active center (14), which can rescue a backtracked complex, is switched off (compare complexes in Fig. 3B and fig. S6B). Such unusual inactivation, as well as impossibility of RNA extension in EC^{polyU} (compare complexes in Fig. 3B and fig. S6B), ensures the formation of a "dead-end" complex, whose only fate is to terminate.

The distance between the Pol III active center (but not necessarily the 3' end of RNA) and the RNA secondary structure required for termination is 7 nt (fig. S7A and supplementary text), which, notably, resembles bacterial termination. Most of the Pol III transcripts contain no or very short spacers between the poly-U signal and the nearest secondary structure (table S1). Therefore, the function of poly-T signal on these templates is to pause Pol III at ~7 nt from the nearest secondary structure (supplementary text and fig. S8). However, some transcripts synthe-

sized by Pol III contain longer spacers between the poly-U tract and the nearest RNA duplex (fig. S3 and table S1), which suggests that the deep backtracking on the poly-T signal of these genes is required to bring Pol III closer to the nearest secondary structure (fig. S8). In the case of short spacers, the 3' penultimate RNA duplex (such as helix IV of 5S RNA and the T ψ C arm of tRNA) can also cause termination, should the 3' proximal hairpin fail to fold and Pol III backtracks (fig. S8).

Backtracking on the poly-T signal results in a strong (G- and C-rich) RNA-DNA hybrid within the termination complex but does not influence termination. Efficient hairpin-dependent termination can also be achieved on a poly-G track (fig. S7A). Therefore, termination by Pol III does not require a weak RNA-DNA hybrid, as was postulated earlier (15). Backtracking and the presence of a nonhomopolymeric RNA-DNA hybrid within the backtracked EC^{polyU} also exclude possibilities of forward translocation (20) and RNA-DNA hybrid shearing (21), respectively, as possible mechanisms for termination. The results are consistent with the recently proposed allosteric mechanism of termination (22), when the RNA hairpin allosterically opens RNAP and leads to its dissociation from the template, though we cannot exclude the possibility that hairpin-dependent destruction of the Pol III elongation complex takes place via a different route.

The above results argue that, in itself, the poly-T signal may not be sufficient for elongation complex destruction. Archaeal RNAP, which was proposed to terminate on the poly-T signal without involvement of additional factors (3), also fails to dissociate on the poly-T signal, whereas an RNA hairpin is sufficient to cause termination (fig. S7B). This finding suggests that Archaea may also use RNA-duplex-dependent termination, the mechanism of which may date back to the last universal common ancestor (LUCA). Termination caused by structures embedded in the functional body of the transcript provides a simple, factor-independent mechanism for the finish of gene transcription and may serve as a checkpoint for proper folding of RNA, which has been essential for the ribozymes of the LUCA and remains essential for structural and/or catalytic RNAs synthesized by Pol III.

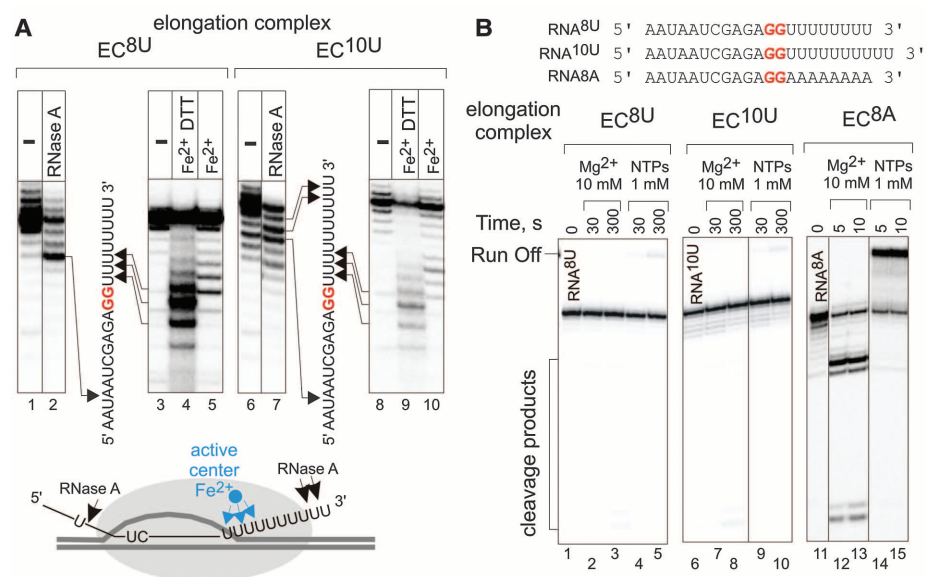


Fig. 3. Complex paused on termination signal undergoes deep backtracking. (A) Probing of EC^{8U} and EC^{10U} with RNase A and hydroxyl radicals generated by Fe^{2+} bound in the Pol III active center (scheme below the gels). Lanes 5 and 10 (without dithiothreitol, DTT) are controls for hydrolysis caused by Fe^{2+} . Radiolabels in transcripts are shown in red. Cleaved positions are shown with arrows. The identity of positions cleaved by RNase A was confirmed with 5'-end-labeled RNA (fig. S5). Interpretation of the probing results is shown schematically below the gels. **(B)** RNA extension and hydrolysis in EC^{8U} , EC^{10U} , and EC^{8A} (see also fig. S6).

References and Notes

1. I. Gusarov, E. Nudler, *Mol. Cell* **3**, 495 (1999).
2. P. Richard, J. L. Manley, *Genes Dev.* **23**, 1247 (2009).
3. T. J. Santangelo, L. Cubonová, K. M. Skinner, J. N. Reeve, *J. Bacteriol.* **191**, 7102 (2009).
4. H. Matsuzaki, G. A. Kassavetis, E. P. Geiduschek, *J. Mol. Biol.* **235**, 1173 (1994).
5. D. F. Bogenhagen, D. D. Brown, *Cell* **24**, 261 (1981).
6. A. Orioli, C. Pascali, A. Pagano, M. Teichmann, G. Dieci, *Gene* **493**, 185 (2012).
7. P. Braglia, R. Percudani, G. Dieci, *J. Biol. Chem.* **280**, 19551 (2005).
8. I. Sidorenkov, N. Komissarova, M. Kashlev, *Mol. Cell* **2**, 55 (1998).

9. N. Zenkin, Y. Yuzenkova, K. Severinov, *Science* **313**, 518 (2006).
10. C. D. Kuhn *et al.*, *Cell* **131**, 1260 (2007).
11. D. Wang *et al.*, *Science* **324**, 1203 (2009).
12. Materials and methods are available as supplementary materials on Science Online.
13. N. Zenkin, T. Naryshkina, K. Kuznedelov, K. Severinov, *Nature* **439**, 617 (2006).
14. S. K. Whitehall, C. Bardeleben, G. A. Kassavetis, *J. Biol. Chem.* **269**, 2299 (1994).
15. T. D. Yager, P. H. von Hippel, *Biochemistry* **30**, 1097 (1991).
16. W. S. Yarnell, J. W. Roberts, *Science* **284**, 611 (1999).
17. N. Komissarova, J. Becker, S. Solter, M. Kireeva, M. Kashlev, *Mol. Cell* **10**, 1151 (2002).
18. E. Zaychikov *et al.*, *Science* **273**, 107 (1996).
19. K. D. Westover, D. A. Bushnell, R. D. Kornberg, *Cell* **119**, 481 (2004).
20. T. J. Santangelo, J. W. Roberts, *Mol. Cell* **14**, 117 (2004).
21. M. H. Larson, W. J. Greenleaf, R. Landick, S. M. Block, *Cell* **132**, 971 (2008).
22. V. Epshtein, C. J. Cardinale, A. E. Ruckenstein, S. Borukhov, E. Nudler, *Mol. Cell* **28**, 991 (2007).

Acknowledgments: This work is dedicated to the memory of Denis Izyumov. We thank J. Roberts, E. Nudler, P. E. Geiduschek, and J. Brown for critical reading of the paper; G. Kassavetis, R. van Nues, H. Murray, N. Proudfoot, and P. Braglia for experimental advice; and J. Chong for help with Archaea. This work was supported by the UK

Biotechnology and Biological Sciences Research Council, the Biotechnology and Biological Sciences Research Council under the SysMO initiative, and the European Research Council [grant ERC-2007-StG 202994-MTP]. Data are available in the supplementary materials.

Supplementary Materials

www.sciencemag.org/cgi/content/full/340/6140/1577/DC1
Materials and Methods

Supplementary Text

Figs. S1 to S8

Table S1

References (23–27)

18 March 2013; accepted 13 May 2013

10.1126/science.1237934

Transcription Under Torsion

Jie Ma,^{1,2} Lu Bai,^{3,4} Michelle D. Wang^{1,2*}

In cells, RNA polymerase (RNAP) must transcribe supercoiled DNA, whose torsional state is constantly changing, but how RNAP deals with DNA supercoiling remains elusive. We report direct measurements of individual *Escherichia coli* RNAPs as they transcribed supercoiled DNA. We found that a resisting torque slowed RNAP and increased its pause frequency and duration. RNAP was able to generate 11 ± 4 piconewton-nanometers (mean \pm standard deviation) of torque before stalling, an amount sufficient to melt DNA of arbitrary sequence and establish RNAP as a more potent torsional motor than previously known. A stalled RNAP was able to resume transcription upon torque relaxation, and transcribing RNAP was resilient to transient torque fluctuations. These results provide a quantitative framework for understanding how dynamic modification of DNA supercoiling regulates transcription.

DNA supercoiling is a regulator of gene expression (1–5). RNA polymerase (RNAP) must transcribe supercoiled DNA, and transcription elongation, in turn, generates DNA supercoiling. As RNAP moves along the helical groove of DNA, it generates (+) DNA supercoiling ahead and (–) DNA supercoiling behind (the “twin supercoiled domain model”) (1, 3–6). DNA supercoiling is broadly present during transcription (3–5). Active transcription can accumulate dynamic DNA supercoiling on DNA templates that are not bound by topological constraints (3), as well as in the presence of a normal complement of topoisomerases in vivo (4). However, little is known about some basic properties of the interplay between transcription and DNA supercoiling. We have developed an assay to directly monitor RNAP translocation in real time as it worked under a defined torque. An RNAP was torsionally anchored to the surface of a coverslip, and either the downstream or upstream end of the DNA template was torsionally anchored to the bottom of a nanofabricated quartz cylinder held in an angular optical trap (AOT) (Fig. 1A and fig. S1) (7–11). An AOT allows simultaneous control and measurement of rotation, torque, displacement, and force of the trapped cylinder (8–11). Analysis of these mea-

surements allowed for the determination of the RNAP position on the DNA template as it transcribed under torque (11).

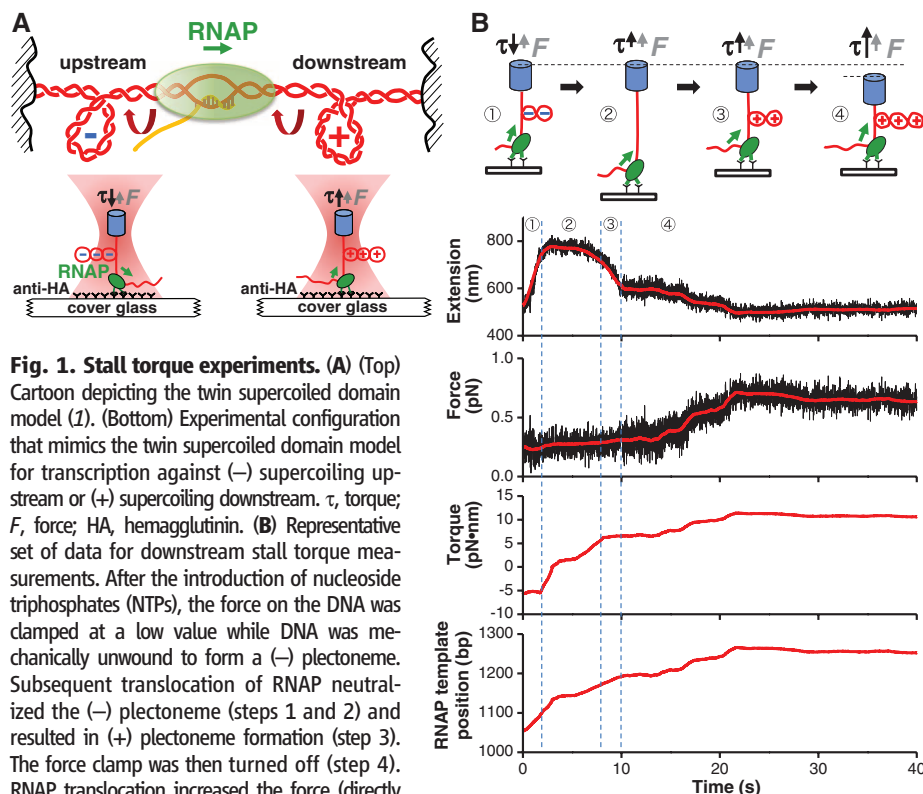


Fig. 1. Stall torque experiments. (A) (Top) Cartoon depicting the twin supercoiled domain model (1). (Bottom) Experimental configuration that mimics the twin supercoiled domain model for transcription against (–) supercoiling upstream or (+) supercoiling downstream. τ , torque; F , force; HA, hemagglutinin. (B) Representative set of data for downstream stall torque measurements. After the introduction of nucleoside triphosphates (NTPs), the force on the DNA was clamped at a low value while DNA was mechanically unwound to form a (–) plectoneme. Subsequent translocation of RNAP neutralized the (–) plectoneme (steps 1 and 2) and resulted in (+) plectoneme formation (step 3). The force clamp was then turned off (step 4). RNAP translocation increased the force (directly measured) and the corresponding torque (derived) (11) until reaching a stall [<1 base pair (bp)/s for 20 to 50 s]. Data were filtered: extension to 200 Hz (black) and 1 Hz (red) and force to 40 Hz (black) and 1 Hz (red). The RNAP template position is defined as the distance of RNAP from the transcription start site (in base pairs).

¹Department of Physics–Laboratory of Atomic and Solid State Physics, Cornell University, Ithaca, NY 14853, USA. ²Howard Hughes Medical Institute, Cornell University, Ithaca, NY 14853, USA. ³Department of Biochemistry and Molecular Biology, Pennsylvania State University, University Park, PA 16801, USA. ⁴Department of Physics, Pennsylvania State University, University Park, PA 16801, USA.

*Corresponding author. E-mail: mwang@physics.cornell.edu

The measured downstream stall torque distribution is well fit by a Gaussian function, yielding a mean torque of 11.0 ± 3.7 pN·nm (mean \pm SD), with the largest measured value being ~ 18 pN·nm (Fig. 2A and fig. S6A). This mean torque is sufficient to create (+) plectonemic DNA under the low forces used in our experiments. In contrast, the upstream stall torque distribution shows an

asymmetry (Fig. 2B and fig. S6B). Unlike (+) supercoiled DNA, which can sustain a much higher torque before structural changes, (−) supercoiled DNA undergoes a transition at 10.5 pN·nm consistent with melting (fig. S3) (11). The upstream stall torque distribution shows a singular peak immediately before a sharp cutoff near the DNA melting torque, and $\sim 60\%$ of RNAPs were stalled

between 10 to 12 pN·nm. These data indicate that RNAP is able to generate an upstream torque sufficient to alter DNA structure. The upstream data were fit with a Gaussian function, yielding a Gaussian centered at 10.6 ± 4.1 pN·nm, comparable to the downstream stall torque (Fig. 2B). The spreads in the measured stall torque distributions are attributed to DNA sequence

Fig. 2. Transcription stalling and resumption.

(A) Distribution of the measured downstream stall torques. The smooth blue curve is a fit with a Gaussian function, yielding a mean of 11.0 ± 3.7 pN·nm (mean \pm SD). (B) Distribution of measured upstream stall torques. The smooth curve is a fit with a Gaussian function assuming that the peaked fraction generated torques of at least 10 pN·nm, yielding a mean of 10.6 ± 4.1 pN·nm (mean \pm SD). (C) Example traces showing RNAP reverse translocation upon stalling. Both axes are shifted for clarity. For each trace, the arrow indicates the entry into a stall. (D) Fraction of RNAPs that resumed transcription after torque release versus time. After stalling, torque on RNAP was relaxed, and transcription was detected by an experiment similar to that shown in step 1 of Fig. 1B. Error bars indicate SEM.

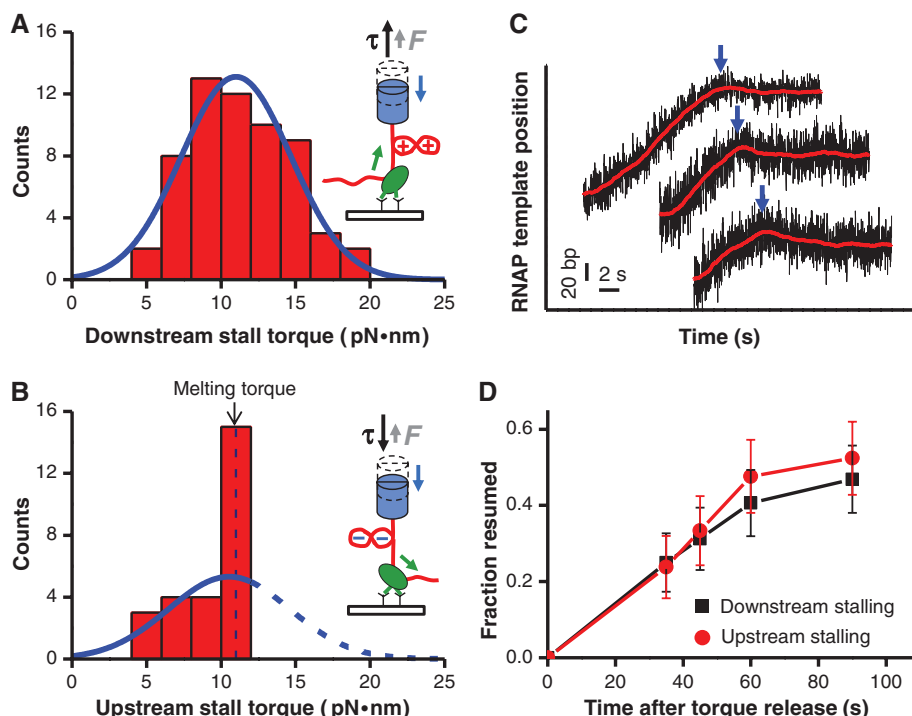
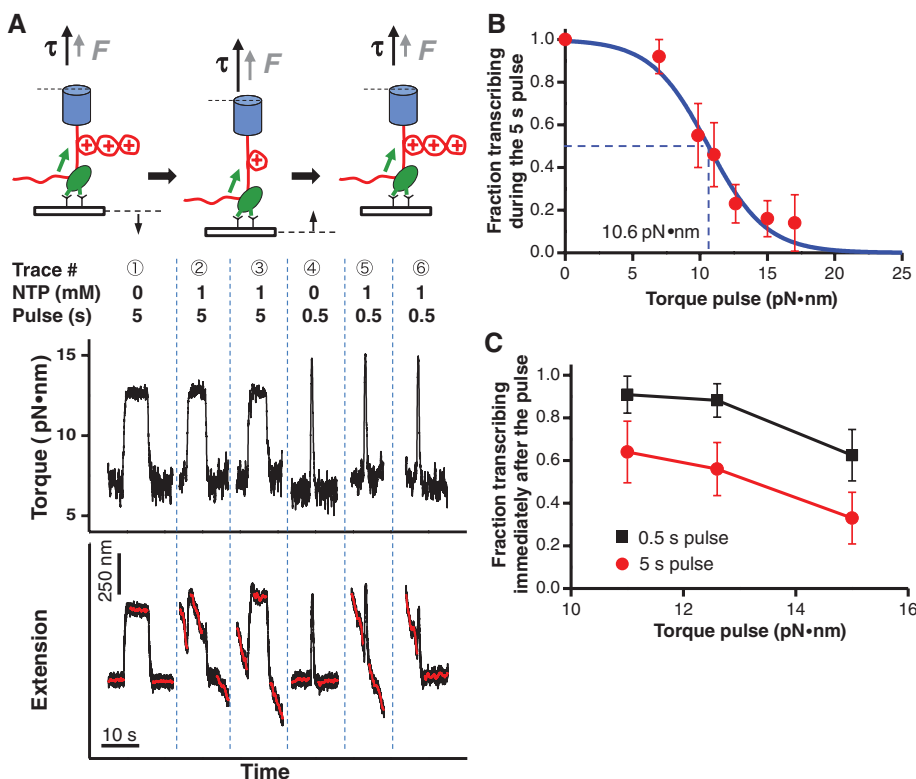


Fig. 3. Transcription response to a transient torque pulse.

(A) (Top) Cartoon illustrating steps of the torque pulse experiments and (bottom) representative traces of data. RNAP initially transcribed under a low downstream torque of ~ 7 pN·nm and then was subjected to a higher torque pulse for either 5 or 0.5 s before restoration of the initial low torque. Traces 1 and 4 are controls. The extension and time axes are shifted for clarity. (B) Probability of maintaining active transcription during the 5-s torque pulse. The blue solid line is a fit to a Boltzmann function: $f = 1/[1 + e^{(\tau - \tau_c)/\tau_0}]$, where τ_c is the characteristic cutoff torque, and τ_0 is the characteristic width of the transition torque. Error bars indicate SEM. (C) Probability of resuming transcription immediately (within 5 s) after the torque pulse. Error bars indicate SEM.



variations and single-molecule stochasticity, according to a thermal-ratchet kinetic model for transcription elongation that we previously developed (15–17).

Thus, RNAP is fully capable of generating torque sufficient to melt DNA of arbitrary sequence (11), not just AT-rich sequences that are prone to melting (3, 4, 11). The strong (–) supercoiling generated by RNAP may facilitate initiation of transcription from adjacent promoters (18), binding of regulatory proteins (3, 4), and initiation of replication (19).

We found that, in some traces, RNAP reverse translocated upon stalling (Fig. 2C). This reverse

motion suggests that torque may induce stalling via backtracking, during which RNAP translocates back along the template DNA and displaces the 3' transcript from the active site, preventing RNA synthesis (20–22).

In vivo, torsional stress accumulated by RNAP may be relaxed by the arrival of a topoisomerase at the DNA template or by DNA rotation. We found that stalled RNAPs gradually resumed transcription following torque release (Fig. 2D). At 90 s after torque release, ~50% of stalled RNAPs had resumed transcription. Thus, in vivo torque relaxation should allow a large fraction of stalled RNAPs to resume transcription, prevent-

ing them from becoming obstacles or inducing DNA damage that disrupts genome stability (23).

In vivo, torsional stress in local DNA segments may be present transiently due to actions of motor proteins and dynamic reconfiguration of topological domains. However, it is not known how these sudden changes in torsional stress might influence a transcribing RNAP. We thus carried out transient torque pulse experiments to determine how RNAP responded to a brief exposure of a resisting torque on a time scale comparable to those of topoisomerases (24–26) (0.5 or 5 s) (Fig. 3A). We found that the fraction of active RNAPs during the 5-s pulse decreased as the torque was jumped to an increasingly higher value (Fig. 3B). The characteristic cutoff torque was 10.6 ± 4.0 pN·nm, a value similar to the mean stall torque. A substantially larger fraction of RNAPs was able to transcribe immediately (within 5 s) after the 0.5-s pulse, as opposed to after the 5-s pulse (Fig. 3C), indicating that a 0.5-s torque pulse does not give sufficient time for RNAP to backtrack substantially. Thus, RNAP can effectively resist transient torque fluctuations (<0.5 s) but is unable to withstand prolonged exposure to a large torque without stalling or arresting.

We investigated the torque-velocity relationship, which characterizes how the transcription speed is regulated by torque (Fig. 4A). To maintain a constant torque, we monitored transcription in the presence of a DNA plectoneme under a small and constant force. The measured transcription traces showed that continuous elongation was interrupted by frequent pausing (Fig. 4B and fig. S7). Because of the sensitivity of the assay, it was possible to resolve pauses as short as 0.2 s. By analyzing the velocity between pauses, we obtained the torque-velocity relation of RNAP. Figure 4C shows how the transcription rate increased with an assisting torque and decreased with a resisting torque. In addition, both pause density and duration decreased with an assisting torque and increased with a resisting torque (Fig. 4D).

We show that RNAP can generate torque; torque, in turn, regulates transcription rate and pausing; and excessive torque accumulation leads to transcription stalling and DNA structural alteration. A transcription-generated supercoiling wave can propagate through DNA to provide action at a distance, not only to alter DNA structure (3, 4) but also to potentially alter or dissociate bound proteins (3, 4, 27). Torsion generated by eukaryotic RNAP may alter chromatin fiber and evict histones (4, 27, 28), and torsional relaxation by chromatin may, in turn, facilitate transcription (28).

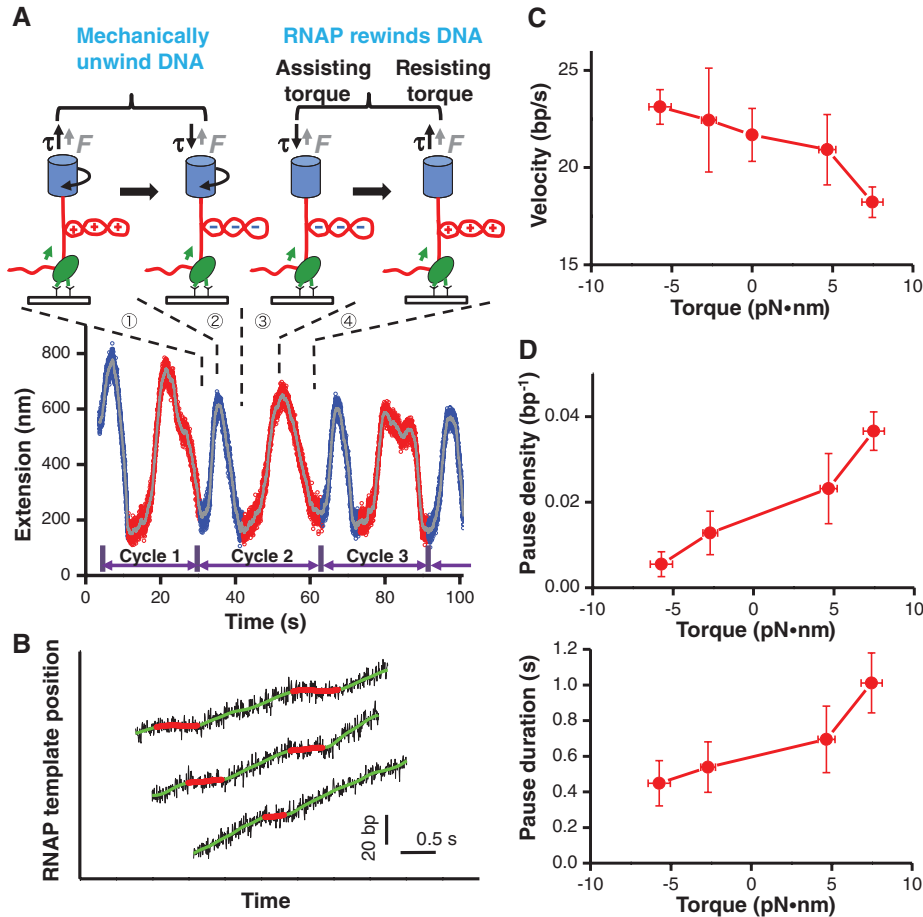


Fig. 4. Determination of transcription torque-velocity relationship. (A) Representative set of data for transcription measurement under a constant torque. Transcribing RNAP, under a small and constant tension of 0.15 pN, was subjected to multiple cycles of resisting and assisting torque. For each cycle, the downstream DNA was mechanically unwound to remove any (+) plectoneme (step 1) and create a (–) plectoneme (step 2). Subsequent RNAP transcription was assisted by the (–) DNA supercoiling (step 3), until the generation of (+) supercoiling, which hindered transcription (step 4). In the presence of a plectoneme, the torque on the DNA was constant for a given force (9) (fig. S3), and RNAP velocity was derived from the slope of the extension-versus-time curve (11). Also, we define a resisting torque to be (+) and an assisting torque to be (–). Data were filtered to 200 Hz (blue and red) and 1 Hz (gray). (B) Representative transcription traces under a torque of +7.5 pN·nm. Continuous transcription (green smoothed data) was interrupted by pauses (red smoothed data). (C) Transcription torque-velocity relationship. Transcription velocity was obtained by weighting each transcript position equally, and the resulting velocity reflected primarily transcription rates between pauses (11, 29). Vertical error bars indicate SEM; horizontal error bars denote SD. (D) Pause density (top) and duration (bottom) as a function of torque. A pause is defined as having a duration of ≥ 0.2 s at a given nucleotide position (11). Zero-torque data (fig. S8) had lower sensitivity to transcription due to lack of plectonemes in DNA, precluding detection of pauses of 0.2 to 2 s in duration, and were thus excluded from pause analysis. Vertical error bars indicate SEM; horizontal error bars denote SD.

References and Notes

1. L. F. Liu, J. C. Wang, *Proc. Natl. Acad. Sci. U.S.A.* **84**, 7024 (1987).
2. A. Travers, G. Muskheishvili, *Nat. Rev. Microbiol.* **3**, 157 (2005).
3. F. Kouzine, J. Liu, S. Sanford, H.-J. Chung, D. Levens, *Nat. Struct. Mol. Biol.* **11**, 1092 (2004).
4. F. Kouzine, S. Sanford, Z. Elisha-Feil, D. Levens, *Nat. Struct. Mol. Biol.* **15**, 146 (2008).

5. K. Matsumoto, S. Hirose, *J. Cell Sci.* **117**, 3797 (2004).
6. H.-Y. Wu, S. H. Shyy, J. C. Wang, L. F. Liu, *Cell* **53**, 433 (1988).
7. A. La Porta, M. D. Wang, *Phys. Rev. Lett.* **92**, 190801 (2004).
8. C. Deufel, S. Forth, C. R. Simmons, S. Dejosha, M. D. Wang, *Nat. Methods* **4**, 223 (2007).
9. S. Forth *et al.*, *Phys. Rev. Lett.* **100**, 148301 (2008).
10. M. Y. Sheinin, S. Forth, J. F. Marko, M. D. Wang, *Phys. Rev. Lett.* **107**, 108102 (2011).
11. Materials and methods are available as supplementary materials on Science Online.
12. Y. Harada *et al.*, *Nature* **409**, 113 (2001).
13. A. Revyakin, R. H. Ebright, T. R. Strick, *Proc. Natl. Acad. Sci. U.S.A.* **101**, 4776 (2004).
14. A. Revyakin, C. Liu, R. H. Ebright, T. R. Strick, *Science* **314**, 1139 (2006).
15. L. Bai, A. Shundrovsky, M. D. Wang, *J. Mol. Biol.* **344**, 335 (2004).
16. L. Bai, R. M. Fulbright, M. D. Wang, *Phys. Rev. Lett.* **98**, 068103 (2007).
17. L. Bai, M. D. Wang, *J. Stat. Mech.* **2010**, P12007 (2010).
18. D. M. J. Lilley, C. F. Higgins, *Mol. Microbiol.* **5**, 779 (1991).
19. D. Kowalski, M. J. Eddy, *EMBO J.* **8**, 4335 (1989).
20. N. Komissarova, M. Kashlev, *Proc. Natl. Acad. Sci. U.S.A.* **94**, 1755 (1997).
21. J. W. Shaevitz, E. A. Abbondanzieri, R. Landick, S. M. Block, *Nature* **426**, 684 (2003).
22. E. A. Galbur *et al.*, *Nature* **446**, 820 (2007).
23. D. Dutta, K. Shatalin, V. Epshtein, M. E. Gottesman, E. Nudler, *Cell* **146**, 533 (2011).
24. T. R. Strick, V. Croquette, D. Bensimon, *Nature* **404**, 901 (2000).
25. D. A. Koster, V. Croquette, C. Dekker, S. Shuman, N. H. Dekker, *Nature* **434**, 671 (2005).
26. J. Gore *et al.*, *Nature* **439**, 100 (2006).
27. V. Levchenko, B. Jackson, V. Jackson, *Biochemistry* **44**, 5357 (2005).
28. C. Lavelle, *Biochimie* **89**, 516 (2007).
29. K. Adelman *et al.*, *Proc. Natl. Acad. Sci. U.S.A.* **99**, 13538 (2002).

Acknowledgments: We thank members of the Wang lab for critical reading of the manuscript. We especially thank R. M. Fulbright for purification of the RNAP and S. Forth, Y. Yang, M. Y. Sheinin, J. T. Inman, and R. A. Forties for assistance with single-molecule assays, data acquisition, data analysis, and figure preparation. We wish to acknowledge support from an NIH grant (GM059849 to M.D.W.) and an NSF grant (MCB-0820293 to M.D.W.).

Supplementary Materials

www.sciencemag.org/cgi/content/full/340/6140/1580/DC1
Materials and Methods
Figs. S1 to S11
References (30–51)
Movie S1

21 January 2013; accepted 21 May 2013
10.1126/science.1235441

Fe-S Cluster Biosynthesis Controls Uptake of Aminoglycosides in a ROS-Less Death Pathway

Benjamin Ezraty,¹ Alexandra Vergnes,¹ Manuel Banzhaf,² Yohann Duverger,¹ Allison Huguenot,¹ Ana Rita Brochado,² Shu-Yi Su,² Leon Espinosa,¹ Laurent Loiseau,¹ Béatrice Py,¹ Athanasios Typas,² Frédéric Barras^{1*}

All bactericidal antibiotics were recently proposed to kill by inducing reactive oxygen species (ROS) production, causing destabilization of iron-sulfur (Fe-S) clusters and generating Fenton chemistry. We find that the ROS response is dispensable upon treatment with bactericidal antibiotics. Furthermore, we demonstrate that Fe-S clusters are required for killing only by aminoglycosides. In contrast to cells, using the major Fe-S cluster biosynthesis machinery, ISC, cells using the alternative machinery, SUF, cannot efficiently mature respiratory complexes I and II, resulting in impendence of the proton motive force (PMF), which is required for bactericidal aminoglycoside uptake. Similarly, during iron limitation, cells become intrinsically resistant to aminoglycosides by switching from ISC to SUF and down-regulating both respiratory complexes. We conclude that Fe-S proteins promote aminoglycoside killing by enabling their uptake.

Reactive oxygen species (ROS) have been recently proposed to be central to cell killing by all classes of bactericidal antibiotics (1). However, using a recently published high-throughput chemical-genetics screen in *Escherichia coli*, we did not detect any functional enrichment for ROS-defense genes in the profiles of two major classes of bactericidal antibiotics: β -lactams, which target the cell wall, and aminoglycosides, which cause mistranslation (fig. S1) (2). Instead, β -lactams and aminoglycosides cause cellular death through unrelated morphological defects (3–5) (fig. S2). We decided to further explore the proposed role of ROS in antibiotic killing by using a series of mutants altered in the protective response of *E. coli* against ROS and testing them with a β -lactam [ampicillin (Amp)] and an aminoglycoside [gentamicin (Gm)] antibiotic.

E. coli mutants, hypersensitive to O_2^- (lacking both cytoplasmic superoxide dismutases, $\Delta sodA$ and $\Delta sodB$) or to H_2O_2 (lacking the H_2O_2 -sensing master activator, $\Delta oxyR$), exhibited similar sensitivities to Gm and Amp as the wild type (WT) in a time-dependent killing experiment, with $\Delta oxyR$ being more resistant to Amp at the last time point, 4.5 hours after drug addition (Fig. 1, A and B). When tested in a concentration-dependent killing experiment, the two mutants were as sensitive as WT to Gm (Fig. 1C) but exhibited small differences to the WT at intermediate Amp concentrations, at levels that provided no support for a prominent role for ROS defense mechanisms during treatment with bactericidal antibiotics (Fig. 1D). In contrast and as expected, both strains were hypersensitive to their respective ROS source, a known O_2^- generator (paraquat) and H_2O_2 (fig. S3). Similarly, an *oxyRc* strain constitutively expressing the OxyR regulon—which is significantly more resistant to H_2O_2 (fig. S3)—showed slight differences to WT in killing experiments with Amp and Gm (Fig. 1, A to D), tending to be more susceptible to both antibiotics than WT (Fig. 1, C and D).

The lack of evidence for a link between oxidative stress and bactericidal antibiotics also held true when testing the same strains for minimal inhibitory concentrations (MIC) and growth rates in subinhibitory antibiotic amounts (table S1 and fig. S4). Taken together, these results revealed no association between ROS and bactericidal antibiotic sensitivity, in agreement with two recent reports using complementary approaches (6, 7).

Kohanski *et al.* (1) proposed that protein-bound Fe-S clusters are required for killing by bactericidal antibiotics because they release Fe^{2+} ions that fuel ROS production by Fenton chemistry. This assumption was based on the fact that mutants lacking the major Fe-S cluster biogenesis system ISC were resistant to both Gm and Amp. The *iscS* gene codes for the ISC cysteine desulfurase that, in addition to Fe-S protein maturation, is involved in all sulfur trafficking pathways (8, 9). We found that the *iscS* mutant, as previously reported (1), was fully resistant to Gm killing and showed partial resistance to Amp in a time-dependent killing experiment using 5 μ g/ml for both drugs (Fig. 2, A and B). However, the enhanced resistance of the *iscS* mutant was only recapitulated for Gm, but not for Amp at lower antibiotic concentrations (fig. S5, A and B) or when measuring MICs and growth rates in subinhibitory antibiotic concentrations (table S1 and fig. S5C).

We then tested an *iscUA* mutant, because in contrast to the pleiotropic *iscS* mutant, it is specifically compromised in Fe-S cluster biogenesis, as it lacks both the scaffold for assembling the Fe-S cluster and the transport machinery that inserts the Fe-S cluster into apo-proteins (9, 10). Interestingly, the *iscUA* mutant was resistant to Gm and sensitive to Amp in all tests used (Fig. 2, A and B, table S1, and fig. S5). We conclude that Fe-S clusters are required for the bactericidal effect of aminoglycosides but not for that of β -lactams.

If killing by aminoglycosides is not caused by ROS, why does eliminating the ISC system render *E. coli* resistant to these antibiotics? Fe-S clusters are essential for growth, and *E. coli* has a second assembly system, called SUF (10). To

¹Laboratoire de Chimie Bactérienne, Aix-Marseille Université, CNRS, UMR 7283, Institut de Microbiologie de la Méditerranée, 31 Chemin Joseph Aiguier, 13009 Marseille France. ²Genome Biology Unit, European Molecular Biology Laboratory, Meyerhofstrasse 1, 69117 Heidelberg, Germany.

*Corresponding author. E-mail: barras@imm.cnrs.fr

dissect the role of *SUF* in aminoglycoside treatment, we made a mutant lacking endogenous *ISC* and *SUF* and instead expressing *SUF* from an arabinose-inducible ectopic copy (*eSUF*). This strain only grew in the presence of arabinose, confirming that *E. coli* needs at least one of the two Fe-S biogenesis systems to survive (11). Moreover, *eSUF* was more resistant to killing by Gm, indicating that Fe-S clusters are not per se detrimental to *E. coli* on aminoglycoside treatment. In contrast, the parental *eSUF isc⁺* strain was Gm sensitive (Fig. 2C and fig. S6A). Thus, *E. coli* without the *ISC* machinery is resistant to Gm, not because it cannot synthesize Fe-S clusters but because it uses *SUF* to build them.

Aminoglycosides' uptake into bacterial cells requires proton motive force (PMF) that is generated by electron flow through the respiratory chain (12–15). We verified the link between the PMF and aminoglycoside uptake by using carbonyl cyanide-*m*-chlorophenylhydrazone (CCCP), a PMF uncoupling reagent. Increasing amounts of CCCP blocked Gm-mediated killing (Fig. 2D) and allowed *E. coli* to grow well under subinhibitory Gm concentrations (fig. S7). Gm uptake was also reduced in cells using exclusively *SUF* (*iscUA* and *eSUF*), but addition of *ISC* to *eSUF* restored Gm uptake (Fig. 2E). Heterologous expression of proteorhodopsin (16), a PMF generating system, restored Gm sensitivity for the

iscUA mutant (Fig. 2F) but played no role in WT cells (fig. S8). We concluded that cells lacking *ISC* are resistant to Gm as a result of a PMF defect.

PMF is largely generated by the respiratory complex I, NADH (reduced form of nicotinamide adenine dinucleotide) dehydrogenase (*Nuo*) and, to some extent, by complex II, succinate dehydrogenase (*Sdh*) (17). Complex I, but not complex II, directly translocates protons, but both also indirectly contribute to PMF production by passing electrons to the proton-translocating cytochrome oxidases (17). Complexes I and II contain nine and three Fe-S clusters, respectively. Although only the single *nuo* mutant, and not the *sdhB* mutant, was significantly more resistant to Gm killing and exhibited lower Gm uptake, the *nuo sdhB* double mutant showed some aggravating effect for both killing and uptake (Fig. 3, A and B, fig. S6B, and fig. S9). This suggests that both systems are targeted by *ISC*, but they are not the only *ISC*-matured systems that are relevant for aminoglycoside resistance, because the *nuo sdhB* double mutant is still more sensitive to Gm than the *iscUA* mutant. Consistent with *ISC* maturing, these complexes—and, as previously reported (8)—an *iscUA* mutant showed close to background activity for respiratory complexes I and II (Fig. 3C and fig. S10). Because the levels of respiratory complex I polypeptides are similar in

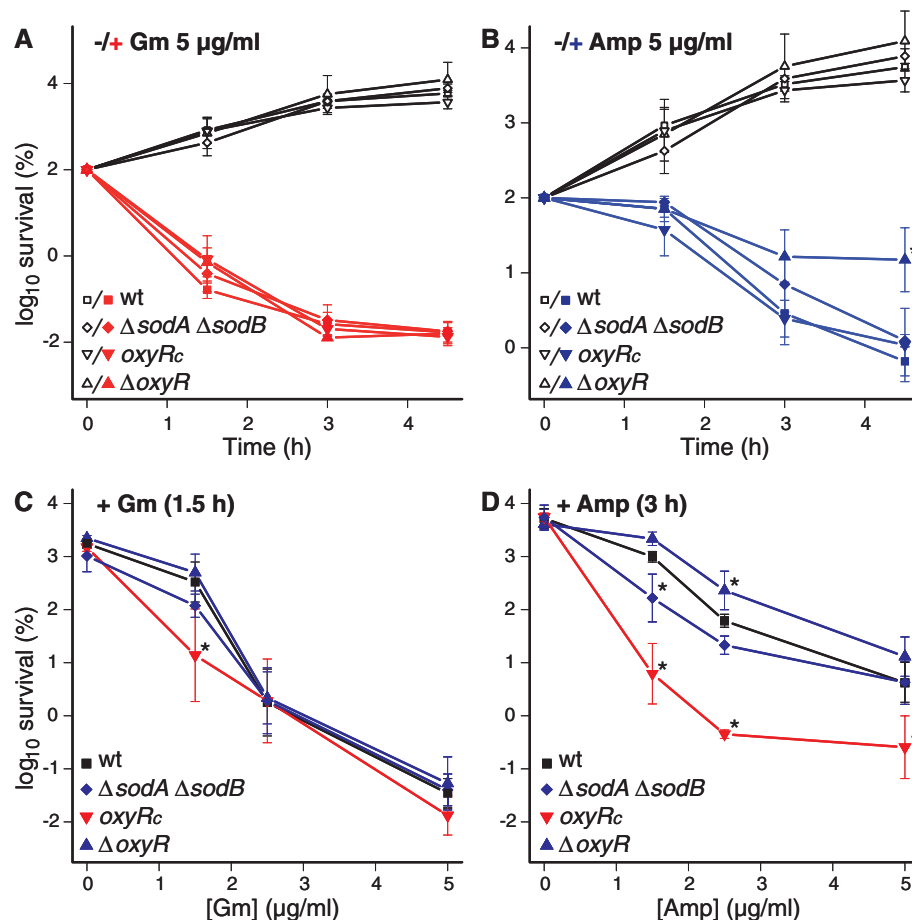
both WT and *iscUA* (fig. S11A), we concluded that the lack of *ISC* impairs efficient Fe-S cluster insertion in main PMF-producing aerobic respiratory complexes, leading to reduced Gm uptake and killing.

The findings above also imply that *SUF* cannot adequately substitute for *ISC* in the maturation of respiratory complexes I and II. Indeed the *ISC*-deficient *eSUF* strain showed reduced activity levels of respiratory complexes I and II (~45% of WT) (Fig. 3C), despite the high *SUF* protein level (fig. S11A). Only a concomitant increase in the respiratory complex I protein level by a factor of about 5 (fig. S11B), using an inducible plasmid (*pNuo⁺*), yielded sufficient increase in complex I activity (~70% of WT) (Fig. 3C) to restore both Gm uptake (Fig. 3B) and sensitivity (Fig. 3D). This suggests that higher than normal levels of both *SUF* and its substrate are required for *SUF* to efficiently mature respiratory complexes I and II. *E. coli* has a second NADH dehydrogenase system, *NdhII*, which lacks Fe-S clusters and does not translocate protons. We found that NADH reduction mediated by *NdhII* is slightly increased in the *iscUA* mutant (fig. S12), but this increase in respiration was not sufficient to support Gm uptake (Fig. 2E).

Under iron limitation, cells use *SUF* instead of *ISC* (11, 18, 19). We suspected that this might be the reason Kohanski *et al.* reported that chelation

Fig. 1. The ROS-stress response is not required for antibiotic killing in *E. coli*. (A and B) Survival of WT and mutants with compromised oxidative stress resistance after Gm (5 μ g/ml) and Amp (5 μ g/ml) treatment was essentially the same (black, no antibiotic; red or blue, with antibiotic). Survival, measured by colony-forming units (CFU) per ml, was normalized relative to time zero at which the antibiotic was added (midexponential phase cells; $\sim 5 \times 10^7$ CFU/ml) and was plotted as \log_{10} of % survival.

$\Delta oxyR$ lacks the H_2O_2 sensing master regulator *OxyR*, which positively controls the expression of ROS-defense genes, whereas *oxyR_c* expresses ROS-defense genes constitutively. The $\Delta soda \Delta sodB$ strain lacks both cytoplasmic superoxide dismutases. (C and D) As above, but survival was measured as a function of antibiotic concentration. \log_{10} of % survival was measured at 1.5 hours after Gm addition (C) and at 3 hours after Amp addition (D). Mutants deviated from the WT behavior only in Amp, but the effects were inconsistent with a need for ROS defense mechanisms during the antibiotic treatment. Values are expressed as means (number of experiments $n = 3$ to 10), and error bars depict standard deviations. Asterisks indicate a statistically significant difference between mutants and the WT, apart from when two mutants are compared, and then this is clearly indicated in the figure. * $P \leq 0.05$; ** $P \leq 0.01$; and *** $P \leq 0.001$ (Mann-Whitney U test). When all the measurements within a curve share the same significance level, asterisks are shown in parentheses after the last measurement point.



of Fe eliminates aminoglycoside killing (1) and misinterpreted it as a role for Fenton chemistry in antibiotic killing. As predicted, adding the intracellular iron chelator 2,2'-dipyridyl (DIP) to growing *E. coli* resulted in low activity levels for respiratory complexes I and II, inhibited Gm uptake, with consequent resistance to Gm killing (Fig. 4, A to C, and fig. S6, C and D). Adding back exogenous iron to DIP-treated cells suppressed the protection to Gm (Fig. 4D) and confirmed that the DIP effect was due to iron limitation. Interestingly, DIP-treated cells were characterized by a decrease in respiratory complex I protein levels, in addition to the higher SUF-lower ISC protein levels (Fig. 4E), which may also have contributed to the low Gm uptake. This effect on protein level was also rapidly reversed after addition of exogenous iron to DIP-treated cells (Fig. 4E). Thus, iron limitation leads to both a switch from ISC to SUF and a reduction of respiratory complex I levels, thereby making cells aminoglycoside resistant.

Iron bioavailability is sensed by Fur, a global repressor of >100 genes involved in iron homeostasis (20, 21). Surprisingly, a *fur*-null mutant, which expresses the iron-limitation response constitutively and hence contains high intracellular iron levels, produced similar, albeit more modest, phenotypes as the DIP-treated cells in terms of respiratory complex I and II activities (Fig. 4A), complex I protein levels (fig. S10C), and Gm uptake (Fig. 4B) and sensitivity (Fig. 4C). Although loaded with intracellular iron, the *fur* mutant was still significantly more resistant to Gm than WT as a result of reduced Gm uptake, supporting the argument that it is not intracellular iron levels per se that control aminoglycoside resistance but rather the iron limitation response. We then wondered whether Fur was directly, or indirectly via one of its downstream targets, responsible for the aminoglycoside resistance. The small non-coding RNA (ncRNA), RyhB, seemed an ideal target, as it is Fur-dependent and itself inhibits the synthesis of nonessential Fe-utilization proteins

(22), including Isc, Nuo, and Sdh (23). Consistent with this scenario, the *ryhB fur* double mutant restored the activities of respiratory complexes I and II (Fig. 4A), the complex I protein levels (fig. S11C), the uptake of Gm (Fig. 4B), and the Gm sensitivity to WT levels (Fig. 4C and fig. S6C). Thus, RyhB expression is the relevant iron-limitation feature that leads to aminoglycoside resistance.

In summary, we have shown that the Fe-S cluster biogenesis machineries play a key role in aminoglycoside resistance by affecting their PMF-energized uptake. Switching from ISC to SUF allows *E. coli* to maintain enough Fe-S clusters to survive, albeit with low PMF levels. As a consequence, aminoglycosides, whose uptake is strongly PMF-dependent, cannot reach the ribosome, their cytoplasmic target. As uptake and target lie in a positive-feedback loop for aminoglycosides (fig. S13) (24), small changes in the otherwise basal uptake of aminoglycosides has a severe impact on their action. At least for *E. coli*, iron

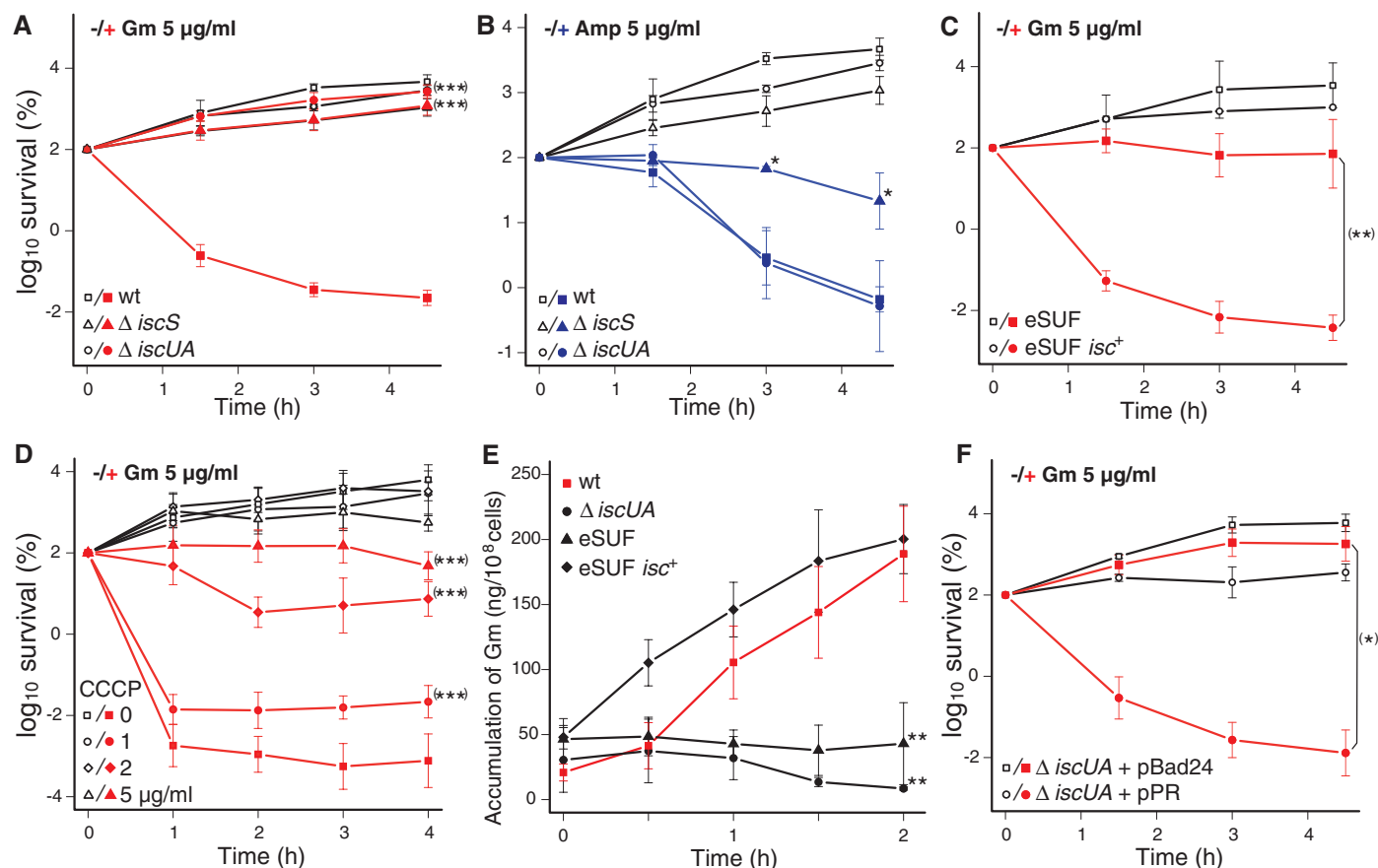


Fig. 2. Mutations in the ISC, but not the SUF, Fe-S cluster biogenesis machinery makes *E. coli* resistant to bactericidal aminoglycosides. Survival of WT and mutants defective in Fe-S cluster biogenesis after (A) Gm (5 $\mu\text{g/ml}$) and (B) Amp (5 $\mu\text{g/ml}$) treatment (black, no antibiotic; red or blue, with antibiotic). The $\Delta iscUA$ mutant was resistant to Gm, but the pleiotropic $\Delta iscS$ also showed some resistance to Amp. (C) The eSUF strain is resistant to Gm. The eSUF strain contains deletions of the endogenous *iscUA* genes and *suf* operon and expresses the *suf* operon from an ectopic chromosomal position under the control of the pBAD promoter. The eSUF *isc*⁺ strain is the parent of the eSUF strain before transduction of the $\Delta iscUA$ deletion. Cultures of

eSUF and eSUF *isc*⁺ were grown in the presence of arabinose (0.2%). (D) CCCP, a PMF uncoupler, increased resistance to killing by Gm in a dosage-dependent manner. (E) Tritiated gentamicin (³H-Gm) uptake was compromised in cells that depend on the SUF rather than the ISC machinery. Uptake was measured by incubating early exponential-phase cultures (OD₆₀₀ ~ 0.3) with 5 $\mu\text{g/ml}$ ³H-Gm at 37°C. (F) Exogenous proteorhodopsin (pPR) restores the Gm susceptibility of cells depending on the SUF machinery for Fe-S cluster formation. For killing experiments, strains were grown, and \log_{10} of % survival was measured as in Fig. 1. Values, error bars, and statistical significance were calculated and are indicated as in Fig. 1.

Fig. 3. The PMF-generating respiratory complexes I and II function in strain using ISC, but not in strain using SUF, Fe-S cluster biogenesis machinery. (A) Survival of WT, complex I and/or II-deficient strains after 5 $\mu\text{g/ml}$ Gm treatment. The Δnuo and $\Delta sdhB$ mutants cannot synthesize respiratory complexes I and II, respectively (black, no antibiotic; red, with antibiotic). **(B)** ^3H -Gm uptake is defective in cells without respiratory complexes I and II ($\Delta nuo \Delta sdhB$) and restored when both SUF and respiratory complex I are over-expressed (eSUF/pNuo $^+$), indicating that SUF can mature sufficient amounts of respiratory complex I to create the necessary PMF. The uptake experiment was performed as described in Fig. 2E. **(C)** Activities of respiratory complexes I and II are altered in cells lacking ISC. Complex I activity can be partially restored when both SUF and respiratory complex I are overexpressed. Complex I (Nuo) activity was assessed by monitoring deamino-NADH consumption in whole-cell lysates. Complex II (Sdh) activity was assayed by monitoring dichloro-phenol-endo-phenol (DCPIP) reduction in membrane preparations (fig. S10 provides an explanation for the higher than basal succinate dehydrogenase activity of the $\Delta nuo \Delta sdhB$ double mutant). **(D)** Cells without ISC become susceptible to Gm only when both SUF and respiratory complex I are overexpressed. For killing experiments, strains were grown and log $_{10}$ of % survival was measured as in Fig. 1. Values, error bars, and statistical significance were calculated and are indicated as in Fig. 1.

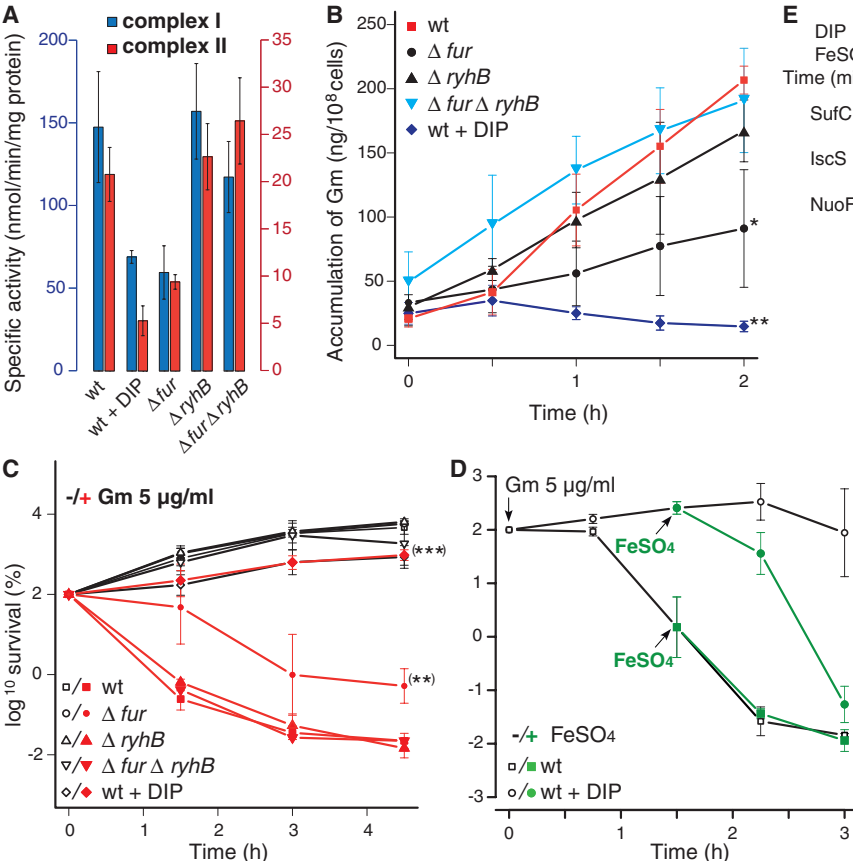
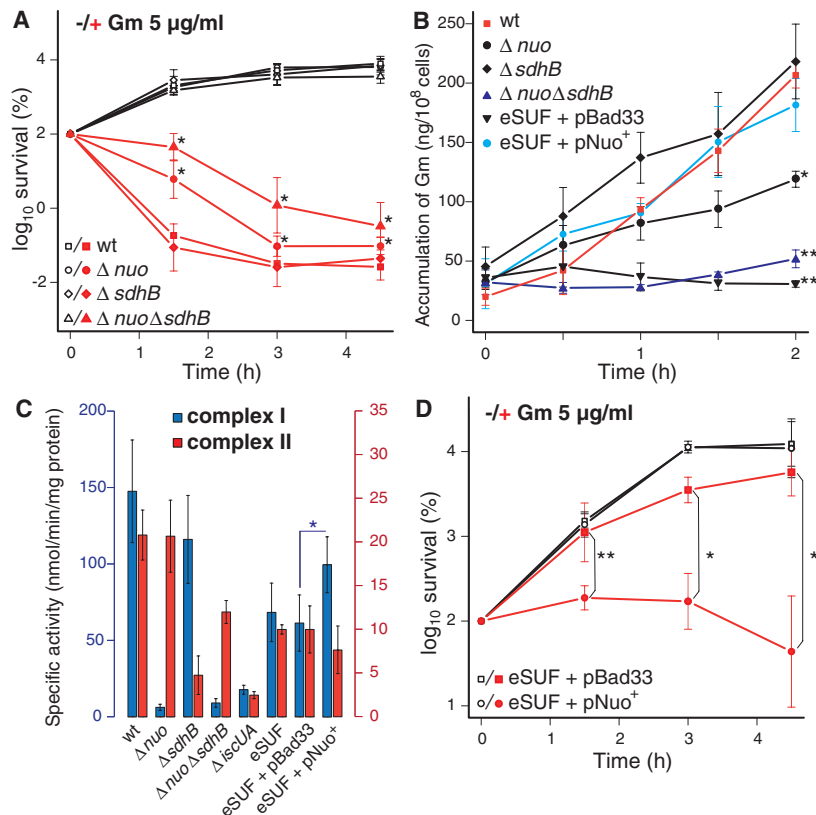


Fig. 4. Iron limitation orchestrates a switch from ISC to SUF and prevents aminoglycoside uptake. Complexes I and II activity assays (A), ^3H -Gm uptake (B), and survival after Gm treatment (5 $\mu\text{g/ml}$) (C) of WT in the presence/absence of an iron chelator (250 μM DIP), and of three mutants affected in iron homeostasis control, Δfur , $\Delta ryhB$, and $\Delta fur \Delta ryhB$. When the iron-limitation response was turned on by the addition of the iron chelator DIP or deletion of the global repressor *fur*, complexes I and II activity and ^3H -Gm uptake were low, which caused Gm resistance. Knocking out one of the central players of the iron response, ncRNA *RyhB*, restored antibiotic sensitivity, indicating that protection against aminoglycosides is mediated by *RyhB*. **(D)** Addition of exogenous iron restored sensitivity to Gm to iron-starved cells (250 μM DIP). FeSO_4 (100 μM) was added 1.5 hours after treatment with 5 $\mu\text{g/ml}$ Gm. **(E)** Iron limitation induced SUF protein levels and reduced that of ISC and complex I. The response was rapidly reversed on addition of exogenous FeSO_4 (100 μM). Western blots were performed with antibodies against specific subunits of the respiratory complex I (NuoF), the SUF (SufC), and the ISC (IscS) machineries. Adding exogenously excess of iron to DIP-treated cells resulted in a 9-fold decrease in SufC protein levels and a 2-fold increase in IscS and NuoF levels after 90 min. Values, error bars, and statistical significance were calculated and are indicated as in Fig. 1.

limitation would be a physiological environment where the cell switches from ISC to SUF, becoming more resistant to aminoglycosides. Bacteria are iron-depleted in the host, but some pathogens induce local increases of iron concentration by lysing host cells and erythrocytes (25), which suggests that aminoglycosides may be to some degree selective against enterobacterial pathogens. In addition, aminoglycosides may be very effective in treating recurrent enterobacterial infections in patients with human genetic disorders associated with iron overload in the blood, such as thalassemia and hemochromatosis (26).

References and Notes

- M. A. Kohanski, D. J. Dwyer, B. Hayete, C. A. Lawrence, J. J. Collins, *Cell* **130**, 797 (2007).
- R. J. Nichols *et al.*, *Cell* **144**, 143 (2011).
- B. G. Spratt, *Proc. Natl. Acad. Sci. U.S.A.* **72**, 2999 (1975).
- B. D. Davis, *Microbiol. Rev.* **51**, 341 (1987).
- Z. Yao, D. Kahne, R. Kishony, *Mol. Cell* **48**, 705 (2012).
- I. Keren, Y. Wu, J. Inocencio, L. R. Mulcahy, K. Lewis, *Science* **339**, 1213 (2013).
- Y. Liu, J. A. Imlay, *Science* **339**, 1210 (2013).
- C. J. Schwartz *et al.*, *Proc. Natl. Acad. Sci. U.S.A.* **98**, 14895 (2001).
- R. Shi *et al.*, *PLoS Biol.* **8**, e1000354 (2010).
- B. Roche *et al.*, *Biochim. Biophys. Acta* **1827**, 455 (2013).
- F. W. Outten, O. Djaman, G. Storz, *Mol. Microbiol.* **52**, 861 (2004).
- P. D. Damper, W. Epstein, *Antimicrob. Agents Chemother.* **20**, 803 (1981).
- L. E. Bryan, S. Kwan, *Antimicrob. Agents Chemother.* **23**, 835 (1983).
- S. M. Mates *et al.*, *Proc. Natl. Acad. Sci. U.S.A.* **79**, 6693 (1982).
- H. W. Taber, J. P. Mueller, P. F. Miller, A. S. Arrow, *Microbiol. Rev.* **51**, 439 (1987).
- J. M. Walter, D. Greenfield, C. Bustamante, J. Liphardt, *Proc. Natl. Acad. Sci. U.S.A.* **104**, 2408 (2007).
- J. Simon, R. J. van Spanning, D. J. Richardson, *Biochim. Biophys. Acta* **1777**, 1480 (2008).
- J. L. Giel *et al.*, *Mol. Microbiol.* **87**, 478 (2013).
- D. Vinella, L. Loiseau, S. O. de Choudens, M. Fontecave, F. Barras, *Mol. Microbiol.* **87**, 493 (2013).
- Z. Chen *et al.*, *Nucleic Acids Res.* **35**, 6762 (2007).
- K. Hantke, *Curr. Opin. Microbiol.* **4**, 172 (2001).
- E. Massé, S. Gottesman, *Proc. Natl. Acad. Sci. U.S.A.* **99**, 4620 (2002).
- G. Desnoyers, A. Morissette, K. Prévost, E. Massé, *EMBO J.* **28**, 1551 (2009).
- B. D. Davis, L. L. Chen, P. C. Tai, *Proc. Natl. Acad. Sci. U.S.A.* **83**, 6164 (1986).
- E. P. Skaar, *PLoS Pathog.* **6**, e1000949 (2010).
- S. Vento, F. Cainelli, F. Cesario, *Lancet Infect. Dis.* **6**, 226 (2006).

Acknowledgments: We are grateful to C. Gross (University of California, San Francisco, USA) for critically reading the manuscript and providing feedback. We thank T. Friedrich (Freiburg University, Germany), T. Yagi and J. Torres Bacete (La Jolla, CA, USA), E. Bouveret (Laboratoire d'Ingénierie des Systèmes Macromoléculaires, Marseille, France), J. Armitage (Oxford, UK), and P. Moreau and T. Mignot (Laboratoire de Chimie Bactérienne, Marseille, France) for providing materials and strains. This work was supported by grants from Agence Nationale Recherche (ANR Blanc SPV 05511), the Institut Universitaire de France, the Fondation pour la Recherche Médicale, and European Molecular Biology Laboratory. Data are deposited in the Dryad Repository: <http://dx.doi.org/10.5061/dryad.3062c>.

Supplementary Materials

www.sciencemag.org/cgi/content/full/340/6140/1583/DC1
Materials and Methods
Figs. S1 to S13
Tables S1 and S2
References (27–40)

26 March 2013; accepted 8 May 2013
10.1126/science.1238328

B Cells Use Mechanical Energy to Discriminate Antigen Affinities

Elizabeth Natkanski,¹ Wing-Yiu Lee,¹ Bhakti Mistry,¹ Antonio Casal,¹ Justin E. Molloy,² Pavel Tolar^{1*}

The generation of high-affinity antibodies depends on the ability of B cells to extract antigens from the surfaces of antigen-presenting cells. B cells that express high-affinity B cell receptors (BCRs) acquire more antigen and obtain better T cell help. However, the mechanisms by which B cells extract antigen remain unclear. Using fluid and flexible membrane substrates to mimic antigen-presenting cells, we showed that B cells acquire antigen by dynamic myosin IIa-mediated contractions that pull out and invaginate the presenting membranes. The forces generated by myosin IIa contractions ruptured most individual BCR-antigen bonds and promoted internalization of only high-affinity, multivalent BCR microclusters. Thus, B cell contractility contributes to affinity discrimination by mechanically testing the strength of antigen binding.

Efficient antibody responses require selective expansion of B cell clones that recognize foreign antigens with high affinity. B cells are initially stimulated by the binding of their B cell receptors (BCRs) to antigens on the surfaces of antigen-presenting cells (APCs) (1–5). During these cellular contacts, termed immune synapses, B cells acquire the antigens from the APCs (1, 2, 6), which leads to B cell antigen processing and presentation to helper T cells. The extent of T cell help, and resulting B cell activation, depends on the BCR affinity for antigen (7–9). Therefore, efficient affinity discrimination during antigen acquisition is essential for B cell clonal selection.

Although B cell synapse formation is sensitive to antigen affinity (10, 11), the mechanisms by which B cells extract antigens from APCs remain poorly understood (12, 13). To study this process, we developed an experimental model for studying immune synapses using immobilized plasma membrane sheets (PMSs).

PMSs are made from plasma membranes of adherent cells (14) and are suspended ~10 nm above the coverslip (fig. S1). Decoration of the exposed surfaces of PMSs with antigens, but not with control proteins, induced B cell spreading and antigen clustering that resembled B cell synapses with planar lipid bilayers (PLBs), an alternative model substrate (10, 15). However, unlike synapses with PLBs, B cells rapidly internalized the antigen from synapses made with PMSs (Fig. 1, A and B, and movie S1). The ability of B cells to internalize antigen was not a result of the composition of the PMSs, as PLBs prepared from plasma

membranes (PM-PLBs) did not support antigen internalization (Fig. 1B). In addition, the internalization did not correlate with lipid or antigen diffusion within these substrates (fig. S2).

To investigate why B cells internalize antigens from PMSs, but not PLBs, we examined the flexibility of these substrates using atomic force microscopy (AFM) and compared them to live APCs. In these experiments, the AFM tip binds to the substrate and then retracts to measure forces between the tip and the substrate until the rupture of the bond (16, 17). On PLBs and PM-PLBs, forces during tip retraction increased rapidly to 30 to 40 pN and produced single-step ruptures of bonds a few nanometers from the surface (Fig. 1, C and D), indicating high membrane stiffness. By contrast, on both PMSs and dendritic cells (DCs), forces initially increased and then plateaued at ~20 pN, with bonds often rupturing hundreds of nanometers away from the surface (Fig. 1, C and D). Thus, in contrast to PLBs or PM-PLBs, PMSs were flexible and similar in their viscoelastic properties to plasma membranes of APCs loaded with physiological antigen complexes.

Labeling PMSs with the hydrophobic dye 1,1'-dioctadecyl-3,3',3'-tetramethylindocarbocyanine perchlorate (DiI) showed that B cells internalized antigen together with small pieces of the PMS membrane (Fig. 1, A and E). We observed similar colocalization of antigen and lipid in B cells that acquired cognate immune complexes from DCs (Fig. 1, E and F). By contrast, B cells that formed synapses with PLBs did not take up any DiI or antigen (Fig. 1, A and E). These results resemble the acquisition of APC membranes by B cells in vivo (18) and, together with the force spectroscopy data, suggest that B cells require flexibility of the presenting membranes to pinch off the antigen together with the phospholipid bilayer.

¹Division of Immune Cell Biology, MRC National Institute for Medical Research, Mill Hill, London NW7 1AA, UK. ²Division of Physical Biochemistry, MRC National Institute for Medical Research, Mill Hill, London, UK.

*Corresponding author. E-mail: ptolar@nimr.mrc.ac.uk

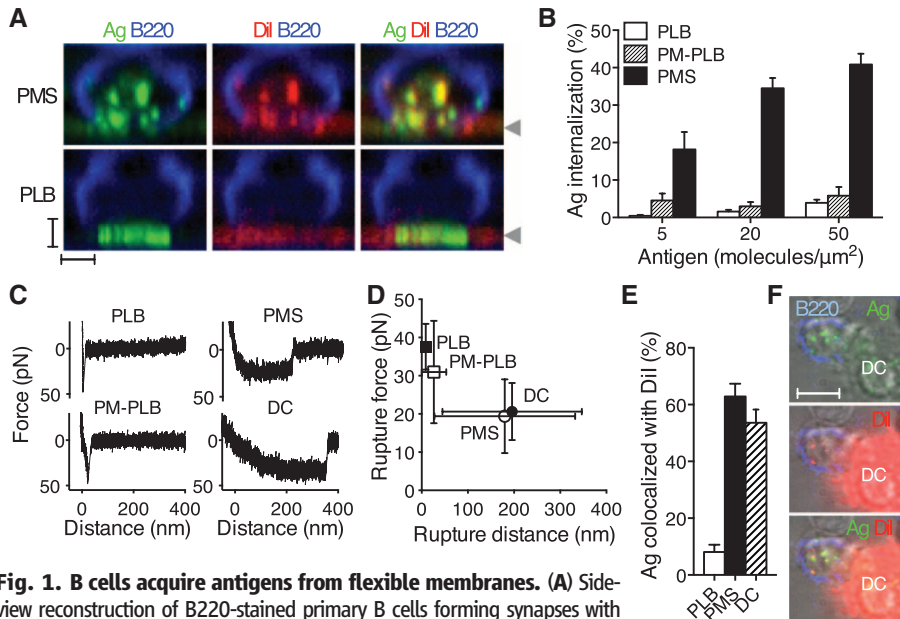


Fig. 1. B cells acquire antigens from flexible membranes. (A) Side-view reconstruction of B220-stained primary B cells forming synapses with DiI-stained and antibody against immunoglobulin κ (anti-Ig κ) antigen-loaded (Ag) PMSs or PLBs. Arrowheads indicate the position of the substrate. Scale bars, 2 μ m. (B) Image quantification of primary B cell antigen internalization (means \pm SEM, n = 23 to 60 cells). (C) AFM force retraction curves of streptavidin-coated AFM tip and biotinylated antigens. Antigens were anti-Ig κ for PLBs, PM-PLBs, and PMSs, and immune complexes of NIP antigen for DCs. Speed of retraction was 0.1 μ m/s. (D) Rupture distances and forces (mean \pm SD, n = 31 to 109 retraction curves). (E) Colocalization of internalized antigen with DiI in primary B cells after internalization from the substrates (means \pm SEM, n = 12 to 21 cells). (F) B220-stained B1-8 primary B cell internalizing immune complexes of NIP antigen from a DC stained with DiI. Scale bar, 5 μ m.

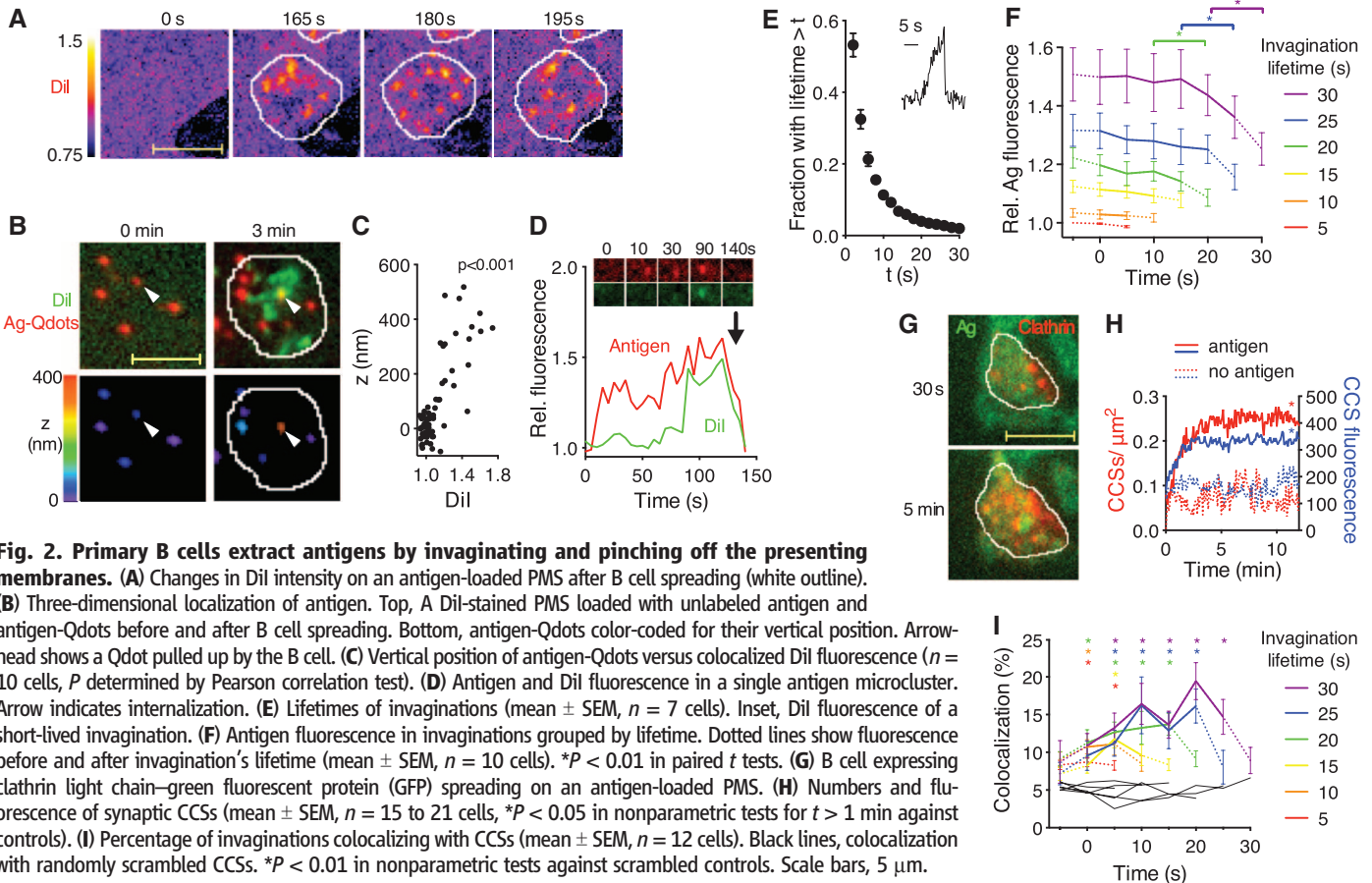


Fig. 2. Primary B cells extract antigens by invaginating and pinching off the presenting membranes. (A) Changes in DiI intensity on an antigen-loaded PMS after B cell spreading (white outline). (B) Three-dimensional localization of antigen. Top, A DiI-stained PMS loaded with unlabeled antigen and antigen-Qdots before and after B cell spreading. Bottom, antigen-Qdots color-coded for their vertical position. Arrowhead shows a Qdot pulled up by the B cell. (C) Vertical position of antigen-Qdots versus colocalized DiI fluorescence (n = 10 cells, P determined by Pearson correlation test). (D) Antigen and DiI fluorescence in a single antigen microcluster. Arrow indicates internalization. (E) Lifetimes of invaginations (mean \pm SEM, n = 7 cells). Inset, DiI fluorescence of a short-lived invagination. (F) Antigen fluorescence in invaginations grouped by lifetime. Dotted lines show fluorescence before and after invagination's lifetime (mean \pm SEM, n = 10 cells). * P < 0.01 in paired t tests. (G) B cell expressing clathrin light chain–green fluorescent protein (GFP) spreading on an antigen-loaded PMS. (H) Numbers and fluorescence of synaptic CCSs (mean \pm SEM, n = 15 to 21 cells, * P < 0.05 in nonparametric tests for t > 1 min against controls). (I) Percentage of invaginations colocalizing with CCSs (mean \pm SEM, n = 12 cells). Black lines, colocalization with randomly scrambled CCSs. * P < 0.01 in nonparametric tests against scrambled controls. Scale bars, 5 μ m.

To visualize the initiation of antigen extraction, we recorded total internal reflection fluorescence (TIRF) time lapses of B cells interacting with the DiI-labeled PMSs. Within a few seconds after B cell spreading, numerous spots of increased DiI fluorescence appeared in the PMSs, and these spots continued to form and disappear dynamically (Fig. 2A and movie S2). By contrast, DiI fluorescence remained diffuse in the absence of antigen (fig. S3A). High-resolution three-dimensional (3D) localization showed that the DiI spots were associated with upward movement of colocalized antigen particles (Fig. 2, B and C). Thus, the increase in DiI fluorescence reports local lipid enrichment caused by antigen-induced B cell pulling-out and invaginating the presenting membranes.

Whereas antigen microclusters typically colocalized with a subset of membrane invaginations just before internalization (Fig. 2D), the membrane invaginations were more frequent and dynamic than antigen microclusters (movie S3). Most invaginations lasted less than 5 s (Fig. 2E) and terminated abruptly (Fig. 2E, inset), suggesting physical rupture. Analysis of DiI and antigen fluorescence showed that the longer-lived invaginations started at sites that contained higher amounts of antigen compared to short-lived invaginations, and there was a significant drop in antigen fluorescence after their termination, indicating antigen internalization (Fig. 2F and fig. S3B). These

results show that B cells pulled out the presenting membranes at sites that contained variable amounts of antigen, but the lifetime of the invaginations and the probability of their internalization depended on prior formation of antigen microclusters.

To understand the mechanisms that regulate antigen internalization from the invaginations, we analyzed the dynamics of clathrin (19, 20). After B cell spreading on PMSs, the numbers of clathrin-coated structures (CCSs), and their brightness, increased compared to PMSs without antigen (Fig. 2, G and H). CCSs formed throughout the synapse, and we observed simultaneous disappearance of long-lived invaginations, antigen microclusters, and CCSs (fig. S4). Short-lived invaginations rarely colocalized with CCSs, but 20% of long-lived invaginations colocalized with CCSs, particularly at the end of their lifetime (Fig. 2I). To assess the importance of CCSs in antigen acquisition, we knocked-down components of CCSs in Ramos B cells using short hairpin RNA (shRNA). Knockdown of AP2 and dynamin2 inhibited antigen internalization from PMSs (Fig. 3A), although pulling of membrane invaginations was

not affected (Fig. 3B). These findings were confirmed in primary B cells by means of a dynamin2 inhibitor (Fig. 3, C and D). Thus, CCSs pinch off invaginated antigen microclusters, leading to internalization of the antigen. However, clathrin-independent mechanisms are required to first pull out the presenting membrane.

Using shRNA-mediated knockdown and pharmacological inhibition, we found that myosin IIa and its activator, Rock1, were required for both membrane invagination and antigen internalization from PMSs (Fig. 3, A to D). By contrast, inhibition of myosin IIa did not prevent internalization of soluble antigen (Fig. 3C) or B cell spreading on the PMSs (fig. S5), suggesting that myosin IIa is not required for all BCR signaling or endocytosis. TIRF microscopy showed that myosin IIa formed dynamic spots and short fibers throughout the synapse (Fig. 3E and movie S4) and specifically accumulated at the sites of membrane invaginations just before their onset (Fig. 3F). Myosin IIa then rapidly cleared from the center of growing invaginations, but remained closely associated with their sides (Fig. 3, E and F). By contrast, F-actin accumulated at the onset

of membrane invaginations, persisted throughout their lifetime, and disappeared after their termination (fig. S6, A to C, and movie S5). In longer-lived invaginations, a second wave of F-actin recruitment was detectable at the end of the invagination's lifetime (fig. S6, B and C). Together, these results show that B cells use actomyosin contractility to pull out and invaginate the presenting membranes, which is required to internalize the antigen via a clathrin- and actin-dependent process (21, 22). The observed short lifetime of most invaginations leads to a prediction that BCR-antigen bonds within small microclusters rupture under the pulling forces, aborting endocytosis. However, BCR-antigen interactions within larger microclusters resist the contractile forces for more than 20 to 30 s, allowing association or maturation of CCSs and internalization. This suggests that contractile forces mechanically test the strength of BCR binding immediately before internalization, providing a possible proofreading mechanism for affinity discrimination.

To extract antigen, BCR-antigen bonds would have to resist forces of up to 20 pN (Fig. 1D). To directly characterize the mechanical strength of individual BCR-antigen bonds, we measured BCR-antigen rupture forces using AFM force spectroscopy (Fig. 4, A to C, fig. S7). In these experiments, we varied the speed of cantilever retraction to subject the bonds to various bond-loading rates. This can reveal dependence of bond dynamics on applied forces (23). We conjugated AFM tips to 4-hydroxy-3-nitrophenylacetyl (NP) or 4-hydroxy-3-iodo-5-nitrophenylacetyl (NIP) antigens, which differ by a factor of ~10 in their 3D affinity for the B1-8 F_{ab} fragment (table S1). Measurements of forces between NIP antigens and the B1-8 F_{ab} attached to coverslips showed a sharp increase of force with cantilever retraction, resulting in single-step ruptures (Fig. 4A, top). The mean rupture forces between the F_{ab} and the NP or NIP antigens rose linearly with the logarithm of the loading rates as expected (24) (Fig. 4, B and C) and yielded extrapolated zero-force off-rates similar to those measured in solution (fig. S7B). Force spectroscopy with living B1-8 B cells showed that forces between the B1-8 BCR and antigens also rose steadily with cantilever retraction (Fig. 4A, bottom), consistent with the BCR being anchored to the submembrane cytoskeleton (16, 25). Consequently, loading rates on the BCR were only slightly lower than on the F_{ab}. However, the rupture forces of the BCR-antigen bonds showed a nonlinear dependence on the logarithm of loading rates (Fig. 4, B and C). For slow loading rates, induced by pulling speeds similar to those generated by myosin IIa contractility, rupture forces for the BCR were lower and had shorter lifetimes than those with the F_{ab}, suggesting that single BCR-antigen bonds break quickly at forces required for antigen extraction (fig. S7D). Thus, the mechanical strength of single BCR-antigen bonds is not sufficient for antigen extraction, highlighting the importance of load-sharing in multivalent BCR microclusters.

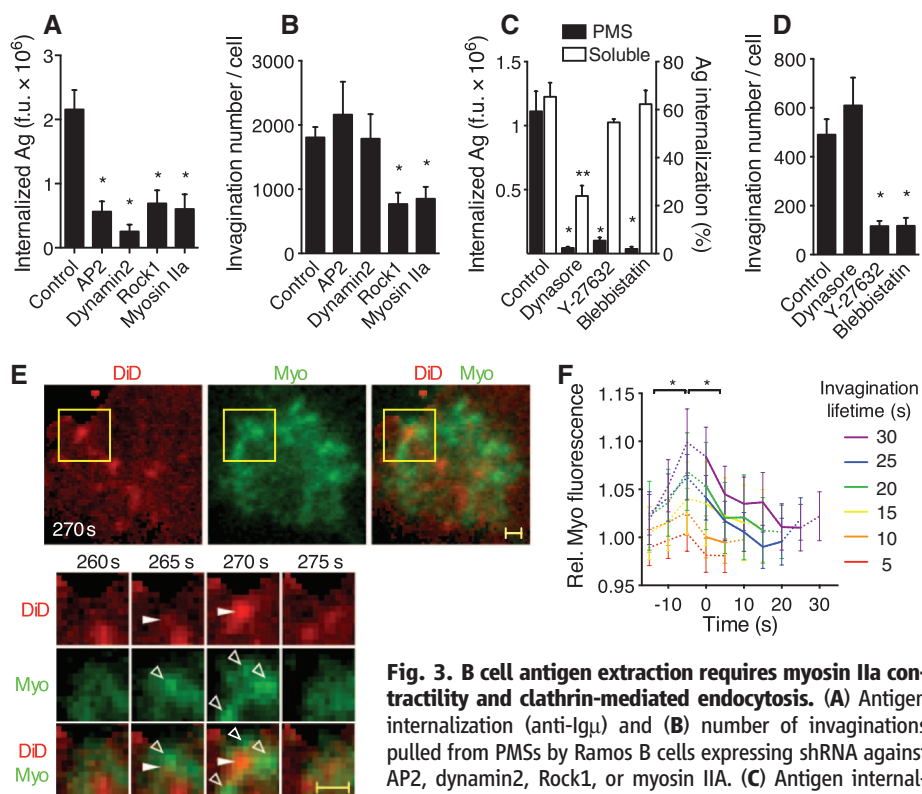


Fig. 3. B cell antigen extraction requires myosin IIa contractility and clathrin-mediated endocytosis. (A) Antigen internalization (anti-Ig α) and (B) number of invaginations pulled from PMSs by Ramos B cells expressing shRNA against AP2, dynamin2, Rock1, or myosin IIa. (C) Antigen internalization (anti-Ig κ) from PMSs (left y axis) or solution (right y axis) by primary B cells treated with inhibitors against dynamin2 (dynasore), Rock1 (Y-23632), or myosin IIa (blebbistatin). (D) Number of invaginations pulled from PMSs by primary B cells treated with inhibitors. (A) to (D), means \pm SEM, $n = 17$ to 25 cells for internalization from PMSs, $n = 7$ to 15 cells for invagination numbers, $n = 3$ experiments for soluble antigen internalization. * $P < 0.01$, ** $P < 0.05$ in nonparametric tests against controls. f.u., fluorescence units. (E) Top, TIRF image of a primary B cell expressing myosin IIa regulatory light chain (RLC)-GFP (Myo) spread on a DiD-labeled PMS loaded with antigen. Yellow squares show the region magnified below. Closed arrowheads show invagination, open arrowheads show myosin IIa structures. Scale bar, 1 μ m. (F) Quantification of myosin IIa RLC fluorescence in invaginations grouped by lifetime (mean \pm SEM, $n = 15$ cells, * $P < 0.01$ in paired t tests).

axis) by primary B cells treated with inhibitors against dynamin2 (dynasore), Rock1 (Y-23632), or myosin IIa (blebbistatin). (D) Number of invaginations pulled from PMSs by primary B cells treated with inhibitors. (A) to (D), means \pm SEM, $n = 17$ to 25 cells for internalization from PMSs, $n = 7$ to 15 cells for invagination numbers, $n = 3$ experiments for soluble antigen internalization. * $P < 0.01$, ** $P < 0.05$ in nonparametric tests against controls. f.u., fluorescence units. (E) Top, TIRF image of a primary B cell expressing myosin IIa regulatory light chain (RLC)-GFP (Myo) spread on a DiD-labeled PMS loaded with antigen. Yellow squares show the region magnified below. Closed arrowheads show invagination, open arrowheads show myosin IIa structures. Scale bar, 1 μ m. (F) Quantification of myosin IIa RLC fluorescence in invaginations grouped by lifetime (mean \pm SEM, $n = 15$ cells, * $P < 0.01$ in paired t tests).

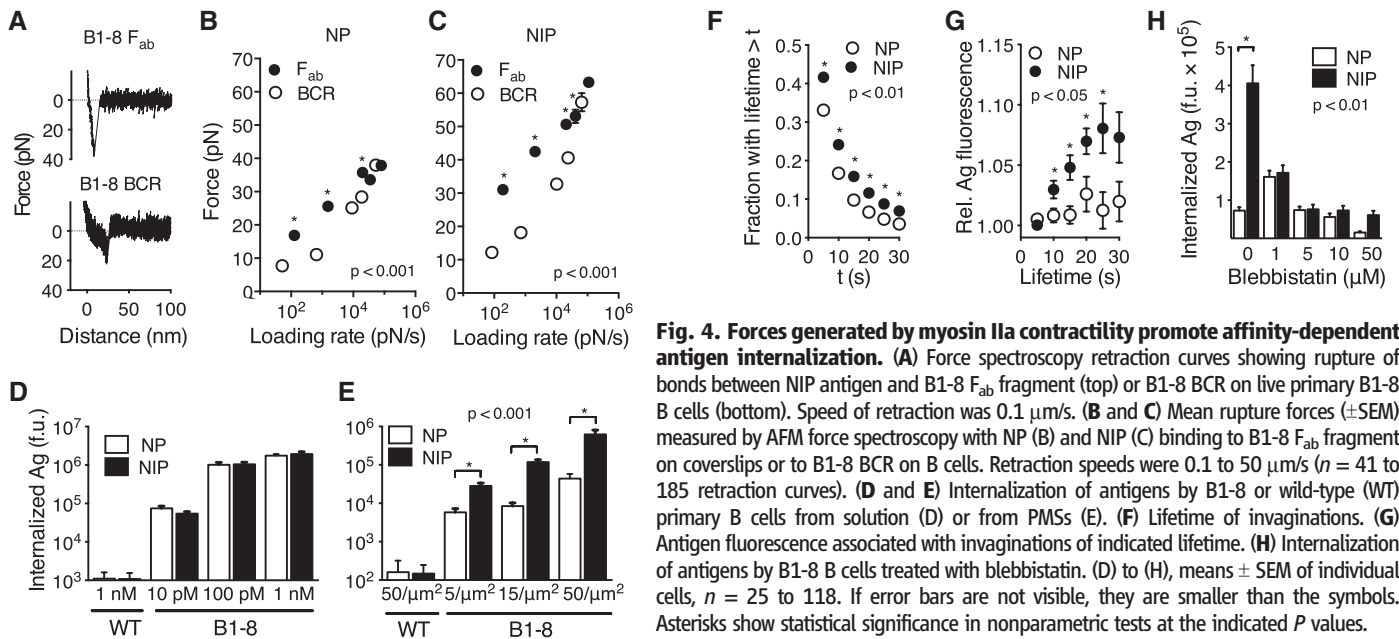


Fig. 4. Forces generated by myosin IIa contractility promote affinity-dependent antigen internalization. (A) Force spectroscopy retraction curves showing rupture of bonds between NIP antigen and B1-8 F_{ab} fragment (top) or B1-8 BCR on live primary B1-8 B cells (bottom). Speed of retraction was 0.1 $\mu\text{m/s}$. (B and C) Mean rupture forces (\pm SEM) measured by AFM force spectroscopy with NP (B) and NIP (C) binding to B1-8 F_{ab} fragment on coverslips or to B1-8 BCR on B cells. Retraction speeds were 0.1 to 50 $\mu\text{m/s}$ ($n = 41$ to 185 retraction curves). (D and E) Internalization of antigens by B1-8 or wild-type (WT) primary B cells from solution (D) or from PMSs (E). (F) Lifetime of invaginations. (G) Antigen fluorescence associated with invaginations of indicated lifetime. (H) Internalization of antigens by B1-8 B cells treated with blebbistatin. (D) to (H), means \pm SEM of individual cells, $n = 25$ to 118. If error bars are not visible, they are smaller than the symbols. Asterisks show statistical significance in nonparametric tests at the indicated P values.

By contrast, with faster loading rates, BCR-antigen rupture forces increased sharply and approached those measured with the F_{ab}. These data suggest that at higher forces, the BCR improves its resistance to mechanical stress, providing an additional layer of regulation.

What are the implications of these findings for antigen affinity discrimination? We found that B1-8 B cells internalized NP and NIP antigens to a similar extent from solution (Fig. 4D). However, when the antigens were presented on PMSs, B1-8 B cells internalized significantly more of the NIP antigen than the NP antigen (Fig. 4E). The NIP antigen also induced faster microcluster formation (fig. S8A), longer lifetime of invaginations (Fig. 4F), and increased amounts of invagination-associated antigen (Fig. 4G). In addition, we found that although inhibition of myosin IIa by a high concentration of blebbistatin abolished internalization of both antigens, modulation of the strength of myosin IIa contraction by low concentrations of blebbistatin reduced internalization of the NIP antigen, whereas it promoted the internalization of the NP antigen (Fig. 4H). This suggests that reduced myosin IIa activity improves low-affinity BCR binding by reducing the mechanical stress on the bonds. Thus, the ability of B cells to discriminate between these two antigens depends on the strength of actomyosin-mediated force, implicating contractile forces in the regulation of affinity discrimination.

Owing to the bivalency of the BCR and the multivalency of most physiologically relevant antigens, the half-lives of BCR-antigen complexes can reach many hours. As a result, B cells typically internalize soluble multivalent antigens in an affinity-independent manner (12). However, in vivo, B cells acquire multivalent antigens in an affinity-dependent manner (7, 18). We suggest that

myosin IIa-generated forces shorten the lifetime of synaptic BCR-antigen bonds, promoting affinity discrimination on a physiologically relevant time scale, i.e., seconds rather than hours. Because the initial growth of BCR microclusters is dependent on affinity (11) (fig. S8A), higher-affinity antigens will form larger microclusters with higher number of bonds faster than lower-affinity antigens. When contractile forces engage, the higher number of bonds in larger microclusters, together with better resistance to force of the individual high-affinity bonds, will provide stability to the microclusters, allowing association with CCSs and endocytosis of the antigen. As a result, the probability of antigen internalization will depend on BCR affinity.

Spending mechanical energy to discriminate between interactions that could not be distinguished passively likely contributes to B cells' ability to develop high-affinity antibodies. This strategy seems to rely on mechanisms linking receptor signaling to myosin IIa contractility and endocytosis (26–28). Understanding of this process may inspire new ideas to improve antibody affinity beyond the nanomolar range, both in vivo and in vitro affinity maturation systems.

References and Notes

- Y. R. Carrasco, F. D. Batista, *Immunity* **27**, 160 (2007).
- T. G. Phan, J. A. Green, E. E. Gray, Y. Xu, J. G. Cyster, *Nat. Immunol.* **10**, 786 (2009).
- T. Jun et al., *Nature* **450**, 110 (2007).
- H. Qi, J. G. Egen, A. Y. C. Huang, R. N. Germain, *Science* **312**, 1672 (2006).
- S. F. Gonzalez et al., *Nat. Immunol.* **11**, 427 (2010).
- F. D. Batista, D. Iber, M. S. Neuberger, *Nature* **411**, 489 (2001).
- T. A. Schwickert et al., *J. Exp. Med.* **208**, 1243 (2011).
- G. D. Victora et al., *Cell* **143**, 592 (2010).
- T.-A. Y. Shih, E. Meffre, M. Roederer, M. C. Nussenzweig, *Nat. Immunol.* **3**, 570 (2002).

- S. J. Fleire et al., *Science* **312**, 738 (2006).
- W. Liu, T. Meckel, P. Tolar, H. W. Sohn, S. K. Pierce, *J. Exp. Med.* **207**, 1095 (2010).
- F. D. Batista, M. S. Neuberger, *EMBO J.* **19**, 513 (2000).
- M.-I. I. Yuseff et al., *Immunity* **35**, 361 (2011).
- M. S. Moore, D. T. Mahaffey, F. M. Brodsky, R. G. Anderson, *Science* **236**, 558 (1987).
- P. Tolar, J. Hanna, P. D. Krueger, S. K. Pierce, *Immunity* **30**, 44 (2009).
- E. A. Evans, D. A. Calderwood, *Science* **316**, 1148 (2007).
- D. J. Müller, J. Helenius, D. Alsteens, Y. F. Dufrène, *Nat. Chem. Biol.* **5**, 383 (2009).
- K. Suzuki, I. Grigorova, T. G. Phan, L. M. Kelly, J. G. Cyster, *J. Exp. Med.* **206**, 1485 (2009).
- A. Stoddart, A. P. Jackson, F. M. Brodsky, *Mol. Biol. Cell* **16**, 2339 (2005).
- A. Chaturvedi, R. Martz, D. Dorward, M. Waisberg, S. K. Pierce, *Nat. Immunol.* **12**, 1119 (2011).
- S. Boulant, C. Kural, J.-C. Zehe, F. Ubelmann, T. Kirchhausen, *Nat. Cell Biol.* **13**, 1124 (2011).
- D. K. Cureton, R. H. Massol, S. P. J. Whelan, T. Kirchhausen, *PLoS Pathog.* **6**, e1001127 (2010).
- O. K. Dudko, G. Hummer, A. Szabo, *Proc. Natl. Acad. Sci. U.S.A.* **105**, 15755 (2008).
- G. I. Bell, *Science* **200**, 618 (1978).
- B. Treanor et al., *Immunity* **32**, 187 (2010).
- F. Vascotto et al., *J. Cell Biol.* **176**, 1007 (2007).
- R. Levayer, A. Pelissier-Monier, T. Lecuit, *Nat. Cell Biol.* **13**, 529 (2011).
- J.-C. Kuo, X. Han, C.-T. Hsiao, J. R. Yates III, C. M. Waterman, *Nat. Cell Biol.* **13**, 383 (2011).

Acknowledgments: We thank S. Martin for help with binding studies. B1-8^{flow} mice were a gift from K. Rajewsky, obtained under material transfer agreement with Mouse Genetics Cologne Foundation. This work was supported by Medical Research Council UK (Unit Programmes numbers U117597138 and U117570592).

Supplementary Materials

www.sciencemag.org/cgi/content/full/science.1237572/DC1
Materials and Methods
Figs. S1 to S8
Table S1
Movies S1 to S5
References (29–36)

8 March 2013; accepted 29 April 2013
Published online 16 May 2013;
10.1126/science.1237572

Deep Cortical Layers Are Activated Directly by Thalamus

Christine M. Constantinople and Randy M. Bruno*

The thalamocortical (TC) projection to layer 4 (L4) is thought to be the main route by which sensory organs communicate with cortex. Sensory information is believed to then propagate through the cortical column along the L4→L2/3→L5/6 pathway. Here, we show that sensory-evoked responses of L5/6 neurons in rats derive instead from direct TC synapses. Many L5/6 neurons exhibited sensory-evoked postsynaptic potentials with the same latencies as L4. Paired *in vivo* recordings from L5/6 neurons and thalamic neurons revealed substantial convergence of direct TC synapses onto diverse types of infragranular neurons, particularly in L5B. Pharmacological inactivation of L4 had no effect on sensory-evoked synaptic input to L5/6 neurons. L4 is thus not an obligatory distribution hub for cortical activity, and thalamus activates two separate, independent “strata” of cortex in parallel.

The conventional model of neocortex is that sensory processing begins in L4, which has been known for a century to be the principal target of thalamic afferents. Cortical layers are believed to transform sensory information as excitation spreads serially along the L4→L2/3→L5/6 pathway (1–4). This hierarchical serial model is consistent with anatomical observations that axons of excitatory L4 neurons primarily innervate L2/3 and that axons of L2/3 pyramidal neurons arborize extensively in L5/6 (1, 4). L5 neurons make up a major output of the cortex, as they have the most substantial axonal innervation of subcortical and cortical structures, whereas L6 neurons transmit feedback to thalamus and cortex (4–6).

The same thalamocortical (TC) axons that arborize so extensively in L4 also have sparser branches in the infragranular layers at the L5–L6 border (7–11), which have been assumed to be modulatory (3, 11, 12). Recent quantitative measurements of reconstructed TC axons suggest, however, that innervation of L5/6 may be extensive, albeit less than that of L4 (8). Therefore, L5/6 neurons might integrate sensory information from at least two classes of inputs: the direct TC pathway and the indirect L4→L2/3→L5/6 pathway. We investigated this in adult rats administered local anesthetics and a sedative, which better approximate wakefulness than does general anesthesia (13, 14). We made *in vivo* whole-cell recordings from 176 neurons in barrel cortex and juxtosomal recordings from 76 neurons in ventral posterior medial (VPM) nucleus of thalamus, areas processing tactile input from the facial whiskers during environment exploration.

The conventional model predicts that the responses of neurons in L5/6 should lag behind those in other layers. We compared the latencies of sensory-evoked sub- and suprathreshold responses of morphologically identified neurons in every layer of barrel cortex. Strong high-velocity

whisker deflection evoked robust postsynaptic potentials (PSPs) in neurons in all cortical layers (Fig. 1A). L4 onset latencies preceded those in L2/3 (L4: 7.76 ± 0.16 ms, $n = 24$; L2/3: 11.04 ± 0.26 ms, $n = 18$; $P < 10^{-13}$) (Fig. 1, B and C). While the average L5 (9.44 ± 0.3 , $n = 53$) and L6 latencies (10.68 ± 0.67 ms, $n = 13$) were longer than that of L4, many L5 cells rivaled L4 in latency. Moreover, the longer-latency PSPs among L5 cells occur simultaneously with, not after, the onsets of L2/3 cells (Fig. 1, B and C). Many L5 cells exhibited spike latencies as short as cells in L4 (Fig. 1, D and F).

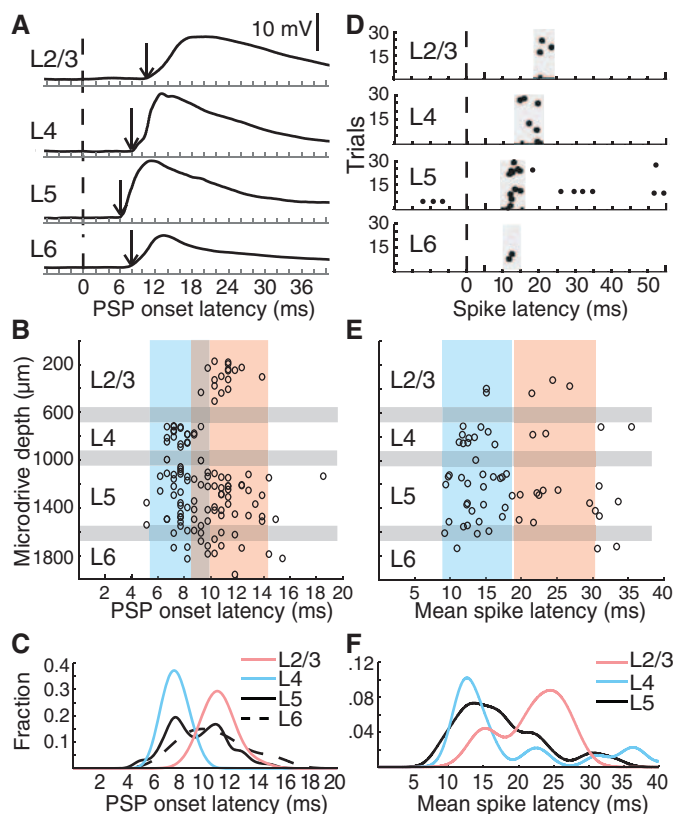
Short L5/6 latencies could result from substantial TC convergence, which can be estimated

from the probability of finding TC–L5/6 connections. Ideally, synaptic measurements are made *in vivo* rather than *in vitro* to avoid issues related to lack of background synaptic input, the concentrations of extracellular ions and neuromodulators, and severing of axons during slice preparation. We used a previously developed technique to identify and quantify individual synaptic connections in living animals (14). Whole-cell recordings were made from neurons in L5/6 during simultaneous juxtosomal recording of action potentials from somatotopically aligned VPM neurons (Fig. 2, A and B). The average PSP (aPSP) that a single thalamic cell produces in a cortical neuron (Fig. 2, C and D) was estimated by spike-triggered averaging and corrected for the contribution of unrecorded inputs [see supplementary materials (SM)].

Monosynaptic connections were observed onto L5/6 neurons (10 of 55 topographically aligned pairs tested, including morphologically identified and unidentified cells). Of the morphologically identified subset (Fig. 2E), connections were observed more frequently onto L5 pyramidal neurons (26%, 7 connected of 27 pairs tested) than onto L6 cells (9%, 1 of 11). Connections were not observed onto topographically unaligned cells or pyramidal neurons with apical trunks extending through the septal region between L4 barrels (Fig. 2E).

Individual TC connections onto infragranular neurons produced relatively small depolarizations (mean \pm SD 571 ± 46.5 μ V, median 463 μ V,

Fig. 1. Many L5/6 cells have response latencies as short as L4's. (A) Example whole-cell traces from histologically identified cells, averaged overall stimulus directions. Dashed line, time of whisker deflection; arrow, PSP onset. (B) PSP onset latencies by microdrive depth ($n = 126$). Gray bars, approximate laminar boundaries determined from the microdrive depths where histologically recovered neurons were found in each layer. Blue and pink boxes, approximate extent of the densities of L4 and L2/3 data, respectively, as in (C). (C) Normalized probability densities of PSP onset latencies. (D) Example raster plots of cells in each layer relative to whisker deflection. (E) Distribution of mean spike latencies for responsive cells ($n = 64$) by microdrive depth. (F) Normalized probability densities of mean spike latencies. L6 density was not calculated because of insufficient spiking.



Department of Neuroscience and Kavli Institute for Brain Science, Columbia University, New York, NY 10032, USA.

*Corresponding author. E-mail: randybruno@columbia.edu

range 137 μ V to 1.18 mV (Fig. 2F), similar to TC-L4 synapses [\sim 500 μ V (14)]. Mean onset latencies and 20 to 80% rise times were 2.40 ± 0.31 and 6.17 ± 4.55 ms, respectively. Neurons in each layer responded to conventional high-velocity stimuli with PSPs proportional to the probability of finding TC connections in that layer (Fig. 2G), consistent with direct TC connections producing sensory-evoked responses.

L5/6 neuronal subclasses having distinct morphology, physiology, and projection targets are spatially intermingled (15, 16) but may be preferentially thalamorecipient (9). Monosynaptic TC connections were observed most frequently on L5 thick-tufted neurons (44%, 4 connected of 9 pairs tested) but were also observed on L5 thin-tufted (17%, 3 of 18) and L6 (9%, 1 of 11) pyramidal neurons (Fig. 2, H and I, and fig. S1A) and smooth interneurons (1 of 3). In vitro L5 thick-tufted neurons are typically “intrinsically bursting” (IB), whereas adapting trains of single spikes are more typical of the “regular-spiking” (RS) L5 thin-tufted neurons (9, 16). The predominant firing type of both morphological classes in vivo, however, was IB (fig. S1, B and C), possibly because of our awakelike conditions, and monosynaptic connections were observed onto

both physiological cell types (fig. S1, D and E). By contrast, most connected cells had somata at depths of 1400 to 1600 μ m, where thalamic axons arborize in L5B/6A (7, 8), even though we sampled substantially from depths shallower than 1400 μ m (Fig. 2J, left). Neurons in the TC arborization zone near L5B had the largest sensory-evoked PSPs (Fig. 2J, right).

Given that a whisker’s representation in VPM contains \sim 200 neurons (14), 9 to 44% convergence is substantial, translating into \sim 20 to 90 thalamic connections per L5/6 cell, depending on its type. Although individual TC synapses are weak, this number of synchronous convergent inputs may provide a second powerful pathway into the cortex, capable of directly driving the activity of L5 and responsive L6 cells. We therefore sought to dissect the contributions of the direct TC pathway and the indirect L4→L2/3→L5/6 pathway to the sensory responses of infragranular neurons, by inactivating L4 during sensory stimulation. Silencing of L4 was achieved by pressure ejection of lidocaine and confirmed by monitoring the local field potential (LFP) through the drug pipette. Beyond blocking action potentials in L4 cells, lidocaine suppresses axonal conduction within L4, along

TC axonal branches that extend directly into L3, and along the radial trunks of axons from L2/3 cells that traverse L4 to synapse in L5/6. This manipulation thus disconnects the upper and lower cortical layers, leaving intact the TC-L5/6 pathway.

To validate our manipulation, we performed whole-cell recordings of L4 neurons located 150 μ m from the LFP and drug pipette (Fig. 3A). Lidocaine injection not only prevented these L4 cells on the other side of the barrel from discharging any action potentials but also robustly and reliably eliminated virtually all spontaneous and sensory-evoked synaptic input ($n = 6$, from 10.71 ± 1.21 to 0.27 ± 0.08 mV, $P = 0.0004$) (Fig. 3, B to D). Given the high connectivity among L4 barrel neurons [$P(\text{connection}) \sim 0.3$ (4)], this dramatic reduction in synaptic input confirms that our manipulation silenced virtually all neurons in a barrel. Replacing the whole-cell pipette with an LFP pipette yielded similar results (fig. S2, A to C), which further demonstrated that lidocaine inactivated a diameter exceeding 300 μ m, more than the size of a barrel (\sim 200 to 300 μ m wide). In addition, L4 inactivation reduced L2/3 synaptic inputs and prevented L2/3 spiking (fig. S2, D to F).

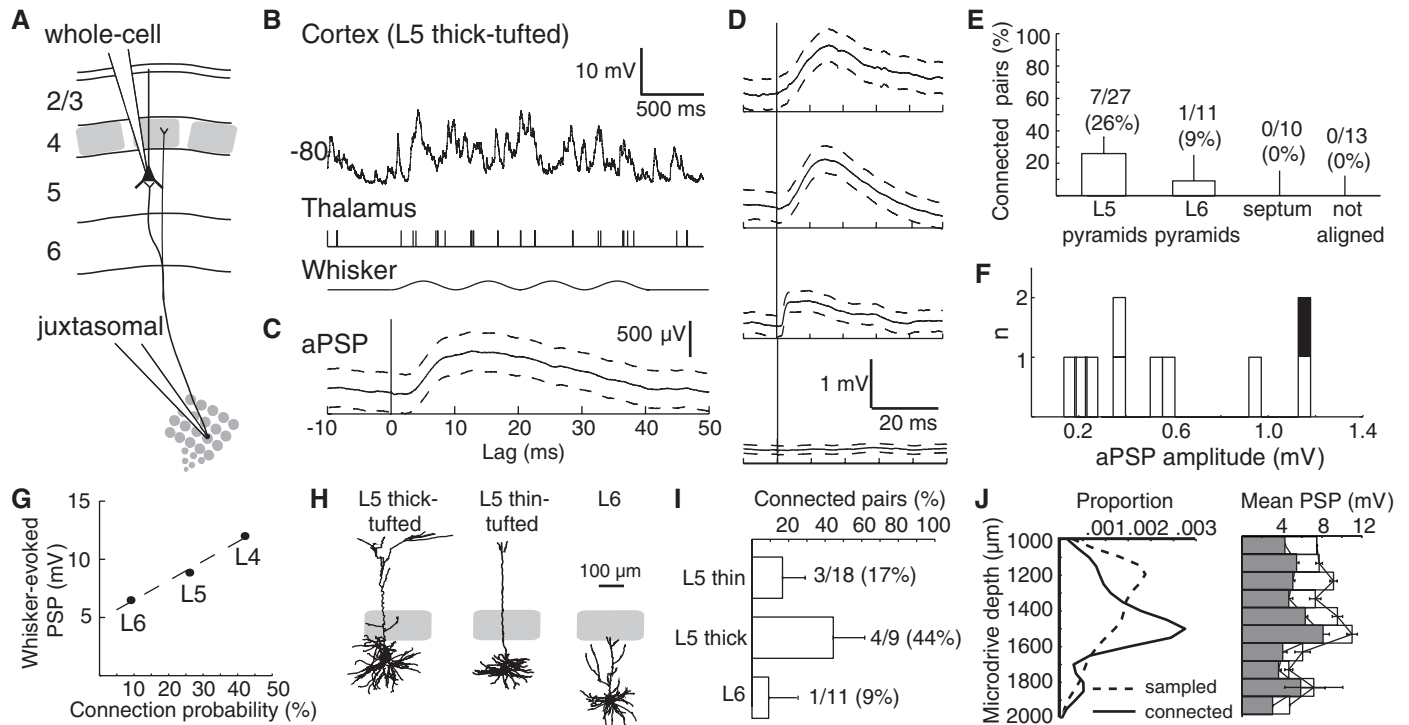


Fig. 2. TC connections onto infragranular neurons are weak but convergent. (A) Schematic of simultaneous in vivo whole-cell recording of a cortical L5 pyramidal neuron and juxtosomal recording of a somatotopically aligned thalamic neuron. (B) Example whole-cell trace from an L5 thick-tufted cell (top), action potentials from a thalamic neuron (middle), and sinusoidal whisker stimulus (bottom). (C) The aPSP measured from the above pair ($n = 1076$ thalamic action potentials). Dashed lines, 95% confidence intervals. (D) Example aPSPs onto L5 thin-tufted, L6, and L5 thick-tufted pyramidal neurons and example unconnected pair (from top to bottom). (E) Percentage of connected pairs by cortical cell location. Error bars, 95% confidence intervals

for a binomial distribution. (F) Distribution of aPSP amplitudes. Black, smooth interneuron. (G) Amplitude of mean sensory-evoked PSPs (10 to 20 deflections in the preferred direction) for L4, L5, and L6 cells ($n = 40, 35$, and 11 , respectively) versus probability of finding connected pairs in each layer. Dashed line, least-squares fit. L4 data are from (14). (H) Example reconstructions. (I) Connection probability by morphological subtype. (J) (Left) Densities of the depths of all sampled cells (dashed line) and cells onto which TC connections were observed (solid line). (Right) Mean sensory-evoked PSP amplitude by depth (means \pm SEM; 100- μ m bins). White bars, preferred direction. Shaded bars, average over eight directions.

We then recorded synaptic inputs from morphologically identified neurons in L5/6 while inactivating the overlying L4 barrel (Fig. 3E). L5/6 pyramidal neurons deeper than 1350 μm from the pia were targeted to avoid direct drug effects on recorded cells and to sample the region of highest TC connectivity (Fig. 2J). Despite reducing the amplitude of the sensory-evoked LFP in L4 ($n = 12$; from 0.69 ± 0.09 to 0.21 ± 0.03 mV, $P = 0.0001$), lidocaine had virtually no effect on the sensory-evoked synaptic inputs of L5/6 neurons (Fig. 3, F and G), in terms of amplitude (from 7.53 ± 0.98 to 7.58 ± 0.75 mV, $P = 0.93$) (Fig. 3H) or onset latency (Fig. S3, A and B). Mean and variance of spontaneous membrane potential fluctuations were similarly unaffected (Fig. S3B).

Even after L4 inactivation, sensory stimuli continued to evoke L5/6 action potentials (0.16 ± 0.07 versus 0.12 ± 0.04 spikes per stimulus, $P = 0.64$) (Fig. 3, I and J). Although L5/6 spiking was unaffected on average, some individual neurons appeared to increase or decrease their firing rates (Fig. 3J). To test whether this was simply because of spiking variability, L5/6 spiking re-

sponses during “test” and subsequent “retest” periods were compared. Individual L5/6 cells exhibited a range of firing rate differences between the test and retest periods similar to the pre- and postlidocaine periods (Fig. S3C).

How can thalamus effectively elicit L5 spikes given that L5 receives less TC convergence and exhibits smaller PSPs than L4? The mean spontaneous membrane potential of each L5 neuron was significantly closer to its spike threshold, compared with neurons in L4 and L6 (Fig. 3K), and the distance to threshold correlated with responsiveness (Fig. S3E). Therefore, the relative depolarization of L5 cells observed here under sedation, as under anesthesia (17), enables less synaptic input than available to L4 to become suprathreshold in 53% of cells (Fig. S3, F and G). In contrast, the smaller sensory-evoked PSPs and relative hyperpolarization of L6 (Figs. 2G and 3K) render 81% of its cells silent (Fig. S3, F and G), consistent with L6 corticothalamic cells being unresponsive to sensory stimulation [see (6)].

Muscimol injection to inactivate VPM neurons but spare fibers of passage substantially re-

duced PSPs of aligned L5/6 neurons (Fig. S4, A and B). Residual PSP did not derive from neighboring cortical columns (Fig. S4, C and D). A likely source is the secondary thalamic area, the posterior medial (POM) nucleus, which arborizes in L1 and L5A, consistent with some L5 cells receiving mixed VPM and POM input (18). We tested whether long-range inputs—including axons from POM, secondary somatosensory cortex, primary motor cortex, and the callosum—contribute to L5 sensory responses via synapses onto apical tufts in L1. Pial application of lidocaine blocks L1 synapses, as indicated by its ability to silence L2 (Fig. S5, A to C). L5 PSPs were unaffected by combined L1/L4 inactivation (Fig. S5, D and E). If ascending pathways such as those from POM contribute to deep-layer sensory responses, it is likely that they do so via axon collaterals in L5/6 rather than in L1.

Our study demonstrates that primary thalamic nuclei, like VPM, can simultaneously copy the same signals to L4 and L5B, where they are processed in parallel (Fig. 4B) instead of serially through L4 (Fig. 4A). The TC→L4→L2/3

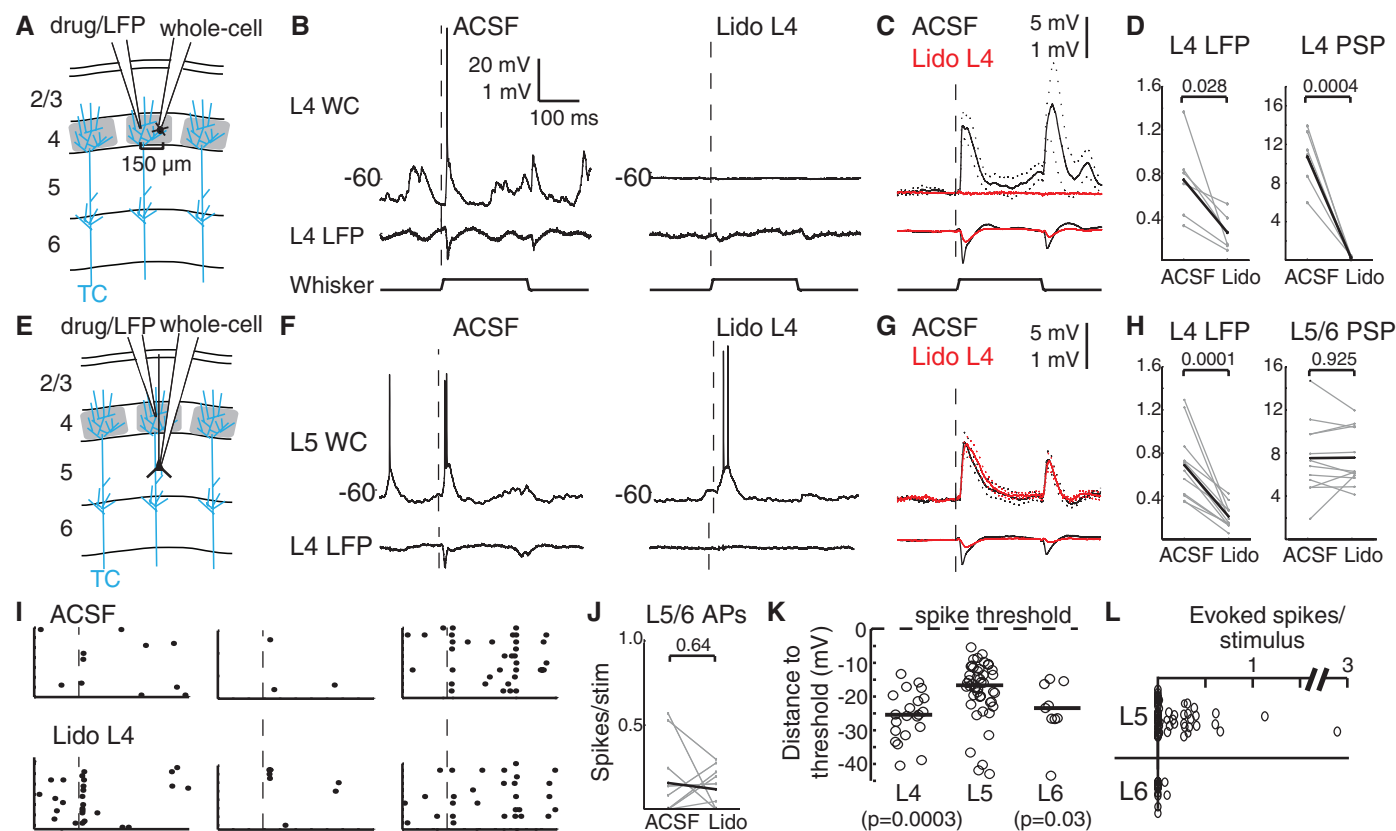


Fig. 3. L5/6 sensory responses do not require L4. (A) Whole-cell recordings were made from L4 cells during inactivation of the barrel by lidocaine injection. Blue lines schematically depict single TC axons, among hundreds per column. (B) Simultaneous whole-cell and LFP recordings during injection of artificial cerebrospinal fluid (ACSF) vehicle and lidocaine. Dashed line, onset of whisker deflection in preferred direction. (C) Population averages of L4 PSPs (top) and LFPs (bottom). Dotted lines, SEM. (D) Summary of responses (in mV). Gray, individual cells; black, means. (E) L5/6 recordings were made while L4 was silenced. (F) Example L5 whole-cell and L4 LFP traces

during injection of ACSF and lidocaine. (G) Population averages of L5/6 PSPs (top) and L4 LFPs (bottom). (H) Summary plots. (I) Rasters of a subset of trials for three example neurons during injection of ACSF (top) and lidocaine (bottom). (J) Plots of the baseline-subtracted evoked spikes per stimulus before and after lidocaine injection. (K) The relation between neurons' mean spontaneous membrane potential and spike threshold (L4: $n = 21$; L5: $n = 46$; L6: $n = 9$). Circles, individual cells; lines, medians; P values, comparison with L5 (Wilcoxon rank-sum test). (L) Baseline-subtracted evoked spikes per stimulus.

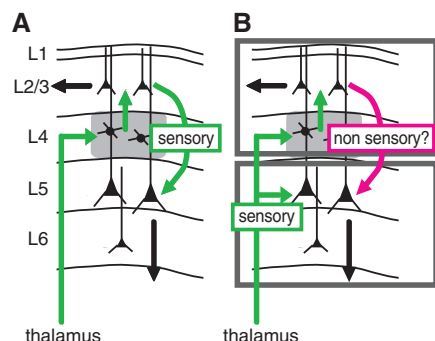


Fig. 4. Schematics of the conventional and proposed models of cortical processing. (A) In the conventional serial model, sensory information is transformed as excitation spreads from thalamus to L4 to L2/3 to L5/6 along the densest axonal pathways (green). (B) In the bistratified model, thalamus copies sensory information to both an upper stratum (L4 and L2/3) and a lower stratum (L5/6), which differ in coding properties and downstream targets.

pathway and the TC→L5/6 pathway appear independent with regard to ascending sensory signals. TC axons innervate both middle and deep layers in multiple species (human, monkey, rat, and cat) and neocortical systems (motor, visual, auditory, and somatosensory) (19–23). Tuning of extracellular units in infragranular layers of cat visual and rodent somatosensory cortex often persists following lesion of L2/3 (24, 25), and some such units respond as early as middle layers (26, 27). Direct TC engagement of infragranular neurons may therefore be a general feature of neocortex.

Neocortical columns may contain two separate processing systems or “strata”: an upper stratum (L4 and L2/3) and a lower stratum (L5/6) possibly subserving different functions. This architecture may elaborate receptive fields via intralaminar cross-columnar rather than in-

terlaminar connections. Moreover, L2/3 targets other neocortical regions, whereas L5/6 targets both cortical and subcortical structures. Although some subcortical projections provide feedback (i.e., to brainstem and primary thalamic nuclei), many of the subcortical targets, especially those of L5, are action-related (striatum and spinal cord) or high-order (secondary thalamic nuclei, which innervate high-order cortical regions). Both strata therefore have direct access to the same sensory information and can alter behavior via different anatomical pathways. Consistent with the idea of two distinct systems, cell fate mapping studies recently demonstrated that the upper and lower strata develop from two distinct populations of radial glial cells (28).

Our results further demonstrate that propagation of excitation cannot be inferred solely from synaptic strength or relative axonal densities. L2/3's extremely low firing rates (13, 29–31) may explain its minimal contribution to sensory signals in deep layers, which, by contrast, are highly active. The activity and interactions of the layers may be behaviorally gated by comparisons of motor, state, and sensory signals (6, 32, 33) or by induction of learning.

References and Notes

1. C. D. Gilbert, T. N. Wiesel, *Nature* **280**, 120 (1979).
2. R. J. Douglas, K. A. Martin, *Annu. Rev. Neurosci.* **27**, 419 (2004).
3. E. M. Callaway, *Neural Netw.* **17**, 625 (2004).
4. D. Feldmeyer, *Frontiers Neuroanat.* **6**, 24 (2012).
5. M. Oberlaender et al., *Proc. Natl. Acad. Sci. U.S.A.* **108**, 4188 (2011).
6. S. Lee, G. E. Carvell, D. J. Simons, *Nat. Neurosci.* **11**, 1430 (2008).
7. V. C. Wimmer, R. M. Bruno, C. P. de Kock, T. Kuner, B. Sakmann, *Cereb. Cortex* **20**, 2265 (2010).
8. M. Oberlaender, A. Ramirez, R. M. Bruno, *Neuron* **74**, 648 (2012).
9. A. Agmon, B. W. Connors, *J. Neurosci.* **12**, 319 (1992).
10. M. Beierlein, B. W. Connors, *J. Neurophysiol.* **88**, 1924 (2002).
11. A. N. Viana, I. Petrof, S. M. Sherman, *J. Neurosci.* **31**, 12738 (2011).
12. R. W. Guillery, S. M. Sherman, *Neuron* **33**, 163 (2002).

13. C. M. Constantinople, R. M. Bruno, *Neuron* **69**, 1061 (2011).
14. R. M. Bruno, B. Sakmann, *Science* **312**, 1622 (2006).
15. Y. Chagnac-Amitai, H. J. Luhmann, D. A. Prince, *J. Comp. Neurol.* **296**, 598 (1990).
16. A. M. Hattox, S. B. Nelson, *J. Neurophysiol.* **98**, 3330 (2007).
17. I. D. Manns, B. Sakmann, M. Brecht, *J. Physiol.* **556**, 601 (2004).
18. I. Bureau, F. von Saint Paul, K. Svoboda, *PLoS Biol.* **4**, e382 (2006).
19. D. Ferster, S. LeVay, *J. Comp. Neurol.* **182**, 923 (1978).
20. G. G. Blasdel, J. S. Lund, *J. Neurosci.* **3**, 1389 (1983).
21. M. Herkenham, *Science* **207**, 532 (1980).
22. C. L. Huang, J. A. Winer, *J. Comp. Neurol.* **427**, 302 (2000).
23. V. Garcia-Marin, T. H. Ahmed, Y. C. Afzal, M. J. Hawken, *J. Comp. Neurol.* **521**, 130 (2013).
24. H. D. Schwark, J. G. Malpeli, T. G. Weyand, C. Lee, *J. Neurophysiol.* **56**, 1074 (1986).
25. W. Huang, M. Armstrong-James, V. Rema, M. E. Diamond, F. F. Ebner, *J. Neurophysiol.* **80**, 3261 (1998).
26. C. P. de Kock, R. M. Bruno, H. Spors, B. Sakmann, *J. Physiol.* **581**, 139 (2007).
27. J. H. Maunsell, J. R. Gibson, *J. Neurophysiol.* **68**, 1332 (1992).
28. S. J. Franco et al., *Science* **337**, 746 (2012).
29. D. H. O'Connor, S. P. Peron, D. Huber, K. Svoboda, *Neuron* **67**, 1048 (2010).
30. T. Hromádka, M. R. Deweese, A. M. Zador, *PLoS Biol.* **6**, e16 (2008).
31. C. P. de Kock, B. Sakmann, *Proc. Natl. Acad. Sci. U.S.A.* **106**, 16446 (2009).
32. C. M. Niell, M. P. Stryker, *Neuron* **65**, 472 (2010).
33. G. B. Keller, T. Bonhoeffer, M. Hübener, *Neuron* **74**, 809 (2012).

Acknowledgments: We thank L. Abbott, R. Axel, A. Losonczy, and K. Miller for manuscript comments; D. Baughman for technical support; and M. Ilardi for morphological reconstruction. Supported by National Institute of Neurological Disorders and Stroke, NIH, NS069679; Rita Allen Foundation; Klingenstein Fund; and an NSF Student Fellowship.

Supplementary Materials

www.sciencemag.org/cgi/content/full/340/6140/1591/DC1
Materials and Methods
Figs. S1 to S5
References (34, 35)

11 February 2013; accepted 26 April 2013
10.1126/science.1236425

HEATED CIRCULATING BATHS

Available in 23 different models, a new line of heated circulating water baths can achieve temperatures as high as 200°C with temperature stabilities as exacting as $\pm 0.005^\circ\text{C}$. These elegantly designed circulators come in reservoir sizes ranging from 7 L to 28 L and are available with six different temperature controllers, including two programmable models. The heated circulators incorporate many ergonomic features that make life in the lab more productive and efficient. Among the many design innovations featured on these baths are a swiveling control head that permits viewing of the temperature display anywhere within a 180° viewing radius, an integral lid docking system for no-mess reservoir cover storage, and a corrosion- and chemical-resistant top plate that dampens noise and remains cooler at high temperatures. Among the temperature controllers available are PolyScience's Performance Programmable, Performance Digital, Advanced Programmable, Advanced Digital, Standard Digital, and MX models.

PolyScience

For info: 800-229-7569 | www.polyscience.com



ELECTROCHEMICAL DETECTOR

The Dionex UltiMate 3000 offers sensitivity and selectivity needed for neurotransmitters, pharmaceuticals, and complex biological samples to UHPLC. The Dionex UltiMate 3000 Electrochemical Detector makes the speed and resolution of ultrahigh performance liquid chromatography (UHPLC) separation available with electrochemical detection. Electrochemical detection offers: the high sensitivity needed to measure neurotransmitters, the robustness to analyze pharmaceutical compounds, and the selectivity to characterize complex samples such as supplements, beverages, and biological samples. Compatible with the current family of Dionex Ultimate 3000 EC-optimized HPLC and UHPLC systems, this detector features coulometric and amperometric sensors that are designed for simple, flexible, and low-maintenance operation. Coulometric sensors are known for their stability and low maintenance. Amperometric sensors are chosen for their very high sensitivity, even with precious, volume-limited samples. Plug-and-play electrochemical sensors with SmartChip intelligence are designed to configure the instrument automatically, optimize parameters, and minimize noise by eliminating cable connections.

Thermo Scientific

For info: 800-532-4752 | www.thermoscientific.com/ECdetection

UNTREATED MICROPLATES

A new range of 12-, 24-, 48-, and 96-well format untreated polystyrene culture microplates are now available for growing cells in stationary suspension or other applications where reduced cell attachment is desired. Untreated polystyrene plates are the lab tool of choice for growing embryoid bodies and other cells where cell attachment needs to be reduced or avoided. Natural, unmodified polystyrene surfaces are hydrophobic and only bind cells and biomolecules through passive hydrophobic interactions. Molded from ultrapure polystyrene in a class 100,000 clean-room production environment, the untreated culture plates are supplied with lids in individual sterile packs. The plates include raised well rims to reduce evaporation, a single position lid to avoid cross contamination, and alphanumeric code marking to enable easy identification of individual wells.

Porvair Sciences

For info: +44-(0)-1372-824290 | www.porvair-sciences.com

MICROPLATE READER

The SpectraMax i3 Multi-Mode Detection Platform is available as a stand-alone reader with the option for users to upgrade to additional applications and detection modes such as cellular imaging with the SpectraMax MiniMax Imaging Cytometer and cartridges for Time-Resolved Fluorescence, Fluorescence Polarization, and AlphaScreen assays. The highly sensitive instrument accommodates the budget and throughput needs of both small and large laboratories alike. The SpectraMax i3 Platform's base system features an integrated optical system enabling top and bottom reads for 6- to 384-well microplates and launches with three broad detection modes: luminescence, absorbance, and fluorescence. Patented user-exchangeable cartridge design expands the system's detection capability making it highly versatile, and able to offer application options far exceeding those of standard readers. The MiniMax Imaging Cytometer module adds first of its kind cellular imaging to a multimode detection platform, enabling fluorescence and brightfield cellular imaging.

Molecular Devices

For info: 800-635-5577 | www.moleculardevices.com/spectramax

MicroRNA INHIBITORS

Mission Synthetic and Lentiviral microRNA (miRNA) Inhibitors are based upon the Tough Decoy (TuD) design for the long-term suppression of any miRNA endogenous to humans or mice. Each miRNA inhibitor is designed using a proprietary algorithm that evaluates all possible sequences for the design predicted to best maintain the TuD structure, providing maximal miRNA recognition and binding. In contrast to current approaches that use single-stranded RNAs, such as sponge decoys and locked nucleic acids, TuD RNAs are double-stranded. This, along with a stem-loop stabilized secondary structure, resists cellular nuclease degradation and facilitates sustained miRNA inhibition for longer than one month. In addition, both strands of a TuD RNA contain an miRNA binding site for more efficient sequestration of target miRNAs at lower, nanomolar concentrations. The TuD RNAs are available in both synthetic and lentiviral formats to support transient miRNA knockdown as well as long-term miRNA suppression without repeated transfections.

Sigma-Aldrich

For info: 800-325-3010 | www.sigma.com/inhibitors

Electronically submit your new product description or product literature information! Go to www.sciencemag.org/products/newproducts.dtl for more information. Newly offered instrumentation, apparatus, and laboratory materials of interest to researchers in all disciplines in academic, industrial, and governmental organizations are featured in this space. Emphasis is given to purpose, chief characteristics, and availability of products and materials. Endorsement by *Science* or AAAS of any products or materials mentioned is not implied. Additional information may be obtained from the manufacturer or supplier.

Discovery Fast Track

Competition



Put your novel concept on the fast track toward new medicines.

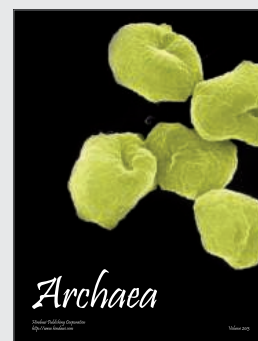
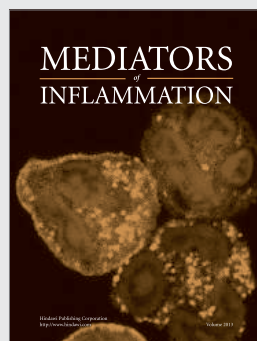
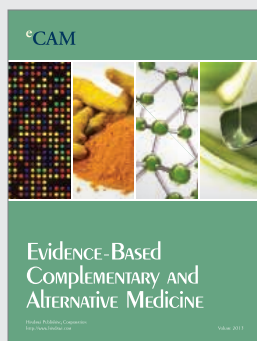
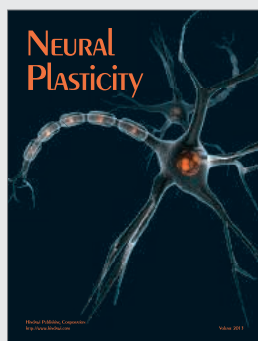
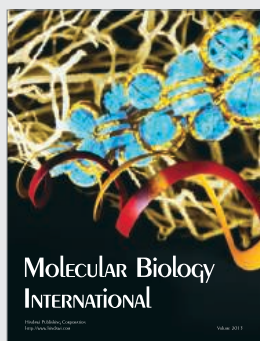
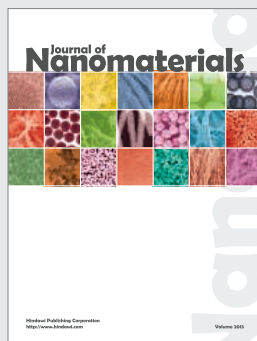
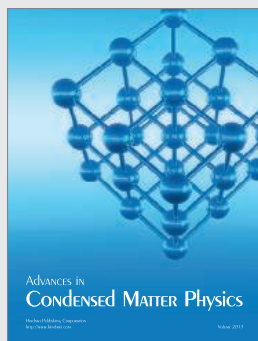
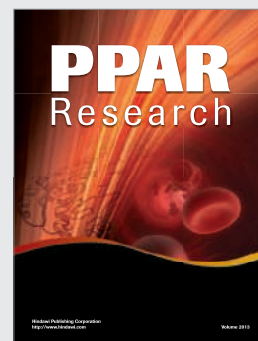
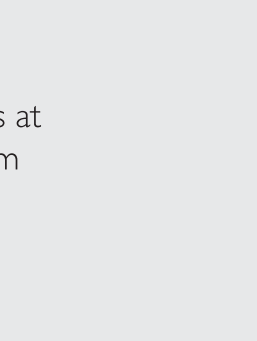
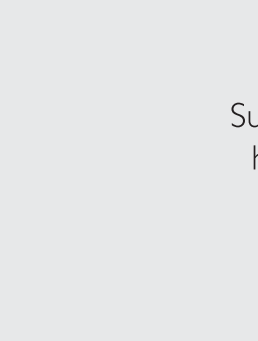
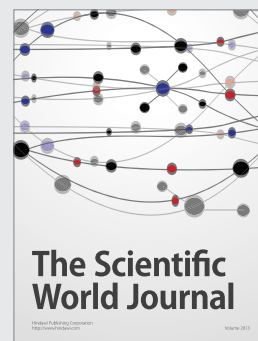
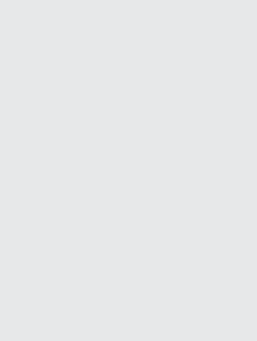
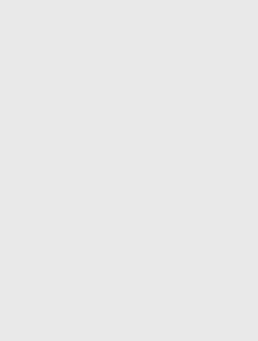
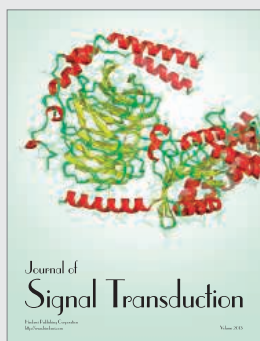
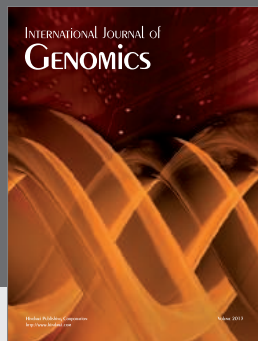
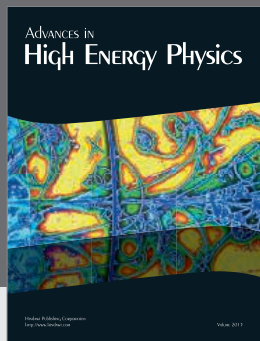
If you're a U.S. or Canadian academic researcher with a novel drug discovery concept, then the Discovery Fast Track competition is for you.

Up to ten winners will have the opportunity to collaborate with the drug discovery experts of GSK, discovering active compounds by taking advantage of our expertise, screening platforms and expansive compound library.

Key results will be shared, providing you with the best possible chemical probes to interrogate your translational biological assays.

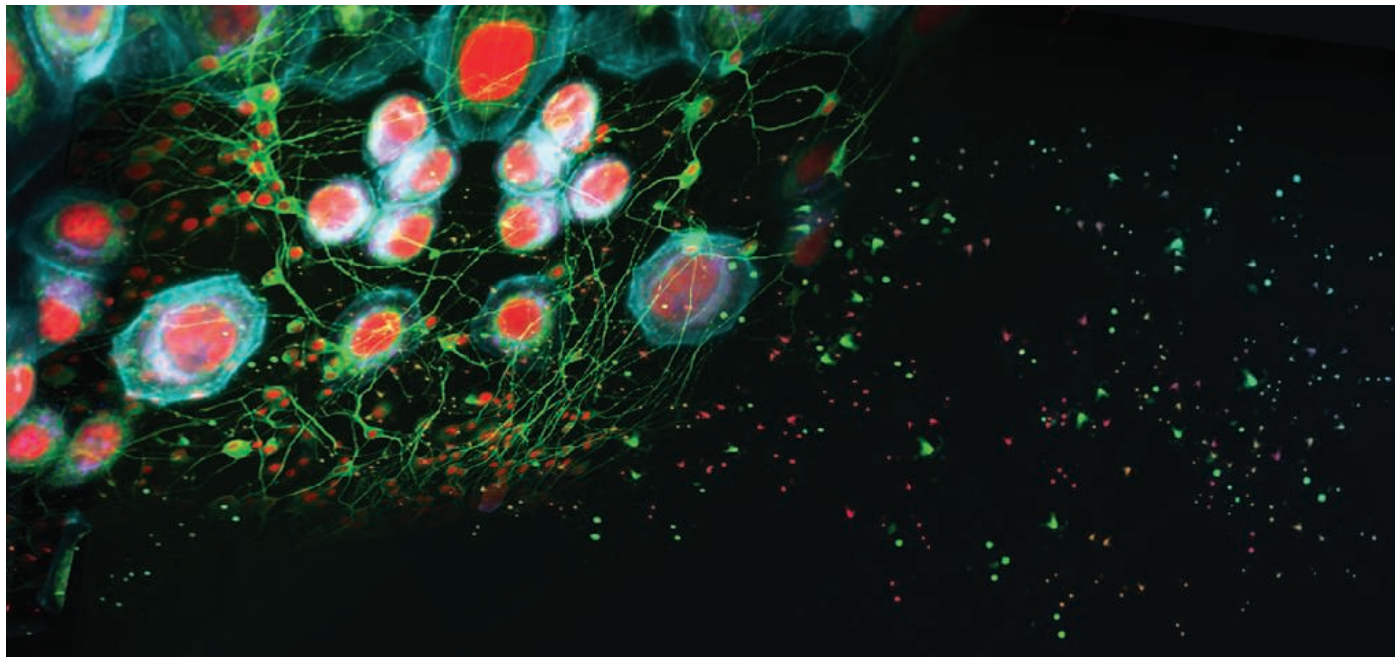
**Applications accepted until
July 19. Enter today at
openinnovation.gsk.com**

**Your idea. Our resources.
It's a winning combination.**



Hindawi

Submit your manuscripts at
<http://www.hindawi.com>



Explore the universe of the cell

Cell imaging and analysis technologies from GE Healthcare Life Sciences

From high-content assays with extensive data analysis, to high- and super-resolution cellular imaging, our cutting-edge technologies give you amazing depth and breadth of investigation, allowing you to analyze interactions as they happen and gain deeper insights into complex cellular mechanisms.

See more. Understand more. Discover more.

www.gelifesciences.com/cellimaging

New
IN Cell Analyzer 2200



IN Cell Analyzer 6000



DeltaVision™



DeltaVision OMX™



imagination at work

Introducing the new BD FACSAria™ Fusion

Integrated cell sorting and biosafety.



The fusion of safety,
performance, and sorting.

The BD FACSAria™ Fusion cell sorter is built on the solid foundation of patented technologies, exceptional multicolor performance and ease-of-use that was first brought to the world of sorting by the launch of the BD FACSAria™ cell sorter in 2003.

Now this sorting know-how is combined with best-in-class biosafety expertise to create the BD FACSAria Fusion, a fully integrated advanced cell sorter and biosafety solution for research laboratories.



Helping all people
live healthy lives

The BD FACSAria Fusion has been verified to meet personnel and product protection standards for a Class II Type A2 biosafety cabinet, the National Sanitation Foundation International Standard 49, the European Standard 12469, and the Australian Standard AS 2252.2–2009.

Choose up to six laser wavelengths and 20 detector positions to measure up to 18 colors simultaneously.

Learn more at bdbiosciences.com/go/fusion.

Class 1 Laser Product.

For Research Use Only. Not for use in diagnostic or therapeutic procedures.

BD, BD Logo and all other trademarks are the property of Becton, Dickinson and Company. © 2013 BD 23-15046-01

BD Biosciences
2350 Qume Drive
San Jose, CA 95131
bdbiosciences.com

Demanding Transfection. Easy Solution.



Focus your efforts on discovery. Efficiently transfect difficult cells, including more than 100 cancer cell lines using **X-tremeGENE DNA Transfection Reagents**.



Free sample and protocols at
www.x-tremegene.roche.com

For life science research only.
Not for use in diagnostic procedures.

X-TREMEGENE is a trademark of Roche.

Roche Diagnostics GmbH
Sandhofer Straße 116
68305 Mannheim, Germany

© 2013 Roche Diagnostics.
All rights reserved.



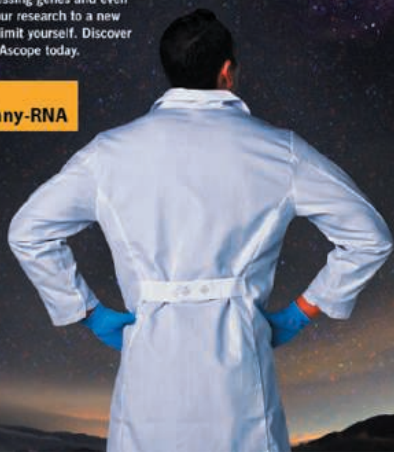


NOW YOU CAN SEE ANY RNA.

Be **amazed** by RNAscope's breakthrough multiplexing technology.

Take your research to the next level with RNAscope. Using this breakthrough technology, now you can target low expressing genes and even non-coding RNA, opening your research to a new world of possibilities. Don't limit yourself. Discover what's so amazing about RNAscope today.

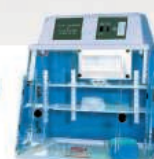
Learn More at
www.acdbio.com/any-RNA



Powder Handling Glove Box used for small-scale handling / weighing of active pharmaceutical ingredients ("API's") in powder form.



Controlled Atmosphere Chambers



PCR (UV) Chambers



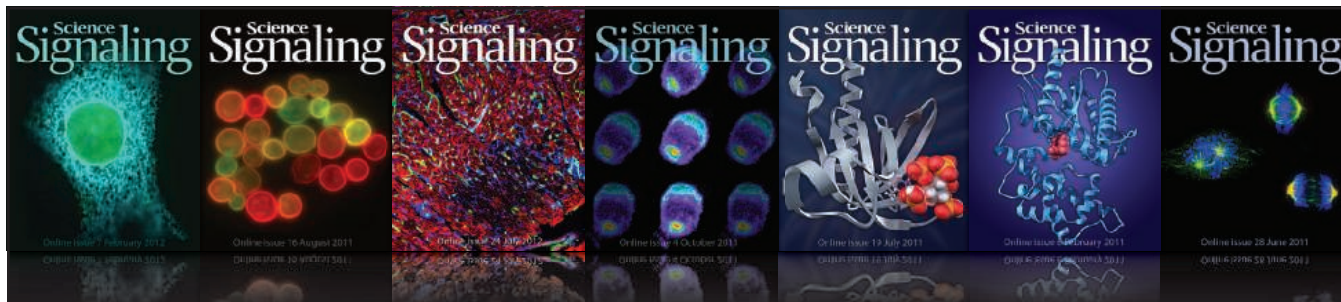
Compact Analytical Balance Chamber

Hypoxia Chambers
Anaerobic Chambers
Temperature & Humidity
Nitrogen Dry Box

PCR (UV) Chambers
HEPA Filtered PCR Chamber

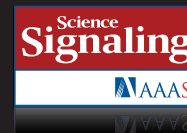
Compact Glove Box
HEPA Filtration
Four (4) Standard Sizes
Custom Sizes Available

PLAS ■ LABS, INC.
www.PLAS-LABS.com
800-866-7527



Science Signaling

The Leading Journal of Cell Signaling



- Peer-reviewed Research Articles and Resources
- Perspectives, Reviews, Protocols, and an interactive Database of Cell Signaling
- Recommend *Science Signaling* to your institution's library
ScienceSignaling.org/recommend

ScienceSignaling.org



INTERNATIONAL SCIENCE & ENGINEERING VISUALIZATION CHALLENGE

Call for Entries

ENTRY DEADLINE:
SEPTEMBER 30, 2013

SCIENCE & ENGINEERING'S
MOST POWERFUL
STATEMENTS ARE NOT
MADE FROM WORDS ALONE



You are invited to submit an entry to this year's International Science & Engineering Visualization Challenge, cosponsored by the National Science Foundation and AAA's journal Science.

Entry categories include: Photography, Illustration, Posters and Graphics, Games & Apps, and Video.

Winning entries will be published in a special section of a February 2014 print issue of Science and ScienceMag.org, and NSF's web site.

ENTRY DEADLINE: SEPTEMBER 30, 2013

For entry forms, rules, and more information, go to:

www.nsf.gov/news/scivis

Award Categories

- Photography
- Illustration
- Posters & Graphics
- Video
- Games & Apps





By your side since 1962

One company, one family of trusted brands. Here to support your research.

As your research needs evolve, we evolve to meet them. We continuously innovate high-quality solutions for every lab and every application, building from technology chosen by scientists for up to 50 years. And we're staffed to support your success, with 3,000 technical sales, service, and support professionals ready to assist you.

Invitrogen™

Applied Biosystems®

Gibco®

Molecular Probes®

Novex®

Ambion®

Ion Torrent™

Find the most cited life science brands at
lifetechnologies.com/trustedbrands

life
technologies™

©2013 Life Technologies Corporation. All rights reserved. The trademarks mentioned herein are the property of Life Technologies Corporation and/or its affiliate(s) or their respective owners. C005619 0613

Elevate your PCR research



Invitrogen™

Applied Biosystems®

PCR essentials:
extraordinarily convenient, high-performing,
and innovative end-to-end workflow solutions

Shop PCR essentials at lifetechnologies.com/elevatepcr

life
technologies™

For research use only. Not for use in diagnostic procedures. ©2013 Life Technologies Corporation. All rights reserved. The trademarks mentioned herein are the property of Life Technologies Corporation and/or its affiliate(s) or their respective owners. C005023 0613

Eppendorf Consumables—
it's Your sample



Future included

50 years of experience in highest quality

Eppendorf consumables are the result of 50 years constant improvement and development. With the new Eppendorf Tubes® 5.0 mL a new tube format in the medium volume range will complete the legendary Eppendorf Tubes family.

Laboratory processes will become easier and more convenient.

Purest assay results are no coincidence:

- > Unique features to make every day routines faster and easier
- > Minimized risk of chemical leaching from consumables
- > Purity grades tailored to even the highest requirements

www.eppendorf.com/consumables

Eppendorf®, the Eppendorf logo and Eppendorf Tubes® are registered Trademarks of Eppendorf AG, Germany. All rights reserved, including graphics and images. Copyright © 2013 by Eppendorf AG.

HEATED CIRCULATING BATHS

Available in 23 different models, a new line of heated circulating water baths can achieve temperatures as high as 200°C with temperature stabilities as exacting as $\pm 0.005^{\circ}\text{C}$. These elegantly designed circulators come in reservoir sizes ranging from 7 L to 28 L and are available with six different temperature controllers, including two programmable models. The heated circulators incorporate many ergonomic features that make life in the lab more productive and efficient. Among the many design innovations featured on these baths are a swiveling control head that permits viewing of the temperature display anywhere within a 180° viewing radius, an integral lid docking system for no-mess reservoir cover storage, and a corrosion- and chemical-resistant top plate that dampens noise and remains cooler at high temperatures. Among the temperature controllers available are PolyScience's Performance Programmable, Performance Digital, Advanced Programmable, Advanced Digital, Standard Digital, and MX models.

PolyScience

For info: 800-229-7569 | www.polyscience.com



ELECTROCHEMICAL DETECTOR

The Dionex UltiMate 3000 offers sensitivity and selectivity needed for neurotransmitters, pharmaceuticals, and complex biological samples to UHPLC. The Dionex UltiMate 3000 Electrochemical Detector makes the speed and resolution of ultrahigh performance liquid chromatography (UHPLC) separation available with electrochemical detection. Electrochemical detection offers: the high sensitivity needed to measure neurotransmitters, the robustness to analyze pharmaceutical compounds, and the selectivity to characterize complex samples such as supplements, beverages, and biological samples. Compatible with the current family of Dionex Ultimate 3000 EC-optimized HPLC and UHPLC systems, this detector features coulometric and amperometric sensors that are designed for simple, flexible, and low-maintenance operation. Coulometric sensors are known for their stability and low maintenance. Amperometric sensors are chosen for their very high sensitivity, even with precious, volume-limited samples. Plug-and-play electrochemical sensors with SmartChip intelligence are designed to configure the instrument automatically, optimize parameters, and minimize noise by eliminating cable connections.

Thermo Scientific

For info: 800-532-4752 | www.thermoscientific.com/ECdetection

UNTREATED MICROPLATES

A new range of 12-, 24-, 48-, and 96-well format untreated polystyrene culture microplates are now available for growing cells in stationary suspension or other applications where reduced cell attachment is desired. Untreated polystyrene plates are the lab tool of choice for growing embryoid bodies and other cells where cell attachment needs to be reduced or avoided. Natural, unmodified polystyrene surfaces are hydrophobic and only bind cells and biomolecules through passive hydrophobic interactions. Molded from ultrapure polystyrene in a class 100,000 clean-room production environment, the untreated culture plates are supplied with lids in individual sterile packs. The plates include raised well rims to reduce evaporation, a single position lid to avoid cross contamination, and alphanumeric code marking to enable easy identification of individual wells.

Porvair Sciences

For info: +44-(0)-1372-824290 | www.porvair-sciences.com

MICROPLATE READER

The SpectraMax i3 Multi-Mode Detection Platform is available as a stand-alone reader with the option for users to upgrade to additional applications and detection modes such as cellular imaging with the SpectraMax MiniMax Imaging Cytometer and cartridges for Time-Resolved Fluorescence, Fluorescence Polarization, and AlphaScreen assays. The highly sensitive instrument accommodates the budget and throughput needs of both small and large laboratories alike. The SpectraMax i3 Platform's base system features an integrated optical system enabling top and bottom reads for 6- to 384-well microplates and launches with three broad detection modes: luminescence, absorbance, and fluorescence. Patented user-exchangeable cartridge design expands the system's detection capability making it highly versatile, and able to offer application options far exceeding those of standard readers. The MiniMax Imaging Cytometer module adds first of its kind cellular imaging to a multimode detection platform, enabling fluorescence and brightfield cellular imaging.

Molecular Devices

For info: 800-635-5577 | www.moleculardevices.com/spectramax

MicroRNA INHIBITORS

Mission Synthetic and Lentiviral microRNA (miRNA) Inhibitors are based upon the Tough Decoy (TuD) design for the long-term suppression of any miRNA endogenous to humans or mice. Each miRNA inhibitor is designed using a proprietary algorithm that evaluates all possible sequences for the design predicted to best maintain the TuD structure, providing maximal miRNA recognition and binding. In contrast to current approaches that use single-stranded RNAs, such as sponge decoys and locked nucleic acids, TuD RNAs are double-stranded. This, along with a stem-loop stabilized secondary structure, resists cellular nuclease degradation and facilitates sustained miRNA inhibition for longer than one month. In addition, both strands of a TuD RNA contain an miRNA binding site for more efficient sequestration of target miRNAs at lower, nanomolar concentrations. The TuD RNAs are available in both synthetic and lentiviral formats to support transient miRNA knockdown as well as long-term miRNA suppression without repeated transfections.

Sigma-Aldrich

For info: 800-325-3010 | www.sigma.com/inhibitors

Electronically submit your new product description or product literature information! Go to www.sciencemag.org/products/newproducts.dtl for more information. Newly offered instrumentation, apparatus, and laboratory materials of interest to researchers in all disciplines in academic, industrial, and governmental organizations are featured in this space. Emphasis is given to purpose, chief characteristics, and availability of products and materials. Endorsement by *Science* or AAAS of any products or materials mentioned is not implied. Additional information may be obtained from the manufacturer or supplier.

WEBINAR

Harnessing Stem Cells for Predictive Toxicology

Meeting the Challenges of Drug Discovery Today

Wednesday, July 17, 2013

12 noon Eastern, 9 a.m. Pacific, 5 p.m. UK, 6 p.m. Central Europe

The core techniques used in toxicology studies have remained largely unchanged for over 40 years. It is acknowledged in the pharmaceutical industry that more predictive, earlier tests need to be established in order to prevent unsafe drugs progressing into the clinic and to stop potentially effective therapeutics being excluded from development. This recognition is driving the development of more relevant, specific, and reliable toxicology models and tests to improve drug safety and reduce the cost of development. In particular, the use of stem-cell-derived models can provide an opportunity to develop a transformative, integrated drug toxicity surveillance system.

IN THIS WEBINAR VIEWERS WILL:

- Gain insight into stem cell differentiation and control of cell fate using hepatocytes as a model, and how stem-cell-derived assays help improve drug toxicity prediction accuracy
- Hear how stem-cell-derived cardiomyocytes could overcome the shortcomings of existing cardiac animal models by providing more predictive assays
- Learn how a human stem-cell-derived cell model, together with high-content analysis, provides deeper insights into drug mechanism of action
- Have their questions answered live by our respected thought leaders!

REGISTER NOW!
webinar.sciencemag.org

Speakers

Hirdesh Uppal, Ph.D., DVM
Genentech
San Francisco, CA



Liz Roquemoire, Ph.D.
GE Healthcare
Cardiff, UK



Webinar sponsored by



Brought to you by the
Science/AAAS Custom
Publishing Office



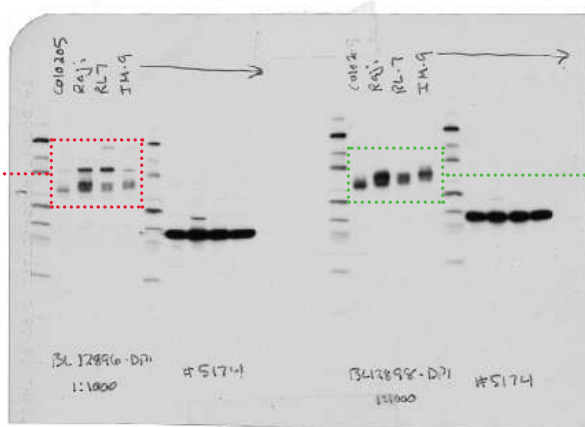
You've carefully
designed your
experiment.

Taylor Ngo started at CST 8
years ago and is currently in
the Molecular Biology group.

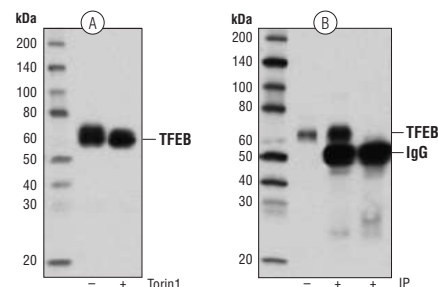
Does your antibody measure up?

We validate all our antibodies in-house. If it's not specific, it doesn't ship.

REJECTED
Extra Band
Weak Signal



**CST
APPROVED**
Clean Band
Strong Signal



TFEB Antibody #4240: (A) WB analysis of Raji cell extracts, untreated (-) or Torin1-treated, using #4240 (Torin1 treatment induces dephosphorylation). (B) IP of TFEB from COLO 205 cells using #4240 (lane 2) or Normal Rabbit IgG #2729 (lane 3). Lane 1 is 10% input.

WB analysis of various cell extracts using two development samples at 1:1000 dilution. GAPDH (D16H11) XP® Rabbit mAb #5174 was used as a loading control.

Please visit our website to request a copy of our new white paper – *A Guide to Successful Western Blotting*.

www.cellsignal.com/successfulWB

© 2013 Cell Signaling Technology, Inc. Cell Signaling Technology® and XP® are trademarks of Cell Signaling Technology, Inc.



Cell Signaling
TECHNOLOGY®

There's only one
Science

Science Careers Advertising

For full advertising details, go to ScienceCareers.org and click For Employers, or call one of our representatives.

Tracy Holmes
Worldwide Associate Director
Science Careers
Phone: +44 (0) 1223 326525

THE AMERICAS
E-mail: advertise@sciencecareers.org
Fax: 202-289-6742

Tina Burks
East Coast/West Coast/South America
Phone: 202-326-6577

Marci Gallan
Midwest/Canada
Phone: 202-326-6582

Candice Nulsen
Corporate
Phone: 202-256-1528

Online Job Posting Questions
Phone: 202-312-6375

**EUROPE/INDIA/AUSTRALIA/
NEW ZEALAND/REST OF WORLD**
E-mail: ads@science-int.co.uk
Fax: +44 (0) 1223 326532

Axel Gesatzki
Phone: +44 (0)1223 326529

Kelly Grace
Phone: +44 (0) 1223 326528

JAPAN
Yuri Kobayashi
Phone: +81-(0)90-9110-1719
E-mail: ykobayas@aaas.org

**CHINA/KOREA/SINGAPORE/
TAIWAN/THAILAND**
Ruolei Wu
Phone: +86-1367-1015-294
E-mail: rwu@aaas.org

All ads submitted for publication must comply with applicable U.S. and non-U.S. laws. Science reserves the right to refuse any advertisement at its sole discretion for any reason, including without limitation for offensive language or inappropriate content, and all advertising is subject to publisher approval. Science encourages our readers to alert us to any ads that they feel may be discriminatory or offensive.

Science Careers
From the journal *Science* AAAS

ScienceCareers.org

POSITIONS OPEN

UC San Diego
Local Impact, National Influence, Global Reach

ASSOCIATE DIRECTOR

University of California San Diego (UCSD) Clinical Translational Research Institute ([website: http://ctri.ucsd.edu/Pages/default.aspx](http://ctri.ucsd.edu/Pages/default.aspx)). The candidate should have a strong administrative, funding, and research record as well as an M.D., Ph.D., or PharmD for this **ASSOCIATE** or **FULL PROFESSOR** position. Please submit a cover letter, curriculum vitae, and summary of professional interests to: **Dr. Michael Ziegler, UCSD San Diego, CA 92103-8341**, or to e-mail: mziegler@ucsd.edu.

UCSD is an Equal Opportunity/Affirmative Action Employer.

**NEURO-ONCOLOGY RESEARCH
FACULTY POSITION**

The Dardinger Neuro-Oncology Center at the Ohio State University Wexner Medical Center is seeking applicants for a faculty position at the rank of Associate or Full professor. The successful candidate will be a funded investigator with research focus on topics that will synergize with existing research in the department with a focus on topics that could include: tumor, migration/invasion, bioinformatics, developmental neurobiology, tumor stem cells, neuroimmunology, infection, inflammation or ischemia. The successful candidate will join a well-established Neuro-Oncology Program that is very active in developmental therapeutics and clinical trials. This position requires a Ph.D. and/or M.D. with relevant experience. Preference will be given to candidates with a track record of publications and successful extramural funding. The chosen candidate will be asked to set up an independent neuro-oncology laboratory within the Dardinger Neuro-Oncology Center. Attractive startup packages commensurate with experience.

Applicants should submit curriculum vitae, statement of research plans, and arrange to have three letters of reference sent to: **Russell R. Lonser, M.D., Professor and Chair, Department of Neurological Surgery, the Ohio State University Wexner Medical Center, N1047 Doan Hall, 410 W. 10th Avenue, Columbus, Ohio 43210.**

You may submit electronically to e-mail: melinda.freed@osumc.edu.

The Ohio State University is an Equal Opportunity/Affirmative Action Employer. Women and minorities are strongly encouraged to apply.

We deliver customized job alerts and more...

Science Careers
From the journal *Science* AAAS

www.ScienceCareers.org

POSITIONS OPEN

ASSISTANT/ASSOCIATE PROFESSOR of Immunology and Infectious Diseases
Harvard School of Public Health
Department of Immunology and Infectious Diseases

The Department of Immunology and Infectious Diseases at the Harvard School of Public Health seeks outstanding candidates for the position of assistant or associate professor of immunology and infectious diseases. This is a tenure-ladder position, with academic rank to be determined in accordance with the successful candidate's experience and productivity.

Applicants must have a Ph.D., M.D., DVM, or equivalent degree. The successful candidate will build and maintain an internationally recognized extramurally funded research program focused on AIDS, with research emphasis on innovative strategies for prevention and control of HIV infection. Evidence of published research excellence in HIV/AIDS is required. Evidence of commitment to collaboration with colleagues in developing countries and in other areas of public health is highly desirable. The candidate should possess the scholarly qualities required to mentor doctoral students in the graduate program in the Division of Biological Sciences.

Please apply at **website: <https://academicpositions.harvard.edu>**.

For questions, please contact **Stephen Heim, Department of Immunology and Infectious Diseases, e-mail: sheim@hsph.harvard.edu**.

Harvard University is committed to increasing representation of women and minority members among its faculty and particularly encourages applications from such candidates.

ASSISTANT/ASSOCIATE PROFESSOR of Immunology and Infectious Diseases
Harvard School of Public Health
Department of Immunology and Infectious Diseases

The Department of Immunology and Infectious Diseases at the Harvard School of Public Health seeks outstanding candidates for the position of assistant or associate professor of immunology and infectious diseases. This is a tenure-ladder position, with academic rank to be determined in accordance with the successful candidate's experience and productivity.

Applicants must have a Ph.D., M.D., DVM, or equivalent degree with extensive training and experience in microbiology and/or immunology. The successful candidate will build and maintain an internationally recognized extramurally funded research program, with a special emphasis on mycobacteria and tuberculosis. We particularly seek individuals whose expertise complements existing programs in the department. The candidate should possess the ability to work collaboratively with other scientists and the scholarly qualities required to mentor doctoral students in the graduate program in the Division of Biological Sciences.

Please apply at **website: <https://academicpositions.harvard.edu>**.

For questions, please contact **Stephen Heim, Department of Immunology and Infectious Diseases, e-mail: sheim@hsph.harvard.edu**.

Harvard University is committed to increasing representation of women and minority members among its faculty and particularly encourages applications from such candidates.

Find your future here.

↓

Science Careers
From the journal *Science* AAAS

www.ScienceCareers.org



The University of Konstanz, with its »Institutional Strategy to promote Top-Level Research«, has been receiving continuous funding since 2007 within the framework of the Excellence Initiative by the German Federal and State Governments.

The *Zukunftskolleg* of the University of Konstanz is offering:

up to six ZIF Marie Curie 5-year Research Fellowships
and

up to four Zukunftskolleg 5-year Research Fellowships

in any discipline represented at the University of Konstanz for the development and implementation of individual research projects (Salary Scale 14 TV-L).

Fellowships will begin on June 1, 2014, and end on May 31, 2019.

Reference number 2013/102

Applications, supporting materials, and two letters of reference should be submitted in English by **September 30, 2013** using the **Online Application Platform**: www.zukunftskolleg.uni-konstanz.de/online-application



Details concerning the application, required documents, and information about the Zukunftskolleg are available on our website: <http://www.zukunftskolleg.uni-konstanz.de>

Contact: Dr. Nani Clow,
e-mail: n.clow@uni.kn

Assistant Professor (Tenure Track) of Social Network Analysis

The Department of Humanities, Social and Political Sciences at ETH Zurich (www.gess.ethz.ch) invites applications for a tenure track assistant professorship in Social Network Analysis. The position is part of the interdisciplinary Behavioral Studies Section and open to applications from all scientific disciplines.

The candidate should have an internationally recognized track record in Social Network Analysis and be able to build and sustain a strong research program. Furthermore, he or she should document an ability to teach effectively and be clearly committed to doing research in an interdisciplinary environment. The new professor will be expected to teach undergraduate level courses (in German or English) and graduate level courses (in English) within the scope of the required electives in the humanities and social sciences. ETH Zurich offers an environment that expects and supports high quality teaching and research.

Assistant professorships have been established to promote the careers of younger scientists. The initial appointment is for four years with the possibility of renewal for an additional two-year period and promotion to a permanent position.

Please apply online at www.facultyaffairs.ethz.ch

Applications should include a curriculum vitae, a list of publications and a statement of future research and teaching interests. The letter of application should be addressed to the **President of ETH Zurich, Prof. Dr. Ralph Eichler**. The closing date for applications is **30 September 2013**. ETH Zurich is an equal opportunity and family friendly employer and is further responsive to the needs of dual career couples. In order to increase the number of women in leading academic positions, we specifically encourage women to apply.

Keck School of Medicine of USC

Emerging Pathogens TENURE-TRACK FACULTY POSITIONS

Department of Molecular Microbiology and Immunology
USC Institute of Emerging Pathogens and Immune Diseases
Keck School of Medicine
University of Southern California
Los Angeles, California

The Department of Molecular Microbiology and Immunology at the Keck School of Medicine of the University of Southern California in Los Angeles, California, has an ongoing expansion to build upon existing strengths in Microbiology, Virology, and Immunology.

The Department invites applicants for tenure-track **Assistant and/or Associate Professor** positions with a specific research emphasis on emerging pathogens and immune responses. We are especially interested in candidates whose research addresses biodefense pathogenesis-related, trans-disciplinary, and translational research topics. Creative scientists with a record of achievement and commitment to excellence in both research and teaching are encouraged to apply. Successful candidates will receive generous start-up packages and laboratory space along with access to a new Biosafety Laboratory 3 facility. The Keck School of Medicine has strong research programs in Cancer, Genomics, Immunology, Stem Cells, Neurobiology, and Virology.

Applicants should submit a letter of application, curriculum vitae, a statement of current and future research plans, and three letters of recommendation. Please complete faculty application through the USC job website at <https://jobs.usc.edu/applicants/Central?quickFind=70592> (Job Code 019806).

USC values diversity and is committed to equal opportunity in employment. Women and men, and members of all racial and ethnic groups are encouraged to apply.

It's not because we all wear white coats that we all do the same job



INRA IS RECRUITING 51 SCIENTISTS

First agricultural institute in Europe and second in the world, the French National Institute for Agricultural is recruiting experienced scientists through open competitions on the basis of a research project:

- 6 Experienced Research Scientists (4 year's experience in research)
- 45 Research Directors (8 year's experience in research)



Applications from
28 June to 2nd September 2013
on <http://jobs.inra.fr/en>



There's only one

DR. SHIRLEY MALCOM



To Dr. Shirley Malcom, born and raised in the segregated South more than 65 years ago, a career based on her studies in science seemed even less likely than the launch of the Soviet's Sputnik. But with Sputnik's success, the Space Race officially started and, in an instant, brought a laser-like focus to science education and ways to deliver a proper response. Not long after, Dr. Malcom entered the picture.

Although black schools at the time received fewer dollars per student and did not have sufficient resources to maintain their labs at a level equivalent to the white schools, Dr. Malcom found her way to the University of Washington where she succeeded in obtaining a B.S. in spite of the difficulties of being an African American woman in the field of science. From there she went on to earn a Ph.D. in ecology from Penn State and held a faculty position at the University of North Carolina, Wilmington.

Dr. Malcom has served at the AAAS in multiple capacities, and is presently Head of the Directorate for Education and Human Resources Programs. Nominated by President Clinton to the National Science Board, she also held a position on his Committee of Advisors on Science and Technology. She is currently a member of the Caltech Board of Trustees, a Regent of Morgan State University, and co-chair of the Gender Advisory Board of the UN Commission on Science and Technology for Development. She has held numerous other positions of distinction and is the principal author of *The Double Bind: The Price of Being a Minority Woman in Science*.

Of her active career in science, Dr. Malcom says, "I guess I have become a poster child for taking one's science background and using that in many other ways: we ask questions; we try to understand what we find; we consider what evidence we would need to confirm or refute hypotheses. And that happens in whatever setting one finds oneself."

At *Science* we are here to help you in your own scientific career with expert career advice, forums, job postings, and more — all for free. Visit *Science* today at ScienceCareers.org.

**AAAS**

For your career in science, there's only one **Science**

ScienceCareers.org



The research group Electron Paramagnetic Resonance (EPR) spectroscopy at the Max Planck Institute for Biophysical Chemistry is offering two

Postdoctoral Positions (Code Number 22-13)

in the field of biomolecular EPR spectroscopy and dynamic nuclear polarization, respectively. The work includes collaborative research within the research groups at our institute and at the international level. The successful candidates should have a PhD degree in Physics or Chemistry. Experience with magnetic resonance techniques or spectroscopy is required. The laboratory is equipped with state-of-the-art EPR spectrometers at frequencies from 9 up to 263 GHz, as well as capabilities for double resonance techniques (ENDOR, PELDOR and DNP) and optical excitation. For additional information please refer to: www.mpibpc.mpg.de/english/research/ags/bennati

The positions will be available from September 1st, 2013. Payment will be according either to the MPI postdoctoral fellowships or to the German TVöD standard.

The Max Planck Society is trying to increase the percentage of women on its scientific staff and strongly encourages applications from qualified women.

Please send your application with reference to the code number 22-13 preferably via e-mail to:

office.bennati@mpibpc.mpg.de

Max Planck Institute
for Biophysical Chemistry
Research Group
"Electron Paramagnetic Resonance"
Prof. Dr. Marina Bennati
Am Fassberg 11, 37077 Göttingen
Germany



The Cluster of Excellence 'Engineering of Advanced Materials – Hierarchical Structure Formation of Functional Devices' (EAM, www.eam.fau.de), funded by the German Research Foundation (DFG), at Friedrich-Alexander-Universität Erlangen-Nürnberg (FAU), Germany, invites applications for a permanent

W2 Professorship in Particle Synthesis

The candidate should have excellent research qualifications in the area of bottom-up particle formation from gases or liquids, nanocrystal engineering, template-based synthesis (e.g. from emulsions), or materials chemistry. The candidate should exhibit strong expertise in particle characterization, particle functionalization and/or product engineering of particles for functional applications. Applicants are expected to have experience in interdisciplinary research and the necessary skills to develop an internationally recognized fundamental research program in close collaboration with other research areas of the Cluster of Excellence. She or he is further expected to play an active role in the 'Center for Functional Particle Systems' at FAU.

The position also includes teaching duties in the curricula of the Department of Chemical and Biological Engineering. The successful candidate will moreover be expected to take on administrative duties and to raise external funding.

Required qualifications include university graduate and doctoral degrees, excellent teaching skills, and a *Habilitation* or equivalent qualification, which may also have been acquired in a non-university context or through a post as a 'Junior Professor'.

The University of Erlangen-Nürnberg pursues a policy of intense student mentoring and therefore expects its teaching staff to be present during lecture periods.

FAU is an equal opportunities employer.

Application documents (curriculum vitae, list of publications and teaching activities, copies of degree certificates but no publications) and a brief summary of research interests should be submitted via e-mail to administration@eam.uni-erlangen.de by **July 18, 2013**.

Cluster of Excellence Engineering of Advanced Materials
Prof. Dr. Wolfgang Peukert, Nögelsbachstraße 49b, 91052 Erlangen, Germany



www.fau.de



Faculty Positions in Genetics, Immunology, Infectious and Inflammatory Diseases

The Department of Molecular Genetics and Microbiology at the University of New Mexico School of Medicine (<http://mgm.unm.edu/index.html>) is seeking two new tenure-track faculty members. Areas of interest are aligned with Institutional Signature Programs including: the Center for Infectious Disease and Immunity (CIDI), the Clinical and Translational Science Center (CTSC), the Brain and Behavioral Health Institute (BBHI), the Cancer Center (CC), and additional initiatives including stem cell research and others described on the MGM website <http://mgm.unm.edu/index.html>.

Appointment is open rank, depending on qualifications and evidence of established research programs. The successful applicant will participate in departmental activities including medical school teaching. Salary and rank commensurate with qualifications and experience.

Minimum Requirements:

- Ph.D., M.D. or equivalent
- Eligible to work in the United States

Desirable Qualifications:

- strong record of scientific accomplishments
- current grant funding with Principal Investigator status
- high probability of obtaining and maintaining external funding
- potential for research and educational interactions with members of the Department of Molecular Genetics and Microbiology
- Synergy with UNM Health Sciences Center signature programs

For best consideration apply by **July 31, 2013**. The position will remain open until filled. For complete details of this position or to apply, please visit this website: <https://unmjobs.unm.edu>. Please reference posting Number: **#0820701**. For additional information you may contact: **Sally Ann Garcia, Search Coordinator, (505) 272-9374, SanGarcia@salud.unm.edu**.

The University of New Mexico's confidentiality policy (Disclosure of Information about Candidates for Employment, UNM Board of Regents' Policy Manual 6.7), which includes information about public disclosure of documents submitted by applicants, is located at <http://www.unm.edu/~brpm/r67.htm>

UNM is an Equal Opportunity/Affirmative Action Employer and Educator.



COLUMBIA UNIVERSITY
MEDICAL CENTER

College of Physicians and Surgeons

Department of Neurology

Assistant Professor in Neurology

The Department of Neurology, Columbia University seeks two full-time neurohospitalists at the level of Assistant Professor. Together with a neurohospitalist already in place, they provide around-the-clock, year-round inpatient and emergency department acute stroke and other consultations at the Allen Hospital. The Allen Hospital is one of five major centers that form the NewYork-Presbyterian Hospital, the nation's largest not-for-profit, nonsectarian hospital, with 2,409 beds. NewYork-Presbyterian/Allen Hospital is located on the northern tip of Manhattan, at Broadway and 220th Street. It is a community hospital and serves northern Manhattan, Riverdale, and other communities in the Bronx.

Faculty appointment is in the Department of Neurology, College of Physicians and Surgeons, the medical school of Columbia University. Applicants must have board certification or eligibility in neurology, with neurohospitalist fellowship training preferred.

Send CV and letter of interest to

Dr. Laura Lennihan, ll18@columbia.edu

Or you may apply directly at:

<https://academicjobs.columbia.edu/applicants/Central?quickFind=57380>

Columbia University is an affirmative action/equal opportunity employer.



AAAS is here – helping scientists achieve career success.

Every month, over 400,000 students and scientists visit ScienceCareers.org in search of the information, advice, and opportunities they need to take the next step in their careers.

A complete career resource, free to the public, *Science* Careers offers a suite of tools and services developed specifically for scientists. With hundreds of career development articles, webinars and downloadable booklets filled with practical advice, a community forum providing answers to career questions, and thousands of job listings in academia, government, and industry, *Science* Careers has helped countless individuals prepare themselves for successful careers.

As a AAAS member, your dues help AAAS make this service freely available to the scientific community. If you're not a member, join us. Together we can make a difference.

To learn more, visit aaas.org/plusyou/sciencecareers





AAAS is here – promoting universal science literacy.

In 1985, AAAS founded Project 2061 with the goal of helping all Americans become literate in science, mathematics, and technology. With its landmark publications *Science for All Americans* and *Benchmarks for Science Literacy*, Project 2061 set out recommendations for what all students should know and be able to do in science, mathematics, and technology by the time they graduate from high school. Today, many of the state standards in the United States have drawn their content from Project 2061.

Every day Project 2061 staff use their expertise as teachers, researchers, and scientists to evaluate textbooks and assessments, create conceptual strand maps for educators, produce groundbreaking research and innovative books, CD-ROMs, and professional development workshops for educators, all in the service of achieving our goal of universal science literacy.

As a AAAS member, your dues help support Project 2061 as it works to improve science education. If you are not yet a AAAS member, join us. Together we can make a difference.

To learn more, visit aaas.org/plusyou/project2061



Women in Science Booklet

Science and the L'Oréal Foundation present



Read inspiring profiles of women
making a difference in biology.

Free download at
ScienceCareers.org/LorealWIS